Fossil riches at risk in Utah monument *p. 218*

Guarding the skin *p. 227*

Agriculture reduces bee diversity *p. 282*

Science

$15
18 JANUARY 2019
sciencemag.org

AAAS

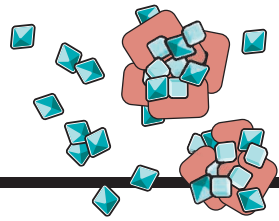


NANOSCALE IMAGING

A close-up view inside the fly brain *p. 245*

CONTENTS

18 JANUARY 2019 • VOLUME 363 • ISSUE 6424



221
Deadly pileups of proteins



218

NEWS

IN BRIEF

208 News at a glance

IN DEPTH

211 SHAKE-UP THREATENS NOVEL U.S. ECOLOGY FACILITY
NEON science head quits, advisers fired after Battelle replaces two top managers *By J. Mervis*

212 DID NEURONS ARISE FROM AN EARLY SECRETORY CELL?
Cell lineage studies of comb jellies and other creatures may suggest a single ancient origin of the nervous system
By E. Pennisi

213 IN CONGO, FIGHTING A VIRUS AND A GROUNDSWELL OF FAKE NEWS
Armed conflict and political tensions stoke rumors and misinformation about Ebola *By L. Spinney*
▸ PODCAST

214 DUELING SPACECRAFT LOOK DEEP INTO SATURN AND JUPITER
NASA probes reveal surprising contrasts between two gas giants *By P. Voosen*
▸ RESARCH ARTICLE BY L. IESS *ET AL.* 10.1126/science.aat2965; PODCAST

216 PAIN SPREADS FROM SHUTDOWN
Historic spending impasse halts paychecks and projects *By D. Malakoff*

217 FLOTILLA LAUNCHES LARGE SURVEY OF ANTARCTIC KRILL
Health of stock is critical to fishery—and to predators *By E. Stockstad*

FEATURES

218 THE BONES OF BEARS EARS
Paleontologists struggle to protect sites that could rewrite Earth's history
By A. Reese

221 THE BRAIN'S TRAFFIC PROBLEMS
Disrupted flow into and out of the nucleus may kill neurons *By E. Dolgin*

INSIGHTS

PERSPECTIVES

224 WHEN EARTH GOT PUMMELED
The frequency of impacts on Earth's surface increased about 290 million years ago *By C. Koeberl*
▸ REPORT P. 253

225 IRON HITS THE MARK
Strongly electron-donating ligands enable nanosecond lifetimes of iron(III) photoexcited states
By E. R. Young and A. Oldacre
▸ REPORT P. 249

227 MICROBIAL GUARDIANS OF SKIN HEALTH
Skin microbes can promote skin immunity, repair, and antimicrobial defense *By A. Stacy and Y. Belkaid*

229 THE CEREBELLUM GETS SOCIAL
The cerebellum can regulate behavior by controlling dopamine release
By E. D'Angelo
▸ RESEARCH ARTICLE P. 248

230 ADAPTATIONS OF AN ANCIENT MODULAR MACHINE
Mechanism of energy conversion is conserved in the complex I superfamily
By U. Brandt
▸ REPORT P. 257

231 GENE THERAPY FOR PATHOLOGIC GENE EXPRESSION
Haploinsufficiency in disease can be overcome by boosting gene expression with CRISPR
By L. E. Montefiori and M. A. Nobrega
▸ RESEARCH ARTICLE P. 246

232 B CELLS, CMV, AND STEM CELL TRANSPLANT
Host antibodies help prevent CMV dissemination after bone marrow transplantation *By M.-L. Alegre*
▸ REPORT P. 288

POLICY FORUM

234 OVERSIGHT OF DIRECT-TO-CONSUMER NEUROTECHNOLOGIES
Efficacy of products is far from clear
By A. Wexler and P. B. Reiner

BOOKS *ET AL.*

236 THE REVEALING HISTORY OF A REVERED WATERWAY
Human and environmental stories interweave in a meandering meditation on the Ganges River *By A. Rademacher*

GRAPHIC: V. ALTOUNIAN/*SCIENCE*; PHOTO: CAVAN SOCIAL/ALAMY STOCK PHOTO

Downloaded from http://science.sciencemag.org/ on January 21, 2019

Published by AAAS

237 NUCLEAR POWER AND PROMISE
Deference to industry trumps safety in the U.S., warns a controversial former regulator
By J. D. Hamblin

LETTERS

239 THE VALUE OF SMALL MANGROVE PATCHES
By D. J. Curnick et al.

240 BRAZIL'S ENDANGERED POSTGRADUATE SYSTEM
By H. Martelli Júnior et al.

240 AIRBORNE IN THE ERA OF CLIMATE CHANGE
By K. Jean and C. Wymant

RESEARCH

IN BRIEF

241 From *Science* and other journals

REVIEW

244 ORGANIC CHEMISTRY
The importance of synthetic chemistry in the pharmaceutical industry *K. R. Campos* et al.
REVIEW SUMMARY; FOR FULL TEXT:
dx.doi.org/10.1126/science.aat0805

RESEARCH ARTICLES

245 IMAGING TECHNIQUES
Cortical column and whole-brain imaging with molecular contrast and nanoscale resolution *R. Gao* et al.
RESEARCH ARTICLE SUMMARY; FOR FULL TEXT:
dx.doi.org/10.1126/science.aau8302

246 GENE THERAPY
CRISPR-mediated activation of a promoter or enhancer rescues obesity caused by haploinsufficiency *N. Matharu* et al.
RESEARCH ARTICLE SUMMARY; FOR FULL TEXT:
dx.doi.org/10.1126/science.aau0629
▸ PERSPECTIVE P. 231

247 ASYMMETRIC CATALYSIS
Prediction of higher-selectivity catalysts by computer-driven workflow and machine learning *A. F. Zahrt* et al.
RESEARCH ARTICLE SUMMARY; FOR FULL TEXT:
dx.doi.org/10.1126/science.aau5631



248 NEUROSCIENCE
Cerebellar modulation of the reward circuitry and social behavior *I. Carta* et al.
RESEARCH ARTICLE SUMMARY; FOR FULL TEXT:
dx.doi.org/10.1126/science.aav0581
▸ PERSPECTIVE P. 229

REPORTS

249 INORGANIC CHEMISTRY
Luminescence and reactivity of a charge-transfer excited iron complex with nanosecond lifetime *K. S. Kjær* et al.
▸ PERSPECTIVE P. 225

253 IMPACT CRATERS
Earth and Moon impact flux increased at the end of the Paleozoic *S. Mazrouei* et al.
▸ PERSPECTIVE P. 224

257 PHOTOSYNTHESIS
Structural adaptations of photosynthetic complex I enable ferredoxin-dependent electron transfer *J. M. Schuller* et al.
▸ PERSPECTIVE P. 230

261 CHEMICAL PHYSICS
Observation of magnetically tunable Feshbach resonances in ultracold $^{23}Na^{40}K + {}^{40}K$ collisions *H. Yang* et al.

265 SOLAR CELLS
A Eu^{3+}-Eu^{2+} ion redox shuttle imparts operational durability to Pb-I perovskite solar cells *L. Wang* et al.

270 ORGANIC CHEMISTRY
Concise total syntheses of (−)-jorunnamycin A and (−)-jorumycin enabled by asymmetric catalysis *E. R. Welin* et al.

276 NEUROSCIENCE
An amygdalar neural ensemble that encodes the unpleasantness of pain *G. Corder* et al.

282 BIODIVERSITY
Agriculturally dominated landscapes reduce bee phylogenetic diversity and pollination services *H. Grab* et al.

285 CILIA
Flagellar microtubule doublet assembly in vitro reveals a regulatory role of tubulin C-terminal tails *M. Schmidt-Cernohorska* et al.

288 IMMUNOTHERAPY
Strain-specific antibody therapy prevents cytomegalovirus reactivation after transplantation *J. P. Martins* et al.
▸ PERSPECTIVE P. 232

294 CELL DIFFERENTIATION
H3K9me3-heterochromatin loss at protein-coding genes enables developmental lineage specification *D. Nicetto* et al.

DEPARTMENTS

207 EDITORIAL
Why we need fetal tissue research
By Sally Temple and Lawrence S. B. Goldstein

314 WORKING LIFE
Lessons from a postdoc gone wrong
By Victor S. C. Wong

ON THE COVER



A three-dimensional micrograph, color coded by depth, of neurons at the ellipsoid body in the brain of a fruit fly (*Drosophila melanogaster*), extracted from a much larger dataset encompassing the entire brain. Combining expansion microscopy with lattice light-sheet microscopy enables rapid fluorescence imaging of neural circuits and their molecular constituents over millimeter dimensions with nanoscale resolution. See page 245. *Image: Betzig Lab, Janelia Research Campus/HHMI; Boyden Lab, MIT Media Lab*

Science Staff 206
New Products 298
AAAS Meeting Program 299
Science Careers 309

SCIENCE (ISSN 0036-8075) is published weekly on Friday, except last week in December, by the American Association for the Advancement of Science, 1200 New York Avenue, NW, Washington, DC 20005. Periodicals mail postage (publication No. 484460) paid at Washington, DC, and additional mailing offices. Copyright © 2019 by the American Association for the Advancement of Science. The title SCIENCE is a registered trademark of the AAAS. Domestic individual membership, including subscription (12 months): $165 ($74 allocated to subscription). Domestic institutional subscription (51 issues): $1971; Foreign postage extra: Mexico, Caribbean (surface mail) $55; other countries (air assist delivery): $98. First class, airmail, student, and emeritus rates on request. Canadian rates with GST available upon request, GST #125488122. Publications Mail Agreement Number 1069624. **Printed in the U.S.A.**
Change of address: Allow 4 weeks, giving old and new addresses and 8-digit account number. **Postmaster:** Send change of address to AAAS, P.O. Box 96178, Washington, DC 20090–6178. **Single-copy sales:** $15 each plus shipping and handling; bulk rate on request. **Authorization to reproduce** material for internal or personal use under circumstances not falling within the fair use provisions of the Copyright Act can be obtained through the Copyright Clearance Center (CCC), www.copyright.com. The identification code for *Science* is 0036-8075. *Science* is indexed in the *Reader's Guide to Periodical Literature* and in several specialized indexes.

PHOTO: EYEWELL PORTRAIT

Downloaded from http://science.sciencemag.org/ on January 21, 2019

Published by AAAS

Science
AAAS
1200 New York Avenue, NW, Washington, DC 20005
Clarendon House, Clarendon Road, Cambridge, UK CB2 8FH

Editor-in-Chief Jeremy Berg
Executive Editor Monica M. Bradford **News Editor** Tim Appenzeller
Editor, Insights Lisa D. Chong **Editors, Research** Valda Vinson, Jake S. Yeston

Research and Insights

DEPUTY EDITORS Julia Fahrenkamp-Uppenbrink(UK), Stella M. Hurtley(UK), Phillip D. Szuromi, Sacha Vignieri **SR. EDITORIAL FELLOW** Andrew M. Sugden(UK) **SR. EDITORS** Gemma Alderton(UK), Caroline Ash(UK), Pamela J. Hines, Paula A. Kiberstis, Marc S. Lavine(Canada), Steve Mao, Ian S. Osborne(UK), Beverly A. Purnell, L. Bryan Ray, H. Jesse Smith, Jelena Stajic, Peter Stern(UK), Brad Wible, Laura M. Zahn **ASSOCIATE EDITORS** Michael A. Funk, Brent Grocholski, Priscilla N. Kelly, Tage S. Rai, Seth Thomas Scanlon(UK), Keith T. Smith(UK) **ASSOCIATE BOOK REVIEW EDITOR** Valerie B. Thompson **LETTERS EDITOR** Jennifer Sills **LEAD CONTENT PRODUCTION EDITORS** Harry Jach, Lauren Kmec **CONTENT PRODUCTION EDITORS** Amelia Beyna, Jeffrey E. Cook, Amber Esplin, Chris Filiatreau, Cynthia Howe, Nida Masiulis **SR. EDITORIAL COORDINATORS** Carolyn Kyle, Beverly Shields **EDITORIAL COORDINATORS** Aneera Dobbins, Joi S. Granger, Jeffrey Hearn, Lisa Johnson, Maryrose Madrid, Shannon McMahon, Jerry Richardson, Alice Whaley(UK), Anita Wynn **PUBLICATIONS ASSISTANTS** Alexander Kief, Ope Martins, Ronmel Navas, Hilary Stewart(UK), Alana Warnke, Brian White **EXECUTIVE ASSISTANT** Jessica Slater **ASI DIRECTOR, OPERATIONS** Janet Clements(UK) **ASI SR. OFFICE ADMINISTRATOR** Jessica Waldock(UK)

News

NEWS MANAGING EDITOR John Travis **INTERNATIONAL EDITOR** Martin Enserink **DEPUTY NEWS EDITORS** Elizabeth Culotta, Lila Guterman, David Grimm, Eric Hand, David Malakoff **SR. CORRESPONDENTS** Daniel Clery(UK), Jon Cohen, Jeffrey Mervis, Elizabeth Pennisi **ASSOCIATE EDITORS** Jeffrey Brainard, Catherine Matacic **NEWS WRITERS** Adrian Cho, Jennifer Couzin-Frankel, Jocelyn Kaiser, Kelly Servick, Robert F. Service, Erik Stokstad(Cambridge, UK), Paul Voosen, Meredith Wadman **INTERN** Frankie Schembri **CONTRIBUTING CORRESPONDENTS** Warren Cornwall, Ann Gibbons, Mara Hvistendahl, Sam Kean, Eli Kintisch, Kai Kupferschmidt(Berlin), Andrew Lawler, Mitch Leslie, Eliot Marshall, Virginia Morell, Dennis Normile(Shanghai), Charles Piller, Tania Rabesandratana(London), Emily Underwood, Gretchen Vogel(Berlin), Lizzie Wade(Mexico City) **CAREERS** Donisha Adams, Rachel Bernstein(Editor), Katie Langin **COPY EDITORS** Julia Cole (Senior Copy Editor), Cyra Master (Copy Chief) **ADMINISTRATIVE SUPPORT** Meagan Weiland

Executive Publisher Rush D. Holt
Publisher Bill Moran

DIRECTOR, BUSINESS STRATEGY AND PORTFOLIO MANAGEMENT Sarah Whalen **DIRECTOR, PRODUCT AND CUSTOM PUBLISHING** Will Schweitzer **MANAGER, PRODUCT DEVELOPMENT** Hannah Heckner **BUSINESS SYSTEMS AND FINANCIAL ANALYSIS DIRECTOR** Randy Yi **DIRECTOR, BUSINESS OPERATIONS & ANALYST** Eric Knott **ASSOCIATE DIRECTOR, PRODUCT MANAGMENT** Kris Bishop **SENIOR SYSTEMS ANALYST** Nicole Mehmedovich **SENIOR BUSINESS ANALYST** Cory Lipman **MANAGER, BUSINESS OPERATIONS** Jessica Tierney **BUSINESS ANALYSTS** Meron Kebede, Sandy Kim, Jourdan Stewart **FINANCIAL ANALYST** Julian Iriarte **ADVERTISING SYSTEM ADMINISTRATOR** Tina Burks **SALES COORDINATOR** Shirley Young **DIRECTOR, COPYRIGHT, LICENSING, SPECIAL PROJECTS** Emilie David **DIGITAL PRODUCT ASSOCIATE** Michael Hardesty **RIGHTS AND PERMISSIONS ASSOCIATE** Elizabeth Sandler **RIGHTS, CONTRACTS, AND LICENSING ASSOCIATE** Lili Catlett **RIGHTS & PERMISSIONS ASSISTANT** Alexander Lee

DIRECTOR, INSTITUTIONAL LICENSING Iquo Edim **ASSOCIATE DIRECTOR, RESEARCH & DEVELOPMENT** Elisabeth Leonard **SENIOR INSTITUTIONAL LICENSING MANAGER** Ryan Rexroth **INSTITUTIONAL LICENSING MANAGERS** Marco Castellan, Chris Murawski **SENIOR OPERATIONS ANALYST** Lana Guz **MANAGER, AGENT RELATIONS & CUSTOMER SUCCESS** Judy Lillibridge

WEB DEVELOPMENT DIRECTOR David Levy **PROJECT MANAGER** Virginia Bramante

DIGITAL MEDIA DIRECTOR OF ANALYTICS Enrique Gonzales **DIGITAL REPORTING ANALYST** Timothy Frailey **MULTIMEDIA MANAGER** Sarah Crespi **MANAGING WEB PRODUCER** Kara Estelle-Powers **DIGITAL PRODUCER** Jessica Hubbard **VIDEO PRODUCERS** Chris Burns, Meagan Cantwell

DIGITAL/PRINT STRATEGY MANAGER Jason Hillman **QUALITY TECHNICAL MANAGER** Marcus Spiegler **DIGITAL PRODUCTION MANAGER** Lisa Stanford **ASSISTANT MANAGER DIGITAL/PRINT** Rebecca Doshi **SENIOR CONTENT SPECIALISTS** Steve Forrester, Antoinette Hodal, Lori Murphy **CONTENT SPECIALISTS** Jacob Hedrick, Kimberley Oster

DESIGN DIRECTOR Beth Rakouskas **DESIGN MANAGING EDITOR** Marcy Atarod **SENIOR DESIGNER** Chrystal Smith **DESIGNER** Christina Aycock **GRAPHICS MANAGING EDITOR** Alberto Cuadra **GRAPHICS EDITOR** Nirja Desai **SENIOR SCIENTIFIC ILLUSTRATORS** Valerie Altounian, Chris Bickel **SCIENTIFIC ILLUSTRATOR** Alice Kitterman **INTERACTIVE GRAPHICS EDITOR** Jia You **SENIOR GRAPHICS SPECIALISTS** Holly Bishop, Nathalie Cary **PHOTOGRAPHY MANAGING EDITOR** William Douthitt **PHOTO EDITOR** Emily Petersen **IMAGE RIGHTS AND FINANCIAL MANAGER** Jessica Adams

SENIOR EDITOR, CUSTOM PUBLISHING Sean Sanders: 202-326-6430 **ASSISTANT EDITOR, CUSTOM PUBLISHING** Jackie Oberst: 202-326-6463 **ADVERTISING PRODUCTION OPERATIONS MANAGER** Deborah Tompkins **SR. PRODUCTION SPECIALIST/GRAPHIC DESIGNER** Amy Hardcastle **SR. TRAFFIC ASSOCIATE** Christine Hall **DIRECTOR OF BUSINESS DEVELOPMENT AND ACADEMIC PUBLISHING RELATIONS, ASIA** Xiaoying Chu: +86-131 6136 3212, xchu@aaas.org **COLLABORATION/CUSTOM PUBLICATIONS/JAPAN** Adarsh Sandhu + 81532-81-5142 asandhu@aaas.org **EAST COAST/E. CANADA** Laurie Faraday: 508-747-9395, FAX 617-507-8189 **WEST COAST/W. CANADA** Lynne Stickrod: 415-931-9782, FAX 415-520-6940 **MIDWEST** Jeffrey Dembksi: 847-498-4520 x3005, Steven Loerch: 847-498-4520 x3006 **UK EUROPE/ASIA** Roger Goncalves: TEL/FAX +41 43 243 1358 **JAPAN** Kaoru Sasaki (Tokyo): + 81 (3) 6459 4174 ksasaki@aaas.org

ASSOCIATE DIRECTOR, BUSINESS DEVELOPMENT Justin Sawyers **GLOBAL MARKETING MANAGER** Allison Pritchard **DIGITAL MARKETING ASSOCIATE** Aimee Aponte **MARKETING MANAGER, JOURNALS** Shawana Arnold **MARKETING ASSOCIATES** Mike Romano, Tori Velasquez **SENIOR DESIGNER** Kim Huynh **TRADE SHOW COORDINATOR** Andrew Clamp

GLOBAL SALES DIRECTOR ADVERTISING AND CUSTOM PUBLISHING Tracy Holmes: +44 (0) 1223 326525 **CLASSIFIED** advertise@sciencecareers.org **SALES MANAGER, US, CANADA AND LATIN AMERICA SCIENCE CAREERS** Claudia Paulsen-Young: 202-326-6577, **EUROPE/ROW SALES** Sarah Lelarge **SALES ADMIN ASSISTANT** Kelly Grace +44 (0)1223 326528 **JAPAN** Miyuki Tani(Osaka): +81 (6) 6202 6272 mtani@aaas.org **CHINA/TAIWAN** Xiaoying Chu: +86-131 6136 3212, xchu@aaas.org

AAAS BOARD OF DIRECTORS, CHAIR Susan Hockfield **PRESIDENT** Margaret A. Hamburg **PRESIDENT-ELECT** Steven Chu **TREASURER** Carolyn N. Ainslie **CHIEF EXECUTIVE OFFICER** Rush D. Holt **BOARD** Cynthia M. Beall, May R. Berenbaum, Rosina M. Bierbaum, Kaye Husbands Fealing, Stephen P.A. Fodor, S. James Gates, Jr., Michael S. Gazzaniga, Laura H. Greene, Robert B. Millard, Mercedes Pascual, William D. Provine

SUBSCRIPTION SERVICES For change of address, missing issues, new orders and renewals, and payment questions: 866-434-AAAS (2227) or 202-326-6417, FAX 202-842-1065. Mailing addresses: AAAS, P.O. Box 96178, Washington, DC 20090-6178 or AAAS Member Services, 1200 New York Avenue, NW, Washington, DC 20005

INSTITUTIONAL SITE LICENSES 202-326-6730 **REPRINTS:** Author Inquiries 800-635-7181 **COMMERCIAL INQUIRIES** 803-359-4578 **PERMISSIONS** 202-326-6765, permissions@aaas.org **AAAS Member Central Support** 866-434-2227 www.aaas.org/membercentral.

Science serves as a forum for discussion of important issues related to the advancement of science by publishing material on which a consensus has been reached as well as including the presentation of minority or conflicting points of view. Accordingly, all articles published in *Science*—including editorials, news and comment, and book reviews—are signed and reflect the individual views of the authors and not official points of view adopted by AAAS or the institutions with which the authors are affiliated.

INFORMATION FOR AUTHORS See www.sciencemag.org/authors/science-information-authors

BOARD OF REVIEWING EDITORS (Statistics board members indicated with **(S)**)

Adriano Aguzzi, *U. Hospital Zürich*
Takuzo Aida, *U. of Tokyo*
Leslie Aiello, *Wenner-Gren Foundation*
Judith Allen, *U. of Manchester*
Sebastian Amigorena, *Institut Curie*
Paola Arlotta, *Harvard U.*
Johan Auwerx, *EPFL*
David Awschalom, *U. of Chicago*
Clare Baker, *U. of Cambridge*
Nenad Ban, *ETH Zürich*
Franz Bauer, *Pontificia Universidad Católica de Chile*
Ray H. Baughman, *U. of Texas at Dallas*
Carlo Beenakker, *Leiden U.*
Yasmine Belkaid, *NIAID, NIH*
Philip Benfey, *Duke U.*
Gabriele Bergers, *VIB*
Bradley Bernstein, *Mass. General Hospital*
Peer Bork, *EMBL*
Chris Bowler, *École Normale Supérieure*
Ian Boyd, *U. of St. Andrews*
Emily Brodsky, *U. of California, Santa Cruz*
Ron Brookmeyer, *U. of California, Los Angeles* **(S)**
Christian Büchel, *UKE Hamburg*
Dennis Burton, *Scripps Research*
Carter Tribley Butts, *U. of California, Irvine*
Gyorgy Buzsaki, *New York U. School of Med.*
Blanche Capel, *Duke U.*
Annmarie Carlton, *U. of California, Irvine*
Lars-Erik Cederman, *ETH Zürich*
Nick Chater, *U. of Warwick*
Ib Chorkendorff, *Denmark TU*
James J. Collins, *MIT*
Robert Cook-Deegan, *Arizona State U.*
Alan Cowman, *Walter & Eliza Hall Inst.*
Carolyn Coyne, *U. of Pittsburgh*
Roberta Croce, *VU Amsterdam*
Jeff L. Dangl, *U. of North Carolina*
Tom Daniel, *U. of Washington*
Chiara Daraio, *Caltech*
Nicolas Dauphas, *U. of Chicago*
Frans de Waal, *Emory U.*
Stanislas Dehaene, *Collège de France*
Claude Desplan, *New York U.*
Sandra Díaz, *Universidad Nacional de Córdoba*
Dennis Discher, *U. of Penn.*
Jennifer A. Doudna, *U. of California, Berkeley*
Bruce Dunn, *U. of California, Los Angeles*
William Dunphy, *Caltech*
Christopher Dye, *U. of Oxford*
Todd Ehlers, *U. of Tübingen*
Jennifer Elisseeff, *Johns Hopkins U.*
Tim Elston, *U. of North Carolina*
Nader Engheta, *U. of Penn.*
Karen Ersche, *U. of Cambridge*
Barry Everitt, *U. of Cambridge*
Vanessa Ezenwa, *U. of Georgia*
Michael Feuer, *The George Washington U.*
Toren Finkel, *U. of Pittsburgh Med. Ctr.*
Kate Fitzgerald, *U. of Mass.*
Gwenn Flowers, *Simon Fraser U.*
Peter Fratzl, *Max Planck Inst. Potsdam*
Elaine Fuchs, *Rockefeller U.*
Eileen Furlong, *EMBL*
Jay Gallagher, *U. of Wisconsin*
Susan Gelman, *U. of Michigan*
Daniel Geschwind, *U. of California, Los Angeles*
Karl-Heinz Glassmeier, *TU Braunschweig*
Ramon Gonzalez, *Rice U.*
Elizabeth Grove, *U. of Chicago*
Nicolas Gruber, *ETH Zürich*
Kip Guy, *U. of Kentucky College of Pharmacy*
Taekjip Ha, *Johns Hopkins U.*
Christian Haass, *Ludwig Maximilians U.*
Sharon Hammes-Schiffer, *Yale U.*
Wolf-Dietrich Hardt, *ETH Zürich*
Louise Harra, *U. College London*
Jian He, *Clemson U.*
Carl-Philipp Heisenberg, *IST Austria*
Ykä Helariutta, *U. of Cambridge*
Janet G. Hering, *Eawag*
Kai-Uwe Hinrichs, *U. of Bremen*
David Hodell, *U. of Cambridge*
Lora Hooper, *UT Southwestern Med. Ctr.*
Fred Hughson, *Princeton U.*
Randall Hulet, *Rice U.*
Auke Ijspeert, *EPFL*
Akiko Iwasaki, *Yale U.*
Stephen Jackson, *USGS and U. of Arizona*
Kai Johnsson, *EPFL*
Peter Jonas, *IST Austria*
Matt Kaeberlein, *U. of Washington*
William Kaelin Jr., *Dana-Farber Cancer Inst.*
Daniel Kammen, *U. of California, Berkeley*
Abby Kavner, *U. of California, Los Angeles*
Masashi Kawasaki, *U. of Tokyo*
V. Narry Kim, *Seoul Nat. U.*
Robert Kingston, *Harvard Med. School*
Nancy Knowlton, *Smithsonian Institution*
Etienne Koechlin, *École Normale Supérieure*
Alexander Kolodkin, *Johns Hopkins U.*
Thomas Langer, *U. of Cologne*
Mitchell A. Lazar, *U. of Penn.*
Stanley Lemon, *U. of North Carolina*
Ottoline Leyser, *U. of Cambridge*
Wendell Lim, *U. of California, San Francisco*
Marcia C. Linn, *U. of California, Berkeley*
Jianguo Liu, *Michigan State U.*
Luis Liz-Marzán, *CIC biomaGUNE*
Jonathan Losos, *Harvard U.*
Ke Lu, *Chinese Acad. of Sciences*
Christian Lüscher, *U. of Geneva*
Fabienne Mackay, *U. of Melbourne*
Anne Magurran, *U. of St. Andrews*
Oscar Marín, *King's College London*
Charles Marshall, *U. of California, Berkeley*
Christopher Marx, *U. of Idaho*
Geraldine Masson, *CNRS*
C. Robertson McClung, *Dartmouth College*
Rodrigo Medellín, *U. of Mexico*
Graham Medley, *London School of Hygiene & Tropical Med.*
Jane Memmott, *U. of Bristol*
Edward Miguel, *U. of California, Berkeley*
Tom Misteli, *NCI, NIH*
Yasushi Miyashita, *U. of Tokyo*
Alison Motsinger-Reif, *NC State U.* **(S)**
Daniel Nettle, *Newcastle U.*
Daniel Neumark, *U. of California, Berkeley*
Kitty Nijmeijer, *TU Eindhoven*
Helga Nowotny, *Austrian Council*
Rachel O'Reilly, *U. of Warwick*
Harry Orr, *U. of Minnesota*
Pilar Ossorio, *U. of Wisconsin*
Andrew Oswald, *U. of Warwick*
Isabella Pagano, *Istituto Nazionale di Astrofisica*
Margaret Palmer, *U. of Maryland*
Elizabeth Levy Paluck, *Princeton U.*
Jane Parker, *Max Planck Inst. Cologne*
Giovanni Parmigiani, *Dana-Farber Cancer Inst.* **(S)**
Samuel Pfaff, *Salk Inst. for Biological Studies*
Julie Pfeiffer, *UT Southwestern Med. Ctr.*
Matthieu Piel, *Institut Curie*
Kathrin Plath, *U. of California, Los Angeles*
Martin Plenio, *Ulm U.*
Albert Polman, *FOM Inst. for AMOLF*
Elvira Poloczanska, *Alfred-Wegener-Inst.*
Julia Pongratz, *Ludwig Maximilians U.*
Philippe Poulin, *CNRS*
Jonathan Pritchard, *Stanford U.*
David Randall, *Colorado State U.*
Félix A. Rey, *Institut Pasteur*
Trevor Robbins, *U. of Cambridge*
Amy Rosenzweig, *Northwestern U.*
Mike Ryan, *U. of Texas at Austin*
Mitinori Saitou, *Kyoto U.*
Shimon Sakaguchi, *Osaka U.*
Miquel Salmeron, *Lawrence Berkeley Nat. Lab*
Nitin Samarth, *Penn. State U.*
Jürgen Sandkühler, *Med. U. of Vienna*
Alexander Schier, *Harvard U.*
Wolfram Schlenker, *Columbia U.*
Susannah Scott, *U. of California, Santa Barbara*
Vladimir Shalaev, *Purdue U.*
Beth Shapiro, *U. of California, Santa Cruz*
Jay Shendure, *U. of Washington*
Brian Shoichet, *U. of California, San Francisco*
Robert Siliciano, *Johns Hopkins U. School of Med.*
Lucia Sivilotti, *U. College London*
Alison Smith, *John Innes Centre*
Richard Smith, *U. of North Carolina* **(S)**
Mark Smyth, *QIMR Berghofer*
Pam Soltis, *U. of Florida*
John Speakman, *U. of Aberdeen*
Tara Spires-Jones, *U. of Edinburgh*
Allan C. Spradling, *Carnegie Institution for Science*
Paula Stephan, *Georgia State U.*
V. S. Subrahmanian, *U. of Maryland*
Ira Tabas, *Columbia U.*
Sarah Teichmann, *U. of Cambridge*
Shubha Tole, *Tata Inst. of Fundamental Research*
Wim van der Putten, *Netherlands Inst. of Ecology*
Bert Vogelstein, *Johns Hopkins U.*
Kathleen Vohs, *U. of Minnesota*
David Wallach, *Weizmann Inst. of Science*
Jane-Ling Wang, *U. of California, Davis* **(S)**
David Waxman, *Fudan U.*
Jonathan Weissman, *U. of California, San Francisco*
Chris Wikle, *U. of Missouri* **(S)**
Terrie Williams, *U. of California, Santa Cruz*
Ian A. Wilson, *Scripps Research* **(S)**
Yu Xie, *Princeton U.*
Jan Zaanen, *Leiden U.*
Kenneth Zaret, *U. of Penn. School of Med.*
Jonathan Zehr, *U. of California, Santa Cruz*
Maria Zuber, *MIT*

Published by AAAS

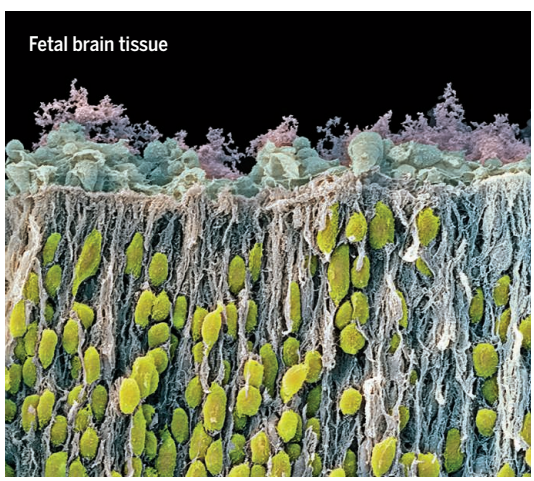
EDITORIAL

Why we need fetal tissue research

A vocal minority in the United States is intent on stopping federal funding for research using human fetal tissue, citing stem cell–based or other alternatives as adequate. This view is scientifically inaccurate. It ignores the current limitations of stem cell research and disregards the value of fetal tissue research in finding therapies for incurable diseases. If there is to be continued rapid progress in treating cancer, birth defects, heart disease, and infectious diseases, then we need fetal tissue research.

Life-saving advances, including the development of vaccines against rubella, rabies, and hepatitis A viruses, and antiviral drugs that prevent HIV/AIDS, required fetal tissue research. Today, fetal tissue is being used to develop new medicines including vaccines for HIV/AIDS, preventives for Zika virus, and immunotherapies to battle untreatable cancers.

Although research into alternatives is worthwhile, there are several aspects of fetal tissue research for which alternatives do not and will not exist. For example, to discover which fetal cells go awry and cause childhood cancers such as retinoblastoma, a cancer of the eye, or rhabdomyosarcoma, a muscle cancer, we must understand which cells are the culprits. For that, we need access to relevant fetal tissues. Zika virus can cross the placenta and attack specific fetal brain cells. To determine the mechanism of viral entry, which cell types are vulnerable, and how to prevent infection and damage, we need access to fetal brain tissue. Beyond diseases affecting children, some forms of hereditary Alzheimer's disease cause neural impairments in utero that persist over decades and manifest later in life. Without access to fetal cells, we cannot understand and effectively combat diseases that begin in utero.



"...fetal tissue remains an essential resource for many applications."

Fetal tissue alternatives for some applications may be developed as science advances, but this will take time. The transition to any new model of research should be data-driven and based on scientific evidence. Opponents of fetal tissue research state that human stem cell–derived organoids are adequate models, supplanting fetal tissue research, but that is incorrect. Organoids typically do not fully mirror the complex cellular composition and architecture of fetal organs. Although organoids may prove valuable to model some diseases, critically, access to fetal tissue is required for validation of these and any proposed alternatives. For example, mice that model the human blood system are produced through transplants of human fetal liver and/or thymus tissue to provide a near full complement of long-lived human blood cells. These animal models are needed to develop therapies that involve the immune system, such as HIV vaccines and new chimeric antigen receptor (CAR) T cell–based cancer treatments. Alternative mouse models using human neonatal thymus are being explored but may lack the variety and sustained production of blood cells produced from fetal liver or autologous bone marrow, and supply is limited to thymus taken from infants undergoing congenital heart surgery, sometimes associated with concomitant immune problems that confound results. It would be a grave injustice to the patients and families afflicted by diseases that benefit from this research to prematurely halt production of fetal tissue models.

Although alternatives may be established in some cases, fetal tissue remains an essential resource for many applications. It is important to remember that the fetal tissue used in research would otherwise be discarded and thus unavailable in the fight against disease. U.S. researchers also follow rigorous, well-established medical and ethical standard practices for this research. Fetal tissue research has been supported for decades by both Republican and Democratic administrations and congresses. Rigorous U.S. government–sponsored review processes have also concluded that this research is ethical and valuable.

If we are to achieve medical advances for currently incurable diseases, the path forward must include fetal tissue research, for which continued public support is most critical at this time.

–Sally Temple and Lawrence S. B. Goldstein



Sally Temple *is the scientific director of the Neural Stem Cell Institute, Rensselaer, NY, USA. sallytemple@neuralsci.org*



Lawrence S. B. Goldstein *is a professor in the Department of Cellular and Molecular Medicine at the University of California, San Diego, CA, USA and the scientific director of the Sanford Consortium for Regenerative Medicine. lgoldstein@ucsd.edu*

10.1126/science.aaw6299

PHOTOS: (INSET) STEVE GSCHMEISSNER/SCIENCE SOURCE; (RIGHT TOP TO BOTTOM) SUZANNE KAWOLA, NSCI; DONNA COLEMAN PHOTOGRAPHY

Downloaded from http://science.sciencemag.org/ on January 21, 2019

Published by AAAS

> “We need a rigorous, scientific postmortem on Russian misinformation to harden our democracy against future attacks.”
>
> **Sinan Aral**, of the Massachusetts Institute of Technology, in *The Washington Post*.

IN BRIEF

Edited by **Lila Guterman**

ENVIRONMENT

Fish kill reignites Australian water fight



Dead carp lie on the shores of Lake Hawthorn, part of the Murray-Darling Basin in Australia, in 2007.

More than 1 million fish have died in the Murray-Darling river system in New South Wales and adjacent states in Australia in recent weeks—despite a 2012 water-sharing agreement, touted as historic, that was supposed to avoid such catastrophes. The die-off is due to the combined effects of a heat wave, low water levels, and algae blooms, which starved the fish of oxygen when they decayed. Farmers blame a monthslong drought, but environmentalists say too much water has been drawn for irrigation from the network of rivers, which stretches through a 1-million-square-kilometer basin in the country’s southeast. The 2012 plan promised to balance the demand for drinking water and irrigation with environmental needs (*Science*, 7 December 2012, p. 1273). But enforcement of water diversion limits has been lax, says John Quiggin, an environmental economist at the University of Queensland in Brisbane, Australia, and the federal government has refused to buy back water rights from farmers, as the plan stipulated. Climate change could exacerbate stresses on the ecosystem, he says, and cause “irrecoverable damage.”

India’s quantum computing push

FUNDING | The Indian government quietly unveiled a $12 million Quantum Enabled Science & Technology program last week. The funds, to be spent over 3 years, will build infrastructure and hire researchers to help realize the country’s ambitious new goal: being at the forefront of the quantum computing revolution within 10 years. Indian policymakers often lament that the country missed the computer hardware revolution of the 1970s, despite having played a significant role in developing software. Now, they don’t want to miss the quantum computing boat.

Radio telescopes plan global pact

ASTRONOMY | Radio astronomers intend to link two of their biggest planned projects, the Square Kilometre Array (SKA)—a 12-nation effort to build thousands of radio antennas across swaths of South Africa and Australia—and the U.S. Next Generation Very Large Array (ngVLA). Designs for the ngVLA include 214 18-meter dishes across New Mexico, Texas, Arizona, and northern Mexico, as well as 30 more far-flung dishes in Hawaii, British Columbia in Canada, the U.S. Virgin Islands, and elsewhere; the dishes will pool their data to achieve unprecedented resolution. Tony Beasley, director of the U.S. National Radio Astronomy Observatory in Charlottesville, Virginia, told the American Astronomical Society meeting in Seattle, Washington, last week that ngVLA planners are in discussions with their SKA counterparts on a reciprocal agreement to allow researchers access to both observatories. Neither array, however, has yet been approved for construction.

Space ‘Cow’ mystery endures

ASTRONOMY | Astronomers admitted last week they are flummoxed by an unusually bright glow in the sky that appeared suddenly one day in June 2018. After months of study, they still aren’t sure what the object—officially called AT2018cow, but universally referred to as the “Cow”—is or what caused it. At the American Astronomical Society meeting last week in Seattle, Washington, researchers described using dozens of

Downloaded from http://science.sciencemag.org/ on January 17, 2019

PHOTO: AMY TOENSING/NATIONAL GEOGRAPHIC IMAGE COLLECTION

Published by AAAS

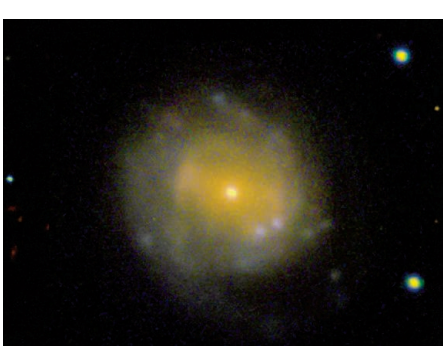


PALEOECOLOGY

A mite-y record of the Incan Empire

The history of the Andes might well be told through llama poop. During the Incan Empire, which lasted from 1438 to 1533, thousands of llamas carrying trade goods such as salt and coca leaves marched through the Marcacocha Basin, once the site of a small lake in highland Peru. Their dung washed into the lake, where it was eaten by oribatid mites, a half-millimeter-long relative of spiders. The more llamas that passed through Marcacocha, the more excrement they left, and the larger the mite populations could grow. Researchers counted the mites in a sediment core and found that their population boomed during the Incan Empire and plummeted after the Spanish arrived, tracking the deaths of huge numbers of the Indigenous people and their animals. A more commonly used environmental proxy, spores of the dung-dwelling fungus *Sporormiella*, didn't track those historical events, the team reports in the *Journal of Archaeological Science*. Rather, the number of spores boomed during dry periods that shrank the lake. The researchers suggest that mites are better than the fungus for tracking llama populations in small, shallow lakes like Marcacocha.

telescopes to study the Cow, located in a small galaxy about 200 million light-years away. It didn't behave like a distant supernova, and its position ruled out a black hole ripping apart a star. Its steady brightness over several weeks suggests it was powered by some kind of "central engine." Whatever the Cow is, says astronomer Liliana Rivera Sandoval of Texas Tech University in Lubbock, "It's super weird."



AT2018cow is the farther right of two bright spots in the lower right of this galaxy.

PHOTOS: (TOP TO BOTTOM) ISTOCK.COM/OGPHOTO; R. MARGUTTI/W. M. KECK OBSERVATORY

James Watson stripped of titles

PEOPLE | Cold Spring Harbor Laboratory (CSHL) in New York has severed its ties to James Watson after the Nobel laureate reiterated the belief that black people are intrinsically less intelligent than white people. Watson retired as CSHL chancellor in 2007 and apologized after his earlier comments appeared in London's *The Times*. But this month, Watson said in a PBS documentary that his views about genetics and intelligence have not changed. In a statement, CSHL said it "unequivocally rejects [Watson's] unsubstantiated and reckless personal opinions" and has revoked Watson's titles of chancellor emeritus, Oliver R. Grace professor emeritus, and honorary trustee.

Plagiarism at integrity meeting

ETHICS | Researchers studying integrity might be expected to be full of that rare quality. That's why organizers of the sixth World Conference on Research Integrity, to be held in Hong Kong, China, in June, were surprised to receive an abstract that was, instead, full of apparent plagiarism. After combing through all 430 submissions, they discovered 11 additional cases of suspected plagiarism. When they reached out to the authors of the abstracts—two of which, ironically, were about plagiarism—six didn't respond, one withdrew their submission, one blamed staff, and two said they had permission to use each other's work. Only two gave "acceptable" explanations, the organizers reported last week on the Retraction Watch blog.

Harassment bill introduced

U.S. CONGRESS | Representative Eddie Bernice Johnson (D–TX), who became chair of the science committee in the U.S. House of Representatives this month, has already introduced three bills that signal her interest in topics that previous Republican leadership has shunned—and her interest

Downloaded from http://science.sciencemag.org/ on January 17, 2019

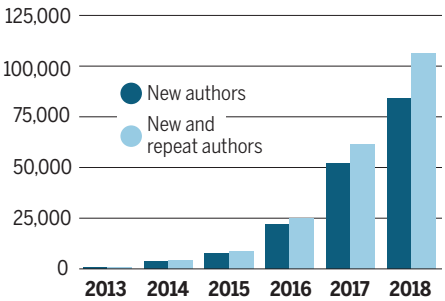
Published by AAAS

in bipartisanship. She teamed up with Representative Frank Lucas (OK), the panel's top Republican, on a bill that would make agencies adopt common policies for handling allegations of sexual harassment and encourage the National Science Foundation (NSF) to do research on the topic. The panel's top lawmakers are also jointly sponsoring legislation to strengthen clean water programs at the Department of Energy. A third bill—likely much more controversial and lacking bipartisan support—would authorize NSF and three other agencies to fund research on the causes and consequences of gun violence.

Biologists flock to preprints

PUBLISHING | Last year saw rapid growth in the number of biologists posting papers to the preprint server bioRxiv and in the total number of papers. The server still hosts only a small fraction of all new biology papers, but it has provided an outlet to authors looking to quickly share research findings. More preprints were posted in the first 11 months of 2018—18,825—than in the years since the server launched in 2013. Nearly two-thirds of preprints posted in 2017 or earlier were later published in journals, report Richard Abdill and Ran Blekhman of the University of Minnesota in Minneapolis this week in a bioRxiv preprint. The researchers also unveiled Rxivist.org, a website that allows users to sort bioRxiv preprints by number of downloads or Twitter mentions.

BioRxiv gains fans



World Bank head resigns early

PEOPLE | Jim Yong Kim, president of the World Bank in Washington, D.C., announced last week that he would step down on 1 February, 3 years before the end of his term. Kim, a physician and anthropologist, was nominated by then-President Barack Obama in 2012 and in 2016 was appointed to a new term that runs through 2021. His departure has raised questions about whether the bank's board will follow a long-standing tradition and accept whomever the U.S. president nominates. In a statement, the World Bank said Kim plans to join a firm that will "focus on increasing infrastructure investments in developing countries" and rejoin the board of Partners in Health, a Boston-based nonprofit organization that provides health care in developing countries.

Germany inks open-access deal

PUBLISHING | This week, a consortium of German libraries, universities, and research institutes signed a first-of-its-kind open-access deal with the publisher Wiley. In exchange for an annual lump sum, Wiley will make papers from authors at more than 700 institutions freely available online. Researchers at the German institutions will also gain access to all Wiley journal papers published since 1997. At Wiley's request, the details of the payment plan won't be disclosed for 30 days. Negotiators for the consortium, called Project DEAL, hope the step will push Elsevier and Springer toward similar deals. Hundreds of institutes in Germany, including the Max Planck Society, lost access to Elsevier journals after contracts ran out.

Europe plans newest collider

PARTICLE PHYSICS | This week, European scientists released a conceptual design for a successor to the world's biggest atom smasher, the 27-kilometer-long Large Hadron Collider (LHC) at CERN, the European particle physics laboratory near Geneva, Switzerland. The plan envisions a ring 100 kilometers in circumference that would collide electrons and positrons and study in detail the Higgs boson, the weird new particle the LHC discovered in 2012. The €9 billion accelerator would begin to operate around 2040, after the LHC shuts down. After the electron-positron collider has done its work, its tunnel might house an even more ambitious €15 billion collider that, like the LHC, would bash protons together, but would reach far higher energies than any previous machine. CERN has competition from physicists in China with similar plans.



CLIMATE

East Antarctica's ice is melting rapidly

The vast majority of Antarctica's ice melt, which is responsible for at least 13.8 millimeters of sea level rise over the past 40 years, was long thought to come from the unstable West Antarctic Ice Sheet. Now, a study using 40 years of satellite imagery finds that the East Antarctic Ice Sheet is losing a substantial quantity of ice as well. Over the past 4 decades, that loss accounted for more than 30% of the sea level rise attributed to the continent, researchers report this week in the *Proceedings of the National Academy of Sciences*. East Antarctica, which has 10 times as much ice as the continent's western half, was long thought to be insulated from climate change because it rests on land, largely protected from warming ocean waters. A 2018 *Nature* paper estimated the region was actually gaining ice. If confirmed, the new results could dramatically reshape projections of sea level rise for the next century.

SCIENCEMAG.ORG/NEWS
Read more news from *Science* online.

CREDITS: (GRAPHIC) J. BRAINARD/*SCIENCE*; (DATA) R. J. ABDILL AND R. BLEKHMAN, BIORXIV, 10.1101/515643 (2019); (PHOTO) TORSTEN BLACKWOOD/POOL/GETTY IMAGES

Downloaded from http://science.sciencemag.org/ on January 17, 2019

Published by AAAS



IN DEPTH

ENVIRONMENTAL RESEARCH

Shake-up threatens novel U.S. ecology facility

NEON science head quits, advisers fired after Battelle replaces two top managers

By **Jeffrey Mervis**

The National Ecological Observatory Network (NEON), a half-billion-dollar facility funded by the National Science Foundation (NSF), hopes to revolutionize ecology by collecting an unprecedented amount of data about long-term environmental changes across North America. But as NEON prepares to begin full operations, an abrupt leadership shake-up threatens to alienate the scientists who will be using those data and, thus, are essential to its success.

On 8 January, Sharon Collinge, NEON's chief scientist and principal investigator, resigned 4 days after Battelle Memorial Institute, which manages the network, fired two senior managers without her knowledge or consent. Within hours of Collinge's resignation, Battelle dissolved NEON's 20-member technical advisory committee, heading off a possible mass resignation of panel members opposed to Battelle's actions. The rapid-fire developments came after years of cost overruns, construction delays, and debate over the project's scientific merits and left many researchers bewildered and concerned.

Battelle "just burned some of the most prominent ecologists in the country," says Ankur Desai, an atmospheric scientist at the University of Wisconsin in Madison who served on NEON's now disbanded Science, Technology & Education Advisory Committee (STEAC). "This has put the project at massive risk." He and other former STEAC members want the advisory panel reinstated and its role strengthened. Disbanding it "leaves NEON open to missteps and … is breeding mistrust in the user community," they wrote in a 14 January letter to Battelle executives and NSF leadership.

The upheaval is NEON's latest self-inflicted wound. First proposed by then–NSF Director Rita Colwell in 2000, the project has chewed up half a dozen scientific directors—Collinge lasted less than a year—ensnared two contractors, prompted a congressional inquiry over spending and management practices, and generated a seemingly endless stream of critical reviews by outside experts. Many ecologists also worry that NEON's $65-million-a-year operating budget will reduce the NSF funding available for ecological research that doesn't rely on data from the 81-site facility, which is headquartered in Boulder, Colorado.

Battelle took over NEON in 2016, after NSF fired the project's original contractor, and the Columbus-based nonprofit is widely credited with putting the project on the right track. By the end of 2018 it had completed work on all but one of NEON's data-collecting sites, for $10 million less than the latest projected cost of $469 million. At a meeting in November 2018, members of the National Science Board, NSF's presidentially appointed oversight body, welcomed the progress. "I feel we are in a very happy place," said Inez Fung, an atmospheric scientist at the University of California, Berkeley, who had led an ad hoc panel created to keep close tabs on NEON. (Fung has since rotated off the board.) "I am looking forward to very great discoveries," she added.

Ecologists take vegetation measurements in 2018 at NEON's Toolik Lake site in northern Alaska.

But this month's events have clouded NEON's future. On 4 January, Battelle executives removed Richard Leonard, who had overseen the project's turnaround, and ecologist Wendy Gram, a senior manager and head of engagement who had worked at NEON since 2008. Within minutes, both had been escorted out of NEON's headquarters.

Collinge, who took a 2-year leave from the University of Colorado in Boulder when she joined NEON in February 2018, says Battelle gave her no notice of the firings. She sees them as the final straw in a series of developments that had undermined her ability to lead the observatory.

"I have not been granted the authority to be successful," she wrote to Battelle officials as she announced her decision to return a year early to her tenured position as a professor of environmental studies. Battelle had promised that she would have the

PHOTO: THOMAS COLBY WRIGHT

Downloaded from http://science.sciencemag.org/ on January 18, 2019

Published by AAAS

power to "allocate resources, both human and financial," Collinge says, and the firings were a breach of that agreement.

Battelle, however, has said Collinge could not have hiring and firing authority because she is not an employee of the nonprofit. And Patrick Jarvis, Battelle's senior vice president of marketing and communications, says a management change was needed as NEON shifts from construction to operation.

"Since we are shifting our focus, we decided to streamline our management structure to use our funds most efficiently," Jarvis told *Science*. He says soil scientist Eugene Kelly, who spent a year as NEON's top scientist during the transition to Battelle, has agreed to return in an acting capacity until a permanent observatory director is hired. The new head will have "a free hand" in deciding how to reconstitute any advisory structure, Jarvis adds.

Restoring the committee is crucial, some former members of NEON's advisory panel say. STEAC was "the primary means of communication and guidance between the scientific community and NEON," they note in their letter. "These [advisory] structures must be able to tell an organization what it may not want to hear, without fear of retaliation," they write. That independence was lacking, say former STEAC members, because the panel reported to Battelle, not to NSF—a relationship that appears to be unique among the many large facilities that NSF has funded and operates through contractors.

How NSF responds to the latest crisis will be key to NEON's future. But its reaction has been muted by the current partial government shutdown, which has furloughed the NSF staffers who oversee the project.

One question is whether Battelle's contract to manage NEON will be renewed when the current agreement ends in September 2020. NSF selected the firm "because they know how to build things and because we were facing a crisis," says Fung, adding that board members expect "a robust competition" for the next contract.

Some scientists wonder whether it's time for a change. "Battelle rescued NEON and did an excellent job of building it out," says plant biologist Scott Collins of the University of New Mexico in Albuquerque, a STEAC member who worked at NSF when NEON was hatched. "But they don't know how to run an ecological observatory."

Despite the current turmoil, ecologists are still rooting for NEON to succeed. But a tweet Desai posted shortly after getting the news about this month's shake-up reflects what many worry might happen instead: "Great data, no users, no trust = failure." ■

EVOLUTION

Did neurons arise from an early secretory cell?

Cell lineage studies of comb jellies and other creatures may suggest a single ancient origin of the nervous system

By **Elizabeth Pennisi**, *in Tampa, Florida*

Swimming through the oceans, voraciously consuming plankton and other small creatures—and occasionally startling a swimmer—the beautiful gelatinous masses known as comb jellies won't be joining Mensa anytime soon. But these fragile creatures have nerve cells—and they offer insights about the evolutionary origins of all nervous systems, including our own. Inspired by studies of a glue-secreting cell unique to these plankton predators, researchers have now proposed that neurons emerged in the last common ancestor of today's animals—and that their progenitors were secretory cells, whose primary function was to release chemicals into the environment.

Joseph Ryan, a computational evolutionary biologist the University of Florida Whitney Laboratory for Marine Bioscience in St. Augustine, suggested that scenario last year after tracing the development of nerve cells in embryos of comb jellies, among the most ancient animals. Earlier this month at the annual meeting of the Society for Integrative and Comparative Biology (SICB) here, he marshaled evidence from developmental studies of other animals, all pointing to common origins for some neuron and secretory cells.

"What Ryan is proposing is novel and important," says David Plachetzki, an evolutionary biologist at the University of New Hampshire in Durham. Among other mysteries, it could resolve a long debate about whether the nervous system evolved twice early in animal life.

Today, nerve cells are among the most specialized cell types in the body, able to transmit electrical signals, for example. Some versions talk to each other, others relay information from the environment to the brain, and still more send directives to muscles and other parts of the body. They are an almost universal feature of animals; only sponges and placozoans, an obscure group of tiny creatures with the simplest of animal structures, lack them.

When and how the animal nervous system arose has remained murky, however. Ryan and Whitney lab postdoctoral fellow Leslie Babonis were drawn into the debate by their recent analysis of the developmental origin of the colloblast, a specialized cell unique to most comb jellies. Studding the tentacles of comb jellies, the cells secrete glue that grabs passing prey.

By tracing the development of individual cells in comb jelly embryos and monitoring each cell's gene activity, Babonis discovered that colloblasts arise from the same progenitor cells as the animal's nerve cells. "That was not expected at all," recalls Ryan, whose team published those results



The rudimentary nervous system of the warty comb jelly may help resolve how nerve cells arose.

PHOTO: ANDREY NEKRASOV/ALAMY STOCK PHOTO

Downloaded from http://science.sciencemag.org/ on January 18, 2019

Published by AAAS

on 30 August 2018 in *Molecular Biology and Evolution*.

Since then, however, he's learned of additional studies pointing to common origins for neurons and other secretory cells in embryonic development—and perhaps in evolution. In his talk at the SICB meeting, he noted that one team showed more than 25 years ago that the stinging cells of jellyfish, another specialized secretory cell type, arise from the same embryonic precursors as the animal's nerve cells. He cited similar evidence for hydra and fruit flies. "It's a really generalizable thing," he says.

The finding could settle a long-standing debate. In 2013, a research team analyzing the newly sequenced genome of a comb jelly known as the sea gooseberry (*Pleurobrachia bachei*) discovered it was missing multiple genes active in the nervous systems of most animals: certain *Hox* genes, which control development, and the gene for the neurotransmitter serotonin. That discovery led the team to propose that comb jellies evolved a nervous system independently from almost all other animals (*Science*, 25 January 2013, p. 391). But many wondered how something so complex could have evolved twice.

Finding a common developmental source for neurons in comb jellies, jellyfish, and many other animals suggests it didn't, Ryan and others now say. The work shows "the platform upon which the nervous system was built was there" in the last common ancestor of animals, says Timothy Jegla, a neurobiologist at Pennsylvania State University in University Park. "Relatively simple reprogramming [of] stem cells during development can lead to whole new cell types and tissues, and the nervous system is probably just another example of that." Other researchers, however, say it's still possible that nerve cells had multiple origins after the last common ancestor, each time arising from the same stem cell lineage.

Next, Ryan, Babonis, and Whitney lab neurophysiologist Yuriy Bobkov hope to learn how progenitor cells develop into neurons by studying a simple sensory organ—the "warts" of the warty comb jelly, or sea walnut (*Mnemiopsis leidyi*). Recent work shows that each wart contains about 500 nerve and muscle cells that react to light, the smell of fish, and mechanical stimuli. Warts regenerate if cut off, and by tracing gene activity of their cells as they regrow and specialize, Ryan hopes his team can pin down the genes directing nerve cell formation—and perhaps, he says, "peel back some of the complexity of the evolution of neurons." ■



A member of UNICEF's Ebola outreach team addresses the public in Beni, in the Democratic Republic of the Congo.

PHOTO: © UNICEF/UN0228985/NAFTALIN

INFECTIOUS DISEASES

In Congo, fighting a virus and a groundswell of fake news

Armed conflict and political tensions stoke rumors and misinformation about Ebola

By **Laura Spinney**

The Ebola epidemic in the Democratic Republic of the Congo (DRC) is providing a natural experiment in fighting fake news. Occurring in a conflict zone, amid a controversial presidential election, the epidemic has proved to be fertile ground for conspiracy theories and political manipulation, which can hamper efforts to treat patients and fight the virus's spread. Public health workers have mounted an unprecedented effort to counter misinformation, saying the success or failure of the Ebola response may pivot on who controls the narrative.

Tensions are expected to rise in the wake of the 10 January declaration by the DRC's election commission that opposition leader Felix Tshisekedi won the election, held on 30 December. Foreign observers and the Roman Catholic Church's monitors say Martin Fayulu, another opposition figure, garnered more votes, and his supporters are alleging fraud. Health workers know rumors thrive amid uncertainty.

"I usually tell my teams that we fight two outbreaks, Ebola and fear," says Carlos Navarro Colorado of the United Nations International Children's Emergency Fund (UNICEF) in New York City. "It is all about information." For the first time in an Ebola outbreak, UNICEF and other agencies have joined forces as a single response team, which answers to the DRC's Ministry of Health in Kinshasa and includes dozens of social scientists. They use the airwaves, social media, and meetings with community and religious leaders to fight misinformation. Responders also foster trust by making their work more transparent—in some cases literally. A new biosecure tent, called the Biosecure Emergency Care Unit for Outbreaks (CUBE), allows relatives to visit and see Ebola patients during treatment.

With 600 confirmed cases and 343 deaths recorded since August 2018, the outbreak is the second largest ever after the massive epidemic that struck West Africa 5 years ago and killed more than 11,000. Conflict has smoldered for years in North Kivu, an anti-government stronghold, and some at-risk areas are inaccessible because they are controlled by armed rebels or can't be reached by road or rail. The outbreak has already reached several urban centers, including Butembo, a city of almost 700,000. An experimental vaccine developed by Merck and

Downloaded from http://science.sciencemag.org/ on January 17, 2019

Published by AAAS

given to nearly 60,000 people so far has likely slowed the virus but hasn't stopped it.

In West Africa, fear kept people away from clinics, causing Ebola cases, as well as diseases such as measles and malaria to go untreated. Mistrust of governments and aid workers ran high and rumors were rife.

That's even more true in the DRC now. In September 2018, an opposition politician, Crispin Mbindule Mitono, claimed on local radio that a government lab had manufactured the Ebola virus "to exterminate the population of Beni," a city that was one of the earliest foci of the outbreak. Another rumor has it that the Merck vaccine renders its recipients sterile. On 26 December, the national election commission decided to exclude Beni and Butembo from the polls because of the epidemic; the following day, an Ebola evaluation center was attacked during protests.

Although opposition organizations condemned the commission's decision, they called for the Ebola response to be protected—which health workers saw as a small but significant victory. "We've managed to get communities to separate in their minds Ebola control from the broader political agenda," says Michael Ryan of the World Health Organization in Geneva, Switzerland. "That's been really helpful." Ryan hands much of the credit to social scientists working for the various agencies involved in the response. Along with community engagement workers, they make up one-third of the workforce.

Part of their role is to chart the social networks through which the virus spreads, but they also gather information about communities' perceptions, which is entered within days into an online "dashboard" created by the International Federation of Red Cross and Red Crescent Societies (IFRC) in Geneva. The government has also recruited young people to report misinformation circulating on WhatsApp, a major information channel in the DRC, says Jessica Ilunga, a spokesperson for the health ministry.

As rumors surface, communications experts rebut them with accurate information via WhatsApp or local radio. They take care not to repeat the misinformation; research has shown this is the best way to help the public "forget" false news and reinforce the truth. The vocal support of Ebola survivors has helped as well. Grateful for their care, some have become volunteers at Ebola treatment centers (ETCs).

So far, the responders believe they are winning the information war. People who might be ill are now far more willing to accept a referral to an ETC than early in the epidemic, says IFRC's Ombretta Baggio.

The CUBE, used for the first time in this outbreak, is also a big help, says Tajudeen Oyewale, UNICEF's deputy representative in the DRC. In the past, visitors were kept at a safe distance from patients at ETCs or not permitted at all. Designed by a Senegal-based organization called ALIMA, the CUBE, with its transparent walls and external arm entries—like those in a laboratory glove box—allows patients and their relatives to see and speak to each other up close. The €15,000, reusable units also improve care, because health workers don't need to wear cumbersome protective gear that limits their movements and can only be worn for a short time.

Organized tours of the ETCs for members of the local community have helped, too, as have creches for the children of sick mothers, located close to the centers. Ambulances in North Kivu no longer use sirens when transporting suspected Ebola patients, as the sound was judged stigmatizing in West Africa.

> ***"I usually tell my teams that we fight two outbreaks, Ebola and fear."***
>
> **Carlos Navarro Colorado**, UNICEF

Burial practices keep evolving as well. In early Ebola epidemics, victims were often buried unceremoniously, sealed in opaque body bags, with no opportunity for relatives and friends to say farewell. That bred resentment and stoked rumors about corpses being stolen to sell their organs. In "safe and dignified" burials, introduced in the West Africa epidemic, families are given more opportunities to spend time with the body. For the current epidemic, responders procured transparent body bags, allowing families to see their loved one until the coffin is closed.

"One of the starkest lessons we learned in West Africa is that we don't need to change everything about a traditional burial," says anthropologist Juliet Bedford, director of a consultancy called Anthrologica in Oxford, U.K. "We just need to make sure it is medically safe." Even touching the body is sometimes allowed, provided relatives wear protective clothing.

Contingency plans are in place in case of further unrest, and the partner agencies have bolstered preparedness in neighboring areas not yet touched by the epidemic. Ryan says the political problems may have an upside: "Communities that resist are energetic," he says. "If you can turn that negative energy into positive energy, then it becomes a force for good. You just have to know how to pick that lock." ■

Laura Spinney is a journalist based in Paris.

PLANETARY SCIENCE

Dueling spacecraft look deep into Saturn and Jupiter

NASA probes reveal surprising contrasts between two gas giants

By **Paul Voosen**

A clever use of radio signals from planetary spacecraft is allowing researchers to pierce the swirling clouds that hide the interiors of Jupiter and Saturn, where crushing pressure transforms matter into states unknown on Earth. The effort, led by Luciano Iess of Sapienza University in Rome, turned signals from two NASA probes, Cassini at Saturn and Juno at Jupiter, into probes of gravitational variations that originate deep inside these gas giants.

What the researchers have found is fueling a high-stakes game of compare and contrast. The results, published last year in *Nature* for Jupiter and this week in *Science* for Saturn, show that "the two planets are more complex than we thought," says Ravit Helled, a planetary scientist at the University of Zurich in Switzerland. "Giant planets are not simple balls of hydrogen and helium."

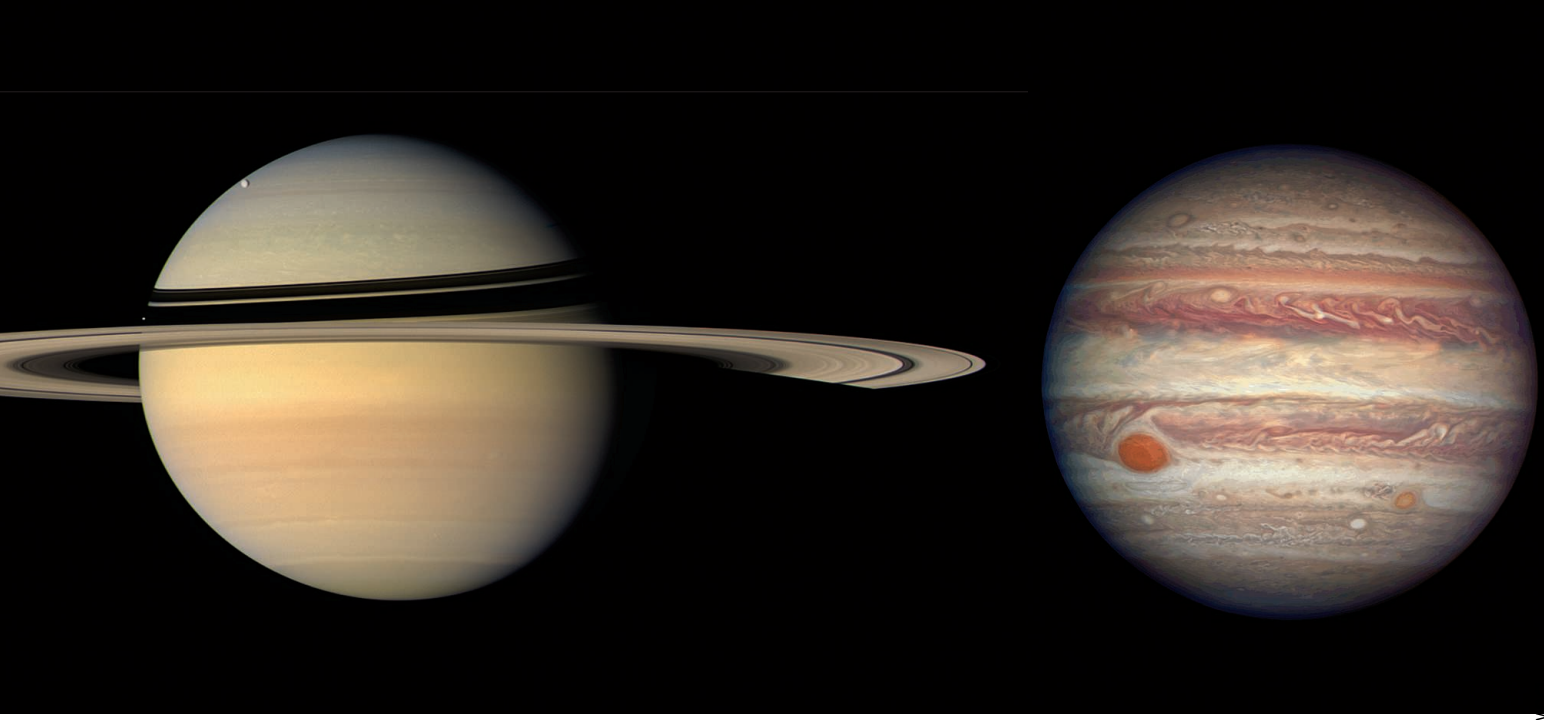
In the 1980s, Iess helped pioneer a radio instrument for Cassini that delivered an exceptionally clear signal because it worked in the Ka band, which is relatively free of noise from interplanetary plasma. By monitoring fluctuations in the signal, the team planned to search for gravitational waves from the cosmos and test general relativity during the spacecraft's journey to Saturn, which began in 1997. Iess's group put a similar device on Juno, which launched in 2011, but this time the aim was to study Jupiter's interior.

Juno skims close to Jupiter's surface every 53 days, and with each pass hidden influences inside the planet exert a minute pull on the spacecraft, resulting in tiny Doppler shifts in its radio signals. Initially,

PHOTOS: NASA/JPL/SPACE SCIENCE INSTITUTE

Downloaded from http://science.sciencemag.org/ on January 17, 2019

Published by AAAS



Material thousands of kilometers below the clouds of Jupiter and Saturn tugs subtly on orbiting spacecraft, revealing hidden structure and motions.

Iess and his team thought measuring those shifts wouldn't be feasible at Saturn because of the gravitational influence of its rings. But that obstacle disappeared earlier this decade, after the Cassini team decided to end the mission by sending the craft on a series of orbits, dubbed the Grand Finale, that dipped below the rings and eliminated their effects. As a result, Iess and colleagues could use radio fluctuations to map the shape of gravity fields at both planets, allowing them to infer the density and movements of material deep inside.

One goal was to probe the roots of the powerful winds that whip clouds on the gas giants into distinct horizontal bands. Scientists assumed the winds would either be shallow, like winds on Earth, or very deep, penetrating tens of thousands of kilometers into the planets, where extreme pressure is expected to rip the electrons from hydrogen, turning it into a metal-like conductor. The results for Jupiter were a puzzle: The 500-kilometer-per-hour winds aren't shallow, but they reach just 3000 kilometers into the planet, some 4% of its radius. Saturn then delivered a different mystery: Despite its smaller volume, its surface winds, which top out at 1800 kilometers per hour, go three times deeper, to at least 9000 kilometers. "Everybody was caught by surprise," Iess says.

Scientists think the explanation for both findings lies in the planets' deep magnetic fields. At pressures of about 100,000 times that of Earth's atmosphere—well short of those that create metallic hydrogen—hydrogen partially ionizes, turning it into a semiconductor. That allows the magnetic field to control the movement of the material, preventing it from crossing the field lines. "The magnetic field freezes the flow," and the planet becomes rigid, says Yohai Kaspi, a planetary scientist at the Weizmann Institute of Science in Rehovot, Israel, who worked with Iess. Jupiter has three times Saturn's mass, which causes a far more rapid increase in atmospheric pressure—about three times faster. "It's basically the same result," says Kaspi, but the rigidity sets in at a shallower depth.

The Juno and Cassini data yield only faint clues about greater depths. Scientists once believed the gas giants formed much like Earth, building up a rocky core before vacuuming gas from the protoplanetary disc. Such a stately process would have likely led to distinct layers, including a discrete core enriched in heavier elements. But Juno's measurements, interpreted through models, suggested Jupiter's core has only a fuzzy boundary, its heavy elements tapering off for up to half its radius. This suggests that rather than forming a rocky core and then adding gas, Jupiter might have taken shape from vaporized rock and gas right from the start, says Nadine Nettelmann, a planetary scientist at the University of Rostock in Germany.

The picture is still murkier for Saturn. Cassini data hint that its core could have a mass of some 15 to 18 times that of Earth, with a higher concentration of heavy elements than Jupiter's, which could suggest a clearer boundary. But that interpretation is tentative, says David Stevenson, a planetary scientist at the California Institute of Technology in Pasadena and a co-investigator on Juno. What's more, Cassini was tugged by something deep within Saturn that could not be explained by the winds, Iess says. "We call it the dark side of Saturn's gravity." Whatever is causing this tug, Stevenson adds, it's not found on Jupiter. "It is a major result. I don't think we understand it yet."

Because Cassini's mission ended with the Grand Finale, which culminated with the probe's destruction in Saturn's atmosphere, "There's not going to be a better measurement anytime soon," says Chris Mankovich, a planetary scientist at the University of California, Santa Cruz. But although the rings complicated the gravity measurements, they also offer an opportunity. For some unknown reason—perhaps its winds, perhaps the pull of its many moons—Saturn vibrates. The gravitational influence of those oscillations minutely warps the shape of its rings into a pattern like the spiraling arms of a galaxy. The result is a visible record of the vibrations, like the trace on a seismograph, which scientists can decipher to plumb the planet. Mankovich says it's clear that some of these vibrations reach the deep interior, and he has already used "ring seismology" to estimate how fast Saturn's interior rotates.

Cassini's last gift may be to show how fortunate scientists are to have the rings as probes. Data from the spacecraft's final orbits enabled Iess's team to show the rings are low in mass, which means they must be young, as little as 10 million years old—otherwise, encroaching interplanetary soot would have darkened them (*Science*, 22 December 2017, p. 1513). They continue to rain material onto Saturn, the Cassini team has found, which could one day lead to their demise. But for now they stand brilliant against the gas giant, with more stories to tell. ■

Downloaded from http://science.sciencemag.org/ on January 21, 2019

Published by AAAS



Furloughed from his work on rocket tests, NASA contractor Jack Lyons spends time in his workshop making props for marching bands.

PHOTO: AP PHOTO/DAVID GOLDMAN

U.S. RESEARCH FUNDING

Pain spreads from shutdown

Historic spending impasse halts paychecks and projects

By **David Malakoff**

No paychecks. No experiments. No reviews of grant applications. And no stink bugs by mail. The financial, empirical, and entomological consequences of the partial shutdown of the U.S. government for science multiplied this week, as it became the longest such closure in history. More than a half-dozen agencies that fund or conduct research, including NASA, the National Science Foundation (NSF), the U.S. Department of Agriculture (USDA), and the Food and Drug Administration (FDA), have been partly paralyzed since 22 December 2018 (*Science*, 11 January, p. 109). As *Science* went to press, the fight between Congress and President Donald Trump over spending $5.7 billion on a border wall, which has shuttered about one-quarter of the federal government, showed no signs of being resolved.

The impasse has already meant a lost paycheck for some 800,000 federal employees, as well as missed payments for thousands more contractors and academic researchers. Agencies have canceled dozens of meetings to review thousands of funding proposals, at one of the busiest times for federal grantmaking. Researchers inside and outside of government have postponed, restructured, or just given up entirely on planned studies.

The shutdown could soon paralyze federally funded scientific facilities and research centers that have been largely insulated from the pain because they are operated by contractors who get paid in advance, often on a quarterly basis. "But now that quarterly check may or may not be coming," says Benjamin Corb, public affairs director at the American Society for Biochemistry and Molecular Biology in Rockville, Maryland. "The uncertainty is creating a real mess."

At the National Center for Atmospheric Research in Boulder, Colorado, which is funded by NSF but operated by a consortium of universities, managers are beginning to consider ways to scale back activities. Staff could be given the option of being furloughed without pay or continuing to work at reduced pay (with back pay once the shutdown ends). That could disrupt efforts to improve climate models and manage massive data sets, officials say.

NSF's closure is also creating anxiety for would-be graduate students hoping to win a prestigious Graduate Research Fellowship (GRF) from NSF. Last year, the agency received more than 12,000 GRF applications and gave out 2000 awards, which provide graduate students with a $34,000 annual stipend for 3 years. Managing that massive operation requires sticking to a tight schedule. Some 2000 reviewers had already agreed to serve on about four dozen virtual panels set for later this month. But if NSF remains closed, those panels will not be able to meet. (The agency had already canceled 33 other proposal review meetings as of 14 January, according to Corb.)

NSF typically announces GRF winners by the beginning of April because U.S. graduate schools require accepted students to make a firm decision by 15 April. So far, the agency has no contingency plan in case its review process is delayed. "Nobody knows what will happen because there's been no guidance," says a former GRF program manager who requested anonymity.

At FDA, reviews of submitted drugs and devices already paid for by industry fees can continue. But some researchers who want to continue other work—developing new tools or methods for evaluating drugs, for example—must show that it is essential for health, safety, or protecting a federal investment (such as continuing an animal experiment that has already begun). The justification process is "a heavily scrutinized rigmarole," says one FDA employee who asked to remain anonymous.

Agricultural research is taking a particularly heavy hit because it often involves collaborations between federal and private or academic laboratories. At the Virginia Polytechnic Institute and State University in Blacksburg, veterinary pathologist Kevin Lahmers has had to halt studies aimed at evaluating the livestock disease threat posed by the Asian longhorned tick, first discovered in the United States in 2017, because he is collaborating with a shuttered USDA laboratory in Pullman, Washington.

Entomologist Don Weber, who works on biocontrol agents at USDA's Beltsville Agricultural Research Center in Maryland, isn't completely immobilized. He is allowed to enter his lab a few times a week to maintain insect and plant populations. But he can't do studies. Nor can he mail invasive stink bugs from his colonies to other researchers who want them, hobbling efforts to find a defense against the farm pest. And Weber hasn't been able to order a synthesized chemical that is key to an upcoming project because his contract office is closed. "I'm going to lose a field season," he predicts.

Weber hasn't let past closures derail his research. During a 16-day funding impasse in 2013, he went ahead and collected the final data in a long-term field study "in defiance of the shutdown," he acknowledged in a 2014 paper. "The way I saw it," Weber says now, "collecting that data was essential to protecting a federal investment. Otherwise, the money that had been spent would have gone to waste." ■

With reporting by Jeffrey Mervis and Kelly Servick.

Downloaded from http://science.sciencemag.org/ on January 18, 2019

Published by AAAS

OCEANS

Flotilla launches large survey of Antarctic krill

Health of stock is critical to fishery—and to predators

By **Erik Stokstad**

Krill, crustaceans smaller than a cigarette, play an outsize role in the ecology of the ocean around Antarctica: Penguins, whales, and other predators feast on vast swarms of the shrimplike animals. Now, researchers have launched a broad international survey of krill's main habitat in and around the Scotia Sea—the first in nearly 20 years—to learn whether a growing fishing industry is leaving enough for krill's natural predators.



Krill feed on phytoplankton and are a critical part of the food web.

The effort, led by the Institute of Marine Research (IMR) in Bergen, Norway, began in earnest last week when Norway's new polar research vessel *Kronprins Haakon* sailed from Punta Arenas, Chile, for the Scotia Sea. It and five other vessels will spend nearly 2 months mapping krill abundance across an area about the size of Mexico. Beside gauging population, the project will test tools for cheaper, more frequent surveys that could improve oversight of the fishery. "With a more dynamic management system, we can be more certain that the fishery is not negatively affecting the krill populations or the predators," says Bjørn Krafft, a marine biologist at IMR who is directing the $5 million Norwegian cruise.

Soviet vessels were the first to ply the Southern Ocean for krill, which was ground into fish meal. By the 1980s, scientists began to worry about the effect on krill-feeding predators. The Convention for the Conservation of Antarctic Marine Living Resources (CCAMLR), a treaty organization established in 1982, set tight limits on fishing, now at 620,000 tons per year. Most fishing stopped after the 1991 collapse of the Soviet Union, but it has been slowly growing again. Norway takes about half the current catch, extracting omega-3 fatty acids for nutritional supplements. "We absolutely need to know whether the catch limit is still precautionary," says Simeon Hill, an ecologist with the British Antarctic Survey in Cambridge, who is not involved in the project.

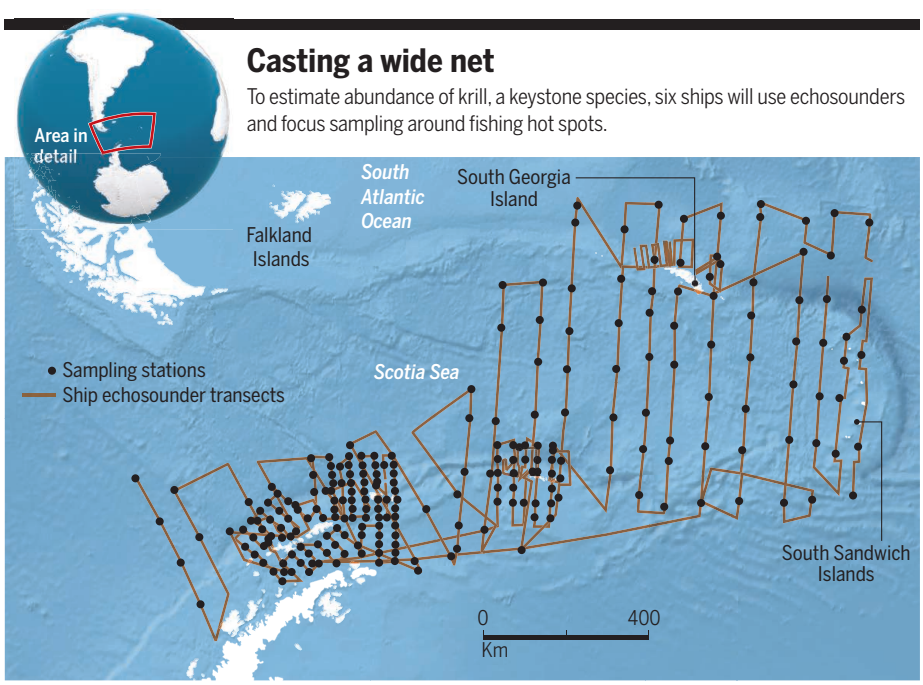
CCAMLR organized the previous large krill survey, in 2000. The central finding—about 60 million tons of krill in the Scotia Sea—reassured managers that they had been adequately conservative. But much smaller surveys, conducted annually in a few places, have shown that regional krill populations go through boom and bust cycles, making it harder to gauge the health of the overall stock from a single survey. "We have pieces, but we are missing the big picture," says marine biologist Rodolfo Werner, an adviser to the Pew Charitable Trusts and the Antarctic and Southern Ocean Coalition, who is based in Bariloche, Argentina.

During the survey, vessels will retrace the previous transects, measuring krill swarms with echosounders, a kind of sonar, and confirming the identification with sampling trawls. Some ships will measure oceanographic variables as well, such as temperature, currents, and plankton, to see whether they can be used to predict krill abundance.

IMR will also test remote devices that could gather krill data continuously and more cheaply. The *Haakon* will deploy moored sensors, as well as wave gliders and a sail-propelled buoy, in order to compare their readings with the net and echosounder data. "This is one of the most beneficial parts of the survey," says Bettina Meyer, a krill ecophysiologist at the Alfred Wegener Institute in Bremerhaven, Germany.

At the same time, land-based teams from IMR and the Norwegian Polar Institute will track seals, whales, and penguins foraging for krill in the Bransfield Strait, an important feeding ground near the Antarctic Peninsula. Matching their feeding behavior with survey results "has big potential to get a better idea of the interactions between the krill fisheries and the predators," says So Kawaguchi, a marine ecologist with the Australian Antarctic Division in Kingston.

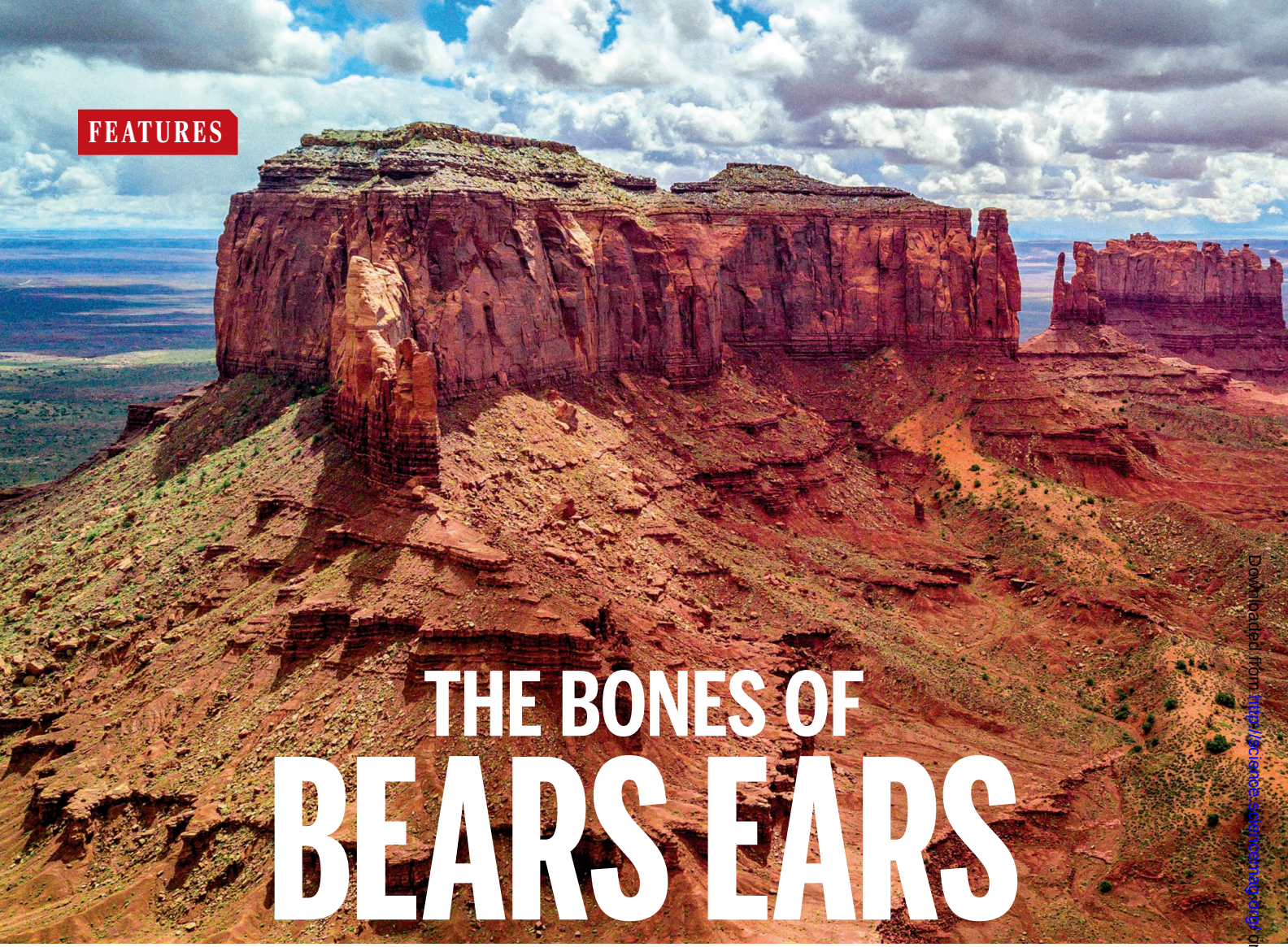
The survey itself won't be able to reveal how the overall krill population in the Scotia Sea might have changed since the 2000 survey, given the variability of krill populations over space and time. Finding out what drives population changes will require more research on the seasonal movement of krill, for example, and the impact of climate change. Loss of sea ice, which protects young krill from predators, is expected to reduce their abundance, and rising water temperatures and acidification could also pose serious threats—ones that even the best management plan might not avert. ■



CREDITS: (PHOTO) AUSCAPE INTERNATIONAL PTY LTD/ALAMY STOCK PHOTO; (MAP) A. CUADRA/*SCIENCE*; (DATA) INSTITUTE OF MARINE RESEARCH

Downloaded from http://science.sciencemag.org/ on January 17, 2019

Published by AAAS



THE BONES OF BEARS EARS

Paleontologists struggle to protect sites that could rewrite Earth's history

By **April Reese**, *at Bears Ears National Monument in Utah*

On a rise with a sweeping view of the Indian Creek valley in southern Utah, skirts of red earth unfurling for kilometers in all directions, Adam Huttenlocker crouches to examine a knee-high nub of Cedar Mesa sandstone. Embedded in the rock is an ivory oval with a smoky center. The paleontologist, from the University of Southern California in Los Angeles, leans in for a closer look. Other researchers gather round, and soon they identify the mysterious eyelike fragment: It is a cross section of limb bone, probably from a synapsid—the group of reptiles that gave rise to mammals—that lived here more than 300 million years ago.

Thousands of such rare fossils pepper Bears Ears, a sweep of buttes and badlands whose candy-striped sedimentary rocks catalog hundreds of millions of years of Earth's history. The region's rich paleontological and archaeological record—and the lobbying of southwestern tribes whose ancestors lived here—persuaded former President Barack Obama to designate the area a national monument just over 2 years ago, in the waning days of his administration.



Looters stole—but later returned—this snout from a fossilized phytosaur, a crocodilelike creature that once roamed Bears Ears.

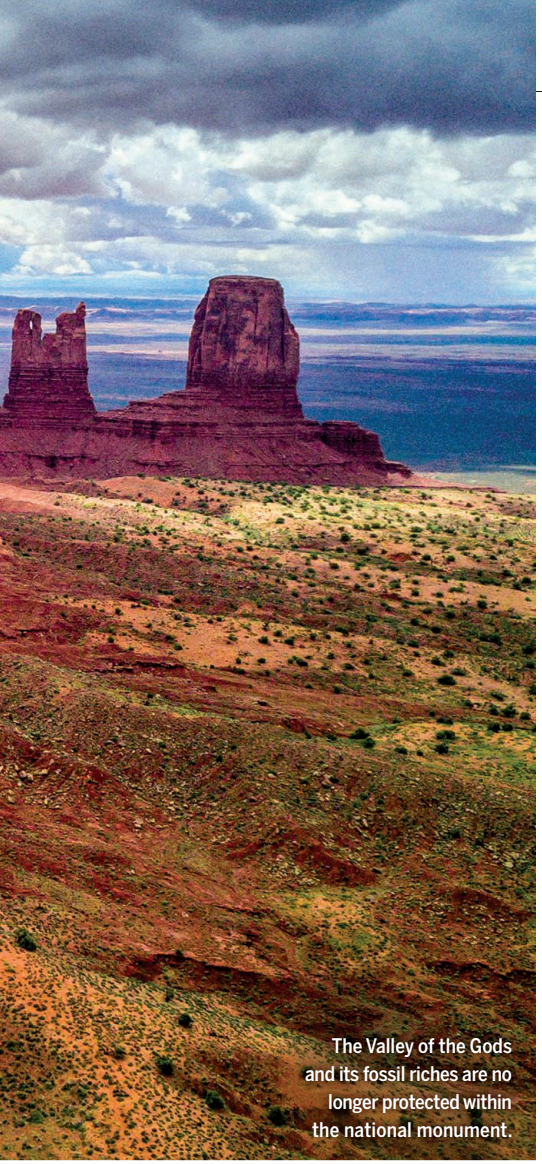
Now, those fossils, and the influx of special research funding that came with the designation, are under threat. In December 2017, urged on by Utah officials, President Donald Trump slashed the size of the 547,000-hectare monument by 85%, leaving just 82,000 hectares split into two separate units. Since Trump's order took effect in February 2018, the excised lands, which hold thousands of Native American artifacts and sites—and possibly the world's densest cache of fossils from the Triassic period, roughly 250 million to 200 million years ago—are open again to mining, expanded grazing, and cross-country trekking by off-road vehicles.

That prospect spurred the typically apolitical Society of Vertebrate Paleontology (SVP), based in Bethesda, Maryland, to sue the Trump administration in federal court, joining archaeologists, environmentalists, outdoor companies, and five Native Ameri-

PHOTOS: (TOP TO BOTTOM) CAVAN SOCIAL/ALAMY STOCK PHOTO; JENNIFER DICKSON/THE WILDERNESS SOCIETY

Downloaded from http://science.sciencemag.org/ on January 17, 2019

Published by AAAS



The Valley of the Gods and its fossil riches are no longer protected within the national monument.

can tribes. Their argument: The 1906 Antiquities Act used to create Bears Ears only allows presidents to establish monuments—not to drastically reduce them. The cutbacks represent an "extreme overreach of authority," SVP said in announcing the lawsuit just days after Trump's move. If SVP wins, the ruling could set a precedent that would help safeguard the boundaries of the 158 national monuments created under presidential authority; if it loses, future presidents could gain new powers to downsize them.

At Bears Ears, the potential loss to science—and society—is sizable, says former SVP President David Polly, a paleontologist at Indiana University in Bloomington. Fossils here chronicle major events that remade the world—from the evolution of early life on land 340 million years ago to the shift in climate at the end of the last ice age that ushered in the era of human civilization.

"It's a landscape of stories," says Rob Gay, a paleontologist and education director with the Colorado Canyons Association in Grand Junction, who has studied the Bears Ears area for more than a decade and was among the first paleontologists to push for monument designation. Without protection, he says, "our knowledge of our planet [will be] diminished forever."

FOR A LESSON in how monument status can pay off for paleontology, Gay motions toward Grand Staircase-Escalante National Monument, 228 kilometers away across the mesas and canyons of southern Utah. A similarly rich fossil trove, from the era when dinosaurs ruled, helped make the case for that monument, which was established by then-President Bill Clinton in 1996 and cut in half by Trump in another December 2017 proclamation. An influx of federal funding followed, which Polly credits with allowing researchers to uncover some of the world's best records of the Late Cretaceous.

Within 10 years, researchers had discovered fossils from 25 taxa new to science and documented the rise of flowering plants, insects, and the ancestors of mammals between 145 million and 66 million years ago. "It was essentially the origin of modern ecosystems happening in the Cretaceous before the extinction of the dinosaurs," Polly says. "And I think it is safe to say that we wouldn't have that concept if it hadn't been for the research at Grand Staircase." He estimates that 40% to 50% of SVP members have used data from Grand Staircase-Escalante studies, and another 10% have conducted research there themselves.

"Bears Ears is sort of like what Grand Staircase was at one time—there were a few sites known [when the monument was created] and clearly a lot of potential," he adds.

Bears Ears's record begins earlier, more than 340 million years ago, when the supercontinent Pangaea spanned much of the planet. A tropical sea that covered the area began to fill with sediment shed by the uplifting Rocky Mountains, leaving thousands of prehistoric sea creatures, mammallike reptiles, and dinosaurs entombed in hardened mudflats. Some of those fossils help tell the story of the "great dying" 252 million years ago, which killed 96% of marine species and 70% of terrestrial ones, clearing the way for dinosaurs. Others chronicle the End Triassic extinction some 50 million years later, which wiped out 76% of terrestrial and marine life.

Amid the red-rock spires of the Valley of the Gods, for example, Huttenlocker and his team are uncovering a trove of 300-million-year-old fossils, including what may be the most complete skeleton of a sail-backed synapsid predator known as *Dimetrodon*. Meanwhile, with the help of high school students, Gay has discovered what could be the largest concentration of Triassic fossils in the United States—and possibly the world. Excavation has just begun, but already Gay and his team have found rare fossil fragments of four phytosaurs—6-meter-long crocodilelike creatures that roamed these lands 212 million years ago. Many other sites remain uninvestigated.

Early on, says paleontologist Allison Stegner of the University of Wisconsin in Madison, some locals skeptical of the monument came to share scientists' enthusiasm for the resources it aimed to protect. When the Bears Ears designation was first proposed, "people were excited to learn about what was in their area. [They] were totally unaware that southeastern Utah is a world-class destination for paleontology," says Stegner, who did local outreach for the Bureau of Land Management (BLM) while the monument was under consideration. But there was little money and staff to nurture the emerging goodwill, and the momentum was lost, she says. "Instead, what's happened is a lot of animosity toward the monument."

Many local and state officials were opposed to the monument from the start, viewing its land use restrictions as too stringent and its designation as an overreach of federal authority. Earlier this month, Trump acknowledged that Utah lawmakers influenced his decision to carve out large pieces of the monument, saying he did it for Senator Mike Lee (R) and a "very special person," now-retired Senator Orrin Hatch (R).

Mining companies, eyeing the area's rich uranium deposits, also sought the rollback. The low price of uranium is likely to keep companies from starting new digs anytime soon, says David Talbot, a uranium and battery metals analyst with Eight Capital in Toronto, Canada. But if the price does spike—it has been on the rise for 2 years—that could change. (Under a September 2018 court ruling, however, BLM must notify the plaintiffs before approving any new development on the former monument lands.)

Now that the boundaries have been redrawn, the Valley of the Gods and much of the area where Gay's Triassic cache lies are outside the monument, as is the Indian Creek bone bed where Huttenlocker spotted the watchful eye. "As far as we can tell, [the administration] gave no consideration to the vertebrate fossil sites when redrawing the new boundaries," Huttenlocker says. The two units that remain include important paleontological and cultural sites, such as a bed of more than 250 dinosaur tracks and ancient Puebloan rock art in Shay Canyon. But most of Bears Ears's richest paleontological treasures are now on the outside, Gay says.

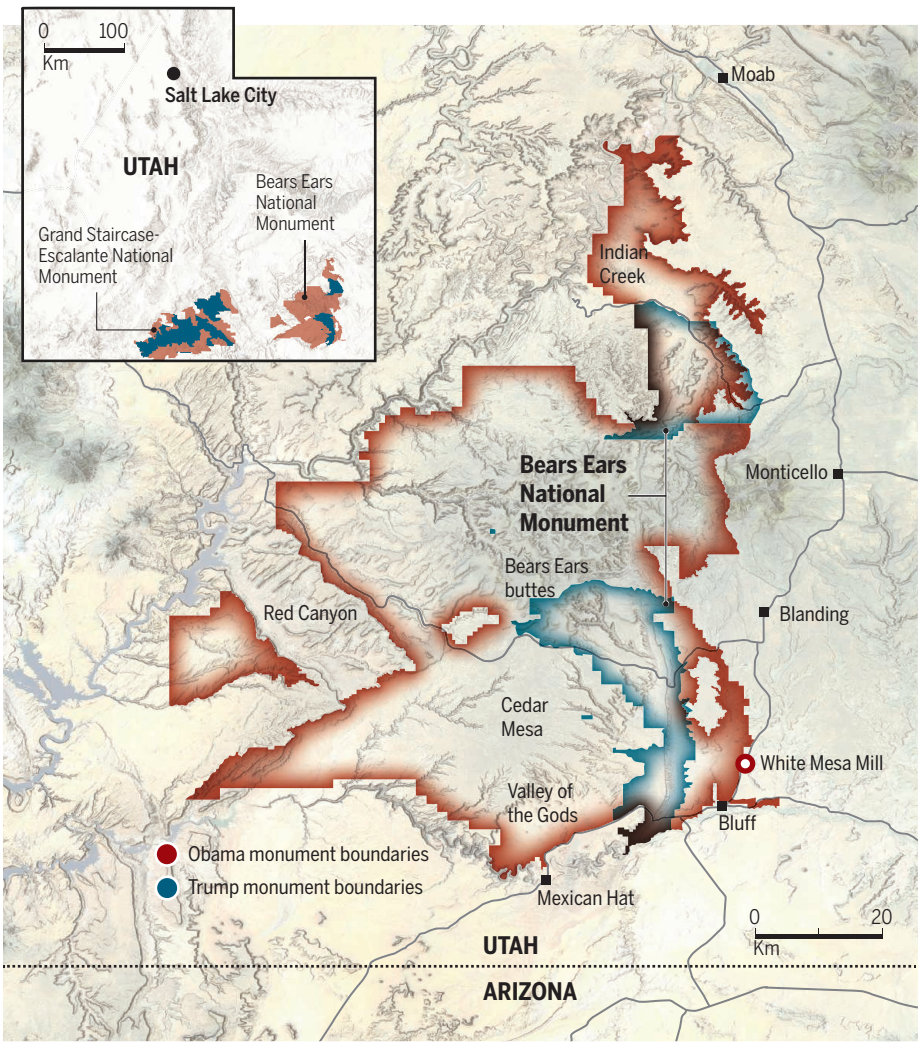
The loss of monument status means those treasures could be exposed to many dangers. Off-road vehicles are now allowed to crisscross the monument's former

Downloaded from http://science.sciencemag.org/ on January 17, 2019

Published by AAAS

Monumental reversal

In December 2017, President Donald Trump issued proclamations shrinking Bears Ears National Monument by 85% and nearby Grand Staircase-Escalante National Monument by nearly half, leaving out fossil-rich areas such as the Valley of the Gods and the northern portion of Indian Creek.



grounds, which are once again open to mining (although new projects must go through BLM's usual review process). The land will also lose out on resources aimed at beefing up research, such as personnel—Grand Staircase got its own paleontologist, for example—and special funding to develop scientific and cultural resources.

That money—part of federal funding for BLM lands protected for their scientific resources—not only funds ongoing projects and spurs new discoveries; it also helps ensure that scientists find those resources before looters do. Looting has long been a problem in San Juan County, where the monument is located. When Gay and his students found the phytosaur cache in 2016, for example, a snout from one of the creatures was missing. It was eventually returned, but looters rarely repent, Gay says. Without the protection and increased attention from BLM officials, he fears the excised areas are more vulnerable to pillaging.

Scientists will also have to compete with law-abiding private fossil collectors. The 2009 Paleontological Resources Preservation Act makes removing vertebrate fossils from federal lands a crime for nonscientists. But the rules are different for plant and invertebrate fossils, which are crucial to understanding ancient ecosystems and evolution. Within a monument, those fossils, too, can be collected only by researchers, but outside monument boundaries, anyone can gather and sell them. "Without special protection, [the sites] are more vulnerable to vandalism, which they have suffered in the past, and [fossils] can be more easily sold away to private buyers or repurposed for other uses," Gay says.

BLM has long insisted that it does what's needed to protect scientific and cultural resources on public land. Its management plan for the newly shrunken monument is still under development, but in an August 2017 statement, BLM's Utah director, Ed Roberson, called Bears Ears a remarkable landscape and said the agency's preferred blueprint provides "maximum management flexibility while protecting Monument objects and resource values." But unlike the other three draft plans, one of which would "prioritize the protection of Monument objects and values over other resources," BLM's preferred plan emphasizes "multiple uses." (Because of the ongoing federal government shutdown, a BLM spokesperson could not respond to specific questions from *Science*.)

Research on the excised lands is now in limbo, and Gay, Huttenlocker, and other paleontologists are racing to do as much as they can before their monument-tied funding dries up. Only one round of Bears Ears funding was doled out before Trump's proclamation. BLM has agreed to let researchers finish their work under those grants, but when that money runs out, projects outside the new monument boundaries may be left without crucial federal support, Polly says. And although paleontologists can still get permits to investigate and dig for fossils on the former Bears Ears lands, the process won't be as easy as before, when science was a priority, Polly says. Now, paleontology is just one of many uses, competing with mining, off-roading, and grazing.

In comments submitted to BLM, SVP urged the agency to treat now-unprotected areas as though they still had monument protection, giving priority to science and conservation. SVP also recommended that the agency hire four paleontologists for the greater Bears Ears area and continue to support research there.

As BLM proceeds with its plans for the shrunken monument, SVP and the other plaintiffs are hoping for a swift victory. They've already notched one win—having the case heard in Washington, D.C., instead of Utah, which the administration considered more welcoming. They now await District Judge Tanya Chutkan's decision on a Department of Justice request to dismiss the lawsuit.

As the case wends its way through the courts, paleontologists are scrambling to unlock Bears Ears's secrets. In Los Angeles, Huttenlocker and his colleagues labor to piece together the story of their newly found *Dimetrodon*. In western Colorado, Gay is eager to return to his phytosaur site before looters do. Meanwhile, scientists hope the sacred twin buttes that gave Bears Ears its name will continue to guard its treasures. ■

April Reese is a freelance journalist based in Santa Fe.

CREDITS: (GRAPHIC) A. CUADRA/*SCIENCE*; (DATA) SOUTHERN UTAH WILDERNESS ALLIANCE

Downloaded from http://science.sciencemag.org/ on January 17, 2019

Published by AAAS





The normal compound fly eye (top) is marred by cell death in a strain (bottom) with a mutation causing amyotrophic lateral sclerosis.

PHOTOS: KIRSTIN MAULDING

THE BRAIN'S TRAFFIC PROBLEMS

Disrupted flow into and out of the nucleus may kill neurons

By **Elie Dolgin**

The compound eyes of the common fruit fly are normally brick red. But in neurologist Tom Lloyd's lab at Johns Hopkins University School of Medicine in Baltimore, Maryland, many of the fly eyes are pocked with white and black specks, a sign that neurons in each of their 800-odd eye units are shriveling away and dying.

Those flies have the genetic equivalent of amyotrophic lateral sclerosis (ALS), the debilitating neurodegenerative disorder also known as Lou Gehrig's disease, and their eyes offer a window into the soul of the disease process. By measuring the extent of damage to each insect's eyes, researchers can quickly gauge whether a drug, genetic modification, or some other therapeutic intervention helps stop neuronal loss.

Those eyes have also offered an answer to the central mystery of ALS: just what kills neurons—and, ultimately, the patient.

The flies carry a mutation found in about 40% of ALS patients who have a family history of the disease, and in about 10% of sporadic cases. The mutation, in a gene called *C9orf72*, consists of hundreds or thousands of extra copies of a short DNA sequence, just six bases long. They lead to unusually large strands of RNA that glom onto hundreds of proteins in the cell nucleus, putting them out of action. Some of those RNA-ensnared proteins, Lloyd and his Hopkins colleague Jeffrey Rothstein hypothesized, might hold the key to ALS.

Over many months, the researchers systematically studied the role of each protein by developing fly strains carrying both the ALS mutation and an incapacitated or hyperactive version of each protein's gene. One set of flies, bred to have elevated levels of a pro-

Downloaded from http://science.sciencemag.org/ on January 20, 2019

Published by AAAS

tein called RanGAP, stood out. Fifteen days after the flies emerged from their pupal casings, their eyes remained a pure burnt sienna. RanGAP "was by far the most potent suppressor of neurodegeneration," Lloyd says. What was known about its function was tantalizing: It serves as a courier, helping shuttle other proteins across the membrane that divides the cell nucleus from the cytoplasm.

The team's result would upend neuroscientists' understanding of ALS and brain disease in general, and others were on the same trail. In 2015, two more research teams reported that defects in the cell's nuclear transport system were hallmark features not only of ALS, but also of frontotemporal dementia (FTD), another progressive brain disease caused by *C9orf72* mutations. Scientists would soon link dysfunctional trafficking across the nuclear divide to other neurodegenerative diseases—Alzheimer's, Huntington, spinocerebellar ataxia—and even to normal aging. In all those ailments, the resulting abnormal pileups of proteins somehow become rogue neuronal killers.

"I often get queasy when someone makes a discovery and tries to explain the rest of the world with it," says Rothstein, a neurologist who directs the Johns Hopkins Brain Science Institute. But here, he says, it seems to be true.

The findings are not merely academic. They are inspiring therapeutic efforts to address the cause of general age-related neurodegeneration—a goal that has largely eluded drug developers. If the gradual loss of nucleocytoplasmic transport is a conserved feature of the aging brain, says Sami Barmada, a neurologist at the University of Michigan in Ann Arbor, preventing it "might be a really broad and effective therapy."

Several biotech companies have jumped on that idea, exploring it in animal models and planning the first human trials this year. Chief among them: Biogen in Cambridge, Massachusetts, which in 2018 bought the rights to develop a drug compound called KPT-350 that directly targets the nuclear transport pathway. The research underpinning that drug's action is brand new. But, "The biology is there," says Chris Henderson, head of neuromuscular and movement disorders research at Biogen. "Here's a drug with a body of rationale," he adds, "and we're optimistic about getting this into trials."

THE LIPID MEMBRANE that divides the DNA-packed nucleus from the rest of the cell is like an international border busy with two-way industrial traffic. DNA-binding proteins and other molecules are constantly flowing into the nucleus to help turn genes on and off, for example. The messenger RNAs produced by those genes stream the other way, into the cytoplasm to protein-assembly platforms. The cell must regulate that traffic through entry points known as nuclear pores. Choke off those portals and it stands to reason cells will suffer.

The first hints that disrupted nuclear transport might underpin ALS came in 2010, when researchers at King's College London, working with human nerve cancer cells, experimentally blocked the expression of proteins involved in the import business. The result was something also seen in cells from ALS patients: clumps of a protein called TDP-43 building up in the cytoplasm.

Few ALS researchers paid much attention to that early report. What might be gumming up the gears of the transport machinery in ALS patients wasn't clear, and the researchers couldn't say whether the buildup of TDP-43—a protein that normally binds both DNA and RNA inside the nucleus to regulate multiple steps in gene expression—was actually killing neurons or was just a consequence of a different toxic process. It would take another 5 years—and Lloyd's and Rothstein's study of the flies with telltale eyes—for ALS scientists to take nuclear transport more seriously.

The Hopkins team's result electrified colleagues in part because it had identified a transport protein, RanGAP, as key to neurodegeneration. The team showed in both the fly model of ALS and in cells from human patients that the lengthy RNA readouts produced by the mutant *C9orf72* gene seemed to stick to RanGAP near the nuclear pore and put the protein out of commission. The loss of functioning RanGAP spurred a backup of the nuclear import system, resulting in the cytoplasmic buildup of proteins such as TDP-43—cluttering a cell like bags of rotting trash during a garbage strike.

Just as galvanizing was the team's finding that a potential drug could preserve neuronal health, at least in the flies. "All of a sudden it threw a potential treatment approach into the ring," says Dorothee Dormann, a biochemist from Ludwig Maximilian University in Munich, Germany.

The team had no drug that could boost levels of RanGAP in the cytoplasm and restore enough inflow to rescue the eye neurons. But Lloyd reasoned that blocking outflow of TDP-43 and other nuclear proteins may have the same beneficial effect. An experimental compound called KPT-276 was known to selectively inhibit a key nuclear export protein called exportin 1 (XPO1). The approach was a hack of sorts, marrying two wrongs—defective inflow and outflow—to make a right, but it worked. When Lloyd gave KPT-276 to his ALS flies, their eyes remained pristine.

KPT IS THE experimental compound code used by Karyopharm Therapeutics, a small drug company in Newton, Massachusetts. Karyopharm formed in 2008 to develop XPO1 inhibitors for treating cancer, the idea

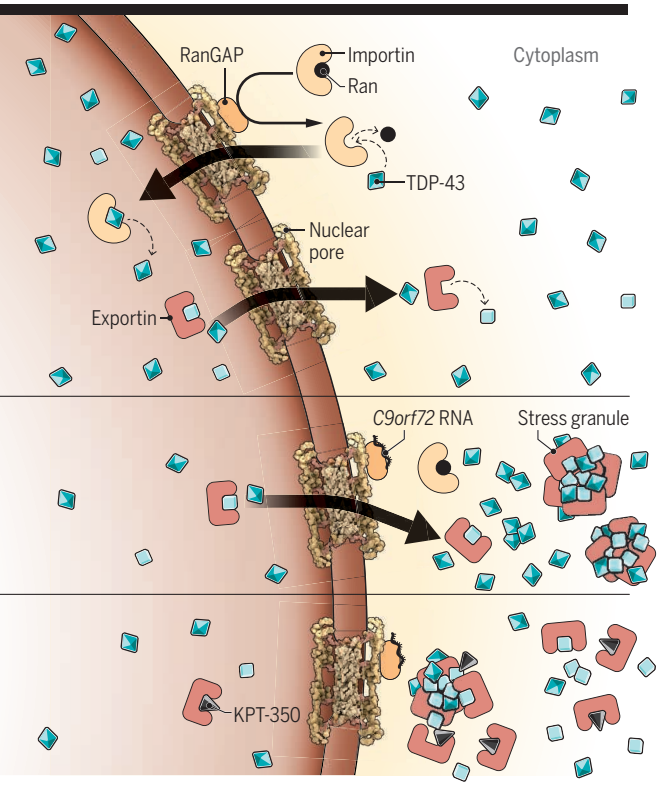
Fixing traffic jams

The flow of molecules through pores in the nucleus is key to the health of cells, particularly neurons. Traffic problems may contribute to amyotrophic lateral sclerosis (ALS) and other brain diseases.

Normal
Importin proteins bring TDP-43 and other cargo from the cytoplasm through the nuclear pore, whereas exportins take molecules out.

ALS
In some ALS cases, abnormal RNA made by a mutant *C9orf72* gene prevents RanGAP from mediating nuclear import, leading to protein buildup in stress granules.

ALS + drug
A possible drug, KPT-350, impairs the specific exportin XPO1 and may normalize nuclear traffic of proteins or bust up stress granules.



GRAPHIC: V. ALTOUNIAN/*SCIENCE*

Downloaded from http://science.sciencemag.org/ on January 20, 2019

Published by AAAS

being to trigger a buildup of tumor suppressor proteins in the nucleus, where they carry out their anticancer watchdog function. A decade on, the company's first clinical candidate, a drug for multiple myeloma, is widely expected to win marketing approval in the coming months.

Chemists at Karyopharm developed a suite of XPO1 inhibitors, including KPT-276 and a relative called KPT-350, that had an important attribute: They crossed the blood-brain barrier more readily than other candidates. KPT-350 proved more potent and less toxic in preclinical testing, so the firm looked for ways to use it to treat brain disease and injury.

Lloyd's and Rothstein's results piqued the company's interest. When Sharon Tamir, its head of neurodegenerative and infectious diseases at the time, learned that the Hopkins researchers were working with KPT-276 and not KPT-350, she called them up to propose a collaboration using the "better" compound. Meanwhile, she began to distribute KPT-350 to other groups in Japan, Belgium, and across the United States. Collectively, those scientists showed the drug's neuroprotective effects across a range of human cell, fly, and rodent models of ALS, Huntington, and other brain diseases.

For example, treatment with KPT-350 preserved the health of axons, the long, signal-transmitting extensions of nerve cells, and improved the motor functions of mice with a multiple sclerosis–like condition, a team led by neuroscientist Jeffery Haines at the Icahn School of Medicine at Mount Sinai in New York City showed. And in the Hopkins group's hands, the drug kept alive mouse neurons harboring the mutation associated with Huntington.

"There's still a lot that needs to be explored about why the nuclear pore complex is so susceptible to problems in different types of neurons in different brain regions causing multiple different diseases," says Gavin Daigle, a former postdoc in Rothstein's lab who worked on the Huntington project and helped link disrupted pore function to Alzheimer's disease before joining AbbVie in Cambridge. But he stresses that all the research is showing one thing: "This is a pathway that can be targeted."

The results proved enough to convince Biogen, which bought the rights to test the drug in humans. "The package of preclinical data that Karyopharm was able to amass really justifies the excitement," says Laura Fanning, R&D project leader for KPT-350 at Biogen (which has renamed the molecule BIIB100). "It's not just a blip of efficacy in one strain of mice. It's a broad base of evidence," she says. A first-in-human dose-escalation study of KPT-350 could begin in ALS patients later this year. If the drug shows promise against that disease, Biogen may expand its clinical testing to other conditions, Henderson says.

ALTHOUGH THE DRUG seems to work in the laboratory, why or how is not at all clear. "The story started to get murkier as more data has come in," notes Haines, now at Regeneron Pharmaceuticals in Tarrytown, New York. Initially, most scientists assumed that because it blocks XPO1, the drug prevents proteins such as TDP-43 from piling up in the cytoplasm by trapping them in the nucleus. But last year, Dormann's team and another led by Philip Thomas, a biochemist at the University of Texas Southwestern Medical Center in Dallas, independently reported that TDP-43 and another protein called FUS seem to exit the nucleus by passive diffusion, not through XPO1-mediated transport. (FUS also clumps in the cytoplasm of motor neurons in some patients with ALS or FTD.)

So if KPT-350 is not acting directly on the transport system, what is it doing? "It looks like the drug is targeting some more general neurotoxic pathway," Dormann says, "but it remains to be clarified what the mechanism really is and which nuclear transport defects we're correcting with this drug."

> ***"Here's a drug with a body of rationale, and we're optimistic about getting this into trials."***
> **Chris Henderson**, Biogen

One possibility, recent research suggests, is that the drug actually targets tiny, dense packets of protein and RNA that form during times of cellular stress. In healthy cells, those membraneless "stress granules" generally break down and their components disperse after a viral infection, thermal shock, or some other environmental insult has passed. Not so in the diseased neurons of people with ALS or FTD. In those cells, the stress granules persist and turn sticky, recruiting proteins such as TDP-43 and FUS and eventually transforming into solid, toxic aggregates.

Over the past year, several research teams have shown that components of the nuclear transport machinery—including importers, exporters, and parts of the nuclear pore itself—also can get tangled up in those aggregates. The transportation system falters, and as more TDP-43 and other proteins are added to the stress granules, a feedback loop takes hold that grinds the molecular traffic to a halt. "TDP-43 is not just a victim of nucleocytoplasmic transport defects," says Wilfried Rossoll, a neuroscientist at the Mayo Clinic in Jacksonville, Florida. "It's also a perpetrator."

In August 2018, findings from a study led by neurobiologist Ludo Van Den Bosch of VIB–Catholic University of Leuven in Belgium suggested that the transport protein XPO1 itself may play a role in stress granules. That means a drug such as KPT-350 may serve primarily as a stress granule buster, and any impact on transport may be secondary. "Things are more complicated than initially presented," says Van Den Bosch, who has collaborated with Karyopharm.

The open questions about KPT-350 have not discouraged other groups from pursuing additional strategies to sort out nuclear traffic problems. In 2017, for example, Guillaume Hautbergue and his colleagues at the University of Sheffield in the United Kingdom implicated another export factor in the neuronal loss experienced by ALS flies with the *C9orf72* mutation. Hautbergue is working on ways to target that protein to prevent the export of mutant RNAs produced by the gene.

Other researchers are focusing on breaking up stress granules. That approach should free up transport factors and pore proteins held hostage in those granules, allowing them to return to their usual posts in the cell, explains James Shorter, a protein biochemist at the University of Pennsylvania. He is developing a way to equip cells with a gene for making a "disaggregase" protein and has begun to test the therapeutic strategy in a mouse model of ALS.

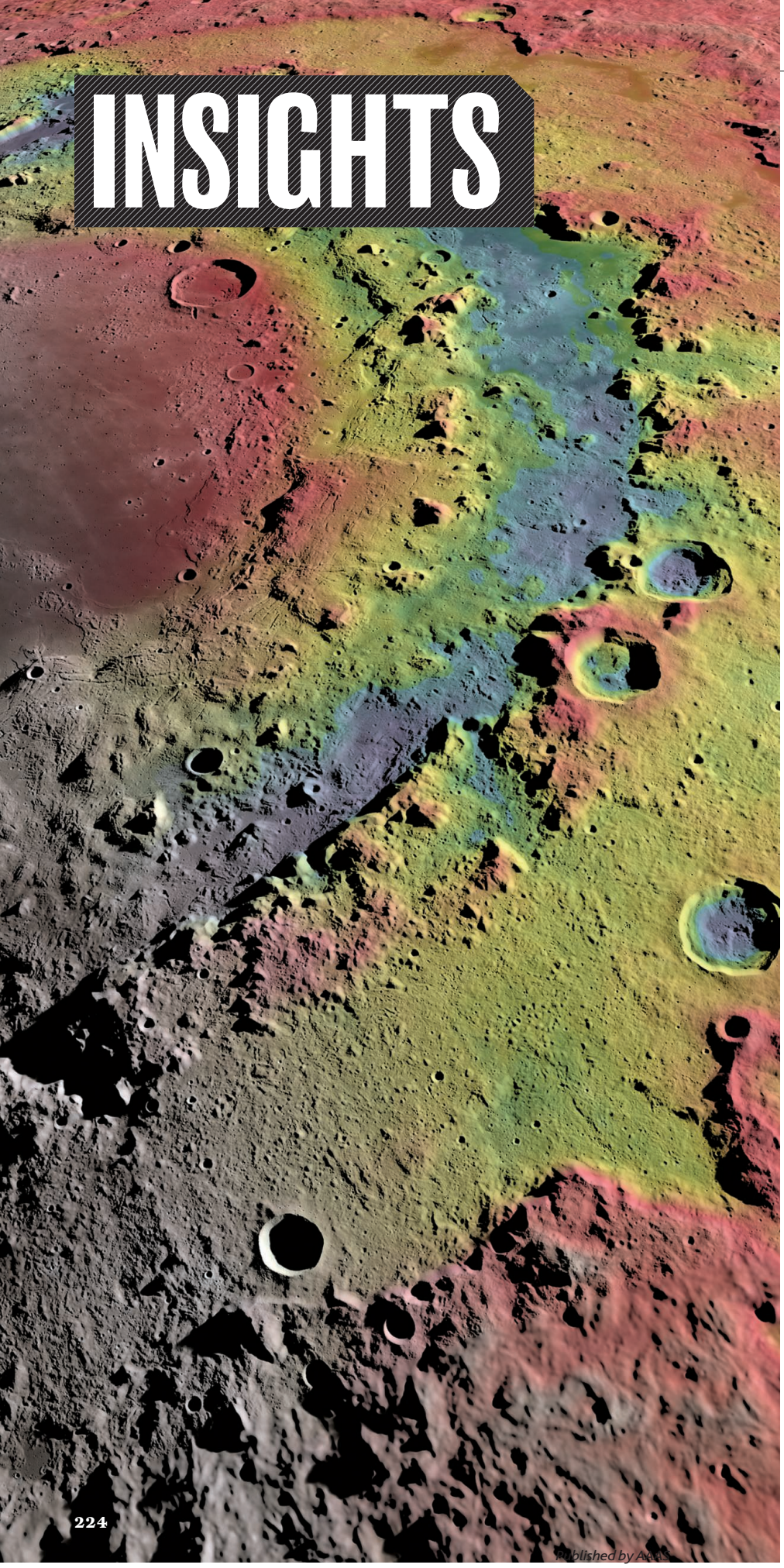
A few drug companies, including Denali Therapeutics of South San Francisco, California, and Aquinnah Pharmaceuticals of Cambridge, are looking for small molecules that can do basically the same thing. Those therapies may not directly target the nuclear transport pathway, but they would get the job done, says Aquinnah co-founder and Chief Scientific Officer Ben Wolozin, a neuropharmacologist at Boston University's School of Medicine, because dismantling stress granules helps restore healthy nuclear transport. "This is all part of an integrated biological response," Wolozin says.

Aquinnah hopes to begin to evaluate its lead compound in ALS patients this year, about the same time that Biogen is aiming to get KPT-350 into the clinic. For now, Biogen scientists are still trying to pin down what the drug is doing in various genetic models of the disease, including the flies with marred eyes. But to some extent, Henderson says, knowing the exact mechanism of action doesn't really matter. "The relevant experiment," he concludes, "is in the human patient." ■

Elie Dolgin is a science journalist based in Somerville, Massachusetts.

Downloaded from http://science.sciencemag.org/ on January 20, 2019

Published by AAAS



PLANETARY SCIENCE

When Earth got pummeled

The frequency of impacts on Earth's surface increased about 290 million years ago

By **Christian Koeberl**[1,2]

Collisions and impact processes have been important throughout the history of the solar system, including that of Earth. Small bodies in the early solar system, the planetesimals, grew through collisions, ultimately forming the planets. Recognizing the remnants of impact events on Earth is difficult because terrestrial processes either cover or erase the surface expression of impact structures in geologically short timespans. Because Earth and the Moon are subjected to the same flux of impactors, the latter's crater record serves as a proxy for that of Earth. On page 253 of this issue, Mazrouei *et al.* (*1*) report that infrared images of the Moon taken by the Lunar Reconnaissance Orbiter Diviner instrument can be used to estimate the ages of young lunar craters. They find the impact rate increased within the last ~500 million years.

Impact cratering is a high-energy event that occurs at more-or-less irregular intervals, although over long periods of time, an average cratering rate can be established (*2*). The terrestrial rock record, in the form of crustal rocks, extends back to only about 89% of Earth's history, to ~4.0 billion years ago, with the oldest rocks showing very limited exposures in Greenland and Canada. The importance of the process of impact cratering on a planetary scale has only recently been recognized in the geological sciences. During the past few decades, planetary scientists and astronomers have demonstrated, with the aid of many space missions, that the surfaces of Earth's moon, Mercury, Venus, Mars, the asteroids, and the moons of the outer gas planets are all covered (some surfaces to saturation) with meteorite impact craters.

Impact craters on the lunar surface persist over billions of years and help to constrain Earth's impact record. Orientale (shaded topographic map shown) is a large and relatively young impact basin on the Moon.

PHOTO: ERNEST WRIGHT, NASA/GSFC SCIENTIFIC VISUALIZATION STUDIO

Downloaded from http://science.sciencemag.org/ on January 17, 2019

Published by AAAS

Part of the problem regarding recognition of the remnants of impact events on Earth is that terrestrial processes, such as sedimentation, erosion, and plate tectonics, either cover or erase the surface expression of impact structures. Many impact structures are covered by younger (post-impact) sediments and are not visible on the surface. Others were mostly destroyed by erosion. To determine if specific rocks have been subjected to impact or not, it is necessary to identify criteria that allow such processes to be distinguished from those resulting from normal terrestrial geological processes. Most of the geological features of meteorite impact structures are not unique. Such features can be the product of conventional processes such as tectonic deformation, salt-dome formation, volcanic eruption, or internal igneous activity. Only the presence of diagnostic shock metamorphic effects and, in some cases, the discovery of meteorites, or traces thereof, provide unambiguous evidence for an impact origin (*3*). As of 2018, about 190 impact structures have been identified on Earth on the basis of these criteria. With one exception, all of these are younger than 2 billion years.

On some other planets and moons, the problem of geological processes destroying or obscuring the impact record is much less severe than on Earth. It has long been known that Earth's companion, the Moon, has been geologically mostly inactive on its surface for the past 3 billion years or so. This makes it an ideal canvas on which asteroids can leave their impact traces. Mazrouei *et al.* used Lunar Reconnaissance Orbiter data to derive the impact flux on the Moon for craters larger than about 10 km in diameter—and by proxy, also on Earth—during the past billion years. This was done by determining the ages of all lunar craters larger than 10 km using an inverse relationship between the absolute ages of craters and the "rockiness" of their ejecta, derived from the Lunar Reconnaissance Orbiter Diviner instrument. In previous studies, it was usually assumed that the paucity of craters on Earth is a direct result of the erosional and other geological forces that destroy or obscure such craters on Earth. Recently, an estimate of the number of impact craters that should be present at Earth's surface was reported (*4*). The study noted no evidence for any systematic incompleteness in the available inventory of the craters larger than about 6 km in diameter exposed at the surface but suggested that more than 90 craters with diameters ranging from 1 to 6 km have yet to be discovered, as well as more than 250 craters between 0.25 and 1 km in diameter. In the larger-size range (larger than a 6-km diameter), Mazrouei *et al.* now demonstrate that instead of an erosional bias for craters in the age range of about 650 to 290 million years ago, there is a lower-impact flux to be blamed, where the Snowball Earth ice ages (when Earth was entirely or nearly entirely frozen) might be responsible for erosion that destroyed any earlier craters. By contrast, a previous study suggested an increase in impact rate during the Phanerozoic period, 541 million years ago to the present (*5*).

This still leaves a large part of Earth's history lacking for impact structures. The early record of impact on Earth is rather limited and mostly circumstantial. Likely impact debris layers (ejecta layers) have been documented in 3.2- to 3.47-billion-year-old Archean successions in the Barberton Greenstone Belt (South Africa) and Pilbara Craton (Australia). The exact number of ejecta layers is not known, but several different events between 3.4 and 2.5 billion years ago, and at 2.1 to 1.8 billion years ago, have been identified (*6*).

"The early record of impact on Earth is rather limited and mostly circumstantial."

The oldest impact structure on Earth dates to 2.02 billion years ago (Vredefort in South Africa), and for the "next" billions of years the impact record on Earth is quite sparse in terms of both craters and ejecta layers. Thus, Earth's impact record is quite limited: nothing for the first billion years, then some ejecta layers until about 2.5 billion years ago, and then less than a handful of impact craters prior to about 750 million years ago. Nevertheless, the discovery of these ejecta layers aids in the discussion of the importance of impact events in Earth's early history. So, despite having a good explanation for why a single time window in Earth's history might have seen as many impacts as originally anticipated, the earlier (pre–600 million years ago) impact record on Earth, which spans most of the age of the planet, is still a wide open field of research. ■

[1]*Natural History Museum, Burgring 78, 1010 Vienna, Austria.* [2]*Department oif Lithospheric Research, University of Vienna, Althanstrasse 14, 1090 Vienna, Austria. Email: christian.koeberl@univie.ac.at*

REFERENCES

1. S. Mazrouei *et al.*, *Science* **363**, 253 (2019).
2. E. M. Shoemaker *et al.* in *Global Catastrophes in Earth History*, V. L. Sharpton, P. D. Ward, Eds. (Geological Society of America, Special Paper 247, 1990), pp. 155–170.
3. B. M. French, C. Koeberl, *Earth Sci. Rev.* **98**, 123 (2010).
4. S. Hergarten, T. Kenkmann, *Earth Planet. Sci. Lett.* **425**, 187 (2015).
5. E. M. Shoemaker, in *Meteorites: Flux with Time and Impact Effects*, M. M. Grady, R. Hutchison, G. J. H. McCall, D. A. Rothery, Eds. (Geological Society of London, Special Publication 140, 1998), pp. 7–10.
6. T. Schulz *et al.*, *Geochim. Cosmochim. Acta* **211**, 322 (2017).

10.1126/science.aav8480

INORGANIC CHEMISTRY

Iron hits the mark

Strongly electron-donating ligands enable nanosecond lifetimes of iron(III) photoexcited states

By **Elizabeth R. Young** *and* **Amanda Oldacre**

Solar energy can enable our society to thrive as we endeavor to reduce our dependence on fossil fuels. However, the Sun is an intermittent form of energy. Solar-cell technology is well suited for daytime electricity generation and usage, but our society uses energy around the clock. Thus, it is not only important to generate electricity for daytime use but also to store solar energy for nighttime use. Chemists see huge potential in molecules and materials that absorb light (that is, solar energy) and use that energy to generate electrons that then carry out chemical reactions to turn low-energy feedstocks into high-energy fuels. To date, the transition metal complex (TMC) photosensitzers that have sufficiently long excited-state lifetimes to enable this chemistry (*1*) contain expensive and scarce metals, such as complexes of ruthenium (Ru), osmium, and iridium. On page 249 of this issue, Kjær *et al.* (*2*) report an iron (Fe)–based photosensitizer with a quantum efficiency surpassing that of $[Ru(bpy)_3]^{2+}$ (where bpy is 2,2′-bipyridine), the historical standard bearer. Furthermore, the new iron-based photosensitizer has an excited-state lifetime of 2 ns, which is sufficiently long to transfer electrons to other compounds (see the figure).

Ruthenium-based TMCs have received much attention as photosensitizers because of their long-lived metal-to-ligand charge-transfer (MLCT) excited state and general photo- and chemical stability (*3*). Despite their superior performance, ruthenium-based TMCs are limited in their usefulness to society because ruthenium is rare and expensive. Not only is there not enough ruthenium to go around, even if there were, it is harmful to the environment. A search for alternative earth-abundant and less expensive metals has been pursued for the past several decades. Iron, being in the same group of the periodic table as ruthenium, shares certain similarities that

Department of Chemistry, Lehigh University, Bethlehem, PA 18015, USA. Email: ery317@lehigh.edu

Downloaded from http://science.sciencemag.org/ on January 17, 2019

Published by AAAS

make it a potentially attractive target metal for use in TMCs. Iron-based TMCs would have several advantages, such as earth-abundancy, low toxicity, and strongly absorbing charge-transfer (CT) excited states (*4*).

However, the photophysics of iron TMCs have made their solar-driven applications relatively rare (*5*). Molecular orbital ordering dictates the ability of TMC excited states to separate charge within the complex and maintain this separation long enough to carry out productive chemical reactions. Ruthenium(II)-based TMCs experience relatively large octahedral splitting that drives the e_g and t_{2g} metal-centered (MC) states of ruthenium(II)-based TMCs far enough apart that a ligand-centered (LC) state falls between them (*6*). This molecular orbital ordering generates a low-lying MLCT excited state that rapidly becomes populated upon photoexcitation of a ruthenium(II)-based TMC (*7*). By moving charge either away from or onto the ligands, the resulting excited state maintains the potential to drive a desired chemical reaction.

Iron(II)-based TMCs experience weak ligand-field splitting, such that the e_g state falls below the LC state. The excited state is a low-energy MC state that cannot be used to carry out productive chemistry. The development of iron(II)-based TMCs that have long-lived CT excited states has been tackled by inorganic chemists who have purposefully designed ligands to overcome this issue. During the past several years, Wärnmark and colleagues have developed iron TMCs containing strong σ-donor ligands based on *N*-heterocyclic carbenes (NHCs). These ligands destabilize the low-lying e_g MC state so that the MLCT excited state becomes the lowest-energy transition.

Further research by the Gros and Wärnmark groups provided critical insight into molecular design for iron(II)-based TMCs. In parallel, they reported on iron(II) NHC complexes with the longest triplet ^{3}MLCT lifetimes to that point, 16.5 and 18 ps, respectively (*8*, *9*). In 2017, Wärnmark and coworkers reported an all-NHC coordination iron(III) complex, $[Fe(btz)_3]^{3+}$, where btz is 3,3′-dimethyl-1,1′-*bis*(*p*-tolyl)-4,4′-*bis*(1,2,3-triazol-5-ylidene), that extended the CT lifetime to 100 ps (*10*).

Kjær *et al.* build off these previous successes using a two-pronged approach. First, they used an exceptionally strongly σ-donating ligand that is also negatively charged and enforces a near perfect octahedral coordination sphere in order to substantially destabilize the otherwise low-lying e_g MC state in the iron-containing complex (*7*), causing the LC state to become the lowest unoccupied molecular orbital. The switch in orbital ordering leads to a low-lying CT excited state that can be used to drive chemical reactions.

Second, the newly reported iron-based TMC contains iron(III) rather than iron(II). The iron(III)-TMC contains an unpaired electron in the t_{2g} ground state, so both the ground and ligand-to-metal charge transfer (LMCT) excited states are doublets. The advantages of the ^{2}LMCT excited state are twofold: There is no excited-state energy loss as a result of singlet-to-triplet conversion that is ubiquitous in many TMCs with singlet character, and the lower-lying MC scavenger states (^{4}MC and ^{6}MC) are less accessible than the scavenger states (^{3}MC and ^{5}MC) of the ^{3}MLCT formed in iron(II)-based TMCs, which reduces nonradiative losses.

For years, the goal of designing ligands for iron-based TMCs has been to separate charge in the excited state (forming LMCT or MLCT states) and to reduce the nonradiative decay through the MC scavenger states. This new ligand design hits both marks. Kjær *et al.* report that $[Fe(phtmeimb)_2]^+$ (where (phtmeimb)$^-$ is {phenyl[tris(3-methylimidazol-1ylidene)]borate}$^-$) has a record quantum yield of 2% {0.3% greater than the standard, $[Ru(bpy)_3]^{2+}$} and a lifetime of 2 ns. The tridentate, facial phtmeimb ligand provides the key design element, namely, large σ-donor ability, which is more pronounced because of the negative charge of the borate ligand.

The combination of time-correlated single-photon counting and transient absorption spectroscopy indicates that emission occurs from the ^{2}LMCT state. Furthermore, the $[Fe(phtmeimb)_2]^+$ complex is a strong photooxidant [a standard reduction potential $E°(III^*/II)$ = 1.0 V versus $Fc^{+/0}$, where Fc is ferrocenium] and photoreductant [$E°(IV/III^*)$ = −1.9 V versus $Fc^{+/0}$] and has been shown to act as a facile photoredox agent in two model reactions. With this demonstration, iron complexes can now feasibly be used as photosensitizers in energy-relevant small-molecule activations, such as water oxidation to produce hydrogen and reduction of carbon dioxide into chemical feedstocks. ■

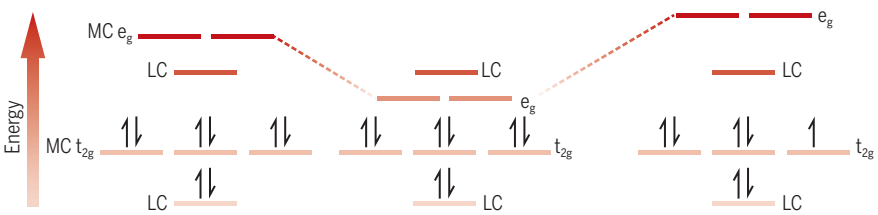
Iron complexes that stay excited

Most iron(II) complexes have short-lived, metal-centered (MC) photoexcited states that are unable to perform chemical reactions. A new iron(III) complex reported by Kjær *et al.* overcomes these limitations.

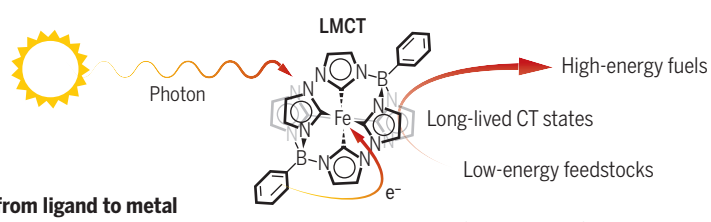
Typical ruthenium(II) complexes
The ligand-centered (LC) orbital lies below the e_g orbitals and receives photoexcited t_{2g} electrons.

Most iron(II) complexes
The LC orbital lies above the e_g orbitals, and excited t_{2g} electrons transfer quickly to the e_g orbitals.

An iron(III) complex
Strong σ-donor ligands drive the e_g orbital above the LC orbital. The stabilized iron(III) center yields a partially filled t_{2g} orbital to receive excited electrons from a lower lying LC state.



Achieving photoinduced electron transfer
Photoexcited electrons must transfer between LC and MC orbitals to generate charge-transfer (CT) excited states and survive long enough to drive subsequent chemical reactions.



Transfer from ligand to metal
In $[Fe(phtmeimb)_2]^+$, the photoexcited electrons transfer from a filled LC orbital to a MC t_{2g} orbital and have been shown to react with electron donors and acceptors in photoinitiated reactions.

REFERENCES

1. Y.-J. Yuan, Z.-T. Yu, D.-Q. Chen, Z.-G. Zou, *Chem. Soc. Rev.* **46**, 603 (2017).
2. K. S. Kjær *et al.*, *Science* **363**, 249 (2019).
3. D. W. Thompson, A. Ito, T. J. Meyer, *Pure Appl. Chem.* **85**, 1257 (2013).
4. B. Bozic-Weber, E. C. Constable, C. E. Housecroft, *Coord. Chem. Rev.* **257**, 3089 (2013).
5. Y. Liu, P. Persson, V. Sundström, K. Wärnmark, *Acc. Chem. Res.* **49**, 1477 (2016).
6. P. A. Scattergood, A. Sinopoli, P. I. P. Elliott, *Coord. Chem. Rev.* **350**, 136 (2017).
7. A. M. Brown, C. E. McCusker, J. K. McCusker, *Dalton Trans.* **43**, 17635 (2014).
8. T. Duchanois *et al.*, *Eur. J. Inorg. Chem.* **2015**, 2469 (2015).
9. T. C. B. Harlang *et al.*, *Nat. Chem.* **7**, 883 (2015).
10. P. Chábera *et al.*, *Nature* **543**, 695 (2017).

10.1126/science.aav9866

GRAPHIC: A. KITTERMAN/*SCIENCE*

Downloaded from http://science.sciencemag.org/ on January 17, 2019

Published by AAAS

MICROBIOLOGY

Microbial guardians of skin health

Skin microbes can promote skin immunity, repair, and antimicrobial defense

By **Apollo Stacy**[1,2,3] *and* **Yasmine Belkaid**[1,2]

Skin, our largest and outermost organ, faces numerous challenges, including wounds, infections, inflammatory disorders, and cancer. Fortunately, it does not meet these challenges alone. Our skin is home to complex microbial communities, the skin microbiota, that play a fundamental role in the protection and control of this barrier surface. Here, we focus on *Staphylococcus epidermidis* as a "poster child" of the skin microbiota to illustrate the remarkable diversity of functions a microbe can exert on skin physiology and health.

Some of the most abundant constituents of the skin microbiota are the coagulase-negative staphylococci, a group of bacteria that includes *S. epidermidis*. Although in the past these microbes were merely considered fast-growing "weeds" and potential pathogens, recent studies highlight that, analogous to the oft-studied gut microbiota, this group also assumes prominent roles in promoting tissue immunity, repair, and antimicrobial defense.

Of note, *S. epidermidis* is more than "one microbe." Individual strains vary dramatically in their genome content, functional potential, and relationship to the host immune system. Furthermore, the context in which *S. epidermidis* is sensed—for example, by intact or inflamed skin—can have a profound impact on interaction outcomes, explaining in part the diverse effects that it exerts on the host and on other microbes (*1*, *2*). These functions can be mediated by defined microbial features (see the figure), some of which are specific to *S. epidermidis* [for example, unique cell wall products (*2*)], whereas others are shared among many members of the skin microbiota [for example, the ability to produce antimicrobials (*3*) or the ability to colonize particular skin niches such as hair follicles (*4*)].

As a skin inhabitant, *S. epidermidis* lives in tight association with keratinocytes, the cells that constitute the top layer of this organ. Keratinocytes represent a first line of defense, yet it remains poorly understood how they peacefully coexist with the skin microbiota. Because unchecked immune tolerance to the skin microbiota could lead to microbial overgrowth, keratinocytes have likely co-opted products of microbial metabolism as cues to curb its proliferation. Short-chain fatty acids (SCFAs) are released by *S. epidermidis* and other skin microbes as metabolic waste. As such, SCFAs serve as effective proxies for the quantity of microbiota, and hence its potential threat to skin integrity. For instance, the SCFAs propionate and valerate inhibit the activity of histone deacetylases (HDACs) in keratinocytes. This promotes gene expression and thereby enables higher keratinocyte production of proinflammatory cytokines (*5*). Thus, the metabolic activity of the skin microbiota may calibrate the activation status of keratinocytes toward either tolerance or inflammation.

In the context of tissue damage, the dialog between the skin microbiota and keratinocytes is shaped by microbial products. Certain cell wall products are sensed by the host through dedicated receptors, such as Toll-like receptors (TLRs). In most host cells, microbial cell wall products trigger inflammation, but in keratinocytes, *S. epidermidis* TLR2 signaling can, in some contexts, dampen inflammation processes (*2*, *6*). This response benefits not only *S. epidermidis*, by ensuring its stable colonization on skin, but also the host in contexts where excess inflammation is deleterious. For instance, *S. epidermidis* TLR2 signaling can limit inflammation after skin injury—an effect that promotes wound healing (*2*)—as well as during infection with the acne-associated microbe *Cutibacterium acnes* (*6*). This anti-inflammatory communication occurs through discrete mechanisms. In the context of wounds, TLR2 activation by *S. epidermidis* inhibits proinflammatory TLR3 signaling in response to double-stranded RNA from damaged host cells (*2*), whereas in the context of *C. acnes* infection, *S. epidermidis* TLR2 signaling induces a microRNA that limits TLR2 expression, counteracting TLR2-driven inflammation (*6*). Given the structural and metabolic complexity of microbial cells, numerous microbiota-derived ligands may yet be discovered that are recognized by other host receptors.

Members of the skin microbiota such as *S. epidermidis* can also fully engage components of the adaptive immune system, including different subsets of T cells. These cells are noted for acquiring target specificity and orchestrating highly dynamic immune responses, ranging from effector (for example, aimed at eliminating a pathogen) to regulatory (suppressive). *S. epidermidis* can finely tune both types of responses. In early life, cells with regulatory function [for example, regulatory T cells (T_{regs})] migrate to skin after the skin microbiota colonizes hair follicles. As these T_{regs} are microbiota-specific, they are instrumental to establishing tolerance to skin microbes including *S. epidermidis* (*4*).

The two major subsets of effector T cells are helper (T_H) and cytotoxic (T_C) cells. Although many skin microbes can promote the accumulation of T_H cells, *S. epidermidis* is rare in its ability to recruit and license the function of T_C cells (*1*). Remarkably, T_C cells acquire specificity to *S. epidermidis* through an evolutionarily ancient arm of immunity. This pathway involves the presentation of *S. epidermidis* peptides on nonclassical antigen-presenting molecules by dendritic cells to T_C cells (*7*). *S. epidermidis*–specific T_C cells can provide multiple benefits to the host through their ability to alter the behavior of keratinocytes. These benefits include protecting the skin against foreign pathogens (*8*) and accelerating the healing of skin wounds (*7*).

Antimicrobial peptides (AMPs) are secreted by keratinocytes to fortify the skin against pathogens. Notably, their production can be augmented by cues from *S. epidermidis*. These cues can be sensed directly via TLR2 (*2*) or transduced by *S. epidermidis*–specific T_C cells that instruct keratinocytes to express AMPs (*1*). Both pathways promote keratinocyte AMP expression and killing of diverse microbial pathogens, including bacteria and fungi (*1*, *2*). Because *S. epidermidis* has built-in defenses, such as modifying its cell wall with positively charged residues that repel AMPs (*9*), these responses may benefit not only the host but also *S. epidermidis* by eliminating its potential competitors.

S. epidermidis also interacts with other microbes directly, independently of the host. Often, these interactions are antagonistic, revolving around competition for space and nutrients. Antagonism is especially prominent in the nasal cavity, a primary reservoir of the pathogen *S. aureus*. In this niche, *S. epidermidis* can displace *S. aureus* by secreting the protease Esp that degrades *S. aureus* adherence proteins (*3*). Microbes can further

[1]*Metaorganism Immunity Section, Laboratory of Immune System Biology, National Institute of Allergy and Infectious Diseases, Bethesda, MD 20892, USA.* [2]*NIAID Microbiome Program, National Institute of Allergy and Infectious Diseases, Bethesda, MD 20892, USA.* [3]*Postdoctoral Research Associate Training Program, National Institute of General Medical Sciences, Bethesda, MD 20892, USA. Email: ybelkaid@niaid.nih.gov*

Downloaded from http://science.sciencemag.org/ on January 21, 2019

Published by AAAS

compete by producing antimicrobials, usually peptides, that directly kill specific species or strains (bacteriocins) (*3*) or interfere with their coordination of microbial group behaviors (quorum-sensing inhibitors) (*10*). In a systematic analysis of nasal isolates, *S. epidermidis* was identified as an especially frequent producer of antimicrobials (*11*). As such, *S. epidermidis* may play a dominant role in shaping the microbiota in defined settings. This is illustrated by the microbiota associated with atopic dermatitis (AD), a type of eczema that is characterized by recurring flares of dry, itchy skin. These flares are thought to be driven by colonization with *S. aureus* and are associated with a loss of *S. epidermidis* strains that produce *S. aureus*–targeting bacteriocins. Reintroduction of a cocktail of bacteriocin-producing microbes decolonizes AD-affected sites of *S. aureus* (*12*), which suggests that this condition may represent a target for ecology-based therapy. This type of therapy, rather than eliminating pathogens by brute force, leverages understanding of the preferred niche of a pathogen in order to make it less habitable. The appeal of this approach is that, compared to antibiotic therapy, it is much less likely to harm the indigenous microbiota in a patient. Such an approach could also provide an important strategy for the control of antibiotic-resistant pathogens.

However, *S. epidermidis* does not always act in the host's interest. Although *S. aureus* predominantly colonizes strong AD flares, mixed populations of *S. epidermidis* strains prevail in less severe flares (*13*). These strains are genetically related to strains acquired in hospitals, where *S. epidermidis* is one of the most frequent causes of sepsis in newborns (*9*). A hallmark of these strains is the presence of staphylococcal chromosome cassette (SCC) *mec* genetic elements that can encode not only methicillin antibiotic resistance but also a potent peptide toxin, the phenol-soluble modulin PSM-mec. During sepsis, this toxin mediates the killing of neutrophils (crucial inflammatory immune cells), the survival of *S. epidermidis* in blood, and ultimately host death (*14*).

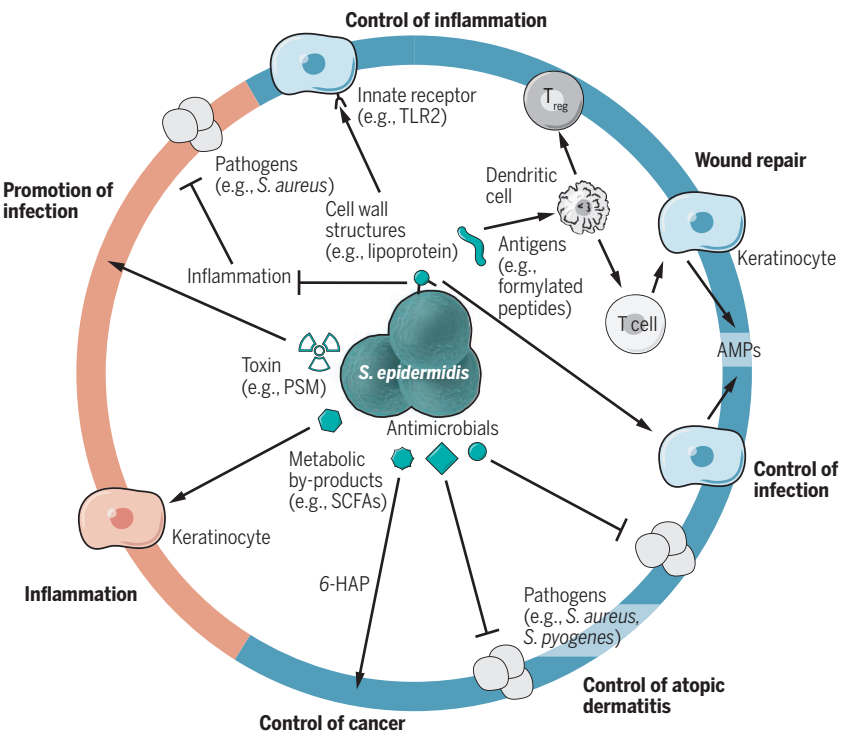
Furthermore, the ability of *S. epidermidis* to limit inflammation can be exploited to the advantage of pathogens such as *S. aureus*. In the liver, macrophage uptake of the cell wall polymer peptidoglycan from *S. epidermidis* or other defined skin microbes strongly suppresses production of antimicrobial reactive oxygen species. Because of this, bloodstream infection by *S. aureus* and *S. epidermidis*—for example, as a consequence of intravascular catheterization—promotes *S. aureus* survival in the liver and reduces its infectious dose (*15*).

Although many of the products made by *S. epidermidis* likely evolved for its survival on skin, these products can also have unexpected, off-target effects. Remarkably, one such product, 6-*N*-hydroxyaminopurine (6-HAP), an antimicrobial that normally targets skin pathogens, has recently been shown to inhibit tumor cell growth. 6-HAP, an analog of the DNA nucleotide base adenine, interferes with the essential process of DNA replication. Keratinocytes, however, are resistant to 6-HAP because, unlike tumor cells, they highly express enzymes that can detoxify 6-HAP. In mice, topical application of 6-HAP–producing strains of *S. epidermidis* protects against ultraviolet-induced skin tumors (*16*). Intriguingly, such strains are commonly found on the skin of healthy human individuals, which suggests that the composition of the skin microbiota could affect the development of skin tumors.

S. epidermidis has emerged as an influential, keystone member of the skin microbiota. Although particular strains are contextually pathogenic, their multifarious roles in skin immunity and antimicrobial defense suggest that most *S. epidermidis* strains bolster our skin health overall. Much remains to be learned about the beneficial role of the numerous other microbes that constitute the skin microbiota. Precise editing of the microbiota, such as by providing nutrients targeted at promoting the growth of defined members of the skin microbiota such as *S. epidermidis*, or the direct application of purified microbiota-derived products may one day hold strong therapeutic value in the fight against skin inflammatory disorders, infections, wounds, and cancer. ■

The multifaceted roles of *S. epidermidis* in skin physiology

S. epidermidis guards skin against inflammation, infections, and cancer through interactions with keratinocytes, T cells, and other members of the skin microbiota. These interactions are strain- and context-dependent, with some leading to negative outcomes for the host, including inflammation and infection.



REFERENCES AND NOTES

1. S. Naik *et al.*, *Nature* **520**, 104 (2015).
2. R. L. Gallo, T. Nakatsuji, *J. Invest. Dermatol.* **131**, 1974 (2011).
3. B. Krismer *et al.*, *Nat. Rev. Microbiol.* **15**, 675 (2017).
4. T. C. Scharschmidt *et al.*, *Cell Host Microbe* **22**, 1 (2017).
5. J. A. Sanford *et al.*, *Sci. Immunol.* **1**, eaah4609 (2016).
6. X. Xia *et al.*, *J. Invest. Dermatol.* **136**, 621 (2016).
7. J. L. Linehan *et al.*, *Cell* **172**, 784 (2018).
8. S. Naik *et al.*, *Science* **337**, 1115 (2012).
9. M. Otto, *Nat. Rev. Microbiol.* **7**, 555 (2009).
10. A. E. Paharik *et al.*, *Cell Host Microbe* **22**, 746 (2017).
11. D. Janek *et al.*, *PLOS Pathog.* **12**, e1005812 (2016).
12. T. Nakatsuji *et al.*, *Sci. Transl. Med.* **9**, eaah4680 (2017).
13. A. L. Byrd *et al.*, *Sci. Transl. Med.* **9**, eaal4651 (2017).
14. L. Qin *et al.*, *PLOS Pathog.* **13**, e1006153 (2017).
15. E. Boldock *et al.*, *Nat. Microbiol.* **3**, 881 (2018).
16. T. Nakatsuji *et al.*, *Sci. Adv.* **4**, eaao4502 (2018).

ACKNOWLEDGMENTS

Supported by the Intramural Research Program of the National Institute of Allergy and Infectious Diseases (project number 1ZIAAI001115-09) (A.S. and Y.B.) and by a Postdoctoral Research Associate Training fellowship from the National Institute of General Medical Sciences (project number 1FI2GM128736-01) (A.S.).

10.1126/science.aat4326

GRAPHIC: N. DESAI/*SCIENCE*

Downloaded from http://science.sciencemag.org/ on January 21, 2019

Published by AAAS



The cerebellum is involved in the main circuits that regulate social behavior in mice.

PHOTO: BILDAGENTUR ZOONAR GMBH/SHUTTERSTOCK

NEUROSCIENCE

The cerebellum gets social

The cerebellum can regulate behavior by controlling dopamine release

By **Egidio D'Angelo**

The cerebellum contains the second main cortex of the brain and ~50% of the neurons that constitute the brain. Although the cerebellum has long been thought to subserve motor learning and coordination, more recently it has been recognized to take part in cognitive and emotional processing. Additionally, evidence for cerebellar involvement in autism spectrum disorder (ASD), schizophrenia, and addiction is growing. On page 248 of this issue, Carta *et al.* (*1*) extend this theme and show that the cerebellum can activate the ventral tegmental area (VTA). The VTA is a mesencephalic nucleus giving rise to the mesocortical and mesolimbic fiber bundles that release dopamine to the prefrontal cortex and ventral striatum. Dopamine, in turn, plays a fundamental role in cognitive and emotional functioning by regulating motivation and reward. This places the cerebellum into the main circuits regulating brain states and social behavior.

Behavior can be defined as a coordinated series of motor acts and neurovegetative changes centered on a certain target (*2*). There are several elements that contribute to the behavioral response, and historically these have been separated and attributed to different parts of the brain. The cerebral cortex is classically thought to play a planning and decisional role; the basal ganglia to control action selection, motivation, and reward; the cerebellum to coordinate motor actions; and the hippocampus to allow spatial navigation (*3*). Although these stereotypes may help to conceptualize how the behavioral response is generated, they are oversimplifications (*4*) because brain circuits are interconnected at multiple levels and influence each other through neuromodulatory systems, as demonstrated by Carta *et al.*

The cerebral cortex is bidirectionally connected with the cerebellum through multiple neural circuits (*5*–*8*). In humans, these circuits involve the motor cortical areas but also areas that regulate cognition, emotion, attention, and social behavior. These nonmotor areas receive more than 80% of all the nerve fiber tracts that travel between the cerebellum and cerebral cortex through the deep cerebellar nuclei and thalamus (*9*).

The prototypical mode of action of the cerebellum has been characterized for motor coordination (*5*). The cerebral cortex elaborates the motor plan as a predictive sensory state (*6*, *7*), which is conveyed to the cerebellum through descending pathways. In the cerebellum this plan is compared to the actual sensory state, which is conveyed through the afferent sensory pathways. According to the motor learning theory, through this comparison the cerebellar circuit learns to minimize motor errors (*10*). It has been argued that this process could be generalized to the cognitive and emotional domains (*11*). The results of Carta *et al.* imply that a similar mechanism could be used to regulate the motivation and reward cycle.

In functional magnetic resonance imaging (fMRI) studies, different areas of the cerebellum are activated depending on the nature of tasks performed by the subjects. The anterior cerebellum is activated in relation to motor commands, whereas the posterior cerebellum and the hemispheres become activated when, for example, we see actions performed by others, we evaluate sensory perceptions, and we feel emotions (*12*). Moreover, the cerebellum shows coherent activation together with several areas of the cerebral cortex and hippocampus in the so-called fMRI resting-state networks. These include the default-mode network, the salience network, and the attention networks, which regulate the switch from an internal reference state to external target-oriented behaviors (*13*). The study of Carta *et al.* implies that the specific modules of the cerebellum, as part of these brain networks, contribute to action selection and behavioral switching.

Surprisingly, Carta *et al.* find that the cerebellum regulates the motivation and reward process that is typically attributed to the basal ganglia. The authors demonstrate that in mice, monosynaptic connections from the fastigial nucleus of the cerebellum regulate the activity of the VTA directly. In this way, the cerebellum can regulate functions related to decision-making, emotional control, and attentional switching. The same group showed that the cerebellum communicates directly with the basal ganglia (*14*). The findings of Carta *et al.* reveal a more complex scenario in which the two main subcortical circuits coordinate dopamine functions in the brain.

Carta *et al.* suggest that dysfunction of the cerebellum-VTA connection could contribute to the pathogenesis of diseases in which the dopaminergic system is dysregulated, including ASD and schizophrenia (*15*), and to conditions such as drug addiction. These proposals need critical validation in humans. This study opens a new avenue for interpreting the function of the cerebellum and also for understanding social behavior and related pathologies, with the potential to discover novel therapies to treat these diseases. ■

Department of Brain and Behavioral Sciences, University of Pavia, Pavia, Italy. Email: dangelo@unipv.it

REFERENCES AND NOTES

1. I. Carta *et al.*, *Science* **363**, eaav0581 (2019).
2. A. S. Pillai *et al.*, *Neuron* **94**, 1010 (2017).
3. S. Arber *et al.*, *Science* **360**, 1403 (2018).
4. S. Grillner, *Curr. Biol.* **28**, R162 (2018).
5. E. D'Angelo, *Handb. Clin. Neurol.* **154**, 85 (2018).
6. S. J. Blakemore *et al.*, *Nat. Neurosci.* **1**, 635 (1998).
7. D. M. Wolpert *et al.*, *Trends Cogn. Sci.* **2**, 338 (1998).
8. J. Ghajar *et al.*, *Neuroscientist* **15**, 232 (2009).
9. F. Palesi *et al.*, *Sci. Rep.* **7**, 12841 (2017).
10. R. R. Llinas *et al.*, *Philos. Trans. R. Soc. London Ser. B* **364**, 1301 (2009).
11. E. D'Angelo *et al.*, *Front. Cell. Neurosci.* **6**, 116 (2013).
12. L. Casiraghi *et al.*, *Cereb. Cortex* 10.1093/cercor/bhy322 (2019).
13. G. Castellazzi *et al.*, *Front. Cell. Neurosci.* **12**, 331 (2018).
14. C. H. Chen *et al.*, *Nat. Neurosci.* **17**, 1767 (2014).
15. J. D. Schmahmann, J. C. Sherman, *Brain* **121**, 561 (1998).

ACKNOWLEDGMENTS

Supported by Human Brain Project SGA720270/SGA785907 and Centro Fermi MNL.

10.1126/science.aaw2571

Downloaded from http://science.sciencemag.org/ on January 17, 2019

Published by AAAS

STRUCTURAL BIOLOGY

Adaptations of an ancient modular machine

Mechanism of energy conversion is conserved in the complex I superfamily

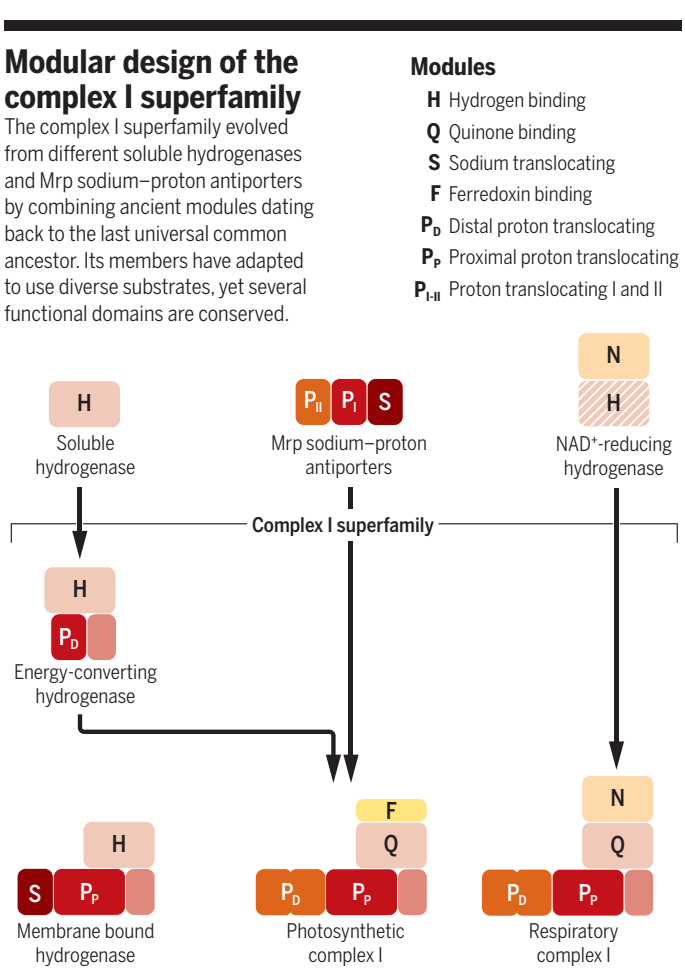
By **Ulrich Brandt**

All expressions of life ultimately depend on energy derived from redox chemistry and photosynthesis. On page 257 of this issue, Schuller *et al.* (*1*) report the structure of photosynthetic complex I at atomic resolution. The authors have analyzed how the distinct NADH [reduced form of oxidized nicotinamide adenine dinucleotide (NAD^+)] dehydrogenase subunit S (NdhS) facilitates electron transfer from ferredoxin, thereby establishing efficient cyclic electron flow around photosystem I. The findings add an important piece to the puzzle of deciphering the enigmatic mechanisms at work in the remarkable molecular machines of the complex I superfamily encompassing photosynthetic and respiratory complex I, as well as proton pumping hydrogenases. In combination with high resolution structures of respiratory complex I from bacteria (*2*), mitochondria (*3*–*5*), and membrane bound hydrogenase (*6*), it is now possible to trace the modular evolution and functional adaptations of the complex I superfamily at the atomic level.

Evolutionary studies suggest that the metabolism of the last universal common ancestor relied on the reduction of carbon dioxide and nitrogen by hydrogen and hydrogen sulfide, assisted by transition metals such as iron, nickel, and molybdenum (*7*). This basal redox chemistry provided the building blocks for organic molecules, nucleic acids, and proteins. The integration of photosynthesis into this primordial power supply tapped sunlight as an unlimited energy source. With the advent of water splitting photosynthesis and terminal oxidases, oxygen became the major player in the overall cycle of biological energy. Thus, going back to the origin of life, biological electron transfer, respiration, and photosynthesis were closely intertwined and accompanied by the modular unfolding of the complex I superfamily of redox enzymes.

The module common to all members of the complex I superfamily is provided by soluble [NiFe] hydrogenases (*8*). These hydrogenases have a [NiFe] active site and catalyze the reversible conversion of hydrogen to protons and electrons. They also feature a chain of three iron-sulfur clusters and harbor a substrate binding site for hydrogen (H-module) or plasto-, mena-, or ubiquinone (Q-module). Although the active site evolved to bind chemically different substrates while concomitantly losing the [NiFe] center—from soluble hydrogenase to mitochondrial complex I—both the sequence and structure of nearby domains are conserved (*3*, *4*, *9*, *10*). Hydrogenases acquired a membrane anchor and a proton-translocating module (P_I) from the multiple resistance and pH (Mrp)–type sodium-proton antiporter, yielding the energy-converting hydrogenase (Ech) that energetically connects electron transfer between ferredoxin and hydrogen to proton translocation across a membrane. The Mrp transporters also trace back to the last universal common ancestor, in which they are proposed to play a role in establishing the sodium gradient across the plasma membrane to drive primordial adenosine triphosphate (ATP)–synthase (*7*). The structure of the hydrogen gas–evolving membrane-bound hydrogenase (Mbh) revealed that it retained the sodium translocating module (S) of Mrp and expanded the P_I-module by adding three additional subunits. This resulted in a composition very similar to that of the proximal proton pumping (P_P) module of complex I (*6*). Instead of the S-module, photosynthetic and respiratory complex I retained the second proton-translocating module of Mrp (P_{II}), duplicating it to form the distal proton pumping (P_D) module. Strikingly, however, as compared with Mbh, the P_P-module is rotated 180° in the membrane plane in complex I, probably retaining the relative topology of the modules in Mrp. This is particularly remarkable because irrespective of the orientation of the P_P-module, proton pumping is driven by the redox chemistry taking place in the homologous Q- or H-module.

The membrane-bound hydrogenases of the complex I superfamily mostly use ferredoxin as the electron donor or acceptor for the H-module. Ferredoxin also reduces the Q-module of photosynthetic complex I, passing on electrons from photosystem I. However, as shown by Schuller *et al.*, an additional NdhS subunit (see the figure, module F) greatly facilitates recognition and binding of the redox protein, thereby optimizing cyclic electron transfer. Respiratory complex I turned into a NADH-dehydrogenase by capturing its electron input module from the NAD^+-reducing hydrogenase. The H-module of this



GRAPHIC: V. ALTOUNIAN/*SCIENCE*

Radboud Institute for Molecular Life Sciences, Department of Pediatrics, Radboud University Medical Center, Geert Grooteplein-Zuid 10, Route 772, 6525 GA Nijmegen, Netherlands. Email: ulrich.brandt@radboudumc.nl

Downloaded from http://science.sciencemag.org/ on January 17, 2019

Published by AAAS

group of [NiFe] hydrogenases is only distantly related to the H/Q-module of the complex I superfamily. Thus, respiratory complex I has evolved by combining ancient modules from two different groups of hydrogenases and Mrp sodium–proton antiporters. This core structure was then retained all the way from bacterial to mammalian complex I.

Several conclusions can be drawn from the adaptive development of the superfamily originating from simple soluble hydrogenases and leading to the large and complicated molecular machine of mammalian complex I. Proton pumping by the P_I/P_P-module is driven by redox chemistry catalyzed by the H/Q module, irrespective of its orientation in the membrane domain. Different additional ion-translocating modules from Mrp are docked onto this central unit. In the P_D-module, even two closely related modules are stacked onto the P_P-module. It seems that this works because the central axes of protonable residues common to all modules of the Mrp transporter can connect flexibly with each other. This is in line with the proposed mechanism of electrostatic energy transmission into the central axis from the H/Q-module and from one pump site to the next, both of which feature broken transmembrane helices found in many ion transporters. During the conversion from the H into the Q-module, the hydrogen reactive [NiFe] center was transformed into binding pockets for different kinds of hydrophobic quinones. Remarkably, the fold surrounding this active site and even a substantial number of critical residues are highly conserved (*9*). This holds in particular for a cluster of three critical loops that connect the active site with the common membrane anchor, which has been implicated in generating the electrostatic pulse transmitted toward the pump modules in the membrane domain of complex I (*4*, *11*) and is already present in membrane-bound hydrogenase (*6*).

Studying the conserved structural elements and understanding the functional adaptions of complex I superfamily members will greatly help to understand the still poorly understood molecular mechanism of these distinct redox-driven ion pumps. ■

REFERENCES

1. J. M. Schuller *et al.*, *Science* **363**, 257 (2019).
2. R. Baradaran *et al.*, *Nature* **494**, 443 (2013).
3. J. Zhu, K. R. Vinothkumar, J. Hirst, *Nature* **536**, 354 (2016).
4. V. Zickermann *et al.*, *Science* **347**, 44 (2015).
5. K. Fiedorczuk *et al.*, *Nature* **538**, 406 (2016).
6. H. Yu *et al.*, *Cell* **173**, 1636 (2018).
7. M. C. Weiss *et al.*, *Nat. Microbiol.* **1**, 16116 (2016).
8. J. W. Peters *et al.*, *Biochim. Biophys. Acta* **1853**, 1350 (2015).
9. N. Kashani-Poor *et al.*, *J. Biol. Chem.* **276**, 24082 (2001).
10. A. Volbeda *et al.*, *Nature* **373**, 580 (1995).
11. A. Cabrera-Orefice *et al.*, *Nat. Commun.* **9**, 4500 (2018).

10.1126/science.aaw0493

THERAPEUTICS

Gene therapy for pathologic gene expression

Haploinsufficiency in disease can be overcome by boosting gene expression with CRISPR

By **Lindsey E. Montefiori** *and* **Marcelo A. Nobrega**

Haploinsufficiency arises when one copy of a gene is functionally lost, often through nonsense or frameshift mutations or small chromosomal deletions. The resulting monoallelic expression is not sufficiently compensated for by the intact allele, ultimately leading to decreased expression of the gene product and resulting in pathologic phenotypes (*1*). What are the therapeutic options for diseases rooted in insufficient gene expression? One possible viable option is to restore normal gene expression levels by enhancing their transcription in a targeted fashion. On page 246 in this issue, Matharu *et al.* (*2*) report a CRISPR-based gene-activation approach that can increase the expression of normal endogenous genes in a tissue-specific manner, setting the stage for the development of new gene-regulating therapies for gene dosage–associated diseases.

Among the emerging applications of CRISPR-based gene editing are techniques that use a catalytically inactive Cas9 enzyme (dCas9) fused to a protein domain to modulate transcription (*3*). These fusion proteins can be recruited by way of guide RNAs (gRNAs) to specific genomic locations, including promoters and cis-regulatory elements such as enhancers, which regulate gene expression. If the recruitment site is transcriptionally competent, the result is activation (CRISPRa) or repression/interference (CRISPRi) of transcription. Although this strategy has been applied in human cell culture and animal models (*4*, *5*), the ultimate task of employing CRISPRa to therapeutically rescue pathologic gene expression has not been fully realized. Matharu *et al.* use CRISPRa to restore the expression of two haploinsufficient genes, single-minded 1 (*Sim1*) and melanocortin 4 receptor (*Mc4r*), to physiological amounts in mouse models of severe early-onset obesity. Haploinsufficiency of either gene causes severe obesity in humans, and previous work in mice established that SIM1 and MC4R control eating behavior through their expression in the hypothalamus (*6*–*8*); therefore, a relevant therapeutic intervention would target gene expression specifically in the hypothalamus.

Department of Human Genetics, University of Chicago, Chicago, IL, USA. Email: nobrega@uchicago.edu

Because *Sim1* and *Mc4r* are expressed in multiple tissues, an important first step was to address whether it is feasible to modulate expression in a tissue-specific manner. The authors tested two approaches, focusing initially on *Sim1*: (i) Target CRISPRa to the promoter of the remaining functional *Sim1* gene to enhance expression wherever *Sim1* was already active, and (ii) target CRISPRa to a 270-kb distal enhancer that controls *Sim1* expression specifically in the hypothalamus (see the figure). Both approaches were employed in transgenic animals expressing the CRISPRa reagents (dCas9 fused to the transcriptional activator VP64), as well as recombinant adeno-associated virus (rAAV)–mediated delivery of CRISPRa directly into the hypothalamus. In all cases, hypothalamic *Sim1* expression was restored to wild-type levels and the mice did not become obese, demonstrating robust prevention of a haploinsufficient phenotype by enhancing endogenous gene expression. Interestingly, the authors found that they could manipulate *Sim1* expression exclusively in the hypothalamus by targeting the hypothalamic enhancer instead of the *Sim1* promoter, indicating that to obtain tissue-specific transcriptional modification, CRISPRa will likely need to be deployed to tissue-specific regulatory elements. Injection of rAAV-based CRISPRa into the hypothalamus of *Mc4r* haploinsufficient mice similarly prevented obesity, further demonstrating the strength of this approach.

This strategy illustrates what could emerge as an important new approach to treating gene expression disorders and raises the possibility of expanding the scope of CRISPRa and CRISPRi technology to treat diseases that involve pathogenic overexpression of a gene, particularly in cancer. For example, somatic mutations in a subset of pediatric T cell acute lymphoblastic leukemia (T-ALL) result in the formation of a highly active enhancer that drives oncogenic *TAL1* gene overexpression (*9*). More-

Downloaded from http://science.sciencemag.org/ on January 17, 2019

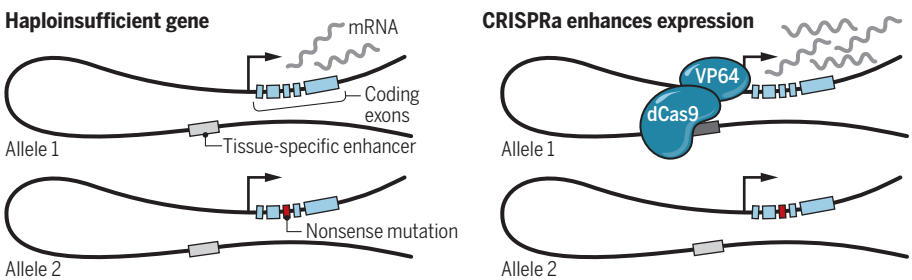
Published by AAAS

over, *MYC* gene expression in human B cell acute myeloid leukemia (AML) was recently shown to be dependent on a 1.7-megabase distal enhancer element (*10*). Both studies demonstrated that disrupting these enhancer elements negatively affected cancer cell survival, providing a precedent for developing CRISPRi as a therapeutic approach to inactivate cancer-promoting enhancers. Although transcription factors such as TAL1 and MYC are among the most potent oncoproteins, targeting them with small-molecule inhibitors has proven challenging. The results presented by Matharu *et al.* suggest that it should be possible to circumvent protein-targeted therapies by quelling oncogene expression at its source—transcription.

phenotype later in life. Many haploinsufficient disorders in humans are likely to be therapeutically actionable only after the disease phenotypes are partially or fully established. Future experiments should test the therapeutic benefit of targeting gene expression with the goal of reversing a haploinsufficient phenotype. Additionally, it is important to recognize that many enhancers are dynamic, meaning that they may act at specific developmental stages and change their tissue specificity with time (*11*). Fortunately, the authors were able to capitalize on a developmentally stable tissue-specific enhancer, although it is unclear how often this will be the case for targeting enhancers of other haploinsufficient genes.

Enhancing endogenous gene expression with CRISPRa

Most genes are biallelically expressed; however, heterozygous mutations can cause haploinsufficiency, resulting in 50% less functional protein. Recruitment of CRISPRa to the endogenous promoter or enhancer of the gene in mouse models causes up-regulation of the wild-type copy, leading to normal expression levels.



A key advancement in the study by Matharu *et al.* is their use of rAAV to deliver CRISPRa reagents in vivo. For a CRISPR-based therapeutic to be relevant for use in humans, it will likely need to be packaged within a virus and administered intravenously, because most targeted cell types will not be available for ex vivo manipulation and implantation. rAAV is nonpathogenic and displays a high delivery potential, making it a viable option for effectively introducing CRISPR reagents to human cells. CRISPRa and CRISPRi approaches have the added benefit of modulating gene expression without modifying the genome, thereby avoiding potential off-target mutations. Thus, pairing CRISPRa with rAAV to treat a gene expression disorder in vivo is an important step forward in the development of expression-based therapeutics.

Although Matharu *et al.* demonstrate that CRISPR-based up-regulation of a haploinsufficient gene can prevent obesity, this study also raises the important question of whether a disease phenotype can be reversed. Because the authors administered CRISPRa reagents to mice at 4 weeks of age—before the onset of obesity—they did not address the potential to rescue the

Naturally occurring and pathogenic gene regulatory DNA elements provide a tailored therapeutic route to targeting gene expression. The results presented by Matharu *et al.* underscore the importance of identifying and carefully characterizing the enhancers that control gene expression. Large-scale efforts have identified thousands of putative enhancers in hundreds of human cell types. However, cell types representing diverse disease states, particularly from human patients, remain understudied. Knowing the full repertoire of gene regulatory elements and their target genes (*12*) in these cell types is likely to provide critical insight that can be exploited for CRISPR-based therapeutic approaches to modify gene expression. ■

REFERENCES AND NOTES

1. N. Huang *et al.*, *PLOS Genet.* **6**, e1001154 (2010).
2. N. Matharu *et al.*, *Science* **363**, eaau0629 (2019).
3. C.-H. Lau, Y. Suh, *Transgenic Res.* **27**, 489 (2018).
4. M. L. Maeder *et al.*, *Nat. Methods* **10**, 977 (2013).
5. H. Zhou *et al.*, *Nat. Neurosci.* **21**, 440 (2018).
6. J. L. Michaud *et al.*, *Hum. Mol. Genet.* **10**, 1465 (2001).
7. M. J. Krashes *et al.*, *Nat. Neurosci.* **19**, 206 (2016).
8. C. Vaisse *et al.*, *J. Clin. Invest.* **106**, 253 (2000).
9. M. R. Mansour *et al.*, *Science* **346**, 1373 (2014).
10. C. Bahr *et al.*, *Nature* **553**, 515 (2018).
11. A. S. Nord *et al.*, *Cell* **155**, 1521 (2013).
12. L. E. Montefiori *et al.*, *eLife* **7**, e35788 (2018).

10.1126/science.aaw0635

IMMUNOLOGY

B cells, CMV, and stem cell transplant

Host antibodies help prevent CMV dissemination after bone marrow transplantation

By **Maria-Luisa Alegre**

Hematopoietic stem cell transplantation (HSCT) is a potentially curative therapy for various malignant and nonmalignant conditions but can be complicated by infections such as reactivation of cytomegalovirus (CMV). CMV is a ubiquitous DNA herpes virus comprising various distinct strains (*1*). Around 60 to 90% of healthy adults are seropositive, indicating past exposure to the virus, although infections in healthy people are often mild or asymptomatic. After initial acute infection, CMV enters a latent phase, similar to other herpes viruses. It has been suggested that CMV infection may confer an immunological benefit, perhaps explaining its prevalence, because comparison of seropositive and seronegative individuals has shown that CMV infection results in greater responses to the flu vaccine (*2*). The immune system is essential to control the initial infection and to prevent later CMV reactivation, as demonstrated by the high incidence of CMV reactivation in immunosuppressed patients such as HSCT recipients. Whereas the incidence and severity of CMV transcriptional reactivation and cell-to-cell dissemination after HSCT has substantially diminished since the adoption of prophylactic or preemptive antiviral therapies (*3*), CMV remains the most important viral infection after HSCT, especially in high-risk patients (such as seropositive recipients of seronegative donors), and can lead to life-threatening CMV disease in ~10% of HSCT recipients (*4*). On page 288 of this issue, Martins *et al.* (*5*) make the unexpected observation, in mice undergoing bone marrow transplantation (BMT) as a model of HSCT, that strain-specific CMV antibodies made by host B cells play a crucial role in preventing CMV dissemination

Section of Rheumatology, Department of Medicine, University of Chicago, Chicago, IL 60637, USA. Email: malegre@midway.uchicago.edu

Downloaded from http://science.sciencemag.org/ on January 17, 2019

GRAPHIC: KELLIE HOLOSKI/*SCIENCE*

Published by AAAS

after BMT. They propose that passive transfer of antibodies that are matched to the latent CMV strain in HSCT recipients might constitute a powerful and easy therapeutic approach to prevent CMV disease.

It is thought that αβ T cells, γδ T cells, natural killer (NK) cells, and B cells all contribute to curbing CMV infection (*6*) and that anti-CMV $CD8^+$ T cells are especially important in CMV immune surveillance and prevention of reactivation and dissemination. Analysis of cadaveric organ donor tissue has revealed potential sites of active T cell–mediated CMV clearance in the blood, bone marrow, and spleen and reservoirs of viral persistence in the lung coexisting with active antiviral T cells (*7*). Indeed, transfer of anti-CMV $CD8^+$ T cells from donors is one of the approaches investigated to treat CMV reactivation in immunosuppressed patients (*8*). Martins *et al.* found that in mice, T cell immunosuppression or depletion alone is insufficient to enable CMV reactivation after BMT, and only when host B cells and plasma cells are eliminated [by graft-versus-host disease (GVHD), a process by which donor T cells can attack host cells, or by genetic deficiency] in addition to T cell and NK cell depletion does infection emerge (see the figure). Moreover, they demonstrate that protection from CMV reactivation conferred by antibodies is much more efficient if it is strain specific. Additionally, protection by antibodies that prevent cell-to-cell dissemination is more effective than by antibodies that prevent cell entry. Whether these discoveries in mice—by using a different conditioning regimen from that used in the clinic and, by necessity, mouse rather than human CMV (which are quite different)—are relevant to the clinical situation merits careful examination.

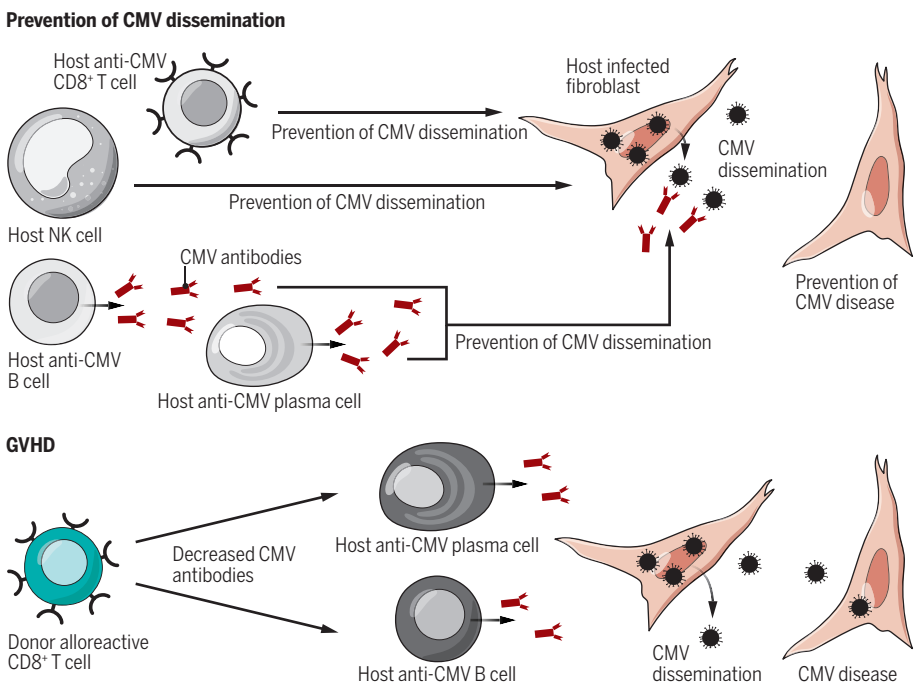
Recipients of allogeneic HSCT can be treated with a variety of regimens to prevent the host immune system from rejecting the allogeneic stem cells, with a heavy focus on T cell immunosuppression. These conditioning regimens may include total-body irradiation at high or low doses, cytoreducing chemotherapy drugs, and antithymocyte globulin (ATG) or anti-CD52 (alemtuzumab) to eliminate host T cells. Given the findings of Martins *et al.*, it is compelling to consider how these clinical treatments may affect antibody-producing B cells and plasma cells because CMV reactivation in the clinic, unlike in mice, can occur in the absence of GVHD. Plasma cells are thought to be somewhat radioresistant, but ATG is a mixture of polyclonal antibodies, some of which can target B cells and plasma cells (*9*), and CD52 is expressed on both T and B cells. HSCT recipients have been reported to experience prolonged B cell depletion (*10*) and might thus develop a reduction in CMV-specific antibody titers after HSCT. Prospective following of CMV-specific antibody titers may be of interest in the clinic to see whether this is indeed the case.

Prevention or treatment of CMV with immunoglobulins has usually been ineffective in HSCT recipients (*11*). The authors argue that this may be because these reagents, which come from sera pooled from many donors, may not contain sufficient concentrations of antibodies specific to the CMV strain infecting a given recipient. That humans can experience successive infections with different CMV strains (*12*) supports the possibility that the protective effect of CMV antibodies is strain specific or at least that antibodies generated after a given CMV infection are not broadly cross-protective against other strains. This is consistent with the observation of Martins *et al.* that in their mouse model, protection against CMV reactivation is only conferred by strain-specific serum and not when this serum is diluted with sera containing antibodies reactive to other strains. If confirmed in the clinic, generation of a collection of sera specific for each CMV genotype may be useful for passive antibody therapy in the future.

An additional point to consider is how antibodies may work to prevent reactivation of CMV that is inside infected cells. The authors show that neutralizing antibodies that prevent cell infection are not as protective when injected in vivo as those that prevent cell-to-cell dissemination in vitro, which may provide insights for vaccine design. Much effort has been devoted to developing vaccines against human CMV (*13*). The study of Martins *et al.* support giving further consideration to the role of humoral immunity in the prevention of reactivation and dissemination of CMV after clinical HSCT, the therapeutic potential of strain-specific serum transfer, and the rational vaccine design either for CMV-seronegative recipients or to boost or broaden responses of seropositive recipients before HSCT. ■

B cells help prevent CMV reactivation

T cells, NK cells, and B cell–derived antibodies contribute to the prevention of mouse CMV dissemination after BMT. Killing of host B cells and plasma cells by alloreactive donor T cells (GVHD) in combination with therapeutic deletion of T cells and NK cells resulted in CMV infection of latently infected hosts.



REFERENCES

1. H. Kaminski, J. A. Fishman, *Am. J. Transplant.* **16**, 2254 (2016).
2. D. Furman *et al.*, *Sci. Transl. Med.* **7**, eaaa2293 (2015).
3. D. Lilleri, G. Gerna, *Immunotherapy* **8**, 1135 (2016).
4. E. Maffini *et al.*, *Expert Rev. Hematol.* **9**, 585 (2016).
5. J. P. Martins *et al.*, *Science* **363**, 288 (2019).
6. A. Huygens *et al.*, *Front. Immunol.* **5**, 552 (2014).
7. C. L. Gordon *et al.*, *J. Exp. Med.* **214**, 651 (2017).
8. M. Cobbold *et al.*, *J. Exp. Med.* **202**, 379 (2005).
9. M. S. Zand *et al.*, *Transplantation* **79**, 1507 (2005).
10. E. Corre *et al.*, *Haematologica* **95**, 1025 (2010).
11. P. Raanani *et al.*, *J. Clin. Oncol.* **27**, 770 (2009).
12. C. Smith *et al.*, *J. Virol.* **90**, 7497 (2016).
13. P. R. Krause *et al.*, *Vaccine* **32**, 4 (2013).

10.1126/science.aav9867

GRAPHIC: N. DESAI/*SCIENCE*

Downloaded from http://science.sciencemag.org/ on January 17, 2019

Published by AAAS



POLICY FORUM

Direct-to-consumer marketing of neurotechnologies is on the rise.

SCIENCE AND REGULATION

Oversight of direct-to-consumer neurotechnologies

Efficacy of products is far from clear

By **Anna Wexler**[1] *and* **Peter B. Reiner**[2]

Marketed for the purpose of modulating cognition or a variety of affective and mental states, a growing ecosystem of neurotechnology products is being sold direct to consumers (DTC) without necessitating the physician as intermediary. Offering individuals the prospect of monitoring and manipulating a range of brain functions from memory to mental health, the major product categories are neuromonitoring devices, cognitive training applications, neurostimulation devices, and mental health apps. The market for these products is predicted to top $3 billion by 2020 (*1*). Yet there are good reasons to conclude that regulatory oversight of DTC neurotechnologies is insufficient. We suggest ways to provide systematic support for regulatory agencies, funding bodies, and a public that is thirsty for knowledge about the efficacy of DTC neurotechnology products.

[1]*Department of Medical Ethics and Health Policy, Perelman School of Medicine, University of Pennsylvania, Philadelphia, PA, USA.* [2]*Department of Psychiatry and the Neuroethics Collective, University of British Columbia, Vancouver, BC, Canada. Email: awex@upenn.edu*

UNCLEAR EFFICACY, POTENTIAL HARMS

These products are neurotechnologies insofar as they appeal to the fruits of the brain and cognitive sciences; indeed, the imprimatur of science is often an integral part of their marketing. One overarching issue is whether DTC neurotechnologies work as advertised. The problem is threefold. First, many companies have conducted little to no original research on the effectiveness of their products. Second, many DTC neurotechnology companies sell products that are loosely based on scientific research, yet it is unclear whether data gathered in the laboratory are applicable to consumer-grade products. For example, consumer electroencephalography (EEG) devices are designed differently from research-grade EEG devices (e.g., they employ fewer electrodes) and are used in different ways (e.g., they require the individual himself or herself, not a trained technician, to position the EEG headset). Third, in many domains of DTC neurotechnology, there is a lack of scientific consensus with regard to efficacy: Questions have been raised about whether devices that deliver transcranial direct current stimulation (tDCS) can improve cognitive performance (*2*), whether cognitive gains from brain-training games are generalizable (*3*), and whether the behavioral effects of EEG neurofeedback (*4*) and mental health apps (*5*) are due to placebo.

tDCS devices present the possibility of overt harms such as skin burns, which are reported by a small portion of users (*6*). Also worth mentioning are the potential psychological harms from DTC neurotechnologies. For example, many consumer EEG devices purport to "read" one's emotional state (e.g., as stressed, meditative, or focused). Yet these devices have not been independently validated and may provide false information. If a consumer EEG device erroneously shows that an individual is in a stressed state, this may cause him or her to become stressed or to enact this stressed state, resulting in unwarranted psychological harm (*7*). Individuals may learn from a smartphone app that they have symptoms of depression—yet the diagnosis is provided without support structures that exist within the medical realm, such as a psychologist or mental health counselor.

PUBLIC UNDERSTANDING AND ETHICS

It is difficult for the public to assess the validity of claims made by DTC neurotechnology companies. Even those who are interested in developments in neurotechnology see navigating product claims as a key concern in the brain fitness field (*8*). Research has found that the public is unsure of which activities actually benefit their cognition. More than a quarter of adults age 40 and older believe that the best way to maintain or improve brain health is to play so-called "brain games" like Lumosity, even though there is little scientific evidence to support this notion (*9*).

No single DTC neurotechnology has yet demonstrated the kind of overwhelming efficacy that would result in widespread public adoption. However, if a new technology were to display the sort of efficacy that the field aspires to, a host of ethical concerns would arise. One common issue brought forward by neuroethicists is distributive justice: To the extent that cognitive ability influences socioeconomic status, premium pricing of cognitive enhancers could serve to exacerbate existing inequality gaps. Moreover, cognitive enhancement technologies hold particular appeal for populations such as the elderly, for whom cognitive decline is among the most frightening of prospects. The popularity of brain fitness software in the face of unproven efficacy is a testament to the appeal of this class of product.

PHOTO: FRANTICOO/SHUTTERSTOCK

Downloaded from http://science.sciencemag.org/ on January 17, 2019

Published by AAAS

REGULATORY INSUFFICIENCIES

One might imagine that DTC neurotechnologies would be classified as medical devices. But in much the same way that dietary supplements can avoid being classified as drugs by refraining from making claims about treating or diagnosing disease, so, too, do most DTC neurotechnologies avoid classification as medical devices by limiting their claims to wellness (e.g., "optimizing focus"). Indeed, a recent guidance from the U.S. Food and Drug Administration (FDA) clarified that the agency would not be enforcing medical device regulations for "low-isk" products marketed for wellness purposes (*10*). This guidance suggested that tDCS products would fall within the agency's jurisdiction, but the FDA has not taken public enforcement action against consumer tDCS products.

Venture capitalists interested in financing neurotechnologies have publicly stated that it would be difficult for them to invest in devices that require a premarket approval path through the FDA (*11*). Although some companies, such as app developer Pear Therapeutics, have pursued FDA approval, there is incentive for companies to market products for wellness to avoid FDA regulation. The regulatory burden for DTC neurotechnologies has largely fallen to the Federal Trade Commission (FTC), which has authority to take action in cases of deceptive advertising. Although the FTC has filed complaints against companies marketing brain-training software, there are thousands of mental health apps on the market (*12*), as well as dozens of devices for cognitive enhancement, relaxation by entraining brain waves, improving motor function, and more.

The challenges of regulating DTC neurotechnologies are in many ways similar to those facing dietary supplements. In both cases, the safety and efficacy of products have not been well established, there are no industry-wide standards, and the market is flooded with companies advertising and selling products directly to consumers with dubious health claims. In the United States, supplements are regulated by the FDA via the Dietary Supplement Health and Education Act (DSHEA) in a largely postmarket approach (*13*). Just as federal regulatory oversight from the FDA and FTC has been critiqued as being ill-suited to monitor the dietary supplement market (*14*), we suggest that similar concerns exist for DTC neurotechnologies: Given the sheer number of products, the dynamic nature of software applications that can change with each update, the flexibility required to oversee them, and the potential ethical issues involved, current regulatory oversight leaves much to be desired.

WHAT SHOULD WE DO?

Looking to the realm of supplements for guidance can be instructive, even if it does not provide a clear pathway forward. DSHEA mandated the creation of the National Institutes of Health (NIH) Office of Dietary Supplements, which conducts scientific research on dietary supplements and translates knowledge for the public and policy-makers. In addition, independent organizations provide evaluations and seals of approval for supplements (*14*).

In the realm of DTC neurotechnology, the analogous needs are twofold: for additional research into the safety and effectiveness of products, as well as how they are used by consumers; and for evaluations that can be made available to the public.

With regard to research, given that the DTC neurotechnology market is smaller than that of supplements and the concomitant public health risks are lower, we do not suggest the creation of a dedicated NIH body at the present time. However, inasmuch as DTC neurotechnology can be viewed as a downstream product of NIH-supported neuroscience research, we recommend that the NIH consider specifically funding research on DTC neurotechnologies, potentially under the umbrella of neuroethics research.

As for evaluation, two approaches exist for mental health apps but none for the remaining DTC neurotechnologies. At one end of the spectrum, the nonprofit organization Psyberguide provides consumer-oriented numerical ratings of individual mental health apps based on factors that include credibility, user experience, and transparency; at the other end of the spectrum, the American Psychiatric Association developed a framework that gives psychiatrists (but not consumers) tools to evaluate the safety, efficacy, and veracity of mental health apps.

We propose an approach that strikes a balance between the two: an independent working group that would survey the main domains of DTC neurotechnology and provide succinct appraisals of potential harms and probable efficacy. Rather than evaluating each and every product, which is resource-intensive, or providing overarching framing questions, the working group's appraisals would outline the evidence base and potential risks and identify gaps in current knowledge. Recent articles on the home use of brain stimulation (*15*) and consumer EEG devices (*7*) provide guidance and critiques without evaluating individual devices or claims and could serve as a model for the working group's appraisals.

The working group would be tasked with broadly circulating its appraisals to the public. Dissemination strategies would involve identifying and partnering with organizations such as the American Association of Retired Persons that are well positioned to communicate with key consumer groups, as well as sharing information with media outlets. The working group would serve as a clearinghouse for regulatory agencies such as the FDA and FTC, third-party organizations that monitor advertising claims, industry, social and medical scientists, funding agencies, and the public at large.

We envision the working group, which would be housed independently or within a reputable third-party organization, as drawing on the expertise of scientists, health professionals, consumer groups, industry representatives, ethicists, regulators, and funders. The working group would survey the current landscape, incorporating new domains of DTC neurotechnology and revising its appraisals. The group's mandate would include anticipating future developments, with an eye toward possible ethical concerns.

Given that government agencies and private enterprises are actively funding research into new methods of modulating brain function, the present generation of DTC neurotechnologies may be only the tip of the iceberg—making it all the more imperative to create an independent body to monitor developments in this domain. ■

Downloaded from http://science.sciencemag.org/ on January 17, 2019

REFERENCES AND NOTES

1. SharpBrains, Market Report on Pervasive Neurotechnology, (2018); https://sharpbrains.com/pervasive-neurotechnology/.
2. J. C. Horvath, J. D. Forte, O. Carter, *Brain Stimul.* **8**, 535 (2015).
3. D. J. Simons *et al*., *Psychol. Sci. Public Interest* **17**, 103 (2016).
4. R. T. Thibault, A. Raz, *Am. Psychol.* **72**, 679 (2017).
5. J. Torous, J. Firth, *Lancet Psychiatry* **3**, 100 (2016).
6. A. Wexler, *J. Cogn. Enhance* **2**, 114 (2018).
7. A. Wexler, R. Thibault, *J. Cogn. Enhance.* (2018); https://doi.org/10.1007/s41465-018-0091-2.
8. SharpBrains, "The Digital Brain Health Market 2012–2020" (2016); https://sharpbrains.com/market-report/.
9. L. Mehegan, C. Rainville, L. Skufca, "2017 AARP Cognitive Activity and Brain Health Survey" (AARP Research, Washington, DC, 2017); https://doi.org/10.26419/res.00044.001.
10. Food and Drug Administration, "General Wellness: Policy for Low Risk Devices" (2016), pp. 1–13.
11. J. Cavuoto, Regulatory Efficacy. Neurotech Business Report (2012); www.neurotechreports.com/pages/publishersletterOct12.html.
12. J. B. Torous *et al*., *Psychiatr. Serv.* **69**, 498 (2018).
13. J. Dwyer, P. Coates, M. Smith, *Nutrients* **10**, 41 (2018).
14. R. L. Bailey, *Crit. Rev. Food Sci. Nutr.* **39**, 1 (2018).
15. R. Wurzman, R. H. Hamilton, A. Pascual-Leone, M. D. Fox, *Ann. Neurol.* **80**, 1 (2016).

ACKNOWLEDGMENTS

This paper is informed by a 2018 meeting at the Banbury Center at Cold Spring Harbor that brought together regulators, scholars, and representatives from various professional organizations. A.W. acknowledges support from the Office of the Director, NIH, under Award Number DP5OD026420. P.B.R.'s funding derives from SSHRC grant 435-2018-0561. The content is solely the responsibility of the authors and does not represent the official views of funders.

10.1126/science.aav0223

Published by AAAS



Offerings are prepared on the banks of the Ganges River in Varanasi, Uttar Pradesh, India.

BOOKS *et al.*

ENVIRONMENTAL STUDIES

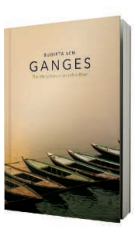
The revealing history of a revered waterway

Human and environmental stories interweave in a meandering meditation on the Ganges River

By **Anne Rademacher**

Invoking the Ganges prompts two very different visions. One imagines a sacred destination for countless devout pilgrims and the site of rituals repeated for thousands of years. Another sees a heavily polluted repository for the sewage and industrial wastes of dozens of Indian cities and yet water source for half a billion people. In this dual vision, the Ganges seems to embody the disjuncture of our time: It is both a dying piece of the planet and an enduring natural symbol of life and absolution.

Sudipta Sen's *Ganges: The Many Pasts of an Indian River* invites its reader across the space and time of this iconic riverscape. Through a sweeping yet carefully textured history, the layers of the Ganges's past assume a life that is both consequential and contemporary. We come to understand the Ganges as an expansive and dynamic social and natural system, and we gain a clearer perspective on the river's present and potential futures.



Ganges
Sudipta Sen
Yale University Press, 2019. 459 pp.

Sen begins this history with the ancient and enduring human practice of pilgrimage. Recounting his own journey from Gangotri, where the Ganges begins its descent, to the river's source at Gaumukh glacier, he asks how it is that this single river came to be imbued with sacred importance—nothing short, he writes, of a "metaphysical threshold."

He begins to explore this question through the long and dynamic history of myths, which narrate the river's powerful centrality in both spiritual cosmology and the political imagination. Although the details of the many myths Sen recounts changed over centuries, their core associations with a feminine form of divinity reproduced the river as both a sacred center and a symbolic locus of political legitimacy.

Ganges is neither social nor environmental history; it is inseparably both. Sen challenges us to notice the myriad ways that social and environmental transformation on this riverscape produced one another, often without a clearly linear story of cause and effect. Rather than composing an explanatory history, then, he emphasizes how social and environmental change melded together as ongoing processes. The approach, like the Ganges's very name, favors dynamism over stasis; Sen notes that the Sanskrit root of Ganges, *gam* ("to go"), invites us to study the river through prisms of motion, flow, direction, and force.

From pilgrimage and myth, the book moves through the heavily contested archaeological quest to find and discern the river's material past. That quest guides the reader along the vast tendrils of settled agriculture, reaching back nearly 15,000 years. We are led to reenvision the many lakes, marshes, forests, and grasslands that preceded the Ganges's present agrarian mosaic, in part through descriptions from the *Matsya Purana*, a collection of texts that date between the 8th and 13th centuries. These accounts bring lush past landscapes, which today are all but lost, back to conceptual life so that habitat transformation made less discernable in spans of centuries now leaves a more vivid trace.

Sen narrates the dramatic reworking of the plant and animal world in part by tracing equally dramatic social transformation. With settled agriculture came land ownership and taxation patterns, crop distribution mosaics, and consequent trade patterns that remade the riverscape and its social composition. The Ganges and the kingdoms and cities that rose around it organized spiritual and political identity, legitimizing successive imperial projects whose armies, merchants, artisans, and new religious practices carved and recarved territorial claims.

Late in the book, Sen arrives at the period of European empire building, the time at which more conventional histories of the present-day Ganges begin. With the benefit of a fuller historical arc, we understand more clearly how and why the Ganges was central to the Victorian imperial imagination and why the lower Ganges plains and the Bengal delta formed the heart of the East India Company's imperial territories in India. It also underscores why countless postcolonial leaders have repeatedly invoked its place, as Sen recounts using Nehru's words, as "a symbol and a memory of the past of India."

Ganges is a study of a river as many simultaneous places, temporalities, and experiences. It offers a way of thinking about a river not only as it flows over a landscape but as it assembles and connects aesthetics, territories, habitats, and human beings. In this sense, the book is an invitation to think about all environmental history not only as a story of a changing natural world but also as a story about ourselves. ■

The reviewer is in the Department of Environmental Studies and the Department of Anthropology, New York University, New York, NY 10003, USA. Email: anne.rademacher@nyu.edu

10.1126/science.aav8514

Downloaded from http://science.sciencemag.org/ on January 18, 2019

PHOTO: ISTOCK.COM/USER3A14F790_939

Published by AAAS

NUCLEAR POLICY

Nuclear power and promise

Deference to industry trumps safety in the U.S., warns a controversial former regulator

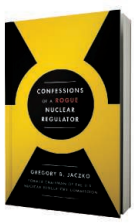
By **Jacob Darwin Hamblin**

Less than a year after the Fukushima nuclear accident in Japan, physicist Gregory B. Jaczko tried to break the "first commandment" of nuclear regulation: Thou shalt not deny a license to operate a reactor. As chairman of the U.S. Nuclear Regulatory Commission (NRC), he knew that the tradition was to encourage doomed applications to be withdrawn. But when one company refused, Jaczko dug in his heels and opposed the license. It turned out to be a futile gesture that the other commissioners opposed. But it was one of many examples, he contends, of the weaknesses in the nation's top nuclear regulatory body and an exemplar of its obeisance to the nuclear power industry.

Confessions of a Rogue Nuclear Regulator is one part engrossing memoir and another part seething diatribe, depicting a government agency that routinely caves to industry pressure. The book cannot help but also feel like a rationalization of Jaczko's own actions during his conflict-ridden tenure as chairman, a position offered to him in 2009 by President Barack Obama.

Jaczko first came to the commission in 2005, after working for Nevada senator Harry Reid fighting the project to store the nation's high-level radioactive waste at Yucca Mountain. He had a notoriously abrasive personality, and that did not change while at the NRC.

Yucca Mountain set the tone for Jaczko's tenure, and his autocratic leadership style alienated Republicans and Democrats alike. When he terminated a licensing review for the storage project, the other commissioners interpreted it as an illegal abuse of authority. The ensuing political fracas convinced Jaczko that the nuclear industry used the NRC as a tool for promoting rather than regulating nuclear power. He believes that a national repository for radioactive waste puts too much responsibility on the taxpayer. "No other industry is able to complain so loudly that someone else has failed to take care of its waste," he laments.



Confessions of a Rogue Nuclear Regulator
Gregory B. Jaczko
Simon and Schuster, 2019. 207 pp.

The answer is to stop producing nuclear waste, argues Jaczko, and indeed stop producing nuclear power at all. He wishes that as chairman, he'd "had the courage to say this, but my courage had its limits."

Most of Jaczko's short book hammers on the theme that industry lobbyists hold sway over the would-be regulators. He highlights the longstanding concept of "enforcement discretion" and skewers it as one of nuclear regulation's "greatest oxymorons."

Rather than demand safety compliance, the NRC historically has allowed nuclear plants to develop alternative approaches and has granted exceptions and exemptions. Recounting an episode in which he tried to abolish enforcement discretion in fire safety, Jaczko writes: "What happened over the next several weeks was more brutal than Roman imperial succession."

The political infighting was particularly intense after the 2011 Fukushima disaster. Jaczko visited Japan and grew impatient with the "litany of guarantees" from industry about American nuclear facilities. He tried to insist on new requirements to mitigate accidents triggered by natural disasters such as floods, earthquakes, and tsunamis. One internal NRC report drafted after Fukushima criticized the practice of relying on voluntary industry initiative to address safety concerns. Jaczko's descriptions of other commissioners' attempts to quash or edit the report provide a disturbing glimpse of the dynamic of trust and betrayal within the agency.

Confessions comes across as a story of one man and his loyal staff against a whole industry and its political toadies. Jaczko portrays himself as a naïve scientist, pushing hard for progressive reforms amid a corrupt bureaucracy. His critics might not be persuaded.

Toward the end of his tenure, Jaczko's fellow commissioners lodged a formal complaint against him, including accusations of mistreatment of women in the workplace. He survived the coup (his term) but ultimately resigned in 2012 at the request of his old mentor Harry Reid, who wanted to use his position as a political bargaining chip.

Although Jaczko's account will become standard reading as an antinuclear book, his reasons have more to do with regulation than nuclear energy per se. Jaczko sees two paths ahead. One has a sustainable future with nuclear reactors that includes widespread recognition that accidents will happen and a greater commitment to safety. The other path is the one he witnessed as NRC chairman, featuring waning public trust in a secretive, uncooperative industry that regards safety regulations as unfair and cumbersome.

The problem that plagued the old Atomic Energy Commission—that the promoters and regulators were too cozy with each other—is clearly alive and well. Jaczko describes the relationship as a "corrupt, toxic environment." It may be a hard warning to hear, but it comes from one who had a fuller view of the nuclear regulatory landscape than most. ■

The reviewer is at the School of History, Philosophy, and Religion, Oregon State University, Corvallis, OR 97331, USA. Email: jacob.hamblin@oregonstate.edu



PHOTO: ALEX WONG/GETTY IMAGES

Gregory Jaczko prepares to testify at a Senate hearing on nuclear reactor safety on 15 December 2011.

10.1126/science.aav8854

Downloaded from http://science.sciencemag.org/ on January 17, 2019

Published by AAAS



LETTERS

Since 2016, when this photo was taken, much of Kulhudhuffushi island's small mangrove patch has been destroyed.

PHOTO: EYEWELL PORTRAIT

Edited by **Jennifer Sills**

The value of small mangrove patches

Mangroves provide crucial services to humanity, including food, coastal protection, fisheries support, and carbon sequestration (*1*). However, up to 35% of mangrove area has been lost since the 1980s, primarily due to coastal development (*2*). Mangroves are protected under a plethora of international agreements, and they are key to meeting commitments of the Paris Climate Agreement and mitigating the impacts of a changing climate on coastal communities (*3*). Despite warnings about the ramifications of losing mangroves (*4*), conversion and degradation still occur (*5*), especially for smaller mangrove patches.

The global disdain for small mangrove patches is exemplified by the 2017 decision by the Maldivian government to construct a new local airport on the regionally significant mangrove patch (12 ha) on Kulhudhuffushi island (*6*). This decision was made despite the socioeconomic importance of the mangrove to the local community, the viable alternative solutions that were identified (*6*), the island's high risk for cyclones and tsunamis (*6*), and the substantial funding the Maldives received for climate change mitigation and adaptation [e.g., (*7*)]. Despite assurances that only 30% of the mangrove would be directly affected by this project, nearly 70% may have already been destroyed (*8*).

The loss of relatively small patches of mangrove may seem less concerning than large-scale deforestation. However, these patches are especially important to low-lying island nations vulnerable to climate change and sea-level rise (*1*). Their interconnectedness with adjacent habitats, such as coral reefs, allows them to provide substantial ecosystem services relative to their size (*9*). The continued loss of mangrove patches further fragments mangrove habitat, which creates barriers to species movement and dispersal (*10*). The loss also drastically erodes local coastal resilience and pushes key mangrove ecosystems toward collapse.

Given the recent Intergovernmental Panel on Climate Change's projections (*11*), we simply cannot afford to lose more mangrove forests, irrespective of their size. We call on governments to move away from policy decisions that prioritize large areas and short-term local political gains and instead adopt a more holistic long-term vision (*12*), whereby the value of smaller mangrove patches is better appreciated and safeguarded.

David J. Curnick[1,2], Nathalie Pettorelli[1,2], A. Aldrie Amir[1,3], Thorsten Balke[1,4], Edward B. Barbier[1,5], Stephen Crooks[1,6], Farid Dahdouh-Guebas[1,7,8], Clare Duncan[1,2], Charlie Endsor[1,9], Daniel A. Friess[1,10], Alfredo Quarto[1,11], Martin Zimmer[1,12], Shing Yip Lee[1,13]

[1]Mangrove Specialist Group, International Union for the Conservation of Nature (IUCN), Conservation Programmes, Zoological Society of London, Regents Park, London NW1 4RY, UK. [2]Zoological Society of London, Institute of Zoology, Regents Park, London NW1 4RY, UK. [3]Institute for Environment and Development (LESTARI), Universiti Kebangsaan Malaysia, 43600 Bangi, Selangor, Malaysia. [4]University of Glasgow, School of Geographical and Earth Sciences, Glasgow G12 8QQ, UK. [5]Department of Economics and School of Global Environmental Sustainability, Colorado State University, Fort Collins, CO 80523, USA. [6]Silvestrum Climate Associates, San Francisco, CA 94103, USA. [7]Systems Ecology and Resource Management, Université Libre de Bruxelles, B-1050 Brussels, Belgium. [8]Department of Ecology and Biodiversity, Vrije Universiteit Brussel, B-1050 Brussels, Belgium. [9]Conservation Programmes, Zoological Society of London, Regents Park, London NW1 4RY, UK. [10]Department of Geography, National University of Singapore, Singapore 117570, Singapore. [11]Mangrove Action Project, Seattle, WA 98104, USA. [12]Leibniz Centre for Tropical Marine Research, ZMT-GmbH, Bremen, Germany. [13]School of Life Sciences and Earth System Science Programme, The Chinese University of Hong Kong, Shatin, New Territories, Hong Kong SAR, China.
*Corresponding author. Email: david.curnick@zsl.org

REFERENCES

1. S. Y. Lee *et al.*, *Glob. Ecol. Biogeogr.* **23**, 726 (2014).
2. B. A. Polidoro *et al.*, *PLOS ONE* **5**, 10.1371/journal.pone.0010095 (2010).
3. P. Taillardat, D. A. Friess, M. Lupascu, *Biol. Lett.* **14**, 20180251 (2018).
4. N. C. Duke *et al.*, *Science* **317**, 41 (2007).
5. S. E. Hamilton, D. Casey, *Glob. Ecol. Biogeogr.* **25**, 729 (2016).
6. Z. Hameed, "Environmental Impact Assessment for the airport development project at Haa Dhaal Kulhudhuffushi" (2017).
7. Green Climate Fund (2018); www.mv.undp.org/content/maldives/en/home/operations/projects/environment_and_energy/GreenClimateFund.html.
8. Transparency Maldives (2018); http://transparency.mv/2018/09/joint-press-statement-we-call-on-the-authorities-to-ensure-the-protection-of-the-kulhudhuffushi-mangrove/.
9. E. B. Barbier, in *Seascape Ecology*, S. J. Pitmann, Ed. (Wiley-Blackwell, NY, 2017), pp. 465–481.
10. L. Triest, *Aquat. Bot.* **89**, 138 (2008).
11. O. Hoegh-Guldberg *et al.*, in "Global warming of 1.5°C," V. Masson-Delmotte *et al.*, Eds. (2018); www.ipcc.ch/sr15/.
12. A. A. Amir, *Science* **359**, 1342 (2018).

10.1126/science.aaw0809

Downloaded from http://science.sciencemag.org/ on January 17, 2019

Published by AAAS

Brazil's endangered postgraduate system

Over the past decade, Brazilian scientists have faced a dramatic reduction in financial support (*1*–*3*). In 2017, the Ministry of Science and Technology had a budget of only 2.8 billion reais, the equivalent of US$700 million (*4*), the lowest in the past 14 years (*5*). Dwindling funding affects a crucial population in Brazil's scientific system: students working toward master's and Ph.D. degrees.

Brazil's postgraduate system plays a pivotal role in scientific output. A major portion of scientific research takes place in publicly funded universities, and most scientific publications are driven by postgraduate programs (*6*, *7*). Brazil's 6303 master's and Ph.D. programs (*8*) are primarily funded by the Coordination for the Improvement of Higher Education Personnel (CAPES), a governmental agency within the Ministry of Education (*9*). The CAPES budget has plunged from the equivalent of US$1.9 billion in 2015 to the equivalent of US$1 billion in 2018 (*10*). The budget for 2019 projects an additional cut of nearly 40% (*11*). The funding cuts will likely translate into a substantial drop in federal grants, postdoctoral fellowships, support for international collaborations, and student scholarships. As student support falls, scientific output will likely decrease as well.

Brazil's scientific enterprise cannot function without qualified human resources, who will in turn strengthen social and economic development. Despite the polarized political atmosphere, Brazil must implement a strategic plan to improve the quality of science and innovation by investing in the postgraduate system.

Hercílio Martelli Júnior[1,2], Daniella R. Martelli[1], Ana Cristina Simões e Silva[2,3], Maria Christina L. Oliveira[3,4], Eduardo A. Oliveira[3,4]*

[1]Health Science/Primary Care Postgraduate Program, State University of Montes Claros (Unimontes), Montes Claros, MG 39401-089, Brazil. [2]Interdisciplinary Programs, CAPES, Brasília, DF 70.040-031, Brazil. [3]Health Sciences Postgraduate Program, School of Medicine, Federal University of Minas Gerais (UFMG), Belo Horizonte, MG 30130-100, Brazil. [4]University of California, San Diego, La Jolla, CA 92093–0630, USA.
*Corresponding author.
Email: eduolive812@gmail.com

REFERENCES

1. E. Gibney, *Nature* **526**, 16 (2015).
2. C. Angelo, *Nature* **533**, 19 (2016).
3. F. Marquez, "Funding in crisis," *Revista Pesquisa FAPESP* **256**, 1 (2017).
4. C. Angelo, *Nature* 10.1038/nature.2017.21766 (2017).
5. Ministério da Ciência, Tecnologia, Inovações e Comunicações, Recursos Aplicados—Governo Federal (2018); www.mctic.gov.br/mctic/opencms/indicadores/detalhe/recursos_aplicados/governo_federal/2_2_4.html [in Portuguese].
6. A. F. Helene, P. L. Ribeiro, *Scientometrics* **89**, 677 (2011).
7. E. A. Oliveira *et al.*, *Scientometrics* **90**, 429 (2011).
8. Coordenação de Aperfeiçoamento de Pessoal de Nível Superior (CAPES), Ministério da Educação, "Avaliação quadrienal em números" (2017); www.ucs.br/site/midia/arquivos/Avalia%C3%A7%C3%A3o_Quadrienal_em_n%C3%BAmeros.pdf [in Portuguese].
9. Coordenação de Aperfeiçoamento de Pessoal de Nível Superior (CAPES), Plano nacional de pós-graduação (PNPG) 2011-2020 (2010); www.capes.gov.br/plano-nacional-de-pos-graduacao [in Portuguese].
10. Coordination for the Improvement of Higher Education Personnel (CAPES), "Budget—Evolution in Reais" (2018); www.capes.gov.br/orcamento-evolucao-em-reais [in Portuguese].
11. A. C. Moreno, "Quase 200 mil bolsistas da Capes podem ficar sem bolsa se orçamento de 2019 sofrer corte, diz conselho," globo.com (2018); https://g1.globo.com/educacao/noticia/2018/08/02/quase-200-mil-podem-ficar-sem-bolsa-se-orcamento-de-2019-sofrer-corte-diz-conselho-da-capes.ghtml [in Portuguese].

10.1126/science.aav9015

Airborne in the era of climate change

The Intergovernmental Panel on Climate Change (IPCC) recently released its special report on limiting global warming to 1.5°C (*1*). The IPCC's 2050 target of carbon neutrality is strongly challenged by sectors with unavoidable emissions, such as aviation. Forecasts of the sector's growth predict that by 2050 it could have consumed up to one-quarter of the total global carbon budget for 1.5°C (*2*). The absence of substantial technical gains in aircraft emissions implies that reduction of aviation impact will be unfeasible without a decrease in demand (*3*). Air travel contributes substantially to the carbon footprint of academic communities (*4*), despite calls to travel less (*5*). In the current academic system, avoiding flying means accepting trade-offs, such as greater challenges to collaboration and networking. However, the cost of inaction and business as usual is the growing global threat of climate change, and scientists, given the alarms they regularly raise, should model responsible behavior to the planet. To encourage low-impact mobility, scientific institutions should adopt an avoid-mitigate-compensate approach similar to that developed in ecosystem conservation (*6*).



Air travel accounts for much of the science community's carbon footprint.

PHOTO: ISTOCK.COM/GUVENDEMIR

To avoid unnecessary journeys, institutions, department heads, and principal investigators should encourage scientists to consider or provide alternatives, such as teleconferencing and virtual scientific conferences. To mitigate emissions resulting from travel, scientists who must travel should replace flights with cleaner modes of travel as much as possible. Participants should prioritize local meetings, and organizers should reduce distances traveled by choosing central locations. To compensate for travel, scientists should financially contribute to credible and traceable projects for reducing and removing carbon emissions. This should be the last resort, given the questionable effectiveness of carbon offsetting (*7*).

There is increasing discussion about the best way to evaluate scientists, teams, and research projects (*8*), and including a carbon sobriety criterion could be a good way to reduce scientists' carbon footprint. Individual involvement is crucial, but supportive institutional environments [e.g., (*9*)] are also required to incentivize carbon-neutral behavior at the scale and speed required. Institutions invariably have policies for preventing and reducing harm, which address problems such as physical safety and data security. Surely the protection of planetary health, through the dramatic carbon cuts that are now urgently required, has a place in institutional policy, too.

Kévin Jean[1,2]* and Chris Wymant[3]

[1]Laboratoire MESuRS, Conservatoire National des Arts et Métiers, Paris, France. [2]Unité PACRI, Institut Pasteur, Conservatoire National des Arts et Métiers, Paris, France. [3]Big Data Institute, Li Ka Shing Centre for Health Information and Discovery, Nuffield Department of Medicine, University of Oxford, Oxford, UK.
*Corresponding author. Email: kevin.jean@lecnam.net

REFERENCES

1. "Global warming of 1.5°C," V. Masson-Delmotte *et al.*, Eds. (2018); www.ipcc.ch/sr15/.
2. "Analysis: Aviation could consume a quarter of 1.5C carbon budget by 2050," *Carbon Brief* (2016); www.carbonbrief.org/aviation-consume-quarter-carbon-budget.
3. A. Macintosh, L. Wallace, *Energ. Pol.* **37**, 264 (2009).
4. A. Stohl, *Atmos. Chem. Phys.* **8**, 6499 (2008).
5. X. Anglaret, *Lancet Planet Health* **2**, e382 (2018).
6. "An integrated framework and guidelines for avoiding, mitigating, and compensating for wetland losses: Resolution XI.9" (Ramsar Convention, 2012); www.ramsar.org/sites/default/files/documents/library/cop11-res09-e.pdf.
7. K. Hyams, T. Fawcett, *Wiley Interdisc. Rev.: Clim. Change* **4**, 91 (2013).
8. D. Moher *et al.*, *PLOS Biol.* **16**, e2004089 (2018).
9. Tyndall Centre, "Tyndall Travel Strategy—Towards a culture of low carbon research for the 21st Century" (2014); https://tyndall.ac.uk/travel-strategy.

10.1126/science.aaw1145

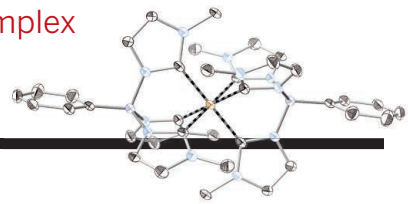
Downloaded from http://science.sciencemag.org/ on January 17, 2019

Published by AAAS

RESEARCH

Presenting a nanosecond-excited iron complex

Kjær et al., *p. 249*



IN *SCIENCE* JOURNALS

Edited by **Stella Hurtley**

BIODIVERSITY

Ancestral history matters

Biodiversity is sometimes quantified purely by the number of species within a system that allow it to function to produce ecosystem services. Grab *et al*. show that simple species counting is too simplistic. They combined remotely sensed land-cover analyses and crop production records with an extensive 10-year pollinator community survey and a complete species-level phylogeny generated using genome-wide phylogenomic methods. They found that the equivalent of millions of years of pollinator evolution were lost in highly altered agricultural environments, which decreased pollination services above and beyond what would be expected from a simple numerical species count. —SNV

Science, this issue p. 282

Mining bee (*Andrena nasonii*) on an apple (*Malus pumila*) flower

IMPACT CRATERS

Impact rates on Earth and the Moon

The rate at which impacts produce craters on the Moon is used to calibrate ages in planetary science. Earth should also have received similar numbers of impacts, but many craters have been hidden by erosion, ice sheets, and so on. Mazrouei *et al*. used infrared images of the Moon to estimate the ages of young lunar craters (see the Perspective by Koeberl). They found that the impact rate increased within the past ~500 million years, a conclusion strengthened by an analysis of known impact craters on Earth. Crater size distributions are the same on Earth and the Moon over this period, implying that terrestrial erosion affects all craters equally, regardless of their size. —KTS

Science, this issue p. 253; see also p. 224

PHOTOSYNTHESIS

Plugging into the pump

Photosynthetic organisms use light to fix carbon dioxide in a process that requires both chemical reducing equivalents and adenosine triphosphate (ATP). Balancing the ratio of these inputs is accomplished by a short circuit in electron flow through photosynthetic complex I, a proton pump that contributes to ATP production but does not increase net reducing equivalents in the cell. Schuller *et al.* solved a cryo–electron microscopy structure of photosynthetic complex I (see the Perspective by Brandt) and went on to reconstitute electron transfer using the electron carrier protein ferredoxin. —MAF

Science, this issue p. 257; see also p. 230

SOLAR CELLS

A redox road to recovery

Device longevity is a key issue for organic-inorganic perovskite solar cells. Encapsulation can limit degradation arising from reactions with oxygen and water, but light, electric-field, and thermal stresses can lead to metastable elemental lead and halide atom defects. Wang *et al*. show that for the lead-iodine system, the introduction of the rare earth europium ion pair Eu^{3+}-Eu^{2+} can shuttle electrons and recover lead and iodine ions (Pb^{2+} and I^-). Devices incorporating this redox shuttle maintained more than 90% of their initial power conversion efficiencies under various aging conditions. —PDS

Science, this issue p. 265

NEUROSCIENCE

The emotional dimension of pain

The unpleasantness of pain is an emotional phenomenon distinct from pain's sensory qualities. To study how the brain processes pain-related emotions, Corder

(PHOTO) KENT LOEFFLER; (GRAPHIC) KJAER *ET AL.*

Published by AAAS

et al. used in vivo neural calcium imaging in freely behaving mice. They identified brain circuits that respond to pain and directly tested their causal role in motivational behaviors associated with acute and chronic pain. —PRS

Science, this issue p. 276

CILIA

Assembly of the ciliary microtubule doublet

The cilium is a conserved organelle that is crucial for motility as well as for sensing the extracellular environment. Its core structure is characterized by nine microtubule doublets (MTDs). The mechanisms of MTD assembly are unclear. Schmidt-Cernohorska *et al*. developed an assay to reconstitute MTD assembly in vitro. Tubulin carboxyl-terminal tails played a critical inhibitory role in MTD formation. Molecular dynamics revealed that carboxyl-terminal tails of the A11 microtubule protofilament regulated MTD initiation. Furthermore, live-cell imaging showed an unexpected bidirectional isotropic elongation of the MTD. —SMH

Science, this issue p. 285

IMMUNOTHERAPY

Serotherapy treats a transplant hurdle

Cytomegalovirus (CMV) infection and reactivation are common and potentially fatal complications after bone marrow or hematopoietic stem cell transplantation (BMT). Martins *et al*. developed faithful preclinical murine models of CMV reactivation following BMT and found that humoral immunity can prevent this process (see the Perspective by Alegre). After BMT, antiviral antibodies that would have kept CMV at bay dwindle because host plasma cells are ablated and the donor B cell pool reconstitutes poorly. CMV reactivation was prevented by transferring antibody-containing immune serum. Such a therapeutic strategy would avoid some limitations of cellular therapies for BMT patients. —STS

Science, this issue p. 288; see also p. 232

FIBROSIS

When cell adhesion promotes fibrosis

Inflammatory macrophages produce the cytokine transforming growth factor–β (TGF-β), which induces the activation of fibroblasts into myofibroblasts that secrete extracellular matrix and promote fibrosis. Lodyga *et al*. found that the adhesion protein cadherin-11 (CDH11) was enriched at contact points between macrophages and myofibroblasts in fibrotic lung tissues from mice and human patients. CDH11-mediated adhesion between macrophages and lung fibroblasts triggered the activation of fibroblasts into myofibroblasts and targeted macrophage-produced TGF-β to myofibroblasts, creating a self-sustaining profibrotic niche. —AV

Sci. Signal. **12**, eaao3469 (2019).

TUMOR IMMUNOLOGY

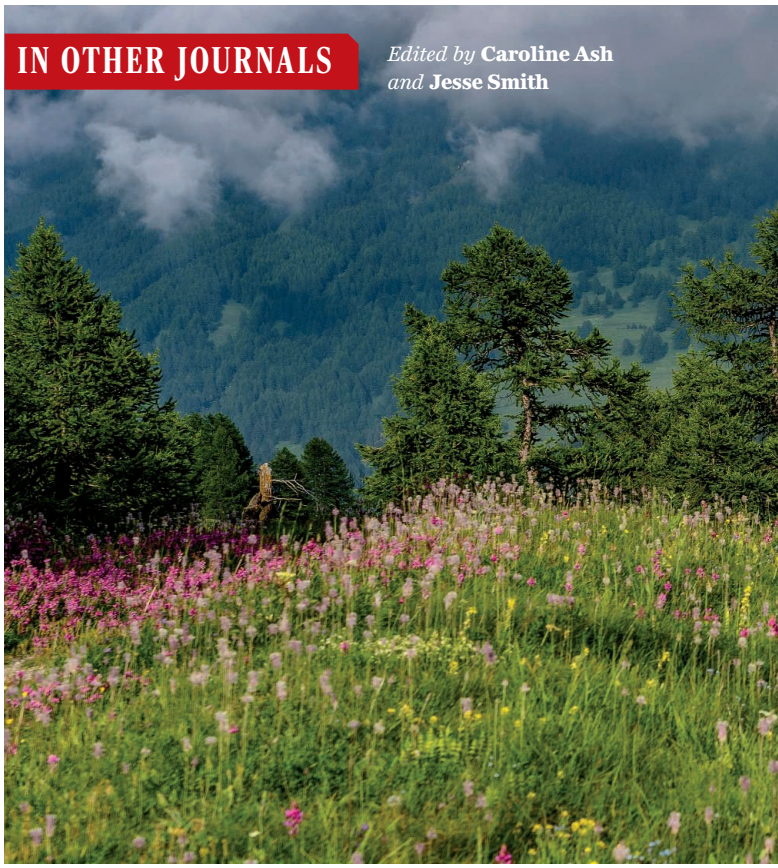
Neoantigen reactivity

Increased frequencies of intratumoral CD4$^+$ regulatory T cells (T_{regs}) have typically been associated with more-rapid tumor progression, but the antigen specificity of these T_{regs} within tumors is not well understood. Ahmadzadeh *et al*. characterized the T cell receptor (TCR) repertoire of intratumoral T_{regs} from patients with metastatic melanoma, gastrointestinal, and ovarian cancers. These T_{regs} had a unique TCR repertoire different from other intratumoral CD4$^+$ T cells, and dominant TCRs were specific to tumors and neoantigens. Similar cells were also found in the periphery, indicating that these T_{regs} may be expanding from both compartments. —CNF

Sci. Immunol. **4**, eaao4310 (2019).

IN OTHER JOURNALS

Edited by **Caroline Ash** *and* **Jesse Smith**



METALLOPROTEINS

A lanthanide secret handshake

Most metal ions in biology have distinct properties determined by atomic number and oxidation state. However, some metals in the lower rows of the periodic table are notorious for mimicking their lighter cousins: Trivalent yttrium and lanthanides, for example, can replace divalent calcium ions in some proteins. Cook *et al.* determined the solution structure of a protein that has evolved exquisite selectivity for these heavier ions over the lighter calcium. Despite superficial similarity to the calcium-binding protein calmodulin, there are large differences in the overall protein structure, and an additional carboxylic acid ligand is likely crucial for recognition of the heavier ions. —MAF

Biochemistry 10.1021/acs.biochem.8b01019 (2018).

PREGNANCY

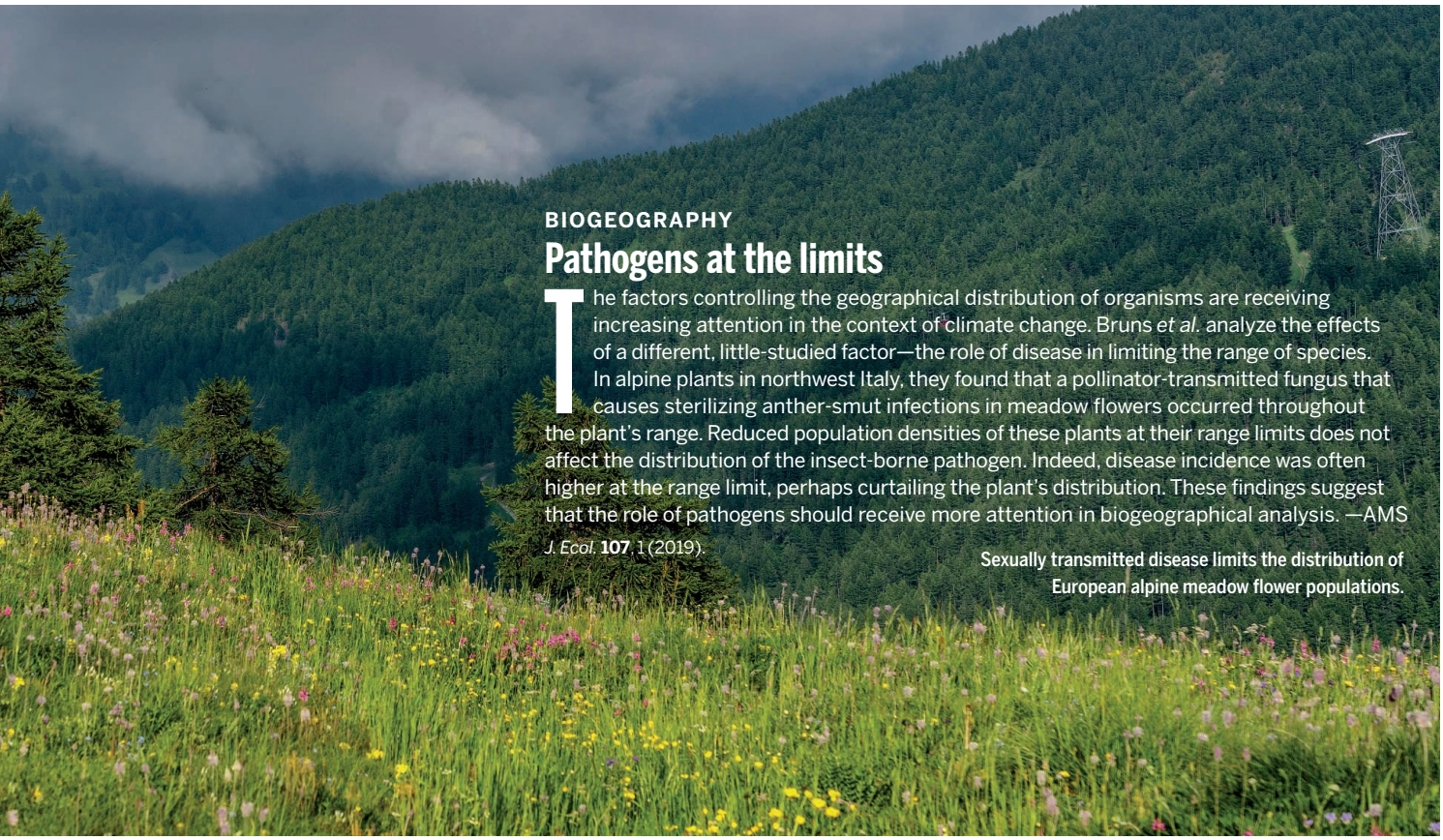
Understanding preeclampsia

Preeclampsia is characterized by the development of hypertension and kidney dysfunction during late stages of pregnancy, and it is an important cause of maternal and fetal mortality. Quitterer *et al.* found that increased complex formation between the G protein–coupled receptors angiotensin II AT1 and bradykinin B2 in vascular smooth muscle cells triggered preeclampsia in pregnant mice. Evidence for the hyperactivity of this heterodimer was also found in vascular structures in samples of placenta from pregnancies that had preeclampsia. Using a small-molecule inhibitor to target AT1-B2 receptor signaling prevented preeclampsia in mice. Initial data in patients with symptoms of preeclampsia indicate that this is an avenue for treatment options. —GKA

Cell **176**, 318 (2019).

PHOTO: CLAUDIO GIOVANNI COLOMBO/ALAMY STOCK PHOTO

Published by AAAS



BIOGEOGRAPHY

Pathogens at the limits

The factors controlling the geographical distribution of organisms are receiving increasing attention in the context of climate change. Bruns *et al.* analyze the effects of a different, little-studied factor—the role of disease in limiting the range of species. In alpine plants in northwest Italy, they found that a pollinator-transmitted fungus that causes sterilizing anther-smut infections in meadow flowers occurred throughout the plant's range. Reduced population densities of these plants at their range limits does not affect the distribution of the insect-borne pathogen. Indeed, disease incidence was often higher at the range limit, perhaps curtailing the plant's distribution. These findings suggest that the role of pathogens should receive more attention in biogeographical analysis. —AMS

J. Ecol. **107**, 1 (2019).

Sexually transmitted disease limits the distribution of European alpine meadow flower populations.

PHYSICS

Dynamics of repulsive Fermi gases

Pump-probe techniques, in which a short light pulse knocks the system out of equilibrium and another pulse is then used to monitor the dynamics, are commonplace in solid-state physics. Amico *et al.* used such a technique in a fermionic atomic gas to study what happens when the gas is plunged into a regime where the atoms strongly repel one another. The nature of this regime in an even mixture of two spin states has been debated—a ferromagnetic state was expected, but instead the atoms had a tendency to form pairs. Here, the researchers disentangled the two pathways and found that correlations consistent with ferromagnetism initially increased faster than the pairs formed, but neither clearly dominated over the other. —JS

Phys. Rev. Lett. **121**, 253602 (2018).

BIOTECHNOLOGY

Precision CRISPR editing

The most popular gene-editing tool, CRISPR-Cas9, generates breaks in the genome that are subsequently repaired by a mix of cellular pathways. Yet, the repair outcomes are not random. Using machine-learning algorithms to analyze large amounts of Cas9-mediated, genome-wide editing events in a range of cells, Shen *et al.*, Allen *et al.*, and Chakrabarti *et al.* uncovered sequence determinants of repair outcomes and devised rules to predict editing products. These findings provide insights into the repair process and instruct the design of guide RNAs to achieve more precise editing. —SYM

Nature **563**, 646 (2018).
Nat. Biotechnol. **37**, 64 (2019).
Mol. Cell 10.1016/j.molcel.2018.11.031 (2018).

ORGANIC CHEMISTRY

Targeting CH_2 sites

Most organic compounds contain numerous carbon-hydrogen (C–H) bonds. The weakest among them are easy to transform selectively, but the stronger ones tend to be hard to discriminate. Zhao *et al.* report a manganese catalyst that can selectively oxidize CH_2 centers in the presence of aromatic C–H bonds. The catalyst activates hydrogen peroxide with the help of chloroacetic acid, and despite targeting strong C–H bonds, it tolerates halogen, oxygen, and nitrogen functionality. The protocol is demonstrated across a variety of pharmaceutically relevant compounds. —JSY

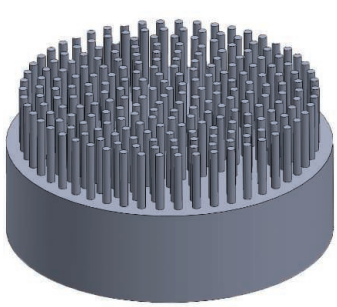
Nat. Chem. 10.1038/s41557-018-0175-8 (2018).

BIOMEDICINE

Addressing a hairy problem

Bioengineered skin grafts have helped many patients who have suffered considerable skin loss caused by disease or injury. However, these grafts often lack hair follicles, which are critical for thermoregulation, barrier function, and wound healing. The generation and function of hair follicles also requires spatial arrangement of skin cells and extracellular matrix, which has been difficult to reproduce in vitro. To address this challenge, Abaci *et al.* used three-dimensional (3D) printing technology to generate hair follicle–like microwells in a three-dimensionally reconstructed dermis. This allowed them to arrange human cells critical for hair growth into a physiologically relevant configuration. Grafting of vascularized versions of these skin constructs onto mice resulted in the growth of human hair. —PAK

Nat. Commun. **9**, 5301 (2018).



3D-printed template used to create hair follicles in reconstructed dermis

GRAPHIC: H. ABACI *ET AL.*, *NAT. COMMUN.* (2018)

Published by AAAS

ALSO IN *SCIENCE* JOURNALS

Edited by **Stella Hurtley**

ORGANIC CHEMISTRY

Synthetic innovation in drug development

Chemical synthesis plays a key role in pharmaceutical research and development. Campos *et al*. review some of the advantages that have come from recent innovations in synthetic methods. In particular, they highlight small-molecule catalysts stimulated by visible light, enzymes engineered for versatility beyond their intrinsic function, and bio-orthogonal reactions to selectively modify proteins for conjugation. High-throughput techniques are also poised to accelerate methods optimization from small-scale discovery to large-scale production, and complementary machine-learning approaches are just coming into focus. —JSY

Science, this issue p. 244

IMAGING TECHNIQUES

Combining expansion and the lattice light sheet

Optical and electron microscopy have made tremendous inroads into understanding the complexity of the brain. Gao *et al*. introduce an approach for high-resolution tracing of neurons, their subassemblies, and their molecular constituents over large volumes. They applied their method, which combines expansion microscopy and lattice light-sheet microscopy, to the mouse cortical column and the entire *Drosophila* brain. The approach can be performed at speeds that should enable high-throughput comparative studies of neural development, circuit stereotypy, and structural correlations to neural activity or behavior. —SMH

Science, this issue p. 245

GENE THERAPY

CRISPRa corrects haploinsufficient obesity

Loss-of-function mutation in one gene copy, termed haploinsufficiency, can lead to insufficient protein levels and result in human disease. Matharu *et al*. tested whether a CRISPR-based activation system (CRISPRa) could rescue a haploinsufficient phenotype by increasing the gene expression levels of the existing normal copy (see the Perspective by Montefiori and Nobrega). By delivering this system into the mouse hypothalamus using adeno-associated virus, they rescued the obesity phenotype caused by haploinsufficiency of either of two genes known to promote obesity when mutated in mice and humans. These results highlight the translational potential of the CRISPR activation system to treat haploinsufficient disease. —BAP

Science, this issue p. 246; see also p. 231

ASYMMETRIC CATALYSIS

Predicting catalyst selectivity

Asymmetric catalysis is widely used in chemical research and manufacturing to access just one of two possible mirror-image products. Nonetheless, the process of tuning catalyst structure to optimize selectivity is still largely empirical. Zahrt *et al*. present a framework for more efficient, predictive optimization. As a proof of principle, they focused on a known coupling reaction of imines and thiols catalyzed by chiral phosphoric acid compounds. By modeling multiple conformations of more than 800 prospective catalysts, and then training machine-learning algorithms on a subset of experimental results, they achieved highly accurate predictions of enantioselectivities. —JSY

Science, this issue p. 247

NEUROSCIENCE

The cerebellum and reward-driven behavior

Damage to the cerebellum manifests itself in various forms of cognitive impairment and abnormal social behavior. However, the exact role the cerebellum plays in these conditions is far from clear. Working in mice, Carta *et al*. found direct projections from the deep cerebellar nuclei to the brain's reward center, a region called the ventral tegmental area (see the Perspective by D'Angelo). These direct projections allowed the cerebellum to play a role in showing a social preference. Intriguingly, this pathway was not prosocial on its own. Cerebellar inputs into the ventral tegmental area were more active during social exploration. Depolarization of ventral tegmental area neurons thus represents a similar reward stimulus as social interaction for mice. —PRS

Science, this issue p. 248; see also p. 229

INORGANIC CHEMISTRY

Orange-glowing iron at room temperature

Many photoactive coordination compounds contain precious metals. Replacing ruthenium with more–earth-abundant iron has been a long-sought goal, but iron compounds generally relax too rapidly after light absorption to channel the energy productively. Kjær *et al*. prepared an iron compound with an excited state stable enough to emit light for nanoseconds, or that could engage in bimolecular electron transfer (see the Perspective by Young and Oldacre). Targeting a ligand-to-metal rather than metal-to-ligand charge-transfer state was key to the achievement, as was the octahedral coordination environment rigidly enforced by two tridentate carbene ligands. —JSY

Science, this issue p. 249; see also p. 225

ORGANIC CHEMISTRY

Journey to jorumycin

Jorumycin is a structurally complex, pentacyclic organic compound produced by a marine mollusk. The success of a similar compound, trabectedin, in treating certain types of cancer has focused attention on exploring jorumycin's pharmaceutical properties. Welin *et al*. developed a succinct route to synthesizing jorumycin and the closely related jorunnamycin A that deliberately diverges from the putative biosynthetic pathway underlying prior chemical syntheses. This route, which hinges on a carefully optimized asymmetric catalytic hydrogenation, can be easily modified to introduce unnatural structural diversity for functional optimization in further drug discovery research. —JSY

Science, this issue p. 270

CHEMICAL PHYSICS

Brief get-togethers between NaK and K

Cooling molecules to nanokelvin temperatures places them under the tightest quantum mechanical constraints. Studies in this intriguing regime have been limited to diatomics: Two cold atoms can be lured together into weakly associated Feshbach resonances, which lasers can then shift into a more stable molecular state. Yang *et al*. now report the observation of triatomic Feshbach resonances in ultracold collisions between potassium (K) atoms and sodium potassium (NaK) diatomics. The findings potentially set the stage for the preparation and study of ultracold triatomic molecules. —JSY

Science, this issue p. 261

Published by AAAS

CELL DIFFERENTIATION

Reversing chromatin dynamics for development

Compacted chromatin regions, marked by trimethylation of histone H3 at position lysine 9 (H3K9me3), occur at highly repeated DNA sequences, helping to suppress recombination and gene expression. Because pluripotent cells contain low levels of H3K9me3 heterochromatin relative to differentiated cells, it has been thought that an increase in such heterochromatin helps to define cell differentiation. Nicetto *et al*. used two independent methods to examine compacted heterochromatic domains and found that H3K9me3 compaction increased at protein-coding genes during early mouse organogenesis. During differentiation, these domains open up to allow cell-specific expression. Loss of heterochromatin by genetic inactivation of the H3K9me3 methyltransferases caused ectopic expression of cell-inappropriate genes and tissue pathology. —BAP

Science, this issue p. 294

MICROBIOLOGY

Dual roles of skin microbiota

Like the gut, the skin is colonized by microbes that can be protective to help maintain homeostasis or be pathogenic. In a Perspective, Stacy and Belkaid discuss the dual roles of *Staphylococcus epidermidis* on skin. This microbe exemplifies how skin microbiota can promote immune and antimicrobial responses against pathogens but, in certain contexts, aggravate pathologies such as eczema and possibly skin cancer. Skin is often termed the largest human organ, so it is important to understand how skin microbiota contribute to health. —GKA

Science, this issue p. 227

METABOLISM

An anti-ammonia probiotic

Hyperammonemia, or excess blood ammonia, is a serious condition that can result in brain damage and death. Kurtz *et al*. modified the metabolism of a probiotic *Escherichia coli* strain to overproduce arginine, thereby sequestering some of the ammonia produced by gut bacteria into the amino acid molecules. The engineered strain, called SYNB1020, lowered blood ammonia and increased survival in mouse hyperammonemia models and showed repeat-dose tolerability in nonhuman primates. A phase 1 dose-escalation study in healthy human volunteers resulted in no serious adverse events and indicated that the bacterium was metabolically active in vivo. —CAC

Sci. Transl. Med. **11**, eaau7975 (2019).

ECOLOGY

Standardizing science for conservation

Assessments of biodiversity and human impacts on the environment often rely on species distribution models that make data-supported predictions of species survival in changing environments. However, no agreed-upon standards for evaluating these models exist, and their application to conservation policy is inconsistent. Araújo *et al.* analyzed 400 model-based studies over the past 20 years to assess the adequacy of the models and their impacts on scientific interpretation and projection. They make the case for the development of best-practice standards and guidelines for the evaluation of data and models used. Such standardized practices should ensure more transparent and consistent translation of scientific results into policy. —PJB

Sci. Adv. 10.1126/sciadv.aat4858 (2019).

Published by AAAS

REVIEW SUMMARY

ORGANIC CHEMISTRY

The importance of synthetic chemistry in the pharmaceutical industry

Kevin R. Campos*, Paul J. Coleman*, Juan C. Alvarez, Spencer D. Dreher, Robert M. Garbaccio, Nicholas K. Terrett, Richard D. Tillyer, Matthew D. Truppo, Emma R. Parmee

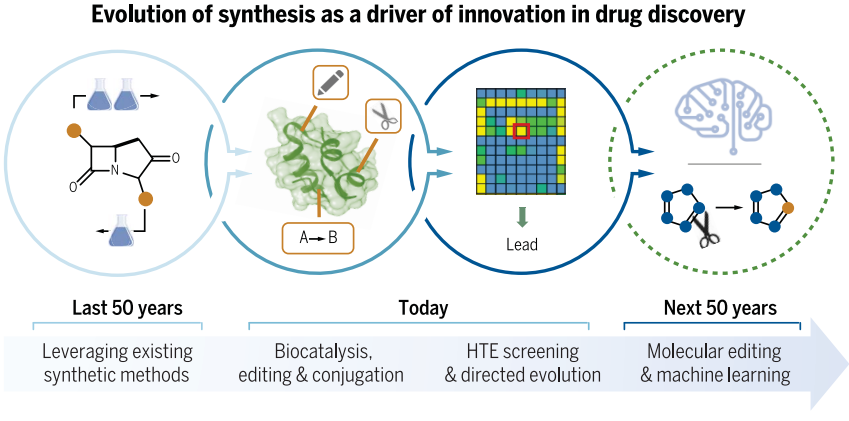
BACKGROUND: Over the past century, innovations in synthetic chemistry have greatly enabled the discovery and development of important life-changing medicines, improving the health of patients worldwide. In recent years, many pharmaceutical companies have chosen to reduce their R&D investment in chemistry, viewing synthetic chemistry more as a mature technology and less as a driver of innovation in drug discovery. Contrary to this opinion, we believe that excellence and innovation in synthetic chemistry continue to be critical to success in all phases of drug discovery and development. Moreover, recent developments in new synthetic methods, biocatalysis, chemoinformatics, and reaction miniaturization have the power to accelerate the pace and improve the quality of products in pharmaceutical research. Indeed, the application of new synthetic methods is rapidly expanding the realm of accessible chemical matter for modulating a broader array of biological targets, and there is a growing recognition that innovations in synthetic chemistry are changing the practice of drug discovery. We identify some of the most enabling recent advances in synthetic chemistry as well as opportunities that we believe are poised to transform the practice of drug discovery and development in the coming years.

ADVANCES: Over the past century, innovations in synthetic methods have changed the way scientists think about designing and building molecules, enabling access to more expansive chemical space and to molecules possessing the essential biological activity needed in future investigational drugs. In order for the pharmaceutical industry to continue to produce breakthrough therapies that address global health needs, there remains a critical need for invention of synthetic transformations that can continue to drive new drug discovery. Toward this end, investment in research directed toward synthetic methods innovation, furthering the nexus of synthetic chemistry and biomolecules, and developing new technologies to accelerate methods discovery is essential. One powerful example of an emerging, transformative synthetic method is the recent discovery of photoredox catalysis, which allows one to harness the energy of visible light to accomplish synthetic transformations on drug-like molecules that were previously unachievable. Furthermore, recent breakthroughs in molecular biology, bioinformatics, and protein engineering are driving rapid identification of biocatalysts that possess desirable stability, unique activity, and exquisite selectivity needed to accelerate drug discovery. Recent developments in the merging fields of synthetic and biosynthetic chemistry have sought to harness these molecules in three distinct ways: as biocatalysts for novel and selective transformations, as conjugates through innovative bioorthogonal chemistry, and in the development of improved therapeutic modalities. The development of high-throughput experimentation and analytical tools for chemistry has made it possible to execute more than 1500 simultaneous experiments at microgram scale in 1 day, enabling the rapid identification of suitable reaction conditions to explore chemical space and accelerate drug discovery. Finally, advances in computational chemistry and machine learning in the past decade are delivering real impact in areas such as new catalyst design, reaction prediction, and even new reaction discovery.

ON OUR WEBSITE

Read the full article at http://dx.doi.org/10.1126/science.aat0805

OUTLOOK: These advances position synthetic chemistry to continue to have an impact on the discovery and development of the next generation of medicines. Key unsolved problems in synthetic chemistry with potential implications for drug discovery include selective saturation and functionalization of heteroaromatics; concise synthesis of highly functionalized, constrained bicyclic amines; and C-H functionalization for the synthesis of α,α,α-trisubstituted amines. Other areas, such as site-selective modification of biomolecules and synthesis of noncanonical nucleosides, are emerging as opportunities of high potential impact. The concept of molecular editing, whereby one could selectively insert, delete, or exchange atoms in highly elaborated molecules, is an area of emerging interest. Continued investment in synthetic chemistry and chemical technologies through partnerships between the pharmaceutical industry and leading academic groups holds great promise to advance the field closer to a state where exploration of chemical space is unconstrained by synthetic complexity and only limited by the imagination of the chemist, enabling the discovery of the optimal chemical matter to treat disease faster than ever before. ■



Evolution of synthesis as a driver of innovation in drug discovery. Past, present, and future advances in synthetic chemistry are poised to transform the practice of drug discovery and development.

The list of author affiliations is available in the full article online.
*Corresponding author. Email: kevin_campos@merck.com (K.R.C.); paul_coleman@merck.com (P.J.C.)
Cite this article as K. R. Campos *et al.*, *Science* **363**, eaat0805 (2019). DOI: 10.1126/science.aat0805

Downloaded from http://science.sciencemag.org/ on January 19, 2019

REVIEW

ORGANIC CHEMISTRY

The importance of synthetic chemistry in the pharmaceutical industry

Kevin R. Campos[1]*, Paul J. Coleman[1]*, Juan C. Alvarez[1], Spencer D. Dreher[1], Robert M. Garbaccio[1], Nicholas K. Terrett[1], Richard D. Tillyer[2], Matthew D. Truppo[2], Emma R. Parmee[1]

Innovations in synthetic chemistry have enabled the discovery of many breakthrough therapies that have improved human health over the past century. In the face of increasing challenges in the pharmaceutical sector, continued innovation in chemistry is required to drive the discovery of the next wave of medicines. Novel synthetic methods not only unlock access to previously unattainable chemical matter, but also inspire new concepts as to how we design and build chemical matter. We identify some of the most important recent advances in synthetic chemistry as well as opportunities at the interface with partner disciplines that are poised to transform the practice of drug discovery and development.

Over the past century, innovations in synthetic chemistry have greatly enabled the discovery and development of important life-changing medicines, improving the health of patients worldwide. In recent years, many pharmaceutical companies have chosen to reduce their R&D investment in chemistry, viewing synthetic chemistry more as a mature technology and less as a driver of innovation in drug discovery (*1*–*3*). Contrary to this opinion, we believe that excellence and innovation in synthetic chemistry continues to be critical to success in all phases of drug discovery and development. Moreover, recent developments in new synthetic methods, biocatalysis, chemoinformatics, and reaction miniaturization have the power to accelerate the pace and improve the quality of products in pharmaceutical research. The application of new synthetic methods is rapidly expanding the realm of accessible chemical matter for modulating a broader array of biological targets, and there is a growing recognition that innovations in synthetic chemistry are changing the practice of drug discovery (*4*, *5*). Here, we identify some of the most enabling recent advances in synthetic chemistry as well as opportunities that we believe are poised to transform the practice of drug discovery and development in the coming years.

The pharmaceutical sector is currently facing multiple challenges: an increasing focus on complex diseases with unknown causal biology, a rapidly changing and highly competitive landscape, and substantial pricing pressures from patients and payers. In this challenging environment, drug discovery scientists must select biological targets of relevance to human disease and find safe and effective therapeutic molecules that appropriately modulate those targets. The current toolbox of synthetic methods and common chemical starting materials provides access to chemical space (*6*) that can be efficiently explored and mined to identify a suitable ligand and subsequently pursue studies of that preliminary lead compound toward its potential development as a successful drug. Brown and Boström have noted that a historical overreliance on just a few robust synthetic transformations (amide bond formation, sp^2-sp^2 C-C cross-coupling, and S_NAr reactions) has biased the output of many drug discovery efforts, leading to narrow sampling of chemical space (*7*). In other cases, the lack of any reasonable method of synthesis has, at minimum, hampered thorough evaluation of chemical space or, at worst, prevented it completely.

Conversely, the discovery of breakthrough synthetic methods can truly transform the process of drug discovery. Innovation in synthetic chemistry provides opportunity to gain more rapid access to biologically active, complex molecular structures in a cost-effective manner that can change the practice of medicine. An outstanding example of the transformative power of synthetic chemistry in drug discovery is the application of carbenoid N-H insertion chemistry to the synthesis of β-lactam antibiotics (*8*). In the 1950s, the synthesis of antibiotics such as penicillin represented a formidable challenge to medicinal chemists, and broad exploration of structure-activity relationships (SAR) within this class of compounds was hindered by a lack of good methods of synthesis for these chemically sensitive structures. Indeed, the first chemical synthesis of penicillin took nearly a decade of dedicated effort to achieve (*9*) despite an intensive effort across multiple laboratories. This lack of synthetic accessibility prevented thorough evaluation of structurally related antibiotics that might have a broader spectrum of activity and an improved resistance profile. The application of intramolecular N-H carbenoid insertion chemistry (Fig. 1) to these structures provided a disruptive solution to the preparation of these fused β-lactams. This synthetic method was applied to the preparation of numerous natural and synthetic anti-infectives, including thienamycin (*10*), which subsequently led to the discovery and industrial manufacture of the antibiotic imipenem. In this example, synthesis enabled design, opening access to previously unattainable molecules of high therapeutic value.

The development of targeted medicines for the treatment of chronic hepatitis C infection, a global health challenge (*11*), illustrates another key advance that innovative synthetic chemistry has contributed to drug discovery in recent years. The design and synthesis of hepatitis C virus (HCV) NS3/4a protease inhibitors represents a formidable challenge for medicinal chemists because the active site of this protease has a shallow, open binding site, and the enzyme possesses both genotypic and mutational diversity. Early studies

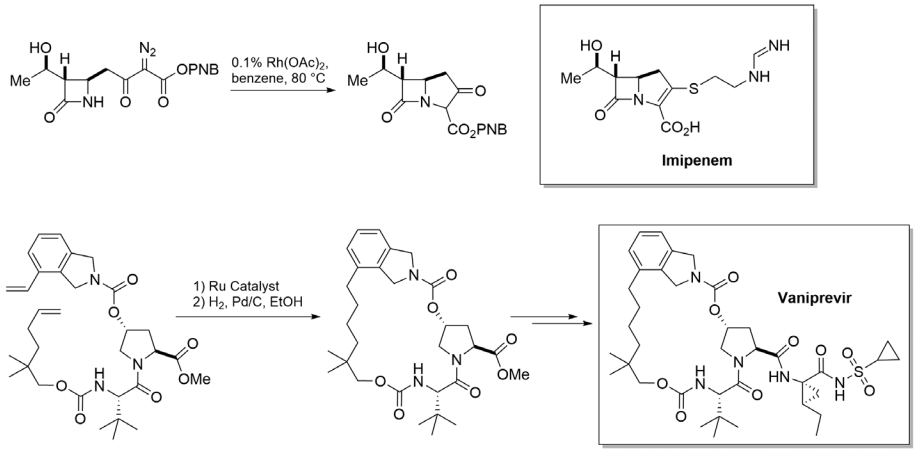


Fig. 1. Synthetic method innovations enable discovery of important anti-infectives, imipenem and vaniprevir.

[1]Global Chemistry, Merck & Co. Inc., Kenilworth, NJ 07033, USA. [2]Janssen Research & Development LLC, Spring House, PA 19477, USA.
*Corresponding author. Email: kevin_campos@merck.com (K.R.C.); paul_coleman@merck.com (P.J.C.)

Downloaded from http://science.sciencemag.org/ on January 19, 2019

of peptide-based inhibitors and subsequent molecular modeling suggested that construction of large, macrocyclic enzyme inhibitors could provide favorable ligand-protein binding and potent inhibition of this essential viral protease (*12*). The relatively flat and featureless protein surface requires a large ligand to gain sufficient binding affinity, while constrained macrocyclic ligands minimize the entropic cost of inhibitor binding. The application of ring-closing metathesis chemistry (*13*) has been transformative in the synthesis of many HCV NS3/4a protease inhibitors of varying ring sizes and complexity, including six approved drugs: simeprevir (*14*), paritaprevir (*15*), vaniprevir (*16*), grazoprevir (*17*), voxilaprevir (*18*), and glecaprevir (*19*). Ring-closing metathesis chemistry enabled the discovery of these and related macrocycles, allowing rapid assembly of complex bioactive molecules and broad exploration of SAR to address a range of properties.

In the two examples described above, the discovery of new synthetic pathways changed the way scientists thought about designing and building molecules, which broadened the accessible chemical space and thereby furnished molecules possessing the biological activity required in future drug candidates. The ability of the pharmaceutical industry to discover molecules to treat unmet medical needs and deliver them to patients efficiently in the face of an increasingly challenging regulatory landscape is dependent on continued invention of transformative, synthetic methodologies. Toward this end, investment in research directed toward synthetic methods innovation, furthering the nexus of synthetic chemistry and biomolecules, and developing new technologies to accelerate methods discovery is absolutely essential. Pertinent examples in these three areas are reviewed below.

Synthetic methods innovation

Over the past 20 years, several scientists have been recognized with the Nobel Prize for the invention of synthetic methodologies that have changed the way chemists design and build molecules. Each of these privileged methods—asymmetric hydrogenation, asymmetric epoxidation, olefin metathesis, and Pd-catalyzed cross-couplings—have broadly influenced the entire field of synthetic chemistry, but they have also enabled new directions in medicinal chemistry research. Of particular interest are new synthetic methods that enable medicinal chemists to control reactivity in complex, drug-like molecules, access non-obvious vectors for SAR development, and rapidly access new chemical space or unique bond formations. Recently, there have been several reported methods in these categories that have been rapidly adopted by medicinal chemists as a result of their practicality and broad utility.

Owing to the diverse biological activity of nitrogen-containing compounds, the discovery of Pd-catalyzed and Cu-catalyzed cross-coupling reactions of amines and aryl halides to form C-N bonds resulted in the rapid implementation of these synthetic methods in the pharmaceutical industry (*20*). The methodology addressed an unsolved problem to quickly and predictably access aromatic and heteroaromatic amines from simple precursors, and as a result it was rapidly adopted by medicinal chemists. Further development of these methodologies by process chemistry groups for scale-up has resulted in optimized ligands and precatalysts, as well as generally reliable protocols that have further advanced the application of this methodology in discovery programs. Consequently, aromatic C-N bonds are common features in pharmaceutical compounds (*21*), highlighting the tremendous impact that controlled construction of C-N bonds in aromatic compounds has had on medicinal chemistry programs. The next frontier is development of reliable methods to accomplish Csp^3-N couplings (*22*).

As the development of transition metal–catalyzed processes has advanced, application of cutting-edge methods to the predictable activation of C-H bonds for functionalization of complex lead structures can enable novel vector elaborations, changing the way analogs are prepared (*23*). In particular, late-stage selective fluorination and trifluoromethylation of C-H bonds in an efficient, high-yielding, and predictable fashion permits the modification of lead compounds to give analogs that potentially possess greater target affinity and metabolic stability without resorting to de novo synthesis. Methodological advances have enabled preparation of fluorinated analogs of lead structures under either nucleophilic or electrophilic conditions (*24*). One promising recent example shows that electrophilic aromatic fluorination can occur under mild conditions with a palladium catalyst and an electrophilic fluorine source such as *N*-fluorobenzenesulfonimide (NFSI) (*25*). In addition, trifluoromethylation of a structurally diverse array of drug discovery candidates using zinc sulfinates, in the presence of iron(III) acetylacetonate, generated analogs with improved metabolic properties (*26*). Visible-light photoredox catalysis has been also been applied to the practical, direct trifluoromethylation of heteroarenes (*27*).

Adoption of photoredox catalysis in the pharmaceutical industry has been rapid, owing to the practicality of the process, the tolerance to functional groups in drug-like candidates, and the activation of nonconventional bonds in drug-like molecules (*28*). Application of photoredox catalysis to the Minisci reaction was reported, enabling the facile and selective introduction of small alkyl groups into a variety of biologically active heterocycles such as camptothecin (*29*). Photoredox catalysis has also been used for the direct and selective fluorination of leucine methyl ester to afford γ-fluoroleucine methyl ester with a decatungstate photocatalyst and NFSI (Fig. 2). Numerous processes have been reported to access γ-fluoroleucine methyl ester, a critical fragment of the late-stage drug candidate odanacatib; however, this method enables the most direct and efficient method to access this key building block in the fewest operations from a commodity feedstock (*30*). More recently, photoredox catalysis was used to generate diazomethyl radicals, equivalents of carbyne species, which induced site-selective aromatic functionalization in a diverse array of drug-like molecules (*31*). This represents the latest of a series of very diverse, practical, and potentially impactful uses of photoredox techniques to assemble libraries of drug-like scaffolds for screening.

Although the preceding examples highlight the power of photoredox catalysis to accomplish previously unimaginable reactivity under very mild conditions (*32*, *33*), even more remarkable transformations are being reported via synergistic catalysis, where both the photocatalyst and a co-catalyst are responsible for distinct steps in a mechanistic pathway that is only accessible

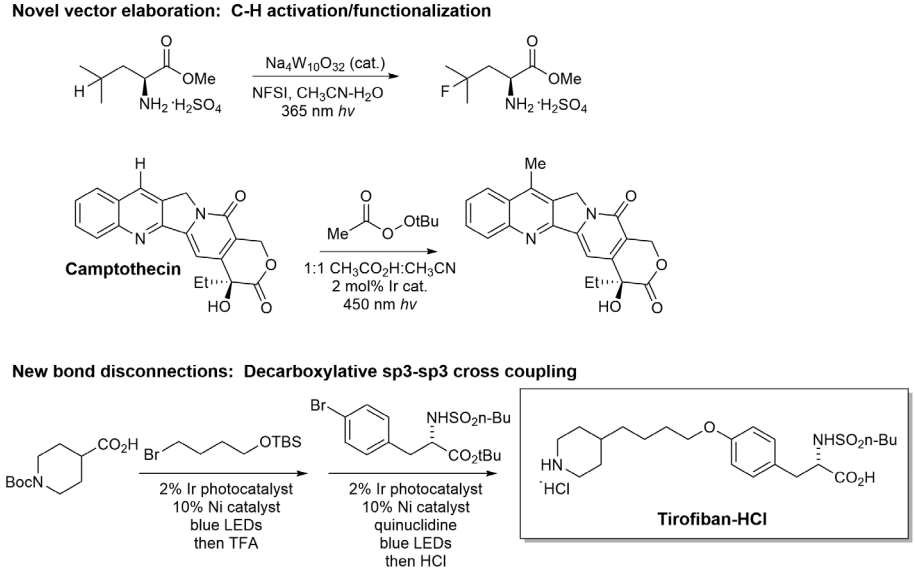


Fig. 2. Synthetic methods with potential to enable drug discovery.

Downloaded from http://science.sciencemag.org/ on January 19, 2019

with both catalysts present. For example, the combination of single-electron transfer–based decarboxylation with nickel-activated electrophiles has provided a general method for the cross-coupling of sp^2-sp^3 and sp^3-sp^3 bonds. This method establishes a new way of thinking about the carboxylic acid functional group as a masked cross-coupling precursor, expanding the synthetic opportunities for a functional group that is ubiquitous in chemical feedstocks (*34*). Furthermore, leveraging synergistic catalysis with photoredox has resulted in the discovery of milder conditions for C-O (*35*) and C-N cross-couplings, allowing application of these methods to more pharmaceutically relevant substrates (*36*). The concise synthesis of the antiplatelet drug tirofiban (*37*) is an excellent example of how the pharmaceutical industry can readily use this methodology to facilitate drug discovery and development. As research continues to surge in this field, additional breakthroughs are anticipated, and these will likely change how molecules are designed and built.

Intersection of synthetic chemistry with biomolecules

Biopolymers including proteins, nucleic acids, and glycans have evolved to achieve exquisite selectivity and function in a highly complex environment. These properties are of great interest to the pharmaceutical industry not only from a target perspective, but also from a therapeutic perspective. The success of monoclonal antibodies, peptides, and RNA-based therapies attests to the power that nature's platforms offer to our industry and patients. Recent advances in merging the fields of synthetic and biosynthetic chemistry have sought to harness these molecules and to expand useful manipulation of biomolecules in three distinct ways: as catalysts for novel and selective transformations, as conjugates through innovative bio-orthogonal chemistry, and in the development of novel and improved therapeutic modalities.

Biocatalysis

Historically, the broad adoption of biocatalysis was held back by a limited availability of robust enzymes, a relatively small scope of reactions, and the long lead time required to optimize a biocatalyst through protein engineering (*38*). The invention of a recombinant engineered Merck/Codexis transaminase biocatalyst for the commercial manufacture of sitagliptin (Januvia) has inspired the broader application of biotransformations in the pharmaceutical industry (*39*). Tremendous advances have been made in molecular biology, bioinformatics, and protein engineering, enabling the development of biocatalysts with desired stability, activity, and exquisite selectivity. The impact of this area of research is exemplified by the 2018 Nobel Prize in Chemistry, recognizing Frances Arnold "for the directed evolution of enzymes." As a result, biocatalysis has become more prevalent as a tool in drug discovery, as a valuable method for drug metabolite synthesis, and as a tool to enable rapid analog synthesis for SAR (*40*). For example, in 2013, the important discovery that cyclic guanosine monophosphate–adenosine monophosphate (2′,3′-cGAMP) is the endogenous agonist of STING, a protein involved in the activation of innate immune cells, triggered an intense interest in the synthesis of cyclic dinucleotide (CDN) analogs (*41*). Typically, the total synthesis of CDNs by purely chemical transformations requires long linear sequences and results in a time-consuming and low-yielding process. The optimization of STING agonists was greatly facilitated by the realization that the endogenous enzyme cGAS, responsible for the in vivo production of 2′,3′-cGAMP, could be engineered and harnessed for the biocatalytic production of non-natural CDNs (Fig. 3). The cyclization of various nucleotide triphosphate derivatives in a single biosynthetic step considerably reduced the cycle time and increased the yield of CDN synthesis, inspiring the design of novel agonists and the generation of SAR in this class (*42*). The continued investment in biocatalysis will lead to innovative solutions for unsolved problems in synthetic chemistry in both the discovery and development arenas. This will be driven by increased speed of protein engineering, access to enzymes with a variety of natural and even unnatural (*43*) catalytic activities, and the implementation of biocatalytic cascade catalysis to efficiently build complex chemical matter from simple starting materials (*44*).

Bio-orthogonal chemistry

Achieving selective reactions with biopolymers such as proteins presents a host of unique challenges to the synthetic chemistry community; proteins have multiple reactive centers, charged residues, higher-order structure, and are usually handled in an aqueous environment. Nonetheless, the opportunity to create improved conjugates as therapies and imaging agents, or to induce covalent interactions to identify protein targets, represents important value to therapeutic drug discovery.

Methods for selective conjugation to biomolecules have undergone major synthetic evolution over the past 20 years. The discovery and development of a suite of click reactions has served as a powerful and broadly applied tool in protein bioconjugation (*45*). This highly bio-orthogonal and biocompatible reaction offers a powerful alternative to heterogeneous conjugation to surface lysines or engineered cysteines, and spurred the development of complementary expression technologies that could incorporate unnatural elements or recognition tags into biopolymers. This evolution in conjugation chemistry is best evidenced in the field of antibody-drug conjugates (ADCs): The first generation of ADCs were heterogeneous conjugates, whereas those of the second generation are now almost entirely homogeneous, with growing evidence that the site of conjugation is an important determinant of overall ADC performance (*46*).

The development of additional bio-orthogonal chemistries that can lead to selective reaction with biomolecules, particularly without the requirement for engineering a recognition element into the biomolecule, is an important new frontier for synthetic impact. Two recent examples of synthetic innovation suggest this toolset is expanding for proteins. In many cases, having the ability to conjugate at either the N or C terminus of a wild-type protein should avoid unintended disruption of its function or secondary structure. The development of selective N-terminal conjugation chemistry (*47*) and complementary

Downloaded from http://science.sciencemag.org/ on January 19, 2019

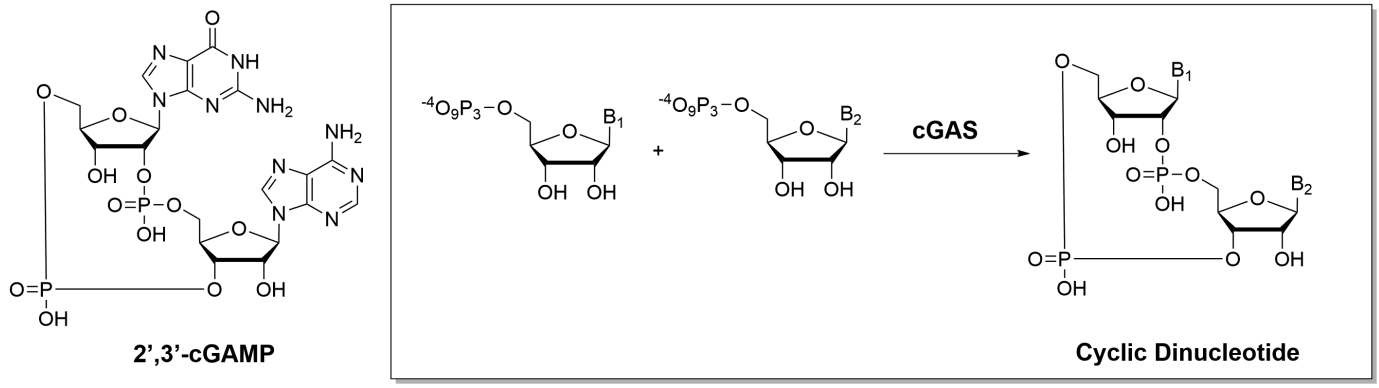


Fig. 3. Biocatalytic synthesis of novel cyclic dinucleotides.

application of decarboxylative alkylation chemistry to the C terminus of a protein substrate (*48*) offer new insights into achieving bio-orthogonal and highly site-selective conjugation with complex biomolecules (Fig. 4). These reactions take advantage of local differences in basicity and ionization potential respectively and, in doing so, leverage the complexity that biopolymers offer.

Synthetic innovation and therapeutic modalities

As these advances in synthetic, biorthogonal, and biosynthetic chemistry merge, so too do our capabilities to improve therapeutic modalities in the space between synthetic small molecules and expressed large monoclonal antibodies. Peptides, oligonucleotides, and bioconjugates have been advanced particularly for biological targets deemed "undruggable" by small-molecule and antibody platforms. Advances in these chemistries inspire new platforms and improve the breadth of biological targets that we can address. Two examples of innovation in therapeutic modalities through synthetic and biosynthetic chemistry are described below, although many others are being invented in academic and industrial settings.

In the first case, it has long been appreciated that a critical element of the success of oligonucleotide-based therapies was the introduction of phosphorothioates into the oligo backbone, which afforded improved stability to biological matrices as well as improved membrane permeability to aid with cytosolic delivery. Although these and other improvements in stability and delivery have advanced the field and enabled novel therapeutics to enter the clinic, many oligo-based therapies require high doses to overcome barriers to delivery, and their use is limited by their toxicity. Further improvements in stability and potency of the oligonucleotide should contribute to a widening of the therapeutic index and dose lowering. Interestingly, the chemistry used to introduce stabilizing phosphorothioates leaves each center as a mixture of two P-stereoisomers. Therefore, most clinical phosphorothioate-containing oligos that have 20 base pairs are, in reality, a large mixture of stereoisomers (2^{19}), each with different potency and stability characteristics. The ability to control phosphorothioate chemistry through an oxazaphospholidine approach by Wada and colleagues (*49*) led to a practical and scalable platform (*50*) for stereopure antisense oligonucleotides that demonstrate preclinical superiority to the corresponding stereomixtures.

Within the peptide arena, there has been a growing recognition that cyclic peptides offer improved starting points for drug discovery programs relative to their linear counterparts, largely due to improvements in entropic cost for binding and proteolytic stability. Early display platforms developed to discover cyclic peptides relied on disulfide formation, and more recently on post-translational introduction of bis-electrophiles

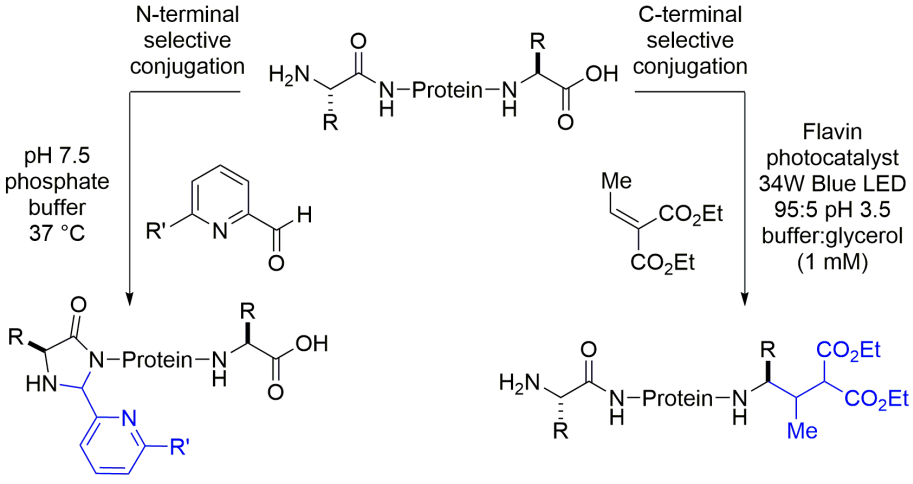


Fig. 4. Bio-orthogonal reactivity with proteins at N and C termini.

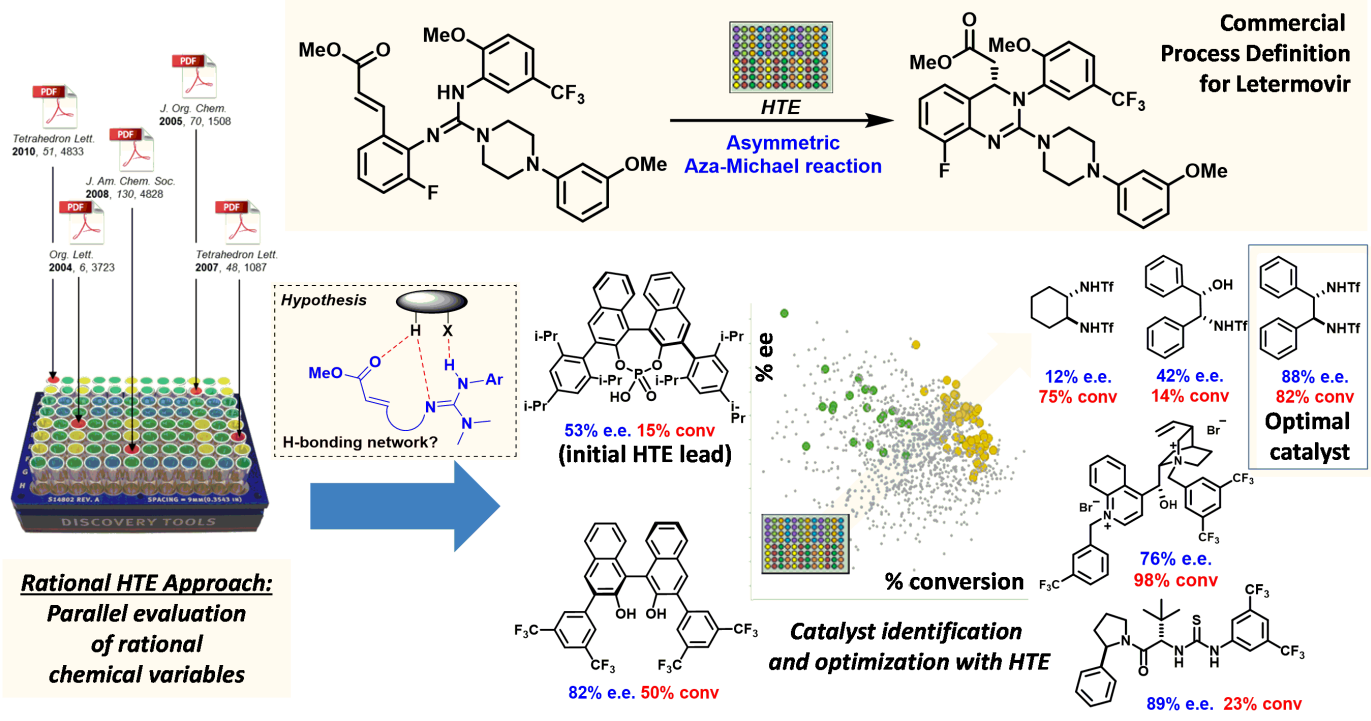


Fig. 5. High-throughput experimentation to accelerating reaction discovery.

Downloaded from http://science.sciencemag.org/ on January 19, 2019

that can cyclize peptides with two cysteine residues (51). Through combined application of a ribozyme biocatalyst to enable unnatural amino acid incorporation into peptides, and then bioorthogonal chemistry for cysteine cyclization through that unnatural amino acid, the Suga lab has developed an improved mRNA display platform (52) that has demonstrated tremendous potential to identify peptide ligands for challenging targets. The merging of chemical synthesis and biosynthesis within a common platform inspires further exploration of cyclic peptide modality; the introduction of selection pressures and forced evolution into this platform begins to resemble aspects of natural product generation that has historically inspired both organic synthesis and drug discovery.

Technologies to accelerate innovation

High-throughput experimentation

Given the need to invent and rapidly deliver medicines to patients, the pharmaceutical industry must invest in capabilities with the potential to radically accelerate the discovery and industrialization of transformative synthetic methodologies. High-throughput screening in biology has been the foundation of hit discovery for decades, and in recent years, the pharmaceutical industry has strategically invested in the creation of high-throughput experimentation (HTE) tools for chemistry that enable scientists to test experimental hypotheses with hundreds of arrayed experiments (53). In the same time frame required for traditional single-reaction evaluation, the different parameters that determine reaction outcome, discrete variables (catalysts, reagents, solvents, additives), and continuous variables (temperatures, concentrations, stoichiometries) can be holistically explored in parallel (54). As a result, the synthetic chemist now has access to exponentially larger amounts of experimental data than ever before. One recent example of the use of end-to-end HTE in process development was the discovery and development of an organo-catalyzed, enantioselective, aza-Michael reaction for the commercial manufacture of the antiviral letermovir (Fig. 5) (55). In this work, a series of efficient synthetic pathways were envisioned by chemists and key transformations were evaluated in parallel using HTE. The emergence of an H-bonding catalysis mechanism was initially discovered with moderate enantioselectivity and low conversion using chiral phosphoric acids. Rapid evaluation of a large number of diverse scaffolds with H-bonding capability in this transformation resulted in the discovery of an efficient and highly selective bissulfonamide catalyst. Further HTE work enabled the mechanistic understanding of the transformation, leading to optimization of both the catalyst structure and definition of optimal processing conditions. In this study and in many others (56, 57), novel bond-forming reactions were conceived by scientists, discovered through HTE, and then rapidly industrialized for the commercial manufacture of late-stage drug candidates.

HTE tools have also begun to have an impact in drug discovery (58). As new catalytic methods emerge that redefine which bonds can be forged, the breadth of the resulting substrate scope is poorly understood, as most test substrates commonly demonstrated in the literature are simple and not representative of the complex functionality common in drug candidates. Pre-dosed, reaction-specific HTE screening kits, containing a lab's most successful and general catalyst systems, are used in discovery chemistry labs to enable the rapid identification of reaction

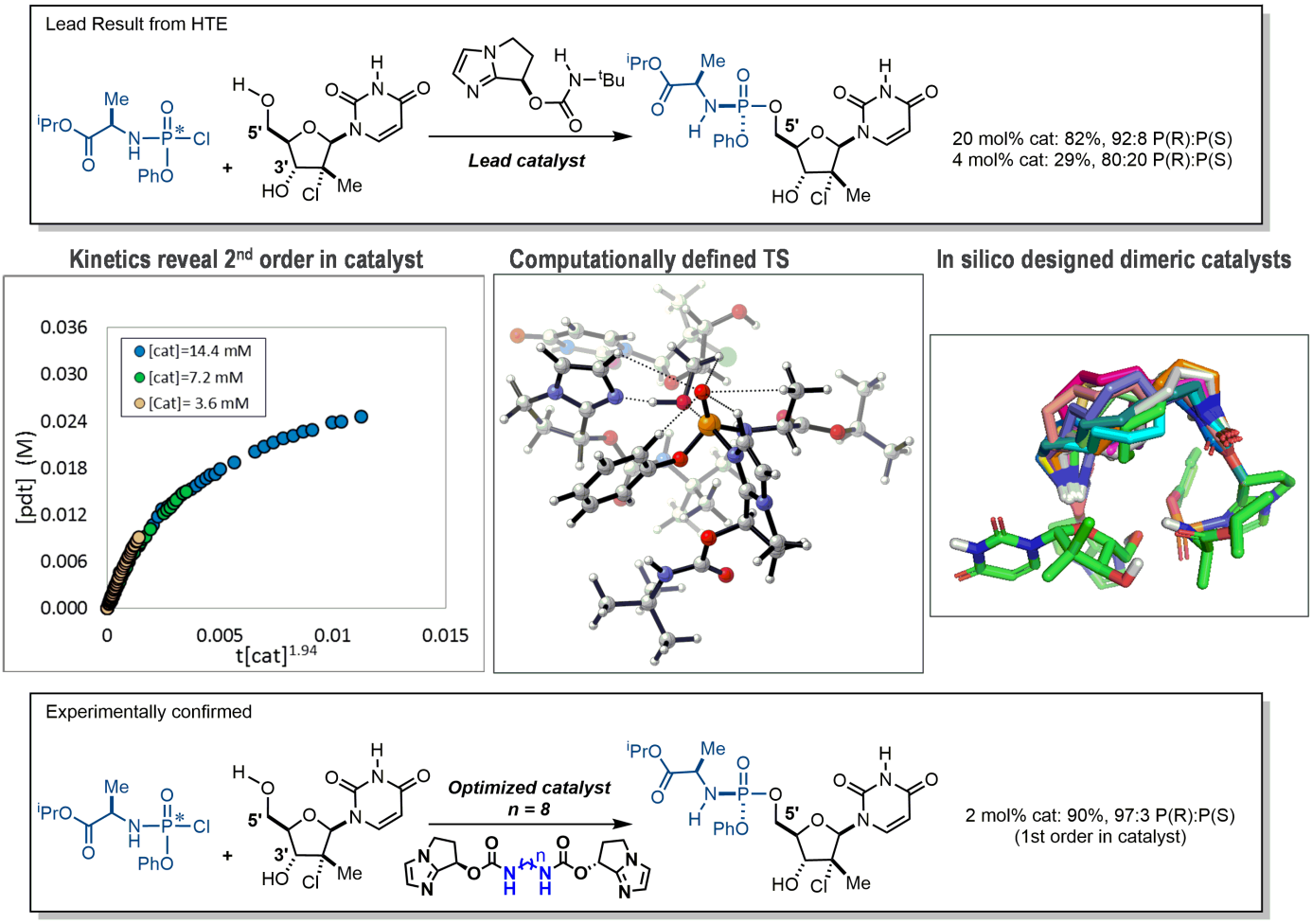


Fig. 6. Application of computational modeling to new catalyst design.

Downloaded from http://science.sciencemag.org/ on January 19, 2019

conditions that work for these complex substrates. Additionally, HTE has recently been leveraged to benchmark emerging methods against different catalytic procedures through the creation of arrays of complex, drug-like substrates known as informer libraries (*59*) or through addition of diverse molecular fragments that can disrupt catalysis (*60*, *61*). The use of these diagnostic methods allows exploration of the relationship between reaction types and diverse complex substrate structures, thus enabling synthetic practitioners to make better decisions about which synthetic methods to prioritize in their problem-solving. Additionally, miniaturization of HTE to nanomole scale—for example, by automated nanomole-scale batch (*62*) and flow (*63*) approaches—now enables the execution of more than 1500 simultaneous experiments at microgram scale in 1 day for rapid identification of suitable reaction conditions to explore chemical space and accelerate drug discovery. This capability is augmented by advances in rapid high-throughput analytics, such as MISER (multiple injections in a single experimental run) and MALDI (matrix-assisted laser desorption/ionization) mass spectrometry techniques (*64*), which have enabled the analysis of as many as 1536 reactions in very short time frames. Finally, nanomole HTE can also expedite the preparation of diverse, complex arrays of molecules and, when coupled directly with biological testing, can radically alter how drug discovery is performed (*65*).

Computational methods

The use of computer-assisted methods to guide synthetic chemistry is emerging as an important component in the practice of drug discovery. Advances in computational chemistry and machine learning in the past decade are delivering real impact in areas such as new catalyst design (*66*) or showing considerable promise in others such as reaction prediction (*67*). The application of deep learning methods has the potential to uncover new chemical reactions, expanding the access to new pharmaceutical chemical matter. Granda *et al.* (*68*) have reported promising results toward this end. By combining automated synthesis with machine learning, they reported the discovery of four chemical transformations with differentiated novelty.

Recently, computer-guided design has been successfully applied to the preparation of catalysts that provide asymmetric control of a cycloisomerization reaction (*69*). Computational methods were used to evaluate the catalytic pathway of a previously unknown reaction, leading to the hypothesis that the electronics of the catalyst ligand influence both the rate and stereoselectivity of the transformation. Application of quantum methods such as density functional theory (DFT) provided optimal ligand designs with markedly enhanced rate and selectivity over the original ligand. A second example where the use of computational methods aided in the design of a superior catalyst is reported in the synthesis of a pronucleotide (ProTide, Fig. 6) (*70*). Achieving selective phosphoramidation of a nucleoside at the 5′ hydroxyl over the 3′ hydroxyl with stereocontrol at the phosphorus center is highly challenging. A combination of mechanistic studies using a variety of chiral catalysts and DFT calculations of a proposed transition state further informed by experimental observations led to the rational design of a dimeric phosphoramidation catalyst with an improved rate and excellent stereoselectivity.

Despite these successes, the process for rational computational design of a catalyst is arduous, requiring the modeling of multiple mechanistic pathways and refinement of numerous molecules and transition states. A program for automating much of this process has been reported (*71*), and the advancement of such methods as well as the continual increase in processing power will drive further use of these tools in the future.

The application of machine learning to synthetic problems has also generated considerable interest and excitement. One area of active research is the use of algorithms for synthetic route planning to a target molecule (*72*, *73*). Segler *et al.* combined Monte Carlo tree search and three neural networks to identify potential synthetic routes (*74*). The success of the approach was qualitatively evaluated through a double-blind A/B test, where 45 chemistry students showed no preference between machine-suggested synthetic routes versus literature routes for representative target molecules. Machine learning has additionally been applied to forward reaction prediction (*75*). Neural networks were used to predict the major product of a reaction using an algorithm that assigns a probability and rank to potential products. Additionally, machine learning was used to successfully predict the performance of a single reaction, a Buchwald-Hartwig amination, against multiple variables: reactants, catalysts, bases, and additives (*76*). Application of machine learning holds considerable promise for synthetic optimization of targets far exceeding those described herein, toward predicting routes, main products, side products, and optimal conditions, among others. The continued advancement of these methods leverages the wealth of public information in the scientific and patent literature as well as within pharmaceutical institutions. The quality, breadth, depth, and density of the data within the domain of the predictions is critical for driving toward high-accuracy models. Inclusion of examples of both successful and unsuccessful transformations is also highly important. HTE is a highly attractive, complementary technology for augmenting existing datasets by generating model-suitable data, maximizing information content through careful design of experiments and capacity to deliver large volumes of data in a rapid and cost-effective manner.

Future directions

As we have discussed, breakthroughs in synthetic chemistry have proven to be the inspiration for the discovery and development of new medicines of important therapeutic value. Despite the many advances described above, the pace and breadth of molecule design is still constrained because of unsolved problems in synthetic chemistry. Many opportunities still remain to advance the field, such that synthetic chemistry will never constrain compound design or program pace, and should actually inspire access to uncharted chemical space in the pharmaceutical industry.

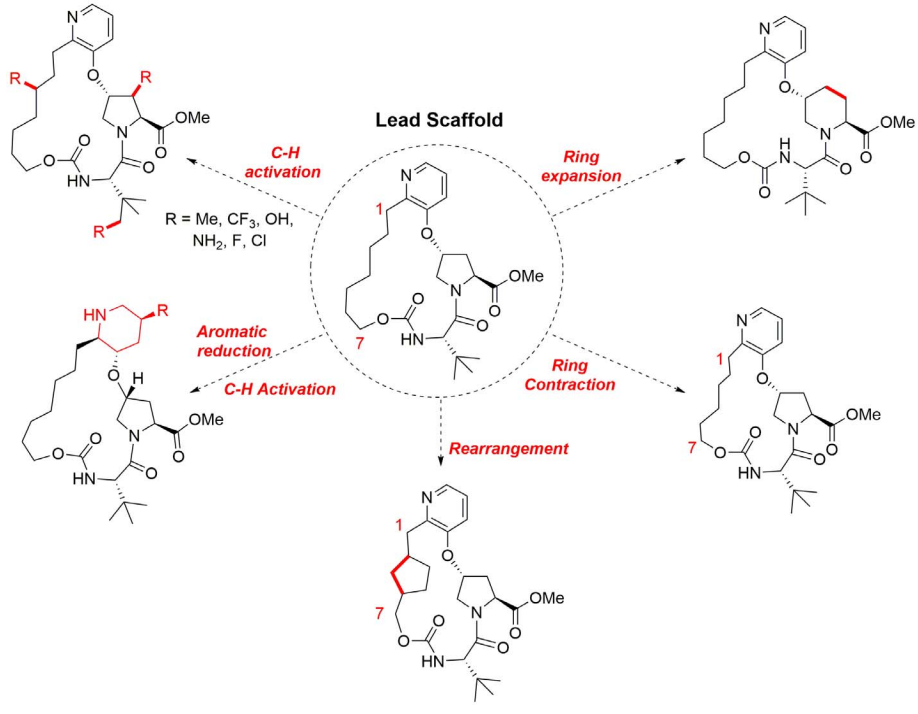


Fig. 7. Molecular editing to enable drug discovery.

Downloaded from http://science.sciencemag.org/ on January 19, 2019

Recently, we conducted a summit with key opinion leaders to assess the state of field and to identify areas of research in synthetic methods that would have critical impact in the pharmaceutical industry. Key unsolved problems in synthetic chemistry included selective saturation and functionalization of heteroaromatics, concise synthesis of highly functionalized, constrained bicyclic amines, and C-H functionalization for the synthesis of α,α,α-trisubstituted amines. Other areas, such as selective functionalization of biomolecules and synthesis of noncanonical nucleosides, were identified as emerging areas of high potential impact. We envision that partnerships between the pharmaceutical industry and leading academic groups in the field hold great promise to spur the invention of disruptive synthetic chemistry to address these areas.

The most intriguing idea to emerge from the discussion was the concept of molecular editing, which would entail insertion, deletion, or exchange of atoms in highly functionalized compounds at will and in a highly specific fashion. Many innovations discussed above possess elements of this aspirational goal; however, a truly general method of this type would substantially change the pace of drug discovery and reduce constraints on compound design. Figure 7 prospectively illustrates how analogs of a complex lead scaffold might be accessed via site selective C-H functionalization, heteroaromatic reduction, ring expansion, or ring contraction. The power to modify this scaffold directly and specifically not only avoids a potentially lengthy synthesis of analogs, but also removes any limitation of molecular design imposed by synthetic hurdles. We anticipate that breakthroughs in the area of molecular editing will improve the pace and quality of molecule invention, enabling the introduction of new and important medicines at a faster rate.

Outlook

Synthetic chemistry has historically been a powerful force in the discovery of new medicines and is now poised to have an even greater impact to accelerate the pace of drug discovery and expand the reach of synthetic chemistry beyond the traditional boundaries of small-molecule synthesis. New methods of synthesis can greatly expand the rate of molecule generation while also providing opportunities to routinely synthesize complex molecules in the course of drug discovery. Manipulation of biomolecules either as catalytic reagents (i.e., engineered enzymes) or as substrates for site-specific modulation is becoming more accessible and creating new opportunities for producing novel therapeutic entities. Academic research continues to be an important venue for producing novel reactivity, and rapid application of new methods has the potential to further drive molecule invention in drug discovery. New technologies such as HTE, automation, and new analytical methods are accelerating the discovery of new reaction methods. Further, integration of computational reaction modeling with the vast quantities of experimental data generated by nanoscale HTE has the potential to build more informative models that can predict successful reaction conditions or even discover new reactions. The field of predictive chemical synthesis remains nascent, but opportunities to build prognostic algorithms via machine-learning processes are likely to expand in the coming years. Continued investment in synthetic chemistry and chemical technologies has the promise to advance the field closer to a state where exploration of chemical space is unconstrained by synthetic complexity and is only limited by the imagination of the chemist. Advancements in synthetic chemistry are certain to remain highly relevant to the mission of inventing new medicines to improve the lives of patients worldwide.

REFERENCES AND NOTES

1. P. Ball, Chemistry: Why synthesize? *Nature* **528**, 327–329 (2015). doi: 10.1038/528327a; pmid: 26672538
2. G. M. Whitesides, Reinventing chemistry. *Angew. Chem. Int. Ed.* **54**, 3196–3209 (2015). doi: 10.1002/anie.201410884; pmid: 25682927
3. T. Laird, Is there a Future for Organic Chemists in the Pharmaceutical Industry outside China and India? *Org. Process Res. Dev.* **14**, 749 (2010). doi: 10.1021/op1001676
4. D. C. Blakemore *et al*., Organic synthesis provides opportunities to transform drug discovery. *Nat. Chem.* **10**, 383–394 (2018). doi: 10.1038/s41557-018-0021-z; pmid: 29568051
5. C. J. Gerry, S. L. Schreiber, Chemical probes and drug leads from advances in synthetic planning and methodology. *Nat. Rev. Drug Discov.* **17**, 333–352 (2018). doi: doi: 10.1038/nrd.2018.53; pmid: 29651105
6. J. L. Reymond, L. Ruddigkeit, L. Blum, R. van Deursen, The Enumeration of Chemical Space. *Wiley Interdiscip. Rev. Comput. Mol. Sci.* **2**, 717–733 (2012). doi: 10.1002/wcms.1104
7. D. G. Brown, J. Boström, Analysis of Past and Present Synthetic Methodologies on Medicinal Chemistry: Where Have All the New Reactions Gone? *J. Med. Chem.* **59**, 4443–4458 (2016). doi: 10.1021/acs.jmedchem.5b01409; pmid: 26571338
8. L. D. Cama, B. G. Christensen, Total synthesis of β-lactam antibiotics IX (±)-1-oxabisnorpenicillin G. *Tetrahedron Lett.* **19**, 4233–4236 (1978). doi: 10.1016/S0040-4039(01)95189-5
9. J. C. Sheehan, K. R. Henery-Logan, The Total Synthesis of Penicillin V. *J. Am. Chem. Soc.* **79**, 1262–1263 (1957). doi: 10.1021/ja01562a063
10. T. N. Salzmann, R. W. Ratcliffe, B. G. Christensen, F. A. Bouffard, A Stereocontrolled Synthesis of (+)-Theinamycin. *J. Am. Chem. Soc.* **102**, 6161–6163 (1980). doi: 10.1021/ja00539a040
11. J. L. Horsley-Silva, H. E. Vargas, New Therapies for Hepatitis C Virus Infection. *Gastroenterol. Hepatol.* **13**, 22–31 (2017). pmid: 28420944
12. J. L. Kim *et al*., Crystal structure of the hepatitis C virus NS3 protease domain complexed with a synthetic NS4A cofactor peptide. *Cell* **87**, 343–355 (1996). doi: 10.1016/S0092-8674(00)81351-3; pmid: 8861917
13. A. H. Hoveyda, A. R. Zhugralin, The remarkable metal-catalysed olefin metathesis reaction. *Nature* **450**, 243–251 (2007). doi: 10.1038/nature06351; pmid: 17994091
14. Å. Rosenquist *et al*., Discovery and development of simeprevir (TMC435), a HCV NS3/4A protease inhibitor. *J. Med. Chem.* **57**, 1673–1693 (2014). doi: 10.1021/jm401507s; pmid: 24446688
15. D. Niu, D. Liu, J. D. Moore, G. Xu, Y. Sun, Y. Gai, D. Tang, Y. S. Or, Z. Wang, US20090005387A1 (2009).
16. J. A. McCauley *et al*., Discovery of vaniprevir (MK-7009), a macrocyclic hepatitis C virus NS3/4a protease inhibitor. *J. Med. Chem.* **53**, 2443–2463 (2010). doi: 10.1021/jm9015526; pmid: 20163176
17. S. Harper *et al*., Discovery of MK-5172, a Macrocyclic Hepatitis C Virus NS3/4a Protease Inhibitor. *ACS Med. Chem. Lett.* **3**, 332–336 (2012). doi: 10.1021/ml300017p; pmid: 24900473
18. K. Bjornson *et al*., Preparation of N-(3-alkyl- and 3-carbocyclyl)prolyl-1-aminocyclopropanecarboxylic acid peptides as inhibitors of hepatitis C virus. WO2014/008285 (2014).
19. Y. S. Or *et al*., Preparation of macrocycles, especially proline-containing cyclic peptides, as hepatitis C virus (HCV) NS3-NS4A protease inhibitors, WO2012/040167 (2012).
20. P. Ruiz-Castillo, S. L. Buchwald, Applications of Palladium-Catalyzed C-N Cross-Coupling Reactions. *Chem. Rev.* **116**, 12564–12649 (2016). doi: 10.1021/acs.chemrev.6b00512; pmid: 27689804
21. E. Vitaku, D. T. Smith, J. T. Njardarson, Analysis of the structural diversity, substitution patterns, and frequency of nitrogen heterocycles among U.S. FDA approved pharmaceuticals. *J. Med. Chem.* **57**, 10257–10274 (2014). doi: 10.1021/jm501100b; pmid: 25255204
22. R. Gianatassio *et al*., Strain-release amination. *Science* **351**, 241–246 (2016). doi: 10.1126/science.aad6252; pmid: 26816372
23. T. Cernak, K. D. Dykstra, S. Tyagarajan, P. Vachal, S. W. Krska, The medicinal chemist's toolbox for late stage functionalization of drug-like molecules. *Chem. Soc. Rev.* **45**, 546–576 (2016). doi: 10.1039/C5CS00628G; pmid: 26507237
24. M. G. Campbell, T. Ritter, Late-Stage Fluorination: From Fundamentals to Application. *Org. Process Res. Dev.* **18**, 474–480 (2014). doi: 10.1021/op400349g; pmid: 25838756
25. K. Yamamoto *et al*., Palladium-catalysed electrophilic aromatic C-H fluorination. *Nature* **554**, 511–514 (2018). doi: 10.1038/nature25749; pmid: 29469096
26. C. A. Kuttruff, M. Haile, J. Kraml, C. S. Tautermann, Late-Stage Functionalization of Drug-Like Molecules Using Diversinates. *ChemMedChem* **13**, 983–987 (2018). doi: 10.1002/cmdc.201800151; pmid: 29534329
27. J. W. Beatty *et al*., Photochemical Perfluoroalkylation with Pyridine *N*-Oxides: Mechanistic Insights and Performance on a Kilogram Scale. *Chem* **1**, 456–472 (2016). doi: 10.1016/j.chempr.2016.08.002; pmid: 28462396
28. M. A. Miranda, M. L. Marin, Photocatalytic Functionalization for the Synthesis of Drugs and Analogs. *Curr. Opin. Green Sustain. Chem.* **6**, 139–149 (2017). doi: 10.1016/j.cogsc.2017.05.001
29. D. A. Dirocco *et al*., Late-stage functionalization of biologically active heterocycles through photoredox catalysis. *Angew. Chem.* **126**, 4902–4906 (2014). doi: 10.1002/ange.201402023; pmid: 24677697
30. S. D. Halperin *et al*., Development of a Direct Photocatalytic C-H Fluorination for the Preparative Synthesis of Odanacatib. *Org. Lett.* **17**, 5200–5203 (2015). doi: 10.1021/acs.orglett.5b02532; pmid: 26484983
31. Z. Wang, A. G. Herraiz, A. M. Del Hoyo, M. G. Suero, Generating carbyne equivalents with photoredox catalysis. *Nature* **554**, 86–91 (2018). doi: 10.1038/nature25185; pmid: 29388953
32. J. Twilton *et al*., The merger of transition metal and photocatalysis. *Nat. Rev. Chem.* **1**, 0052 (2017). doi: 10.1038/nature25185; pmid: 29388953
33. C. R. J. Stephenson, T. P. Yoon, D. W. C. Macmillan, *Visible Light Photocatalysis in Organic Chemistry* (Wiley-VCH, 2018).
34. A. Noble, S. J. McCarver, D. W. C. MacMillan, Merging photoredox and nickel catalysis: Decarboxylative cross-coupling of carboxylic acids with vinyl halides. *J. Am. Chem. Soc.* **137**, 624–627 (2015). doi: 10.1021/ja511913h; pmid: 25521443
35. J. A. Terrett, J. D. Cuthbertson, V. W. Shurtleff, D. W. C. MacMillan, Switching on elusive organometallic mechanisms with photoredox catalysis. *Nature* **524**, 330–334 (2015). doi: 10.1038/nature14875; pmid: 26266976
36. E. B. Corcoran *et al*., Aryl amination using ligand-free Ni(II) salts and photoredox catalysis. *Science* **353**, 279–283 (2016). doi: 10.1126/science.aag0209; pmid: 27338703
37. C. P. Johnston, R. T. Smith, S. Allmendinger, D. W. C. MacMillan, Metallaphotoredox-catalysed sp3-sp3 cross-coupling of carboxylic acids with alkyl halides. *Nature* **536**, 322–325 (2016). doi: 10.1038/nature19056; pmid: 27535536
38. Y. Li, P. C. Cirino, Recent advances in engineering proteins for biocatalysis. *Biotechnol. Bioeng.* **111**, 1273–1287 (2014). doi: 10.1002/bit.25240; pmid: 24802032
39. C. K. Savile *et al*., Biocatalytic asymmetric synthesis of chiral amines from ketones applied to sitagliptin manufacture. *Science* **329**, 305–309 (2010). doi: 10.1126/science.1188934; pmid: 20558668
40. M. D. Truppo, Biocatalysis in the Pharmaceutical Industry: The Need for Speed. *ACS Med. Chem. Lett.* **8**, 476–480 (2017). doi: 10.1021/acsmedchemlett.7b00114; pmid: 28523096
41. K. W. Knouse *et al*., Unlocking P(V): Reagents for chiral phosphorothioate synthesis. *Science* **361**, 1234–1238 (2018). doi: 10.1126/science.aau3369

Downloaded from http://science.sciencemag.org/ on January 19, 2019

42. M. D. Altman *et al*., Cyclic Di-Nucleotide Compounds as STING Agonists, WO2017/027646A1 (2017).
43. F. H. Arnold, Directed Evolution: Bringing New Chemistry to Life. *Angew. Chem. Int. Ed.* **57**, 4143–4148 (2018). doi: 10.1002/anie.201708408; pmid: 29064156
44. S. P. France, L. J. Hepworth, N. J. Turner, S. L. Flitsch, Constructing Biocatalytic Cascades: In Vitro and in Vivo Approaches to de Novo Multi-Enzyme Pathways. *ACS Catal.* **7**, 710–724 (2017). doi: 10.1021/acscatal.6b02979
45. E. M. Sletten, C. R. Bertozzi, Bioorthogonal chemistry: Fishing for selectivity in a sea of functionality. *Angew. Chem. Int. Ed.* **48**, 6974–6998 (2009). doi: 10.1002/anie.200900942; pmid: 19714693
46. P. Strop *et al*., Location matters: Site of conjugation modulates stability and pharmacokinetics of antibody drug conjugates. *Chem. Biol.* **20**, 161–167 (2013). doi: 10.1016/j.chembiol.2013.01.010; pmid: 23438745
47. J. I. MacDonald, H. K. Munch, T. Moore, M. B. Francis, One-step site-specific modification of native proteins with 2-pyridinecarboxyaldehydes. *Nat. Chem. Biol.* **11**, 326–331 (2015). doi: 10.1038/nchembio.1792; pmid: 25822913
48. S. Bloom *et al*., Decarboxylative alkylation for site-selective bioconjugation of native proteins via oxidation potentials. *Nat. Chem.* **10**, 205–211 (2018). doi: 10.1038/nchem.2888; pmid: 29359756
49. N. Oka, M. Yamamoto, T. Sato, T. Wada, Solid-phase synthesis of stereoregular oligodeoxyribonucleoside phosphorothioates using bicyclic oxazaphospholidine derivatives as monomer units. *J. Am. Chem. Soc.* **130**, 16031–16037 (2008). doi: 10.1021/ja805780u; pmid: 18980312
50. N. Iwamoto *et al*., Control of phosphorothioate stereochemistry substantially increases the efficacy of antisense oligonucleotides. *Nat. Biotechnol.* **35**, 845–851 (2017). doi: 10.1038/nbt.3948; pmid: 28829437
51. C. Heinis, T. Rutherford, S. Freund, G. Winter, Phage-encoded combinatorial chemical libraries based on bicyclic peptides. *Nat. Chem. Biol.* **5**, 502–507 (2009). doi: 10.1038/nchembio.184; pmid: 19483697
52. C. J. Hipolito, H. Suga, Ribosomal production and in vitro selection of natural product-like peptidomimetics: The FIT and RaPID systems. *Curr. Opin. Chem. Biol.* **16**, 196–203 (2012). doi: 10.1016/j.cbpa.2012.02.014; pmid: 22401851
53. M. Shevlin, Practical High-Throughput Experimentation for Chemists. *ACS Med. Chem. Lett.* **8**, 601–607 (2017). doi: 10.1021/acsmedchemlett.7b00165; pmid: 28626518
54. K. D. Collins, T. Gensch, F. Glorius, Contemporary screening approaches to reaction discovery and development. *Nat. Chem.* **6**, 859–871 (2014). doi: 10.1038/nchem.2062; pmid: 25242480
55. C. K. Chung *et al*., Asymmetric Hydrogen Bonding Catalysis for the Synthesis of Dihydroquinazoline-Containing Antiviral, Letermovir. *J. Am. Chem. Soc.* **139**, 10637–10640 (2017). doi: 10.1021/jacs.7b05806; pmid: 28737937
56. H. Li *et al*., Enantioselective Synthesis of Hemiaminals via Pd-Catalyzed C-N Coupling with Chiral Bisphosphine Monooxides. *J. Am. Chem. Soc.* **137**, 13728–13731 (2015). doi: 10.1021/jacs.5b05934; pmid: 26414910
57. S. W. Krska, D. A. DiRocco, S. D. Dreher, M. Shevlin, The Evolution of Chemical High-Throughput Experimentation To Address Challenging Problems in Pharmaceutical Synthesis. *Acc. Chem. Res.* **50**, 2976–2985 (2017). doi: 10.1021/acs.accounts.7b00428; pmid: 29172435
58. T. Cernak *et al*., Microscale High-Throughput Experimentation as an Enabling Technology in Drug Discovery: Application in the Discovery of (Piperidinyl)pyridinyl-1H-benzimidazole Diacylglycerol Acyltransferase 1 Inhibitors. *J. Med. Chem.* **60**, 3594–3605 (2017). doi: 10.1021/acs.jmedchem.6b01543; pmid: 28252959
59. P. S. Kutchukian *et al*., Chemistry informer libraries: A chemoinformatics enabled approach to evaluate and advance synthetic methods. *Chem. Sci.* **7**, 2604–2613 (2016). doi: 10.1039/C5SC04751J; pmid: 28660032
60. K. D. Collins, F. Glorius, A robustness screen for the rapid assessment of chemical reactions. *Nat. Chem.* **5**, 597–601 (2013). doi: 10.1038/nchem.1669; pmid: 23787750
61. J. Richardson, J. C. Ruble, E. A. Love, S. Berritt, A Method for Identifying and Developing Functional Group Tolerant Catalytic Reactions: Application to the Buchwald-Hartwig Amination. *J. Org. Chem.* **82**, 3741–3750 (2017). doi: 10.1021/acs.joc.7b00201; pmid: 28245358
62. A. Buitrago Santanilla *et al*., Nanomole-scale high-throughput chemistry for the synthesis of complex molecules. *Science* **347**, 49–53 (2015). doi: 10.1126/science.1259203; pmid: 25554781
63. D. Perera *et al*., A platform for automated nanomole-scale reaction screening and micromole-scale synthesis in flow. *Science* **359**, 429–434 (2018). doi: 10.1126/science.aap9112; pmid: 29371464
64. S. Lin *et al*., Mapping the dark space of chemical reactions with extended nanomole synthesis and MALDI-TOF MS. *Science* **361**, eaar6236 (2018). doi: 10.1126/science.aar6236; pmid: 29794218
65. N. J. Gesmundo *et al*., Nanoscale synthesis and affinity ranking. *Nature* **557**, 228–232 (2018). doi: 10.1038/s41586-018-0056-8; pmid: 29686415
66. M. Orlandi, F. D. Toste, M. S. Sigman, Multidimensional Correlations in Asymmetric Catalysis through Parameterization of Uncatalyzed Transition States. *Angew. Chem. Int. Ed.* **56**, 14080–14084 (2017). doi: 10.1002/anie.201707644; pmid: 28902441
67. D. T. Ahneman, J. G. Estrada, S. Lin, S. D. Dreher, A. G. Doyle, Predicting reaction performance in C-N cross-coupling using machine learning. *Science* **360**, 186–190 (2018). doi: 10.1126/science.aar5169; pmid: 29449509
68. J. M. Granda, L. Donina, V. Dragone, D.-L. Long, L. Cronin, Controlling an organic synthesis robot with machine learning to search for new reactivity. *Nature* **559**, 377–381 (2018). doi: 10.1038/s41586-018-0307-8; pmid: 30022133
69. R. N. Straker, Q. Peng, A. Mekareeya, R. S. Paton, E. A. Anderson, Computational ligand design in enantio- and diastereoselective ynamide [5+2] cycloisomerization. *Nat. Commun.* **7**, 10109 (2016). doi: 10.1038/ncomms10109; pmid: 26728968
70. D. A. DiRocco *et al*., A multifunctional catalyst that stereoselectively assembles prodrugs. *Science* **356**, 426–430 (2017). doi: 10.1126/science.aam7936; pmid: 28450641
71. Y. Guan, S. E. Wheeler, Automated Quantum Mechanical Predictions of Enantioselectivity in a Rhodium-Catalyzed Asymmetric Hydrogenation. *Angew. Chem. Int. Ed.* **56**, 9101–9105 (2017). doi: 10.1002/anie.201704663; pmid: 28586140
72. B. Liu *et al*., Retrosynthetic Reaction Prediction Using Neural Sequence-to-Sequence Models. *ACS Cent. Sci.* **3**, 1103–1113 (2017). doi: 10.1021/acscentsci.7b00303; pmid: 29104927
73. C. W. Coley, L. Rogers, W. H. Green, K. F. Jensen, Computer-Assisted Retrosynthesis Based on Molecular Similarity. *ACS Cent. Sci.* **3**, 1237–1245 (2017). doi: 10.1021/acscentsci.7b00355; pmid: 29296663
74. M. H. S. Segler, M. Preuss, M. P. Waller, Planning chemical syntheses with deep neural networks and symbolic AI. *Nature* **555**, 604–610 (2018). doi: 10.1038/nature25978; pmid: 29595767
75. C. W. Coley, R. Barzilay, T. S. Jaakkola, W. H. Green, K. F. Jensen, Prediction of Organic Reaction Outcomes Using Machine Learning. *ACS Cent. Sci.* **3**, 434–443 (2017). doi: 10.1021/acscentsci.7b00064; pmid: 28573205
76. D. T. Ahneman, J. G. Estrada, S. Lin, S. D. Dreher, A. G. Doyle, Predicting reaction performance in C-N cross-coupling using machine learning. *Science* **360**, 186–190 (2018). doi: 10.1126/science.aar5169; pmid: 29449509

ACKNOWLEDGMENTS

We thank M. Kress, J. Hale, L.-C. Campeau, D. Schultz, S. Krska, D. DiRocco, and A. Walji for their critical review of the manuscript; C. T. Liu for preparation of Fig. 1; and D. MacMillan, R. Sarpong, M. Gaunt, F. Arnold, and G. Dong for their participation in the Disruptive Chemistry Summit at Merck. The authors declare no competing financial interests.

10.1126/science.aat0805

Downloaded from http://science.sciencemag.org/ on January 19, 2019

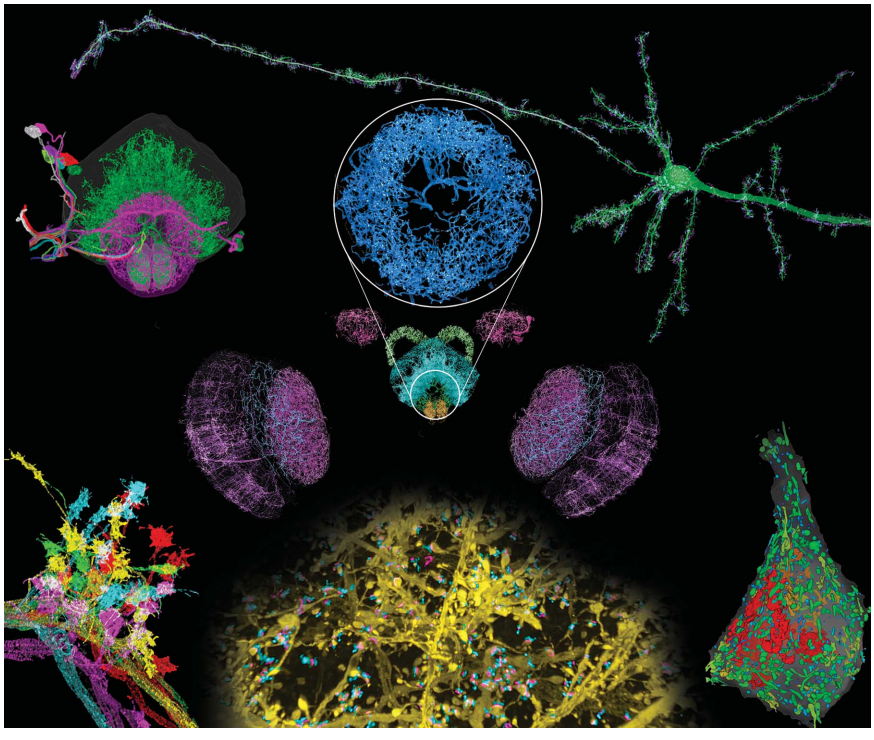
RESEARCH ARTICLE SUMMARY

IMAGING TECHNIQUES

Cortical column and whole-brain imaging with molecular contrast and nanoscale resolution

Ruixuan Gao*, Shoh M. Asano*, Srigokul Upadhyayula*, Igor Pisarev, Daniel E. Milkie, Tsung-Li Liu, Ved Singh, Austin Graves, Grace H. Huynh, Yongxin Zhao, John Bogovic, Jennifer Colonell, Carolyn M. Ott, Christopher Zugates, Susan Tappan, Alfredo Rodriguez, Kishore R. Mosaliganti, Shu-Hsien Sheu, H. Amalia Pasolli, Song Pang, C. Shan Xu, Sean G. Megason, Harald Hess, Jennifer Lippincott-Schwartz, Adam Hantman, Gerald M. Rubin, Tom Kirchhausen, Stephan Saalfeld, Yoshinori Aso, Edward S. Boyden†, Eric Betzig†

INTRODUCTION: Neural circuits across the brain are composed of structures spanning seven orders of magnitude in size that are assembled from thousands of distinct protein types. Electron microscopy has imaged densely labeled brain tissue at nanometer-level resolution over near-millimeter-level dimensions but lacks the contrast to distinguish specific proteins and the speed to readily image multiple specimens. Conversely, confocal fluorescence microscopy offers molecular contrast but has insufficient resolution for dense neural tracing or the precise localization of specific molecular players within submicrometer-sized structures. Last, superresolution fluorescence microscopy bleaches fluorophores too quickly for large-volume imaging and also lacks the speed for effective brain-wide or cortex-wide imaging of multiple specimens.



Nanoscale brain-wide optical imaging. ExLLSM images neural structures with molecular contrast over millimeter-scale volumes, including (clockwise from top right) mouse pyramidal neurons and their processes; organelle morphologies in somata; dendritic spines and synaptic proteins across the cortex; stereotypy of projection neuron boutons in *Drosophila*; projection neurons traced to the central complex; and (center) dopaminergic neurons across the brain, including the ellipsoid body (circular inset).

RATIONALE: We combined two imaging technologies to address these issues. Expansion microscopy (ExM) creates an expanded, optically clear phantom of a fluorescent specimen that retains its original relative distribution of fluorescent tags. Lattice light-sheet microscopy (LLSM) then images this phantom in three dimensions with minimal photobleaching at speeds sufficient to image the entire *Drosophila* brain or across the width of the mouse cortex in ~2 to 3 days, with multiple markers at an effective resolution of ~60 by 60 by 90 nm for 4× expansion.

ON OUR WEBSITE

Read the full article at http://dx.doi.org/10.1126/science.aau8302

RESULTS: We applied expansion/LLSM (ExLLSM) to study a variety of subcellular structures in the brain. In the mouse cortex, we quantified the volume of organelles, measured morphological parameters of ~1500 dendritic spines, determined the variation of distances between pre- and postsynaptic proteins, observed large differences in postsynaptic expression at adjacent pyramidal neurons, and studied both the azimuthal asymmetry and layer-specific longitudinal variation of axonal myelination. In *Drosophila*, we traced the axonal branches of olfactory projection neurons across one hemisphere and studied the stereotypy of their boutons at the calyx and lateral horn across five animals. We also imaged all dopaminergic neurons (DANs) across the brain of another specimen, visualized DAN morphologies in all major brain regions, and traced a cluster of eight DANs to their termini to determine their respective cell types. In the same specimen, we also determined the number of presynaptic active zones (AZs) across the brain and the local density of all AZs and DAN-associated AZs in each brain region.

CONCLUSION: With its high speed, nanometric resolution, and ability to leverage genetically targeted, cell type–specific, and protein-specific fluorescence labeling, ExLLSM fills a valuable niche between the high throughput of conventional optical pipelines of neural anatomy and the ultrahigh resolution of corresponding EM pipelines. Assuming the development of fully validated, brain-wide isotropic expansion at 10× or beyond and sufficiently dense labeling, ExLLSM may enable brainwide comparisons of even densely innervated neural circuits across multiple specimens with protein-specific contrast at 25-nm resolution or better. ■

The list of author affiliations can be found in the full article online.
*These authors contributed equally to this work.
†Corresponding author. Email: esb@media.mit.edu (E.S.B.); betzige@janelia.hhmi.org (E.B.)
Cite this article as R. Gao *et al.*, *Science* **363**, eaau8302 (2019). DOI: 10.1126/science.aau8302

Downloaded from http://science.sciencemag.org/ on January 19, 2019

RESEARCH ARTICLE

IMAGING TECHNIQUES

Cortical column and whole-brain imaging with molecular contrast and nanoscale resolution

Ruixuan Gao[1,2,3]*, Shoh M. Asano[1,2]*†, Srigokul Upadhyayula[3,4,5,6]*, Igor Pisarev[3], Daniel E. Milkie[3], Tsung-Li Liu[3]‡, Ved Singh[3]§, Austin Graves[3]¶, Grace H. Huynh[1]#, Yongxin Zhao[1], John Bogovic[3], Jennifer Colonell[3], Carolyn M. Ott[3], Christopher Zugates[7], Susan Tappan[8], Alfredo Rodriguez[8], Kishore R. Mosaliganti[9], Shu-Hsien Sheu[3], H. Amalia Pasolli[3], Song Pang[3], C. Shan Xu[3], Sean G. Megason[9], Harald Hess[3], Jennifer Lippincott-Schwartz[3], Adam Hantman[3], Gerald M. Rubin[3], Tom Kirchhausen[3,4,5,6], Stephan Saalfeld[3], Yoshinori Aso[3], Edward S. Boyden[1,2,10,11,12,13]††, Eric Betzig[3,14,15,16,17,18]††**

Optical and electron microscopy have made tremendous inroads toward understanding the complexity of the brain. However, optical microscopy offers insufficient resolution to reveal subcellular details, and electron microscopy lacks the throughput and molecular contrast to visualize specific molecular constituents over millimeter-scale or larger dimensions. We combined expansion microscopy and lattice light-sheet microscopy to image the nanoscale spatial relationships between proteins across the thickness of the mouse cortex or the entire *Drosophila* brain. These included synaptic proteins at dendritic spines, myelination along axons, and presynaptic densities at dopaminergic neurons in every fly brain region. The technology should enable statistically rich, large-scale studies of neural development, sexual dimorphism, degree of stereotypy, and structural correlations to behavior or neural activity, all with molecular contrast.

The human brain is a 1.5-kg organ that, despite its small size, contains more than 80 billion neurons (*1*) that connect through approximately 7000 synapses each in a network of immense complexity. Neural structures span a size continuum greater than seven orders of magnitude in extent and are composed of more than 10,000 distinct protein types (*2*) that collectively are essential to build and maintain neural networks. Electron microscopy (EM) can image down to the level of individual ion channels and synaptic vesicles (*3*) across the ~0.03 mm^3 volume of the brain of the fruitfly *Drosophila melanogaster* (*4*, *5*). However, EM creates a grayscale image in which the segmentation of specific subcellular components or the tracing of the complete arborization of specific neurons remains challenging and in which specific proteins can rarely be unambiguously identified. Optical microscopy combined with immunofluorescence, fluorescent proteins, or fluorescence in situ hybridization (FISH) enables high-sensitivity imaging of specific protein expression patterns in brain tissue (*6*, *7*), brain-wide tracing of sparse neural subsets in flies (*8*, *9*) and mice (*10*), and in situ identification of specific cell types (*11*, *12*) but has insufficient resolution for dense neural tracing or the precise localization of specific molecular players within critical subcellular structures such as dendritic spines. Diffraction-unlimited superresolution (SR) fluorescence microscopy (*13*, *14*) combines nanoscale resolution with protein-specific contrast but bleaches fluorophores too quickly for large-volume imaging and, like EM, would require months to years to image even a single *D. melanogaster* brain (table S1).

Given the vast array of molecular species that contribute to neural communication through many mechanisms in addition to the synaptic connections determined by EM connectomics (*15*), and given that the anatomical circuits for specific tasks can vary substantially between individuals of the same species (*16*, *17*), high-resolution three-dimensional (3D) imaging with molecular specificity of many thousands of brains may be necessary to yield a comprehensive understanding of the genesis of complex behaviors in any organism. Here, we describe a combination of expansion microscopy (ExM) (*18*, *19*), lattice light-sheet microscopy (LLSM) (*20*), and terabyte-scale image processing and analysis tools (*21*) that achieves single-molecule sensitivity and ~60- by 60- by 90-nm resolution at volumetric acquisition rates ~700× and 1200× faster than existing high-speed SR (*22*) and EM (*5*) methods, respectively, at comparable or higher resolution (table S1). We demonstrate its utility through multicolor imaging of neural subsets and associated proteins across the thickness of the mouse cortex and the entirety of the *Drosophila* brain while quantifying nanoscale parameters, including dendritic spine morphology, myelination patterns, stereotypic variations in boutons of fly projection neurons, and the number of synapses in each fly brain region.

Combining expansion and lattice light-sheet microscopy (ExLLSM)

In protein-retention ExM (proExM) (*19*), fluorophore-conjugated antibodies (Abs) and/or fluorescent proteins (FPs) that mark the features of interest within a fixed tissue are chemically linked to an infused polyacrylamide/polyacrylate gel. After protease digestion of the tissue, the gel can be expanded in water isotropically, creating an enlarged phantom of the tissue that faithfully retains the tissue's original relative distribution of fluorescent tags (fig. S1 and supplementary note 1). This yields an effective resolution given by the original resolution of the imaging microscope divided by the expansion factor. Another advantage of digestion is that lipids, protein fragments, and other optically inhomogeneous organic components that are not anchored to the gel are sufficiently removed so that the expanded gel has a refractive index nearly indistinguishable from water and therefore can be imaged aberration-free to a postexpansion depth of at least 500 μm (fig. S2) by using conventional water immersion objectives. ProExM has been applied to a range of model animals, including mouse (*19*), zebrafish (*23*), and *Drosophila* (*24*–*28*). Although up to 20× expansion has been reported (*29*), at 8× expansion by using an iterated form of

[1]MIT Media Lab, Massachusetts Institute of Technology (MIT), Cambridge, MA 02139, USA. [2]McGovern Institute for Brain Research, MIT, Cambridge, MA 02139, USA. [3]Janelia Research Campus, Howard Hughes Medical Institute, Ashburn, VA 20147, USA. [4]Department of Cell Biology, Harvard Medical School, 200 Longwood Avenue, Boston, MA 02115, USA. [5]Program in Cellular and Molecular Medicine, Boston Children's Hospital, 200 Longwood Avenue, Boston, MA 02115, USA. [6]Department of Pediatrics, Harvard Medical School, 200 Longwood Avenue, Boston, MA 02115, USA. [7]arivis AG, 1875 Connecticut Avenue NW, 10th floor, Washington, DC 20009, USA. [8]MBF Bioscience, 185 Allen Brook Lane, Suite 101, Williston, VT 05495, USA. [9]Department of Systems Biology, Harvard Medical School, 200 Longwood Avenue, Boston, MA 02115, USA. [10]Department of Biological Engineering, MIT, Cambridge, MA 02139, USA. [11]MIT Center for Neurobiological Engineering, MIT, Cambridge, MA 02139, USA. [12]Department of Brain and Cognitive Sciences, MIT, Cambridge, MA 02139, USA. [13]Koch Institute, MIT, Cambridge, MA 02139, USA. [14]Department of Molecular and Cell Biology, University of California, Berkeley, CA 94720, USA. [15]Department of Physics, University of California, Berkeley, CA 94720, USA. [16]Howard Hughes Medical Institute, Berkeley, CA 94720, USA. [17]Helen Wills Neuroscience Institute, Berkeley, CA 94720, USA. [18]Molecular Biophysics and Integrated Bioimaging Division, Lawrence Berkeley National Laboratory, Berkeley, CA 94720, USA.

*These authors contributed equally to this work. †Present address: Internal Medicine Research Unit, Pfizer, Cambridge, MA 02139, USA. ‡Present address: Vertex Pharmaceuticals, 3215 Merryfield Row, San Diego, CA 92121, USA. §Present address: Intel, 2501 Northwest 229th Avenue, Hillsboro, OR 97124, USA. ¶Present address: Department of Neuroscience, Johns Hopkins University School of Medicine, Baltimore, MD 21205, USA. #Present address: Microsoft Research Lab, 14820 NE 36th Street, Redmond, WA 98052, USA. **Present address: Department of Biological Sciences, Carnegie Mellon University, Pittsburgh, PA 15143, USA.
††Corresponding author. Email: esb@media.mit.edu (E.S.B.); betzige@janelia.hhmi.org (E.B.)

Downloaded from http://science.sciencemag.org/ on January 19, 2019

the N,N-dimethylacrylamide-gel expansion protocol, we observed regions where the expansion superficially appears accurate (fig. S3A) and other regions of clear distortion, such as irregularly shaped somata and nuclei (fig. S3B). High expansion ratios also require exceptionally high fluorescence labeling densities to take advantage of the theoretically achievable resolution and take longer to image. Thus, for this work we chose to focus only on applications (table S2) enabled by 4× expansion.

Several challenges emerge when attempting to extend ExM to specimens at the millimeter scale of the fly brain or a mouse cortical column. First, even 4× expansion requires effective voxel dimensions of ~30 to 50 nm on each side to match the full resolution potential of ExM, or ~20 trillion voxels/mm^3/color. This in turn necessitates imaging at speeds on the order of 100 million voxels/s to complete the acquisition in days rather than weeks or more, as well as an image-processing and -storage pipeline that can handle such high sustained data rates. Second, photobleaching often extinguishes the fluorescence signal from deeper regions of 3D specimens before they can be imaged—a problem that becomes more severe with thicker specimens, longer imaging durations, and/or the higher illumination intensities needed for faster imaging. Last, because ExM resolution is proportional to imaging resolution, the latter should be as high as possible within these other constraints while also striving for near-isotropic resolution, so that neural tracing and quantification of nanoscale structures is not limited by the axis of poorest resolution.

To address these challenges, we turned to LLSM (*20*), which sweeps an ultrathin sheet of laser light through a specimen and collects the resulting fluorescence from above with a high numerical aperture (NA) objective to image it on a high-speed camera (supplementary note 2). Confinement and propagation of excitation light within the detection focal plane permits parallel acquisition of data at rates of 10 million to 100 million voxels/s at low intensities that minimize photobleaching within the plane and eliminates bleaching in the unilluminated regions above and below. Consequently, we could image large volumes of expanded tissue expressing yellow fluorescent protein (YFP) in a subset of mouse cortical neurons with uniform signal from top to bottom (Fig. 1A, left). By contrast, at a comparable signal in the acquired images, the out-of-focus excitation and high peak power at the multiple foci of a spinning disk confocal microscope (SDCM) photobleached the expanded tissue ~10× faster than LLSM (Fig. 1C), rendering deeper regions completely dark (Fig. 1, A and B, center), while the sparse illumination of the SDCM focal array slowed volumetric acquisition by ~7× (table S1). Another commercial alternative, Airyscan, efficiently images the fluorescence generated at the excitation focus and uses this information to extend the imaging resolution approximately 1.4× beyond the diffraction limit (*30*, *31*). However, Airyscan imaged expanded tissue ~40× slower (table S1) and with ~20× faster bleaching (Fig. 1C) than LLSM.

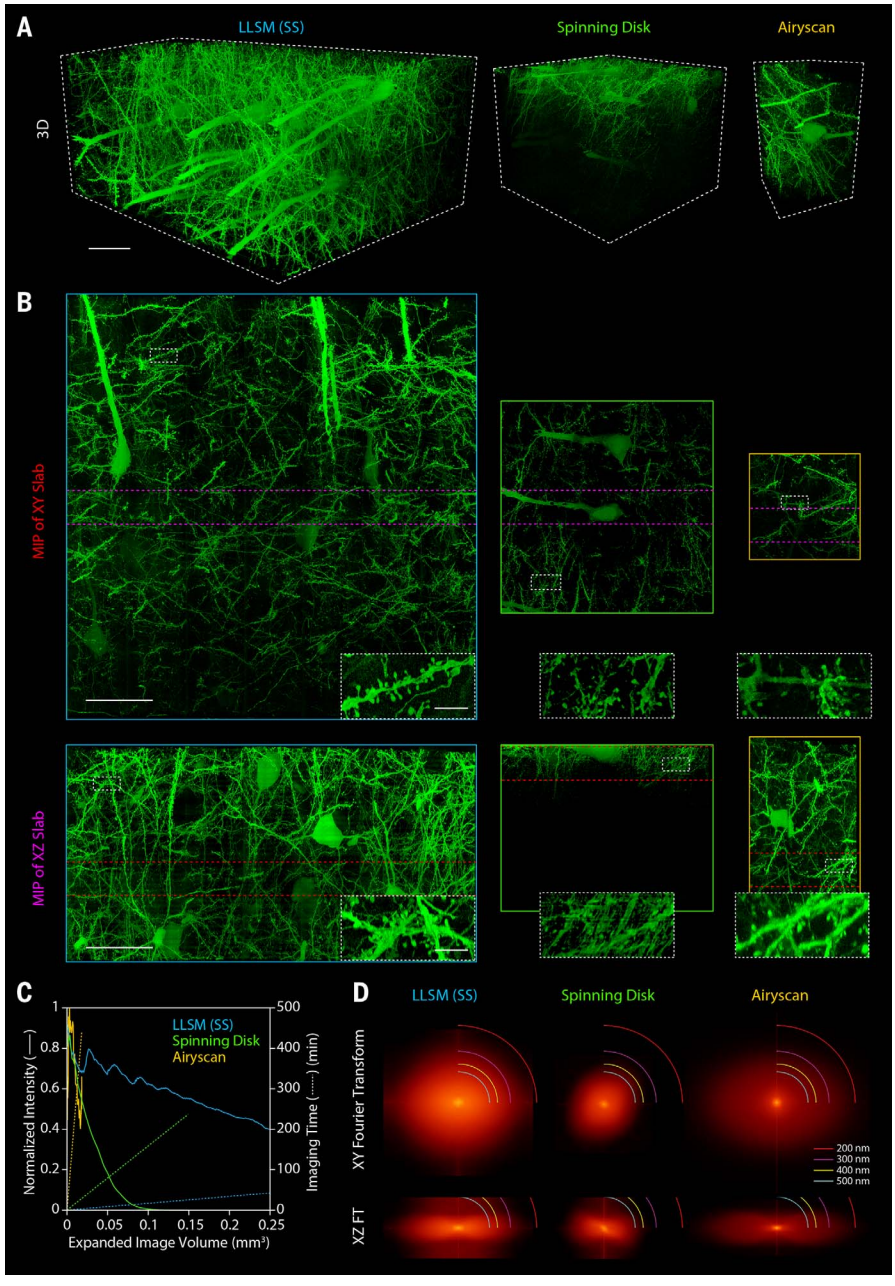


Fig. 1. Comparing modalities to image-expanded mouse brain tissue. (**A**) 3D rendered volumes at equal magnification of tissue sections from the primary somatosensory cortex of a Thy1-YFP transgenic mouse, expanded ~4× by using the protein-retention expansion microscopy (proExM) protocol and imaged by means of (left to right) LLSM in sample scan mode [LLSM (SS), blue]; spinning disk confocal microscopy (Spinning Disk, green); and Airyscan in fast mode (Airyscan, orange). Scale bars, 50 μm, here and elsewhere given in preexpanded (biological) dimensions. (**B**) (Top) *xy* and (bottom) *xz* maximum intensity projections (MIPs) of 25-μm-thick slabs cut from the image volumes in (A) at the locations denoted by the red and purple lines in the slabs perpendicular to them, respectively. (Insets) Regions in the white rectangles at higher magnification. Scale bars, 50 μm, full MIPs; 5 μm, insets. (**C**) Comparative imaging and photobleaching rates for the three modalities (table S1). (**D**) (Top) *xy* and (bottom) *xz* spatial frequency content in the same three image volumes as measured from mitochondria-targeted antibody puncta, with different resolution bands as shown (fig. S4).

LLSM can operate in two modes: objective scan (fig. S4), in which the sample is stationary while the light-sheet and detection objective move in discrete steps across the image volume, and sample scan (Fig. 1), in which the sample is swept continuously through the light sheet. Sample scan is faster (tables S1) but yields slightly lower *yz* resolution (fig. S4) than that of

Downloaded from http://science.sciencemag.org/ on January 19, 2019

objective scan because information in the sample scanning direction is slightly blurred by simultaneous image acquisition and sample movement. Of the methods above, Airyscan should in principle achieve the highest lateral (*xy*) resolution, followed by SDCM (owing to pinhole filtering), and last, the two modes of LLSM. In practice, however, dendritic spines and axons appeared more clearly and faithfully resolved in lateral views with LLSM than with SDCM or even Airyscan (Fig. 1B, top row), a conclusion corroborated by its higher lateral spatial frequency content (Fig. 1D and fig. S4A, top rows) as measured from mitochondria-targeted Ab puncta. Likewise, the thinness of the lattice light sheet contributes to the axial (*z*) resolution of LLSM (Fig. 1D and fig. S4A, bottom rows) and therefore yielded *xz* views of spines and axons only slightly poorer than in the lateral plane and substantially sharper than those obtained with SDCM or Airyscan (Fig. 1B, bottom row).

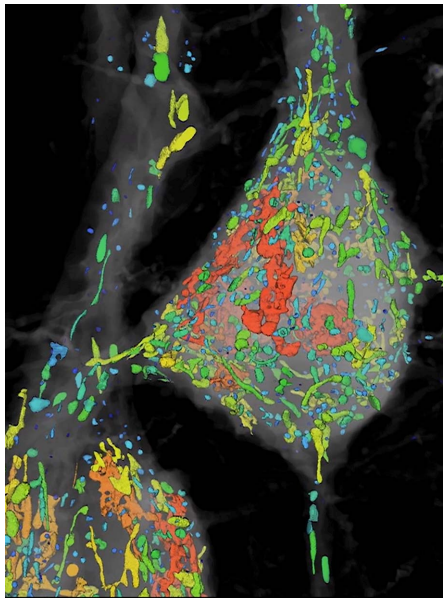
One additional challenge in millimeter-scale ExLLSM involves the processing of multiterabyte data sets. In LLSM, the lateral extent of the light sheet (table S2) is far smaller than an expanded fly brain or cortical column, so the final image volumes had to be computationally stitched together from as many as 25,000 (table S2) tiled subvolumes per color. However, because of systematic sample stage errors and slight swelling or shrinking of expanded samples over many hours, many tiles did not perfectly overlap with their neighbors on all six sides. To address this, we developed an Apache Spark–based high-performance computing pipeline (supplementary note 3 and figs. S5 to S7) that first performed a flat-field correction for each tile to account for intensity variations across the light sheet and then stitched the intensity-corrected tiles together by using an automated and iteratively refined prediction model of tile coordinates. In a separate track, each intensity-corrected tile was deconvolved by using a measured point spread function (PSF) so that when the final set of coordinates for all tiles was available, the deconvolved image volume of the entire specimen could be assembled and visualized (supplementary note 4 and 5) with minimal stitching artifacts.

Quantification of subcellular structures in mouse cortical neurons

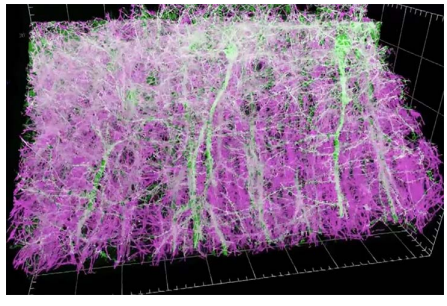
The protein-specific fluorescence contrast of ExLLSM enabled rapid, computationally efficient, and purely automated segmentation and nanoscale quantification of subcellular neural structures over large volumes. For example, dense cytosolic expression of YFP under the *thy1* promotor in mouse pyramidal neurons revealed sharply delineated voids (Movie 1) representing subcellular compartments (Fig. 2A) of various shapes and sizes whose volumes we could quantify accurately (Fig. 2B and supplementary note 4d). Simultaneous immunofluorescence labeling against Tom20 and LAMP1, although comparatively sparse (movie S1), was sufficient to identify the subset of these that represented mitochondria or lysosomes (Fig. 2C)—in the latter case, the specific subset with LAMP1 that likely represented multivesicular bodies or autolysosomes (supplementary note 6a) (*32*). As expected, we found that mitochondria were generally both longer and larger in volume than lysosomes (Fig. 2D and table S3). Mitochondria ranged in length from 0.2 to 8.0 μm, which is consistent with EM measurements in the cortex (*33*) or other regions (*34*) of the mouse brain, whereas the subset of LAMP1 compartments ranged from 0.1 to ~1.0 μm, which is also consistent with EM (*35*).

Given this agreement—and the important roles mitochondria play in dendrite development, synapse formation, calcium regulation, and neurodegenerative disease (*34*, *36*, *37*)—we extended our analysis across ~100 by 150 by 150 μm of the mouse somatosensory cortex. We classified length, aspect ratio, and volume (Fig. 2E and fig. S8) of 2893 mitochondria and 222 lysosomes across the somata and initial portions (78 μm mean length) of the apical dendrite of five-layer V pyramidal neurons, as well as the initial portions (95 μm mean length) of three descending axon segments. As noted previously in the hippocampus (*36*), we found that long and high-aspect-ratio mitochondria were far more prevalent in apical dendrites than in axons, with mitochondria longer than 3 μm comprising 6.5% all dendritic mitochondria (~12 per 100 μm of dendrite length) versus 0.7% of all axonal ones. These differences may represent the difficulty in assembling and maintaining large organelles within the narrow confines of the axon, or they may reflect functional differences in the regulation of calcium in axons versus dendrites.

We next turned our attention to the myelination of axons, which is essential for the rapid (*38*, *39*) and energy-efficient (*40*) propagation of action potentials (APs) and which, when disrupted, can lead to neurodegenerative diseases such as multiple sclerosis (*41*). The propagation velocity is affected by the g-ratio, the diameter of the axon normalized to the diameter of its surrounding myelin sheath (*42*). Most EM measurements of the g-ratio come from 2D images of single sections cut transversely to axonal tracts (*43*–*45*) and therefore lack information on how the g-ratio might vary along the length of a given axon. To address this, we used ExLLSM to image a 320- by 280- by 60-μm volume in the primary somatosensory cortex of a Thy1-YFP transgenic mouse immunostained against myelin basic protein (MBP) (Fig. 2F and Movie 2). At every longitudinal position z along a given myelinated axon, we measured the local g-ratio at every azimuthal position θ by dividing the radius $\rho_{axon}(\theta, z)$ of the axon along the radial vector from the axon center by the radius $\rho_{myelin}(\theta, z)$ of the outer edge of the myelin sheath along the same vector (Fig. 2G, fig. S9, and supplementary note 4e). Across one 56-μm-long segment, the mean g-ratio of 0.57 calculated from mean axon and sheath diameters of 0.52 and 0.90 μm, respectively, fell at the lower end of a distribution previously reported in the central nervous system yet was consistent with a theoretical estimate of 0.60 for the ratio that optimizes propagation velocity (*42*). However, these values do not reflect the substantial variability we observed, with the outer axon–to–outer myelin distance ranging from 0.12 to 0.35 μm (fig. S10) and the local g-ratio ranging from ~0.4 to 0.8 (Fig. 2H and Movie 2). Furthermore, the axon and the sheath were rarely concentric (Fig. 2G), leading to rapid longitudinal changes in capacitance and impedance that may



Movie 1. Organelle analysis of layer V pyramidal neurons in the mouse somatosensory cortex. Segmentation of cytosolic voids in Thy1-YFP–expressing neurons, quantification of their volumes, and immunostaining-based classification of those voids that represent mitochondria or multivesicular bodies or autolysosomes (Fig. 2, A to E; fig. S8; and movie S1).



Movie 2. Axon myelination and local g-ratio of layer V pyramidal neurons of the mouse primary somatosensory cortex. Thy1-YFP–expressing neurons and immunostained myelin sheaths across 320 by 280 by 60 μm, with quantification of the local g-ratio on the surface of a specific myelin sheath (Fig. 2, F and G, and figs. S9 and S10).

Downloaded from http://science.sciencemag.org/ on January 19, 2019

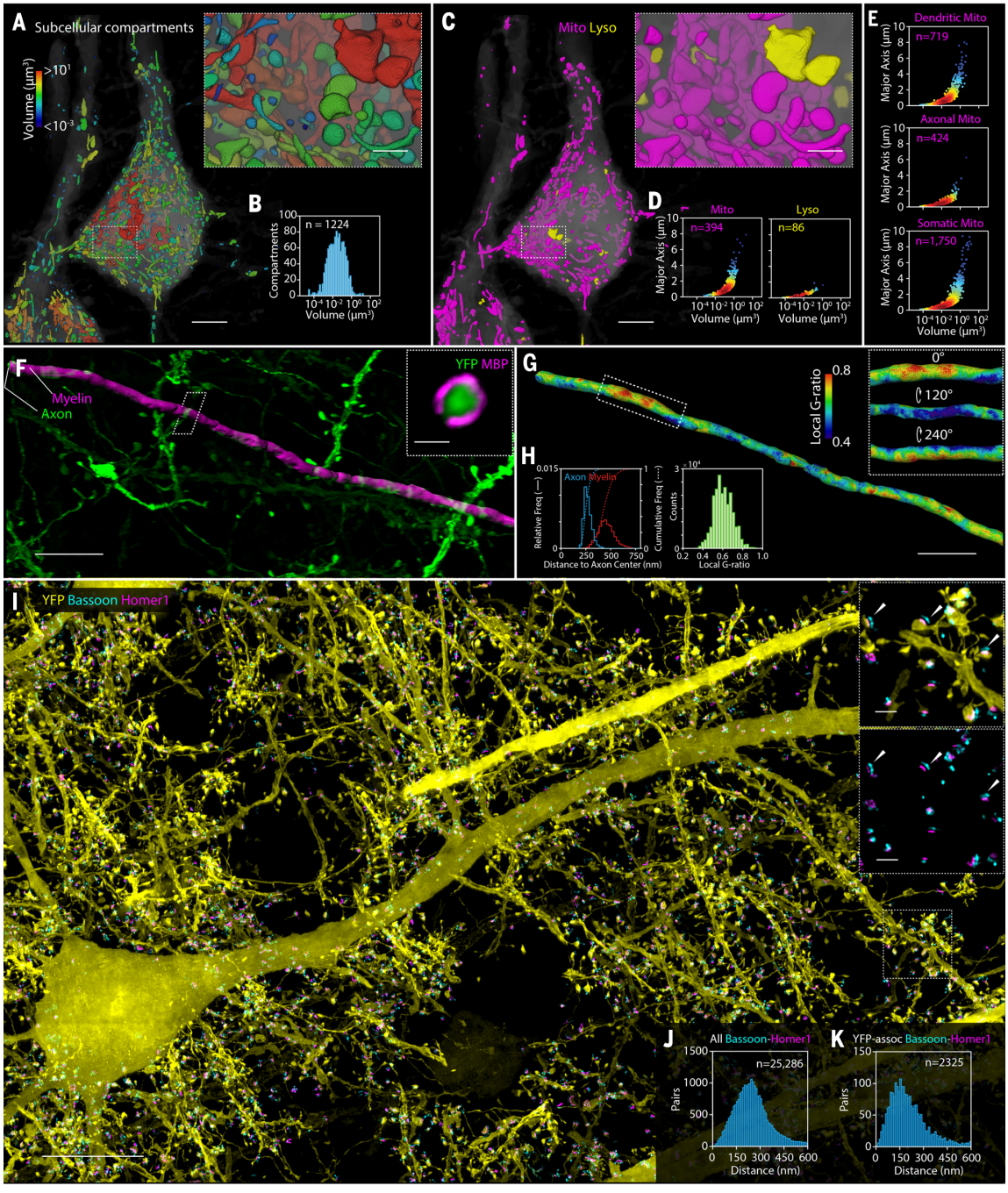


Fig. 2. Nanoscale, protein-specific 3D imaging of subcellular neural structures. (**A**) Segmented compartments void of cytosolic YFP (gray), color-coded by volume, in portions of the somata and apical dendrites of two layer V pyramidal neurons from the somatosensory cortex of a Thy1-YFP mouse (Movie 1). Scale bars, 5 μm and (inset) 1 μm. (**B**) Distribution of the compartment volumes. (**C**) Same region as (A), with voids identified with immunostaining (movie S1) as either mitochondria (magenta) or multivesicular bodies or autolysosomes (yellow). (**D**) Scatter plots of the major axis (long axis) length versus volume for the two organelle types. Point colors in (D) and (E) indicate relative data point density (blue, low; red, high). (**E**) Similar scatter plots for mitochondria only, separated by cellular region (fig. S8). (**F**) Axon of a layer V pyramidal neuron and its surrounding myelin sheath, from the primary somatosensory cortex of another Thy1-YFP mouse, immunostained against myelin (Movie 2). (Inset) A cross-sectional view through the white parallelogram. Scale bars, 5 μm and (inset) 500 nm. (**G**) Same region as (F), with the myelin sheath color coded according to the local g-ratio (fig. S10). (Inset) Azimuthal variation in g-ratio in the region within the rectangle. Scale bar, 5 μm. (**H**) (Left) Distribution of axon radius and myelin outer radius and (right) distribution of g-ratio at all points on the axon in (G). (**I**) *xy* MIP of a 9.3-μm-thick slab within a 75- by 100- by 125-μm volume from the primary somatosensory cortex of a Thy1-YFP mouse, immunostained against synaptic proteins Bassoon and Homer1 (Movie 3 and fig. S10). Only YFP-associated Bassoon/Homer1 pairs are shown for clarity. (Insets) (Top) magnified *xy* MIP of a 2.2-μm-thick slab from boxed region at right. (Bottom) All Bassoon/Homer1 pairs in the same region. Three pairs are indicated with arrows. Scale bars, 10 μm and (insets) 1 μm. (**J**) Distribution of distances between paired Bassoon and Homer1 centroids across the entire volume. (**K**) Distribution when restricted to only those pairs associated with YFP-expressing neurons.

Downloaded from http://science.sciencemag.org/ on January 19, 2019

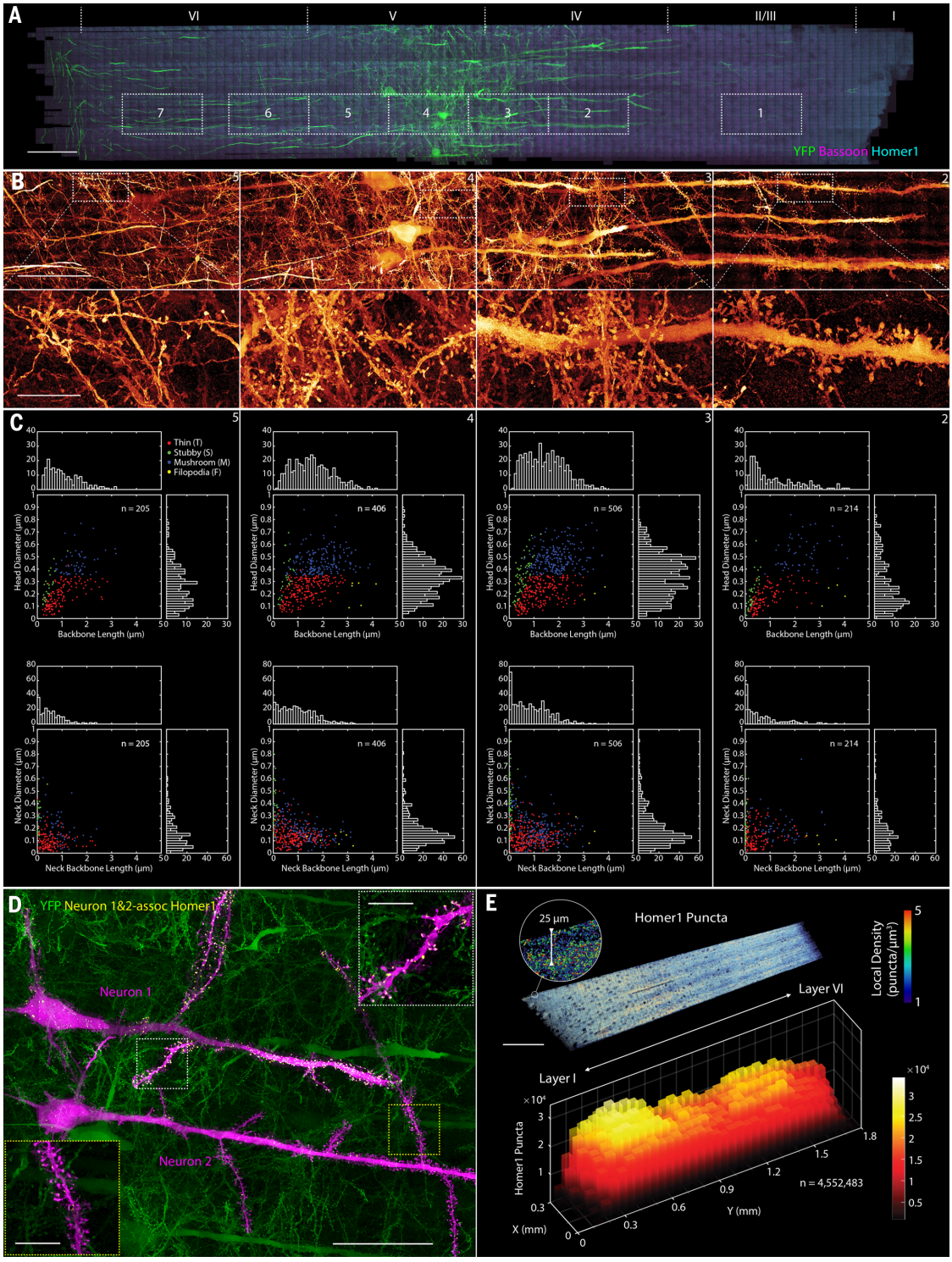


Fig. 3. Characterizing dendritic spine morphologies and postsynaptic Homer1 across the mouse primary somatosensory cortex. (**A**) Coronal MIP of a 1900- by 280- by 70-μm tissue section spanning the pia to the white matter of the primary somatosensory cortex of a Thy1-YFP mouse (Movie 4), additionally immunostained against Bassoon and Homer1. Boxes denote seven regions for quantitative morphological analysis of dendritic spines. Scale bar, 100 μm. (**B**) (Top) Magnified MIPs of YFP-expressing neurons in four of the regions from (A), with (bottom) further magnified subregions showing differing spine morphologies. Scale bars, (top) 50 μm and (bottom) 10 μm. (**C**) Scatter plots and histograms indicating relationships between (top) spine backbone length and head diameter and (bottom) spine neck length and neck diameter in the four regions from (B) (figs. S13 to S15 and movie S2). (**D**) Two adjacent layer V pyramidal neurons selected within the volume (magenta), one exhibiting strong Homer 1 expression (neuron 1) and the other exhibiting weak expression (neuron 2). (Insets) Homer1 localization or lack thereof at apical dendritic spines (fig. S17). Scale bars, 50 μm and (insets) 10 μm. (**E**) (Top) MIP of the local density of Homer1 puncta across a ~25-μm-thick coronal slab, and (bottom) the cumulative number of puncta in 50- by 50- by 25-μm subvolumes across the cortex.

Downloaded from http://science.sciencemag.org/ on January 19, 2019

influence the speed and efficiency of signal propagation. We subsequently confirmed these observations with EM (fig. S11 and supplementary note 2h).

ExLLSM is also well suited to study the nanoscale organization of synaptic proteins over large tissue volumes. Imaging a 75- by 100- by 125-μm tissue section cut from layer IV/V of the primary somatosensory cortex of a transgenic Thy1-YFP mouse, we identified 25,286 synapses that have closely juxtaposed concentrations of immunolabeled pre- and postsynaptic proteins Bassoon and Homer1 (fig. S12A), 2325 of which had Homer1 localized at YFP-labeled dendritic spines (Fig. 2I and Movie 3). These tended to form nested caps, with major axis lengths of 856 ± 181 nm and 531 ± 97 nm for Bassoon and Homer1, respectively [median ± median absolute deviation (MAD)] (fig. S12, B and C). The Homer1 distribution was consistent with SR measurements in dissociated hippocampal neurons (DHN) (*46*), but our Bassoon values were slightly larger. The centroid-to-centroid distance we measured between Bassoon/Homer1 pairs was 243 ± 69 nm for all pairs within the volume (Fig. 2J) and 185 ± 70 nm for those associated with YFP-filled spines (Fig. 2K). The difference between these values suggests that mature glutamatergic synapses of layer V pyramidal neurons, which are the ones expressing YFP, are narrower than other types across the primary somatosensory cortex. The difference between these values and previous SR measurements of 150 ± 20 nm in the ventral orbital cortex (n = 252 Bassoon/Homer1 pairs) (*47*), 165 ± 9 nm in DHN (n = 43 pairs) (*46*), and 179 ± 42 nm in the middle of the primary somatosensory cortex (n = 159 pairs) (*29*) may reflect natural variations in different brain regions (*29*) or a systematic bias in these earlier studies arising by measuring the distance between 1D Gaussian fits to the Bassoon/Homer1 distributions in a manually selected slice through the heart of each synapse, versus our approach of calculating the distance between the 3D centroids calculated across the complete distributions.

Somatosensory cortex–spanning measurement of dendritic spines and excitatory synapses

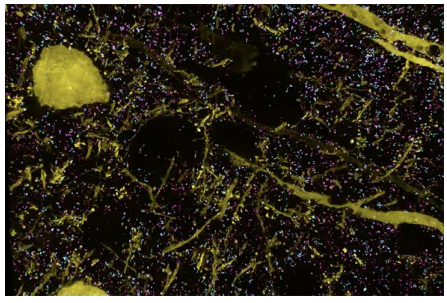
The combination of fast imaging (table S1) and targeted sparse labeling enables ExLLSM-based quantification of nanoscale neural structures to be extended to millimeter-scale dimensions over multiterabyte data sets. This yields statistically large sample populations that can reveal subtle changes in the distributions of specific morphological parameters across different regions of the brain.

One such application involves the morphology of dendritic spines in different layers of the mouse cerebral cortex. A spine is a small (~0.01 to 1.0 μm^3) membranous protrusion from a neuronal dendrite that receives synaptic input from the closely juxtaposed axon of another neuron. Spine morphology has been extensively studied with a variety of imaging methods (*48*), in part because it is related to synaptic strength (*49*), whose time- and activity-dependent change (plasticity) (*50*) is implicated in learning and memory consolidation (*51*). However, although optical methods such as Golgi impregnations (*52*), array tomography (*6*), and confocal (*53*) and two-photon microscopy (*54*, *55*) can image the complete arborization of neurons spanning the cortex, they lack the 3D nanometric resolution needed to measure the detailed morphology of spines. Conversely, EM (*56*, *57*) and SR fluorescence microscopy (*58*, *59*) have the requisite resolution but not the speed to scale readily to cortical dimensions. ExLLSM, however, has both.

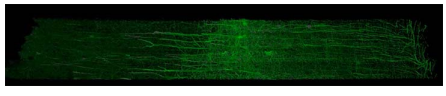
To demonstrate this, we imaged a 1900- by 280- by 70-μm tissue slice spanning the pia to the white matter in the primary somatosensory cortex of a transgenic Thy1-YFP mouse expressing cytosolic fluorescence within a sparse subset of layer V pyramidal neurons. The slice was additionally immunostained against Bassoon and Homer1 (Fig. 3A and Movie 4). In each of seven different regions across the cortex (Fig. 3B and fig. S13A), we selected four 27- by 27- by 14-μm subvolumes and used a modified commercial analysis pipeline (supplementary note 4f) (*60*) to segment (fig. S14 and movie S2) and measure spine ultrastructure. Across the ~1500 spines so measured, the range of spine head diameters, neck diameters, overall backbone lengths (spine root to tip), and neck backbone lengths (Fig. 3C and figs. S13B and S15) were consistent with those seen in an EM study of layer II/III pyramidal neurons in the mouse visual cortex (*56*). Furthermore, the absence of spines in the initial segment of the distal apical dendrite, and prevalence of much larger spines on smaller dendritic branches than on the remainder of the distal apical dendrite (Fig. 3D), were in line with an EM study of pyramidal neurons in the primary somatosensory cortex of the cat (*61*). Mean spine head diameter and mean neck backbone length each approximately doubled from layer II/III (position 1) to the regions of layers IV and V (positions 3 and 4) nearest the somata before falling again in layer VI (positions 6 and 7) to levels similar to layer II/III (table S4). This is consistent with a longitudinal in vivo study of spine morphology that found that spines closer to the soma, including those on proximal apical dendrites, were more mature and formed stronger synaptic connections than those on basal dendrites or the distal apical dendrite (*62*). We also found that head diameter and backbone length or neck backbone length were correlated across all layers of the cortex (Fig. 3C, top row; figs. S13B, top row, and S15; and table S4), but neck diameter and neck backbone length were not correlated across all regions (Fig. 3C, bottom row; fig. S13B, bottom row; and table S4).

Colabeling with Homer1-specific antibodies allowed us also to map excitatory synapses and their density (Fig. 3E) across the primary somatosensory cortex. In particular, when 4.5 million Homer1 puncta were binned in 50- by 50- by 25-μm subvolumes to average across local fluctuations, their density was revealed to be ~1.5 to 2.0× greater in layers II/III and V (~40 to 50 puncta/μm^3) than in adjacent layers I, IV, and VI. Similar dual maxima in synaptic density are seen in sparsely sampled EM images of the rat somatosensory (*63*) and mouse barrel cortex (*64*), although in different cortical layers (rat, II and IV; mouse, I and IV) than seen in this work.

Focusing on the subset of Homer1 puncta colocalized with YFP-expressing dendritic spines, we found that thin spines were approximately twice as likely to coexpress Homer1 as spines classified as stubby, mushroom, or filopodial (fig. S16). As a synaptic scaffold protein, Homer1 plays an important role in the recruitment and cross-linking of other proteins that lead to the maturation and enlargement of spines (*65*–*67*), so Homer1's relative abundance at thin spines may presage their transformation to more mature forms. Surprisingly, we also observed dramatic variations in the expression of Homer1 within neighboring layer V pyramidal neurons: Homer1 was present at nearly all spines and throughout the cytosol of one neuron (Fig. 3D, neuron 1), whereas a parallel neuron ~57 μm away of similar morphology exhibited very little Homer1,



Movie 3. Synaptic proteins and their associations to neuronal processes in layers IV and V of the mouse primary somatosensory cortex. Thy1-YFP–expressing neurons and immunostained pre- and postsynaptic proteins Bassoon and Homer1 across 75 by 100 by 125 μm, sequentially showing all Bassoon and Homer1 puncta, and only YFP-associated Bassoon and Homer1 pairs (Fig. 2, I to K, and fig. S12).



Movie 4. Relationship of postsynaptic Homer1 to neuronal processes across the mouse primary somatosensory cortex. Thy1-YFP–expressing neurons and immunostained postsynaptic protein Homer1 across 1900 by 280 by 70 μm in the primary somatosensory cortex, with specific focus on two adjacent layer V pyramidal neurons that exhibit substantially different patterns of Homer1 expression (Fig. 3, figs. S13 to S17, and movie S2).

Downloaded from http://science.sciencemag.org/ on January 19, 2019

even at its dendritic spines (Fig. 3D, neuron 2). This difference did not result from differential labeling efficiency because the density of Homer1 puncta in the immediate surrounds of each neuron was similar (fig. S17). Instead, because Homer1 levels are known to change rapidly under different neuronal states [for example, asleep versus awake (*68*)], it may reflect the different excitatory states of these two neurons at the time the animal was sacrificed.

Visual cortex–spanning neuronal tracing and myelination patterns

Although the radial anisotropy of axonal myelination (Fig. 2E) can affect the speed and efficiency of AP propagation, so too can its

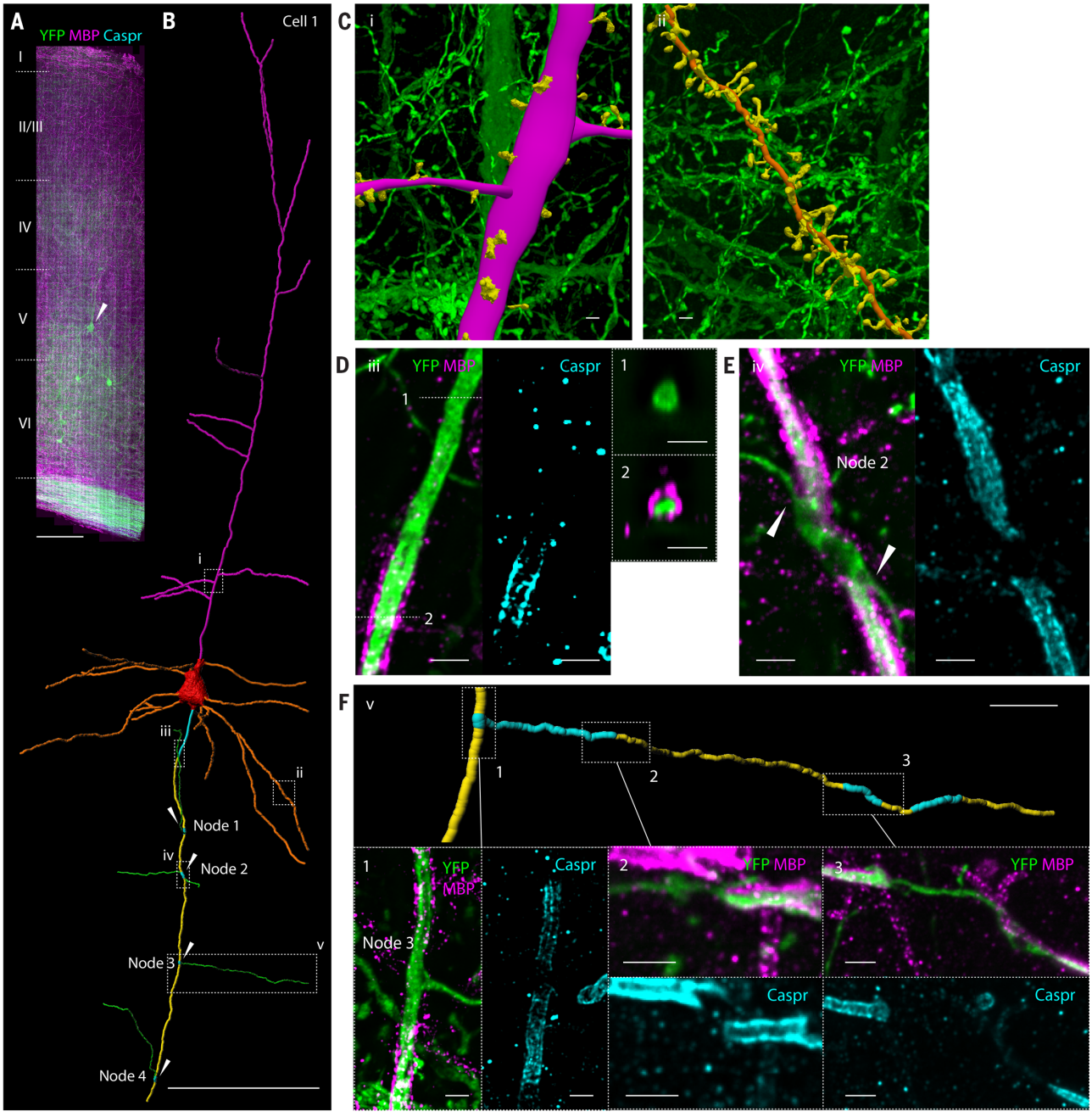


Fig. 4. Neural tracing and longitudinal myelination analysis across the mouse primary visual cortex. (**A**) Coronal MIP of a 25-μm-thick slab within a 1100- by 280- by 83-μm tissue section spanning the pia to the white matter of the primary visual cortex of a Thy1-YFP mouse (Movie 5), additionally immunostained against MBP and Caspr to highlight myelin sheaths and nodes of Ranvier, respectively. Scale bar, 100 μm. (**B**) Traced arborization (Movie 6) of a specific layer V pyramidal neuron denoted by the arrowhead in (A), showing the soma (red), apical (magenta), and basal (orange) dendrites; myelinated (yellow) and unmyelinated (cyan) axon segments; and collateral axon branches (green). Arrows indicate nodes of Ranvier. Scale bar, 100 μm. (**C**) Magnified segmented views of (left) the distal apical dendrite and two of its branches and (right) a basal dendrite and its spines, from boxed regions i and ii in (B), respectively. Scale bars, 1 μm. (**D**) MIP view of boxed region iii in (B), showing (left) the distal end of the PMAS; (middle) Caspr at the start of myelination; and (right) cross-sectional views of the axon (1) before and (2) after the start of myelination. Scale bars, 1 μm. (**E**) MIP view of boxed region iv in (B), showing (left) break in myelination and two branching collateral axons at a node of Ranvier and (right) Caspr highlighting the two ends of the node. Scale bars, 1 μm. (**F**) (Top) Segmented view of a collateral axon with myelinated and unmyelinated sections from boxed region v in (B). (Bottom) Three MIP views of breaks in myelination with flanking Caspr. Scale bars, (top) 10 μm; (bottom) 1 μm.

Downloaded from http://science.sciencemag.org/ on January 19, 2019

longitudinal variation. The repeated gaps in myelination at the nodes of Ranvier house ion channels that are essential to regenerate the AP during saltatory conduction (*69*), the hallmark of high-speed signal propagation in vertebrates. Recently, however, high-throughput EM imaging and axonal tracing at 30 by 30 by 240 nm/voxel (*70*) has revealed additional gaps in the axonal myelination of layer II/III neurons in the mouse primary visual cortex much larger (for example, 55 μm) than either the ~2 μm typical of the nodes of Ranvier or the shorter and rarer gaps observed in layers III to VI of the primary somatosensory cortex.

To determine whether these differences are more reflective of the layer of origination of the axon or the functional role of the cortical region studied (the somatosensory versus the visual cortex), we imaged at 27 by 27 by 50 nm/voxel a ~280- by 1100- by 83-μm tissue section from the primary visual cortex extending from the pia to the white matter of a Thy1-YFP mouse. The tissue was additionally immunostained against MBP and contactin-associated protein (Caspr) (*71*) to visualize myelin sheaths and their terminations, respectively (Fig. 4A and Movie 5). Although the dense global staining of EM makes long-range 3D tracing of small neurites challenging, expression of YFP in a sparse subset of layer V and layer VI pyramidal neurons (*72*) enabled rapid semiautomatic tracing (supplementary note 4h) of axons, their myelination, and the entire arborization of selected neurons across the tissue section (Fig. 4B and Movie 6). This included the distal apical dendrite and its branches (Fig. 4C, i), basal dendrites and their spines (Fig. 4C, ii), the premyelin axonal segment (PMAS) (Fig. 4D), the nodes of Ranvier (Fig. 4E), and collateral branches of the main axon originating at the nodes (Fig. 4F). All these features matched the known morphologies of layer V pyramidal neurons (*73*) and were recapitulated in a second neuron traced throughout the volume (Fig. 5A and Movie 6).

Given this assurance, we traced the axons and their longitudinal myelination patterns for 10 neurons in layer V and 11 more in layer VI (Fig. 5B). Within the imaged volume, all of the layer V axons in the primary visual cortex exhibited continuous myelination beyond the end of the PMAS, except for the expected small gaps at the nodes of Ranvier. This is consistent with the myelination pattern seen previously for layer III to VI axons in the primary somatosensory cortex (*70*). The range of PMAS lengths we measured for these neurons (28 to 41 μm, mean = 34.9 ± 1.1 μm) was also consistent with the range found in layers V and VI of the primary somatosensory cortex (25 to 40 μm, mean = 33.7 ± 2.4 μm). The internodal spacing of the

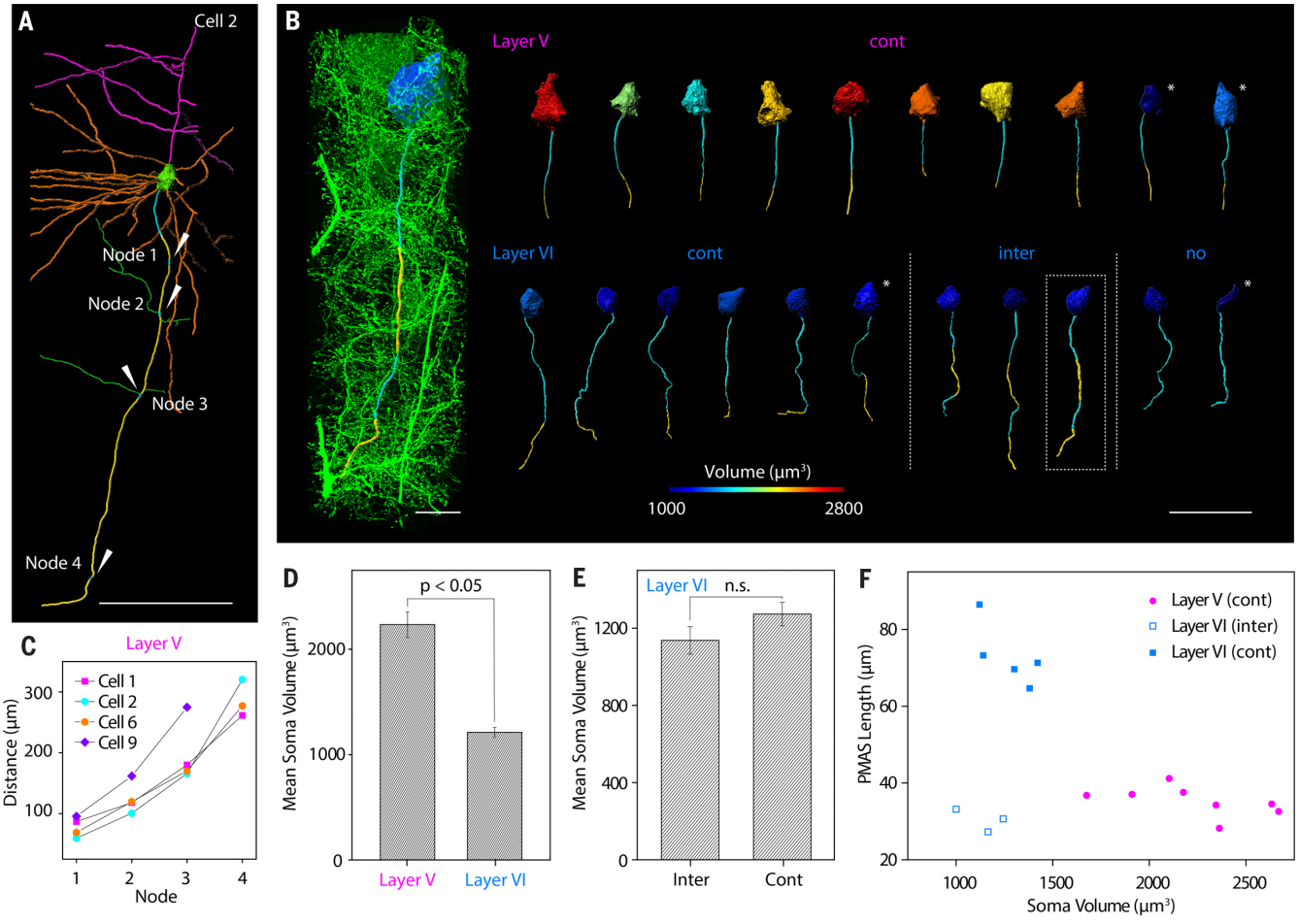


Fig. 5. Longitudinal myelination profiles of layer V and VI pyramidal neurons in the mouse primary visual cortex. (**A**) Traced arborization of a second layer V pyramidal neuron within the volume in Fig. 4A. Scale bar, 100 μm. (**B**) (Left) Segmented soma and axon of a pyramidal neuron shown in the context of its surroundings in layer VI. (Right) Segmented somata (color coded by volume) and axons, showing myelinated (yellow) and unmyelinated (cyan) segments, for 10 pyramidal neurons from layer V (top row) and 11 more from layer VI (bottom row). Boxed neuron is shown at left. Scale bars, (left) 10 μm and (right) 50 μm. (**C**) Node spacing for four layer V neurons from (B) (fig. S18). (**D**) Volumes of eight layer V and nine layer VI somata fully within the image volume [no asterisks in (B)] (mean ± SEM). (**E**) Volumes of the three somata with intermittently myelinated axons and five somata with continuously myelinated axons in layer VI (mean ± SEM). The *P* values are calculated from a permutation test for medians. n.s., not significant. (**F**) Scatter plot of soma volume versus PMAS length for the neurons in (B) (fig. S19).

Downloaded from http://science.sciencemag.org/ on January 19, 2019

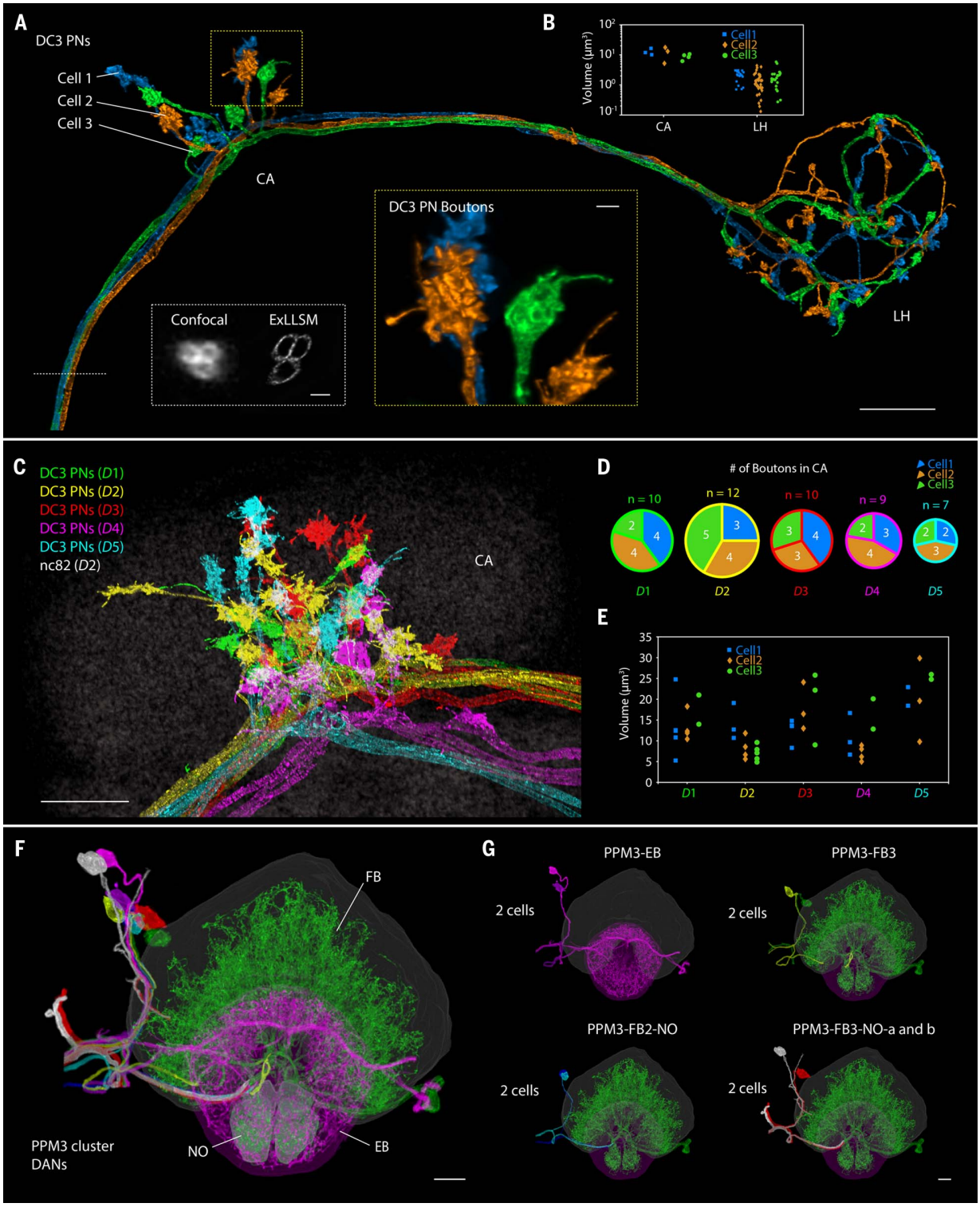


Fig. 6. Long-range tracing and stereotypy of neuron bundles in *Drosophila*. (**A**) MIP view of DC3 olfactory projection neurons (PNs) projecting from the antenna lobe of an adult *Drosophila* brain and partially traced here (Movie 7) to the calyx (CA) and lateral horn (LH). Scale bar, 10 μm. (Inset) (White box) Comparison of cross-sectional views of the axon bundle by means of (left) confocal microscopy and (right) ExLLSM. Scale bar, 1 μm. (Inset) (Yellow box) A magnified view of DC3 PN boutons in CA. Scale bar, 1 μm. (**B**) Volume of each individual DC3 PN bouton in CA and LH. (**C**) Overlaid MIP view of DC3 PNs from five adult *Drosophila* brains (D1 to D5) near CA. Scale bar, 10 μm. (**D**) Number of DC3 PN boutons in CA for D1 to D5 shown in (C). (**E**) Volume of DC3 PN boutons in CA for D1 to D5 shown in (C). (**F**) MIP view of individually traced PPM3 DANs in the right hemisphere of an adult *Drosophila* brain (Movie 8), innervating the fan-shaped body (FB) (green), ellipsoid body (EB) (magenta), and noduli (NO) (green). The fine neurites arborizing FB, EB, and NO are from both hemispheres of the brain. Scale bar, 10 μm. (**G**) MIP view of the identified cell types of PPM3 DANs (fig. S20). Scale bar, 10 μm.

Downloaded from http://science.sciencemag.org/ on January 19, 2019

four layer V neurons that could be traced to the white matter increased with increasing distance from the soma (Fig. 5C and fig. S18). By contrast, in layer VI only six axons were continuously myelinated, whereas two were completely unmyelinated, and three exhibited intermittent myelination with long unmyelinated segments more reminiscent of the layer II and III axons in the primary somatosensory cortex than the layer VI axons there (*70*). Thus, myelination patterns of axons in the primary visual cortex and the primary somatosensory cortex can differ, even for neurons in the same cortical layer.

Although the volumes of the somata and the diameters of the PMAS in layer V of the primary visual cortex were twice as large as those in layer VI (Fig. 5D and fig. S19, respectively), there was not a strong relationship between soma volume and myelination pattern (for example, intermittent or continuous) within layer VI (Fig. 5E). However, the PMAS lengths of the six continuously myelinated and the three intermittently myelinated axons in layer VI of the primary visual cortex split into distinct populations (Fig. 5F), with the intermittent ones of mean length (30.3 ± 1.7 μm) similar to the axons of layer V, and the continuous ones more than twice as long (70.6 ± 3.6 μm). Thus, continuously myelinated axons in different layers of the primary visual cortex need not have similar PMAS lengths. Given that the distal end of the PMAS is the site of AP initiation (*74*), perhaps PMAS length might be one mechanism by which neurons control the AP to account for differences in myelination or overall axon length in different layers and cortical regions.

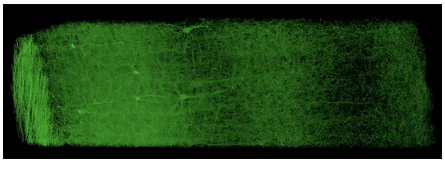
Long-range tracing of clustered neurons in *Drosophila* and their stereotypy

Although millimeter-scale tissue sections present no problem for LLSM, the entire mouse brain is far too large, given the short working distances of commercially available high-resolution objectives. The brain of the fruitfly *D. melanogaster*, on the other hand, fits comfortably within the microscope, even in its 4× expanded form. Furthermore, a vast array of genetic tools have been developed for *Drosophila*, such as split-GAL4 drivers and MultiColor FlipOut (MCFO) (*17*), which enable precise labeling of user-selected subsets of its ~100,000 neurons, such as the dorsal paired medial (DPM) neurons that innervate the mushroom bodies (MBs) (movie S3). Fluorescence imaging of thousands of such subsets across thousands of transgenic flies and collation of the results then yields brain-wide 3D reconstructions of complete neural networks at single-cell resolution (*8*, *9*). However, to trace fine neuronal processes and identify synaptic connections, nanoscale resolution is needed. For all these reasons, the *Drosophila* brain is well matched to the capabilities of ExLLSM.

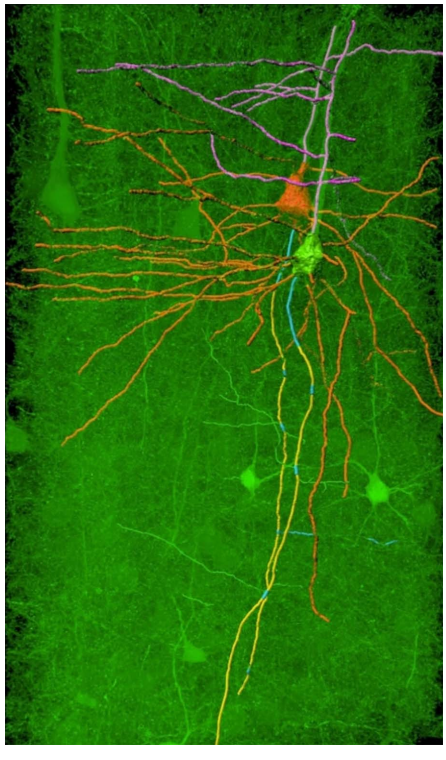
We thus chose to start with a relatively simple case: three olfactory projection neurons (PNs) originating at the DC3 glomerulus of the antennal lobes that feed most prominent sensory inputs to the calyx (CA) of the MB and lateral horn (LH) (*75*, *76*). Imaging a ~250- by 175- by 125-μm volume, we were able to trace the axonal branches of all three DC3 PNs across one hemisphere (Fig. 6A and Movie 7), although tracing of fine dendritic processes was still difficult at 4× expansion. We were also able to precisely assign boutons to each cell within the CA (cell 1, 3 boutons; cell 2, 3 boutons; cell 3, 4 boutons) and the LH (cell 1, 19 boutons; cell 2, 32 boutons; cell 3, 23 boutons) and determine the shapes and sizes of the boutons in these regions (Fig. 6B).

The neuronal circuits of the olfactory pathways to the MB have been extensively described by using light microscopy and have been reconstructed completely in the L1 instar larva and partially in the adult brain by using EM (*5*, *77*). However, the variation among individual animals has not been well studied at the level of detailed subcellular circuitry. The speed of ExLLSM now makes this possible. We studied the stereotypy of DC3 PNs by comparing their morphologies in the CA across five different animals (Fig. 6C). As expected, we consistently observed the restriction of boutons to the ends of the neurites in CA. However, we found that both the number and size of boutons differed among the three cells from the same hemisphere as well as between animals. For example, the total number of boutons in CA varied from 7 to 12, and none of the bouton assignments to each cell was the same among all five brains studied (Fig. 6D). The bouton size also showed substantial variability among the brains (Fig. 6E). These variations might arise from the distinct developmental histories of the individual animals. It is not yet clear whether they also indicate differences in synaptic strength and connection with Kenyon cells or how they might affect processing of olfactory information for associative learning in the MB. ExLLSM will enable such questions to be answered, thanks to its high throughput and its precise descriptions of neuronal morphology.

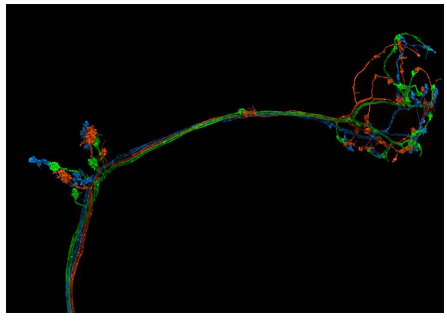
Given our success with this relatively simple example, we next applied ExLLSM to a much more challenging sample by imaging a ~340- by 660- by 90-μm volume covering nearly the entire brain of a TH-GAL4 transgenic *Drosophila* specimen. The sample was immunostained in one color against the membranes of all dopaminergic neurons (DANs) and in a second color with nc82 antibodies against Bruchpilot (Brp), a major structural and functional component of presynaptic active zones (AZs) (*78*, *79*). Among the ~110 DANs within the image volume, we focused our efforts on tracing the protocerebral posterior medial 3 (PPM3) cluster of DANs that project to the central complex, a key brain region essential for navigation, visual memory, sleep, and aggression (*80*–*82*). With manual annotation, we identified and traced all eight



Movie 5. Neuronal processes and myelination patterns across the mouse primary visual cortex. Thy1-YFP–expressing neurons across 1100 by 280 by 83 μm, immunostained against myelin and Caspr, a marker of the nodes of Ranvier, with specific emphasis on the neuronal processes and longitudinal myelination profile of a selected layer V pyramidal neuron (Figs. 4 and 5 and figs. S18 and S19).



Movie 6. Segmentation of pyramidal neurons in layer V of the mouse primary visual cortex. Segmentation of two neurons, with specific emphasis on their branches and axonal myelination patterns (Fig. 4 and 5 and figs. S18 and S19).



Movie 7. Tracing of DC3 olfactory projection neurons (PNs) in an adult *Drosophila* brain. Volumetric view of three individually traced neurons projecting from the antenna lobe in a bundle, with magnified views of their boutons at the calyx and lateral horn (Fig. 6, A to E).

Downloaded from http://science.sciencemag.org/ on January 19, 2019

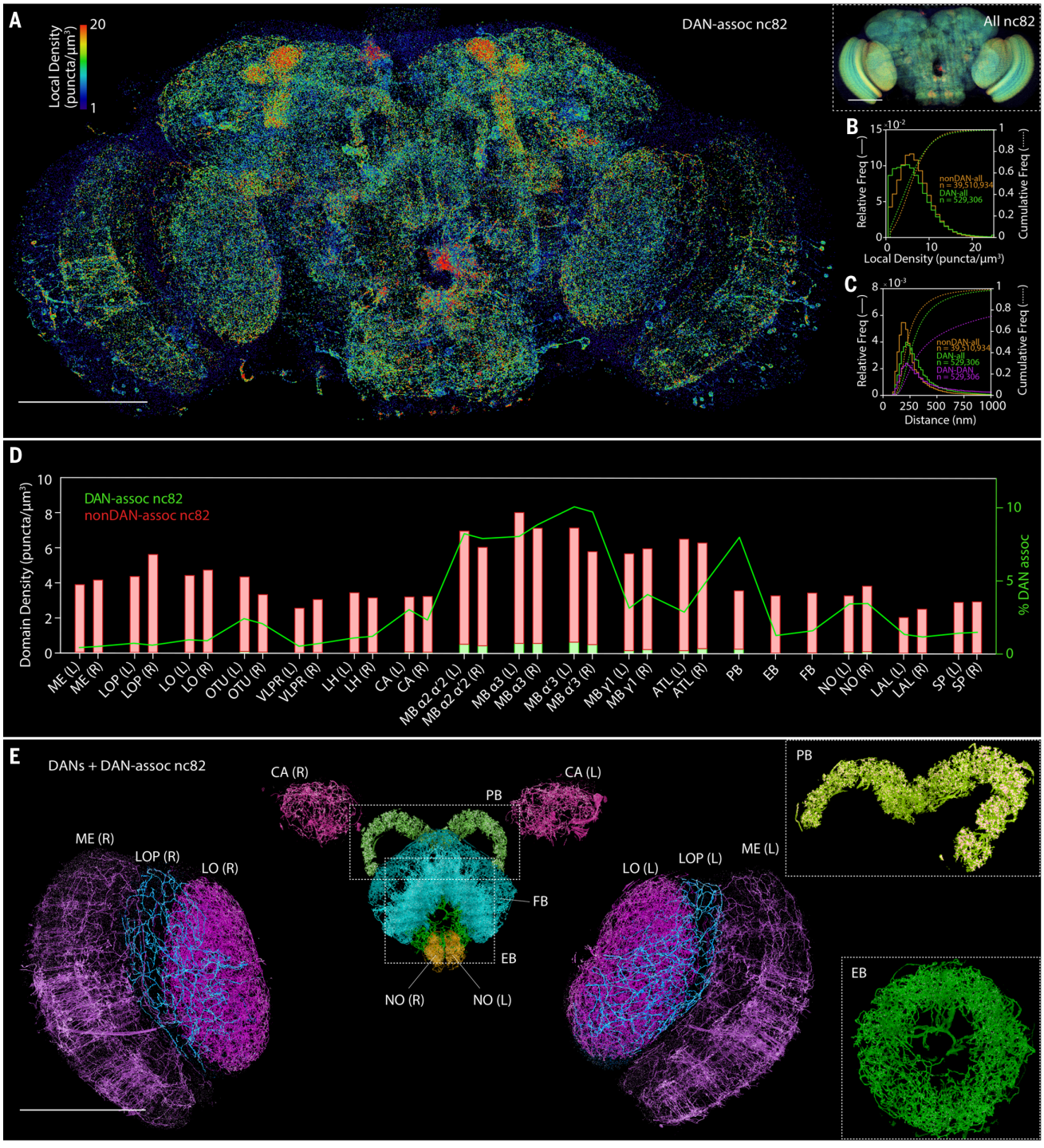


Fig. 7. Whole-brain analysis of presynaptic sites and DANs in *Drosophila*. (**A**) MIP view of the subset of nc82 puncta marking presynaptic sites that are associated with DANs (DAN-assoc nc82), color coded by the local puncta density, in an adult *Drosophila* brain (Movie 9). Scale bar, 100 µm. (Inset) (Right) MIP view of all nc82 puncta, using identical color coding of local density. Scale bar, 100 µm. (**B**) Distribution of local densities of (green) DAN-associated nc82 puncta and (orange) nonDAN-associated nc82 puncta in (A) (fig. S28). (**C**) Distribution of distances from DAN-associated nc82 puncta (green) and nonDAN-associated nc82 puncta (orange) to the nearest nc82 punctum of any kind, and nearest-neighbor distances from one DAN-associated nc82 to another (magenta) (fig. S29). (**D**) Volumetric density of DAN-associated nc82 puncta (green bars) and nonDAN-associated nc82 puncta (red bars), and the percentage of nc82 puncta that are DAN-associated (green curve), within each of the 33 brain regions of the adult *Drosophila* brain (fig. S30). (**E**) MIP view of DANs and DAN-associated nc82 puncta, color coded by 13 representative brain region (Movie 10). Scale bar, 100 µm. (Insets) Magnified views of the (top, angled view) PB and (bottom) EB. Brain regions are ME, medulla; LOP, lobula plate; LO, lobula; OTU, optical tubercle; VLPR, ventrolateral protocerebrum; LH, lateral horn; CA, calyx; MB, mushroom body; ATL, antler; PB, protocerebral bridge; EB, ellipsoid body; FB, fan-shaped body; NO, noduli; LAL, lateral accessory lobe; and SP, superior protocerebrum. "L" and "R" indicate the left and right hemispheres of the brain, respectively.

Downloaded from http://science.sciencemag.org/ on January 19, 2019

individual cells within the cluster (Fig. 6F, figs. S20 and S21, Movie 8, table S5, and movie S4). Although tracing of fine processes inside the central complex was difficult, we were able to trace the main axonal branches and precisely determine the number of cell types and the number of cells belonging to each cell type. Within the PPM3 cluster, we found that two cells (PPM3-EB) mainly projected to the ellipsoid body (EB) (*82*); two cells (PPM3-FB3) projected to layer 3 of the fan-shaped body (FB); two cells (PPM3-FB2-NO) projected to layer 2 of the FB and noduli (NO); and two cells, which could be further categorized into two cell types (PPM3-FB3-NO-a and PPM3-FB3-NO-b), projected to layer 3 of the FB and NO (Fig. 6G, figs. S20 and S21, table S5, and supplementary note 6f). Using stochastic labeling of individual neurons and split-GAL4 intersection, we were able to identify and confirm the individual cell types we assigned (figs. S20 and S21, table S5, and supplementary note 6f).

Whole-brain analysis of presynaptic sites and DANs

We next turned our attention to the nc82 channel of this specimen because recent EM measurements of the nearest-neighbor distances between synapses in the α lobe of the MB (fig. S22) (*83*) suggest that quantitative counting of synapses across the *Drosophila* brain should be possible with ExLLSM at 4× expansion. However, to have confidence in the results, we needed to show that nc82 puncta larger than 100 nm represented true AZs and not nonfunctional Brp monomers or nonspecific background. To do so, we imaged two additional nc82-stained brains: one coimmunostained against V5-tagged Brp and the other coimmunostained against the AZ protein Syd1 (supplementary note 6c) (*84*, *85*). In both cases, the distribution of distances from each nc82 punctum to its nearest costained neighbor was consistent with their mutual incorporation in a single AZ (fig. S23). In addition, we imaged another brain sample of the output neuron from the α1 compartment of the MB (MBON-α1) to validate the specificity of nc82 antibody. We measured a 70-fold–higher surface density of nc82 puncta at the axons and boutons of MBON-α1 than at its dendrites (fig. S24 and supplementary note 6d), which is consistent with the near-absence of dendritic presynaptic densities observed for the same neuron with EM (*83*). Furthermore, we counted ~44,000 nc82 puncta in the α3 compartment (fig. S25), compared with ~34,000 presynaptic densities in the EM study (fig. S22 and supplementary note 6e). The distribution of distances between the presynaptic densities was also similar in the two cases (figs. S22B and S25B).

To see whether these differences were within typical specimen variability, we imaged three additional wild-type females and counted between ~34,000 and ~49,000 n82 puncta in the α3 compartments of four MBs (fig. S26). Conversely, for the two animals in which we studied both α3 compartments (the original TH-GAL4 specimen and the wild type), the number of nc82 puncta in the left and right compartments were within ~10% of one another. This suggests that the variability we observed between animals, including the EM result, is indeed natural and not due to errors from our counting methodology.

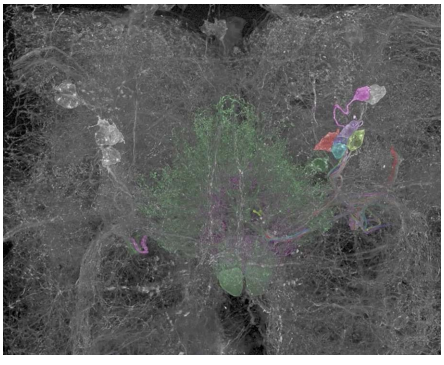
Given confidence from these results, we then extended our analysis across nearly the entire brain (the medial lobes of the MB were not imaged because TH-GAL4 does not express in the DANs in that region). In total, we counted ~40 million nc82 puncta, ~530,000 of them localized at DANs (Fig. 7A and Movie 9), and calculated the brain-wide distribution of puncta density (Fig. 7B) and nearest-neighbor distances between any puncta or only DAN-associated ones (Fig. 7C).

We observed substantial differences when we further subdivided our analysis into 33 major brain regions (fig. S28 to S30 and table S6). The volume density of all puncta, for example, varied from ~2 to 3 per cubic micrometer in the lateral accessory lobe (LAL) and superior protocerebrum (SP) to ~6 to 8 in the compartments of the MB (Fig. 7D), perhaps reflecting the distinct computational needs of different brain regions. The high density in the MB, for example, is likely beneficial for increasing capacity and sensory specificity of memory in associative learning.

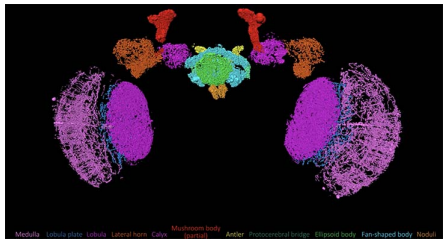
When focusing on only those nc82 puncta associated with DANs, we found additional differences. For example, the distance between non-DAN nc82 puncta and DAN-associated nc82 puncta differed substantially between brain regions (fig. S29), indicating that the proportion of synapses that can be modulated by dopamine may differ between brain regions. We also found that the percentage of puncta associated with DANs was approximately 10-fold higher in the MB than in the optic lobes (Fig. 7D), which is consistent with dopamine-dependent heterosynaptic plasticity being the basis of associative learning in the MB (*83*, *86*, *87*). On the other hand, the FB and the EB, which are known for visual and place memory formation (*88*), exhibited surprisingly low DAN association, whereas the protocerebral bridge (PB) and the antler (ATL), which are not particularly known for heterosynaptic plasticity, showed high DAN association second only to the MB. Despite these differences, the variation in surface density of nc82 puncta on DANs in different brain regions was considerably less pronounced (fig. S30B) because the percentage volume occupied by DAN in each domain (fig. S30D) followed similar trends to the percentage of DAN-associated puncta (Fig. 7D). This could also be seen directly in volume renderings of the DANs and DAN-associated puncta in each brain region (Fig. 7E and Movie 10), although local intradomain variations in the spatial distribution of nc82 were also seen.

Discussion

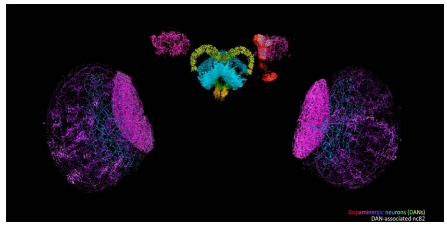
Thanks to its combination of high imaging speed, low photobleaching rate, and 3D nanoscale resolution, ExLLSM extends, by at least 1000-fold in volume, the ability of SR fluorescence microscopy to generate detailed images of subcellular ultrastructure. This fills a valuable niche between the high throughput of conventional optical pipelines of neural anatomy



Movie 8. Tracing and classification of PPM3 dopaminergic neurons (DANs) in an adult *Drosophila* brain. Section of brain near the central complex with eight neurons from the protocerebral posterior medial 3 (PPM3) cluster in the right hemisphere (colored) shown in relation to surrounding DANs (white), and tracing of the individual neurons to their paired innervations in different regions of the central complex (Fig. 6, F and G, and figs. S20 and S21).



Movie 9. Local density map of DAN-associated presynaptic sites across an adult *Drosophila* brain. Color-coded brain regions and 3D color-coded map of the local density of DAN-associated nc82 puncta in each domain (Fig. 7, A to D, and figs. S28 to S30).



Movie 10. DANs and DAN-associated presynaptic sites in different brain regions of an adult *Drosophila* brain. Volume rendered DANs, DAN-associated nc82 puncta, and all nc82 puncta across the entire brain, color coded by brain region, followed by magnified 3D and orthoslice views of DANs and DAN-associated nc82 in each of nine different domains (Fig. 7E).

Downloaded from http://science.sciencemag.org/ on January 19, 2019

(*8*, *9*) and the ultrahigh resolution of corresponding EM pipelines (*5*, *70*, *83*). With genetically targeted cell type–specific labeling (*17*, *89*–*91*) and protein-specific immunostaining, ExLLSM enables sparse neural subsets and dense synaptic connections to be recorded, visualized, and quantified at ~60- by 60- by 90-nm resolution with ~100 person-hours of effort over cortex-spanning volumes in the mouse or brain-wide volumes in *Drosophila*. This compares with 5 weeks to image and ~16,000 person-hours to trace all neurons and count all synapses in a volume only 1/80th of a fly brain encompassing the α lobe of the MB in a recent EM study at 8-nm isotropic resolution (*83*). The fluorescence contrast of ExLLSM also raises the possibility of correlating (*92*) fluorescence-based genetic indicators of neural activity (*93*, *94*) with neural ultrastructure over much larger volumes and without the labeling compromises common to correlative EM/fluorescence studies (*95*).

Although we have focused on the mouse cortex and the *Drosophila* brain in this work, we have also applied ExLLSM to image the mossy fiber innervation of granule cells in glomeruli in the cerebellum of the mouse (fig. S31 and movie S5) as well as a complete human kidney glomerulus section (fig. S32). However, the application of ExM to any biological system must be examined on a case-by-case basis through careful controls and comparisons with known aspects (such as with EM) of the specific ultrastructural elements under investigation. In particular, extrapolating the faithful nanoscale expansion of delicate membranous structures and vesicles in a specimen from images of more robust components such as cytoskeletal elements, clathrin-coated pits, or nuclear histones (*18*, *29*, *96*, *97*) should be avoided. Elastic inhomogeneity of the specimen after digestion, such as from collagen-rich connective tissue or adhesion to a rigid substrate, can also interfere with expansion, although newer protocols with more aggressive digestion may help (*98*). In this regard, brain tissue may represent a best case for ExM studies, owing to its comparatively homogenous mechanical properties and ready digestion. It should always be remembered that any image of a once-living specimen is an imperfect representation of that specimen, and the more steps that intrude in the process from one to the other the more imperfect it becomes. Overexpression, chemical fixation, permeabilization, and immunostaining already introduce numerous structural artifacts (*99*–*101*) in all forms of high-resolution fluorescence microscopy, including ExM, but ExM also requires additional steps of polymer infusion, gelation, label attachment, digestion, expansion, and handling that can perturb ultrastructure even more. Careful controls are essential.

At 4× expansion, the resolution of ExLLSM is close, but not quite sufficient, to trace fine, highly innervated neuronal processes—such as the PPM3 cluster, which terminates in the central complex—and would therefore benefit from higher expansion ratios. However, even if specimen-wide isotropic expansion can be validated at higher ratios with newer protocols of iterated expansion (*29*), ExM is still heir to the problems that bedevil other forms of high-resolution fluorescence microscopy. Chief among these is that because of the stochastic nature of labeling, the mean separation between fluorophores must be ~5× to 10× smaller than the desired resolution in each dimension in order to distinguish with high confidence two or more structures for which no a priori knowledge exists (*102*). We met this requirement at the level of ~60- by 60- by 90-nm resolution in most cases owing to the dense expression of cytosolic label in Thy1-YFP transgenic mice and DAN membrane label in a TH-GAL4 transgenic fly, as well as the exceptional specificity of Abs targeting MBP and nc82. Other Abs in our study did not meet this standard but were sufficient to identify organelles responsible for voids of cytosolic label, mark Homer1 at synapses and Caspr at nodes of Ranvier, and measure statistical distributions of synapse breadth and pre- and postsynaptic separation. However, immunostaining in any form is probably not dense enough to achieve true 3D resolution much beyond that already obtainable at 4× expansion, and the long distance between epitope and fluorophore, particularly with secondary Abs, further limits resolution. Likewise, loss of FP fluorescence upon linking and digestion, as well as the slow continued loss of fluorescence, which we alleviated here with a highly basic imaging buffer (supplementary note 2, c and d), probably preclude study at high resolution of many FP-linked proteins at the endogenous levels produced through genome editing. Indeed, even at 4× expansion, we rarely found sufficient residual fluorescence to image targets labeled with red FPs of the *Anthozoa* family, despite reports to the contrary (*19*).

Despite these challenges and limitations, the high speed and nanometric 3D resolution of ExLLSM make it an attractive tool for comparative anatomical studies, particularly in the *Drosophila* brain. For example, although we imaged the entire TH-GAL4/nc82 brain in 62.5 hours (3.2×10^5 μm^3/hour), with subsequent improvements in scanning geometry and field of view (FOV) we imaged mouse brain tissue in two colors at 4.0×10^6 μm^3/hour. If transferrable to the fly, this would allow whole-brain imaging in ~5.0 hours. This limit is not fundamental; with simultaneous multicolor imaging and multiple cameras to cover even broader FOVs, rates up to ~10^8 μm^3/hour may be achievable, or ~12 min/fly brain at 4× expansion. Assuming the future development of (i) robust, isotropic expansion at 10× or greater; (ii) longer working distance high NA water immersion objectives or lossless sectioning (*103*) of expanded samples; and (iii) a ubiquitous, dense, and cell-permeable fluorescent membrane stain analogous to heavy-metal stains in EM, even densely innervated circuits might be traced, particularly when imaged in conjunction with cell type–specific or stochastically expressed multicolor labels for error checking (*104*). With such a pipeline in place, 10 or more specimens might be imaged in a single day at 4× to 10× expansion, enabling statistically rich, brain-wide studies with protein-specific contrast and nanoscale resolution of neural development, sexual dimorphism, degree of stereotypy, and structure/function or structure/behavior correlations, particularly under genetic or pharmacological perturbation.

Materials and methods

Preparation of ExM samples

Mouse, *D. melanogaster*, and human samples were dissected, fixed, and immunostained following the protocols in supplementary note 1. Sample genotypes and antibodies are summarized in table S2. Unless otherwise noted, all samples were processed by using a protein-retention ExM (proExM) protocol with minor modifications (*19*, *105*) or an expansion pathology (ExPath) protocol (*98*). Prepared ExM samples were stored in 1× phosphate-buffered saline at 4°C and expanded in doubly deionized water immediately before imaging with LLSM.

Lattice light-sheet imaging

With the exception of Fig. 1, all ExM samples were imaged in objective scan mode (*20*) by using a LLSM described previously (*106*), except with adaptive optics capability disabled. The ExM sample in the left column of Fig. 1 was imaged by using a LLSM optimized for ExM, featuring a broader 160-μm FOV, a 1.5-mm scan range, and software optimized for rapid sample scan acquisition (supplementary note 2a). All expanded samples were large compared with the LLS FOV and were therefore imaged in a series of overlapping 3D tiles that covered the desired sample volume (supplementary note 2b). For imaging sessions of several hours or more, focus was maintained through the periodic imaging of reference beads (supplementary note 2c). Raw data from each tile were deskewed (for sample scan mode), flat-fielded, deconvolved, and stored for subsequent processing.

Computing pipeline for flat-field correction, stitching, and export of 3D image tiles

Because automatic tools for 3D stitching (*107*–*111*) do not scale to datasets with thousands of 3D image tiles, we developed a scalable high-performance computing (HPC) pipeline to robustly flat-field correct, deconvolve, and assemble 3D image tiles into the final volume (supplementary note 3). First, we extended and parallelized CIDRE (*107*) for 3D volumes to calculate 3D flat fields (figs. S5 and S6). We then corrected the raw image tiles using these flat-fields and deconvolved each. Next, we parallelized the globally optimizing 3D stitching method (*108*) to automatically stitch the thousands of raw image tiles, without manual intervention, in an iteratively refined prediction model that corrects for systematic stage coordinate errors (fig. S7). Last, we exported the stitched datasets using the flat-field–corrected and deconvolved image tiles as multiresolution hierarchies

Downloaded from http://science.sciencemag.org/ on January 19, 2019

into a custom file format (N5) (*21*) that enabled parallel blockwise export and compression on a HPC cluster. Bindings for N5 format for the ImgLib2 library (*112*) are provided for the ImageJ distribution Fiji (*113*). For interactive visualization, we developed a BigDataViewer-based viewer plugin (*114*) including a crop and export tool to make arbitrary subvolumes available in legacy formats such as TIFF image series.

REFERENCES AND NOTES

1. S. Herculano-Houzel, The human brain in numbers: A linearly scaled-up primate brain. *Front. Hum. Neurosci.* **3**, 31 (2009). doi: 10.3389/neuro.09.031.2009; pmid: 19915731
2. K. Sharma *et al.*, Cell type- and brain region-resolved mouse brain proteome. *Nat. Neurosci.* **18**, 1819–1831 (2015). doi: 10.1038/nn.4160; pmid: 26523646
3. J. E. Heuser, T. S. Reese, Evidence for recycling of synaptic vesicle membrane during transmitter release at the frog neuromuscular junction. *J. Cell Biol.* **57**, 315–344 (1973). doi: 10.1083/jcb.57.2.315; pmid: 4348786
4. C. S. Xu *et al.*, Enhanced FIB-SEM systems for large-volume 3D imaging. *eLife* **6**, e25916 (2017). doi: 10.7554/eLife.25916; pmid: 28500755
5. Z. Zheng *et al.*, A complete electron microscopy volume of the brain of adult *Drosophila melanogaster*. *Cell* **174**, 730–743.e22 (2018). doi: 10.1016/j.cell.2018.06.019; pmid: 30033368
6. K. D. Micheva, S. J. Smith, Array tomography: A new tool for imaging the molecular architecture and ultrastructure of neural circuits. *Neuron* **55**, 25–36 (2007). doi: 10.1016/j.neuron.2007.06.014; pmid: 17610815
7. J.-C. Rah *et al.*, Thalamocortical input onto layer 5 pyramidal neurons measured using quantitative large-scale array tomography. *Front. Neural Circuits* **7**, 177 (2013). doi: 10.3389/fncir.2013.00177; pmid: 24273494
8. A. S. Chiang *et al.*, Three-dimensional reconstruction of brain-wide wiring networks in *Drosophila* at single-cell resolution. *Curr. Biol.* **21**, 1–11 (2011). doi: 10.1016/j.cub.2010.11.056; pmid: 21129968
9. A. Jenett *et al.*, A GAL4-driver line resource for *Drosophila* neurobiology. *Cell Reports* **2**, 991–1001 (2012). doi: 10.1016/j.celrep.2012.09.011; pmid: 23063364
10. M. N. Economo *et al.*, A platform for brain-wide imaging and reconstruction of individual neurons. *eLife* **5**, e10566 (2016). doi: 10.7554/eLife.10566; pmid: 26796534
11. S. Shah, E. Lubeck, W. Zhou, L. Cai, In situ transcription profiling of single cells reveals spatial organization of cells in the mouse hippocampus. *Neuron* **92**, 342–357 (2016). doi: 10.1016/j.neuron.2016.10.001; pmid: 27764670
12. J. R. Moffitt *et al.*, High-throughput single-cell gene-expression profiling with multiplexed error-robust fluorescence in situ hybridization. *Proc. Natl. Acad. Sci. U.S.A.* **113**, 11046–11051 (2016). doi: 10.1073/pnas.1612826113; pmid: 27625426
13. J. Tønnesen, U. V. Nägerl, Superresolution imaging for neuroscience. *Exp. Neurol.* **242**, 33–40 (2013). doi: 10.1016/j.expneurol.2012.10.004; pmid: 23063602
14. H. Zhong, Applying superresolution localization-based microscopy to neurons. *Synapse* **69**, 283–294 (2015). doi: 10.1002/syn.21806; pmid: 25648102
15. C. I. Bargmann, Beyond the connectome: How neuromodulators shape neural circuits. *BioEssays* **34**, 458–465 (2012). doi: 10.1002/bies.201100185; pmid: 22396302
16. J. Lu, J. C. Tapia, O. L. White, J. W. Lichtman, The interscutularis muscle connectome. *PLOS Biol.* **7**, e32 (2009). pmid: 19209956
17. A. Nern, B. D. Pfeiffer, G. M. Rubin, Optimized tools for multicolor stochastic labeling reveal diverse stereotyped cell arrangements in the fly visual system. *Proc. Natl. Acad. Sci. U.S.A.* **112**, E2967–E2976 (2015). doi: 10.1073/pnas.1506763112; pmid: 25964354
18. F. Chen, P. W. Tillberg, E. S. Boyden, Expansion microscopy. *Science* **347**, 543–548 (2015). doi: 10.1126/science.1260088; pmid: 25592419
19. P. W. Tillberg *et al.*, Protein-retention expansion microscopy of cells and tissues labeled using standard fluorescent proteins and antibodies. *Nat. Biotechnol.* **34**, 987–992 (2016). doi: 10.1038/nbt.3625; pmid: 27376584
20. B. C. Chen *et al.*, Lattice light-sheet microscopy: Imaging molecules to embryos at high spatiotemporal resolution. *Science* **346**, 1257998 (2014). doi: 10.1126/science.1257998; pmid: 25342811
21. I. Pisarev, S. Saalfeld, Stitcher and N5 viewer; https://github.com/saalfeldlab/stitching-spark, https://github.com/saalfeldlab/n5-viewer.
22. J. Tønnesen, V. V. G. K. Inavalli, U. V. Nägerl, Super-resolution imaging of the extracellular space in living brain tissue. *Cell* **172**, 1108–1121.e15 (2018). doi: 10.1016/j.cell.2018.02.007; pmid: 29474910
23. L. Freifeld *et al.*, Expansion microscopy of zebrafish for neuroscience and developmental biology studies. *Proc. Natl. Acad. Sci. U.S.A.* **114**, E10799–E10808 (2017). doi: 10.1073/pnas.1706281114; pmid: 29162696
24. T. J. Mosca, D. J. Luginbuhl, I. E. Wang, L. Luo, Presynaptic LRP4 promotes synapse number and function of excitatory CNS neurons. *eLife* **6**, e27347 (2017). doi: 10.7554/eLife.27347; pmid: 28606304
25. C. K. Cahoon *et al.*, Superresolution expansion microscopy reveals the three-dimensional organization of the *Drosophila* synaptonemal complex. *Proc. Natl. Acad. Sci. U.S.A.* **114**, E6857–E6866 (2017). doi: 10.1073/pnas.1705623114; pmid: 28760978
26. A. Tsai *et al.*, Nuclear microenvironments modulate transcription from low-affinity enhancers. *eLife* **6**, e28975 (2017). doi: 10.7554/eLife.28975; pmid: 29095143
27. N. Jiang *et al.*, Superresolution imaging of *Drosophila* tissues using expansion microscopy. *Mol. Biol. Cell* **29**, 1413–1421 (2018). doi: 10.1091/mbc.E17-10-0583; pmid: 29688792
28. F. Guo, M. Holla, M. M. Diaz, M. Rosbash, A circadian output circuit controls sleep-wake arousal threshold in *Drosophila*. *bioRxiv* (2018). doi: 10.1101/298067
29. J. B. Chang *et al.*, Iterative expansion microscopy. *Nat. Methods* **14**, 593–599 (2017). doi: 10.1038/nmeth.4261; pmid: 28417997
30. C. J. L. Sheppard, Super resolution in confocal imaging. *Optik (Stuttg.)* **80**, 53–54 (1988).
31. C. B. Müller, J. Enderlein, Image scanning microscopy. *Phys. Rev. Lett.* **104**, 198101 (2010). doi: 10.1103/PhysRevLett.104.198101; pmid: 20867000
32. X.-T. Cheng *et al.*, Characterization of LAMP1-labeled nondegradative lysosomal and endocytic compartments in neurons. *J. Cell Biol.* **217**, 3127–3139 (2018). doi: 10.1083/jcb.201711083; pmid: 29695488
33. N. Kasthuri *et al.*, Saturated reconstruction of a volume of neocortex. *Cell* **162**, 648–661 (2015). doi: 10.1016/j.cell.2015.06.054; pmid: 26232230
34. Q. A. Liu, H. Shio, Mitochondrial morphogenesis, dendrite development, and synapse formation in cerebellum require both Bcl-w and the glutamate receptor δ2. *PLOS Genet.* **4**, e1000097 (2008). doi: 10.1371/journal.pgen.1000097; pmid: 18551174
35. W. Kuehnel, *Color Atlas of Cytology, Histology, and Microscopic Anatomy* (Thieme Flexibook, ed. 4, 2003).
36. V. Popov, N. I. Medvedev, H. A. Davies, M. G. Stewart, Mitochondria form a filamentous reticular network in hippocampal dendrites but are present as discrete bodies in axons: A three-dimensional ultrastructural study. *J. Comp. Neurol.* **492**, 50–65 (2005). doi: 10.1002/cne.20682; pmid: 16175555
37. M. R. Duchen, Mitochondria in health and disease: Perspectives on a new mitochondrial biology. *Mol. Aspects Med.* **25**, 365–451 (2004). doi: 10.1016/j.mam.2004.03.001; pmid: 15302203
38. S. G. Waxman, M. V. I. Bennett, Relative conduction velocities of small myelinated and non-myelinated fibres in the central nervous system. *Nat. New Biol.* **238**, 217–219 (1972). doi: 10.1038/newbio238217a0; pmid: 4506206
39. K. A. Nave, Myelination and support of axonal integrity by glia. *Nature* **468**, 244–252 (2010). doi: 10.1038/nature09614; pmid: 21068833
40. J. J. Harris, D. Attwell, The energetics of CNS white matter. *J. Neurosci.* **32**, 356–371 (2012). doi: 10.1523/JNEUROSCI.3430-11.2012; pmid: 22219296
41. A. Compston, A. Coles, Multiple sclerosis. *Lancet* **372**, 1502–1517 (2008). doi: 10.1016/S0140-6736(08)61620-7; pmid: 18970977
42. W. A. H. Rushton, A theory of the effects of fibre size in medullated nerve. *J. Physiol.* **115**, 101–122 (1951). doi: 10.1113/jphysiol.1951.sp004655; pmid: 14889433
43. R. La Marca *et al.*, TACE (ADAM17) inhibits Schwann cell myelination. *Nat. Neurosci.* **14**, 857–865 (2011). doi: 10.1038/nn.2849; pmid: 21666671
44. L.-J. Oluich *et al.*, Targeted ablation of oligodendrocytes induces axonal pathology independent of overt demyelination. *J. Neurosci.* **32**, 8317–8330 (2012). doi: 10.1523/JNEUROSCI.1053-12.2012; pmid: 22699912
45. M. Zonouzi *et al.*, GABAergic regulation of cerebellar NG2 cell development is altered in perinatal white matter injury. *Nat. Neurosci.* **18**, 674–682 (2015). doi: 10.1038/nn.3990; pmid: 25821912
46. O. O. Glebov, S. Cox, L. Humphreys, J. Burrone, Neuronal activity controls transsynaptic geometry. *Sci. Rep.* **6**, 22703 (2016). doi: 10.1038/srep22703; pmid: 26951792
47. A. Dani, B. Huang, J. Bergan, C. Dulac, X. Zhuang, Superresolution imaging of chemical synapses in the brain. *Neuron* **68**, 843–856 (2010). doi: 10.1016/j.neuron.2010.11.021; pmid: 21144999
48. N. L. Rochefort, A. Konnerth, Dendritic spines: From structure to in vivo function. *EMBO Rep.* **13**, 699–708 (2012). doi: 10.1038/embor.2012.102; pmid: 22791026
49. H. Hering, M. Sheng, Dendritic spines: Structure, dynamics and regulation. *Nat. Rev. Neurosci.* **2**, 880–888 (2001). doi: 10.1038/35104061; pmid: 11733795
50. E. A. Nimchinsky, B. L. Sabatini, K. Svoboda, Structure and function of dendritic spines. *Annu. Rev. Physiol.* **64**, 313–353 (2002). doi: 10.1146/annurev.physiol.64.081501.160008; pmid: 11826272
51. M. Segal, Dendritic spines and long-term plasticity. *Nat. Rev. Neurosci.* **6**, 277–284 (2005). doi: 10.1038/nrn1649; pmid: 15803159
52. S. Konur, D. Rabinowitz, V. L. Fenstermaker, R. Yuste, Systematic regulation of spine sizes and densities in pyramidal neurons. *J. Neurobiol.* **56**, 95–112 (2003). doi: 10.1002/neu.10229; pmid: 12838576
53. D. Dumitriu, A. Rodriguez, J. H. Morrison, High-throughput, detailed, cell-specific neuroanatomy of dendritic spines using microinjection and confocal microscopy. *Nat. Protoc.* **6**, 1391–1411 (2011). doi: 10.1038/nprot.2011.389; pmid: 21886104
54. M. Jiang *et al.*, Dendritic arborization and spine dynamics are abnormal in the mouse model of MECP2 duplication syndrome. *J. Neurosci.* **33**, 19518–19533 (2013). doi: 10.1523/JNEUROSCI.1745-13.2013; pmid: 24336718
55. X. Yu, Y. Zuo, Two-photon in vivo imaging of dendritic spines in the mouse cortex using a thinned-skull preparation. *J. Vis. Exp.* **87**, e51520 (2014). pmid: 24894563
56. J. I. Arellano, R. Benavides-Piccione, J. Defelipe, R. Yuste, Ultrastructure of dendritic spines: Correlation between synaptic and spine morphologies. *Front. Neurosci.* **1**, 131–143 (2007). doi: 10.3389/neuro.01.1.1.010.2007; pmid: 18982124
57. C. Bosch *et al.*, FIB/SEM technology and high-throughput 3D reconstruction of dendritic spines and synapses in GFP-labeled adult-generated neurons. *Front. Neuroanat.* **9**, 60 (2015). doi: 10.3389/fnana.2015.00060; pmid: 26052271
58. K. Takasaki, B. L. Sabatini, Super-resolution 2-photon microscopy reveals that the morphology of each dendritic spine correlates with diffusive but not synaptic properties. *Front. Neuroanat.* **8**, 29 (2014). doi: 10.3389/fnana.2014.00029; pmid: 24847215
59. J. Tønnesen, G. Katona, B. Rózsa, U. V. Nägerl, Spine neck plasticity regulates compartmentalization of synapses. *Nat. Neurosci.* **17**, 678–685 (2014). doi: 10.1038/nn.3682; pmid: 24657968
60. D. L. Dickstein *et al.*, Automatic dendritic spine quantification from confocal data with neurolucida 360. *Curr. Protoc. Neurosci.* **77**, 1, 21 (2016). doi: 10.1002/cpns.16; pmid: 27696360
61. E. G. Jones, T. P. S. Powell, Morphological variations in the dendritic spines of the neocortex. *J. Cell Sci.* **5**, 509–529 (1969). pmid: 5362339
62. J. Grutzendler, N. Kasthuri, W. B. Gan, Long-term dendritic spine stability in the adult cortex. *Nature* **420**, 812–816 (2002). doi: 10.1038/nature01276; pmid: 12490949
63. L. Anton-Sanchez *et al.*, Three-dimensional distribution of cortical synapses: A replicated point pattern-based analysis. *Front. Neuroanat.* **8**, 85 (2014). doi: 10.3389/fnana.2014.00085; pmid: 25206325
64. J. DeFelipe, L. Alonso-Nanclares, J. I. Arellano, Microstructure of the neocortex: Comparative aspects. *J. Neurocytol.* **31**, 299–316 (2002). doi: 10.1023/A:1024130211265; pmid: 12815249
65. C. Sala *et al.*, Regulation of dendritic spine morphology and synaptic function by Shank and Homer. *Neuron* **31**, 115–130 (2001). doi: 10.1016/S0896-6273(01)00339-7; pmid: 11498055

Downloaded from http://science.sciencemag.org/ on January 19, 2019

66. U. Thomas, Modulation of synaptic signalling complexes by Homer proteins. *J. Neurochem.* **81**, 407–413 (2002). doi: 10.1046/j.1471-4159.2002.00869.x; pmid: 12065649
67. A. Dosemeci, R. J. Weinberg, T. S. Reese, J.-H. Tao-Cheng, The postsynaptic density: There is more than meets the eye. *Front. Synaptic Neurosci.* **8**, 23 (2016). doi: 10.3389/fnsyn.2016.00023; pmid: 27594834
68. G. H. Diering *et al*., Homer1a drives homeostatic scaling-down of excitatory synapses during sleep. *Science* **355**, 511–515 (2017). doi: 10.1126/science.aai8355; pmid: 28154077
69. D. Debanne, E. Campanac, A. Bialowas, E. Carlier, G. Alcaraz, Axon physiology. *Physiol. Rev.* **91**, 555–602 (2011). doi: 10.1152/physrev.00048.2009; pmid: 21527732
70. G. S. Tomassy *et al*., Distinct profiles of myelin distribution along single axons of pyramidal neurons in the neocortex. *Science* **344**, 319–324 (2014). doi: 10.1126/science.1249766; pmid: 24744380
71. S. Einheber *et al*., The axonal membrane protein Caspr, a homologue of neurexin IV, is a component of the septate-like paranodal junctions that assemble during myelination. *J. Cell Biol.* **139**, 1495–1506 (1997). doi: 10.1083/jcb.139.6.1495; pmid: 9396755
72. C. Porrero, P. Rubio-Garrido, C. Avendaño, F. Clascá, Mapping of fluorescent protein-expressing neurons and axon pathways in adult and developing Thy1-eYFP-H transgenic mice. *Brain Res.* **1345**, 59–72 (2010). doi: 10.1016/j.brainres.2010.05.061; pmid: 20510892
73. S. Ramaswamy, H. Markram, Anatomy and physiology of the thick-tufted layer 5 pyramidal neuron. *Front. Cell. Neurosci.* **9**, 233 (2015). doi: 10.3389/fncel.2015.00233; pmid: 26167146
74. L. M. Palmer, G. J. Stuart, Site of action potential initiation in layer 5 pyramidal neurons. *J. Neurosci.* **26**, 1854–1863 (2006). doi: 10.1523/JNEUROSCI.4812-05.2006; pmid: 16467534
75. S. J. C. Caron, V. Ruta, L. F. Abbott, R. Axel, Random convergence of olfactory inputs in the Drosophila mushroom body. *Nature* **497**, 113–117 (2013). doi: 10.1038/nature12063; pmid: 23615618
76. N. J. Butcher, A. B. Friedrich, Z. Lu, H. Tanimoto, I. A. Meinertzhagen, Different classes of input and output neurons reveal new features in microglomeruli of the adult Drosophila mushroom body calyx. *J. Comp. Neurol.* **520**, 2185–2201 (2012). doi: 10.1002/cne.23037; pmid: 22237598
77. K. Eichler *et al*., The complete connectome of a learning and memory centre in an insect brain. *Nature* **548**, 175–182 (2017). doi: 10.1038/nature23455; pmid: 28796202
78. W. Fouquet *et al*., Maturation of active zone assembly by *Drosophila* Bruchpilot. *J. Cell Biol.* **186**, 129–145 (2009). doi: 10.1083/jcb.200812150; pmid: 19596851
79. N. Ehmann *et al*., Quantitative super-resolution imaging of Bruchpilot distinguishes active zone states. *Nat. Commun.* **5**, 4650 (2014). doi: 10.1038/ncomms5650; pmid: 25130366
80. Z. Mao, R. L. Davis, Eight different types of dopaminergic neurons innervate the *Drosophila* mushroom body neuropil: Anatomical and physiological heterogeneity. *Front. Neural Circuits* **3**, 5 (2009). doi: 10.3389/neuro.04.005.2009; pmid: 19597562
81. E. C. Kong *et al*., A pair of dopamine neurons target the D1-like dopamine receptor DopR in the central complex to promote ethanol-stimulated locomotion in *Drosophila*. *PLOS ONE* **5**, e9954 (2010). doi: 10.1371/journal.pone.0009954; pmid: 20376353
82. O. V. Alekseyenko *et al*., Single serotonergic neurons that modulate aggression in *Drosophila*. *Curr. Biol.* **24**, 2700–2707 (2014). doi: 10.1016/j.cub.2014.09.051; pmid: 25447998
83. S. Y. Takemura *et al*., A connectome of a learning and memory center in the adult *Drosophila* brain. *eLife* **6**, e26975 (2017). doi: 10.7554/eLife.26975; pmid: 28718765
84. D. Owald *et al*., A Syd-1 homologue regulates pre- and postsynaptic maturation in *Drosophila*. *J. Cell Biol.* **188**, 565–579 (2010). doi: 10.1083/jcb.200908055; pmid: 20176924
85. S. Holbrook, J. K. Finley, E. L. Lyons, T. G. Herman, Loss of syd-1 from R7 neurons disrupts two distinct phases of presynaptic development. *J. Neurosci.* **32**, 18101–18111 (2012). doi: 10.1523/JNEUROSCI.1350-12.2012; pmid: 23238725
86. Y. Aso *et al*., The neuronal architecture of the mushroom body provides a logic for associative learning. *eLife* **3**, e04577 (2014). doi: 10.7554/eLife.04577; pmid: 25535793
87. Y. Aso, G. M. Rubin, Dopaminergic neurons write and update memories with cell-type-specific rules. *eLife* **5**, e16135 (2016). doi: 10.7554/eLife.16135; pmid: 27441388
88. L. Kahsai, T. Zars, Learning and memory in *Drosophila*: Behavior, genetics, and neural systems. *Int. Rev. Neurobiol.* **99**, 139–167 (2011). doi: 10.1016/B978-0-12-387003-2.00006-9; pmid: 21906539
89. H. Luan, N. C. Peabody, C. R. Vinson, B. H. White, Refined spatial manipulation of neuronal function by combinatorial restriction of transgene expression. *Neuron* **52**, 425–436 (2006). doi: 10.1016/j.neuron.2006.08.028; pmid: 17088209
90. B. D. Pfeiffer *et al*., Refinement of tools for targeted gene expression in *Drosophila*. *Genetics* **186**, 735–755 (2010). doi: 10.1534/genetics.110.119917; pmid: 20697123
91. M. J. Dolan *et al*., Facilitating neuron-specific genetic manipulations in *Drosophila melanogaster* using a split GAL4 repressor. *Genetics* **206**, 775–784 (2017). doi: 10.1534/genetics.116.199687; pmid: 28363977
92. D. D. Bock *et al*., Network anatomy and in vivo physiology of visual cortical neurons. *Nature* **471**, 177–182 (2011). doi: 10.1038/nature09802; pmid: 21390124
93. T.-W. Chen *et al*., Ultrasensitive fluorescent proteins for imaging neuronal activity. *Nature* **499**, 295–300 (2013). doi: 10.1038/nature12354; pmid: 23868258
94. B. F. Fosque *et al*., Neural circuits. Labeling of active neural circuits in vivo with designed calcium integrators. *Science* **347**, 755–760 (2015). doi: 10.1126/science.1260922; pmid: 25678659
95. P. de Boer, J. P. Hoogenboom, B. N. G. Giepmans, Correlated light and electron microscopy: Ultrastructure lights up! *Nat. Methods* **12**, 503–513 (2015). doi: 10.1038/nmeth.3400; pmid: 26020503
96. T. J. Chozinski *et al*., Expansion microscopy with conventional antibodies and fluorescent proteins. *Nat. Methods* **13**, 485–488 (2016). doi: 10.1038/nmeth.3833; pmid: 27064647
97. T. Ku *et al*., Multiplexed and scalable super-resolution imaging of three-dimensional protein localization in size-adjustable tissues. *Nat. Biotechnol.* **34**, 973–981 (2016). doi: 10.1038/nbt.3641; pmid: 27454740
98. Y. Zhao *et al*., Nanoscale imaging of clinical specimens using pathology-optimized expansion microscopy. *Nat. Biotechnol.* **35**, 757–764 (2017). doi: 10.1038/nbt.3892; pmid: 28714966
99. U. Schnell, F. Dijk, K. A. Sjollema, B. N. G. Giepmans, Immunolabeling artifacts and the need for live-cell imaging. *Nat. Methods* **9**, 152–158 (2012). doi: 10.1038/nmeth.1855; pmid: 22290187
100. D. R. Whelan, T. D. M. Bell, Image artifacts in single molecule localization microscopy: Why optimization of sample preparation protocols matters. *Sci. Rep.* **5**, 7924 (2015). doi: 10.1038/srep07924; pmid: 25603780
101. D. Li *et al*., ADVANCED IMAGING. Extended-resolution structured illumination imaging of endocytic and cytoskeletal dynamics. *Science* **349**, aab3500 (2015). doi: 10.1126/science.aab3500; pmid: 26315442
102. W. R. Legant *et al*., High-density three-dimensional localization microscopy across large volumes. *Nat. Methods* **13**, 359–365 (2016). doi: 10.1038/nmeth.3797; pmid: 26950745
103. K. J. Hayworth *et al*., Ultrastructurally smooth thick partitioning and volume stitching for large-scale connectomics. *Nat. Methods* **12**, 319–322 (2015). doi: 10.1038/nmeth.3292; pmid: 25686390
104. Y.-G. Yoon *et al*., Feasibility of 3D reconstruction of neural morphology using expansion microscopy and barcode-guided agglomeration. *Front. Comput. Neurosci.* **11**, 97 (2017). doi: 10.3389/fncom.2017.00097; pmid: 29114215
105. S. M. Asano *et al*., Expansion microscopy: Protocols for imaging proteins and RNA in cells and tissues. *Curr. Protoc. Cell Biol.* **80**, e56 (2018). doi: 10.1002/cpcb.56; pmid: 30070431
106. T. L. Liu *et al*., Observing the cell in its native state: Imaging subcellular dynamics in multicellular organisms. *Science* **360**, eaaq1392 (2018). doi: 10.1126/science.aaq1392; pmid: 29674564
107. K. Smith *et al*., CIDRE: An illumination-correction method for optical microscopy. *Nat. Methods* **12**, 404–406 (2015). doi: 10.1038/nmeth.3323; pmid: 25775044
108. S. Preibisch, S. Saalfeld, P. Tomancak, Globally optimal stitching of tiled 3D microscopic image acquisitions. *Bioinformatics* **25**, 1463–1465 (2009). doi: 10.1093/bioinformatics/btp184; pmid: 19346324
109. D. Hörl *et al*., BigStitcher: Reconstructing high-resolution image datasets of cleared and expanded samples. *bioRxiv* (2018). doi: 10.1101/343954
110. M. Emmenlauer *et al*., XuvTools: Free, fast and reliable stitching of large 3D datasets. *J. Microsc.* **233**, 42–60 (2009). doi: 10.1111/j.1365-2818.2008.03094.x; pmid: 19196411
111. A. Bria, G. Iannello, TeraStitcher—A tool for fast automatic 3D-stitching of teravoxel-sized microscopy images. *BMC Bioinformatics* **13**, 316 (2012). doi: 10.1186/1471-2105-13-316; pmid: 23181553
112. T. Pietzsch, S. Preibisch, P. Tomancák, S. Saalfeld, ImgLib2—Generic image processing in Java. *Bioinformatics* **28**, 3009–3011 (2012). doi: 10.1093/bioinformatics/bts543; pmid: 22962343
113. J. Schindelin *et al*., Fiji: An open-source platform for biological-image analysis. *Nat. Methods* **9**, 676–682 (2012). doi: 10.1038/nmeth.2019; pmid: 22743772
114. T. Pietzsch, S. Saalfeld, S. Preibisch, P. Tomancak, BigDataViewer: Visualization and processing for large image data sets. *Nat. Methods* **12**, 481–483 (2015). doi: 10.1038/nmeth.3392; pmid: 26020499

ACKNOWLEDGMENTS

We thank D. Bock, K. Svoboda, N. Ji, N. Spruston, L. Scheffer, E. Snapp, P. Tillberg, L. Lavis, E. Bloss, W. Legant, D. Hoffman, and K. Hayworth at Howard Hughes Medical Institute (HHMI) Janelia Research Campus (JRC) and B. Sabatini and D. Van Vactor at Harvard Medical School (HMS) for invaluable discussions and comments. We also thank K. Schaefer, T. Wolff, C.-L. Chang, and H. Choi at JRC for help with sample preparation and imaging. We gratefully acknowledge the shared resources and project teams at JRC, including D. Alcor, J. Heddleston, and A. Taylor of the Advanced Imaging Center and Light Microscopy Facility for help with imaging; I. Negrashov and jET for manufacturing expertise; and O. Malkesman, K. Salvesen, C. Christoforou, G. Meissner, and the FlyLight project team for sample handling and preparation. Last, we are grateful to C. Pama and R. Karadottir at the University of Cambridge; J. Melander and H. Zhong at OHSU; T. Herman at the University of Oregon; and E. Karagiannis, J.-S. Kang, and F. Chen at MIT for help with sample preparation and H. Otsuna, T. Kawase, and E. Bas at JRC; C. Wietholt at FEI Amira; M. Gastinger at Bitplane; and J. McMullen and T. Tetreault at MBF Bioscience for data analysis and visualization. **Funding**: I.P., D.E.M., T.-L.L., V.S., A.G., J.B., J.C., C.M.O., J.L.-S., A.H., G.M.R., S.S., Y.A., and E.B. are funded by HHMI. E.S.B. acknowledges, for funding, John Doerr, the Open Philanthropy Project, NIH 1R01NS087950, NIH 1RM1HG008525, NIH 1R01DA045549, NIH 2R01DA029639, NIH 1R01NS102727, NIH 1R41MH112318, NIH 1R01EB024261, NIH 1R01MH110932, the HHMI–Simons Faculty Scholars Program, IARPA D16PC00008, U.S. Army Research Laboratory and the U. S. Army Research Office under contract/grant W911NF1510548, U.S.–Israel Binational Science Foundation Grant 2014509, and NIH Director's Pioneer Award 1DP1NS087724. S.U. and T.K. are funded by grants from Biogen, Ionis Pharmaceuticals, and NIH grant R01GM075252 (to T.K.). S.U. gratefully acknowledges the Fellows program of the Image and Data Analysis Core at Harvard Medical School and the MATLAB code repository received from the Computational Image Analysis Workshop, supported by NIH grant GM103792. K.R.M. and S.G.M. are funded by NIH grant R01DC015478. S.T. and A.R. are funded by NIH grant R44MH093011. **Author contributions:** E.B., E.S.B., and R.G. supervised the project and wrote the manuscript with input from all coauthors. T.-L.L. and J.C. built the microscopes with input from E.B., D.E.M., and jET (JRC) and performed all microscope characterization experiments. D.E.M. created the instrument control software. R.G., S.M.A., T.-L.L., V.S., J.C., and C.M.O. acquired all biological data with coauthors. G.H.H. provided the Thy1-YFP mice, and R.G. and S.M.A. prepared the ExM samples. A.G. and A.H. provided the Slc17a7-cre X TCGO mice and prepared the ExM samples. Y.Z. provided the human kidney sections and prepared the ExPath samples. Y.A. and G.M.R. created the split-GAL4 fly strains, Y.A. optimized the IHC conditions, and R.G. and S.M.A prepared the ExM samples. K.R.M., S.G.M., S.M.A., and T.-L.L. provided the initial stitching software packages. I.P. and S.S. created the automated flat-field, stitching, and N5 visualization pipeline, and I.P., R.G., J.B., and S.S. deconvolved, flat-fielded, and stitched all image data. Y.A. performed segmentation and tracing and supervised analyses of all fly image data. C.Z., S.T., and A.R. provided customized commercial software packages and helped with segmentation, tracing and reconstruction of neurites and dendritic spines using these packages. S.-H.S. and H.A.P. designed experimental protocols and performed sample preparation for FIB-SEM. S.P., C.S.X., and H.H. performed FIB-SEM sample preparation, image acquisition, and data processing. J.L.-S. and T.K. provided essential discussion on the subcellular ultrastructure analysis and access to instrumentation and computational resources. S.U. and R.G. processed and performed quantitative analysis of all image data. S.U., R.G., E.B., and Y.A. produced all figures and

Downloaded from http://science.sciencemag.org/ on January 19, 2019

movies. **Competing interests:** Portions of the technology described here are covered by U.S. patent 7,894,136 issued to E.B., assigned to Lattice Light of Ashburn, VA, and licensed to Carl Zeiss Microscopy; U.S. patents 8,711,211 and 9,477,074 issued to E.B., assigned to HHMI, and licensed to Carl Zeiss Microscopy; U.S. patent application 13/844,405 filed by E.B. and assigned to HHMI; and U.S. patent 9,500,846 issued to E.B. and assigned to HHMI. E.S.B. is a co-inventor on multiple patents related to ExM and is also a cofounder of a company that aims to provide kits and services relating to ExM to the public. R.G. is a co-inventor on multiple patents related to ExM. Y.Z. is a co-inventor on multiple patents related to ExM. **Data and materials availability:** All data needed to evaluate the conclusions in the paper are present in the paper or the supplementary materials. The compressed size of the datasets used in generating the figures and movies exceeds 100 terabytes, and it is therefore not practical to upload to a public data repository. All data used in this paper will be made freely available to those who request and provide a mechanism for feasible data transfers (such as physical hard disk drives or cloud storage). Documentation for construction of a LLSM can be obtained by execution of a research license agreement with HHMI.

SUPPLEMENTARY MATERIALS

www.sciencemag.org/content/363/6424/eaau8302/suppl/DC1
Supplementary Text
Figs. S1 to S33
Table S1 to S6
References (*115*–*133*)
Movies S1 to S7

19 July 2018; accepted 30 November 2018
10.1126/science.aau8302

Downloaded from http://science.sciencemag.org/ on January 19, 2019

RESEARCH ARTICLE SUMMARY

GENE THERAPY

CRISPR-mediated activation of a promoter or enhancer rescues obesity caused by haploinsufficiency

Navneet Matharu, Sawitree Rattanasopha, Serena Tamura, Lenka Maliskova, Yi Wang, Adelaide Bernard, Aaron Hardin, Walter L. Eckalbar, Christian Vaisse, Nadav Ahituv*

INTRODUCTION: Loss-of-function mutations in one gene copy can lead to reduced amounts of protein and, consequently, human disease, a condition termed haploinsufficiency. It is currently estimated that more than 660 genes cause human disease as a result of haploinsufficiency. The delivery of extra copies of the gene by way of gene therapy is a promising therapeutic strategy to increase gene dosage in such conditions. Recombinant adeno-associated virus (rAAV) provides a promising tool for delivery of transgenes in an efficient and safe way for gene therapy. However, it has some limitations, including an optimal DNA packaging constraint of 4700 base pairs and ectopic expression.

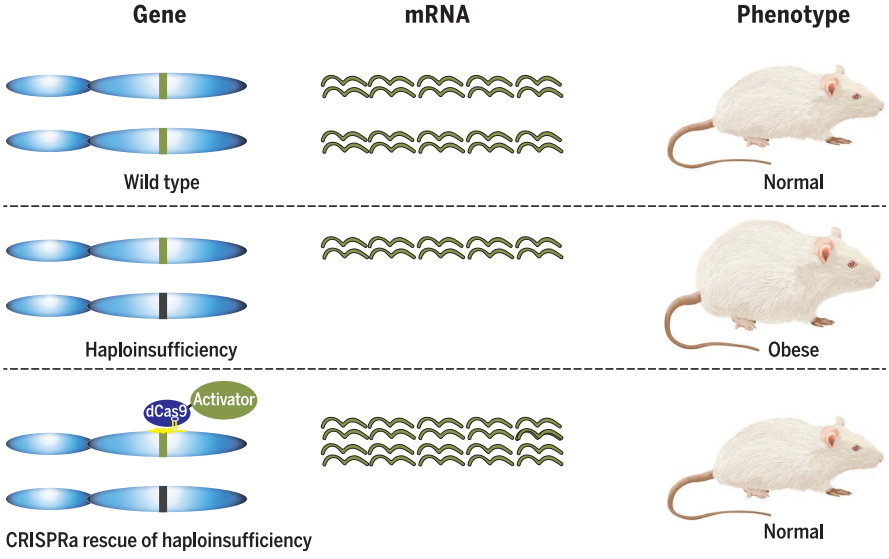
RATIONALE: Increasing the expression levels of the normal gene copy by directly targeting the endogenous gene regulatory elements that control it could potentially correct haploinsufficiency. CRISPR-mediated activation (CRISPRa), whereby a nuclease-deficient Cas9 (dCas9) is used to target a transcriptional activator to the gene's regulatory element (promoter or enhancer), could be used for this purpose. Such an approach could overcome the ectopic expression and DNA packaging limitations of rAAV. Using obesity as a model, we tested in mice whether CRISPR-mediated activation of the existing normal copy of two different genes, *Sim1* or *Mc4r*, where loss-of-function mutations that lead to haploinsufficiency are a major cause of human obesity, can rescue their obesity phenotype.

RESULTS: We first generated a transgenic CRISPRa system using dCas9 fused to a transcriptional activator, VP64, to test whether it can rescue the obesity phenotype in a *Sim1* haploinsufficient mouse model. CRISPRa targeting of the *Sim1* promoter or its hypothalamus-specific enhancer, which is 270 kilobases away from the gene, in *Sim1* haploinsufficient mice increased the expression of the normal copy of *Sim1*. This up-regulation was sufficient to rescue the obesity phenotype of *Sim1* heterozygous mice and led to significantly reduced food intake and body fat content in these mice. We assessed the off-targeting effects of CRISPRa using both RNA sequencing (RNA-seq) and Cas9 chromatin immunoprecipitation sequencing (ChIP-seq) analyses. We found CRISPRa targeting to be highly specific and without any overt changes in the expression of other genes. We also observed that *Sim1* up-regulation occurred only in tissues where the regulatory element (promoter or enhancer) that was being targeted was active. Although promoter-CRISPRa–targeted mice up-regulated *Sim1* in all the tissues where it is expressed, the enhancer-CRISPRa–targeted mice showed *Sim1* up-regulation only in the hypothalamus. We then delivered CRISPRa packaged into rAAV targeting the *Sim1* promoter or its hypothalamus-specific enhancer using either *Streptococcus pyogenes* or the shorter *Staphylococcus aureus* CRISPRa system. We show that postnatal injection of CRISPRa-rAAV into the hypothalamus can up-regulate *Sim1* expression and rescue the obesity phenotype in *Sim1* haploinsufficient mice in a long-lasting manner. To further highlight the therapeutic potential of this approach to rescue other haploinsufficient genes, we targeted *Mc4r*, where haploinsufficiency leads to severe obesity in mice and humans. CRISPRa-rAAV targeting of the *Mc4r* promoter rescued the obesity phenotype of *Mc4r* heterozygous mice.

ON OUR WEBSITE

Read the full article at http://dx.doi.org/10.1126/science.aau0629

CONCLUSION: These findings show that the CRISPRa system can rescue a haploinsufficient phenotype in vivo. This CRISPR-mediated activation strategy is different from a conventional gene therapy strategy, as it uses the endogenous regulatory elements to up-regulate the existing functional gene copy. As such, it can overcome the problem of ectopic gene expression. In addition, it could be used for genes that are not amenable to conventional gene therapy because their coding sequences are longer than the rAAV packaging limit. Our results provide a framework to further develop CRISPRa as a potential tool to treat gene dosage–sensitive diseases. ■



CRISPRa up-regulation of the existing normal gene copy rescues obesity caused by haploinsufficiency. Loss-of-function mutations in one allele lead to reduced amounts of mRNA and protein and can cause human disease, a condition termed haploinsufficiency. By up-regulating the existing normal allele using CRISPR-mediated activation (CRISPRa), whereby a nuclease-deficient Cas9 is fused to a transcriptional activator and targeted to a gene's regulatory element (promoter or enhancer), the haploinsufficient phenotype could be rescued.

The list of author affiliations is available in the full article online.
*Corresponding author. Email: nadav.ahituv@ucsf.edu
Cite this article as N. Matharu *et al.*, *Science* **363**, eaau0629 (2019). DOI: 10.1126/science.aau0629

Downloaded from http://science.sciencemag.org/ on January 20, 2019

RESEARCH ARTICLE

GENE THERAPY

CRISPR-mediated activation of a promoter or enhancer rescues obesity caused by haploinsufficiency

Navneet Matharu[1,2], Sawitree Rattanasopha[1,2,3], Serena Tamura[1,2], Lenka Maliskova[1,2], Yi Wang[4], Adelaide Bernard[4], Aaron Hardin[1,2], Walter L. Eckalbar[1,2], Christian Vaisse[4], Nadav Ahituv[1,2]*

A wide range of human diseases result from haploinsufficiency, where the function of one of the two gene copies is lost. Here, we targeted the remaining functional copy of a haploinsufficient gene using CRISPR-mediated activation (CRISPRa) in *Sim1* and *Mc4r* heterozygous mouse models to rescue their obesity phenotype. Transgenic-based CRISPRa targeting of the *Sim1* promoter or its distant hypothalamic enhancer up-regulated its expression from the endogenous functional allele in a tissue-specific manner, rescuing the obesity phenotype in *Sim1* heterozygous mice. To evaluate the therapeutic potential of CRISPRa, we injected CRISPRa-recombinant adeno-associated virus into the hypothalamus, which led to reversal of the obesity phenotype in *Sim1* and *Mc4r* haploinsufficient mice. Our results suggest that endogenous gene up-regulation could be a potential strategy to treat altered gene dosage diseases.

More than 660 genes are currently estimated to cause human disease due to haploinsufficiency (table S1) (*1*, *2*), leading to a wide range of phenotypes that include cancer, neurological diseases, developmental disorders, immunological diseases, metabolic disorders, infertility, kidney disease, limb malformations, and many others (*1*, *2*). Large-scale exome sequencing analyses estimate that there could be over 3000 human genes that are haploinsufficient (*3*). Gene therapy in which a functional recombinant copy or copies replace the mutant gene holds great promise in addressing diseases caused by haploinsufficiency. Numerous clinical trials are being carried out for gene therapy, most of which use recombinant adeno-associated virus (rAAV) to deliver the transgene (*4*). rAAV is a preferred gene delivery method because of its ability to provide long-lasting gene expression of the transgene, delivering DNA without integrating into the genome, and with limited pathogenicity (*5*). However, current rAAV approaches tend to use promoters to drive transgenes that can lead to nondesirable ectopic expression (*6*, *7*). Another crucial limitation is that AAV has an optimal 4.7-kilobase (kb) packaging capacity (*8*), limiting its gene therapy use for genes longer than 3.5 kb (taking into account additional regulatory sequences needed for its stable expression). Analysis of the 660 haploinsufficiency disease-causing genes and 3230 predicted heterozygous loss-of-function (LoF) genes reveals that 135 (20%) and 730 (23%) of them, respectively, have coding sequences longer than 3.5 kb (fig. S1), rendering them unsuitable for rAAV gene therapy.

CRISPR gene editing can potentially fix haploinsufficient mutations; however, this would require that the editing strategy be custom-tailored for each mutation. Moreover, it may not be feasible to correct heterozygous LoF microdeletions. To address these challenges, we devised a strategy that could potentially treat haploinsufficiency by using CRISPR activation (CRISPRa). CRISPRa takes advantage of the RNA-guided targeting ability of CRISPR to direct a nuclease-deficient Cas9 (*dCas9*) fused with a transcriptional activator to regulatory element(s) of a specific gene, thus increasing its expression (*9*–*15*). Here, we tested whether this system can be used to rescue a haploinsufficient phenotype by increasing the transcription of the normal endogenous gene. As a proof-of-concept model, we chose a quantitative trait, obesity caused by haploinsufficiency of either the single-minded family basic helix-loop-helix (bHLH) transcription factor 1 (*Sim1*) or the melanocortin 4 receptor (*Mc4r*) gene.

SIM1 is a transcription factor that is expressed in the developing kidney and central nervous system and is essential for the formation of the supraoptic nuclei (SON) and paraventricular nuclei (PVN) of the hypothalamus (*16*). *SIM1* also plays a role in the maintenance of long-term energy homeostasis by acting downstream of the leptin-melanocortin pathway (*17*). In humans, haploinsufficiency of *SIM1* due to chromosomal aberrations results in hyperphagic obesity (*18*), and *SIM1* coding mutations, many of which are LoF mutations, are thought to be a major cause of severe obesity in humans (*19*–*21*). *Sim1* homozygous null mice die perinatally, whereas *Sim1* heterozygous mice ($Sim1^{+/-}$) survive, are hyperphagic, and develop early-onset obesity with increased linear growth, hyperinsulinemia, and hyperleptinemia (*22*). A postnatal conditional knockout of hypothalamic *Sim1* leads to a similar phenotype in heterozygous mice (*23*), delineating an additional role for *Sim1* as an important regulator of energy homeostasis in adults. Overexpression of *SIM1*, by using a human bacterial artificial chromosome in mice, rescues diet-induced obesity and reduced food intake (*24*), suggesting a potential role for *SIM1* in preventing development of an obesity phenotype.

MC4R is a heterotrimeric guanine nucleotide–binding protein (G protein)–coupled receptor that is essential for the long-term regulation of energy homeostasis and other physiological processes. MC4R expression in the PVN of the hypothalamus is both necessary and sufficient for most of its effects on the regulation of body weight (*25*). Heterozygous mutations in *MC4R* are the most common cause of monogenic severe obesity, estimated at 2.6 to 5% of cases of early-onset and/or adult class 3 obesity (body mass index >40 kg/m^2) (*26*–*28*). Mice haploinsufficient for *Mc4r* become obese with hyperphagia, hyperinsulinemia, and hyperglycemia (*29*).

We initially tested the ability of a transgenic CRISPRa system to rescue the obesity phenotype in $Sim1^{+/-}$ mice. CRISPRa using a single guide RNA (sgRNA) targeted to either the *Sim1* promoter or its ~270-kb distant enhancer up-regulated *Sim1* expression and rescued *Sim1*-mediated obesity in haploinsufficient animals. This transgenic approach also showed that *Sim1* up-regulation occurred only in tissues where the promoter or enhancer is active, suggesting that the targeted cis-regulatory elements can determine CRISPRa tissue specificity. We also used these transgenic mice to assess the targeting specificity of CRISPRa by using RNA sequencing (RNA-seq) and chromatin immunoprecipitation sequencing (ChIP-seq), which we found to be highly specific and without any apparent off-target effects. To further show that CRISPRa could be used as a potential strategy to treat haploinsufficient phenotypes, we used rAAV-mediated delivery of CRISPRa to the hypothalamus, preventing excessive weight gain in postnatal $Sim1^{+/-}$ mice. To demonstrate that this strategy could be used for other haploinsufficient genes, we also targeted the *Mc4r* promoter by means of a similar CRISPRa-rAAV approach and reduced weight gain in $Mc4r^{+/-}$ mice. Our results present a potential strategy for treating haploinsufficiency and additional gene dosage–related functional abnormalities.

Results

Up-regulation of Sim1 in vitro by CRISPRa

To increase expression of the wild-type *Sim1* gene, we optimized CRISPRa conditions in vitro.

[1]Department of Bioengineering and Therapeutic Sciences, University of California San Francisco, San Francisco, CA 94158, USA. [2]Institute for Human Genetics, University of California San Francisco, San Francisco, CA 94158, USA. [3]Doctor of Philosophy Program in Medical Sciences, Faculty of Medicine, Chulalongkorn University, Bangkok, Thailand. [4]Diabetes Center, University of California San Francisco, San Francisco, CA 94143, USA.
*Corresponding author. Email: nadav.ahituv@ucsf.edu

Downloaded from http://science.sciencemag.org/ on January 20, 2019

Sim1 has a well-characterized promoter (*30*) and distant and robust hypothalamic enhancer (~270 kb from the transcription start site) denoted *Sim1* candidate enhancer 2 [SCE2 (*31*)] (Fig. 1A). To target *Sim1* using CRISPRa, we designed two sgRNAs for either the *Sim1* promoter or SCE2. Using these guides, we tested whether *Streptococcus pyogenes* dCas9 fused to VP64 (spdCas9-VP64), a transcriptional activator that carries four tandem copies of VP16 (a herpes simplex virus type 1 transcription factor) (*32*), can up-regulate *Sim1* in mouse neuroblastoma cells (Neuro-2a). The VP64 activator domain was chosen primarily because of its small size (so that it could later fit in our rAAV plasmid). It is also known to have a moderate activation potential compared to other known activators for a wide variety of genes (*33*), which could be advantageous in obtaining physiologically relevant *Sim1* dosage levels in vivo. Cells were transfected with spdCas9-VP64 and the various guide RNAs. After 48 hours, *Sim1* mRNA levels were measured by quantitative polymerase chain reaction (qPCR). We identified one sgRNA for either promoter or SCE2 that could up-regulate endogenous *Sim1* by 13- and 4-fold respectively (Fig. 1B and fig. S2, A and B). We also carried out ChIP-seq using an antibody against *S. pyogenes* Cas9 in both CRISPRa-promoter– and CRISPRa-enhancer–transfected cells and found on-target binding for the promoter and enhancer, respectively (fig. S2, C and D). We did not observe any peaks that overlapped with predicted sgRNA off-targets (table S2).

Up-regulation of Sim1 in vivo by transgenic CRISPRa rescues obesity

To test the ability of the CRISPRa system to rescue obesity in $Sim1^{+/-}$ mice, we generated knockin mouse lines using TARGATT technology (*34*). Using this technology, we inserted *spdCas9-VP64* into the mouse *Hipp11* locus [a region that is known to allow robust transgene expression (*35*)] having three copies of attP ($H11P3^{CAG\text{-}dCas9\text{-}VP64}$) and either sgRNA, targeting the *Sim1* promoter ($R26P3^{Sim1Pr\text{-}sgRNA}$) or SCE2 ($R26P3^{SCE2En\text{-}sgRNA}$), in the *Rosa26* locus that has three attP sites (Fig. 1C and fig. S3). We then crossed these mice to $Sim1^{+/-}$ mice that develop severe obesity (*22*). Mice having all three alleles ($Sim1^{+/-}$ × $H11P3^{CAG\text{-}dCas9\text{-}VP64}$ and $R26P3^{Sim1Pr\text{-}sgRNA}$ or $R26P3^{SCE2En\text{-}sgRNA}$) were weighed weekly until 16 weeks of age along with wild-type littermates and $Sim1^{+/-}$ and $Sim1^{+/-}$ × $H11P3^{CAG\text{-}dCas9\text{-}VP64}$ mice, both of which become severely obese (negative controls). Analysis of at least 10 females and 10 males per condition showed that $Sim1^{+/-}$ mice carrying both spdCas9-VP64 and either *Sim1* promoter or enhancer sgRNA had a significant reduction in body weight compared to $Sim1^{+/-}$ × $H11P3^{CAG\text{-}dCas9\text{-}VP64}$ and $Sim1^{+/-}$ (Fig. 1, D and E, and fig. S4). $Sim1^{+/+}$ mice carrying *spdCas9-VP64* and either *Sim1* promoter or enhancer sgRNA also showed a reduction in body weight compared to wild-type mice (fig. S4). We also analyzed body fat content and food intake for all genotypes: $Sim1^{+/-}$ × $H11P3^{CAG\text{-}dCas9\text{-}VP64}$ × $R26P3^{Sim1Pr\text{-}sgRNA}$ (Prm CRISPRa), $Sim1^{+/-}$ × $H11P3^{CAG\text{-}dCas9\text{-}VP64}$ × $R26P3^{SCE2En\text{-}sgRNA}$ (Enh-CRISPRa), $Sim1^{+/-}$, and wild-type mice. Both Prm-CRISPRa and Enh-CRISPRa mice showed significantly reduced body fat content and food intake compared to $Sim1^{+/-}$ in both females and males (fig. S5). Of note, we observed slight differences in body weight trajectories between female and male mice (i.e., when compared to wild-type mice, $Sim1^{+/-}$ females gained weight more rapidly than males), similar to what was observed in previous *Sim1* knockout studies (*22*, *23*). Taken together, these results show that both Prm-CRISPRa and Enh-CRISPRa mice have reduced body weight due to lower food intake, which likely leads to their reduced body fat levels.

CRISPRa up-regulation of Sim1 is tissue specific

To test for *Sim1* activation levels and tissue specificity in Prm-CRISPRa and Enh-CRISPRa mice, we measured its mRNA expression levels in different tissues. We selected two tissues where *Sim1* is expressed, hypothalamus and kidney, and two tissues where it is not expressed, lung and liver, based on previous studies (*36*, *37*) and our analysis of *Sim1* expression in different tissues (fig. S6). We first measured *spdCas9* expression and found it to be expressed in all four tissues, as expected, because we used a ubiquitous cytomegalovirus (CMV) enhancer chicken β-actin (CAG) promoter to drive its expression (Fig. 2A). By contrast, for *Sim1*, we observed significantly higher mRNA levels in both the hypothalamus and kidney in Prm-CRISPRa mice but only in the hypothalamus of Enh-CRISPRa mice compared to $Sim1^{+/-}$ mice (Fig. 2B). In $Sim1^{+/-}$ mice, we observed half the levels of mRNA expression when compared to wild-type mice, both in the hypothalamus and kidney.

Because we did not observe any significant differences between the obesity phenotype of Prm-CRISPRa and Enh-CRISPRa mice, we speculate that the activation of *Sim1* in the hypothalamus is sufficient to rescue the $Sim1^{+/-}$ obesity phenotype. In tissues where *Sim1* is not expressed (i.e., liver and lung), we could not detect *Sim1* expression in Prm-CRISPRa or Enh-CRISPRa mice despite *spdCas9* being expressed. These results imply that despite ubiquitous expression, spdCas9-VP64 could only up-regulate *Sim1* in tissues where its target cis-regulatory elements are active. This suggests that cis-regulatory elements could be used to define the tissue specificity of CRISPRa.

Sim1 CRISPRa targeting is highly specific

To check for CRISPRa off-target effects, we undertook two genomic-level approaches: We analyzed the hypothalamic transcriptome (RNA-seq) of wild-type, $Sim1^{+/-}$, Prm-CRISPRa, and Enh-CRISPRa mice. Three males and three females were used for each genotype (total of 24 samples; 6 biological replicates per condition). We also carried out ChIP-seq using an antibody against *S. pyogenes* Cas9 in the hypothalamus of Prm-CRISPRa, Enh-CRISPRa, and *spdCas9-VP64* (negative control) mice. A pool of four mice was used for each genotype, and two biological replicates.

In the RNA-seq analyses, we identified 24 differentially expressed genes [at a false discovery rate (FDR) of 0.1] between $Sim1^{+/-}$ and wild-type mice, of which 17 were up-regulated and 7 were down-regulated. For all of the 17 up-regulated and 6 of the 7 down-regulated genes, we observed fold changes that were similar to that of wild-type versus $Sim1^{+/-}$ for Prm-CRISPRa or Enh-CRISPRa when compared to $Sim1^{+/-}$ (Fig. 2, C and D, and table S3). We also observed that genes that were significantly up-regulated or down-regulated in Prm-CRISPRa versus $Sim1^{+/-}$ were also up-regulated or down-regulated in Enh-CRISPRa and vice versa, highlighting that the overall gene expression profile in Prm-CRISPRa and Enh-CRISPRa was similar (Fig. 2, C and D, and table S3). None of the *Sim1* neighboring genes within a 500-kb window were differentially expressed in Prm-CRISPRa or Enh-CRISPRa in the RNA-seq analysis. Using qPCR, we also analyzed the mRNA expression levels of *Sim1* neighboring genes, activating signal cointegrator 1 complex subunit 3 (*Ascc3*) and G protein–coupled receptor class C group 6 member A (*Gprc6a*). We did not observe any differences in expression levels for these genes in Prm-CRISPRa and Enh-CRISPRa compared to wild-type mice (fig. S7, A and B). These results suggest that Sim1-CRISPRa changes the transcription profile of $Sim1^{+/-}$ mice to one that is more similar to that of the wild type.

Next, we carried out ChIP-seq analysis to identify off-target spdCas9-VP64 binding. We found the most significant on-target enrichment at the *Sim1* promoter in Prm-CRISPRa and SCE2 in Enh-CRISPRa mice (fig. S8, A and B, and table S2). In addition, we found 91 and 136 significant peaks (FDR adjusted p value ≤ 10^{-1}) in Prm-CRISPRa and Enh-CRISPRa, respectively (table S2). We then looked for predicted sequence-specific genomic off-targets due to Prm-sgRNA or Enh-sgRNA mismatches, allowing for zero to three nucleotide mismatches, using Cas-OFFfinder (*38*). For the promoter-targeting sgRNA, we found the one expected on-target site, and one off-target site with three nucleotide mismatches (fig. S8C and table S2). For the enhancer-targeting sgRNA, we found the one expected on-target site and eight off-target sites with three nucleotide mismatches (fig. S8D and table S2). None of the Prm-CRISPRa or Enh-CRISPRa ChIP-seq peaks overlapped a corresponding predicted off-target site (table S2).

We next analyzed the RNA-seq datasets for the expression of the neighboring genes (±500 kb upstream and downstream) near the ChIP-seq peaks and sgRNA off-target sites, including the *Sim1* target-specific peaks (fig. S8, C and D, and table S3). Of the genes within 500 kb of the off-target ChIP-seq peaks or predicted off-target sites, none showed differential gene expression (Fig. 2, E and F, and fig. S8, E and F). In addition, ChIP for dCas9 followed by qPCR for *Ascc3*, *Gprc6a*, and the *Sim1* promoter or SCE2 showed binding

Downloaded from http://science.sciencemag.org/ on January 20, 2019

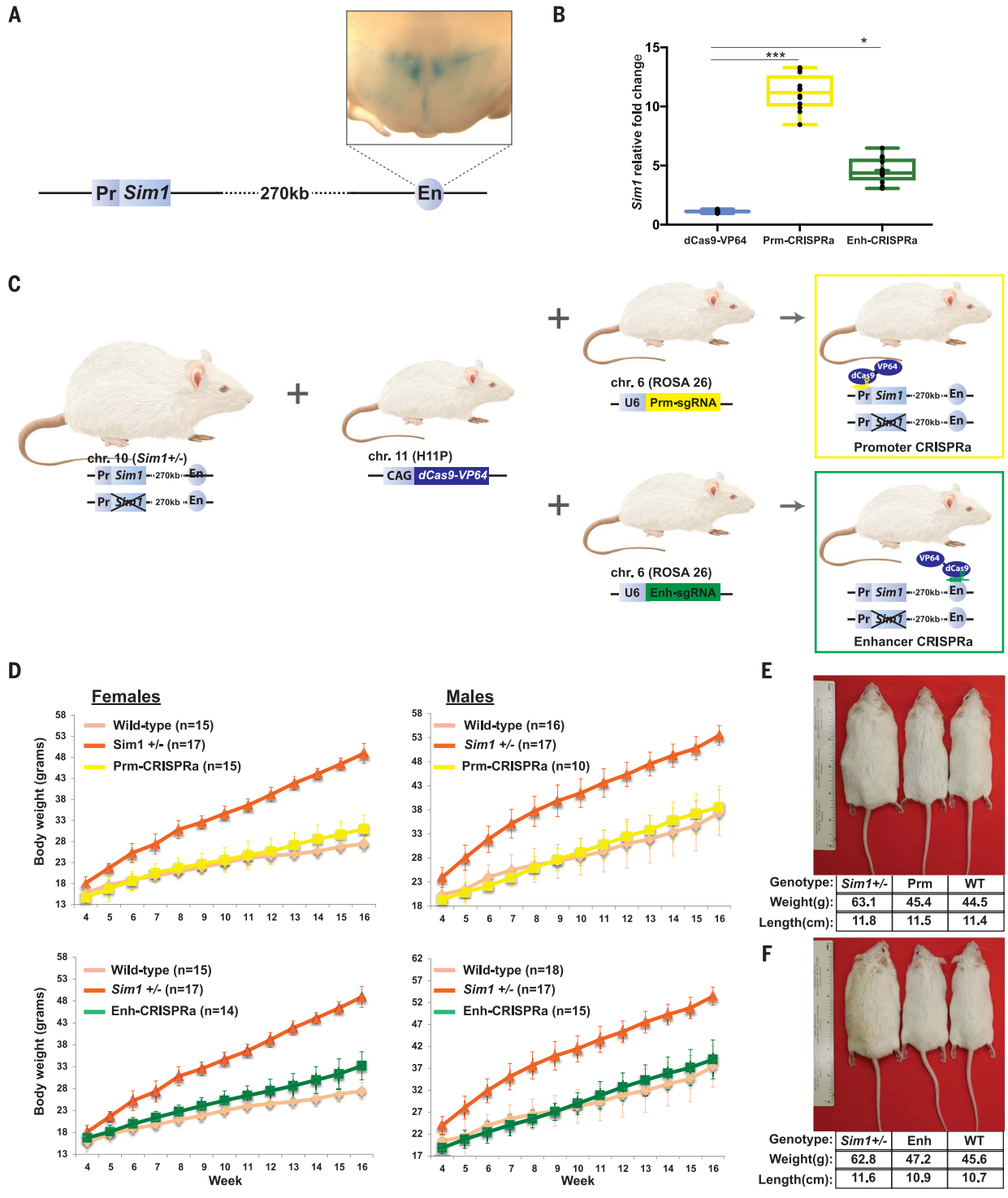


Fig. 1. CRISPRa *Sim1* up-regulation in vitro and obesity rescue in vivo. (**A**) Schema of the mouse *Sim1* genomic locus, showing the LacZ-driven hypothalamic expression of SCE2 (En) from 56-day-old mice. (**B**) CRISPRa in Neuro-2a cells targeting the *Sim1* promoter (Prm-CRISPRa) or enhancer (Enh-CRISPRa). Results are expressed as mRNA fold increase normalized to *Actb* using the ΔΔCT method. The data are represented as means ± the lower and upper quartile, and lines represent the minimum and maximum from three independent experiments and three technical replicates. *$p < 0.001$; ***$p < 0.0005$ (ANOVA, Tukey test). (**C**) Schema showing the mating scheme used to generate $Sim1^{+/-}$ CRISPRa mice. A CAG-dCas9-VP64 cassette was knocked into the *Hipp11* (H11P3) locus, and an sgRNA targeting either the *Sim1* promoter (U6-Prm-sgRNA) or SCE2 (U6-Enh-sgRNA) was knocked into the *Rosa26* locus. (**D**) Weekly weight measurements of wild-type, $Sim1^{+/-}$, $H11P3^{CAG\text{-}dCas9\text{-}VP64}$ × $R26P3^{Sim1Pr\text{-}sgRNA}$ (Prm-CRISPRa), and $H11P3^{CAG\text{-}dCas9\text{-}VP64}$ × $R26P3^{SCE2En\text{-}sgRNA}$ (Enh-CRISPRa). At least 10 male and female mice were measured per genotype. Mean values ± SD are shown. *p*-value statistics are listed in table S5. (**E** and **F**) Photos of 26-week-old male mice for each genotype: $Sim1^{+/-}$, $H11P3^{CAG\text{-}dCas9\text{-}VP64}$ × $R26P3^{Sim1Pr\text{-}sgRNA}$ (Prm), and wild type (WT) (E) and $Sim1^{+/-}$, $H11P3^{CAG\text{-}dCas9\text{-}VP64}$ × $R26P3^{SCE2En\text{-}sgRNA}$ (Enh), and wild type (WT) (F). Genotype, weight, and length of each mouse are depicted below.

Downloaded from http://science.sciencemag.org/ on January 20, 2019

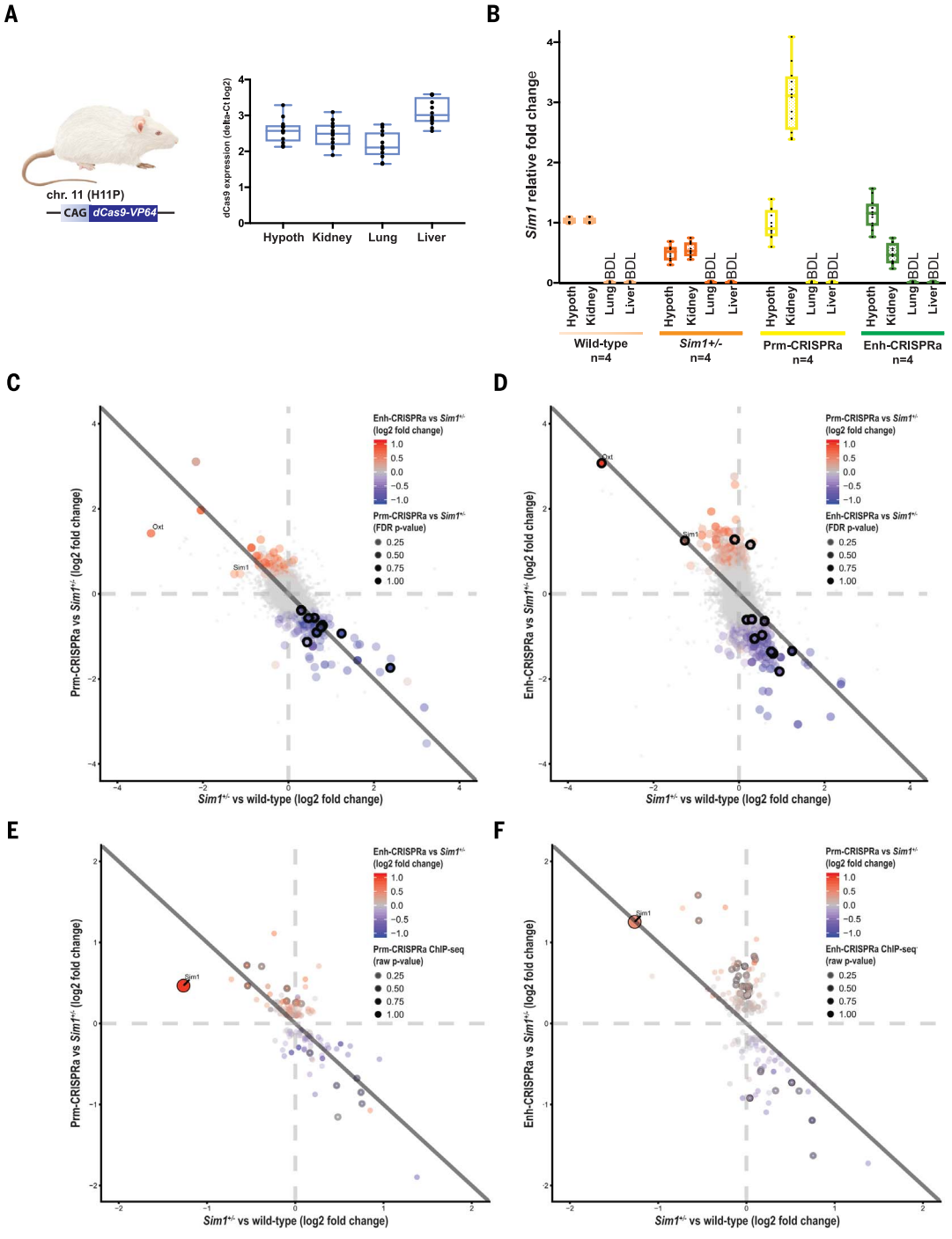


Fig. 2. *dCas9* and *Sim1* mRNA expression levels in CRISPRa transgenic mice. (**A**) *dCas9* mRNA expression in the hypothalamus, kidney, lung, and liver from four $Sim1^{+/-}$ × $H11P3^{CAG\text{-}dCas9\text{-}VP64}$ mice. The data are represented as means ± the lower and upper quartile, and lines represent the minimum and maximum from at least four mice with three technical replicates. (**B**) *Sim1* mRNA expression in the hypothalamus, kidney, lung, and liver for the following genotypes: wild type, $Sim1^{+/-}$, $H11P3^{CAG\text{-}dCas9\text{-}VP64}$ × $R26P3^{Sim1Pr\text{-}sgRNA}$ (Prm-CRISPRa), and $H11P3^{CAG\text{-}dCas9\text{-}VP64}$ × $R26P3^{SCE2En\text{-}sgRNA}$ (Enh-CRISPRa). The data are represented as means ± the lower and upper quartile, and lines represent the minimum and maximum from four mice (two females and two males) and three technical replicates. All experiments were determined based on mRNA fold increase compared to wild type and normalized to *Actb* or *Rpl38* using the ΔΔCT method or ΔCT for (A). BDL, below detectable levels. (**C** and **D**) A Michaelis-Menten plot showing differentially expressed genes in the hypothalamus between $Sim1^{+/-}$ and wild-type mice on the *x* axis and Prm-CRISPRa (C) or Enh-CRISPRa (D) versus $Sim1^{+/-}$ mice on the *y* axis. The larger circles are genes that are differentially expressed with a raw *p* value ≤0.05, and the outlined circles have a FDR ≤0.1. (**E** and **F**) A Michaelis-Menten plot showing differentially expressed genes in the hypothalamus that are nearby ChIP-seq peaks and predicted off-target sgRNAs between $Sim1^{+/-}$ and wild-type mice on the *x* axis and Prm-CRISPRa (E) or Enh-CRISPRa (F) versus $Sim1^{+/-}$ mice on the *y* axis. The outlined circles are genes that show differential expression with a raw *p* value ≤0.05, and the larger circles are genes that overlap nearby off-target sites (both *Sim1* promoter and SCE2 were predicted targets even up to three mismatches).

Downloaded from http://science.sciencemag.org/ on January 20, 2019

only in the *Sim1* promoter for Prm-CRISPRa and SCE2 in Enh-CRISPRa mice (fig. S7, C and D), similar to what we observed in the ChIP-seq data. Our results show that *Sim1* Prm-CRISPRa and Enh-CRISPRa are highly specific, without any apparent off-target effects.

Delivery of Sim1 CRISPRa rAAV to the PVN rescues the weight gain phenotype in Sim1$^{+/-}$ mice

To further investigate the translational potential of this approach to rescue haploinsufficiency in adult mice, we took advantage of rAAV to deliver CRISPRa into the hypothalamus of *Sim1*$^{+/-}$ mice. We generated the following three rAAV vectors: (i) *S. pyogenes* dCas9-VP64 driven by a CMV promoter (*pCMV-spdCas9-VP64*); (ii) *Sim1* promoter sgRNA along with mCherry (*pU6-Sim1Pr-CMV-mCherry*); and (iii) SCE2 sgRNA along with mCherry (*pU6-SCE2-CMV-mCherry*) (Fig. 3A). These vectors were packaged individually into AAV-DJ serotype (*39*). We first tested if the rAAV CRISPRa vectors could up-regulate *Sim1* in vitro using Neuro-2a cells. We observed a four- and fivefold increase in *Sim1* mRNA expression when targeting the promoter or enhancer, respectively (Fig. 3B and fig. S9).

Next, we performed stereotactic injections to deliver virus carrying *pCMV-spdCas9-VP64* and either *pU6-Sim1Pr-CMV-mCherry* (Prm-CRISPRa-AAV) or *pU6-SCE2-CMV-mCherry* (Enh-CRISPRa-AAV) into the PVN of the hypothalamus of *Sim1*$^{+/-}$ mice at 4 weeks of age, before the mice start becoming obese. As an injection-based negative control, we also injected *Sim1*$^{+/-}$ mice with *pCMV-spdCas9-VP64* virus only. We first optimized the stereotaxic injection conditions and coordinates (see Methods) and tested for the expression of mCherry from the *pU6-Sim1Pr-CMV-mCherry* cassette in the PVN by performing immunostaining on the hypothalami of injected mice (Fig. 3C and fig. S10). Next, we carried out stereotaxic injections into the PVN of *Sim1*$^{+/-}$ mice at 4 weeks of age using *S. pyogenes* CRISPRa-AAV. To test whether *Sim1* expression levels were increased by delivering CRISPRa-AAV to the hypothalamus of *Sim1*$^{+/-}$ mice, we measured mRNA expression levels for both *dCas9* and *Sim1* from 11-week-old AAV-injected mice. *dCas9* was expressed in the hypothalami of all the *pCMV-spdCas9-VP64* AAV–injected mice (Fig. 3D). *Sim1* up-regulation was observed in both Prm-CRISPRa-AAV– and Enh-CRISPRa-AAV–injected hypothalami, but not in mice injected with only *pCMV-spdCas9-VP64*-AAV (Fig. 3E). To observe the extent of *Sim1* up-regulation that could be achieved, we injected Prm-CRISPRa-AAV into the hypothalami of wild-type mice using two different titers. We observed up to 1.8-fold up-regulation with the higher viral titer (fig. S11).

Because the length of *S. pyogenes* dCas9-VP64 exceeds the optimal packaging load for AAV (i.e., 4.7 kb), we generated a *Staphylococcus aureus*

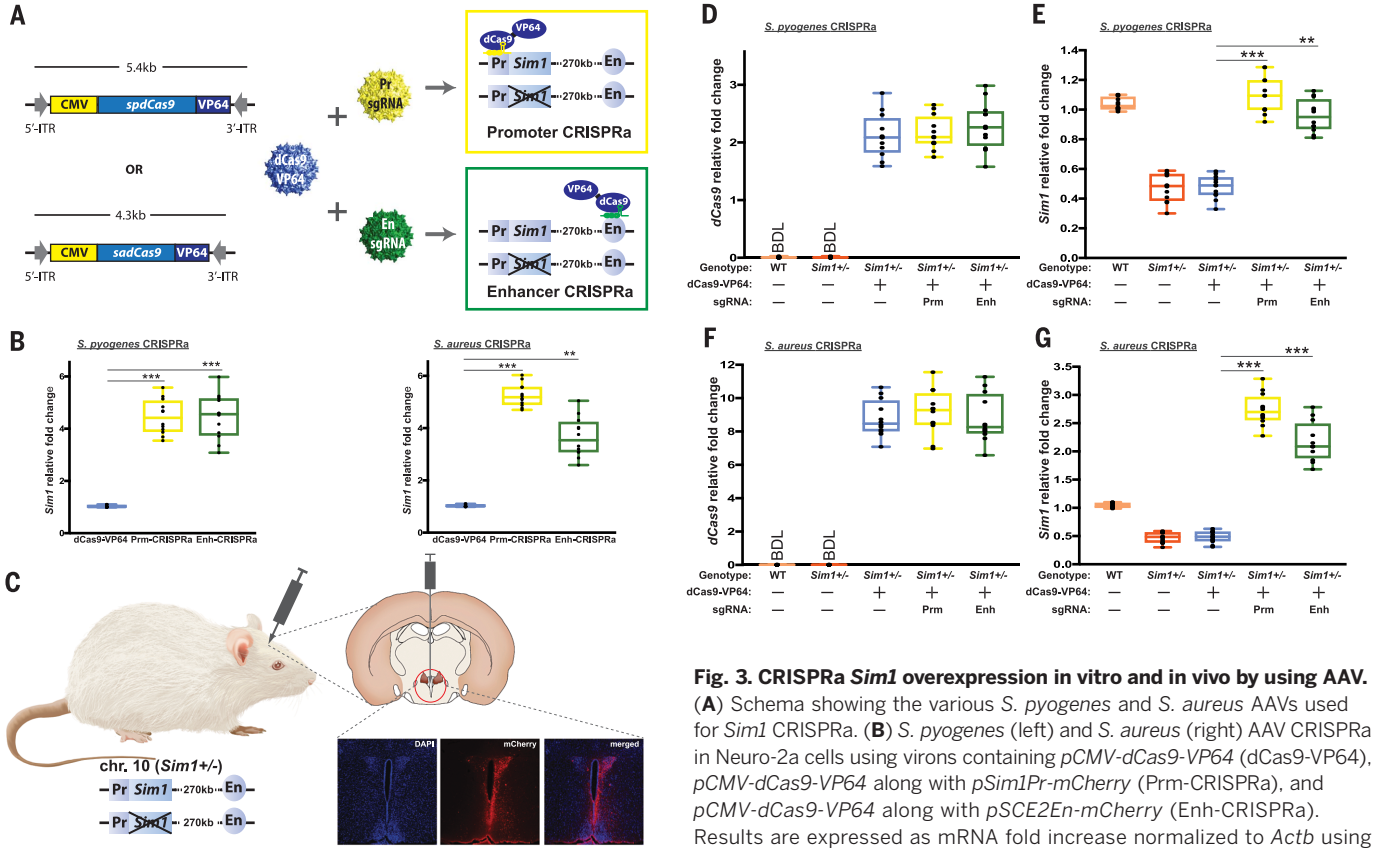


Fig. 3. CRISPRa *Sim1* overexpression in vitro and in vivo by using AAV. (**A**) Schema showing the various *S. pyogenes* and *S. aureus* AAVs used for *Sim1* CRISPRa. (**B**) *S. pyogenes* (left) and *S. aureus* (right) AAV CRISPRa in Neuro-2a cells using virons containing *pCMV-dCas9-VP64* (dCas9-VP64), *pCMV-dCas9-VP64* along with *pSim1Pr-mCherry* (Prm-CRISPRa), and *pCMV-dCas9-VP64* along with *pSCE2En-mCherry* (Enh-CRISPRa). Results are expressed as mRNA fold increase normalized to *Actb* using the ΔΔCT method. The data are represented as means ± the lower and upper quartile, and lines represent the minimum and maximum from four independent experiments with three technical replicates. ***$p < 0.0005$; **$p < 0.001$ (ANOVA, Tukey test). (**C**) Schema showing location of the single midline stereotactic injection in the PVN (red circle) followed by immunohistochemistry results from *pSim1Pr-mCherry*–injected hypothalami of 12-week-old mice showing DAPI (4′,6-diamidino-2-phenylindole) staining, mCherry expression, and merged staining of both. (**D** and **E**) *dCas9* (D) and *Sim1* (E) mRNA expression from noninjected wild-type and *Sim1*$^{+/-}$ mice along with *pCMV-spdCas9-VP64* (dCas9-VP64)–, *pCMV-spdCas9-VP64* + *pSim1Pr-mCherry* (Prm-CRISPRa)–, and *pCMV-spdCas9-VP64* + *pSCE2En-mCherry* (Enh-CRISPRa)–injected *Sim1*+/− mice for *S. pyogenes*. (**F** and **G**) *dCas9* (F) and *Sim1* (G) mRNA expression from noninjected wild-type and *Sim1*$^{+/-}$ mice along with *pCMV-sadCas9-VP64* (dCas9-VP64)–, *pCMV-sadCas9-VP64* + *pSim1Pr-mCherry* (Prm-CRISPRa)–, and *pCMV-sadCas9-VP64* + *pSCE2En-mCherry* (Enh-CRISPRa)–injected *Sim1*+/− mice for *S. aureus*. Four mice were used for each genotype. The data are represented as means ± the lower and upper quartile, and lines represent the minimum and maximum. Values from four independent experiments with three technical replicates were determined based on mRNA fold increase compared to wild-type mice and normalized to *Actb* using the ΔΔCT method for *Sim1* expression and relative *Actb* ΔCT log2 for *dCas9* expression.

Downloaded from http://science.sciencemag.org/ on January 20, 2019

dCas9–fused VP64 vector, which has an AAV packaging load of 4.3 kb (Fig. 3A; *pCMV-sadCas9-VP64*). As *S. aureus* uses a different protospacer adjacent motif site, we designed and cloned sgRNAs for *pU6-Sim1Pr-CMV-mCherry* and *pU6-SCE2-CMV-mCherry*. We identified several sgRNAs that can increase *Sim1* expression by targeting its promoter or SCE2 in Neuro-2a cells through transient transfection (fig. S12, A and B). We also carried out ChIP-seq using an antibody against *S. aureus* Cas9 in both Prm-CRISPRa– and Enh-CRISPRa–transfected cells and found on-target binding for the promoter and enhancer, respectively (fig. S12, C and D). We did not observe any peaks that overlapped with predicted sgRNA off-targets (table S2). We then generated an AAV-DJ serotype of the *S. aureus* CRISPRa vectors, obtaining higher titers for dCas9-VP64 virons than *S. pyogenes* CRISPRa-AAVs (see Methods). We infected Neuro-2a cells with the viruses and selected a single sgRNA for the promoter or SCE2 that significantly increased *Sim1* expression (Fig. 3B and fig. S12E). Next, we carried out stereotactic injections into the PVN of *Sim1*$^{+/-}$ mice at 4 weeks of age using *S. aureus* CRISPRa-AAV. To test whether *Sim1* expression levels were increased by delivering *S. aureus* CRISPRa-AAV to the hypothalamus of *Sim1*$^{+/-}$ mice, we measured mRNA expression levels from hypothalami of 11-week-old AAV-injected mice. Compared to *S. pyogenes* dCas9 expression levels (Fig. 3D), we found higher expression levels of *S. aureus dCas9* in the hypothalami of all *pCMV-saCas9-VP64* AAV–injected mice (Fig. 3F). We also observed higher *Sim1* up-regulation (Fig. 3G) compared to *S. pyogenes* CRISPRa (Fig. 3E).

Next, we tested whether *Sim1* up-regulation by CRISPRa-AAV can lead to a reduction in body weight of *Sim1* haploinsufficient mice. CRISPRa-AAV–injected *Sim1*$^{+/-}$ mice were measured for body weight up to 11 weeks of age (Fig. 4A). We observed a significant weight reduction in the Prm-CRISPRa-AAV– or Enh-CRISPRa-AAV–injected mice compared to the *Sim1*$^{+/-}$ or *pCMV-dCas9-VP64*-AAV–injected *Sim1*$^{+/-}$ mice both for *S. pyogenes* (Fig. 4B) and *S. aureus* (Fig. 4C). These results suggest that CRISPRa-AAV can rescue the *Sim1* haploinsuficiency obesity phenotype.

Finally, we analyzed whether CRISPRa would have a long-term body weight effect on these mice. Although many of the injected mice were analyzed in the aforementioned gene expression studies, a few were maintained and showed significant weight reduction compared to the *Sim1*$^{+/-}$ or *pCMV-spdCas9-VP64*-AAV–injected *Sim1*$^{+/-}$ mice 9 months after injection (Fig. 4, D and E). Similar results were also observed in *S. aureus*–injected mice (fig. S13). These results show that CRISPRa-AAV–mediated up-regulation could have a long-lasting effect on phenotype.

Delivery of Mc4r CRISPRa rAAV to the PVN rescues the weight gain phenotype in Mc4r$^{+/-}$ *mice*

To further investigate whether CRISPRa can rescue an additional haploinsufficient obesity model, we carried out *S. aureus* CRISPRa targeting of the *Mc4r* promoter in *Mc4r*$^{+/-}$ mice, which become obese as a result of heterozygous LoF of *Mc4r* (*29*). We first screened five sgRNAs targeting the *Mc4r* promoter and selected one that led to robust *Mc4r* up-regulation in Neuro-2a cells using both transient transfection and rAAV infections (fig. S14). We then carried out stereotactic injections into the PVN of 4-week-old *Mc4r*$^{+/-}$ mice with either *pCMV-sadCas9-VP64*-AAV as a negative control or *pCMV-sadCas9-VP64*-AAV and *pU6-Mc4rPr-CMV-mCherry* (Mc4rPrm-CRISPRa-AAV) (Fig. 5, A and B). We observed an increase in *Mc4r* expression up to 2.7-fold in Mc4rPrm-CRISPRa-AAV mice (Fig. 5C). Body weight measurements 8 weeks after injection showed a significant weight reduction in the Mc4rPrm-CRISPRa-AAV–injected mice compared to the *Mc4r*$^{+/-}$ or *pCMV-sadCas9-VP64*-AAV–injected *Mc4r*$^{+/-}$ mice (Fig. 5, D and E). These results further suggest that CRISPRa can be used to rescue other haploinsufficient phenotypes.

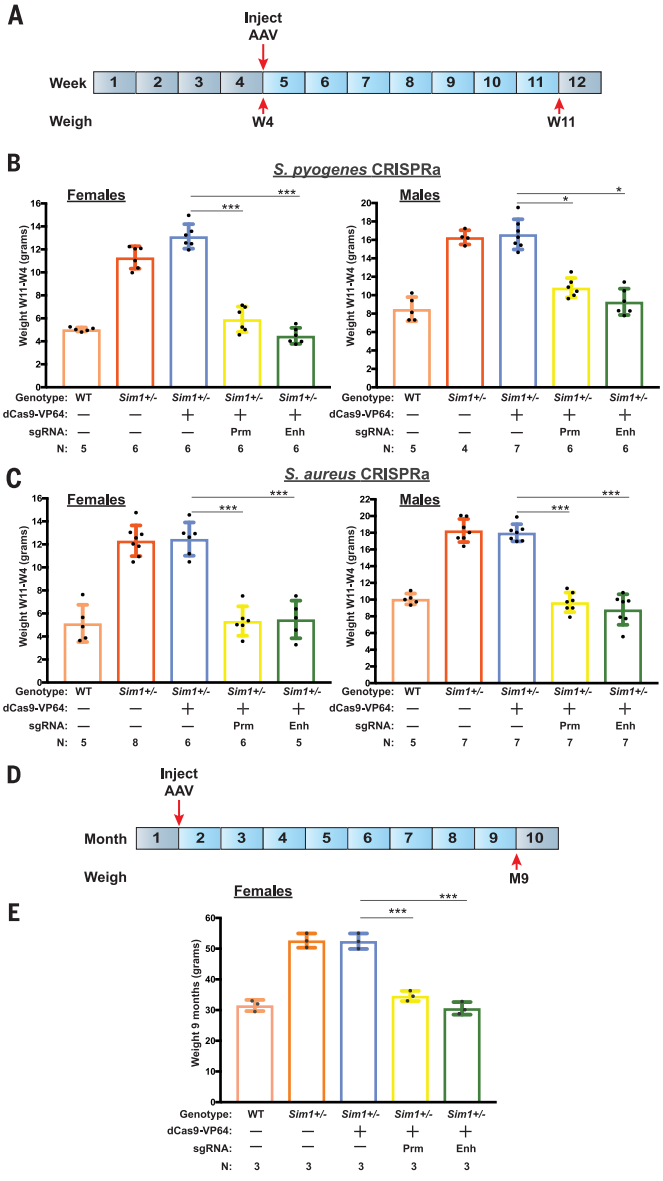


Fig. 4. CRISPRa-AAV injection in the PVN decreases weight gain in *Sim1*$^{+/-}$ mice. (**A**) Timeline for weight measurement after CRISPRa-AAV injection in PVN. (**B** and **C**) Weight gain determined over a 7-week period from *Sim1*$^{+/-}$ mice injected with *pCMV-dCas9-VP64* (dCas9-VP64), *pCMV-dCas9-VP64* + *pSim1Pr-mCherry* (Prm-CRIPSRa), or *pCMV-dCas9-VP64* + *pSCE2En-mCherry* (Enh-CRISPRa) compared to uninjected wild-type littermates and *Sim1*$^{+/-}$ mice using *S. pyogenes* (B) or *S. aureus* (C) CRISPRa. Means ± SD and number of mice (*N*) are shown per condition. *$p < 0.001$; ***$p < 0.0005$; n.s., not significant (ANOVA, Tukey test). (**D**) Monthly timeline for weight measurement after CRISPRa-AAV injection in PVN. (**E**) dCas9-VP64, Prm-CRIPSRa, and Enh-CRISPRa compared to uninjected wild-type littermates and *Sim1*$^{+/-}$ mice 9 months after injection. Means ± SD and number of mice (*N*) are shown per condition. ***$p < 0.0005$.

Discussion

CRISPR-based gene editing is a promising therapeutic technology for correcting genetic mutations. However, it is a challenging approach for treating haploinsufficiency, limited by low homology-directed repair efficiencies (i.e., editing only a small portion of cells) and the need to custom-tailor specific guides and donor sequences for each individual mutation. In addition, it may not be a feasible therapeutic strategy for microdeletions, more than 200 of which are known to cause human disease (*40*), primarily because of haploinsufficiency. In this study, we used a CRISPR-mediated activation approach to tackle these hurdles and show how a haploinsufficient phenotype could be corrected by increasing the transcriptional output from the existing functional allele with CRISPRa.

Downloaded from http://science.sciencemag.org/ on January 20, 2019

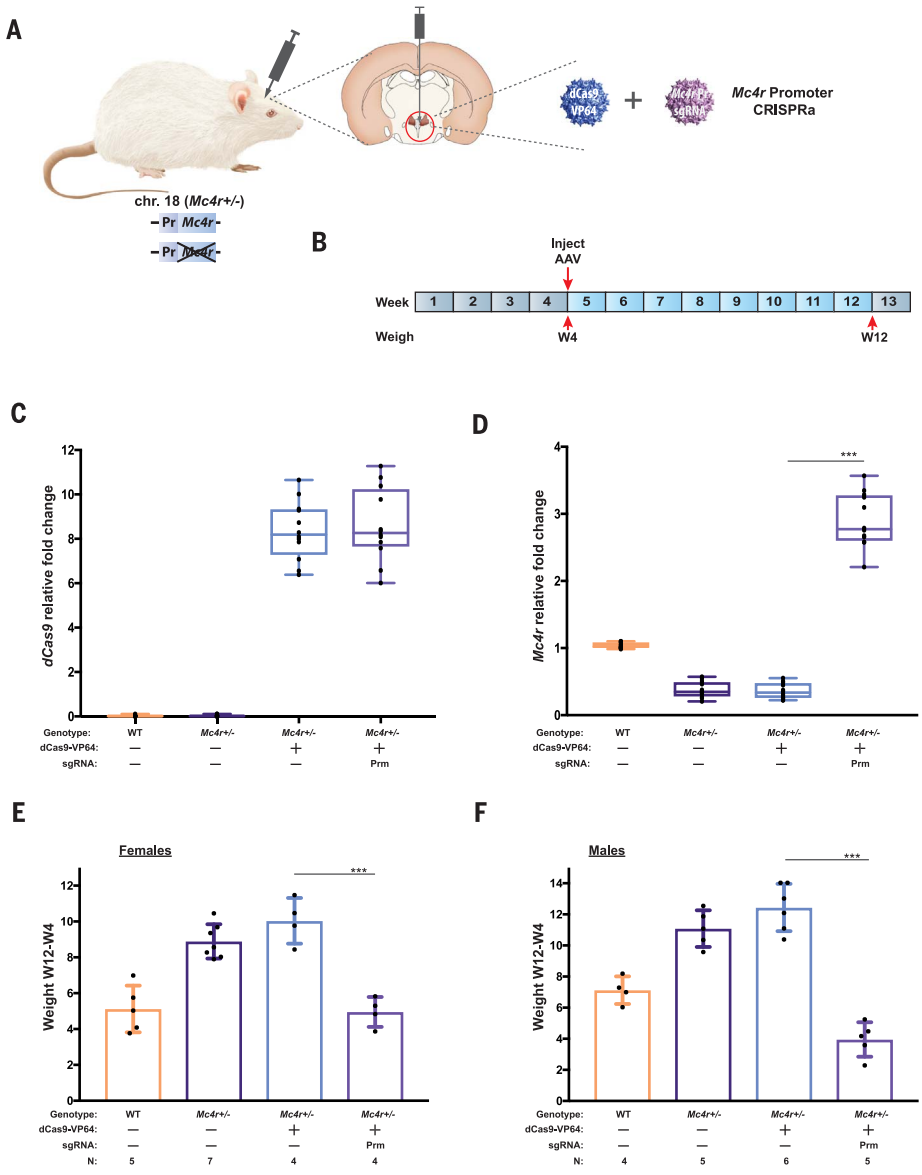


Fig. 5. CRISPRa-AAV injection in the PVN decreases weight gain in *Mc4r*$^{+/-}$ mice. (**A**) Schema showing the CRISPR AAVs used for injection into *Mc4r*$^{+/-}$ mice. (**B**) Timeline for weight measurement post CRISPRa-AAV injection in PVN. (**C** and **D**) *dCas9* (C) and *Mc4r* (D) mRNA expression from uninjected wild-type and *Mc4r*$^{+/-}$ mice along with *pCMV-sadCas9-VP64* (dCas9-VP64)– and *pCMV-sadCas9-VP64* + *pMc4rPr-mCherry* (Prm-CRISPRa)–injected *Mc4r*+/– mice. Four mice were used for each genotype with three technical replicates. The data are represented as means ± the lower and upper quartile, and lines represent the minimum and maximum. Values were determined based on mRNA fold increase compared to wild-type mice and normalized to *Actb* using the ΔΔCT method for *Mc4r* expression and relative *Actb* ΔCT log2 for *dCas9* expression. (**E** and **F**) Weight gain determined over an 8-week period from *Mc4r*$^{+/-}$ female (E) or male (F) mice injected with *pCMV-sadCas9-VP64* (dCas9-VP64) or *pCMV-sadCas9-VP64* + *pMc4rPr-mCherry* (Prm-CRISPRa) compared to uninjected wild-type littermates and *Mc4r*$^{+/-}$ mice. Means ± SD and number of mice (*N*) are shown for each condition. ***$p < 0.0005$; (ANOVA, Tukey test).

Using CRISPRa targeting for either the promoter or enhancer of *Sim1*, we could rescue the obesity phenotype in a tissue-specific manner in mice that are haploinsufficient for *Sim1*. Because this approach takes advantage of the existing functional allele, it has several benefits: (i) It overcomes the need to custom-tailor CRISPR gene editing approaches for different haploinsufficiency-causing mutations in the same gene. (ii) This approach could potentially be used to target two or more genes. It could serve as a potential therapeutic strategy for microdeletions-related diseases that are caused by the heterozygous LoF of more than one gene. (iii) CRISPRa-AAV could be used to rescue haploinsufficient phenotypes caused by genes that are longer than its optimal packaging capability. (iv) Tissue specificity is a major concern for gene therapy. CRISPRa-based approaches can take advantage of cis-regulatory elements to guide tissue specificity (Fig. 6A). The availability of large-scale tissue-specific maps of gene regulatory elements could provide ample candidates for this approach. We observed distinct differences in tissue-specific activation of *Sim1* based on the targeted cis-regulatory element, which can be attributed to chromatin accessibility of the locus in various tissues. Previous large-scale Cas9 and dCas9 cell culture screens have shown a targeting preference for regions with low nucleosome occupancy (*41*, *42*). Active promoters or enhancers would have lower nucleosome occupancy, thus being more amenable to dCas9 targeting.

CRISPRa uses a nuclease-deficient Cas9 (dCas9) fused to a transcriptional activator and as such does not edit the genome. However, it can lead to transcriptional modulated off-target effects. To test for such effects, we carried out both RNA-seq and ChIP-seq in vitro and in vivo. We did not observe any apparent CRISPRa off-target binding that resulted in significant transcriptional changes. Additional analyses of predicted off-targeting loci due to sgRNA mismatches did not find any transcriptional changes surrounding these loci. The dCas9-VP64 fusion used in our CRISPRa system is known to activate loci that are programmed for transcription, such as promoters or enhancers (*14*, *42*). Taken together, our results suggest that CRISPRa has high specificity.

Our dCas9-VP64 mouse and rAAV vectors can be a useful tool for targeted gene activation in vivo by delivering sgRNA(s) targeted to a specific gene in certain tissues or cell types. This approach could be used to assess gene-gene interactions or for the identification of the target gene(s) of a specific regulatory element in vivo by measuring its expression level following activation. Another potential area of study could be neuronal circuit manipulation. Discrepancies between acute and chronic neuronal circuit manipulations have been observed (*43*) that could potentially be addressed by rAAV-CRISPRa and transgenic-CRISPRa strategies, respectively.

Haploinsufficiency of *SIM1* is associated with severe obesity (*19*–*21*) in humans and mice (*22*). Whether this is caused by the reduction in PVN

Downloaded from http://science.sciencemag.org/ on January 20, 2019

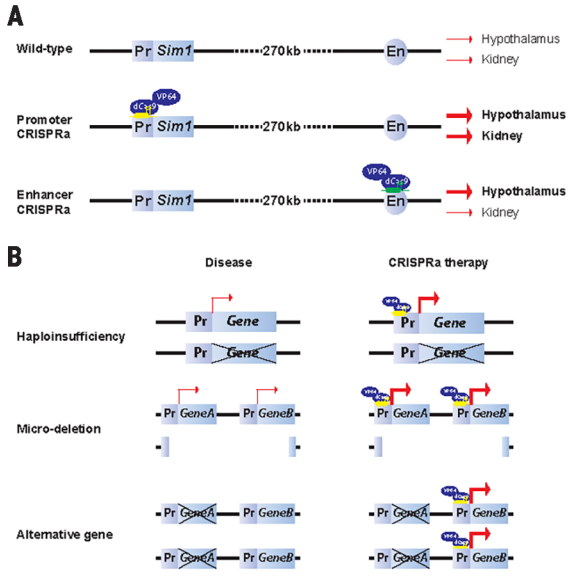


Fig. 6. CRISPRa potential therapeutic strategy. (**A**) Tissue-specific differences in gene activation due to the type of targeted cis-regulatory element (promoter or enhancer). (**B**) CRISPRa can be used as a tool to rescue haploinsufficiency by up-regulating the expression of the endogenous functional allele. It can also be used to up-regulate a gene or genes that are deleted in microdeletions or an alternate gene with a function similar to that of the disease-mutated gene.

size during development that is observed in *Sim1*$^{+/-}$ mice (*22*) or by disturbed energy homeostasis during adulthood was largely unknown. The obesity phenotype observed in the postnatal conditional knockout of hypothalamic *Sim1* (*23*) reinforced the hypothesis that *Sim1* does indeed have a role in energy homeostasis later during adulthood. Our results showing phenotypic rescue in adult mice by rAAV CRISPRa further corroborate this role.

Mutations in *MC4R* are the most commonly found in individuals with class 3 obesity (body mass index >40 kg/m^2), with an estimated 2.6 to 5% of this population having mutations in this gene (*26*–*28*). Heterozygous LoF mutations in this gene are associated with an obesity phenotype (*26*–*28*). MC4R is a promising drug target for anti-obesity drugs, and several agonists have been developed to target this receptor (*44*, *45*). Here, we decreased the weight gain in *Mc4r*$^{+/-}$ mice using rAAV-CRISPRa targeting of the *Mc4r* promoter.

CRISPRa-based gene activation is highly dependent on the nature of the fused activator (*33*) and sgRNA target (*41*) and would need to be optimized for a particular gene, along with the delivery method. It is important to note that overexpressing genes beyond their physiologically relevant doses could have undesirable side effects. The use of a shorter dCas9, such as the *S. aureus* (*46*) that was used in this study, could reduce the packaging load and improve dCas9 delivery, with optimal up-regulation levels to achieve physiologically relevant results. This approach can also lead to increased expression of the mutant allele, if the targeted promoter or enhancer is not deleted, and may not be useful in cases where this allele is not a complete LoF. In addition, targeting rAAV to specific neuronal populations in primates may require multiple injections or other DNA delivery methods.

We demonstrate that CRISPRa can be used to activate genes in vivo not only by targeting their promoters but also by targeting distal cis-regulatory elements such as enhancers. We were able to rescue a haploinsufficient phenotype in a long-lasting manner (9 months) with CRISPRa-rAAV by targeting either the promoter or enhancer of a gene. Previous studies have shown that these elements can be potential therapeutic targets. For example, by targeting a globin enhancer with zinc finger nucleases fused to a chromatin looping factor, the LIM domain binding 1 (*LDB1*) gene, activation of fetal hemoglobin was achieved in vitro, providing a potential therapy for sickle cell disease (*47*). In another study, reactivation of fetal hemoglobin was achieved by deactivating the enhancer of its repressor B cell CLL/lymphoma 11A (*BCL11A*) using CRISPR gene editing (*48*). Our study provides an approach in preclinical mouse model systems that takes advantage of cis-regulatory elements and can aid in designing potential therapeutic strategies. Numerous phenotypes caused by lower gene dosage could potentially be targeted with CRISPRa (Fig. 6B). In addition, several human diseases could potentially be rescued by the activation of another gene with a similar function (Fig. 6C). These could include, for example, *Utrophin* for Duchenne muscular dystrophy (DMD) (*49*, *50*), survival of motor neuron 2 (*SMA2*) for spinal muscular atrophy (*51*), or fetal globin for sickle cell disease. For example, a CRISPR-based approach (CRISPR/Cas9 TGA) was recently shown to ameliorate the dystrophic phenotype upon up-regulation of either the *Utrophin*, *Klotho,* or *Fst* genes in a mouse model of DMD (*50*). Further development of gene up-regulation by CRISPRa or other techniques could provide a potential therapy for dosage-related diseases.

Materials and methods

Plasmids

The *pMSCV-LTR-dCas9-VP64-BFP* vector, encoding a mammalian codon-optimized *Streptococcus pyogenes* dCas9 fused to two C-terminal SV40 NLSs and tagBFP along with a VP64 domain and the U6-sgRNA-CMV-mCherry-T2A-Puro plasmids were used for cell line transfections (both kind gifts from J. S. Weissman and S. Qi). sgRNAs (table S4) were cloned using the In-Fusion HD-cloning kit (Clontech) following the manufacturer's protocol into the Bst XI and Xho I sites. Mouse knockin vectors were generated by cloning dCas9-VP64 and U6-sgRNA-CMV-mCherry expression cassettes from the aforementioned vectors into the TARGATT (CAG + Poly A) plasmid (Applied StemCell). For AAV vectors, *pcDNA-dCas9-VP64* (Addgene 47107), and U6-sgRNA-CMV-mCherry-WPREpA were cloned replacing the *Ef1a-FAS-hChR2(H134R)-mCherry-WPRE-pA* with that of the U6-sgRNA-CMV-mCherry-WPREpA into the backbone of *pAAV-Ef1a-FAS-hChR2(H134R)-mCherry-WPRE-pA* (Addgene 37090). *S. aureus* dCas9-VP64 vector was constructed from Addgene Plasmid #68495, AAV_NLS-dSaCas9-NLS-VPR by removing the RelA(p65) activation domain and Rta Activation domain using XbaI and EcoRI enzymes and introducing a stop codon after the VP64 domain followed by bGHPolyA. We named it *pAAV-CMV-sadCas9-VP64-pA*. *pAAV*-U6-sasgRNA-CMV-mCherry-WPREpA was cloned by replacing the *CMV-sadCas9-VP64-pA cassette in pAAV-CMV-sadCas9-VP64-pA* backbone with that of *U6-sasgRNA-CMV-mCHerry-WPREpA* cassette from *pLTR-1120-MP177-U6-sasgRNA-mcherry* (a kind gift from B. Huang at UCSF). *S. aureus* sgRNAs (table S4) were cloned using the In-Fusion HD-cloning kit (Clontech) following the manufacturer's protocol into the Bst XI and Xho I restriction enzyme sites.

AAV production

Particles of rAAV-DJ serotype, which is a chimera of type 2, 8, and 9 that was shown to achieve high expression levels in multiple tissues (*39*), were produced for all vectors using the Stanford Gene Vector and Virus core. The packaging load for *pCMV-spdCas9-VP64* was 5.4 kb and for *pU6-Sim1Pr-CMV-mCherry* and *pU6-SCE2-CMV-mCherry* 2.5 kb. Genomic titers were ascertained by WPRE and ITR probes to be 1.40 × 10^{10} viral genome (vg)/ml for *pCMV-spdCas9-VP64* and around 3.30 × 10^{13} vg/ml for *pU6-Sim1Pr-CMV-mCherry* and 2.20 × 10^{13} vg/ml for *pU6-SCE2-CMV-mCherry*. The packaging load for *pCMV-sadCas9-VP64-pA* was 4.3 kb and for *pU6-sasgRNA-CMV-mCherry* was 2.5 kb. Genomic titers for *pAAV-CMV-sadCas9-VP64-pA were* 1.60 × 10^{12} vg/ml, for *pU6-sasgRNA3Sim1Pr-CMV-mCherry* 1.58 × 10^{13} vg/ml, for *pU6-sasgRNA3SCE2-CMV-mCherry* 2.0 × 10^{13} vg/ml, and for *pU6-sasgRNA2Mc4rpr-CMV-mCherry* 1.0 × 10^{13} vg/ml.

Cell culture

Neuroblastoma 2a cells (Neuro-2a; ATCC® CCL-131) were grown following ATCC guidelines. Plasmids were transfected into Neuro-2a cells using X-tremeGENE HP DNA transfection reagent (Roche) following the manufacturer's protocol. AAV particles were infected into Neuro-2a cells at different multiplicity of infection (MOI) ratios (figs. S9 and S12E). Neuro-2a cells were

Downloaded from http://science.sciencemag.org/ on January 20, 2019

harvested 48 hours after transfection and 5 days after infection to isolate RNA for qRT-PCR analysis.

RNA isolation, RNA-seq, and quantitative reverse-transcription PCR

RNA was isolated from cells or tissues using RNeasy Mini Kit (Qiagen) following the manufacturer's protocol. For mice, animals were euthanized and tissues were harvested directly into the RNA lysis buffer of the RNeasy Mini Kit. The hypothalamus was dissected using a mouse brain matrix and slicers (Zivic Instruments). Each hypothalamus was sampled the same way for each animal with 1.0-mm coronal section slice intervals. The coronal brain section of the hypothalamus was sliced with two blades 3 mm apart (fig. S15, A to C). The hypothalmaus was dissected out from this coronal section. Care was taken to orient the brain on the matrix and to align the hypothalamus each time corresponding to the same coronal section slots. For qRT-PCR, cDNA was prepared using SuperScript III First-Strand Synthesis System (Invitrogen) using the manufacturer's protocol along with deoxyribonuclease I digestion. qPCR was performed with SsoFast EvaGreen Supermix (Bio-Rad) using the primers indicated in table S4. To further validate our qPCR results for *Sim1*, we also performed qPCR on wild-type, $Sim1^{+/-}$ and $Sim1^{+/-}$ Prm-CRISPRa-AAV–, Enh-CRISPRa-AAV–, or *pCMV-dCas9-VP64*-AAV–injected mice with primers that overlap the region that was knocked out (Sim1-5′ primers listed in table S4), obtaining similar results (fig. S13, D to G). The results were expressed as fold-increase mRNA expression of the gene of interest normalized to either *Actb* or *Rpl38* expression by the ΔΔCT method followed by analysis of variance (ANOVA) and Tukey test for statistical analysis. Reported values are the mean ± SEM from three independent experiments performed on different days ($N = 3$) with technical duplicates that were averaged for each experiment. For RNA-seq, three males and three females were used for each genotype (24 samples total; 6 biological replicates per condition). cDNA was amplified using Ovation V2 kit (NuGEN), and sequencing libraries were generated using NexteraXT kit (Illumina). RNA-seq was carried out on an Illumina HiSeq 4000. Sequence alignment was performed using STAR (*52*). Mappings were restricted to those that were uniquely assigned to the mouse genome and unique read alignments were used to quantify expression and aggregated on a per-gene basis using the Ensembl (GRCm38.67) annotation. Analyses of individual hypothalamus expressed genes (*Agrp*, *Crh*, *Oxt*, *Pomc* and *Trh*) showed a good correlation between individual samples in each condition (fig. S15, D to H). We analyzed these raw data using DESeq2 (*53*) to assess variance and differential expression between sample groups. All RNA-seq data was deposited in NCBI as Bioproject PRJNA438712.

Chromatin immunoprecipitation

Fresh tissue was homogenized using a hand-held dounce homogenizer, cross-linked in phosphate-buffered saline (PBS) containing 1% formaldehyde for 10 min, quenched with 125 mM glycine for 5 min, and washed three times with PBS. Cross-linked tissue pellet was processed further for chromatin immunoprecipitation using the Low cell Chip Kit (Diagenode; catalog no. C01010072) following the manufacturer's protocol. An *S. pyogenes* Cas9 polyclonal antibody (Diagenode; catalog no. C15310258) and an *S. aureus* Cas9 monoclonal antibody (Diagenode; catalog no. C15200230) were used for the pull-down. Enrichment of target regions were assessed by RT-qPCR using SsoFast EvaGreen Supermix (Bio-Rad) and primers listed in table S4. Results were expressed as %input using the ΔCT method. Reported values are the mean ± SEM from three independent experiments performed on different days ($N = 2$) with technical duplicates that were averaged for each experiment. For ChIP-seq, a pool of four mice was used for each genotype and two biological replicates. Libraries were made by using the ThruPLEX DNA-seq kit (Rubicon Genomics; catalog no. R400428) and sequencing was carried out with an Illumina HiSeq-4000. Sequencing reads were mapped to the genome using STAR (*52*). Mapping was restricted to reads that were uniquely assigned to the mouse genome (GRCm38.67). Replicates were pooled to call peaks against a background of the nontargeting VP64 ChIP using MACS2 (*54*). All ChIP-seq data were deposited in NCBI as Bioproject PRJNA438723.

Mice

$Sim1^{+/-}$ mice (*22*) on a mixed genetic background were obtained as a kind gift from J. Michaud's lab. In these mice, a 1-kb fragment containing 750 bp of the 5′ region, the initiation codon, and the sequence coding for the basic domain (the first 17 amino acids) was replaced by a *Pgk–neo* cassette that was used for genotyping (see table S4 for primers) with KAPA mouse genotyping kit (KAPA Biosystems). To generate dCas9-VP64 and sgRNA mice, we used TARGATT technology (*34*). DNA for injection was prepared and purified as minicircles by using the TARGATT Transgenic Kit, V6 (Applied StemCell). The injection mix contained 3 ng/μl DNA and 48 ng/μl of in vitro–transcribed φC31o mRNA in microinjection TE buffer [0.1 mM EDTA, 10 mM Tris (pH 7.5)], and injections were done using standard mouse transgenic protocols (*55*). dCas9-VP64 was inserted into the mouse *Hipp11* locus and sgRNAs into the *Rosa26* locus. Mice were genotyped using the KAPA mouse genotyping kit. F_0 H11P33 TARGATT knockins were assessed using PCR primers SH176 + SH178 + PR432 and for ROSA26 primers ROSA10 + ROSA11 + PR432 described in (*34*) along with vector insertion–specific dCas9-VP64 primers as well as mCherry-specific primers (described in table S4). $Mc4r^{+/-}$ mice on C57BL/6 background were genotyped using MC4R1, MC4F3, and PGKR3 primers (table S4). In these mice, a deletion of 1.5 kb starting from 20 nucleotides downstream of the *Mc4r* initiation codon to ~500 bp after 3′ of the gene was replaced by a *Pgk–neo* cassette (*29*). All mice were fed ad libitum Picolab mouse diet 20, 5058 containing 20% protein, 9% fat, 4% fiber for the whole study. Calories were provided by protein (23.210%), fat (ether extract) (21.559%), and carbohydrates 55.231%. All animal work was approved by the UCSF Institutional Animal Care and Use Committee.

Transgenic mice body weight measurements

$H11P3^{CAG\text{-}dCas9\text{-}VP64}$, $R26P3^{Sim1Pr\text{-}sgRNA}$ and $R26P3^{SCE2En\text{-}sgRNA}$ mice were mated with FVB mice for three to five generations to assess germline transmission. Three independent integrants were used from each line to set up matings. $H11P3^{CAG\text{-}dCas9\text{-}VP64}$ were mated with $Sim1^{+/-}$ and subsequent $Sim1^{+/-} \times H11P3^{CAG\text{-}dCas9\text{-}VP64}$ mice were crossed with either $R26P3^{Sim1Pr\text{-}sgRNA}$ or $R26P3^{SCE2En\text{-}sgRNA}$ to generate mice having all three unlinked alleles. Mice were maintained at Picodiet 5058 throughout the study, and at least 10 females and 10 males from all genotypes (wild type, $Sim1^{+/-}$, $Sim1^{+/-} \times H11P3^{CAG\text{-}dCas9\text{-}VP64}$, $Sim1^{+/-} \times H11P3^{CAG\text{-}dCas9\text{-}VP64} \times R26P3^{Sim1Pr\text{-}sgRNA}$, $Sim1^{+/-} \times H11P3^{CAG\text{-}dCas9\text{-}VP64} \times R26P3^{SCE2En\text{-}sgRNA}$) were measured for their body weights from 4 to 16 weeks of age on a weekly basis.

Body composition and food intake analyses

Body composition was measured using either dual energy x-ray absorptiometry (DEXA) or Echo Magnetic Resonance Imaging (EchoMRI; Echo Medical System). For DEXA, mice were anesthetized with isoflurane and measured for bone mineral density and tissue composition (fat mass and lean mass) with the Lunar PIXImus. EchoMRI (Echo Medical System) was used to measure whole-body composition parameters such as total body fat, lean mass, body fluids, and total body water in live mice without the need for anesthesia or sedation. Food intake was measured by using the Columbus Instruments Comprehensive Lab Animal Monitoring System (CLAMS; Columbus Instruments). Mice were housed individually and acclimatized on powdered picodiet 5058 for 3 to 4 days, and food intake measurements were done over 4 to 5 days. Three males and three females from each genotype: wild-type littermates, $Sim1^{+/-}$, $Sim1^{+/-} \times H11P3^{CAG\text{-}dCas9\text{-}VP64} \times R26P3^{Sim1Pr\text{-}sgRNA}$, $Sim1^{+/-} \times H11P3^{CAG\text{-}dCas9\text{-}VP64} \times R26P3^{SCE2En\text{-}sgRNA}$ were measured.

Stereotaxic injections

Four-week-old $Sim1^{+/-}$ or $Mc4r^{+/-}$ males or females, weighing between 20 and 26 g were housed individually in cages for at least 2 days before surgical interventions. Mice were anesthetized with 3% isoflurane for induction and 1% isoflurane for maintenance in a vaporizer chamber. The skull was immobilized in a stereotaxic apparatus (Model 1900, Stereotaxic Alignment Systems, 1micron resolution, David Kopf Instruments). The stereotaxic coordinates for injection into the PVN were 0.80 mm caudal to bregma, 0 mm at the midline, and 5.2 mm below the surface of the skull, similar to the midline

Downloaded from http://science.sciencemag.org/ on January 20, 2019

injections carried out in a previous study (*56*). A 0.5-mm hole was created in the cranium with a high-speed model 1911 Stereotaxic Drill with a 0.02-inch drill bit (David Kopf Instruments). Using a 31-gauge 1-μl Hamilton microsyringe, we injected a dose of 0.5×10^7 vg/ml of sgRNA-AAV along with 2.5×10^6 vg/kg of spdCas9-VP64-AAV or 0.8×10^7 vg/ml of sadCas9-VP64-AAV in a total injection volume of 1 μl per animal into the PVN unilaterally over a 10-min period. This titer and double the amount (1×10^7 vg/ml of sgRNA-AAV along with 5×10^6 vg/ml of spdCas-VP64-AAV) were also injected into 5-week-old wild-type FVB mice (fig. S11). After rAAV delivery, the needle was left in place for 20 min to prevent reflux and slowly withdrawn in several steps, over 10 min. Mice were administered two doses of buprenorphine (100 mg/kg) before and 24 hours after surgery. Mice were only excluded from the study for the following reasons (table S6): (i) having shorter bregma lambda length during surgery; (ii) having profuse bleeding during surgery; or (iii) did not survive surgery or died during the experiment. All surviving mice were included in the phenotypic analysis, and we did not eliminate mice because of a missed injection. Immunostaining for mCherry, as described below, was used to validate PVN injection coordinates 8 weeks after injection in several mice with single midline injections showing one side of the PVN to have stronger mCherry expression (Fig. 3C and fig. S10). The majority of mice did not undergo immunostaining as they were used for RNA analyses. Mice were maintained on a picodiet 5058 and weighed on a weekly basis.

Immunostaining

For immunostaining, mice were anesthetized with pentobarbital (7.5 mg/0.15 ml, intraperitoneally) and transcardially perfused with 10 ml of heparinized saline (10 U/ml, 2 ml/min) followed by 10 ml of phosphate-buffered 4% paraformaldehyde (PFA). Brains were removed, postfixed for 24 hours in 4% PFA, and then equilibrated in 30% sucrose in PBS for 72 hours. Brains were coronally sectioned (35 μm for immunostaining, 50 μm for stereology) on a sliding microtome (Leica SM 2000R). Immunohistochemistry was performed as previously described (*24*, *57*, *58*). Coronal brain sections that had been stored in PBS at 4°C were permeabilized and blocked in 3% normal goat serum–0.3% Triton X-100 for 1 hour and incubated at 4°C overnight using an antibody to mCherry at a dilution of 1:500 (Abcam ab167453). Sections were placed in 4′,6- diamidino-2-phenylindole (DAPI) (0.2 g/ml; 236276; Roche) for 10 min and then mounted on Plus coated slides and coverslipped using Vectashield (H-1000; Vector Laboratories). Images of sections containing PVN were captured on a Zeiss Apotome.

REFERENCES AND NOTES

1. V. T. Dang, K. S. Kassahn, A. E. Marcos, M. A. Ragan, Identification of human haploinsufficient genes and their genomic proximity to segmental duplications. *Eur. J. Hum. Genet.* **16**, 1350–1357 (2008). doi: 10.1038/ejhg.2008.111; pmid: 18523451
2. M. J. Landrum *et al*., ClinVar: Public archive of interpretations of clinically relevant variants. *Nucleic Acids Res.* **44**, D862–D868 (2016). doi: 10.1093/nar/gkv1222; pmid: 26582918
3. M. Lek *et al*., Analysis of protein-coding genetic variation in 60,706 humans. *Nature* **536**, 285–291 (2016). doi: 10.1038/nature19057; pmid: 27535533
4. E. Bender, Gene therapy: Industrial strength. *Nature* **537**, S57–S59 (2016). doi: 10.1038/537S57a; pmid: 27602741
5. M. A. Kotterman, D. V. Schaffer, Engineering adeno-associated viruses for clinical gene therapy. *Nat. Rev. Genet.* **15**, 445–451 (2014). doi: 10.1038/nrg3742; pmid: 24840552
6. R. J. Samulski, N. Muzyczka, AAV-mediated gene therapy for research and therapeutic purposes. *Annu. Rev. Virol.* **1**, 427–451 (2014). doi: 10.1146/annurev-virology-031413-085355; pmid: 26958729
7. E. A. Lykken, C. Shyng, R. J. Edwards, A. Rozenberg, S. J. Gray, Recent progress and considerations for AAV gene therapies targeting the central nervous system. *J. Neurodev. Disord.* **10**, 16 (2018). doi: 10.1186/s11689-018-9234-0; pmid: 29776328
8. Z. Wu, H. Yang, P. Colosi, Effect of genome size on AAV vector packaging. *Mol. Ther.* **18**, 80–86 (2010). doi: 10.1038/mt.2009.255; pmid: 19904234
9. L. A. Gilbert *et al*., CRISPR-mediated modular RNA-guided regulation of transcription in eukaryotes. *Cell* **154**, 442–451 (2013). doi: 10.1016/j.cell.2013.06.044; pmid: 23849981
10. P. Perez-Pinera *et al*., RNA-guided gene activation by CRISPR-Cas9-based transcription factors. *Nat. Methods* **10**, 973–976 (2013). doi: 10.1038/nmeth.2600; pmid: 23892895
11. S. Konermann *et al*., Genome-scale transcriptional activation by an engineered CRISPR-Cas9 complex. *Nature* **517**, 583–588 (2015). pmid: 25494202
12. I. B. Hilton *et al*., Epigenome editing by a CRISPR-Cas9-based acetyltransferase activates genes from promoters and enhancers. *Nat. Biotechnol.* **33**, 510–517 (2015). doi: 10.1038/nbt.3199; pmid: 25849900
13. A. Chavez *et al*., Highly efficient Cas9-mediated transcriptional programming. *Nat. Methods* **12**, 326–328 (2015). doi: 10.1038/nmeth.3312; pmid: 25730490
14. M. L. Maeder *et al*., CRISPR RNA-guided activation of endogenous human genes. *Nat. Methods* **10**, 977–979 (2013). doi: 10.1038/nmeth.2598; pmid: 23892898
15. S. Kiani *et al*., Cas9 gRNA engineering for genome editing, activation and repression. *Nat. Methods* **12**, 1051–1054 (2015). doi: 10.1038/nmeth.3580; pmid: 26344044
16. J. L. Michaud, T. Rosenquist, N. R. May, C. M. Fan, Development of neuroendocrine lineages requires the bHLH-PAS transcription factor SIM1. *Genes Dev.* **12**, 3264–3275 (1998). doi: 10.1101/gad.12.20.3264; pmid: 9784500
17. S. Beckers, D. Zegers, L. F. Van Gaal, W. Van Hul, The role of the leptin-melanocortin signalling pathway in the control of food intake. *Crit. Rev. Eukaryot. Gene Expr.* **19**, 267–287 (2009). doi: 10.1615/CritRevEukarGeneExpr.v19.i4.20; pmid: 19817705
18. J. L. Holder Jr., N. F. Butte, A. R. Zinn, Profound obesity associated with a balanced translocation that disrupts the SIM1 gene. *Hum. Mol. Genet.* **9**, 101–108 (2000). doi: 10.1093/hmg/9.1.101; pmid: 10587584
19. N. Ahituv *et al*., Medical sequencing at the extremes of human body mass. *Am. J. Hum. Genet.* **80**, 779–791 (2007). doi: 10.1086/513471; pmid: 17357083
20. S. Ramachandrappa *et al*., Rare variants in single-minded 1 (SIM1) are associated with severe obesity. *J. Clin. Invest.* **123**, 3042–3050 (2013). doi: 10.1172/JCI68016; pmid: 23778139
21. A. Bonnefond *et al*., Loss-of-function mutations in SIM1 contribute to obesity and Prader-Willi-like features. *J. Clin. Invest.* **123**, 3037–3041 (2013). doi: 10.1172/JCI68035; pmid: 23778136
22. J. L. Michaud *et al*., Sim1 haploinsufficiency causes hyperphagia, obesity and reduction of the paraventricular nucleus of the hypothalamus. *Hum. Mol. Genet.* **10**, 1465–1473 (2001). doi: 10.1093/hmg/10.14.1465; pmid: 11448938
23. K. P. Tolson *et al*., Postnatal Sim1 deficiency causes hyperphagic obesity and reduced Mc4r and oxytocin expression. *J. Neurosci.* **30**, 3803–3812 (2010). doi: 10.1523/JNEUROSCI.5444-09.2010; pmid: 20220015
24. B. M. Kublaoui, J. L. Holder Jr., K. P. Tolson, T. Gemelli, A. R. Zinn, SIM1 overexpression partially rescues agouti yellow and diet-induced obesity by normalizing food intake. *Endocrinology* **147**, 4542–4549 (2006). doi: 10.1210/en.2006-0453; pmid: 16709610
25. M. J. Krashes, B. B. Lowell, A. S. Garfield, Melanocortin-4 receptor-regulated energy homeostasis. *Nat. Neurosci.* **19**, 206–219 (2016). doi: 10.1038/nn.4202; pmid: 26814590
26. C. Lubrano-Berthelier *et al*., Melanocortin 4 receptor mutations in a large cohort of severely obese adults: Prevalence, functional classification, genotype-phenotype relationship, and lack of association with binge eating. *J. Clin. Endocrinol. Metab.* **91**, 1811–1818 (2006). doi: 10.1210/jc.2005-1411; pmid: 16507637
27. C. Vaisse *et al*., Melanocortin-4 receptor mutations are a frequent and heterogeneous cause of morbid obesity. *J. Clin. Invest.* **106**, 253–262 (2000). doi: 10.1172/JCI9238; pmid: 10903341
28. I. S. Farooqi *et al*., Clinical spectrum of obesity and mutations in the melanocortin 4 receptor gene. *N. Engl. J. Med.* **348**, 1085–1095 (2003). doi: 10.1056/NEJMoa022050; pmid: 12646665
29. D. Huszar *et al*., Targeted disruption of the melanocortin-4 receptor results in obesity in mice. *Cell* **88**, 131–141 (1997). doi: 10.1016/S0092-8674(00)81865-6; pmid: 9019399
30. C. Yang, F. Boucher, A. Tremblay, J. L. Michaud, Regulatory interaction between arylhydrocarbon receptor and SIM1, two basic helix-loop-helix PAS proteins involved in the control of food intake. *J. Biol. Chem.* **279**, 9306–9312 (2004). doi: 10.1074/jbc.M307927200; pmid: 14660629
31. M. J. Kim, N. Oksenberg, T. J. Hoffmann, C. Vaisse, N. Ahituv, Functional characterization of SIM1-associated enhancers. *Hum. Mol. Genet.* **23**, 1700–1708 (2014). pmid: 24203700
32. J. Flint, T. Shenk, Viral transactivating proteins. *Annu. Rev. Genet.* **31**, 177–212 (1997). doi: 10.1146/annurev.genet.31.1.177; pmid: 9442894
33. A. Chavez *et al*., Comparison of Cas9 activators in multiple species. *Nat. Methods* **13**, 563–567 (2016). doi: 10.1038/nmeth.3871; pmid: 27214048
34. B. Tasic *et al*., Site-specific integrase-mediated transgenesis in mice via pronuclear injection. *Proc. Natl. Acad. Sci. U.S.A.* **108**, 7902–7907 (2011). doi: 10.1073/pnas.1019507108; pmid: 21464299
35. S. Hippenmeyer *et al*., Genetic mosaic dissection of Lis1 and Ndel1 in neuronal migration. *Neuron* **68**, 695–709 (2010). doi: 10.1016/j.neuron.2010.09.027; pmid: 21092859
36. A. I. Su *et al*., A gene atlas of the mouse and human protein-encoding transcriptomes. *Proc. Natl. Acad. Sci. U.S.A.* **101**, 6062–6067 (2004). doi: 10.1073/pnas.0400782101; pmid: 15075390
37. R. Petryszak *et al*., Expression Atlas update—An integrated database of gene and protein expression in humans, animals and plants. *Nucleic Acids Res.* **44** (D1), D746–D752 (2016). doi: 10.1093/nar/gkv1045; pmid: 26481351
38. S. Bae, J. Park, J. S. Kim, Cas-OFFinder: A fast and versatile algorithm that searches for potential off-target sites of Cas9 RNA-guided endonucleases. *Bioinformatics* **30**, 1473–1475 (2014). doi: 10.1093/bioinformatics/btu048; pmid: 24463181
39. C. Zincarelli, S. Soltys, G. Rengo, J. E. Rabinowitz, Analysis of AAV serotypes 1-9 mediated gene expression and tropism in mice after systemic injection. *Mol. Ther.* **16**, 1073–1080 (2008). doi: 10.1038/mt.2008.76; pmid: 18414476
40. A. Weise *et al*., Microdeletion and microduplication syndromes. *J. Histochem. Cytochem.* **60**, 346–358 (2012). doi: 10.1369/0022155412440001; pmid: 22396478
41. M. A. Horlbeck *et al*., Nucleosomes impede Cas9 access to DNA in vivo and in vitro. *eLife* **5**, e12677 (2016). doi: 10.7554/eLife.12677; pmid: 26987018
42. D. R. Simeonov *et al*., Discovery of stimulation-responsive immune enhancers with CRISPR activation. *Nature* **549**, 111–115 (2017). doi: 10.1038/nature23875; pmid: 28854172
43. T. M. Otchy *et al*., Acute off-target effects of neural circuit manipulations. *Nature* **528**, 358–363 (2015). doi: 10.1038/nature16442; pmid: 26649821
44. J. P. L. Gonçalves, D. Palmer, M. Meldal, MC4R Agonists: Structural overview on antiobesity therapeutics. *Trends Pharmacol. Sci.* **39**, 402–423 (2018). pmid: 29478721
45. T. H. Collet *et al*., Evaluation of a melanocortin-4 receptor (MC4R) agonist (Setmelanotide) in MC4R deficiency. *Mol. Metab.* **6**, 1321–1329 (2017). doi: 10.1016/j.molmet.2017.06.015; pmid: 29031731
46. F. A. Ran *et al*., In vivo genome editing using Staphylococcus aureus Cas9. *Nature* **520**, 186–191 (2015). doi: 10.1038/nature14299; pmid: 25830891
47. W. Deng *et al*., Reactivation of developmentally silenced globin genes by forced chromatin looping. *Cell* **158**, 849–860 (2014). doi: 10.1016/j.cell.2014.05.050; pmid: 25126789
48. M. C. Canver *et al*., BCL11A enhancer dissection by Cas9-mediated in situ saturating mutagenesis. *Nature* **527**, 192–197 (2015). doi: 10.1038/nature15521; pmid: 26375006

Downloaded from http://science.sciencemag.org/ on January 20, 2019

49. R. C. Hirst, K. J. McCullagh, K. E. Davies, Utrophin upregulation in Duchenne muscular dystrophy. *Acta Myol.* **24**, 209–216 (2005). pmid: 16629055
50. H. K. Liao *et al*., In vivo target gene activation via CRISPR/Cas9-mediated trans-epigenetic modulation. *Cell* **171**, 1495–1507.e15 (2017). doi: 10.1016/j.cell.2017.10.025; pmid: 29224783
51. D. M. Sproule, P. Kaufmann, Therapeutic developments in spinal muscular atrophy. *Ther. Adv. Neurol. Disord.* **3**, 173–185 (2010). doi: 10.1177/1756285610369026; pmid: 21179609
52. A. Dobin *et al*., STAR: Ultrafast universal RNA-seq aligner. *Bioinformatics* **29**, 15–21 (2013). doi: 10.1093/bioinformatics/bts635; pmid: 23104886
53. M. I. Love, W. Huber, S. Anders, Moderated estimation of fold change and dispersion for RNA-seq data with DESeq2. *Genome Biol.* **15**, 550 (2014). doi: 10.1186/s13059-014-0550-8; pmid: 25516281
54. Y. Zhang *et al*., Model-based analysis of ChIP-Seq (MACS). *Genome Biol.* **9**, R137 (2008). doi: 10.1186/gb-2008-9-9-r137; pmid: 18798982
55. A. Nagy, M. Gertsenstein, K. Vintersten, R. Behringer, *Manipulating the Mouse Embryo: A Laboratory Manual* (Cold Spring Harbor, New York, ed. 3, 2002).
56. J. E. Siljee *et al*., Subcellular localization of MC4R with ADCY3 at neuronal primary cilia underlies a common pathway for genetic predisposition to obesity. *Nat. Genet.* **50**, 180–185 (2018). doi: 10.1038/s41588-017-0020-9; pmid: 29311635
57. C. T. Beuckmann *et al*., Expression of a poly-glutamine-ataxin-3 transgene in orexin neurons induces narcolepsy-cataplexy in the rat. *J. Neurosci.* **24**, 4469–4477 (2004). doi: 10.1523/JNEUROSCI.5560-03.2004; pmid: 15128861
58. B. M. Kublaoui, T. Gemelli, K. P. Tolson, Y. Wang, A. R. Zinn, Oxytocin deficiency mediates hyperphagic obesity of Sim1 haploinsufficient mice. *Mol. Endocrinol.* **22**, 1723–1734 (2008). doi: 10.1210/me.2008-0067; pmid: 18451093

ACKNOWLEDGMENTS

We thank J. Michaud for the *Sim1*$^{+/-}$ mice; M. J. Kim for the SCE2 hypothalamus picture; J. S. Weissman and S. Qi for the dCas9-VP64 plasmids; B. Huang for the *S. aureus* sgRNA vector; C. Paillart for assistance with the metabolic profiling; S. K. Matharu and Y. Ahituv for graphic assistance with the figures; and M. T. McManus, P. Devine, and S. H. Ahanger for helpful discussions. **Funding:** This article was supported in part by grant 1R01DK090382 from the National Institute of Diabetes and Digestive and Kidney Diseases (NIDDK), the UCSF Nutrition Obesity Research Center funded by National Institutes of Health grant P30DK098722, and the UCSF School of Pharmacy 2017 Mary Anne Koda-Kimble Seed Award for Innovation. N.A. is also supported by grants by the National Human Genome Research Institute (NHGRI) and Division of Cancer Prevention, National Cancer Institute grant no. 1R01CA197139, National Institute of Mental Health grant no. 1R01MH109907, National Institute of Child and Human Development 1P01HD084387, and NHGRI grant no. 1UM1HG009408. N.M. was supported in part by the UCSF School of Pharmacy 2017 Mary Anne Koda-Kimble Seed Award for Innovation and the UCSF Catalyst Program. S.R. was supported by the Royal Golden Jubilee Ph.D. Program grant no. PHD/0071/2554. C.V. is also supported by NIDDK grant nos. R01DK106404 and R01 DK60540-09 and Y.W. by the American Diabetes Association Mentor Based Award-7-12-MN-79. A.H. is supported by the National Institute of General Medical Sciences IRACDA award K12GM081266. **Author contributions:** N.M. and N.A. conceived and designed the study. N.M., S.T., and L.M. carried out the cloning and in vitro studies. N.M., S.R., S.T. and A.B. performed the mouse experiments. N.M. and Y.W. carried out the immunostaining, and N.M. performed the stereotactic surgeries and phenotypic analyses. A.H. and W.L.E. helped in making fig. S1. W.L.E. carried out computational analyses of genomic data; N.M., S.R., and N.A. analyzed the data; C.V. and N.A. provided resources and critical suggestions; and N.M. and N.A. wrote the manuscript. **Competing interests:** N.A. is an equity holder of, and heads the scientific advisory board for, Encoded Therapeutics, a gene regulation therapeutics company, and N.A. and N.M. are cofounders of Enhancer Therapeutics Inc. N.M. and N.A. are co-inventors on a patent (U.S. Patent US2018017186) submitted by the University of California, San Francisco, that covers gene therapy for haploinsufficiency. **Data and materials availability:** All RNA-seq data were deposited in NCBI as Bioproject PRJNA438712. All ChIP-seq data were deposited in NCBI as Bioproject PRJNA438723.

SUPPLEMENTARY MATERIALS

www.sciencemag.org/content/363/6424/eaau0629/suppl/DC1
Figs. S1 to S15
Tables S1 to S6

6 May 2018; accepted 6 December 2018
Published online 13 December 2018
10.1126/science.aau0629

Downloaded from http://science.sciencemag.org/ on January 20, 2019

RESEARCH ARTICLE SUMMARY

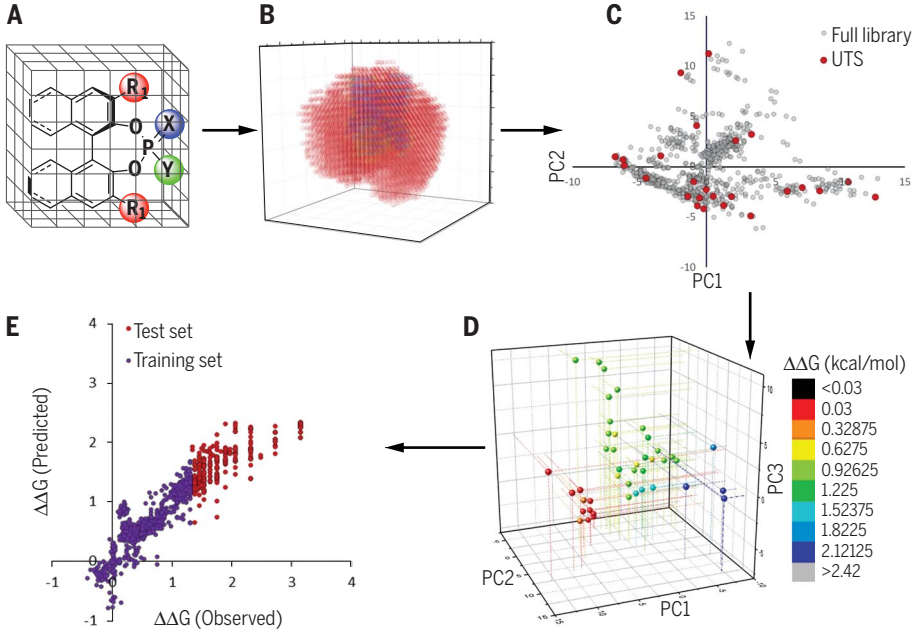
ASYMMETRIC CATALYSIS

Prediction of higher-selectivity catalysts by computer-driven workflow and machine learning

Andrew F. Zahrt*, Jeremy J. Henle*, Brennan T. Rose, Yang Wang, William T. Darrow, Scott E. Denmark†

INTRODUCTION: The development of new synthetic methods in organic chemistry is traditionally accomplished through empirical optimization. Catalyst design, wherein experimentalists attempt to qualitatively identify correlations between catalyst structure and catalyst efficiency, is no exception. However, this approach is plagued by numerous deficiencies, including the lack of mechanistic understanding of a new transformation, the inherent limitations of human cognitive abilities to find patterns in large collections of data, and the lack of quantitative guidelines to aid catalyst identification. Chemoinformatics provides an attractive alternative to empiricism for several reasons: Mechanistic information is not a prerequisite, catalyst structures can be characterized by three-dimensional (3D) descriptors (numerical representations of molecular properties derived from the 3D molecular structure) that quantify the steric and electronic properties of thousands of candidate molecules, and the suitability of a given catalyst candidate can be quantified by comparing its properties with a computationally derived model trained on experimental data. The ability to accurately predict a selective catalyst by using a set of less than optimal data remains a major goal for machine learning with respect to asymmetric catalysis. We report a method to achieve this goal and propose a more efficient alternative to traditional catalyst design.

RATIONALE: The workflow we have created consists of the following components: (i) construction of an in silico library comprising a large collection of conceivable, synthetically accessible catalysts derived from a particular scaffold; (ii) calculation of relevant chemical descriptors for each scaffold; (iii) selection of a representative subset of the catalysts [this subset is termed the universal training set (UTS) because it is agnostic to reaction or mechanism and thus can be used to optimize any reaction catalyzed by that scaffold]; (iv) collection of the training data; and (v) application of machine learning methods to generate models that predict the enantioselectivity of each member of the in silico library. These models are evaluated with an external test set of catalysts (predicting selectivities of catalysts outside of the training data). The validated models can then be used to select the optimal catalyst for a given reaction.



Chemoinformatics-guided optimization protocol. (**A**) Generation of a large in silico library of catalyst candidates. (**B**) Calculation of robust chemical descriptors. (**C**) Selection of a UTS. (**D**) Acquisition of experimental selectivity data. (**E**) Application of machine learning to use moderate- to low-selectivity reactions to predict high-selectivity reactions. R, any group; X, O or S; Y, OH, SH, or NHTf; PC, principal component; ΔΔG, mean selectivity.

ON OUR WEBSITE

Read the full article at http://dx.doi.org/10.1126/science.aau5631

RESULTS: To demonstrate the viability of our method, we predicted reaction outcomes with substrate combinations and catalysts different from the training data and simulated a situation in which highly selective reactions had not been achieved. In the first demonstration, a model was constructed by using support vector machines and validated with three different external test sets. The first test set evaluated the ability of the model to predict the selectivity of only reactions forming new products with catalysts from the training set. The model performed well, with a mean absolute deviation (MAD) of 0.161 kcal/mol. Next, the same model was used to predict the selectivity of an external test set of catalysts with substrate combinations from the training set. The performance of the model was still highly accurate, with a MAD of 0.211 kcal/mol. Lastly, reactions forming new products with the external test catalysts were predicted with a MAD of 0.236 kcal/mol. In the second study, no reactions with selectivity above 80% enantiomeric excess were used as training data. Deep feed-forward neural networks accurately reproduced the experimental selectivity data, successfully predicting the most selective reactions. More notably, the general trends in selectivity, on the basis of average catalyst selectivity, were correctly identified. Despite omitting about half of the experimental free energy range from the training data, we could still make accurate predictions in this region of selectivity space.

CONCLUSION: The capability to predict selective catalysts has the potential to change the way chemists select and optimize chiral catalysts from an empirically guided to a mathematically guided approach. ■

The list of author affiliations is available in the full article online.
*These authors contributed equally to this work.
†Corresponding author. Email: sdenmark@illinois.edu
Cite this article as A. F. Zahrt *et al.*, *Science* **363**, eaau5631 (2019). DOI: 10.1126/science.aau5631

Downloaded from http://science.sciencemag.org/ on January 18, 2019

RESEARCH ARTICLE

ASYMMETRIC CATALYSIS

Prediction of higher-selectivity catalysts by computer-driven workflow and machine learning

Andrew F. Zahrt*, Jeremy J. Henle*, Brennan T. Rose, Yang Wang, William T. Darrow, Scott E. Denmark†

Catalyst design in asymmetric reaction development has traditionally been driven by empiricism, wherein experimentalists attempt to qualitatively recognize structural patterns to improve selectivity. Machine learning algorithms and chemoinformatics can potentially accelerate this process by recognizing otherwise inscrutable patterns in large datasets. Herein we report a computationally guided workflow for chiral catalyst selection using chemoinformatics at every stage of development. Robust molecular descriptors that are agnostic to the catalyst scaffold allow for selection of a universal training set on the basis of steric and electronic properties. This set can be used to train machine learning methods to make highly accurate predictive models over a broad range of selectivity space. Using support vector machines and deep feed-forward neural networks, we demonstrate accurate predictive modeling in the chiral phosphoric acid–catalyzed thiol addition to *N*-acylimines.

The development of synthetic methods in organic chemistry has historically been driven by Edisonian empiricism. Catalyst design, wherein experimentalists attempt to qualitatively recognize patterns in catalyst structures to improve catalyst selectivity and efficiency, is no exception. However, this approach is hindered by a number of factors, including the lack of mechanistic understanding of a new transformation, the inherent limitations of the human brain to find patterns in large collections of data, and the lack of quantitative guidelines to aid catalyst selection. Chemoinformatics (*1*–*3*) provides an attractive alternative for several reasons: No mechanistic information is needed, catalyst structures can be characterized by three-dimensional (3D) descriptors (numerical representations of molecular properties derived from the 3D structure of the molecule) that quantify the steric and electronic properties of thousands of candidate molecules, and the suitability of a given catalyst candidate can be quantified by comparing its properties with a computationally derived model on the basis of experimental data. Although artificial intelligence was applied to problems in chemistry as early as 1965, the use of machine learning methods has yet to affect the daily workflow of organic chemists (*4*). However, recent developments represent the dawn of a new era in organic chemistry, with the emergence of "big-data" methods to facilitate rapid advances in the field. Computer-assisted synthetic planning (*5*, *6*), the prediction of organic reaction outcomes (*7*, *8*), assisted medicinal chemistry discovery (*9*, *10*), catalyst design (*11*, *12*), the use of continuous molecular representations for automatic generation of new chemical structures (*13*), materials discovery (*14*), the enhancement of computer simulation techniques (*15*), and the optimization of reaction conditions (*16*) all provide examples in which leveraging machine learning methods facilitates advances in chemistry. The power of these methods is particularly notable for catalyst design; modern machine learning methods have the capacity to find patterns in large sets of data that are incomprehensible to experimental practitioners (*17*). Discovering these structure-activity relationships may facilitate catalyst identification, thus enabling the rapid optimization of catalytic transformations.

Lipkowitz *et al.* and Kozlowski *et al.* first reported the application of a 3D quantitative structure-activity relationship (QSAR) to asymmetric catalysis, wherein they used different molecular interaction field (MIF) approaches to study copper bis(oxazoline) complexes in enantioselective Diels-Alder reactions and enantioselective alkylations of aryl aldehydes, respectively (*18*, *19*). Although similar MIF-based approaches have since been employed (*12*, *20*, *21*), we suspect that such methods have not achieved widespread use because of the reliance on only one conformer in descriptor generation. To address this problem, Sigman and co-workers have employed multivariate regression techniques and catalyst-specific descriptors to glean mechanistic information (*22*–*24*). These researchers attribute some of their success to the use of Sterimol values; these substituent-based descriptors have multiple parameters designed to capture the rotation of the group of interest, thus providing a more accurate picture of how the molecule behaves in solution (*25*). Furthermore, preliminary studies in which predictions are made beyond the bounds of the training data have been described; Sigman and co-workers have demonstrated the ability to predict ~10% enantiomeric excess (ee) beyond the training data (*26*). However, no examples exist wherein the prediction is far outside the selectivity regime comprising the training data. A very recent example of the utility of machine learning methods in catalysis is the prediction of reaction yields by Doyle and co-workers (*27*, *28*). These authors use many easily calculable descriptors to predict the outcomes of C–N coupling reactions and deoxyfluorination reactions with random forest models (*29*). Although this method excels in predicting the outcomes of reactions when the predicted value falls within the range of values in the training data, this method has not been used to make predictions beyond the range of observed values in the training set.

The ability to accurately predict a selective catalyst by using a set of nonoptimal data remains a primary objective of machine learning with respect to asymmetric catalysis. This feat is sometimes erroneously referred to as "extrapolation"—an understandable mistake, given that predictions are being made outside the bounds of previously observed selectivities. However, the term "extrapolation" does not refer to the selectivity space of the training data but rather to the descriptor space. Thus, a better statement of this goal is to predict high selectivity values far beyond the bounds of what is encompassed in the training data. Herein, we describe a method to achieve this goal by proposing a more efficient alternative to traditional catalyst design.

This endeavor is challenging for a number of reasons. First, very small energy differences (~1 kcal/mol) can give rise to vastly different selectivities—even modern quantum chemical methods struggle to reproduce these energy differences in diastereomeric transition structures. Subtle changes in catalyst structure can also lead to large changes in catalyst performance, whereas descriptors capable of capturing fundamental chemical properties (*30*) and the subtle features of catalyst structure responsible for enantioinduction remain imperfect. Moreover, off-cycle or background reactivity can erode enantioselectivity, and selectivity data are rarely uniformly distributed, adding the challenge of modeling on a skewed dataset. Predicting reactions that are more selective than anything in the training data (essential for machine learning to optimize a reaction) requires the model to accurately predict to a fringe case, a formidable challenge in its own right.

Roger Adams Laboratory, Department of Chemistry, University of Illinois, Urbana, IL 61801, USA.
*These authors contributed equally to this work.
†Corresponding author. Email: sdenmark@illinois.edu

Downloaded from http://science.sciencemag.org/ on January 18, 2019

Perhaps the greatest impediment to accurate prediction in this manner is that no widely accepted workflow implementing chemoinformatics at all stages of development has been introduced to date. Using training set selection algorithms is essential to guarantee that the maximal breadth of feature space is covered in the training data; thus, by design, there should theoretically be no need for extrapolation. Failure to use training set selection algorithms introduces a greater level of uncertainty for predictions—if the domain of applicability is completely unknown, predictions may be outside the well-described region of feature space, and those predictions may be unfounded. If such methods are to be successful, chemical properties must be represented by robust descriptors. This aspect is especially challenging for asymmetric catalysis, as currently no mathematical representation of organic molecules exists that satisfies the following critical criteria: The descriptors must be rapidly calculable, must contain 3D information about an ensemble of conformers for each molecule, must be general for any given scaffold, and must capture the subtle features of catalyst structure responsible for enantioinduction. We describe the development of a workflow that uses chemoinformatic methods at every stage. Further, we report a molecular representation that facilitates this workflow and that enables the prediction of enantioselective reactions in a manner simulating new reaction optimization.

This new workflow consists of the following components (Fig. 1): (i) construction of an in silico library of a large (*31*) collection of conceivable, synthetically accessible catalysts of a particular scaffold; (ii) calculation of robust chemical descriptors for each scaffold, thereby creating the chemical space comprising the in silico library; and (iii) selection of a representative subset of the catalysts in this space. This subset is termed the universal training set (UTS), so named because it is agnostic to reaction or mechanism. Thus, the same set of compounds can be used to collect training data for any reaction that can be catalyzed by the common functional group and will cover the maximum breadth of feature space. The continuation of the workflow involves (iv) collection of the training data and (v) application of machine learning methods to generate models that predict the enantioselectivity of each member of the in silico library. These models are evaluated with an external test set of catalysts (predicting selectivities of catalysts outside of the training data). The validated models can then be used to select the optimal catalyst for a given reaction. At this point, either the predicted catalyst obtains the desired level of selectivity (success) or the predicted catalyst data can be recombined with the training data to make more robust models. The process can then be repeated iteratively until optimal selectivity is achieved (Fig. 1).

To develop this workflow, we chose the BINOL (1,1′-bi-2-naphthol)–derived family of chiral phosphoric acids as the catalyst scaffold. This family possesses a number of beneficial features, including synthetic accessibility and ease of diversification by installation of an array of substituents at the 3,3′ positions. Additionally, the acidity of the phosphoryl group can be easily modulated, and the backbone can be unsaturated (binaphthyl backbone) or saturated (H_8 backbone). These catalysts can be used for a vast number of synthetically useful reactions; thus, a UTS of this scaffold could be very powerful for method development (*32*).

Development of average steric occupancy descriptors

The plan began with the formulation of an in silico library containing 806 chiral phosphoric acid catalysts. For this class, two scaffolds were selected: catalysts with a fully aromatic binaphthyl backbone and catalysts wherein the second ring of the binaphthyl moiety is saturated (H_8). Then a dataset of 403 synthetically feasible substituents (from a database of readily available commercial sources or fragments that require no more than four well-established synthetic steps) was added to the 3,3′ positions of these scaffolds by using Python2 scripts (for full details,

Downloaded from http://science.sciencemag.org/ on January 18, 2019

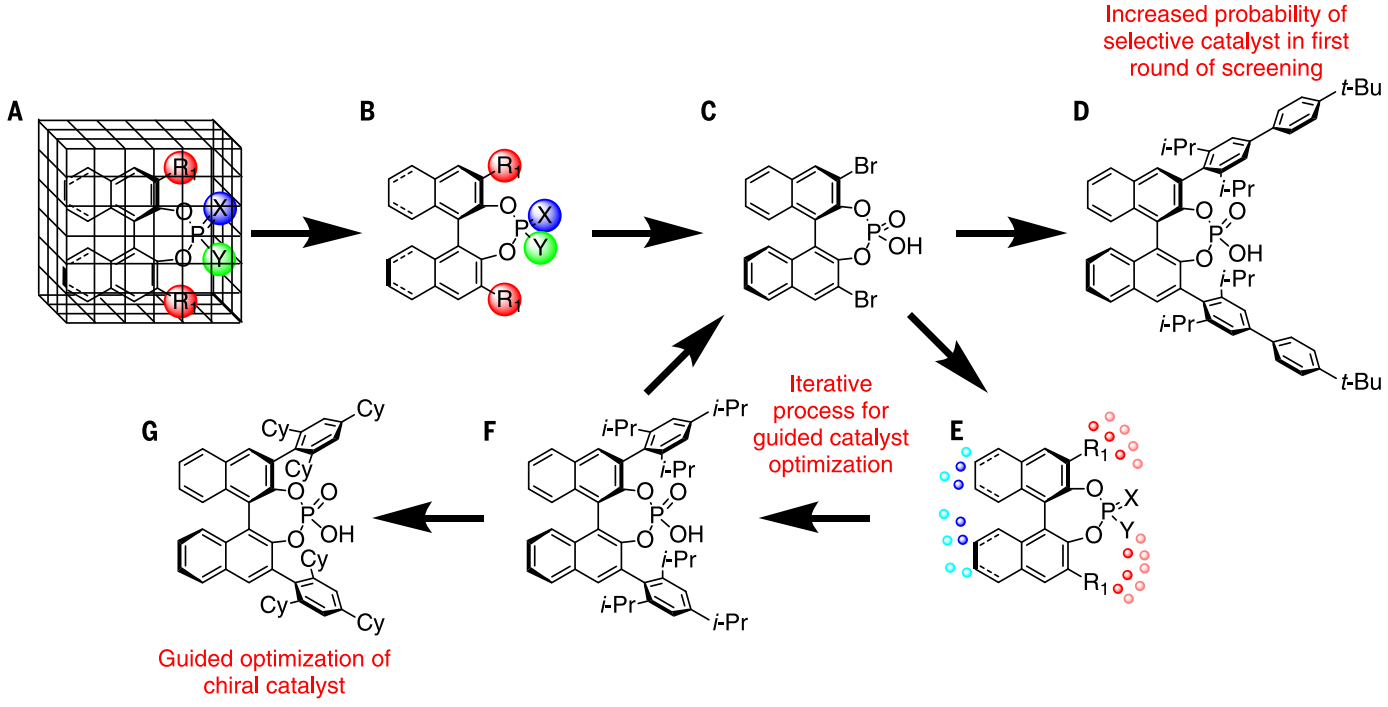


Fig. 1. Summary of chemoinformatics-guided workflow. (**A**) An in silico library of synthetically accessible catalysts is defined. For each member in the library, descriptors are calculated. (**B**) A representative subset is algorithmically selected on the basis of intrinsic chemical properties. (**C**) The representative subset is synthesized and experimentally tested. (**D**) The probability of identifying a highly selective catalyst in the first round of screening should be greater than that by random sampling alone. (**E**) The data from the training set are used to train statistical learning methods. (**F**) The models predict selectivity values for every member of the greater in silico library. (**G**) If successful, the model will predict the optimal catalyst for the reaction. If unsuccessful, the new data can be used as training data to make a stronger prediction in successive rounds of modeling. R, any group; X, O or S; Y, OH, SH, or NHTf; *i*-Pr, isopropyl; *t*-Bu, *tert*-butyl; Cy, cyclohexyl.

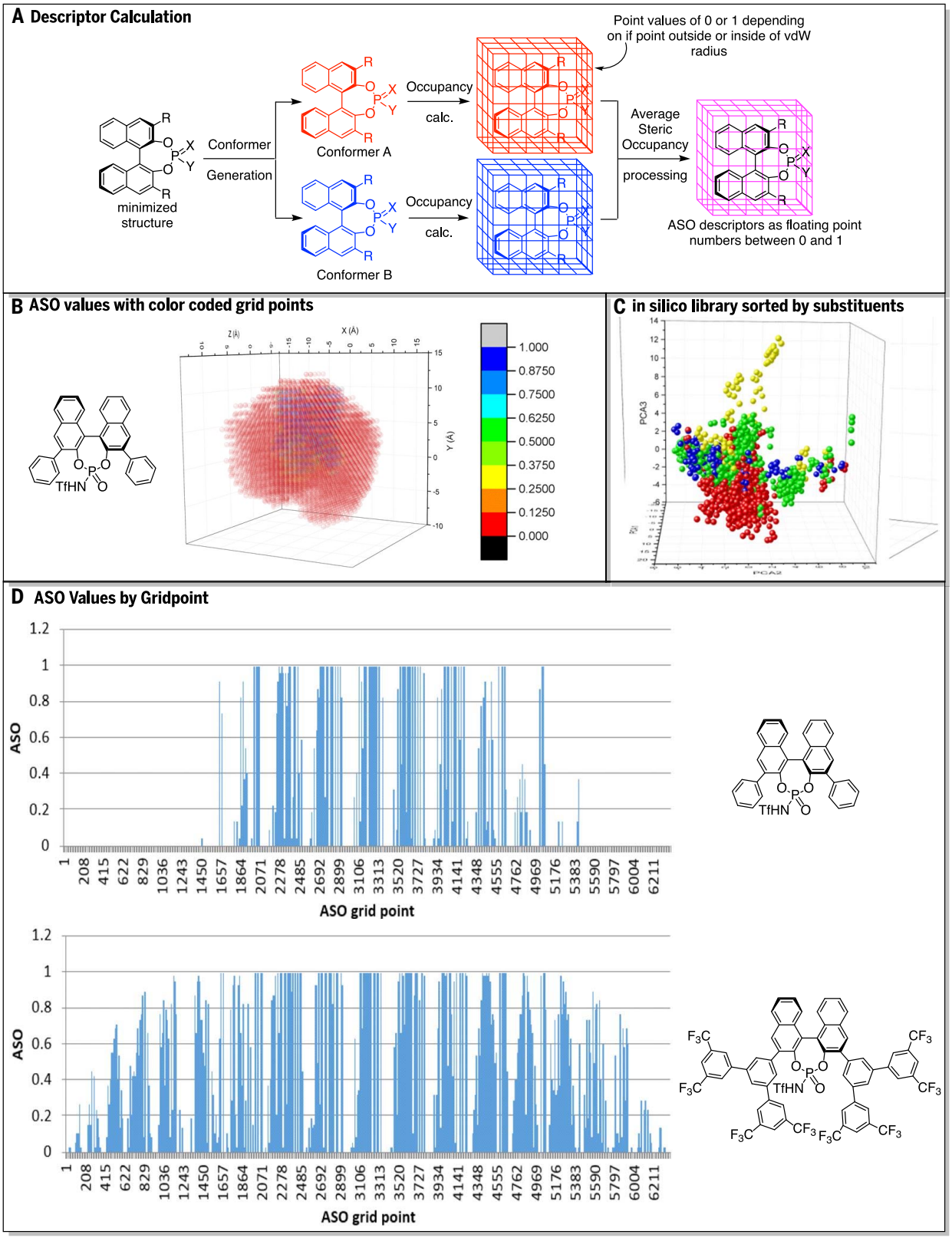


Fig. 2. Generation of ASO descriptors. (**A**) Pictorial description of the ASO calculation process. (**B**) ASO grid points away from the catalyst have values of 0 (red), whereas grid points occupied in all conformers have a value of 1 (blue); flexible substituents can be seen in the green and yellow regions. (**C**) ASO discrimination of 3,3′-substituent groups: ortho-substituted arenes (red), fused-ring substituents (blue), 3,5-disubstituted arenes (yellow), and all other groups (green). (**D**) Bar graph representation of ASO descriptors for two different Brønsted acid catalysts. calc., calculated; vdW, van der Waals.

Downloaded from http://science.sciencemag.org/ on January 18, 2019

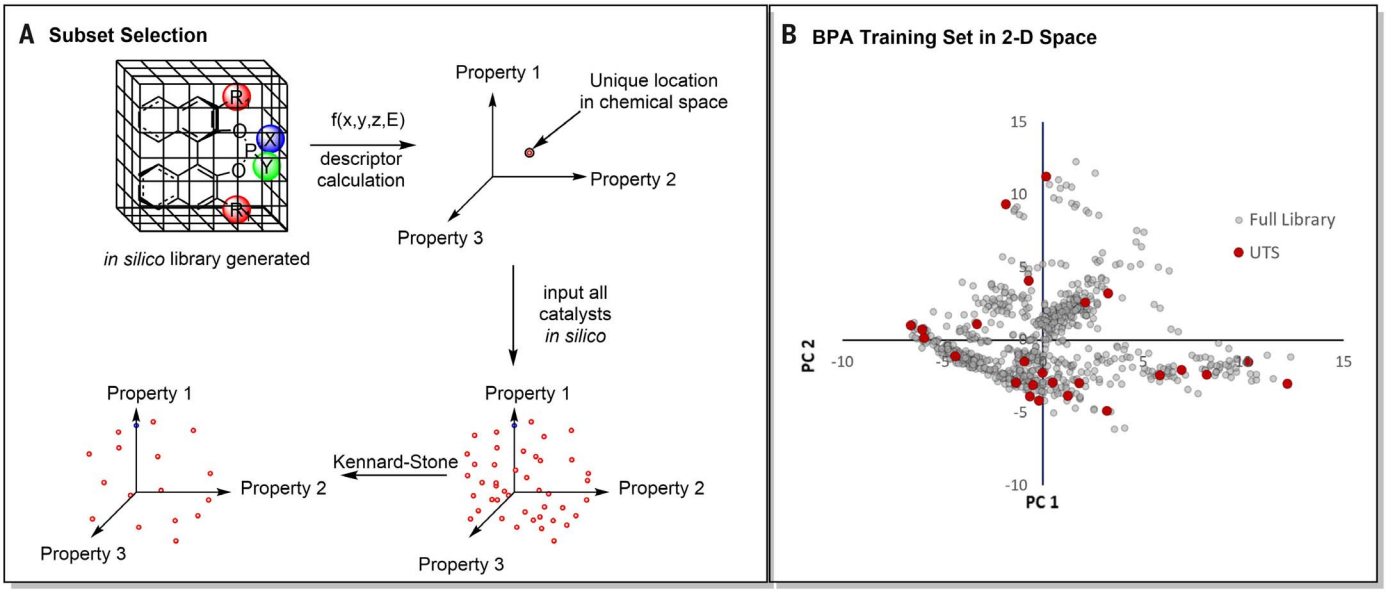


Fig. 3. Construction of the UTS. (**A**) Subset selection with the Kennard-Stone algorithm. The algorithm then selects a representative subset of points, as qualitatively depicted. (**B**) Locations of the catalysts selected by the Kennard-Stone algorithm in 2D chemical space [constructed from the first two principal components (18% and 12% of variance, respectively) of the full catalyst chemical space].

see computational methods in the supplementary materials). The substituents were chosen by surveying catalogs of boronic acids, aryl halides, aldehydes, alkyl boranes, and Grignard reagents and adding all members that were compatible with the reaction conditions necessary to install that substituent (such as Suzuki coupling, use of organolithium reagents, and Kumada coupling). Thus, we are confident that our in silico library covers a large breadth of chemical space that is synthetically accessible. To construct the chemical space representing this library, chemically meaningful descriptors were calculated. However, using many types of readily available 0D, 1D, 2D, and 3D descriptors (the latter derived mostly from MIFs) led to failure because the calculated features did not adequately represent those catalyst properties responsible for enantioinduction [comparative molecular field analysis (CoMFA), grid-independent descriptors (GRIND), and all descriptors available in RDKit and MOE 2015 are some examples of previous attempts] (*33*–*35*). The likely cause of failure was that only a single conformation of each of the catalysts was included. Thus, a new set of descriptors had to be developed that included information about the entire conformer ensemble, could be used for any catalyst scaffold, and would be easily calculable for large libraries of compounds.

To achieve this goal, we invented a new descriptor called average steric occupancy (ASO). The ASO descriptors were inspired by 3.5D and 4D descriptors, simplifying the conformer population information into a location-specific numerical form (*36*, *37*). The protocol for ASO calculation is illustrated in Fig. 2A. First, a conformer distribution for each catalyst in the in silico library was obtained. Second, for each molecule, the conformers were aligned and individually placed in identical grids. If a grid point was within the van der Waals radius of an atom, it was assigned a value of 1; otherwise, it was assigned a value of 0. This process was repeated for n conformers, and upon completion each grid point had a cumulative value ranging from 0 to n. The values were then normalized by dividing by n, such that all grid points had a value between 0 and 1. These values constituted the steric descriptors for the structures. These features are represented in Fig. 2B, wherein the ASO values around a phosphoric acid catalyst are depicted. The red grid points mark areas away from the catalyst where ASO values are 0.000 to 0.125, whereas the blue represents grid points where the ASO values are 0.875 to 1.000. Because the catalysts are aligned to the backbone, the corresponding grid points all have a value of nearly 1, and the backbone is visible as the two overlapping blue bands. Below the blue bands are regions of green and yellow; these represent conformers that differ by the rotation of the P–NH–Tf (triflyl) moiety and the phenyl substituents at the 3,3′ positions. The capacity of these descriptors to distinguish among catalysts of different classes is illustrated in Fig. 2C. The distribution of the different catalyst classes in chemical space (from the first three principal components of the ASO chemical space) demonstrates that ASO qualitatively groups like-structured catalysts.

The electronic descriptors were derived from the perturbation that a substituent exerts on the electrostatic potential map of a quaternary ammonium ion (see the computational methods in the supplementary materials for details). These substituent-based electronic descriptors were combined with the ASO descriptors. In total, this process amounted to 16,384 features per catalyst, which was later reduced upon the removal of all features with a variance of zero.

To select a representative subset of the chemical space spanned by the in silico library, the dimensionality of the chemical space must be reduced (*38*). The data were transformed with principal components analysis (PCA) (*39*), which selects new dimensions such that the variance retained is maximized per dimension kept.

A representative subset (including boundary cases) was selected from this space by using the Kennard-Stone algorithm (*40*) (Fig. 3). This sampling method is of paramount importance; it guarantees that catalysts from uniform regions of feature space are sampled. Thus, predictions made later in method development should still be in a region of feature space described by the initial training set, giving more confidence in these predictions. The subset of selected catalysts constitutes the UTS, which can then be used to optimize any reaction that can be catalyzed by that catalyst type. The 24 members of the UTS for the chiral phosphoric acid scaffold are given in Fig. 4A. To evaluate the predictions made from the UTS, a separate test set of 19 external catalysts (**52** to **70**) (Fig. 5B) was selected from the in silico library. These external catalysts were selected on the basis of intuitive chemical differences and synthetic accessibility.

Application of the catalyst optimization protocol to asymmetric *N*,*S*-acetal formation

To validate the ASO and training set selection protocol, the training set was evaluated on a previously optimized model reaction. The enantioselective formation of *N*,*S*-acetals (Fig. 5A)

Downloaded from http://science.sciencemag.org/ on January 18, 2019

developed by Antilla and co-workers (*41*) was selected for several reasons. The reaction is high yielding and highly reproducible; it can be performed under air at room temperature, thus facilitating rapid screening; and a range of selectivities (0 to 99%) has been reported with different catalysts (six reported catalysts). Accordingly, we judged this reaction to be a good candidate for empirically evaluating the selectivity space covered in the UTS. By calculating ASO and electronic descriptors for reactants and products as well and concatenating these descriptors with catalyst descriptors, individual reaction profiles could be constructed that also took into account substrate properties. The inclusion of substrate descriptors also increased the number of data points obtained per catalyst synthesized. As a general note on the use of reactant and product descriptors, we find that it provides the following benefits: More data points can be collected per catalyst

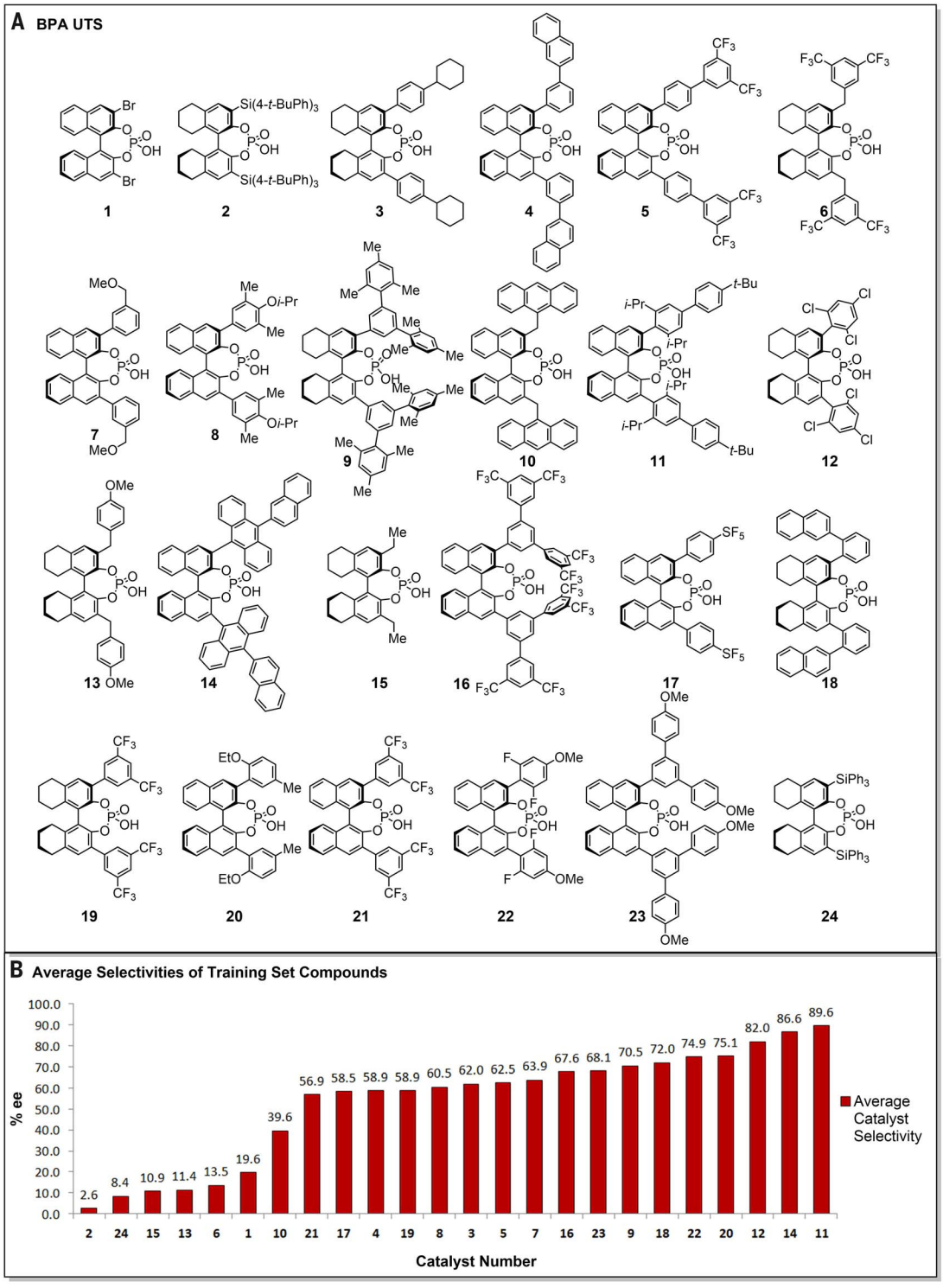


Fig. 4. BINOL phosphoric acid (BPA) UTS. (**A**) UTS of phosphoric acid catalysts selected by the Kennard-Stone algorithm. (**B**) Average selectivity of training catalysts across the 16 training reactions. Ph, phenyl; Me, methyl; Et, ethyl.

Downloaded from http://science.sciencemag.org/ on January 18, 2019

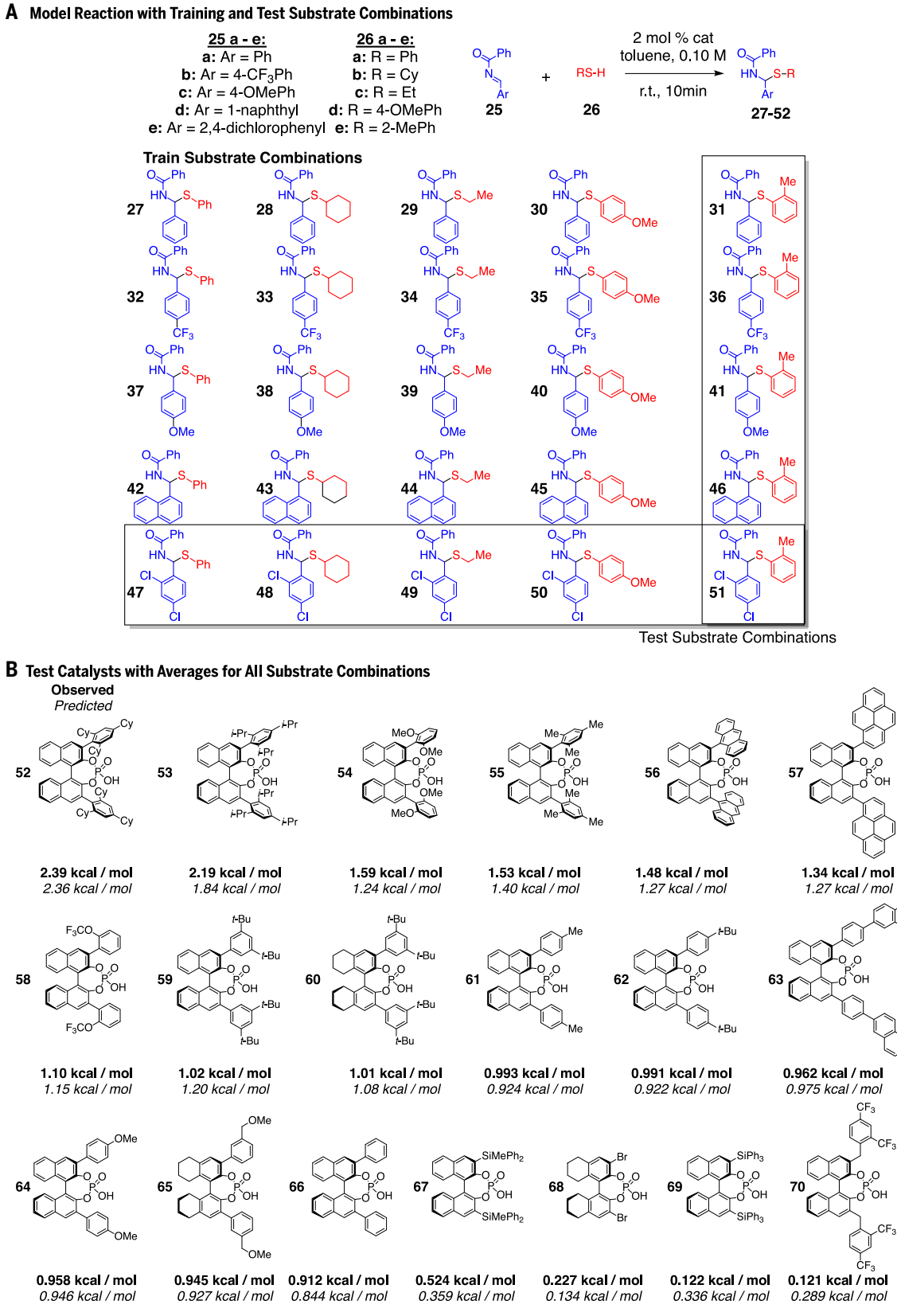
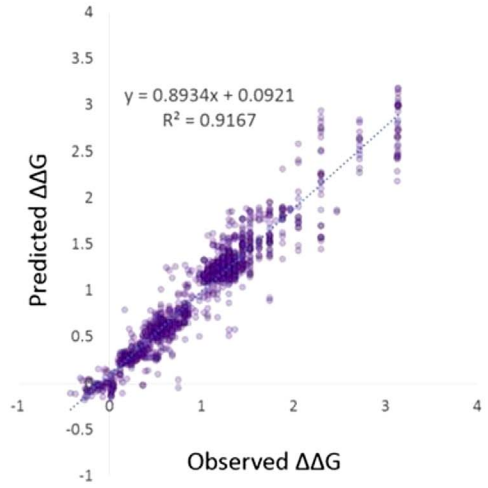


Fig. 5. Model validation on thiol addition to *N*-acyl imines.
(**A**) Model reaction screened over 16 training substrate combinations and nine test substrate combinations. (**B**) Test set of catalysts. Each catalyst was evaluated by the average selectivity across all 25 substrate combinations. The experimentally observed selectivity is in bold, and the predicted selectivity (reported as the free energy differential between the transition structures leading to each enantiomer) is in italics. r.t., room temperature.

Downloaded from http://science.sciencemag.org/ on January 18, 2019

A Plot of Observed vs. Predicted Selectivity.



B Mean Absolute Deviation.

	MAD (ΔΔG, kcal / mol)
Trial 1	0.1487
Trial 2	0.1501
Trial 3	0.1509
Trial 4	0.1519
Trial 5	0.1476
Trial 6	0.1569
Trial 7	0.1550
Trial 8	0.1547
Trial 9	0.1428
Trial 10	0.1572
Average	**0.1516 +/- 0.0050**

Fig. 6. The averaged predicted selectivity values for external test sets plotted against observed enantioselectivity data. (**A**) The vertical bands result from the accuracy in the analytical method, wherein the limit of detection determines enantiomeric purity to the nearest 0.5% ee. Because of the exponential relationship between ee and free energy, detectable differences in selectivity appear greater at larger free energy differentials. (**B**) The MAD data are listed in the table for each of the 10 replicate runs.

synthesized, allowing for stronger models to be produced, and we can use our technology to predict the outcome of reactions with a known catalyst on new substrate combinations, thus creating another powerful tool.

Generation of models by using all selectivity data

To ensure that our descriptors capture the structural information pertaining to enantioinduction and can be used to construct predictive models, 2150 separate experiments were performed, wherein the catalysts shown in Figs. 4A and 5B (43 catalysts in total) were used in the reactions with pairwise combinations of imines and thiols, leading to the 25 different products shown in Fig. 5A. This process creates 43 × 25 = 1075 reactions, which were run in duplicate, and the average of duplicate runs was used as the experimental selectivity data. From these 1075 reactions, 475 were randomly selected as an external test set by using a Python random-number generator, and the remaining 600 reactions were used to train the model. To ensure that model efficacy and training set–test set partitioning were unbiased, this process was repeated 10 times. Models were then developed with support vector machines by using a grid-based optimization of hyperparameters with fivefold cross validation (see supplementary materials for details). The average predicted selectivities of the 475 external test set reactions (i.e., those which were not used in the model training process) reveal very good correlation when plotted against the experimental selectivity data (a high coefficient of determination R^2, a y intercept very close to zero, and a slope approaching unity) (Fig. 6A). The mean absolute deviation (MAD) for each of the 10 randomized trials is listed in Fig. 6B. As is evident from the low MAD of each run, the models make highly accurate predictions of selectivity, confirming that our descriptor set is a valid, numerical representation of molecules capable of capturing the relevant features of catalysts responsible for enantioselectivity.

As experimentalists, we were interested in establishing whether these tools could be used to predict the results of either new substrate combinations or new catalysts that have not previously been tested or to identify new reactions (i.e., substrates and catalysts) that are more selective than any reaction in the training data. We therefore performed two modeling studies to evaluate each hypothesis by partitioning the available data in two different ways. For the first study, the data from reactions of four imines (imines **25a** to **25d**) and four thiols (thiols **26a** to **26d**) (i.e., 16 reactions per catalyst) were evaluated (Fig. 5A). Using the 24-member catalyst training set (Fig. 4A) with each substrate combination then gave rise to 16 × 24 = 384 training reactions that could be used for model development. This process also generated 1075 – 384 = 691 test reactions for external validation (the test reactions were later divided into three different sets, detailed below). For the second study, we investigated whether new, more selective reactions could be predicted. To investigate this possibility, the 1075 experimental selectivity data points were divided such that every catalyst-imine-thiol combination that gave products below 80% ee was included in the training set and no reactions above 80% ee were used at any stage in model development. These remaining, highly selective reactions were instead used as an external test set. Both data division methods violate the iid (independent and identically distributed) assumption (*42*). Thus, we make no claims as to the generalizability of these studies and simply propose this method as a tool to facilitate the experimental optimization of catalysts and the exploration of substrate scope.

Generation of models derived from the UTS

It was very rewarding to find a highly selective catalyst in the training set (compound **11**) (Fig. 4A), supporting our hypothesis that using the UTS increases the probability of finding an effective catalyst in the first round of screening (catalyst selectivity data are summarized in Fig. 4B). 3,3′-Benzyl-substituted catalysts used in reactions with aliphatic thiols as nucleophiles gave rise to the opposite stereoisomer as the major product compared with the other cases. Thus, the range of selectivities covered by the UTS in the 16 training reactions spans from –43% ee to >99% ee with the same enantiomer of catalyst, further supporting the hypothesis that the UTS covers a broad range of selectivity space, as illustrated in the full compilation of experimental results (table S1). From this dataset, a suite of models was generated and used to predict the selectivity of three families of test sets: a substrate test set of reactions generating new products (i.e., those formed from substrates not included in the training set but using catalysts in the training set), a catalyst test set of reactions generating the same products in the training set but with catalysts not included in the training data, and a substrate-catalyst (sub-cat) test set of reactions creating new products and also using catalysts not included in the training data. For the substrate test set, nine distinct compounds (**31**, **36**, **41**, and **46** to **51**) (Fig. 5A) generated from substrate combinations with unknown results in the model reaction were selected, totaling 216 reactions (24 training catalysts × 9 test substrates). For the catalyst test set, the 19 external catalysts (**52** to **70**) (Fig. 5B) were evaluated in reactions generating the same products as the training reactions, totaling 304 reactions (19 test catalysts from Fig. 5B × 16 training substrates from Fig. 5A). For the sub-cat test set, the 19 external test set catalysts were used in reactions producing the nine new products, thus evaluating the capability to predict reaction outcomes with external substrate combinations and external catalysts, totaling 171 reactions [19 test catalysts × 9 test substrates (Fig. 5B catalysts with Fig. 5A test substrate combinations)].

By using a variety of data preprocessing methods (see supplementary materials for details), we generated a suite of models. Of these, the support vector machines method gave the highest performance on the basis of the MAD from the combined external test sets (Fig. 7A). The first test set evaluated the ability of the models to predict the selectivity only of reactions forming new products. In this role, the model performed well, with an MAD of 0.161 kcal/mol. Next, the same model was used to predict the selectivity of the external test set of catalysts. The performance of the model was still highly accurate, with a MAD of 0.211 kcal/mol. Lastly, reactions forming new products with the external test

Downloaded from http://science.sciencemag.org/ on January 18, 2019

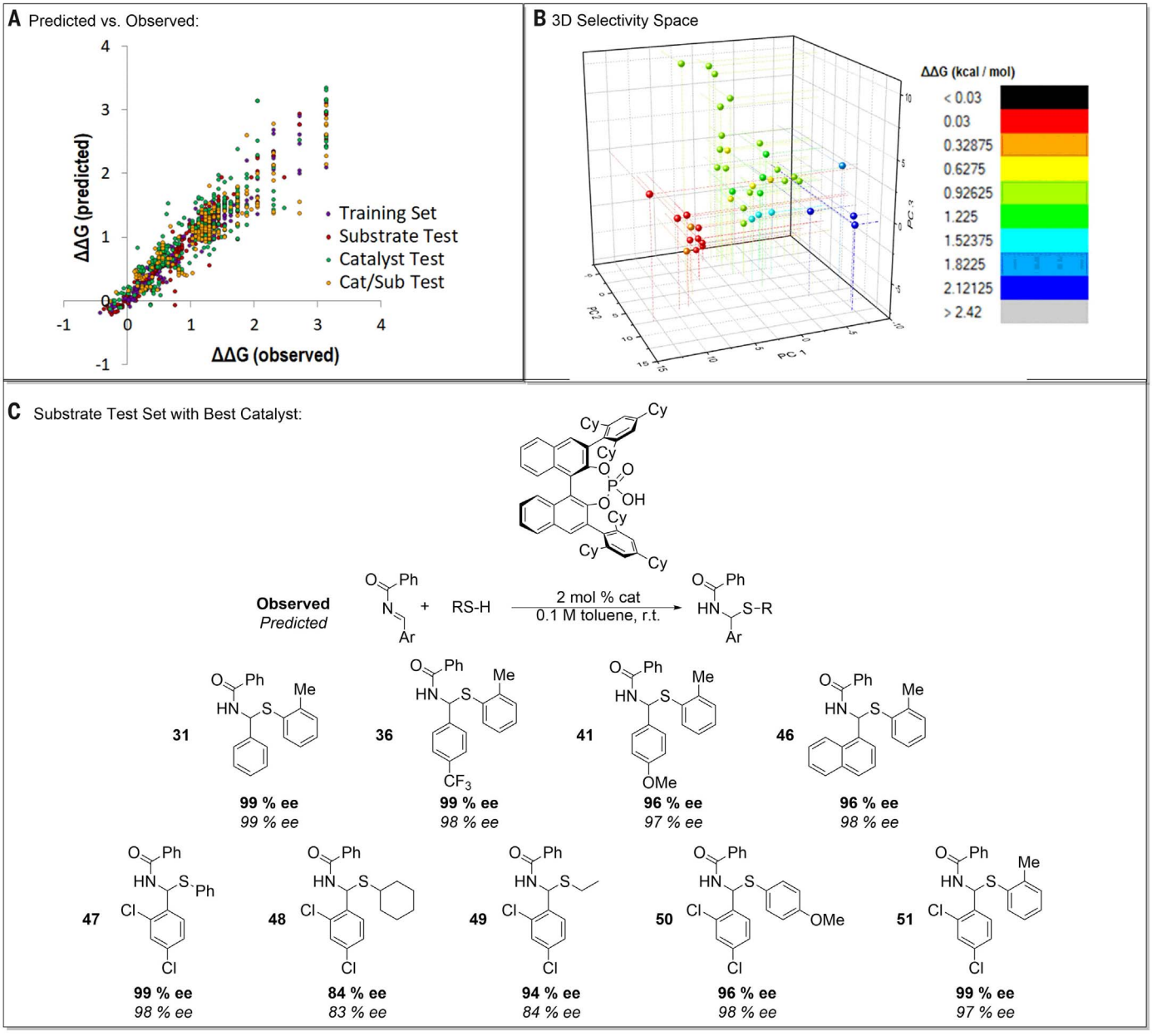


Fig. 7. Application of models from UTS. (**A**) The predicted versus observed plots for the training set, substrate test set, catalyst test set, and sub-cat test set. The support vector machines method (second-order polynomial kernel, q^2 = 0.748 by *k*-fold cross validation) performs well on all external test sets, predicting reaction outcomes within 0.25 kcal/mol (MAD = 0.161, 0.211, and 0.238 kcal/mol, respectively). The vertical bands result from the limit of accuracy in the analytical method. (**B**) The 3D chemical space of all catalysts (from the first three principal components of the full chemical space, 13, 8, and 8% of variance, respectively). The red points are unselective catalysts, the green and yellow points are more selective, and the blue points are the most selective, with the average selectivity across all 25 reactions as a metric of catalyst selectivity. (**C**) Observed and predicted outcomes of reactions with substrate combinations that were not also included in the training data.

catalysts were predicted with a MAD of 0.236 kcal/mol. All three test sets were predicted at a level of accuracy equal to or greater than that of most quantum chemistry methods (*43*). To evaluate catalyst performance, the mean selectivity ($\Delta\Delta G$ in kilocalories per mole) of each test catalyst across all 25 reactions was calculated (Fig. 5B). The model predicted this efficacy metric with notable accuracy, predicting all catalysts within 0.4 kcal/mol, with only two catalysts (**53** and **54**) predicted outside of 0.3 kcal/mol from the experimentally observed $\Delta\Delta G$. Catalyst **53** gave the best selectivity in the original study (*41*), and our results were in good agreement with what has been previously reported. Similarly, aliphatic thiols gave diminished selectivity with respect to thiophenol derivatives. The first three principal components of catalyst space also reveal distinct regions of high, medium, and low space (Fig. 7B). Similarly, the predicted reaction outcomes for the nine test reactions with the best catalyst are illustrated in Fig. 7C. All reaction selectivities except one (**49**) are predicted within 2% ee of the measured value. Despite not being included at any stage of model development, compound **52** was still predicted to be the most selective catalyst in the in silico library for this transformation. A complete list of predicted selectivity values for the entire in silico library of reactions can be found in data S1.

Reaction prediction beyond the training set

Although modeling with data spanning the entire range (e.g., up to 99% ee) of interest can be

Downloaded from http://science.sciencemag.org/ on January 18, 2019

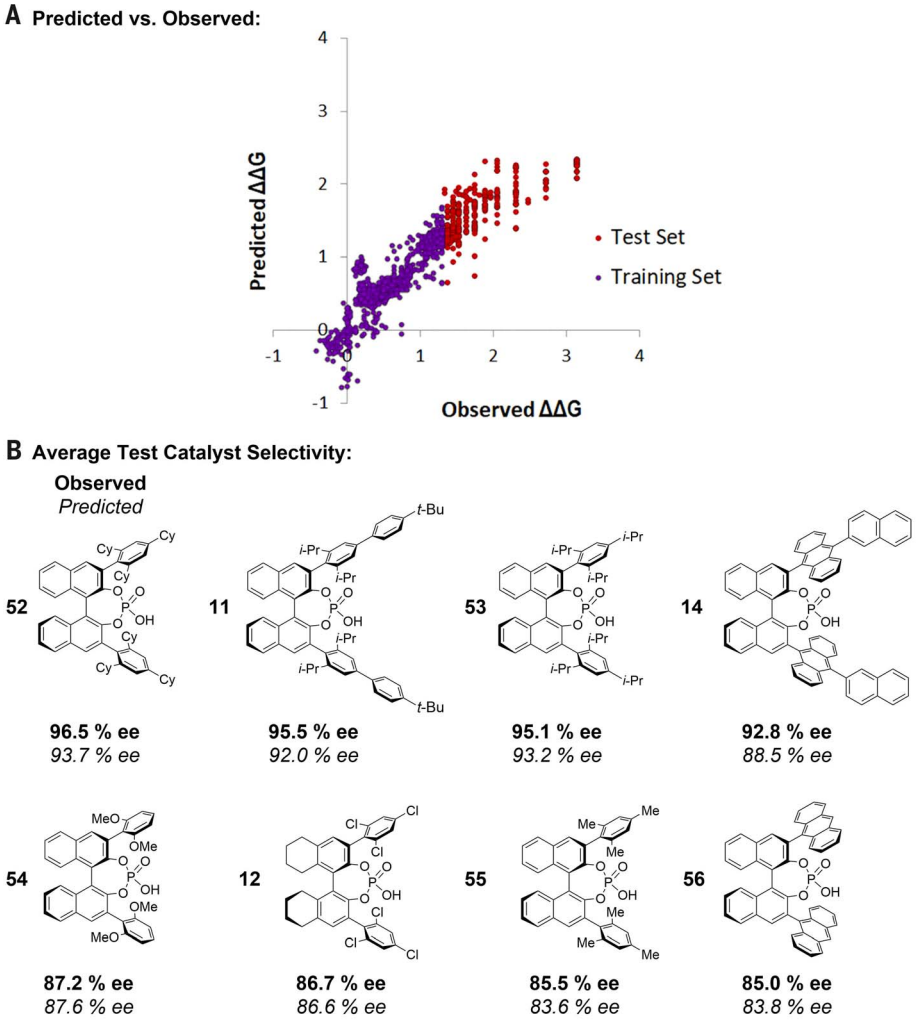


Fig. 8. Reaction prediction beyond the selectivity spanned by the training set. (**A**) A model generated by using a deep feed-forward neural network simulating the optimization of an unoptimized reaction by using all data below 80% ee to train the model. The vertical bands result from the limit of accuracy in the analytical method. (**B**) Predicted and observed average selectivities for the eight catalysts with average enantioselectivity over 80% ee. Only the common reactions (i.e., those forming the same product) that were in the test set for each of the eight catalysts were used to calculate the average selectivities. The identity of these reactions and the predicted and observed values are available in data S3.

valuable for predicting the outcome of new substrate combinations, modeling beyond this range can be leveraged to enhance the rate at which catalytic enantioselective reactions are optimized. To demonstrate this potential in our method, we simulated a situation in which highly selective reactions (i.e., combinations of substrates and catalysts) have not been identified. Accordingly, we partitioned all 1075 reactions as follows: All reactions below 80% ee were used as training data (718 reactions), and all reactions above 80% ee were used as test data (357 reactions). (The identities of the training and test datasets can be found in the supplementary materials.) A variety of modeling methods were tested, and although a number of methods, including support vectors, Lasso, LassoLars, ridge regression, elastic net, and random forest (by no means the state of the art in machine learning; see computational methods for a complete explanation), provided acceptable qualitative results, deep feed-forward neural networks accurately reproduced the experimental selectivities (MAD = 0.33 kcal/mol) (Fig. 8A). More notably, the general trends in selectivity, on the basis of average catalyst selectivity, were correctly identified. As shown in Fig. 8B, the most selective catalyst, ***52***, was predicted with the highest accuracy, within 3% ee of the experimental value. Catalysts ***53*** and ***54*** were the next two to follow experimentally and computationally (the order is inverted, but they are within experimental error from each other), followed by catalyst ***55***. The remaining catalysts shown in Fig. 8B were predicted very accurately, likely because the experimental values are closer to the training set cutoff of 80% ee. Despite omitting about half of the experimental free energy range from the training data, we could still make accurate predictions in this region of selectivity space.

Outlook

The capability to successfully predict the selectivity of higher-performing catalysts has the potential to change the way chemists select and optimize chiral catalysts. This method has not been "pressure tested" in a number of scenarios; reactions that are susceptible to electronic perturbation must be investigated, more flexible catalyst scaffolds need to be explored, and catalyst scaffolds with multiple points of diversity must be examined.

Materials and methods

General information

All reactions were performed in glassware that had been flame-dried under vacuum or oven-dried (140°C) overnight. All reactions were conducted under an atmosphere of dry nitrogen or argon by using a drying tube equipped with phosphorus pentoxide and calcium sulfate. All reaction temperatures are noted as the oil bath temperature, the internal temperature as monitored by a Teflon-coated thermocouple, or the room temperature (~23°C). Solvents used for extraction were reagent grade, and chromatography solvents were technical grade. Column chromatography was performed using ultrapure silica gel (40 to 69 μm) from Silicycle with a column mixed as a slurry, packed, and eluted at 6 to 8 psi. Retention factors, R_f, are reported for analytical thin-layer chromatography performed on Merck silica gel plates treated with F-254 indicator. Visualizations were accomplished by using ultraviolet (UV) light, aqueous $KMnO_4$, ceric ammonium molybdate solution, or iodine. Reaction solvents tetrahydrofuran [Fischer; high-performance liquid chromatography (HPLC) grade], hexanes (Fischer; HPLC grade), diethyl ether [Fischer; butylated hydroxytoluene–stabilized American Chemical Society (ACS) grade], methylene chloride (Fischer; unstabilized HPLC grade), and *N*,*N*′-dimethylformamide (Fischer; HPLC grade) were dried by percolation through two columns packed with neutral alumina under positive pressure of argon. Toluene (Fischer; ACS grade) was dried by percolation through a column packed with neutral alumina and a column packed with Q5 reactant, a supported copper catalyst for scavenging oxygen, under a positive pressure of argon. Amines were distilled fresh before use, and pyridine (Fischer; ACS grade) used as a solvent was distilled and stored over 4-Å molecular sieves before use.

Instrumentation

^{1}H, ^{13}C, ^{19}F, and ^{31}P nuclear magnetic resonance (NMR) spectra were recorded on a Varian Unity Inova 400 spectrometer (^{19}F and ^{31}P), a Varian Unity 500 spectrometer (^{1}H and ^{13}C), a Bruker Advance 500 spectrometer (^{1}H, ^{13}C, ^{19}F, ^{29}Si, and ^{31}P), a Varian VXR 500 spectrometer (^{1}H), or a Unity 500 NB spectrometer (^{1}H). Spectra are referenced to chloroform [δ = 7.26 parts per

Downloaded from http://science.sciencemag.org/ on January 18, 2019

million (ppm), ^{1}H; 77.0 ppm, ^{13}C], residual benzene (δ = 7.15 ppm, ^{1}H; 128.62 ppm, ^{13}C), or dimethyl sulfoxide (δ = 2.50 ppm, ^{1}H; 39.52 ppm, ^{13}C). Chemical shifts are reported in parts per million, and multiplicities are indicated by s (singlet), d (doublet), t (triplet), q (quartet), p (pentet), h (hextet), m (multiplet), and br (broad). Coupling constants *J* are reported in hertz, integration is provided, and assignments are indicated. Mass spectrometry was performed by the University of Illinois Mass Spectrometry Laboratory. Mass spectrometric data were collected on a Waters Q-TOF Ultima (ESI) spectrometer, a Waters Synapt G2-Si spectrometer (ESI), a Waters Quattro Ultima spectrometer (ESI), or a Waters 70-VSE spectrometer (EI). Low-resolution spectral data are reported as (mass, intensity), and high-resolution data are reported as calculated and measured masses to 10^{-4} mass accuracy. Infrared spectra were recorded on a Perkin-Elmer UATR-2 FT-IR spectrophotometer. Peaks are reported as reciprocal centimeters, with relative intensities indicated as s (strong, 67 to 100%), m (medium, 34 to 66%), or w (weak, 0 to 33%). Analytical chiral stationary-phase supercritical fluid chromatography was performed on an Agilent 1100 high-performance liquid chromatograph equipped with an Aurora Systems A-5 supercritical CO_2 adapter for supercritical fluid chromatography and a UV detector (220 or 254 nm) by using Daicel Chiralcel OD, OJ, and OB or Chiralpak AD and AS columns.

Descriptor calculations

To describe the steric environment around a given structure, the strategy taken in these laboratories used grid point–type descriptors. However, instead of using van der Waals potential energy values at grid point locations, this descriptor incorporates steric data from a population of conformers of a given compound. The new calculation process is as follows (see section S3 in the supplementary materials), demonstrated by using a BINOL-based phosphoric acid derivative scaffold. (i) For each base compound within an in silico library, a set of conformers within a given energy window (generally 7 to 10 kcal/mol) is generated. (ii) The full set of compounds and associated conformer libraries are aligned to a common core. (iii) A spherical grid of points is then calculated to encompass the entire set of aligned compounds to a depth of 3 Å. (iv) For each conformer, an indicator field is created by determining which grid point locations are within the van der Waals radius of an atom. Locations determined to be within atoms are given a value of 1; those outside are given a value of 0. (v) The ASO of a given catalyst is calculated as the average of the indicator fields for each conformer of that catalyst. This gives a descriptor value of $0 \leq \text{ASO} \leq 1$ at each grid point. When compiled, the descriptor set acts both to describe the shape of the molecule and to weight that shape with how often the molecule occupies different regions of space. The process of calculating the ASO descriptor set is completed for every catalyst in the in silico library (fig. S4). The same protocol is used to calculate starting material and product descriptors, and concatenation of the descriptors generates the reaction profiles.

The ASO descriptor can be used to visually compare the shapes and sizes of different compounds by plotting the descriptor values as bar charts. Shown in figure S5 is a comparison between 3,3′-diphenyl-substituted BINOL-phosphoramide **1_iv** and the much larger catalyst **182_iv**. As can be seen in the plots, the ASO descriptor values for **182_iv** are much more varied, and nonzero ASO values can be seen for much more of the available descriptor range, indicating that this catalyst is much larger and covers more of the space available to the catalyst. This type of comparative analysis shows that the descriptors are capturing the shape of the molecule as well as distinguishing between catalysts of different sizes and constitutions (Fig. 2D).

To capture the electrostatic effects of substituents on the compounds of interest, a separate set of descriptors was considered. Electrostatic MIF descriptors have underperformed in the applications tested in these laboratories, and these 3D MIF-based electrostatic descriptors do not incorporate conformation-dependent information. Additionally, most descriptor calculation methods based on electrostatic field determinations fail to distinguish between through-bond and through-space effects (*44*). Although others have used 1D and 2D descriptors, such as Hammett parameters (*45*), to describe such changes, the substituent libraries used in these laboratories are too diverse to have these parameters derived for them. To that end, a new electrostatic parameter that correlates well with known 1D parameters has been devised.

This electrostatic parameter was calculated for individual substituents represented in the catalyst in silico library and is used to estimate the electronic effects of the substituents on the core molecule. The calculation was performed by attaching the substituent group to a tetramethylammonium cation, generating a benzyltrimethylammonium cation if the substituent is aryl, a homobenzyl-trimethylammonium cation if the substituent is benzyl, or an tetraalkylammonium ion if the substituent is alkyl. An electrostatic potential MIF is then calculated by using NWChem (*46*) at the B3LYP/6-31G* level of theory, specifying a specific probe and range for the grid to give a single layer of grid points 0.025 Å apart. An example of the grid and calculated electrostatic potential for a 4-nitrobenzyltrimethylammonium cation is shown in figure S6. After the energies are calculated, the maximum and minimum energies calculated in the single-layer MIF are saved, giving the substituent electrostatic potential energy minimum (ESPMIN) and substituent electrostatic potential energy maximum (ESPMAX) descriptors. The ESPMAX descriptors correlated well with known Hammett parameters, suggesting that the descriptor was describing the electron-donating or -withdrawing nature of the given substituents (fig. S7). These electronic parameters were also used for the nucleophiles and electrophiles, wherein the corresponding thioether and aryl moieties, respectively, were appended to the ammonium ion. Further, natural bond orbital (NBO) charges for sulfur and sulfur molecular orbital energies from the NBO calculation were used as electronic descriptors for the thiols.

Model generation

All machine learning methods except deep neural networks were implemented with Python2 scripts by using scikit-learn (*47*), a Python machine learning package. A collection of models was generated by using a variety of feature selection methods with experimental $\Delta\Delta G$ as the observable. Before modeling, all data descriptors were scaled by removing the mean and scaling to unit variance. A variety of feature selection or transform methods were surveyed (variance threshold method, mutual information, f-regression, and PCA). For the feature selection methods, 100, 500, 1000, and 2000 features were selected. Additionally, by using a percentile cutoff, the 10th, 25th, and 50th percentiles were selected. By using PCA, models were generated with 10, 20, 30, 50, and 100 principal components (64, 78, 84, 89, and 94% of variance, respectively). These methods were all performed separately on the scaled descriptor data (PCA and a feature selection method were never used together). The enantioselectivity data (expressed as the free energy differential between the diastereomeric transition structures leading to the different enantiomers) were also highly skewed, so these data were transformed with the Box-Cox transformation by using SciPy before model generation. Each set of preprocessed data (meaning one of the selection methods or PCA on the features with the transformed or untransformed Y-data) were then used to make a collection of models. Models generated include partial least squares PLSn (where n = 2, 4, 6, 8, 10, 14, 18 and in which $n <$ number of principal components), random forest, LassoCV, LassoLarsCV, ElasticNetCV, RidgeCV, kernel RidgeCV [kernel = radial basis function (rbf)] [k (number of folds in k-fold cross-validation) = 5], k-nearest neighbors (kNN), and support vector machines with linear, rbf, and polynomial kernels (second-, third-, and fourth-order polynomials). Grid optimization of hyperparameters was performed (example code can be found on the GitLab site) (*48*). This hyperparameter optimization was performed with a fivefold train-validation split (e.g., in the case of the UTS data, the 384 "training reactions" were split). Models were evaluated via q^2 (cross-validated R^2), R^2, and MAD from an external test set of reactions (not used in hyperparameter optimization). Three examples are given in fig. S8. Each model used the transformed (Box-Cox) selectivity data and the top 25% of features selected by mutual information regression. SVR_poly2 (support vector regressor with second-order polynomial kernel) was the only member of the best models to accurately predict the most selective test reactions.

Whereas SVR_poly2 qualitatively selected the best reactions when attempting to predict

Downloaded from http://science.sciencemag.org/ on January 18, 2019

beyond the range of selectivities in the training data, the models quantitatively underpredicted these reactions. By using Keras (*49*) with the Theano backend, a Python package that can facilitate deep learning, we generated a deep feed-forward network. Grid-based hyperparameter optimization was used with linear, relu, elu, and selu activation functions; 0.05, 0.1, and 0.2 dropouts on the layers; 4, 40, 400, and 4000 nodes per layer; and 0 to 6 hidden layers. Further, all optimizers available in Keras were tested. This method of hyperparameter optimization was very time intensive, and it is strongly recommended that practitioners instead use a Bayesian optimization of hyperparameters. Attempts to use this kind of optimization and more modern machine learning methods are currently under way.

REFERENCES AND NOTES

1. T. Engel, Basic overview of chemoinformatics. *J. Chem. Inf. Model.* **46**, 2267–2277 (2006). doi: 10.1021/ci600234z; pmid: 17125169
2. P. Willett, Chemoinformatics: A history. *Wiley Interdiscip. Rev. Comput. Mol. Sci.* **1**, 46–56 (2011). doi: 10.1002/wcms.1
3. D. K. Agrafiotis, D. Bandyopadhyay, J. K. Wegner, Hv. Vlijmen, Recent advances in chemoinformatics. *J. Chem. Inf. Model.* **47**, 1279–1293 (2007). doi: 10.1021/ci700059g; pmid: 17511441
4. E. A. Feigenbaum, B. G. Buchanan, DENDRAL and Meta-DENDRAL: Roots of knowledge systems and expert system applications. *Artif. Intell.* **59**, 233–240 (1993). doi: 10.1016/0004-3702(93)90191-D
5. M. H. S. Segler, M. Preuss, M. P. Waller, Planning chemical syntheses with deep neural networks and symbolic AI. *Nature* **555**, 604–610 (2018). doi: 10.1038/nature25978; pmid: 29595767
6. S. Szymkuć *et al.*, Computer-assisted synthetic planning: The end of the beginning. *Angew. Chem. Int. Ed. Engl.* **55**, 5904–5937 (2016). doi: 10.1002/anie.201506101; pmid: 27062365
7. J. N. Wei, D. Duvenaud, A. Aspuru-Guzik, Neural networks for the prediction of organic chemistry reactions. *ACS Cent. Sci.* **2**, 725–732 (2016). doi: 10.1021/acscentsci.6b00219; pmid: 27800555
8. C. W. Coley, R. Barzilay, T. S. Jaakkola, W. H. Green, K. F. Jensen, Prediction of organic reaction outcomes using machine learning. *ACS Cent. Sci.* **3**, 434–443 (2017). doi: 10.1021/acscentsci.7b00064; pmid: 28573205
9. H. Chen, O. Engkvist, Y. Wang, M. Olivecrona, T. Blaschke, The rise of deep learning in drug discovery. *Drug Discov. Today* **23**, 1241–1250 (2018). doi: 10.1016/j.drudis.2018.01.039; pmid: 29366762
10. J. Ma, R. P. Sheridan, A. Liaw, G. E. Dahl, V. Svetnik, Deep neural nets as a method for quantitative structure-activity relationships. *J. Chem. Inf. Model.* **55**, 263–274 (2015). doi: 10.1021/ci500747n; pmid: 25635324
11. S. E. Denmark, N. D. Gould, L. M. Wolf, A systematic investigation of quaternary ammonium ions as asymmetric phase-transfer catalysts. Synthesis of catalyst libraries and evaluation of catalyst activity. *J. Org. Chem.* **76**, 4260–4336 (2011). doi: 10.1021/jo2005445; pmid: 21446721
12. S. E. Denmark, N. D. Gould, L. M. Wolf, A systematic investigation of quaternary ammonium ions as asymmetric phase-transfer catalysts. Application of quantitative structure activity/selectivity relationships. *J. Org. Chem.* **76**, 4337–4357 (2011). doi: 10.1021/jo2005457; pmid: 21446723
13. R. Gómez-Bombarelli *et al.*, Automatic chemical design using a data-driven continuous representation of molecules. *ACS Cent. Sci.* **4**, 268–276 (2018). doi: 10.1021/acscentsci.7b00572; pmid: 29532027
14. P. Raccuglia *et al.*, Machine-learning-assisted materials discovery using failed experiments. *Nature* **533**, 73–76 (2016). doi: 10.1038/nature17439; pmid: 27147027
15. A. P. Bartók, M. J. Gillan, F. R. Manby, G. Csányi, Machine-learning approach for one- and two-body corrections to density functional theory: Applications to molecular and condensed water. *Phys. Rev. B* **88**, 054104 (2013). doi: 10.1103/PhysRevB.88.054104
16. Z. Zhou, X. Li, R. N. Zare, Optimizing chemical reactions with deep reinforcement learning. *ACS Cent. Sci.* **3**, 1337–1344 (2017). doi: 10.1021/acscentsci.7b00492; pmid: 29296675
17. J. B. O. Mitchell, Machine learning methods in chemoinformatics. *Wiley Interdiscip. Rev. Comput. Mol. Sci.* **4**, 468–481 (2014). doi: 10.1002/wcms.1183; pmid: 25285160
18. K. B. Lipkowitz, M. Pradhan, Computational studies of chiral catalysts: A comparative molecular field analysis of an asymmetric Diels-Alder reaction with catalysts containing bisoxazoline or phosphinooxazoline ligands. *J. Org. Chem.* **68**, 4648–4656 (2003). doi: 10.1021/jo0267697; pmid: 12790567
19. M. C. Kozlowski, S. L. Dixon, M. Panda, G. Lauri, Quantum mechanical models correlating structure with selectivity: Predicting the enantioselectivity of β-amino alcohol catalysts in aldehyde alkylation. *J. Am. Chem. Soc.* **125**, 6614–6615 (2003). doi: 10.1021/ja0293195; pmid: 12769554
20. J. L. Melville, B. I. Andrews, B. Lygo, J. D. Hirst, Computational screening of combinatorial catalyst libraries. *Chem. Commun.* **2004**, 1410–1411 (2004). doi: 10.1039/b402378a; pmid: 15179489
21. S. Sciabola *et al.*, Theoretical prediction of the enantiomeric excess in asymmetric catalysis. An alignment-independent molecular interaction field based approach. *J. Org. Chem.* **70**, 9025–9027 (2005). doi: 10.1021/jo051496b; pmid: 16238344
22. K. C. Harper, M. S. Sigman, Predicting and optimizing asymmetric catalyst performance using the principles of experimental design and steric parameters. *Proc. Natl. Acad. Sci. U.S.A.* **108**, 2179–2183 (2011). doi: 10.1073/pnas.1013331108; pmid: 21262844
23. K. C. Harper, M. S. Sigman, Three-dimensional correlation of steric and electronic free energy relationships guides asymmetric propargylation. *Science* **333**, 1875–1878 (2011). doi: 10.1126/science.1206997; pmid: 21960632
24. M. S. Sigman, K. C. Harper, E. N. Bess, A. Milo, The development of multidimensional analysis tools for asymmetric catalysis and beyond. *Acc. Chem. Res.* **49**, 1292–1301 (2016). doi: 10.1021/acs.accounts.6b00194; pmid: 27220055
25. K. C. Harper, E. N. Bess, M. S. Sigman, Multidimensional steric parameters in the analysis of asymmetric catalytic reactions. *Nat. Chem.* **4**, 366–374 (2012). doi: 10.1038/nchem.1297; pmid: 22522256
26. Y. Park, Z. L. Niemeyer, J.-Q. Yu, M. S. Sigman, Quantifying structural effects of amino acid ligands in Pd(II)-catalyzed enantioselective C–H functionalization reactions. *Organometallics* **37**, 203–210 (2018). doi: 10.1021/acs.organomet.7b00751
27. D. T. Ahneman, J. G. Estrada, S. Lin, S. D. Dreher, A. G. Doyle, Predicting reaction performance in C-N cross-coupling using machine learning. *Science* **360**, 186–190 (2018). doi: 10.1126/science.aar5169; pmid: 29449509
28. M. K. Nielsen, D. T. Ahneman, O. Riera, A. G. Doyle, Deoxyfluorination with sulfonyl fluorides: Navigating reaction space with machine learning. *J. Am. Chem. Soc.* **140**, 5004–5008 (2018). doi: 10.1021/jacs.8b01523; pmid: 29584953
29. L. Breiman, Random forests. *Mach. Learn.* **45**, 5–32 (2001). doi: 10.1023/A:1010933404324
30. G. Skoraczyński *et al.*, Predicting the outcomes of organic reactions via machine learning: Are current descriptors sufficient? *Sci. Rep.* **7**, 3582 (2017). doi: 10.1038/s41598-017-02303-0; pmid: 28620199
31. In this case, meaning as many as can be accessed by the synthesis of fragments that require no more than four well-established synthetic steps before being combined with a common scaffold.
32. D. Parmar, E. Sugiono, S. Raja, M. Rueping, Addition and correction to complete field guide to asymmetric BINOL-phosphate derived Brønsted acid and metal catalysis: History and classification by mode of activation; Brønsted acidity, hydrogen bonding, ion pairing, and metal phosphates. *Chem. Rev.* **117**, 10608–10620 (2017). doi: 10.1021/acs.chemrev.7b00197; pmid: 28737901
33. K. Roy, S. Kar, R. N. Das, in *Understanding the Basics of QSAR for Applications in Pharmaceutical Sciences and Risk Assessment*, K. Roy, S. Kar, R. N. Das, Eds. (Academic Press, 2015), pp. 291–317.
34. V. L. Cruz, S. Martinez, J. Ramos, J. Martinez-Salazar, 3D-QSAR as a tool for understanding and improving single-site polymerization catalysts. A review. *Organometallics* **33**, 2944–2959 (2014). doi: 10.1021/om400721v
35. P. Braiuca, K. Lorena, V. Ferrario, C. Ebert, L. Gardossi, A three-dimensional quantitative structure-activity relationship (3D-QSAR) model for predicting the enantioselectivity of *Candida antarctica* lipase B. *Adv. Synth. Catal.* **351**, 1293–1302 (2009). doi: 10.1002/adsc.200900009
36. C. L. Senese, J. Duca, D. Pan, A. J. Hopfinger, Y. J. Tseng, 4D-fingerprints, universal QSAR and QSPR descriptors. *J. Chem. Inf. Comput. Sci.* **44**, 1526–1539 (2004). doi: 10.1021/ci049898s; pmid: 15446810
37. J. L. Melville *et al.*, Exploring phase-transfer catalysis with molecular dynamics and 3D/4D quantitative structure-selectivity relationships. *J. Chem. Inf. Model.* **45**, 971–981 (2005). doi: 10.1021/ci050051l; pmid: 16045291
38. R. E. Bellman, *Dynamic Programming* (Princeton Univ. Press, 1957).
39. K. Pearson, LIII. On lines and planes of closest fit to systems of points in space. *London Edinb. Dublin Philos. Mag. J. Sci.* **2**, 559–572 (1901). doi: 10.1080/14786440109462720
40. R. W. Kennard, L. A. Stone, Computer aided design of experiments. *Technometrics* **11**, 137–148 (1969). doi: 10.1080/00401706.1969.10490666
41. G. K. Ingle, M. G. Mormino, L. Wojtas, J. C. Antilla, Chiral phosphoric acid-catalyzed addition of thiols to *N*-acyl imines: Access to chiral *N*,*S*-acetals. *Org. Lett.* **13**, 4822–4825 (2011). doi: 10.1021/ol201899c; pmid: 21842841
42. I. Steinwart, D. Hush, C. Scovel, Learning from dependent observations. *J. Multivar. Anal.* **100**, 175–194 (2009). doi: 10.1016/j.jmva.2008.04.001
43. L. Simón, J. M. Goodman, Theoretical study of the mechanism of Hantzsch ester hydrogenation of imines catalyzed by chiral BINOL-phosphoric acids. *J. Am. Chem. Soc.* **130**, 8741–8747 (2008). doi: 10.1021/ja800793t; pmid: 18543923
44. S. E. Wheeler, K. N. Houk, Through-space effects of substituents dominate molecular electrostatic potentials of substituted arenes. *J. Chem. Theory Comput.* **5**, 2301–2312 (2009). doi: 10.1021/ct900344g; pmid: 20161573
45. C. Hansch, A. Leo, R. W. Taft, A survey of Hammett substituent constants and resonance and field parameters. *Chem. Rev.* **91**, 165–195 (1991). doi: 10.1021/cr00002a004
46. M. Valiev *et al.*, NWChem: A comprehensive and scalable open-source solution for large scale molecular simulations. *Comput. Phys. Commun.* **181**, 1477–1489 (2010). doi: 10.1016/j.cpc.2010.04.018
47. F. Pedregosa *et al.*, Scikit-learn: Machine learning in Python. *J. Mach. Learn. Res.* **12**, 2825–2830 (2011).
48. Denmark Lab Chemoinformatics, ccheminfolib, Project ID 8113486, GitLab (2018); https://gitlab.com/SEDenmarkLab/ccheminfolib.
49. F. Chollet, Keras: Deep learning for humans, GitHub; https://github.com/fchollet/keras.

ACKNOWLEDGMENTS

We thank K. A. Robb and Z. Wickenhauser for experimental assistance and N. Russell for informative discussions about machine learning. We are also grateful for the support services of the NMR, mass spectrometry, and microanalytical laboratories of the University of Illinois at Urbana-Champaign. **Funding:** We are grateful for generous financial support from the W. M. Keck Foundation. A.F.Z. is grateful to the University of Illinois for graduate fellowships. Y.W. thanks Janssen Research Development, San Diego, CA, for a postdoctoral fellowship. **Author contributions:** A.F.Z. contributed to catalyst synthesis, acquisition of experimental selectivity data, and computer modeling and composed the manuscript. J.J.H. contributed to creating ccheminfolib, designing and implementing the ASO descriptors, and revising the manuscript. B.T.R., Y.W., and W.T.D. contributed to catalyst synthesis. S.E.D. secured funding, supervised the project, analyzed data, and revised the manuscript. **Competing interests:** The authors declare no competing interests. **Data and materials availability:** Full experimental procedures, characterization data, and copies of ^{1}H, ^{13}C, ^{31}P, and ^{19}F spectra can be found in the supplementary materials, along with analytical supercritical fluid chromatography traces of all products. The computer code used in these studies is available in GitLab (*48*).

SUPPLEMENTARY MATERIALS

www.sciencemag.org/content/363/6424/eaau5631/suppl/DC1
Materials and Methods
Supplementary Text
Figs. S1 to S10
Table S1
References (*50*–*86*)
Data S1 to S3

22 June 2018; accepted 3 December 2018
10.1126/science.aau5631

Downloaded from http://science.sciencemag.org/ on January 18, 2019

RESEARCH ARTICLE SUMMARY

NEUROSCIENCE

Cerebellar modulation of the reward circuitry and social behavior

Ilaria Carta*, Christopher H. Chen*, Amanda L. Schott, Schnaude Dorizan, Kamran Khodakhah†

INTRODUCTION: Although the cerebellum has long been considered to be a purely motor structure, recent studies have revealed that it also has critical nonmotor functions. Cerebellar dysfunction is implicated in addictive behavior and in mental disorders such as autism spectrum disorder (ASD), cognitive affective syndrome, and schizophrenia. The cerebellum is well poised to contribute to behavior because it receives a wide array of cortical and sensory information and is subject to control by a number of neuromodulators. To perform its function, the cerebellum is believed to integrate these diverse inputs to provide the rest of the brain with predictions required for optimal behavior. Although there are many pathways for this to occur in the motor domain, fewer exist for the nonmotor domain.

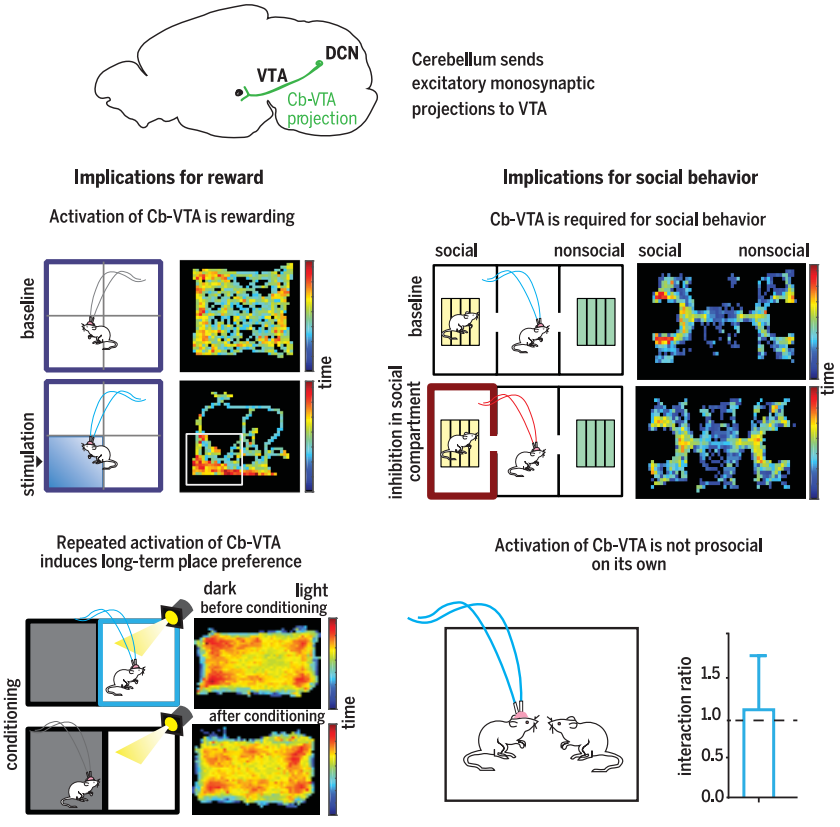
RATIONALE: There are no direct pathways emanating from the cerebellum that have been shown to serve nonmotor functions. We hypothesized that the cerebellum may contribute to motivated behavior by a direct projection to the ventral tegmental area (VTA), a structure that is critical for the perception of reward and control of social behaviors. Such a projection would explain why functional imaging experiments indicate that the cerebellum plays a role in addiction and would provide one potential mechanism by which cerebellar dysfunction might contribute to the symptoms of mental disorders.

RESULTS: In mice, we found that monosynaptic excitatory projections from the cerebellar nuclei to the VTA powerfully activate the reward circuitry and contribute to social behavior. Using anatomical tracing, we showed that axonal projections from the cerebellar nuclei form synapses with both dopaminergic and nondopaminergic neurons in the VTA. The cerebello-VTA (Cb-VTA) projections were powerful and their optogenetic stimulation robustly increased the activity of VTA neurons both in vivo and in vitro. Behavioral tests to examine reward processing showed that stimulation of the Cb-VTA projections was sufficient to cause short-term and long-term place preference, thereby demonstrating that the pathway was rewarding. Although optogenetic inhibition of Cb-VTA projections was not aversive, it completely abolished social preference in the three-chamber test for sociability, which suggests that the cerebellar input to the VTA is required for normal social behavior. A role for the cerebellum in social behavior was also indicated by correlation between calcium activity in these axons and performance in the three-chamber test. However, optogenetic activation of the Cb-VTA inputs was not prosocial, hence the pathway was not sufficient for social behavior.

ON OUR WEBSITE

Read the full article at http://dx.doi.org/10.1126/science.aav0581

CONCLUSION: The Cb-VTA pathway described here is a monosynaptic projection from the cerebellum to a structure known primarily for its nonmotor functions. Our data support a role for the cerebellum in reward processing and in control of social behavior. We propose that this Cb-VTA pathway may explain, at least in part, the association between the cerebellum and addictive behaviors, and provides a basis for a role for the cerebellum in other motivated and social behaviors. In addition to contributing to reward processing, the VTA also targets a number of other brain regions, such as the prefrontal cortex, that in turn sustain a large repertoire of motor and nonmotor behaviors. Direct cerebellar innervation of the VTA provides a pathway by which the cerebellum may modulate these diverse behaviors. The Cb-VTA pathway delineated here provides a mechanism by which cerebellar dysfunction, by adversely affecting the VTA and its targets, might contribute to mental disorders such as ASD and schizophrenia. ■



The cerebellum sends direct excitatory projections to the ventral tegmental area (Cb-VTA). These projections likely play a role in reward processing and addictive behavior, are required (but not sufficient) for social behavior, and may constitute one of the major pathways by which cerebellar dysfunction contributes to mental disorders.

The list of author affiliations is available in the full article online.
*These authors contributed equally to this work.
†Corresponding author. Email: k.khodakhah@einstein.yu.edu
Cite this article as I. Carta *et al.*, *Science* **363**, eaav0581 (2019). DOI: 10.1126/science.aav0581

Downloaded from http://science.sciencemag.org/ on January 18, 2019

RESEARCH ARTICLE

NEUROSCIENCE

Cerebellar modulation of the reward circuitry and social behavior

Ilaria Carta[1]*, Christopher H. Chen[1]*, Amanda L. Schott[1], Schnaude Dorizan[1], Kamran Khodakhah[1,2,3]†

The cerebellum has been implicated in a number of nonmotor mental disorders such as autism spectrum disorder, schizophrenia, and addiction. However, its contribution to these disorders is not well understood. In mice, we found that the cerebellum sends direct excitatory projections to the ventral tegmental area (VTA), one of the brain regions that processes and encodes reward. Optogenetic activation of the cerebello-VTA projections was rewarding and, in a three-chamber social task, these projections were more active when the animal explored the social chamber. Intriguingly, activity in the cerebello-VTA pathway was required for the mice to show social preference in this task. Our data delineate a major, previously unappreciated role for the cerebellum in controlling the reward circuitry and social behavior.

The cerebellum is perhaps most appreciated for its role in motor coordination (*1*). However, there is ample evidence to suggest that the cerebellum also contributes to a myriad of nonmotor functions. Human functional magnetic resonance imaging (fMRI) studies show robust cerebellar activation associated with addiction (*2*–*4*), social cognition (*5*), and even emotional processing (*6*). Conversely, cerebellar lesions or resections can lead to various forms of cognitive impairment and abnormal social behavior (*7*). Cerebellar abnormalities are linked to autism spectrum disorders (ASD) and schizophrenia (*8*–*25*). However, despite the associations between the cerebellum and ASD, schizophrenia, and addiction, the role that the cerebellum plays in these conditions is not clear.

A potential common thread might be an adverse impact of the cerebellum on the association, processing, perception, and/or interpretation of reward in these disorders. Functional imaging studies have highlighted a disruption in the reward system in individuals suffering from schizophrenia (*26*, *27*) or ASD (*28*, *29*), which suggests that people affected by either condition are unable to distinguish between positive and negative valence of cues. In rodents, decades-old data suggest that stimulation of the cerebellar nuclei is rewarding (*30*, *31*), and it has been shown that cerebellar granule cells encode expectation of reward (*32*) and that climbing fibers encode a temporal-difference prediction error similar to that seen in the dopaminergic neurons embedded at the heart of the reward circuitry (*33*). Collectively, these observations suggest that cerebellar activity might somehow impinge on reward processing in the brain.

The brain-wide dopaminergic projections of the ventral tegmental area (VTA) constitute one of the major pathways by which the brain controls reward and motivational and social behaviors (*34*–*36*). Indeed, a role for the VTA in addiction is well established (*37*). The VTA also has robust projections to the prefrontal cortex (*38*), which is thought to mediate many of the higher-order functions. Compromised dopaminergic function, including alterations in dopaminergic signaling in the prefrontal cortex, has been noted in a number of individuals suffering from schizophrenia and ASD (*26*, *39*, *40*).

Repeated stimulation of the cerebellum increases dopamine in the mouse medial prefrontal cortex (*41*). More intriguingly, the cerebellum's ability to do so is compromised in several mouse models of ASD (*42*). It was thus proposed that modulation of the VTA might be one of the mechanisms engaged by the cerebellum to increase dopamine in the prefrontal cortex. However, the pathways proposed for cerebellar modulation of the VTA are indirect (cerebellum→ reticulotegmental nucleus → pedunculopontine nucleus → VTA) and do not envision a direct projection from the cerebellum to the VTA (*41*–*43*). We explored the possibility that there might be a direct cerebello-VTA (Cb-VTA) pathway that allows for robust cerebellar modulation of the reward circuitry and social behavior.

Cerebellar projections to the VTA reliably drive activity in vivo

To explore the presence and delineate the efficacy of direct cerebellar projections to the VTA, we expressed channelrhodopsin (ChR2) in the cerebellum by injecting an adeno-associated virus carrying channelrhodopsin2 and yellow fluorescent protein (AAV1-hSyn-ChR2-YFP) into the deep cerebellar nuclei (DCN) (Fig. 1A). In agreement with prior observations (*44*–*47*), cerebellar axons were present in the VTA (fig. S1C). We performed single-unit recordings in the VTA of awake, head-restrained mice (Fig. 1, A and B, and fig. S1). Activation of ChR2-expressing axons near the recording site with 1-ms pulses of light rapidly increased firing (mean latency, 5.9 ± 0.5 ms; median, 6 ms; number of cells n = 117; number of animals N = 17) in about one-third of the VTA neurons examined (Fig. 1, B to F). This finding suggested that the cerebellar fibers in the VTA could, in principle, make functional synapses with the neurons in the VTA. Because cerebellar output neurons are spontaneously active and can fire action potentials at tens of spikes per second, we explored whether the Cb-VTA synapses could follow repeated activation. We thus monitored the activity of VTA neurons in response to a train of stimuli (Fig. 1G). After the initial response, a few of the subsequent responses depressed with repeated stimulation; however, the remaining stimuli reliably drove activity even at the end of the 1-s, 20-Hz train (Fig. 1, G to I, and fig. S1, D and E).

Monosynaptic cerebellar inputs to the VTA are glutamatergic

To confirm that cerebellar neurons made monosynaptic connections with the neurons in the VTA, and to explore the nature of the transmitter at the Cb-VTA synapses, we performed patch-clamp recordings in acutely prepared VTA slices from mice injected with AAV1-hSyn-ChR2-YFP in the DCN (Fig. 2A). In the cell-attached configuration, optogenetic activation of cerebellar axons in the VTA caused patched neurons to fire a number of action potentials, indicating that the cerebellar projections are strong enough to drive activity in the VTA without the need for additional inputs from other regions (Fig. 2B). In the whole-cell voltage-clamp configuration, 1-ms light pulses elicited excitatory postsynaptic currents (EPSCs) in about half of the cells recorded (23/50 cells). At −70 mV, the EPSCs had a fast decay time constant [τ = 3.6 ± 0.6 ms (SEM), n = 10] and the currents were effectively blocked by cyanquixaline (CNQX), which blocks both AMPA (α-amino-3-hydroxy-5-methyl-4-isoxazolepropionic acid)–mediated and kainate-mediated currents. [n = 9; pre-CNQX, 211 ± 50 pA (SEM); post-CNQX, 15 ± 3 pA; Fig. 2C]. Setting the command voltage to a potential of +50 mV revealed a second, slower decay time constant (τ = 52.7 ± 14.5 ms), which was blocked by the NMDA (*N*-methyl-D-aspartate) receptor blocker AP5 (Fig. 2, E and F).

To directly explore whether the EPSCs were generated by monosynaptic connections between cerebellar projections and VTA neurons, we blocked voltage-gated sodium channels with tetrodotoxin (TTX). Doing so prevented the generation of action potentials and eliminated optogenetically evoked responses in the patched cells. However, subsequent addition of the potassium channel blocker 4-AP to the bathing

[1]Dominick P. Purpura Department of Neuroscience, Albert Einstein College of Medicine, New York, NY 10461, USA. [2]Department of Psychiatry and Behavioral Sciences, Albert Einstein College of Medicine, New York, NY 10461, USA. [3]Saul R. Korey Department of Neurology, Albert Einstein College of Medicine, New York, NY 10461, USA.
*These authors contributed equally to this work.
†Corresponding author. Email: k.khodakhah@einstein.yu.edu

Downloaded from http://science.sciencemag.org/ on January 18, 2019

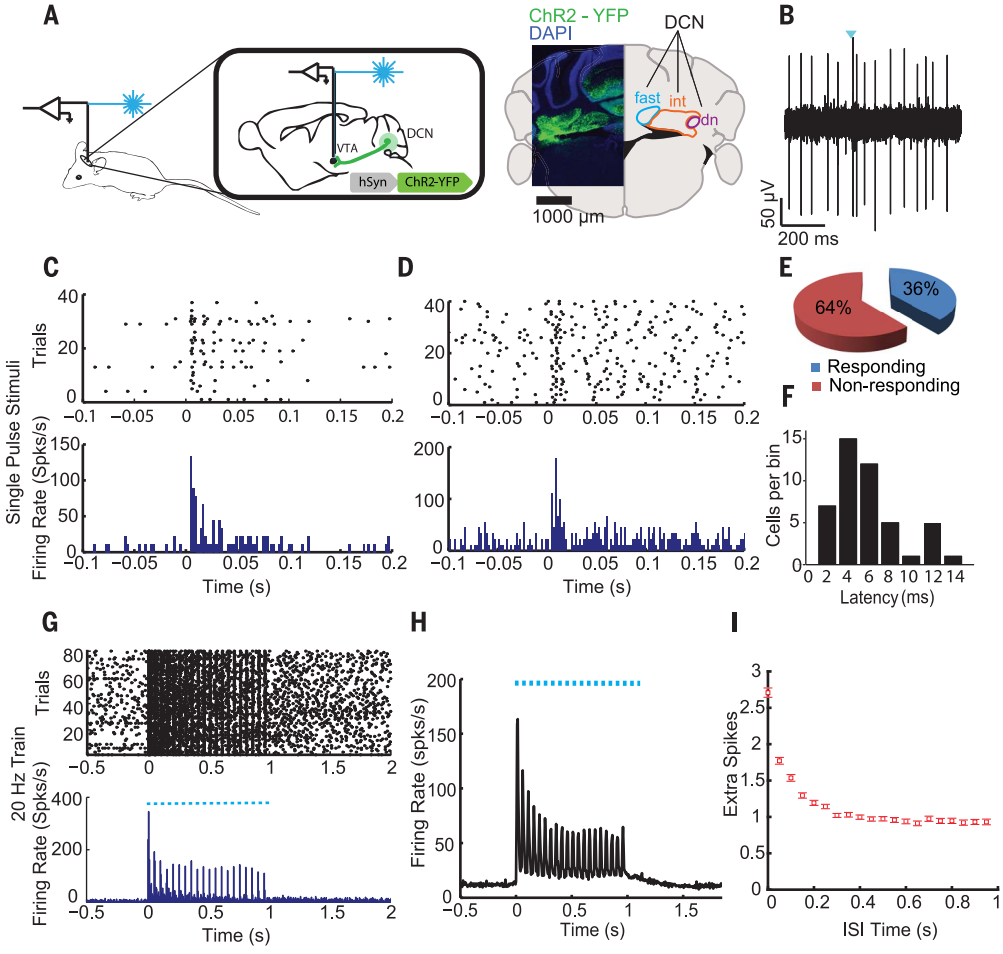


Fig. 1. Optogenetic activation of cerebellar axons in the VTA drives VTA activity in vivo. (**A**) ChR2 was expressed in the DCN. An optrode was lowered into the VTA to simultaneously stimulate cerebellar axons in the VTA and record single-unit activity of VTA neurons. An example injection site is shown at the right (fast, fastigial nucleus; int, interposed nuclei; dn, dentate nucleus). DAPI, 4′,6-diamidino-2-phenylindole. (**B**) Example single-unit recording from the VTA. The timing of the stimulus (1 ms, 2 mW) is indicated by the blue triangle. (**C** and **D**) Example activity rasters and resulting firing-rate histograms following repeated trials of single-pulse optical stimulation of cerebellar axons in two neurons in the VTA. Stimulus was delivered at time zero. (**E**) Pie chart showing response of VTA cells to optogenetics activation of cerebellar axons in the VTA (n = 103, N = 14). (**F**) Latency histogram of VTA neurons excited by optogenetic activation of cerebellar axons in the VTA [mean latency, 5.9 ± 0.5 ms (SEM); median, 6 ms]. (**G**) Example raster and firing-rate histogram following a 20-Hz train of light pulses to optogenetically activate cerebellar axons in the VTA. Train begins at time zero; each pulse is indicated by a blue marker. (**H**) Average response to 20-Hz trains in all VTA neurons examined (n = 14, N = 3). Train begins at time zero; each pulse is indicated by a blue marker. (**I**) Average extra spikes elicited by a 20-Hz train (n = 14, N = 3; means ± SEM).

solution, intended to increase the magnitude and prolong the duration of optogenetically evoked depolarizations in the cerebellar axons, recovered the synaptic responses in all cases examined (Fig. 2D, n = 9). Because no action potentials could be generated in the continued presence of TTX, the finding that 4-AP recovered the EPSCs indicated that the ChR2-expressing cerebellar axons in the VTA made monosynaptic connections with the VTA neurons.

We further examined the properties of the Cb-VTA synapses by applying stimulation trains of varying frequencies. In agreement with our observation in driving neuronal activity with stimuli trains in vivo, although the EPSCs initially depressed with repeated stimulation, thereafter they remained constant for all train frequencies examined (5, 10, and 20 Hz; Fig. 2G).

The VTA is populated by different cell types: About 60% are dopaminergic, 35% are GABAergic, and a small fraction are glutamatergic neurons (*48*). In a subset of experiments, we post hoc examined whether the responsive cells were dopaminergic by staining for tyrosine hydroxylase (TH). Although the bulk of the responsive cells were TH-positive, a number of responsive neurons were TH-negative (Fig. 2H), which suggests that it is unlikely that the cerebellum selectively targets specific neuron types in the VTA.

We also used an anatomical approach to explore the Cb-VTA projections. We injected the green fluorescent protein (GFP)–tagged H129 strain of the anterograde trans-synaptic tracer herpes simplex virus type 1 (H129-GFP) into the cerebellar nuclei and examined GFP expression in the VTA 50 hours after surgery (N = 5; Fig. 2I). This time point was chosen because 50 hours of incubation allows the virus to jump only a single synapse (fig. S2). In agreement with the electrophysiological data delineated above, we found that the virus transfected both dopaminergic and nondopaminergic neurons in the VTA (Fig. 2I).

Cerebellar inputs to the VTA are rewarding

The VTA is involved in reward (*49*), and direct stimulation of the VTA cell bodies and the medial forebrain bundle is rewarding in rodents (*50*, *51*). Given the efficacy of cerebellar projections in increasing the firing rate of the VTA neurons, it is plausible that their activity may be rewarding. A common paradigm to explore whether a pathway is rewarding is to examine

Downloaded from http://science.sciencemag.org/ on January 18, 2019

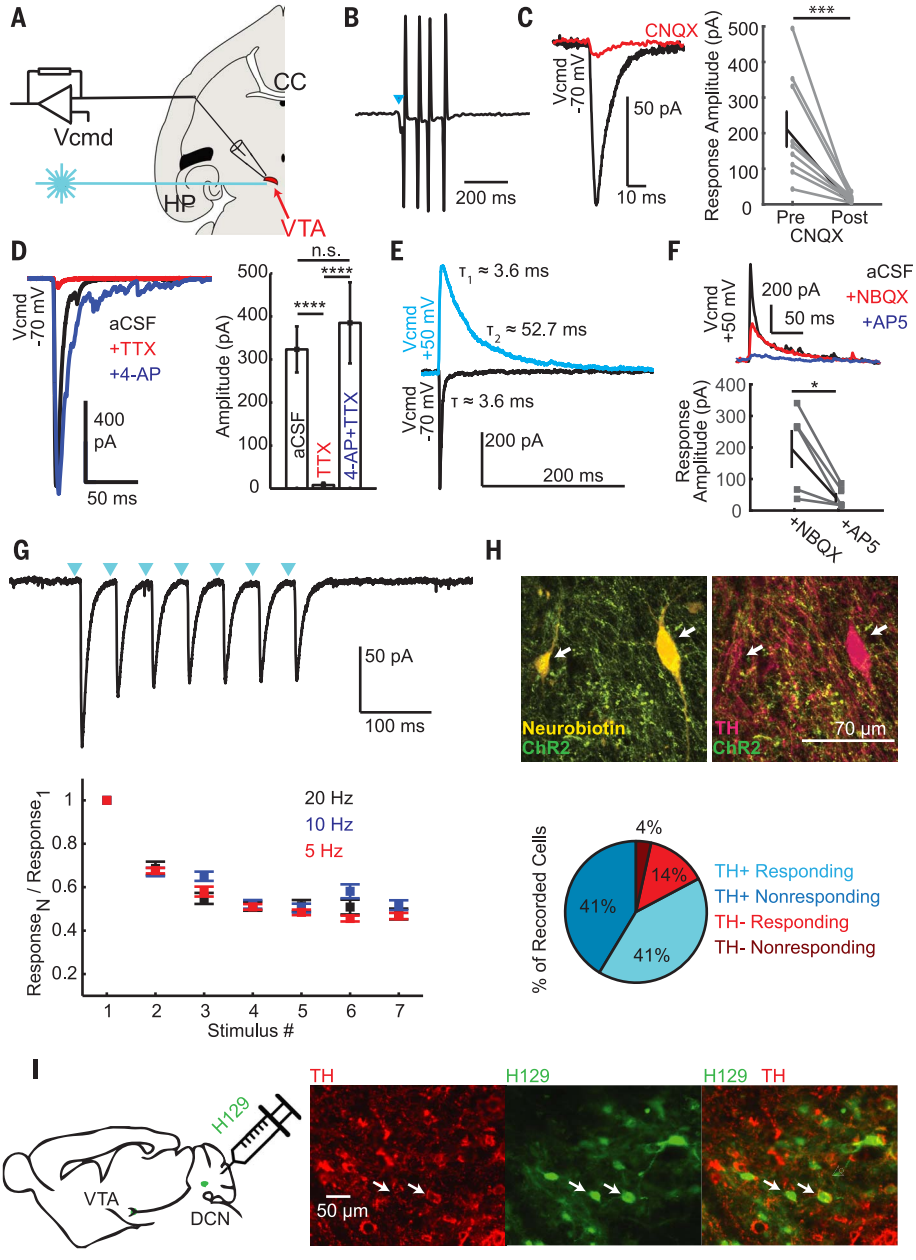


Fig. 2. Cerebellar axons in the VTA form monosynaptic glutamatergic synapses. (**A**) ChR2 was expressed in the DCN. Whole-cell recordings were made in the VTA (indicated in red). Blue light (447 nm) was delivered through the objective to stimulate cerebellar axons in the VTA. The cells were voltage-clamped at a command potential (Vcmd) of −70 mV or +50 mV, as noted. HP, hippocampus; CC, corpus callosum. (**B**) Cells in the VTA fired action potentials in response to stimulation of cerebellar axons in cell-attached recordings. Blue triangle indicates timing of the 1-ms laser pulse. (**C**) Optogenetic activation of cerebellar axons in the VTA resulted in EPSCs in the VTA neurons that were blocked by CNQX. Left: Response of a VTA neuron clamped at −70 mV to stimulation of cerebellar axons before (black) and after (red) bath application of CNQX. Right: Average decrease in response amplitude after application of CNQX. Each symbol represents a cell; data are means ± SEM (n = 9, Wilcoxon signed rank test). (**D**) Optogenetically activated responses were monosynaptic. Optically evoked responses were blocked by bath application of 1 µM TTX. Responses could be recovered with subsequent application of 200 µM 4-AP. Left: Response example. Right: Summary data for cells recorded in artificial cerebrospinal fluid (aCSF) (n = 24), TTX (n = 9), and 4-AP + TTX (n = 11) (Wilcoxon rank sum test). (**E**) When the VTA neurons were clamped at +50 mV (blue), a second, slower decay time constant was observed in addition to the fast decay time constant seen at a holding potential of −70 mV (black, n = 10), which corresponded with the AMPA-mediated component. (**F**) Currents observed at +50 mV are due to NMDA; NMDA currents were isolated using NBQX and blocked by AP5. Top: Example currents at +50 mV. Bottom: Group data. Each symbol represents a cell; data are means ± SEM (n = 5, Wilcoxon signed rank test). (**G**) Cerebellar inputs to the VTA show synaptic depression. An example 20-Hz stimulus trace is shown on top. Average responses to 5, 10, and 20 Hz trains (n = 5, 6, 11, respectively) are shown. (**H**) Cerebellar stimulation produces responses in both TH^+ and TH^- neurons in the VTA. Cells within the VTA were whole-cell patch-clamped with an internal solution containing neurobiotin and post hoc stained for TH (n = 29). Two example cells (indicated by white arrows) are shown; one was co-stained with TH (right) while the other was not (left). Approximate response percentages are shown below; the proportion of responding TH^+ cells was not significantly different from the proportion of TH^- cells (χ^2 test). (**I**) Anterograde trans-synaptic tracing indicates that the cerebellum sends inputs to both TH^+ and TH^- neurons within the VTA. A GFP-tagged H129 strain of herpes simplex virus type 1 (H129-GFP) was injected into the DCN and incubated for 50 hours, which is sufficient time to cross only one synapse (fig. S2). *P < 0.05, ***P < 0.001, ****P < 0.0001; n.s., not significant.

whether test subjects voluntarily self-stimulate to activate the pathway. We expressed channelrhodopsin in the cerebellar output neurons of mice and bilaterally implanted optical fibers targeting the VTA, thereby allowing selective stimulation of the cerebellar axon terminals in the VTA (Fig. 3, A to C). Test animals were allowed to freely explore a square behavioral chamber. After a baseline period, one quadrant was randomly assigned as the "reward quadrant"; every time the animal entered the target quadrant, it automatically received a train of light pulses that activated cerebellar axons in the VTA. The train of light pulses was repeated every 10 s as long as the animal remained in the reward quadrant. In every case examined (N = 22), the mouse showed strong preference for the reward quadrant, and on average spent more than 70% of time in that area (Fig. 3, D, E, and Q). Control GFP-expressing mice that were similarly stimulated did not show a preference for the reward quadrant (N = 12; Fig. 3Q and fig. S3). Optogenetic stimulation of the cerebellar axons in the VTA was as rewarding as direct optogenetic stimulation of dopaminergic neurons in the VTA (N = 8; Fig. 3, F, G, H, and Q). At the intensities

Downloaded from http://science.sciencemag.org/ on January 18, 2019

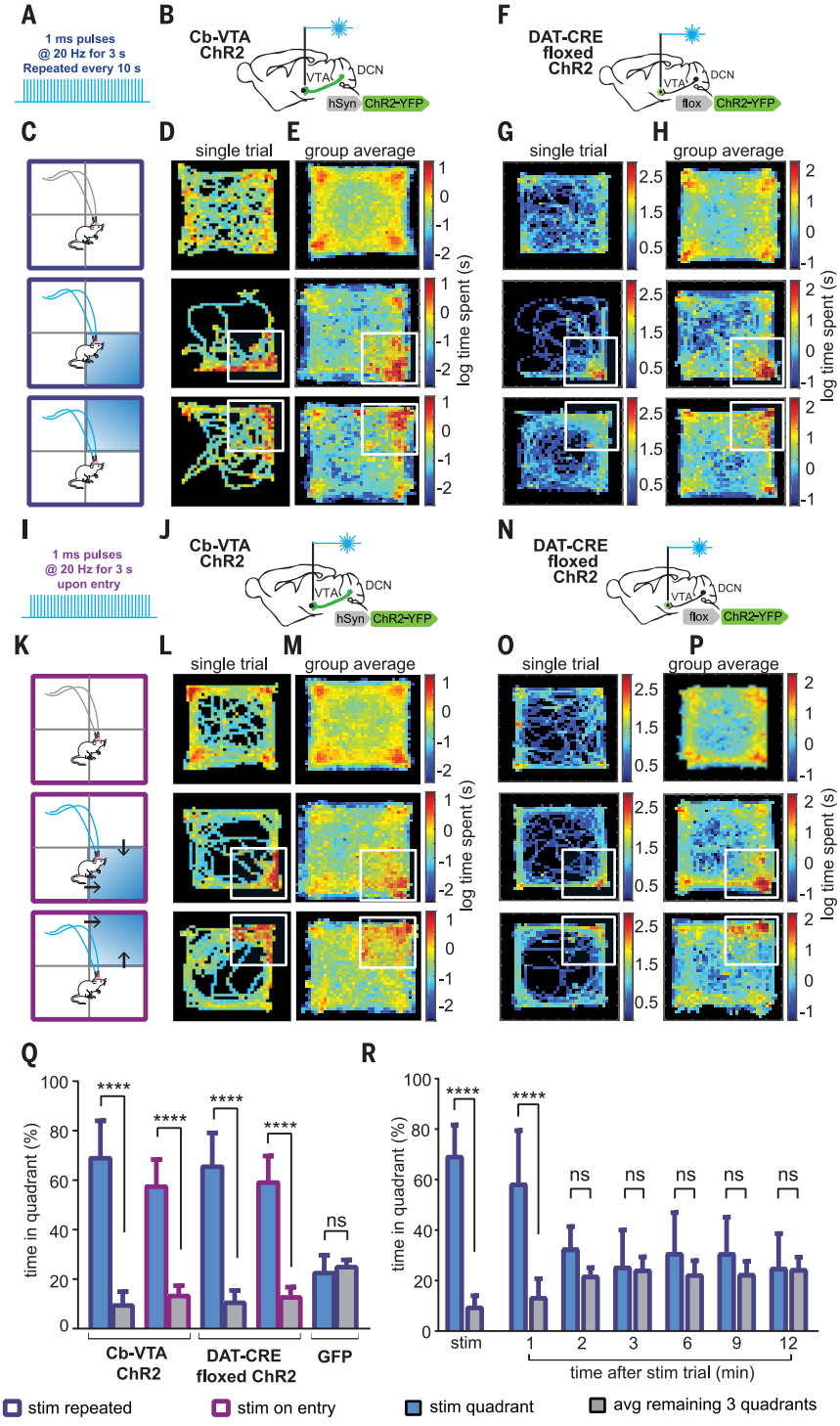


Fig. 3. Stimulation of cerebellar axons in the VTA is rewarding. (**A**) Optogenetic stimulation protocol. A train of 1-ms pulses at 20 Hz for 3 s was delivered repeatedly every 10 s in a randomly assigned quadrant of the experimental chamber. (**B** and **J**) ChR2 was expressed in the DCN and fiber optics were bilaterally implanted targeting the VTA. (**C**) Mice were placed in a square chamber and allowed to explore it at will. After obtaining a 10-min baseline (top), one of the quadrants was randomly chosen as the reward quadrant and the mice were allowed to explore for another 10 min (middle). Upon entry into the reward quadrant, cerebellar axons in the VTA were optically stimulated as described in (A). This stimulus was repeated every 10 s as long as the mouse stayed in the reward quadrant. Afterward (bottom), the reward quadrant was reassigned to a different quadrant in the chamber and the experiment repeated. (**D** and **E**) Mice expressing ChR2 in the Cb-VTA pathway exhibited a marked preference for the reward quadrant. (D) Single-trial example. (E) Average of all mice during the behavioral task outlined above. Here and below, the reward quadrant is indicated by the white box. (**F** and **N**) In a cohort of DAT-CRE mice, ChR2 was expressed in the VTA dopaminergic cells and fiber optics were bilaterally implanted targeting the VTA. (**G** and **H**) DAT-CRE mice expressing ChR2 in dopaminergic cells exhibited a preference for the reward quadrant. (G) Single-trial example. (H) Average of all mice during the behavioral task. (**I**) Variation of optogenetic stimulation protocol in (A): A train of 1-ms pulses at 20 Hz for 3 s was delivered only upon entry in a chosen quadrant of the test arena. (**K**) Behavioral paradigm as in (C). However, the stimulus was delivered only upon entry into the chosen quadrant. To receive more stimulation, the mice are required to leave and reenter the quadrant. (**L** and **M**) Mice expressing ChR2 in the Cb-VTA pathway exhibited a preference for the reward quadrant in the modified self-stimulation task. (L) Single-trial example. (M) Average session across all mice tested. (**O** and **P**) DAT-CRE mice expressing ChR2 in dopaminergic VTA cells exhibited a preference for the reward quadrant in the modified self-stimulation task. (O) Single-trial example. (P) Average session across all mice tested. (**Q**) When stimulated with the protocol in (A), mice expressing ChR2 in the Cb-VTA pathway exhibited a strong preference for the reward quadrant (N = 22); DAT-CRE mice exhibited a similar preference (N = 8). When stimulated with the protocol in (I), both groups exhibited a strong preference for the reward quadrant [Cb-VTA, N = 17 (16 with bilateral, 1 with unilateral implant) DAT-CRE, N = 8]. GFP-expressing animals stimulated with the protocol in (A) did not show a preference for any of the quadrants (N = 12). Stimulation trials 1 and 2 were averaged. Data are means ± SD [two-way analysis of variance (ANOVA) followed by Bonferroni post hoc test]. (**R**) After each stimulation trial, a subset of mice expressing ChR2 in the Cb-VTA pathway was examined for an additional 15 min without delivering additional laser stimulations. A residual preference for the last reward quadrant was noted only during the first minute (N = 16). Stimulation trials 1 and 2 were averaged. Data are means ± SD (two-way ANOVA followed by Bonferroni post hoc test). ****P < 0.0001.

used, light pulses did not have any adverse effects on the speed at which the mice explored the chamber (fig. S4, I to L) or on their motor coordination (fig. S4, M and N).

The self-stimulation task described above is reminiscent of a real-time place preference. In a subset of animals, we determined the length of time after the self-stimulation trial that the mice sought the reward quadrant by allowing them to explore the chamber without delivering any stimulation pulses (N = 16; Fig. 3R). The mice preferred the prior reward quadrant only for a brief period of time, and within minutes they resumed unbiased exploration of all quadrants.

In a slightly modified test, mice had to work harder to get repeated rewards. Mice only received one train of stimuli upon entry to the

Downloaded from http://science.sciencemag.org/ on January 18, 2019

reward quadrant. To receive the stimulation again, they had to leave the quadrant and reenter it (Fig. 3, I to K, and movie S1). With this paradigm as well, mice spent most of their time in the stimulation area (N = 17; Fig. 3, L, M, and Q), which suggests that activation of the cerebellar projections to the VTA is so rewarding that mice will readily and repeatedly work to self-stimulate. This is consistent with previous observations that rats self-stimulate their cerebellar nuclei (*31*).

We used conditioned place preference to examine the rewarding value of optogenetic activation of cerebellar axons in the VTA. Mice expressing ChR2 in their cerebellar axons could freely explore a rectangular experimental chamber, half of which was dark while the other half was brightly lit. Because mice naturally prefer dark places, they spent a larger fraction of time exploring the dark side of the chamber. The mice then underwent conditioning whereby on alternate days they were confined to the bright chamber for 30 min and bilateral fiber optics targeting the VTA delivered 3-s trains of light stimuli at 20 Hz every 10 s to activate the ChR2-expressing cerebellar axons (N = 12; Fig. 4, A to C). After conditioning, mice were allowed to freely explore the entire chamber. Mice spent substantially more time in the bright compartment of the chamber after conditioning (Fig. 4, D and E). GFP control mice were not affected by the conditioning and maintained their bias for the dark side (N = 9; Fig. 4E).

Cerebellar inputs to the VTA contribute to social behavior

Cerebellar activation is observed in humans during social cognition tasks (*52*). Recent evidence has also demonstrated a role for the VTA in social behavior (*34*), although it is not known which of the VTA inputs contribute to social behavior. We postulated that the cerebellar projections to the VTA may contain information relevant for social behavior. Historically, the cerebellum has been thought to be a neuronal learning machine (*1*, *53*) whose function is to learn, and subsequently recognize, associations among a wide range of sensory and cortical information to predict the next set of "command" signals that are needed to coordinate body posture and movement. One can imagine that the same model can, in principle, be adopted to account for the nonmotor cognitive and behavioral functions of the cerebellum. For example, cerebellar circuitry could transform the wide-ranging information it receives into predictions about social reward likelihood. Given that the cerebellum receives inputs from virtually all sensory modalities and cortical regions, it certainly has the appropriate contextual information to perform such a task.

We used the three-chamber social task (*54*), the most widely used and accredited test for social behavior, which has been routinely used to delineate social deficits in rodent models of ASD. A mouse freely explores three connected chambers. The central chamber is empty, whereas the two side chambers contain either an unfamiliar juvenile mouse placed inside a small holding cage (the social chamber) or an empty holding cage (the object chamber). Mice actively explore all three chambers but typically spend the majority of their time in the social chamber (*54*). We postulated that cerebellar inputs to the VTA may provide information that contributes to, or at the very least is relevant for, expression of social behavior. We therefore optogenetically inhibited the activity of cerebellar axons in the VTA as mice performed the task (Fig. 5 and figs. S6 and S7, A to C).

In one group of mice, we injected a virus (AAV5-CAG-ArchT-GFP) containing archaerhodopsin (ArchT) into the cerebellum, and bilaterally implanted fiber optics that targeted the VTA. In baseline conditions, the mice preferred to spend more time in the social chamber than in the object chamber. Once we had established the baseline, we optogenetically silenced the Cb-VTA projections when the mice entered the social chamber (Fig. 5, A to C). When cerebellar axons in the VTA were optically silenced, the mice no longer showed a preference for the social chamber and spent equal time in the social and object chambers (N = 11; Fig. 5, D to F). There was no change in the social preference of control GFP-expressing mice tested under identical conditions (Fig. 5F).

A similar outcome would be expected if silencing of the Cb-VTA projection is aversive. Direct inhibition of VTA neurons is aversive (*55*). It is possible that a continuous input from the cerebellum to the VTA might be required to sustain spontaneous activity of VTA neurons. Thus, by inhibiting the activity of the Cb-VTA pathway in the social chamber, we might have thus prompted the mice to spend less time in the social chamber. We therefore used the "self-stimulation"

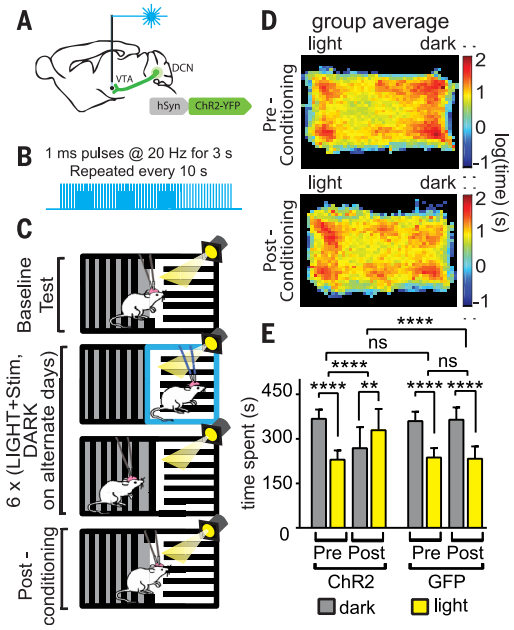


Fig. 4. Activation of cerebellar inputs to VTA promotes conditioned place preference. (**A**) ChR2 was expressed in the DCN and fiber optics were bilaterally implanted targeting the VTA to allow optogenetic activation of cerebellar axons. (**B** and **C**) Experimental paradigm. Mice were tested in a conditioned place preference apparatus containing two chambers, differentiated by lighting conditions and walls of each chamber showing stripes of opposing orientations. On day 1, animals were allowed to freely explore the apparatus for 15 min to establish a baseline chamber preference. Beginning on day 2, mice were conditioned for 30 min per day, on 4 consecutive days, for 3 weeks. Mice were alternately restricted to either the lighted or dark chamber. While confined to the lighted chamber, subjects received 3-s, 20-Hz trains of optical stimulation, repeating every 10 s for the duration of the session. No stimulation was delivered when the subjects were restricted to the dark chamber. Twenty-four hours after the final conditioning session, mice were again allowed to explore the entire apparatus without stimulation for 15 min. (**D**) During the baseline test, mice showed a marked preference for the dark chamber. This preference was noticeably reduced after conditioning. The heat maps depict the average sessions for all mice tested. (**E**) After conditioning, the mice changed their preference for the dark chamber [N = 13 (11 with bilateral and 2 with unilateral fiber optic implants)] versus the lighted one and, on average, showed a preference for the lighted chamber. GFP control mice that underwent the same conditioning treatment maintained their bias for the dark chamber (N = 10 before and after). Therefore, the optogenetic conditioning had a significant effect on the ChR2-expressing mice but not in the GFP-expressing mice. Data are means ± SD (two-way ANOVA followed by Bonferroni post hoc test). $^{**}P < 0.01$, $^{****}P < 0.0001$.

Downloaded from http://science.sciencemag.org/ on January 18, 2019

paradigm described earlier to explore whether mice find silencing of this pathway aversive. We used the same protocol described earlier, except that we expressed ArchT rather than ChR2 in the cerebellar axons. We allowed ArchT-expressing mice to freely explore the open field chamber, and then optically silenced the Cb-VTA projections every time the mouse entered a randomly assigned quadrant. Inhibition of this pathway had no impact on exploration of the mice; the mice spent equal time in all quadrants, which suggests that inhibition of Cb-VTA projections is neither aversive nor rewarding (N = 7; fig. S5).

In a second set of three-chamber test experiments, we inhibited the Cb-VTA projection for the full duration of the task. With the pathway silenced throughout the test, even if silencing is aversive, one should not see a preferential reduction in the time spent in the social chamber because the alleged aversive stimulus is continuously present in all three chambers. However, if the inputs from the cerebellum to the VTA are required for expression of social behavior, silencing the pathway in all chambers throughout the task might be expected to be as effective as silencing it only when the mice enter the social chamber. Indeed, optogenetically silencing the Cb-VTA projections continuously was as effective in preventing the expression of the social behavior in the three-chamber task as when the optical inhibition was applied only when the mouse was in the social chamber (N = 23; Fig. 5, C to F). These experiments indicate that cerebellar inputs to the VTA are necessary for the mice to show social preference.

In these experiments, the inhibition of cerebellar inputs to the VTA seems to selectively inhibit social behavior and not exploratory behavior in general. The mice continued to explore the two side chambers and spent relatively little time in the center chamber, similar to their performance under baseline conditions. Moreover, inhibiting the pathway did not have a significant effect on the number of entries that the mice made to each compartment, nor on the amount of time that they spent grooming (Fig. 5, G and H).

We also examined whether optogenetic activation of the cerebellar axons in the VTA when the mice entered the object chamber increased the fraction of time they spent in that chamber. In a group of mice, we expressed ChR2 in the cerebellum and, as before, implanted fiber optics targeting the VTA (N = 15; Fig. 6A and fig. S7, D to F). Once we had established the baseline, we optogenetically manipulated the Cb-VTA projections by ensuring that every time the test mouse entered the object chamber, it received a train of light pulses to activate the cerebellar axons in the VTA. The stimulation was repeated every 10 s if the animal remained in the object

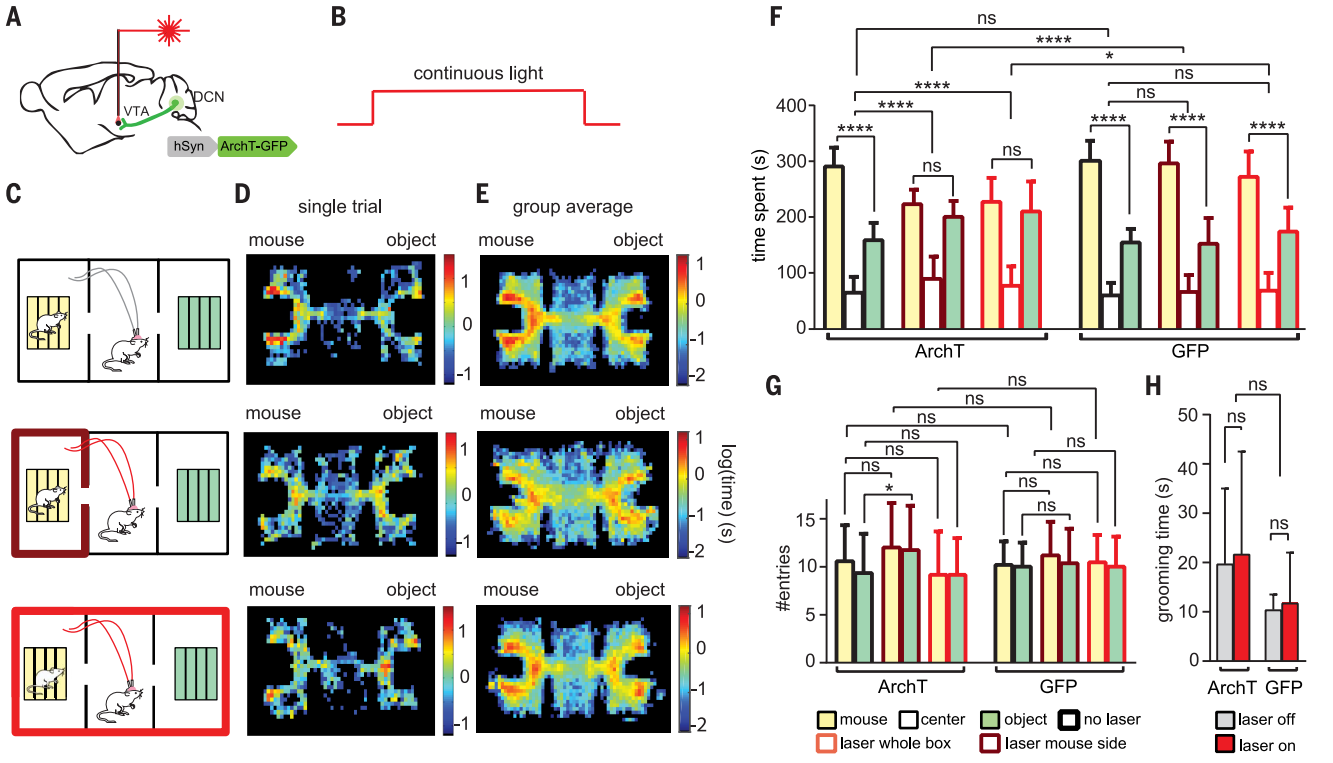


Fig. 5. Manipulating the activity of cerebellar axons in the VTA alters social preference. (**A**) ArchT was expressed in the DCN and fiber optics were bilaterally implanted targeting the VTA to allow optogenetic inhibition of cerebellar axons. (**B** and **C**) Experimental paradigm. Mice were tested using a three-chamber social task. Mice were allowed to approach a juvenile confined to one side chamber or an object placed on the opposite side chamber. On the first trial day, the mice explored the chambers at will. On the second day, a continuous light was delivered to inactivate the cerebellar axons in the VTA whenever the mouse visited the mouse chamber and was terminated immediately if the mouse exited the mouse chamber. On the third trial day, the mice were allowed to explore the chamber again while receiving continuous light independently of their location in the apparatus and for the entire 10-min trial. (**D** and **E**) Position heat maps for a single mouse (D) and average for all mice (E) during social interaction, in the absence (top row) and in the presence of optogenetic inhibition of cerebellar axons in the VTA in the mouse chamber (middle row) or in the entire field (bottom row). (**F**) Optogenetic inhibition of cerebellar axons in the VTA while the animal explored the mouse chamber made the mouse chamber less attractive than on day 1 (days 1 and 2; N = 11). Optogenetic inhibition delivered throughout the three chambers similarly decreased the preference for the social compartment (day 3; N = 20). Data are means ± SD (regular and repeated-measures two-way ANOVA followed by Bonferroni post hoc test). (**G**) Inhibition of cerebellar axons in the VTA while the animal explored the mouse chamber slightly increased the number of entries in the object chamber (N = 11); however, the number of entries in both chambers were not significantly affected by continuous light inhibition throughout the apparatus (N = 20). Data are means ± SD (two-way ANOVA followed by Bonferroni post hoc test). (**H**) Inhibition of cerebellar fibers in the VTA as the mice performed the three-chamber social task did not affect grooming time (N = 23). Data are means ± SD (two-way ANOVA followed by Bonferroni post hoc test). *P < 0.05, ****P < 0.0001.

Downloaded from http://science.sciencemag.org/ on January 18, 2019

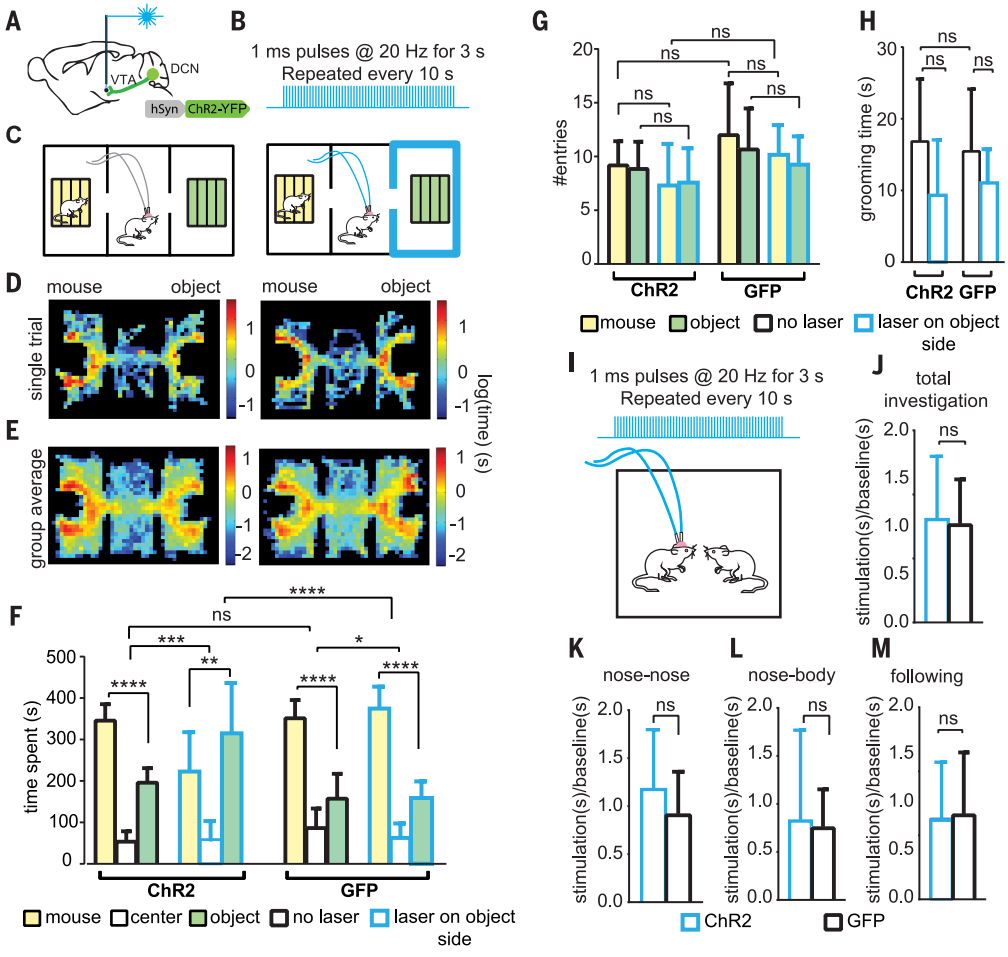


Fig. 6. Three-chamber social test: Optogenetic stimulation in the object compartment. (**A**) ChR2 was expressed in the DCN and fiber optics were bilaterally implanted targeting the VTA to allow optogenetic activation of cerebellar axons. (**B**) Stimulation paradigm. A train of 1-ms optical light pulses (20 Hz for 3 s) was delivered to activate the cerebellar axons in the VTA whenever the mouse entered the object chamber. This optical train was repeated every 10 s as long as the mouse remained in the object chamber, and was terminated immediately if the mouse exited the object chamber. (**C**) Experimental paradigm. Mice were tested using a three-chamber social task. Mice were allowed to approach a juvenile confined to one side chamber or an object placed on the opposite side chamber. On the first trial day, the mice explored the chambers at will. On the second day, mice received optogenetic stimulation in the object chamber as described in (B). (**D** and **E**) Position heat maps for a single mouse (D) and average for all mice (E) during social interaction, in the absence (left) and in the presence of optogenetic activation of cerebellar axons in the VTA (right) in the object chamber. (**F**) On day 1, during baseline testing, all groups preferred spending time in the mouse chamber rather than in the object chamber (ChR2, N = 15, GFP N = 12). On day 2, optogenetic activation of cerebellar axons in the VTA while the animal explored the object chamber made the object chamber slightly more attractive than the social chamber housing the juvenile mouse (N = 15). The same treatment did not produce any change in preference in sham GFP mice (N = 12). Data are means ± SD of time spent in the three chambers (two-way ANOVA followed by Bonferroni post hoc test). (**G**) Activation of cerebellar axons in the VTA while the animal explored the mouse chamber did not affect the number of entries in the social or in the object chamber (N = 15). Similarly, sham GFP mice were not affected by the laser stimulation (N = 12). Data are means ± SD (two-way ANOVA followed by Bonferroni post hoc test). (**H**) Activation of cerebellar fibers in the VTA as the mice performed the three-chamber social task slightly decreased grooming time relative to baseline, although not significantly (N = 15). Grooming was not affected by laser stimulation in the GFP group (N = 12). Data are means ± SD (two-way ANOVA followed by Bonferroni post hoc test). (**I**) Mice were allowed to freely interact with a juvenile mouse in an open field and received trains of stimulation every 10 s for 10 min. (**J** to **M**) Activation of cerebellar fibers in the VTA while the mice were free to interact in an open field did not significantly affect nose-nose (K) or nose-body interactions (L), following behavior (M), or total investigations (J) in ChR2-expressing mice (N = 7) relative to GFP-expressing mice (N = 8). *P < 0.05, **P < 0.01, ***P < 0.001, ****P < 0.0001.

chamber, and immediately terminated if it left the chamber (Fig. 6, B and C). Mice showed slightly greater preference for the object chamber and spent less time investigating the juvenile mouse in the social chamber, which suggests that stimulation of the VTA can be at least as rewarding as socialization (Fig. 6, D to F). In control GFP-expressing mice, stimulation did not affect performance in the three-chamber task (N = 12; Fig. 6F). Although the stimulation paradigm showed a trend toward slightly decreased grooming time, it did not affect exploration as measured by the number of entries to each compartment (Fig. 6, G and H).

These results might support the hypothesis that stimulation of the Cb-VTA projections is sufficient to promote social behavior. However, mice found stimulation of this pathway to be

Downloaded from http://science.sciencemag.org/ on January 18, 2019

rewarding in general and, as described earlier, self-stimulated. Thus, the fact that in the three-chamber test the mice spent more time in the object chamber when the pathway was optogenetically stimulated could be simply a manifestation of a form of self-stimulation. We therefore examined whether optogenetic activation of the Cb-VTA projection while the test mouse explored an open field promoted social interactions with an unfamiliar juvenile mouse. There was no evidence that optogenetic activation of the Cb-VTA projection, on its own, promoted social interactions (Fig. 6, I to M). This implies that in the three-chamber test, the mice spent equal time in the social and object chambers when the Cb-VTA projection was optogenetically activated not because the pathway is prosocial on its own, but perhaps because activation of this pathway can be as rewarding as social interaction.

Collectively, the data suggest that the cerebellar projections to the VTA provide information that is necessary, but not sufficient, for expression of social behavior. This is in contrast to projections made by the paraventricular nucleus oxytocin-releasing neurons, whose activity and release of oxytocin in the VTA is both required and sufficient for prosocial behavior (*55*).

The cerebellar inputs to the VTA are more active during social exploration

To further delineate the role of Cb-VTA projections in social behavior, it would be instructive to examine the activity of the relevant cerebellar projection neurons as the animal performs a social task. Because it is not currently feasible to identify and electrophysiologically monitor the activity of cerebellar neurons that project to the VTA, we used fiber photometry to monitor changes in calcium in cerebellar axons in the VTA as a proxy for neuronal activity. The genetically encoded calcium indicator GCaMP was expressed in the deep cerebellar nuclei, and an imaging fiber optic was implanted in the VTA (Fig. 7A, top). We first established that electrical stimulation of the cerebellum while monitoring GCaMP-expressing axons in the VTA elicited robust calcium transients (fig. S8, B to E). Using the three-chamber social task, we then monitored the changes in the calcium concentration in cerebellar axons in the VTA as the mice performed the task (Fig. 7A, bottom). The calcium levels in the cerebellar axons were higher when mice explored the social chamber (N = 8; Fig. 7, B and C, and fig. S8G).

Different mice show varying levels of social behavior. We explored whether the average calcium levels in the cerebellar axons in the VTA correlated with the fraction of time that each mouse spent in the social chamber. There was a clear correlation with the extent of activity in the Cb-VTA pathway and social preference (Fig. 7D and fig. S8H). Averaging the fluorescence in each chamber revealed that there was significantly greater activity in the social and center chambers relative to the object chamber (Fig. 7E and fig. S8G). Imaging of control mice expressing GFP instead of GCaMP in cerebellar axons in the VTA did not show the same trend (N = 7; fig. S8J). Collectively, the data suggest that the cerebellum dynamically encodes social-related signals and relays them to the VTA to modulate behavior.

Discussion

Our results demonstrate a robust projection from the cerebellum to the VTA, which is powerful enough to modulate reward-driven behavior. This pathway likely constitutes one of the projections that enable the cerebellum to contribute to nonmotor behaviors and, speculatively, may indeed be an important substrate for its role in addictive behaviors (*2*–*4*). The role of the VTA in addictive behaviors is well established (*37*), and although the cerebellum is known to encode reward-related information (*32*, *33*), the exact nature of the information that the cerebellum contributes to the reward circuitry remains to be uncovered.

The Cb-VTA pathway was more active when the mouse explored the social chamber in a

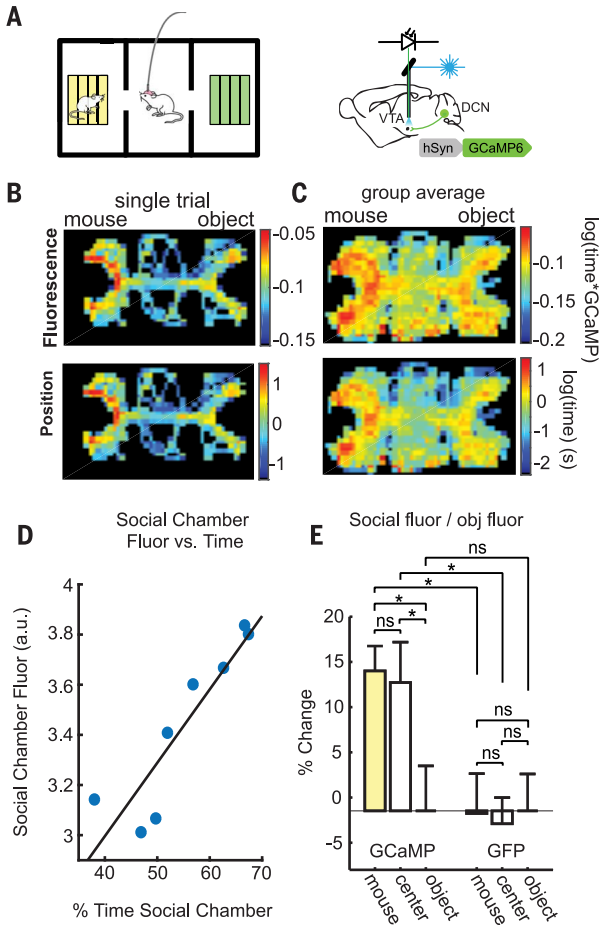


Fig. 7. Calcium activity in cerebellar axons in the VTA increases as the mice explore the social chamber. (**A**) Fiber photometry was used to monitor activity of cerebellar axons in the VTA. GCaMP6 was expressed in the DCN and an imaging fiber-optic was implanted in the VTA. Mice were tested on the same three-chamber social task described in Fig. 5, and changes in GCaMP6 fluorescence in the axons were monitored. (**B** and **C**) Mice showed greater GCaMP6 fluorescence in cerebellar axons while they explored the social chamber. (B) Single-trial example. (C) Group average of the photometry session (N = 8). Top row: Total GCaMP fluorescence with respect to position in the chamber. Bottom row: Time spent by the mouse with respect to position in the chamber during the test. (**D**) Average GCaMP fluorescence per position pixel in the social chamber correlated with the percent of time spent in the social chamber for each mouse (N = 8, R = 0.904). (**E**) Average GCaMP fluorescence per position was greater in the social chamber than in the object chamber. Fluorescence values for each chamber in the fluorescence heat maps in (C) were averaged and normalized to the fluorescence in the object chamber. There was significantly greater fluorescence in the social and central chambers between GCaMP-expressing mice (N = 8) and GFP-expressing mice (N = 7). Within the GCaMP group, there was significantly greater fluorescence between the social and central chambers relative to the object chamber (two-way ANOVA followed by Bonferroni post hoc test). *P < 0.05.

Downloaded from http://science.sciencemag.org/ on January 18, 2019

three-chamber social task. This input may be a necessary, but not sufficient, component of social behavior. Surgical cerebellar resections in adults can result in significant changes in social behavior, cognition, and emotional responses of the patients (*7*). The VTA affects social behavior via its connections with the nucleus accumbens (*34*). Thus, our findings indicate that some of the cerebellar projections probably contact the VTA neurons that project to the nucleus accumbens.

Our conclusions heavily rely on the use of optogenetics in vivo. By stimulating the cerebellar axons in the VTA, we reduced, as much as possible, unintentional nonspecific activation of other pathways. We cannot rule out the possibility that some of the behavioral effects might be the consequence of backpropagation of action potentials in the activated cerebellar axons and subsequent activation of other brain regions targeted by potential (unknown) collaterals of the Cb-VTA projection. However, slice recordings unambiguously showed the presence of strong, functional, monosynaptic projections from the cerebellum to the VTA. The most parsimonious interpretation of our data is that cerebellar activation of the VTA plays a major role in the behaviors examined here. Moreover, the silencing experiments using the inhibitory opsins do not suffer from the same caveat, thus supporting our conclusions.

It remains unclear whether the information encoded by the cerebellum and conveyed to the VTA is related to recognition of a reward cue, or to the reward associated with the cue. Some have hypothesized that the cerebellum may refine higher-order functions and behaviors as it refines movements (*13*, *56*). We favor the possibility that the cerebellar circuitry transforms the wide-ranging information it receives into predictions about reward likelihood, thereby encoding information that is necessary for expression of some forms of behavior. To differentiate between these hypotheses, and to unravel how the cerebellum contributes to reward processing and social behavior, will require a better understanding of the nature of the information encoded and conveyed from the cerebellum to the VTA and other related brain structures.

Our experimental approach treated all cerebellar projections to the VTA as a single unit. However, it is likely that the Cb-VTA projection neurons originate from different parts of the cerebellum, select neuron types within the cerebellar nuclei, follow a specific connectivity pattern with the neurons within the VTA, and convey different information. The available data suggest that all cerebellar nuclei rather diffusely contribute to the Cb-VTA projections (*44*, *46*, *47*, *57*). Nonetheless, it is plausible that a subset of neurons that form the cerebellar projections to the VTA may selectively contact the neurons that project to the nucleus accumbens and affect social behavior, others target VTA neurons that project to the prefrontal cortex, and yet others form synapses with VTA neurons that deal with other forms of reward processing.

Although our data support the function of the Cb-VTA pathway in sociability and reward, this does not exclude the possibility that other structures are also involved, nor does it limit the functions of this pathway to just those described. The VTA, for example, also sends dopaminergic projections to the prefrontal cortex, and selective activation of this pathway in mice can be aversive (*34*). We did not explore this possibility, but it is plausible that the cerebellar projections to the VTA also target the neurons that project to the prefrontal cortex, thus providing a route by which the cerebellum can affect dopamine levels in the prefrontal cortex. Further study of these pathways should delineate the functions of different outputs from the cerebellum to provide points of intervention for management of related disorders. Regardless, these are exciting times for cerebellar research, and it is clear that further studies will unveil more circuits by which the cerebellum contributes to our behaviors.

REFERENCES AND NOTES

1. M. Ito, *The Cerebellum and Neural Control* (Raven, 1984).
2. E. A. Moulton, I. Elman, L. R. Becerra, R. Z. Goldstein, D. Borsook, The cerebellum and addiction: Insights gained from neuroimaging research. *Addict. Biol.* **19**, 317–331 (2014). doi: 10.1111/adb.12101; pmid: 24851284
3. N. D. Volkow *et al*., Expectation enhances the regional brain metabolic and the reinforcing effects of stimulants in cocaine abusers. *J. Neurosci.* **23**, 11461–11468 (2003). doi: 10.1523/JNEUROSCI.23-36-11461.2003; pmid: 14673011
4. M. Miquel, R. Toledo, L. I. García, G. A. Coria-Avila, J. Manzo, Why should we keep the cerebellum in mind when thinking about addiction? *Curr. Drug Abuse Rev.* **2**, 26–40 (2009). doi: 10.2174/1874473710902010026; pmid: 19630735
5. F. Van Overwalle, K. Baetens, P. Mariën, M. Vandekerckhove, Social cognition and the cerebellum: A meta-analysis of over 350 fMRI studies. *Neuroimage* **86**, 554–572 (2014). doi: 10.1016/j.neuroimage.2013.09.033; pmid: 24076206
6. J. D. Schmahmann, D. Caplan, Cognition, emotion and the cerebellum. *Brain* **129**, 290–292 (2006). doi: 10.1093/brain/awh729; pmid: 16434422
7. J. D. Schmahmann, J. C. Sherman, The cerebellar cognitive affective syndrome. *Brain* **121**, 561–579 (1998). doi: 10.1093/brain/121.4.561; pmid: 9577385
8. E. Courchesne, R. Yeung-Courchesne, G. A. Press, J. R. Hesselink, T. L. Jernigan, Hypoplasia of cerebellar vermal lobules VI and VII in autism. *N. Engl. J. Med.* **318**, 1349–1354 (1988). doi: 10.1056/NEJM198805263182102; pmid: 3367935
9. E. Courchesne, J. R. Hesselink, T. L. Jernigan, R. Yeung-Courchesne, Abnormal neuroanatomy in a nonretarded person with autism. Unusual findings with magnetic resonance imaging. *Arch. Neurol.* **44**, 335–341 (1987). doi: 10.1001/archneur.1987.00520150073028; pmid: 3827686
10. S. S. Wang, A. D. Kloth, A. Badura, The cerebellum, sensitive periods, and autism. *Neuron* **83**, 518–532 (2014). doi: 10.1016/j.neuron.2014.07.016; pmid: 25102558
11. S. J. Webb *et al*., Cerebellar vermal volumes and behavioral correlates in children with autism spectrum disorder. *Psychiatry Res.* **172**, 61–67 (2009). doi: 10.1016/j.pscychresns.2008.06.001; pmid: 19243924
12. P. T. Tsai *et al*., Autistic-like behaviour and cerebellar dysfunction in Purkinje cell Tsc1 mutant mice. *Nature* **488**, 647–651 (2012). doi: 10.1038/nature11310; pmid: 22763451
13. N. C. Andreasen, R. Pierson, The role of the cerebellum in schizophrenia. *Biol. Psychiatry* **64**, 81–88 (2008). doi: 10.1016/j.biopsych.2008.01.003; pmid: 18395701
14. B. C. Ho, C. Mola, N. C. Andreasen, Cerebellar dysfunction in neuroleptic naive schizophrenia patients: Clinical, cognitive, and neuroanatomic correlates of cerebellar neurologic signs. *Biol. Psychiatry* **55**, 1146–1153 (2004). doi: 10.1016/j.biopsych.2004.02.020; pmid: 15184033
15. J. W. Murakami, E. Courchesne, G. A. Press, R. Yeung-Courchesne, J. R. Hesselink, Reduced cerebellar hemisphere size and its relationship to vermal hypoplasia in autism. *Arch. Neurol.* **46**, 689–694 (1989). doi: 10.1001/archneur.1989.00520420111032; pmid: 2730382
16. J. W. Jeong, V. N. Tiwari, M. E. Behen, H. T. Chugani, D. C. Chugani, In vivo detection of reduced Purkinje cell fibers with diffusion MRI tractography in children with autistic spectrum disorders. *Front. Hum. Neurosci.* **8**, 110 (2014). doi: 10.3389/fnhum.2014.00110; pmid: 24592234
17. P. E. Rasser *et al*., Cerebellar grey matter deficits in first-episode schizophrenia mapped using cortical pattern matching. *Neuroimage* **53**, 1175–1180 (2010). doi: 10.1016/j.neuroimage.2010.07.018; pmid: 20633666
18. H. Picard, I. Amado, S. Mouchet-Mages, J. P. Olié, M. O. Krebs, The role of the cerebellum in schizophrenia: An update of clinical, cognitive, and functional evidences. *Schizophr. Bull.* **34**, 155–172 (2008). doi: 10.1093/schbul/sbm049; pmid: 17562694
19. T. J. Eluvathingal *et al*., Cerebellar lesions in tuberous sclerosis complex: Neurobehavioral and neuroimaging correlates. *J. Child Neurol.* **21**, 846–851 (2006). doi: 10.1177/08830738060210100301; pmid: 17005099
20. J. Skefos *et al*., Regional alterations in purkinje cell density in patients with autism. *PLOS ONE* **9**, e81255 (2014). doi: 10.1371/journal.pone.0081255; pmid: 24586223
21. C. Bottmer *et al*., Reduced cerebellar volume and neurological soft signs in first-episode schizophrenia. *Psychiatry Res.* **140**, 239–250 (2005). doi: 10.1016/j.pscychresns.2005.02.011; pmid: 16288852
22. J. Ellegood *et al*., Clustering autism: Using neuroanatomical differences in 26 mouse models to gain insight into the heterogeneity. *Mol. Psychiatry* **20**, 118–125 (2015). doi: 10.1038/mp.2014.98; pmid: 25199916
23. R. M. Reith *et al*., Loss of Tsc2 in Purkinje cells is associated with autistic-like behavior in a mouse model of tuberous sclerosis complex. *Neurobiol. Dis.* **51**, 93–103 (2013). doi: 10.1016/j.nbd.2012.10.014; pmid: 23123587
24. L. T. Lotta, K. Conrad, D. Cory-Slechta, N. F. Schor, Cerebellar Purkinje cell p75 neurotrophin receptor and autistic behavior. *Transl. Psychiatry* **4**, e416 (2014). doi: 10.1038/tp.2014.55; pmid: 25072321
25. D. Cupolillo *et al*., Autistic-Like Traits and Cerebellar Dysfunction in Purkinje Cell PTEN Knock-Out Mice. *Neuropsychopharmacology* **41**, 1457–1466 (2016). doi: 10.1038/npp.2015.339; pmid: 26538449
26. O. D. Howes, S. Kapur, The dopamine hypothesis of schizophrenia: Version III—the final common pathway. *Schizophr. Bull.* **35**, 549–562 (2009). doi: 10.1093/schbul/sbp006; pmid: 19325164
27. J. J. Simon *et al*., Reward System Dysfunction as a Neural Substrate of Symptom Expression Across the General Population and Patients With Schizophrenia. *Schizophr. Bull.* **41**, 1370–1378 (2015). doi: 10.1093/schbul/sbv067; pmid: 26006262
28. G. S. Dichter *et al*., Reward circuitry function in autism spectrum disorders. *Soc. Cogn. Affect. Neurosci.* **7**, 160–172 (2012). doi: 10.1093/scan/nsq095; pmid: 21148176
29. G. S. Dichter, J. A. Richey, A. M. Rittenberg, A. Sabatino, J. W. Bodfish, Reward circuitry function in autism during face anticipation and outcomes. *J. Autism Dev. Disord.* **42**, 147–160 (2012). doi: 10.1007/s10803-011-1221-1; pmid: 22187105
30. D. Corbett, E. Fox, P. M. Milner, Fiber pathways associated with cerebellar self-stimulation in the rat: A retrograde and anterograde tracing study. *Behav. Brain Res.* **6**, 167–184 (1982). doi: 10.1016/0166-4328(82)90012-2; pmid: 7138644
31. G. G. Ball, D. J. Micco Jr., G. G. Berntson, Cerebellar stimulation in the rat: Complex stimulation-bound oral behaviors and self-stimulation. *Physiol. Behav.* **13**, 123–127 (1974). doi: 10.1016/0031-9384(74)90313-8; pmid: 4850937
32. M. J. Wagner, T. H. Kim, J. Savall, M. J. Schnitzer, L. Luo, Cerebellar granule cells encode the expectation of reward. *Nature* **544**, 96–100 (2017). doi: 10.1038/nature21726; pmid: 28321129
33. S. Ohmae, J. F. Medina, Climbing fibers encode a temporal-difference prediction error during cerebellar learning in mice. *Nat. Neurosci.* **18**, 1798–1803 (2015). doi: 10.1038/nn.4167; pmid: 26551541
34. L. A. Gunaydin *et al*., Natural neural projection dynamics underlying social behavior. *Cell* **157**, 1535–1551 (2014). doi: 10.1016/j.cell.2014.05.017; pmid: 24949967
35. H. L. Fields, G. O. Hjelmstad, E. B. Margolis, S. M. Nicola, Ventral tegmental area neurons in learned appetitive behavior and positive reinforcement. *Annu. Rev. Neurosci.* **30**, 289–316

Downloaded from http://science.sciencemag.org/ on January 18, 2019

(2007). doi: 10.1146/annurev.neuro.30.051606.094341; pmid: 17376009
36. R. A. Wise, P. P. Rompre, Brain dopamine and reward. *Annu. Rev. Psychol.* **40**, 191–225 (1989). doi: 10.1146/annurev.ps.40.020189.001203; pmid: 2648975
37. E. J. Nestler, Is there a common molecular pathway for addiction? *Nat. Neurosci.* **8**, 1445–1449 (2005). doi: 10.1038/nn1578; pmid: 16251986
38. A. Björklund, S. B. Dunnett, Dopamine neuron systems in the brain: An update. *Trends Neurosci.* **30**, 194–202 (2007). doi: 10.1016/j.tins.2007.03.006; pmid: 17408759
39. M. Ernst, A. J. Zametkin, J. A. Matochik, D. Pascualvaca, R. M. Cohen, Low medial prefrontal dopaminergic activity in autistic children. *Lancet* **350**, 638 (1997). doi: 10.1016/S0140-6736(05)63326-0; pmid: 9288051
40. K. Nakamura *et al*., Brain serotonin and dopamine transporter bindings in adults with high-functioning autism. *Arch. Gen. Psychiatry* **67**, 59–68 (2010). doi: 10.1001/archgenpsychiatry.2009.137; pmid: 20048223
41. T. D. Rogers *et al*., Connecting the dots of the cerebro-cerebellar role in cognitive function: Neuronal pathways for cerebellar modulation of dopamine release in the prefrontal cortex. *Synapse* **65**, 1204–1212 (2011). doi: 10.1002/syn.20960; pmid: 21638338
42. T. D. Rogers *et al*., Reorganization of circuits underlying cerebellar modulation of prefrontal cortical dopamine in mouse models of autism spectrum disorder. *Cerebellum* **12**, 547–556 (2013). doi: 10.1007/s12311-013-0462-2; pmid: 23436049
43. G. Mittleman, D. Goldowitz, D. H. Heck, C. D. Blaha, Cerebellar modulation of frontal cortex dopamine efflux in mice: Relevance to autism and schizophrenia. *Synapse* **62**, 544–550 (2008). doi: 10.1002/syn.20525; pmid: 18435424
44. K. T. Beier *et al*., Circuit Architecture of VTA Dopamine Neurons Revealed by Systematic Input-Output Mapping. *Cell* **162**, 622–634 (2015). doi: 10.1016/j.cell.2015.07.015; pmid: 26232228
45. S. Geisler, D. S. Zahm, Afferents of the ventral tegmental area in the rat-anatomical substratum for integrative functions. *J. Comp. Neurol.* **490**, 270–294 (2005). doi: 10.1002/cne.20668; pmid: 16082674
46. W. Menegas *et al*., Dopamine neurons projecting to the posterior striatum form an anatomically distinct subclass. *eLife* **4**, e10032 (2015). doi: 10.7554/eLife.10032; pmid: 26322384
47. O. T. Phillipson, Afferent projections to the ventral tegmental area of Tsai and interfascicular nucleus: A horseradish peroxidase study in the rat. *J. Comp. Neurol.* **187**, 117–143 (1979). doi: 10.1002/cne.901870108; pmid: 489776
48. R. G. Nair-Roberts *et al*., Stereological estimates of dopaminergic, GABAergic and glutamatergic neurons in the ventral tegmental area, substantia nigra and retrorubral field in the rat. *Neuroscience* **152**, 1024–1031 (2008). doi: 10.1016/j.neuroscience.2008.01.046; pmid: 18355970
49. W. Schultz, P. Dayan, P. R. Montague, A neural substrate of prediction and reward. *Science* **275**, 1593–1599 (1997). doi: 10.1126/science.275.5306.1593; pmid: 9054347
50. H. C. Tsai *et al*., Phasic firing in dopaminergic neurons is sufficient for behavioral conditioning. *Science* **324**, 1080–1084 (2009). doi: 10.1126/science.1168878; pmid: 19389999
51. C. Bielajew, P. Shizgal, Evidence implicating descending fibers in self-stimulation of the medial forebrain bundle. *J. Neurosci.* **6**, 919–929 (1986). doi: 10.1523/JNEUROSCI.06-04-00919.1986; pmid: 3486258
52. F. Van Overwalle, T. D'aes, P. Mariën, Social cognition and the cerebellum: A meta-analytic connectivity analysis. *Hum. Brain Mapp.* **36**, 5137–5154 (2015). pmid: 26419890
53. M. Ito, Cerebellar circuitry as a neuronal machine. *Prog. Neurobiol.* **78**, 272–303 (2006). doi: 10.1016/j.pneurobio.2006.02.006; pmid: 16759785
54. M. Yang, J. L. Silverman, J. N. Crawley, Automated three-chambered social approach task for mice. *Curr. Protoc. Neurosci.* Chapter 8, Unit 8 26 (2011). doi: 10.1002/0471142301.ns0826s56; pmid: 21732314
55. A. Ilango *et al*., Similar roles of substantia nigra and ventral tegmental dopamine neurons in reward and aversion. *J. Neurosci.* **34**, 817–822 (2014). doi: 10.1523/JNEUROSCI.1703-13.2014; pmid: 24431440
56. C. J. Stoodley, J. D. Schmahmann, Functional topography in the human cerebellum: A meta-analysis of neuroimaging studies. *Neuroimage* **44**, 489–501 (2009). doi: 10.1016/j.neuroimage.2008.08.039; pmid: 18835452
57. R. S. Snider, A. Maiti, S. R. Snider, Cerebellar pathways to ventral midbrain and nigra. *Exp. Neurol.* **53**, 714–728 (1976). doi: 10.1016/0014-4886(76)90150-3; pmid: 1001395

ACKNOWLEDGMENTS

We thank D. Reato who provided much of the initial code used for acquisition of the behavioral data, H. Staab and J. V. Buschmann for collecting some of the data and J. L. Pena, S. Nicola, A. Kohn, J. Spiro, K. Narasimhan, and the Khodakhah lab for feedback and comments on the manuscript. **Funding:** Supported by NIH grants NS050808, DA044761, MH115604, and RR027888. **Author contributions:** C.H.C., I.C., S.D., A.S., and K.K. designed the experiments; C.H.C., I.C., A.S., and S.D. performed the experiments and analyzed the data; and C.H.C., I.C., A.S., and K.K. contributed to writing the manuscript. **Competing interests:** The authors declare no competing interests. **Data and materials availability:** All the data required to support the conclusions of the paper are presented within the paper and its supplementary materials. All other data are available at http://academiccommons.einsteinmed.org.

SUPPLEMENTARY MATERIALS

www.sciencemag.org/content/363/6424/eaav0581/suppl/DC1
Materials and Methods
Figs. S1 to S8
Movie S1

9 August 2018; accepted 21 November 2018
10.1126/science.aav0581

Downloaded from http://science.sciencemag.org/ on January 18, 2019

REPORT

INORGANIC CHEMISTRY

Luminescence and reactivity of a charge-transfer excited iron complex with nanosecond lifetime

Kasper Skov Kjær[1]*, Nidhi Kaul[2]*, Om Prakash[3]*, Pavel Chábera[1], Nils W. Rosemann[1], Alireza Honarfar[1], Olga Gordivska[3], Lisa A. Fredin[4]†, Karl-Erik Bergquist[3], Lennart Häggström[5], Tore Ericsson[5], Linnea Lindh[1], Arkady Yartsev[1], Stenbjörn Styring[2], Ping Huang[2], Jens Uhlig[1], Jesper Bendix[6], Daniel Strand[3], Villy Sundström[1]‡, Petter Persson[4]‡, Reiner Lomoth[2]‡, Kenneth Wärnmark[3]‡

Iron's abundance and rich coordination chemistry are potentially appealing features for photochemical applications. However, the photoexcitable charge-transfer states of most iron complexes are limited by picosecond or subpicosecond deactivation through low-lying metal-centered states, resulting in inefficient electron-transfer reactivity and complete lack of photoluminescence. In this study, we show that octahedral coordination of iron(III) by two mono-anionic facial *tris*-carbene ligands can markedly suppress such deactivation. The resulting complex $[Fe(phtmeimb)_2]^+$, where phtmeimb is {phenyl[tris(3-methylimidazol-1-ylidene)] borate}$^-$, exhibits strong, visible, room temperature photoluminescence with a 2.0-nanosecond lifetime and 2% quantum yield via spin-allowed transition from a doublet ligand-to-metal charge-transfer (^{2}LMCT) state to the doublet ground state. Reductive and oxidative electron-transfer reactions were observed for the ^{2}LMCT state of $[Fe(phtmeimb)_2]^+$ in bimolecular quenching studies with methylviologen and diphenylamine.

Photoactive transition metal complexes play an important role in processes ranging from solar light harvesting (*1*–*3*) and light-emitting technology (*4*) to photocatalysis (*5*) and photodynamic therapy (*6*). Such applications almost always rely on charge-transfer (CT) excited states with sufficient lifetime and energy to drive electron transfer and visible light emission. Iron complexes provide an earth-abundant and environmentally benign alternative to noble metal systems (*7*) but have until recently been limited by subpicosecond deactivation of their CT states (*8*) to low-energy metal-centered (MC) states (*9*–*12*). These dynamics arise from the moderate ligand field splitting of Fe complexes with commonly used oligopyridyl ligands (*8*, *11*, *12*). Early work on Fe-centered oligopyridyl systems suggested the involvement of MC states with nanosecond lifetime in electron-transfer reactions (*13*). However, these results were later shown to be incompatible with the excited-state dynamics of the systems (*14*); the MC states are now generally considered too low in energy to participate in photochemistry of interest. Efforts to develop Fe-centered photofunctional systems have therefore focused on inhibiting the ultrafast CT → MC transitions (*8*).

We recently showed that strongly electron donating *N*-heterocyclic carbene (NHC) ligands raise the energy of MC states relative to CT states of iron complexes, thereby increasing the lifetime of the excited CT states (*15*). For Fe^{II} complexes with four NHC moieties and two pyridine moieties, we and others have recently demonstrated triplet metal-to-ligand charge-transfer (^{3}MLCT) state lifetimes of a few tens of picoseconds (*15*–*17*), thereby crossing the threshold for efficient interfacial electron injection from surface-bound Fe photosensitizers to a TiO_2 electrode (*17*).

To further increase the lifetime of the CT states in iron complexes, we very recently saturated the iron center with six coordinating NHC moieties, leading to the $[Fe(btz)_3]^{2+/3+}$ complex [btz, 3,3′-dimethyl-1,1′-bis(p-tolyl)-4,4′-bis(1,2,3-triazol-5-ylidene)]. This complex featured order-of-magnitude-higher charge-transfer lifetimes in both its Fe^{III} [100-ps ligand-to-metal charge-transfer (^{2}LMCT)] and Fe^{II} (528-ps ^{3}MLCT) states (*18*, *19*). Moreover $[Fe(btz)_3]^{3+}$ exhibited room temperature photoluminescence (PL) from a CT state in the visible regime, albeit with an extremely low quantum yield (0.03%). The picosecond CT lifetimes still preclude most light-harvesting and light-emitting applications, but these results suggested that further improvements of Fe^{II} and Fe^{III} complexes are notable in the broader context of development of photoactive and photoluminescent $3d^6$ and $3d^5$ complexes, respectively (*20*, *21*).

We identified maximal ligand field strength and an optically allowed lowest CT excited state (*18*, *19*) as key design elements for extending lifetimes and further increasing PL. For superior ligand field strength, we targeted anions for even more pronounced σ-donor ability. Near-perfect octahedral coordination capability (*22*–*24*) was another factor that drew us to the tridentate facial NHC ligand {phenyl[tris(3-methylimidazol-1-ylidene)]borate}$^-$ (phtmeimb$^-$) (*25*). This ligand has very recently been shown to support weak low-temperature solid-state LMCT and d-d emission in the d^3 complex $[Mn^{IV}(phtmeimb)_2](OTf)_2$ (OTf, triflate) (*26*).

In this study, we demonstrate that the combination of a ^{2}LMCT lowest excited state with the exceptional electronic and steric properties of the phtmeimb$^-$ ligand results in a $[Fe^{III}(phtmeimb)_2]PF_6$ complex featuring a CT state with nanosecond lifetime. $[Fe^{III}(phtmeimb)_2]PF_6$ was efficiently synthesized from $Fe^{II}Br_2$ and in situ generated *tris*-NHC-carbene (phtmeimb)$^-$ as illustrated in Fig. 1A. During the workup procedure in air, Fe^{II} is spontaneously oxidized to Fe^{III}, resulting in an analytically pure product (see supplementary materials). Counterion metathesis with $NaBPh_4$ provided access to the corresponding BPh_4^- salt (Ph, phenyl). The oxidation state of iron in both complexes was confirmed by single-crystal x-ray diffraction analysis. The cation in both $[Fe^{III}(phtmeimb)_2]X$ [X = PF_6^- (Fig. 1B) or BPh_4^-] salts displays a near-perfect octahedral geometry (table S4) in contrast to $[Fe(btz)_3](PF_6)_3$ (*19*).

Mößbauer spectroscopy and magnetometry identified the ground state of the isolated sample of $[Fe^{III}(phtmeimb)_2]PF_6$ as low spin (S = ½), containing <1% Fe^{II} (figs. S12 to S14). Surprisingly, but similar to some low-spin Fe^{III}-porphyrin complexes (*27*), the ^{1}H nuclear magnetic resonance (NMR) spectrum of the paramagnetic $[Fe^{III}(phtmeimb)_2]PF_6$ in CD_3CN shows narrow peaks (<15 Hz at 298 K) (table S1), whereas the X-band electron paramagnetic resonance (EPR) spectrum in frozen solvent glasses at T = 4 to 20 K displays no distinct assignable bands (see the supplementary materials section).

Cyclic voltammetry of $[Fe^{III}(phtmeimb)_2]^+$ (Fig. 2A) illustrates that both reduction to Fe^{II} and oxidation to Fe^{IV} are reversible, with half-wave potentials of $E_{½}$ = −1.16 and 0.25 V versus Ferrocene (Fc), respectively. The pronounced shift toward negative potentials compared with potentials of previously reported Fe-NHC complexes (*15*, *17*, *19*) illustrates the exceptionally strong electron donor properties of the negatively charged *tris*-NHC ligands. Further oxidation of the Fe^{IV} complex at 1.67 V is irreversible (fig. S17). Previous observation of irreversible oxidation of

[1]Division of Chemical Physics, Department of Chemistry, Lund University, Box 124, SE-22100 Lund, Sweden. [2]Department of Chemistry, Ångström Laboratory, Uppsala University, Box 523, SE-75120 Uppsala, Sweden. [3]Center for Analysis and Synthesis (CAS), Department of Chemistry, Lund University, Box 124, SE-22100 Lund, Sweden. [4]Division of Theoretical Chemistry, Department of Chemistry, Lund University, Box 124, SE-22100 Lund, Sweden. [5]Department of Physics and Astronomy, Ångström Laboratory, Uppsala University, Box 516, SE-751 20 Uppsala, Sweden. [6]Department of Chemistry, University of Copenhagen, Universitetsparken 5, DK-2100 Copenhagen, Denmark.
*These authors contributed equally to this work.
†Present address: Department of Chemistry, Lehigh University, 6 E Packer Avenue, Bethlehem, PA 18015, USA.
‡Corresponding author. Email: villy.sundstrom@chemphys.lu.se (V.S.); petter.persson@teokem.lu.se (P.P.); reiner.lomoth@kemi.uu.se (R.L.); kenneth.warnmark@chem.lu.se (K.W.)

Downloaded from http://science.sciencemag.org/ on January 22, 2019

$[Fe(btz)_3]^{3+}$ (*19*) at very similar potential indicates the assignment of this process to ligand oxidation as the potentials of metal-centered couples are lowered substantially by the phtmeimb ligand. With this assignment, the electrochemical potentials agree consistently with the energies of the LMCT transitions found for $[Fe(btz)_3]^{3+}$ (*19*) and the Fe^{III} and Fe^{IV} states of $[Fe^{III}(phtmeimb)_2]$ (see fig. S18 and associated discussion). Reduction of the Fe^{II} complex does not occur within the solvent-electrolyte potential window, demonstrating that the ligand reduction potential is below −3.3 V, which is again consistent with the interpretation of the electronic spectra (see supplementary materials).

The visible absorption spectrum of $[Fe(phtmeimb)_2]^+$ in acetonitrile (Fig. 2B, left curve) is dominated by a single band peaking at 502 nm (molar decadic absorption coefficient ε_{max} = 2950 M^{-1} cm^{-1}) with a minor shoulder around 545 nm. This band is bleached upon oxidation and reduction of the metal center, and its energy matches relatively well the difference in electrochemical potential between the Fe^{III}-Fe^{II} couple and ligand oxidation. The lowest-energy absorption band of $[Fe(phtmeimb)_2]^+$ is therefore assigned to a LMCT transition.

Excitation of $[Fe(phtmeimb)_2]^+$ in acetonitrile with visible light below 600 nm results in strong orange PL (Fig. 2C). The spectral profile of the PL shown in Fig. 2B, right, peaks at 655 nm and has no appreciable structure besides a broad shoulder around 620 nm, which mirrors the LMCT absorption band of the complex. The PL intensity tracks the absorption cross section throughout the visible region, as illustrated by the superimposable absorption and excitation spectra (red circles in Fig. 2B).

The measured emission quantum yield of $[Fe(phtmeimb)_2]^+$ in air-saturated dry acetonitrile at room temperature was 2.1% (Φ_e = 0.021 ± 0.002). Notably, this value is a factor of 70 higher than the quantum yield measured for $[Fe(btz)_3]^{3+}$ (*19*) and is even slightly higher than the 1.8% quantum yield of the prototypical transition metal photosensitizer $[Ru(bpy)_3]^{2+}$ (bpy, 2,2′-bipyridine) under air-saturated conditions, used as reference for the quantification (*28*). The emission decay kinetics measured by time-correlated single-photon counting (TCSPC) (Fig. 3A) show a single exponential with a lifetime of τ = 1.96 ± 0.04 ns, a factor of 20 longer than τ observed in $[Fe(btz)_3]^{3+}$ (*19*). The photophysical properties of $[Fe(phtmeimb)_2]^+$, $[Fe(btz)_3]^{3+}$, and $[Ru(bpy)_3]^{2+}$ are compared in Table 1.

Taken together, the emission quantum yield and excited-state lifetime provide a radiative rate constant of $k_r = \Phi_e/\tau = 1.1 \pm 0.2 \times 10^7\ s^{-1}$. The good agreement of this value with the approximate radiative rate constant $k_r = 1.5 \times 10^7\ s^{-1}$ estimated from the integrated extinction coefficient A (Table 1) of the LMCT band via the Strickler-Berg relationship strongly suggests that the emission occurs directly from the ^{2}LMCT state. Thus, the intersection of the normalized absorption and emission bands at 582 nm provides the energy of the ^{2}LMCT excited state, $E_{0\text{-}0}$ = 2.13 eV (17,200 cm^{-1}). From the photophysical parameters, the 70-fold increase in emission quantum yield from 0.03% for $[Fe(btz)_3]^{3+}$ to 2.1% for $[Fe(phtmeimb)_2]^+$ can be rationalized in terms of a 20-fold slower nonradiative decay ($k_{nr} = [1 - \Phi_e]/\tau$) and a 3.5-fold faster radiative rate constant ($k_r = \Phi_e/\tau$).

The transient absorption (TA) spectra of $[Fe(phtmeimb)_2]^+$ recorded after excitation of the LMCT band at 500 nm are dominated by excited-state absorption (ESA) below 450 nm and exhibit a clear stimulated emission band between 600 and 800 nm. The ESA can be attributed to the transiently reduced iron center of the ^{2}LMCT state. The stimulated emission indicates that the ground-state recovery is spin allowed, offering further support for the ^{2}LMCT assignment of the excited state (see supplementary materials). The TA decay kinetics of $[Fe(phtmeimb)_2]^+$ (Fig. 3A, green) are in perfect agreement with the TCSPC results.

The long-term photostability of $[Fe(phtmeimb)_2]^+$ was measured and compared with that of $[Ru(bpy)_3]^{2+}$ by irradiating aerated acetonitrile solutions of both complexes with an 11-W compact fluorescent lamp for a total of 156 hours and measuring the absorption and emission spectra at intervals during this time period. Whereas clear signs of degradation set in for $[Ru(bpy)_3]^{2+}$ after 48 hours, the $[Fe(phtmeimb)_2]^+$ sample was virtually unchanged throughout the 156-hour experiment (figs. S21 and S22).

Density functional theory (DFT) revealed the minimum energies of the ^{4}MC and ^{6}MC states of $[Fe(phtmeimb)_2]^+$ (Fig. 3B) that are destabilized by 13 and 23% with respect to the ground-state minimum as compared with the previously reported $[Fe(btz)_3]^{3+}$ (*19*). The increased energies of the MC states together with the fact that the ^{2}LMCT states are isoenergetic within the experimental uncertainty for the two systems suggest that the increase in the experimentally observed lifetime is related to an effective increase of the activation barrier for the decay of the ^{2}LMCT state into the ^{4}MC state.

Temperature-dependent emission lifetime measurements (fig. S23) show that the excited-state lifetime of $[Fe(phtmeimb)_2]^+$ increases by a factor of 4 (from 2.0 to 7.8 ns) upon decreasing

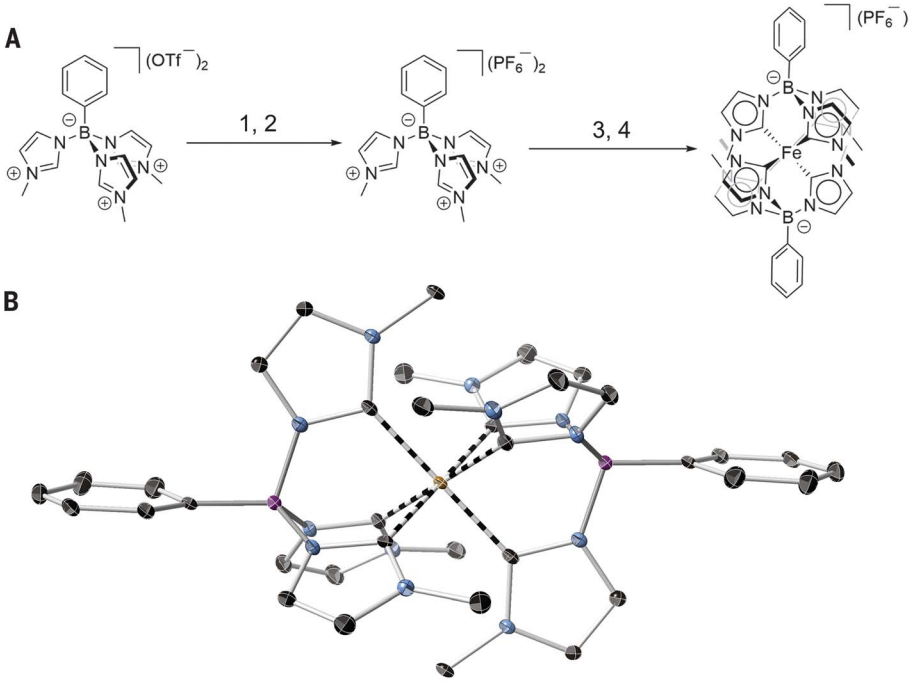


Fig. 1. Synthesis and structure of $[Fe(phtmeimb)_2]PF_6$. (**A**) Synthetic route: 1, precipitation with tetra-*n*-butylammonium bromide in acetone; 2, dissolution in water and precipitation with ammonium hexafluorophosphate; 3, dissolution in tetrahydrofuran under N_2, then cooling to −78°C and addition of *tert*-butoxide; 4, addition of $FeBr_2$, stirring under N_2 at room temperature for 24 hours. (**B**) X-ray crystal structure. Thermal ellipsoids are shown at 50% probability with the six Fe–C bonds highlighted in black and gray stripes. Hydrogen atoms, counterions, and solvent molecules are omitted for clarity. Fe, orange; B, purple; N, blue; C, black.

Downloaded from http://science.sciencemag.org/ on January 22, 2019

the temperature to 100 K, in near-perfect agreement with the behavior of $[Fe(btz)_3]^{3+}$. Fitting the temperature-dependent lifetimes by an Arrhenius model retrieves an activation barrier of 3 kJ mol^{-1} and preexponential factor of 1×10^9 s^{-1}, suggesting that for the decay channels that dominate this temperature dependence, the energy barriers for deactivation of $[Fe(phtmeimb)_2]^+$ and $[Fe(btz)_3]^{3+}$ are almost identical but that the preexponential factor for $[Fe(phtmeimb)_2]^+$ is lower. It is thus the decreased preexponential factor for the transition that results in an increased lifetime, and we tentatively ascribe this to an effective reduction of the crossing frequency from the ^{2}LMCT state to the ^{4}MC state, owing to the combined effect of several structural factors, including the higher symmetry and tighter spatial confinement of the $[Fe(phtmeimb)_2]^+$ ligand system.

With excited-state redox potentials of E^o(III*/II) = 1.0 V and E^o(IV/III*) = −1.9 V versus Fc [1.6 V and −1.3 V versus NHE (normal hydrogen electrode)], the ^{2}LMCT state should be potent as both a photo-oxidant and photoreductant; furthermore, its nanosecond lifetime should enable efficient

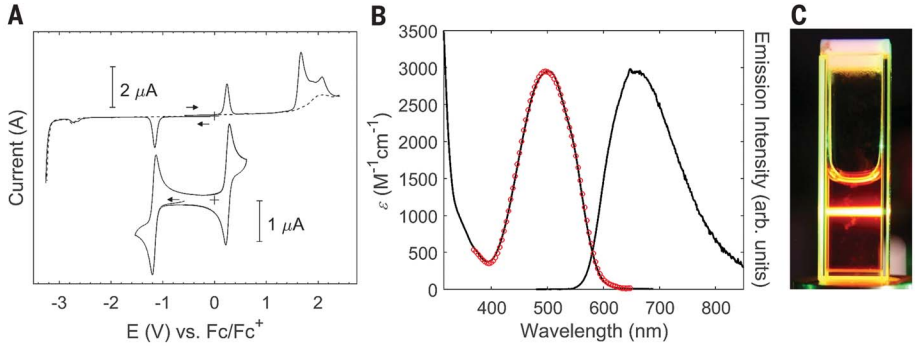


Fig. 2. Electrochemistry and spectroscopy of $[Fe(phtmeimb)_2]^+$ in dry, air-saturated acetonitrile at room temperature. (**A**) Cyclic and differential pulse voltammetry. (**B**) Optical absorption (left black curve), normalized PL (right black curve), and normalized excitation spectra (red circles). (**C**) Visible orange PL of 50 μM $[Fe(phtmeimb)_2]^+$ in dry, air-saturated acetonitrile upon 532-nm excitation.

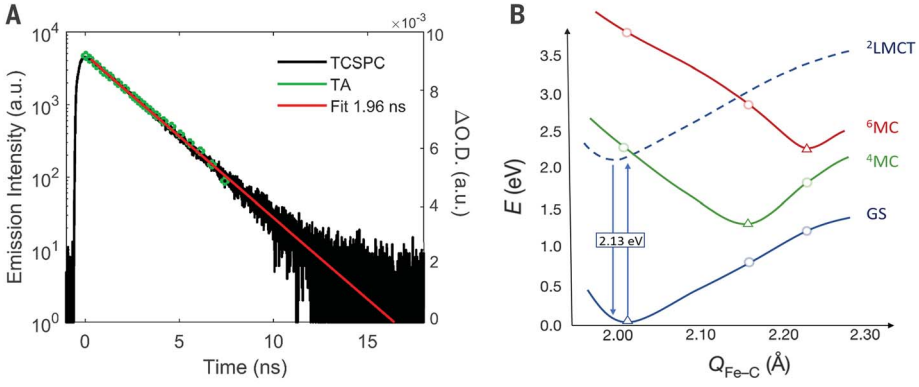


Fig. 3. Excited-state dynamics and computational analysis of $[Fe(phtmeimb)_2]^+$ photophysics. (**A**) Time-correlated single-photon counting data (black, left *y* axis), transient absorption data at 390 nm (green circles, right *y* axis), and monoexponential fit of 1.96 ± 0.04 ns (red). a.u., arbitrary units; O.D., optical density. (**B**) Potential energies and Fe–C equilibrium bond lengths (*Q*) for relevant electronic states of $[Fe(phtmeimb)_2]^+$ (triangles) and potential surfaces (lines) drawn through the energy of each state at the geometry of the two other states (circles). The ^{2}LMCT surface was extrapolated from the ground-state (GS) shape and experimental energy as described in the supplementary materials section.

Table 1. Photophysical parameters of $[Fe(phtmeimb)_2]^+$, $[Fe(btz)_3]^{3+}$, and $[Ru(bpy)_3]^{2+}$ in air-saturated acetonitrile at room temperature. $[Fe(btz)_3]^{3+}$ data are from (*19*); $[Ru(bpy)_3]^{2+}$ data are from (*28*, *34*). $\lambda_{max,abs}$, maximum absorption wavelength; $\lambda_{max,emiss}$, maximum emission wavelength; τ, CT excited-state lifetime.

Complex	$\lambda_{max,abs}$ (ε_{max}) [nm ($10^3 \cdot M^{-1} cm^{-1}$)]	$\lambda_{max,emiss}$ [nm]	A [$10^7 \cdot M^{-1} cm^{-2}$]	k_r [$10^6 \cdot s^{-1}$]	k_{nr} [$10^7 \cdot s^{-1}$]	τ [ns]	Φ_e [%]
$[Fe(phtmeimb)_2]^+$	502 (3.0)	655	2.5	15	49	2	2.1
$[Fe(btz)_3]^{3+}$	558 (1.2)	600	0.47	4	990	0.1	0.03
$[Ru(bpy)_3]^{2+}$	452 (14.6)	625	7.5	0.1	0.56 | 0.10*	180 | 930*	1.8 | 9.5*

*Parameters for oxygen-free acetonitrile solution of $[Ru(bpy)_3]^{2+}$.

Downloaded from http://science.sciencemag.org/ on January 22, 2019

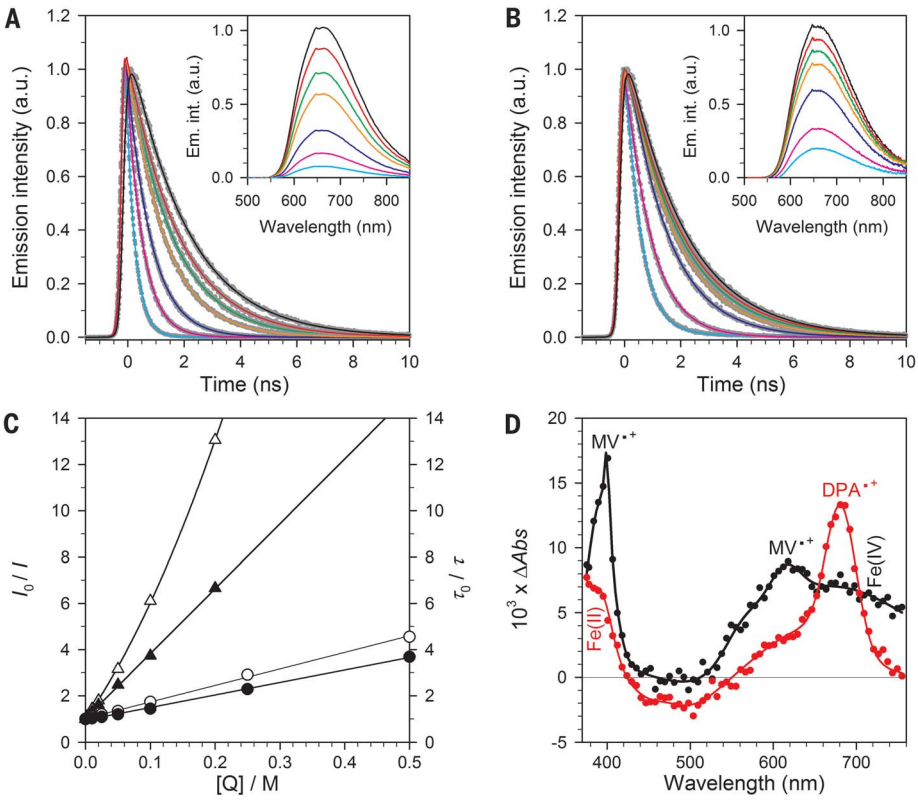


Fig. 4. Reactivity of the ^{2}LMCT excited state of $[Fe(phtmeimb)_2]^+$ toward electron donors and acceptors. Emission quenching was monitored by emission lifetime (TCSPC traces with exponential fits) and steady-state emission spectra (insets) for increasing concentrations (black to cyan) of (**A**) diphenylamine donor (0, 0.005, 0.01, 0.02, 0.05, 0.1, and 0.2 M) and (**B**) methylviologen acceptor (0, 0.01, 0.025, 0.05, 0.1, 0.25, and 0.5 M) in acetonitrile. (**C**) Stern-Volmer plots for steady-state intensity (open symbols) and lifetime data (solid symbols) from quenching experiments with diphenylamine (triangles) and methylviologen (circles). (**D**) Transient absorption spectra after laser flash excitation (465 nm) of $[Fe(phtmeimb)_2]^+$, monitoring products of oxidative quenching by methylviologen (0.25 M) 500 ns after excitation (black) and of reductive quenching by diphenylamine (0.2 M) 100 ns after excitation (red).

bimolecular electron transfer as long as rate constants are not too far from their diffusion-controlled limit. The reactivity of the ^{2}LMCT state toward both electron donors and acceptors was studied by monitoring the impact of the quenchers on both steady-state emission intensity as well as emission lifetime (Fig. 4, A and B). The methylviologen dication (MV^{2+}) and arylamines such as diphenylamine (DPA) are widely used electron-transfer quenching agents with suitable redox properties. The observed emission quenching results were attributed to oxidative and reductive electron transfer, respectively, generating $[Fe^{IV}(phtmeimb)_2]^{2+}$ and $MV^{\bullet+}$ (change in Gibbs free energy $\Delta G^o = -1.08$ eV) in the former case and $[Fe^{II}(phtmeimb)_2]$ and $DPA^{\bullet+}$ ($\Delta G^o = -0.55$ eV) in the latter.

Bimolecular quenching rate constants in acetonitrile for dynamic quenching were determined from Stern-Volmer plots of emission lifetimes τ_0/τ (Fig. 4C); rates were diffusion controlled for DPA ($k_q = 1.4 \times 10^{10}$ M^{-1} s^{-1}) and only somewhat lower even for MV^{2+} ($k_q = 2.7 \times 10^9$ M^{-1} s^{-1}). Although no indications of ground-state complexation were observed with MV^{2+}, additional static quenching by DPA was evident from the curved Stern-Volmer plot of steady-state intensities I_0/I. With both quenchers, the formation of electron transfer products was unambiguously confirmed by transient absorption spectroscopy (Fig. 4D). Spectra after quenching by DPA show characteristic absorption of the donor cation radical peaking at 680 nm (*29*) and of the Fe^{II} state rising toward the ultraviolet region (<420 nm) (see also fig. S18). Also quenching by MV^{2+} resulted in transient absorption spectra that display the well-known absorption features of the acceptor radical $MV^{\bullet+}$ (at 396 and 606 nm) (*30*) together with the broad 700-nm band of the Fe(IV) complex (see fig. S18). In the flash photolysis experiments, the excited state at an initial concentration of ~1.5×10^5 M (determined by actinometry with $[Ru(bpy)_3]^{2+}$) was quenched with efficiencies of ~0.7 by 0.25 M MV^{2+} and nearly unity by 0.2 M DPA. From the initial concentrations of $MV^{\bullet+}$ ($\Delta\varepsilon_{396}$ = 41,800 M^{-1} cm^{-1}) (*30*) and $DPA^{\bullet+}$ ($\Delta\varepsilon_{680}$ = 19,200 M^{-1} cm^{-1}) (*29*), we estimate that in both quenching reactions about 5% of the charge-separated products escape geminate recombination in the solvent cage. The diffusional recombination of the separated products occurs on the time scale of 100 μs and, in case of DPA, proceeds via oxidation of the Fe^{III} ground state by the donor radical (see supplementary materials). Although the cage escape yields values three to five times lower than those typically observed in the quenching of the ^{3}MLCT state of $[Ru(bpy)_3]^{2+}$, that latter process benefits from spin restrictions to back electron transfer in the triplet radical pair (*31*); the yields compare very favorably to the negligible cage escape encountered in other cases of spin-allowed back electron transfer in the quenching of, for instance, singlet excited states of porphyrins (*32*).

The extended CT lifetimes in $[Fe(phtmeimb)_2]^+$ were accomplished without substantial loss of the >2-eV excited-state energy, providing the ^{2}LMCT state with a superior combination of oxidative and reductive power exceeding the corresponding values of the archetypal $[Ru(bpy)_3]^{2+}$ sensitizer (fig. S26). Thermodynamically, the ^{2}LMCT state should be capable of oxidizing or reducing a wide range of molecular donors and acceptors and p- or n-type semiconductor materials and of driving demanding photocatalytic reactions such as water oxidation or carbon dioxide reduction, which could further benefit from the complex's intrinsic stability (fig. S26).

The 2% PL quantum yield also raises the prospect of applying Fe-NHC systems to biosensors and organic light-emitting diodes (*33*). These applications would benefit from the intrinsic low toxicity and earth abundance of Fe complexes, as well as the insensitivity of the ^{2}LMCT excited state of $[Fe(phtmeimb)_2]^+$ to oxygen. Moreover, because both the ground and LMCT excited states of the Fe^{III} light-emitting complex are doublets, they will not suffer from the endemic singlet-versus-triplet formation problem (*33*) of typical rare-earth light emitting complexes. Taken together, our results suggest that the ^{2}LMCT state deserves more attention as a photofunctional state for iron and other transition metals as well.

REFERENCES AND NOTES

1. V. Balzani, G. Bergamini, S. Campagna, F. Puntoriero, in *Photochemistry and Photophysics of Coordination Compounds I* (Topics in Current Chemistry Series, Springer, 2007), pp. 1–36.
2. C. S. Ponseca Jr., P. Chábera, J. Uhlig, P. Persson, V. Sundström, *Chem. Rev.* **117**, 10940–11024 (2017).
3. M. Graetzel, R. A. J. Janssen, D. B. Mitzi, E. H. Sargent, *Nature* **488**, 304–312 (2012).
4. R. C. Evans, P. Douglas, C. J. Winscom, *Coord. Chem. Rev.* **250**, 2093–2126 (2006).
5. S. Ardo, G. J. Meyer, *Chem. Soc. Rev.* **38**, 115–164 (2009).
6. C. B. Larsen, O. S. Wenger, *Chem. Eur. J.* **24**, 2039–2058 (2018).
7. B. Bozic-Weber, E. C. Constable, C. E. Housecroft, *Coord. Chem. Rev.* **257**, 3089–3106 (2013).
8. Y. Liu, P. Persson, V. Sundström, K. Wärnmark, *Acc. Chem. Res.* **49**, 1477–1485 (2016).
9. C. Creutz, M. Chou, T. L. Netzel, M. Okumura, N. Sutin, *J. Am. Chem. Soc.* **102**, 1309–1319 (1980).
10. J. K. McCusker *et al.*, *J. Am. Chem. Soc.* **114**, 6919–6920 (1992).
11. W. Zhang *et al.*, *Nature* **509**, 345–348 (2014).
12. J. E. Monat, J. K. McCusker, *J. Am. Chem. Soc.* **122**, 4092–4097 (2000).
13. K. J. Brewer, W. R. Murphy, K. J. Moore, E. C. Eberle, J. D. Petersen, *Inorg. Chem.* **25**, 2470–2472 (1986).

Downloaded from http://science.sciencemag.org/ on January 22, 2019

14. K. S. Kjær *et al.*, *Struct. Dyn.* **4**, 044030 (2017).
15. Y. Liu *et al.*, *Chem. Commun.* **49**, 6412–6414 (2013).
16. T. Duchanois *et al.*, *Eur. J. Inorg. Chem.* **2015**, 2469–2477 (2015).
17. T. C. B. Harlang *et al.*, *Nat. Chem.* **7**, 883–889 (2015).
18. P. Chábera *et al.*, *J. Phys. Chem. Lett.* **9**, 459–463 (2018).
19. P. Chábera *et al.*, *Nature* **543**, 695–699 (2017).
20. V. W.-W. Yam, K. M.-C. Wong, *Chem. Commun.* **47**, 11579–11592 (2011).
21. O. S. Wenger, *J. Am. Chem. Soc.* **140**, 13522–13533 (2018).
22. M. Abrahamsson *et al.*, *J. Am. Chem. Soc.* **128**, 12616–12617 (2006).
23. K. Ulrich, R. Matthias, L. Peter, W. P. Fehlhammer, *Angew. Chem. Int. Ed. Engl.* **35**, 310–312 (1996).
24. L. L. Jamula, A. M. Brown, D. Guo, J. K. McCusker, *Inorg. Chem.* **53**, 15–17 (2014).
25. A. P. Forshaw, R. P. Bontchev, J. M. Smith, *Inorg. Chem.* **46**, 3792–3794 (2007).
26. V. Baslon *et al.*, *Can. J. Chem.* **95**, 547–552 (2017).
27. C. T. Watson, S. Cai, N. V. Shokhirev, F. A. Walker, *Inorg. Chem.* **44**, 7468–7484 (2005).
28. K. Suzuki *et al.*, *Phys. Chem. Chem. Phys.* **11**, 9850–9860 (2009).
29. K. Kalyanasundaram, *J. Chem. Soc., Faraday Trans. 2* **82**, 2401–2415 (1986).
30. T. Watanabe, K. Honda, *J. Phys. Chem.* **86**, 2617–2619 (1982).
31. J. Olmsted, T. J. Meyer, *J. Phys. Chem.* **91**, 1649–1655 (1987).
32. A. Harriman, G. Porter, A. Wilowska, *J. Chem. Soc., Faraday Trans. 2* **79**, 807–816 (1983).
33. C. Bizzarri, E. Spuling, D. M. Knoll, D. Volz, S. Bräse, *Coord. Chem. Rev.* (2017).
34. D. M. Arias-Rotondo, J. K. McCusker, *Chem. Soc. Rev.* **45**, 5803–5820 (2016).

ACKNOWLEDGMENTS

Funding: K.S.K. and J.B. acknowledge the Danish Council for Independent Research (5051-00095A and 8021-00410B) and the Carlsberg Foundation. N.W.R. acknowledges the Alexander von Humboldt Foundation within the Feodor-Lynen Fellowship program. P.P., R.L., and K.W. acknowledge the Swedish Foundation for Strategic Research. P.P. and K.W. acknowledge the Swedish Research Council. P.P. acknowledges the Swedish Energy Agency, the Knut and Alice Wallenberg Foundation, and the Swedish National Supercomputing Centers LUNARC and NSC via SNIC. K.W. acknowledges the LMK Foundation, Stiftelsen Olle Engkvist Byggmästare, the Carl Trygger Foundation, the Wenner-Gren Foundation, the Crafoord Foundation, Sten K Johnsons Stiftelse, and the Royal Physiographic Society.
Author contributions: K.S.K., P.C., A.H., O.G., N.W.R., J.U., V.S., A.Y., and L.L. conducted the femtosecond-to-nanosecond TA and PL measurements. N.K. conducted all steady-state and time-resolved spectroscopy related to the excited-state quenching studies and analyzed the data. O.P. conducted the synthesis. L.A.F. and P.P. conducted the DFT calculations and theoretical analysis. K.-E.B. conducted NMR spectroscopy. L.H. and T.E. conducted Mößbauer spectroscopy. S.S., P.H., and J.B. conducted EPR spectroscopy. J.B. conducted magnetic susceptibility and magnetization measurements. D.S. conducted x-ray crystallography. K.S.K., V.S., and P.P. conceived of and interpreted the photophysics and excited-state cascade. R.L. conducted electro- and spectroelectrochemistry and emission spectroscopy; interpreted the electrochemical, spectroscopic, and photophysical properties; and conceived of and interpreted the excited-state quenching studies. K.W. conceived of the design and the synthesis of the ligand and the metal complex. K.S.K., O.P., V.S., P.P., R.L., and K.W. wrote the paper with co-writing input from K.-E.B., T.E., L.H., P.H., J.B., D.S., and N.W.R. All authors read and commented on the paper. **Competing interests:** The authors declare no competing interests. **Data and materials availability:** Crystallographic data are available free of charge from the Cambridge Crystallographic Data Centre under reference numbers CCDC-1842079 {[Fe(phtmeimb)$_2$]PF_6} and CCDC-1842084 {[Fe(phtmeimb)$_2$]BPh_4}. All other data are available in the main text or the supplementary materials.

SUPPLEMENTARY MATERIALS

www.sciencemag.org/content/363/6424/249/suppl/DC1
Materials and Methods
Figs. S1 to S26
Tables S1 to S5
References (*35*–*56*)

2 August 2018; accepted 14 November 2018
Published online 29 November 2018
10.1126/science.aau7160

Downloaded from http://science.sciencemag.org/ on January 22, 2019

IMPACT CRATERS

Earth and Moon impact flux increased at the end of the Paleozoic

Sara Mazrouei[1]*, Rebecca R. Ghent[1,2], William F. Bottke[3], Alex H. Parker[3], Thomas M. Gernon[4]

The terrestrial impact crater record is commonly assumed to be biased, with erosion thought to eliminate older craters, even on stable terrains. Given that the same projectile population strikes Earth and the Moon, terrestrial selection effects can be quantified by using a method to date lunar craters with diameters greater than 10 kilometers and younger than 1 billion years. We found that the impact rate increased by a factor of 2.6 about 290 million years ago. The terrestrial crater record shows similar results, suggesting that the deficit of large terrestrial craters between 300 million and 650 million years ago relative to more recent times stems from a lower impact flux, not preservation bias. The almost complete absence of terrestrial craters older than 650 million years may indicate a massive global-scale erosion event near that time.

The abundance of terrestrial craters with diameters (D) ≥ 20 km decreases substantially with age. A common assumption is that this loss is driven by erosive and tectonic processes operating over hundreds of millions of years. Unfortunately, it is challenging to quantitatively test this hypothesis with existing terrestrial data. An alternative is to estimate terrestrial crater loss rates by comparing Earth's crater record with the Moon's. Earth and the Moon have been struck by the same impactor population over time, but large lunar craters have experienced limited degradation over billions of years. An obstacle to performing this test has been obtaining accurate dates for large lunar craters.

We used an analysis of the thermophysical characteristics of lunar impact ejecta as measured with the Diviner thermal radiometer on NASA's Lunar Reconnaissance Orbiter (LRO) (*1*, *2*) to estimate the ages of lunar craters with D >10 km and younger than 1 billion years (Ga). The formation of large lunar craters excavates numerous ≥1m ejecta fragments onto the Moon's surface. These recently exposed rocks have high thermal inertia and remain warm during the lunar night relative to the surrounding lunar soils (called regolith), which have low thermal inertia. The nighttime temperatures were calculated from three of Diviner's thermal infrared channels. Rock abundance values, defined as the fractional coverage of a Diviner pixel by exposed meter-scale rocks (Fig. 1), were obtained, simultaneously with rock-free lunar regolith temperatures, by exploiting the fact that a mixture of lunar rocks and regolith produces a mixed spectral radiance and therefore different estimates of brightness temperature in each of the three thermal infrared channels (*1*).

Using these data, an inverse relationship between rock abundance in large crater ejecta and crater age has been demonstrated by calculating ejecta rock abundance values for nine "index" craters with independently determined ages (*2*). Young craters were found to have high rock abundance in their ejecta, whereas rock abundance decreases with increasing crater age, eventually becoming indistinguishable from the background for craters older than ~1 Ga. The breakdown of lunar rocks has most likely occurred at a steady rate over the past billion years through the constant influx of tiny impactors and the thermal effects of lunar day-night cycling (*3*). We derived a crater age–rock abundance regression function shown in Fig. 1 and fig. S1 (*3*).

We identified 111 rocky craters on the Moon with D ≥10 km between 80°N and 80°S, with ejecta blankets that have rock abundance values high enough to distinguish them from the background regolith (Fig. 2A and table S1). We used the 95th percentile rock abundance values ($RA_{95/5}$), which are those that separate the upper 5% from the lower 95% of RA values for a given crater's ejecta. We chose 10 km as a minimum size for this analysis because those craters have penetrated the surface regolith deeply enough to have excavated large blocks from the underlying bedrock. This approach minimizes the influence of variations in original

[1]Department of Earth Sciences, University of Toronto, Toronto, ON, Canada. [2]Planetary Science Institute, Tucson, AZ, USA. [3]Southwest Research Institute, Boulder, CO, USA. [4]School of Ocean and Earth Science, University of Southampton, Southampton, UK.
*Corresponding author. Email: sara.mazrouei.seidani@mail.utoronto.ca

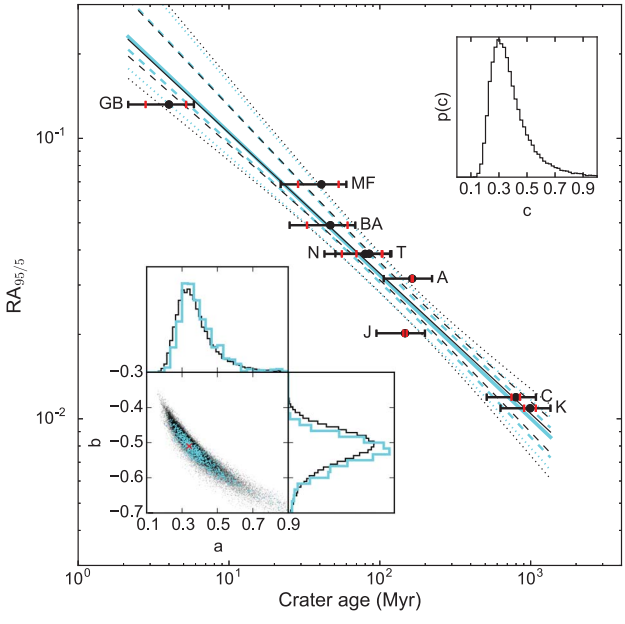


Fig. 1. Regression of lunar crater age versus 95th percentile rock abundance. Updated from (*1*, *2*). Data point labels correspond to dated lunar craters (*2*) listed in table S1. Rock cover is defined as materials with rocklike thermal inertia and minimum diameters larger than the diurnal thermal skin depth (~0.5 m). This regression differs from previous analysis (*2*) because of use of an updated rock abundance dataset and an updated age for Aristarchus crater (*26*), together with a statistical treatment that marginalizes over unacknowledged uncertainties for the published crater ages (*3*). Red error bars illustrate uncertainties for each crater, and black error bars show the uncertainties implied by the median value of the uncertainty scaling factor c given its posterior PDF (eq. S2). The best fitting parameters in the relation $RA_{95/5} = a \times (age/Ma)^b$ are a, 0.33; b, −0.50 (black solid curve); black dashed and dotted curves indicate the 68 and 95% credible intervals. After propagation through the joint terrestrial/lunar Approximate Bayesian Computation rejection (ABCr) analysis (*3*), the best fitting parameters are a, 0.34; b, −0.51 (cyan solid curve); cyan dashed and dotted curves show the 68 and 95% credible intervals. (Insets) The two-dimensional (2D) distribution of the posterior PDF sample of parameters (a, b) before and after ABCr analysis (black and cyan points, respectively), their marginalized distributions, and $p(c)$, the 1D marginalized posterior PDF of the uncertainty scaling factor c (eq. S2).

Downloaded from http://science.sciencemag.org/ on January 17, 2019

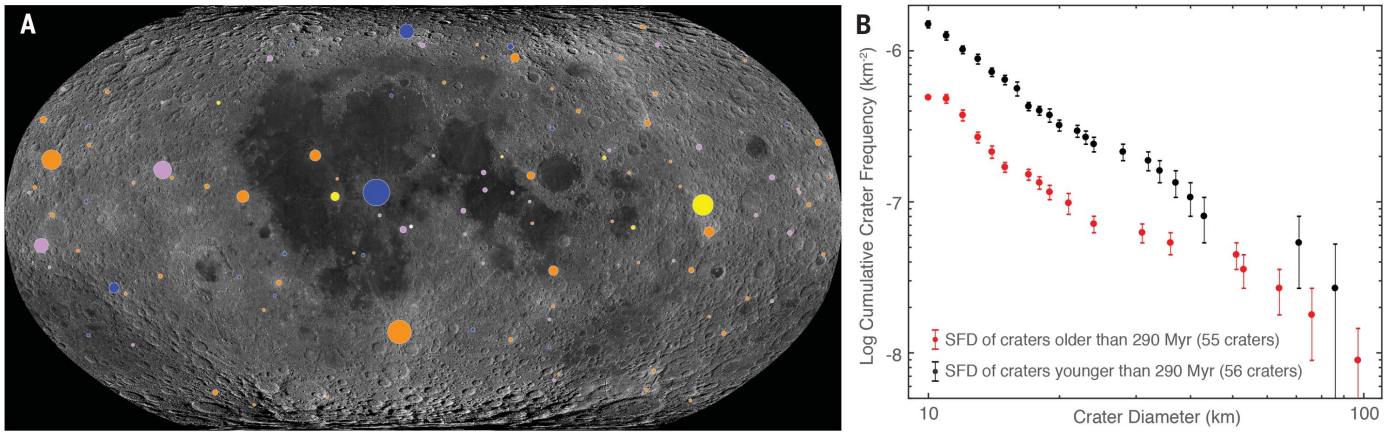


Fig. 2. Geographic and SFD of rocky lunar craters. (**A**) Geographic distribution of 111 rocky (young) craters with $D \geq 10$ km between 80°N and 80°S on the Moon (listed in table S1), scaled by size and color coded according to age. Orange (dark yellow deuteranopia) indicates craters younger than 290 Ma; pink (light blue deuteranopia) indicates craters 290 to 580 Ma old; dark blue indicates craters 580 to 870 Ma old; yellow indicates craters 870 to 1160 Ma old; and white indicates craters older than 1160 Ma. [Background image is from https://astrogeology.usgs.gov/search/map/Moon/LRO/LROC_WAC/Lunar_LRO_LROC-WAC_Mosaic_global_100m_June2013 (*27*)]. (**B**) Cumulative SFDs of craters. Red indicates average SFD of craters older than 290 Ma (55 craters; average of cumulative distribution in three age bins: 290 to 580 Ma old; 580 to 870 Ma old; and 870 to 1160 Ma old), black indicates craters younger than 290 Ma (56 craters), and error bars show Poisson noise. The lunar cratering rate has increased by a factor of 2.6 in the past 290 Ma compared with the preceding ~710 Ma.

ejecta block population that are due to spatial variations in surface soil thickness (*4*, *5*).

Using Fig. 1, we calculated ages for these craters and found that they were not formed uniformly with time (Fig. 2B). This implies that the small- and large-body impact fluxes striking the Moon are probably decoupled from one another at a modest level, with small impactors more likely to maintain a steady impact flux than large impactors (fig. S2) (*3*). Our analysis also showed no statistical evidence for a leading versus trailing hemisphere asymmetry in the calculated ages of these large craters, nor for a latitudinal dependence in rocky crater abundance, although our relatively small sample size might make such a trend difficult to detect. We also identified no correlation between crater sizes and crater ages, meaning differently sized craters are randomly distributed in time.

To quantify the change in flux exhibited by these lunar craters, we adopted a piecewise-constant rate model in which a uniform cratering rate at early times changes instantaneously to a different rate at later times. Sampling from among all possible values of the crater age–rock abundance regression parameters, using conservative estimates on the lunar index crater ages (Fig. 1) (*3*), we found that this model shows statistical evidence for a break at some time between 220 and 770 Ma ago (95% credible intervals), with the peak of the marginalized probability density function (PDF) at a break age of 400 Ma (fig. S1). The ratio of the crater rate after the break age to the prebreak rate is 2.1, with 95% credible interval values of 1.4 to 20.6.

Supporting evidence for an increase of a factor of 2 to 3 in the lunar impact flux since ~400 Ma ago may come from the ages and abundances of lunar impact spherules. Created by energetic cratering events, these glassy melt droplets have been identified in the regolith samples returned from the Apollo landing sites. Their age distribution is a potential proxy for the impact flux of larger bodies and suggests that the impact flux increased by a factor of 3.7 ± 1.2 over the past 400 Ma (*6*, *7*), which is in broad agreement with our results. However, the abundance of young impact spherules found in Apollo lunar regolith samples could be a bias (*7*). Lunar craters formed over the past 300 to 400 Ma may have also degraded faster by means of diffusion processes than those that formed between 700 and 3100 Ma ago (*8*). This observation may be explained if large impacts enhance diffusive processes through, for example, seismic shaking, and the large-body impact flux has increased over recent times.

Rayed lunar craters have previously been used to compute impact flux rates, with the assumption often made that they formed in the past

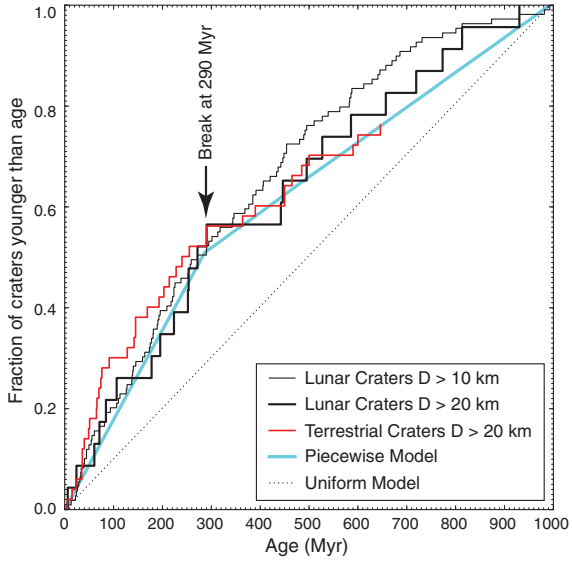


Fig. 3. Age-frequency distributions of lunar and terrestrial craters. The lunar crater $D \geq 10$ and 20 km curves are shown by the black line, whereas terrestrial craters with $D \geq 20$ km (table S2) are shown with the red line. All terrestrial craters are younger than 650 Ma. The lunar impact flux increases by a factor of 2.6 near 290 Ma ago (fig. S1). A simple piecewise model (cyan) demonstrates the break between two rates compared with a simple uniform model (dashed black). The similarity between the lunar and terrestrial distributions suggests that the inferred increase in terrestrial impacts is not a preservation bias.

Downloaded from http://science.sciencemag.org/ on January 17, 2019

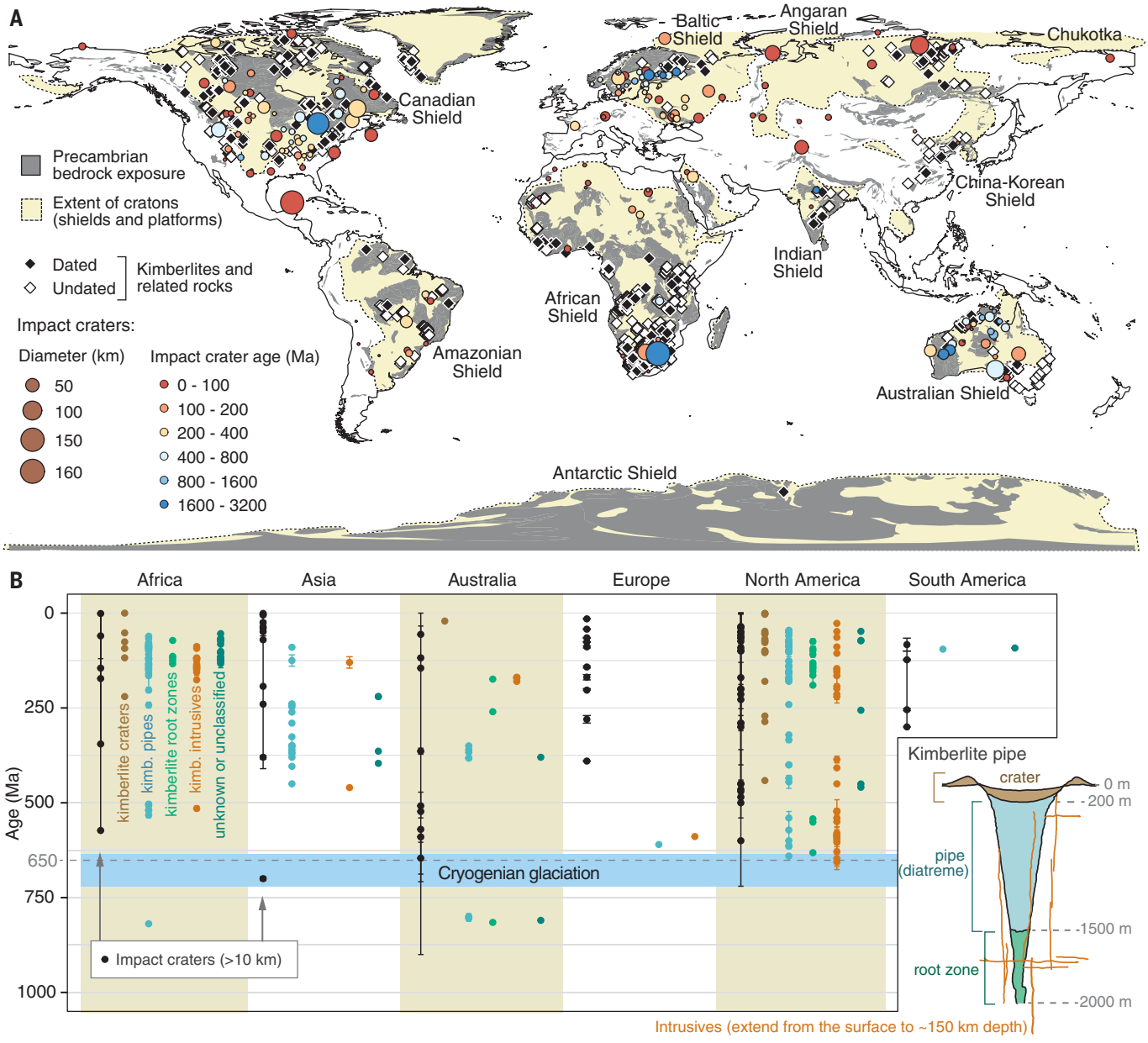


Fig. 4. Positions of terrestrial impact craters and kimberlites in space and time. (**A**) Locations of all impact craters identified in the Planetary and Space Science Centre (PASSC) Earth Impact Database (*24*), scaled by size and colored by age. Kimberlite occurrences are also shown; solid symbols denote those craters with well-defined ages (n = 624), and white diamonds indicate undated kimberlites (n = 3645) (*25*). Gray regions correspond to major exposures of Precambrian basement rocks (*28*), which together with platform areas shown in beige (*29*) form the stable cratons, where 84% of craters with $D \geq 20$ km (and 84.6% of craters with $D \geq 10$ km) occur. (**B**) Chronology of large impacts (>10 km) and well-dated kimberlites for each continent, excluding Antarctica. Colored symbols indicate depth-diagnostic kimberlite zones (labeled and illustrated in the inset). There is an abrupt cut-off in impact crater and kimberlite pipe frequency at ~650 Ma ago, which is coincident with Snowball Earth glaciation during the Cryogenian Period, 720 to 635 Ma ago (*17*–*19*).

1 Ga. We found 11 farside rocky craters with $D \geq 20$ km formed in the past 1 Ga, compared with 28 to 32 farside rayed craters assumed to be this age (*9*, *10*). This discrepancy suggests that rayed craters may have a much wider spread of ages than commonly thought (supplementary text).

These results for the Moon provide insights into Earth's crater record. Interpretation of the terrestrial record is problematic because (i) an unknown number of older craters have been erased at unknown times by erosion or tectonics, (ii) stable continental surfaces capable of recording ancient impacts have potentially been buried and exhumed multiple times since they formed, (iii) it is difficult to precisely quantify which terrains have been adequately searched for craters, and (iv) not all craters are exposed at the surface but instead have to be identified through geophysical anomalies and explored through drilling (*11*).

Lunar craters have experienced comparatively little erosion over the past 1 Ga, and the proximity of Earth to the Moon implies that both have been struck by the same population of impactors. A comparison of records on both bodies therefore provides an opportunity to quantify terrestrial selection effects.

Downloaded from http://science.sciencemag.org/ on January 17, 2019

Contrary to our expectations, we found that the size-frequency distributions (SFDs) of the lunar and terrestrial craters for $D \geq 20$ km, normalized by the total number of craters, are highly similar (fig. S3A). We found no evidence for size bias in retention of terrestrial craters; in an average sense, for a given region, it appears that Earth either keeps all or loses all of its $D \geq 20$ craters at the same rate, independent of size.

We compared the ages of the 38 known terrestrial craters with $D \geq 20$ km (table S2) with the computed age distribution for lunar craters with $D \geq 10$ and ≥ 20 km (Fig. 3 and table S1). Using the same statistical method for the terrestrial craters as for the lunar craters, we found that the terrestrial craters also have a break age and ratio of present-day to past crater rate close to lunar values (fig. S1). Because there is evidence for a nonuniform terrestrial cratering rate similar to the lunar cratering rate, and considering that Earth and the Moon share a similar bombardment history, we combined both records. The inclusion of terrestrial craters provides an absolute age chronology supplement to the nine index craters we have for the Moon.

The model adopted to fit these data includes a single break between two uniform rates, but we do not rule out other simple models (for example, cratering rate linearly increasing in time) or more complex models (for example, multiple breaks). Rather, we used the single-break piecewise model as a simple and physically plausible hypothesis to demonstrate that the lunar and terrestrial cratering rates have not been constant over the past billion years.

Our joint lunar and terrestrial analysis yields a ratio of the crater rate after the break age to the prebreak rate of 2.6, with a 95% credible interval value of 1.7 to 4.7. The most probable break age is 290 Ma. The impact rate change is reflected in the SFD curves, with craters younger than 290 Ma substantially higher in frequency at all diameters than those older than 290 Ma (Fig. 2B). The deficit of large terrestrial craters between 290 and 650 Ma old can therefore be interpreted to reflect a lower impact flux relative to the present day and not a bias (supplementary text).

The erosion history of Earth's continents can also be constrained by using uranium-lead (U-Pb) thermochronology, or temperature-sensitive radiometric dating. Thermochronologic data suggest that stable continental terrains experience low erosion or burial rates of up to 2.5 m Ma^{-1} (*12*), which equates to a maximum of 1.6 km vertical erosion (or deposition) over the past 650 Ma. This would likely be insufficient to eradicate craters with $D \geq 20$ km, given that crater depths are approximately equal to ~10% of their original diameter (*13*).

Support for limited erosion on cratered terrains can also be found in the record of kimberlite pipes. Kimberlites are formed during explosive volcanism from deep mantle sources, generating carrot-shaped pipes 1 to 2 km deep (Fig. 4) (*14*, *15*), and commonly preserve volcanic features (such as volcanic craters and pipes) that are depth-diagnostic (*16*). Impact craters and kimberlites are frequently found in common regions on stable continental surfaces (Fig. 4A), so kimberlites are a proxy that indicate the depth of erosion for surfaces of different ages. Deep erosion of stable continental surfaces (>2 km) should have removed most kimberlite pipes, leaving behind deep-seated intrusive rocks, but kimberlite pipes are relatively common throughout the Phanerozoic Eon (541 Ma ago to the present). Their spatiotemporal distribution (Fig. 4B) suggests only modest erosion (<1 km) on most cratons since 650 Ma ago, favoring the survival of $D \geq 20$ km impact craters (*3*).

There is a sharp cut-off in the number of terrestrial craters at ~650 Ma ago (Figs. 3 and 4). Given erosion rates on stable continental terrains after 650 Ma ago, similar conditions further back in time would have allowed most craters of Precambrian age (older than 541 Ma) to survive. Instead, the paucity of Precambrian craters is coincident with major episodes of globally extensive "Snowball Earth" glaciation (Fig. 4B) (*17*). Pervasive subglacial erosion at ~650 to 720 Ma ago is thought to have removed kilometers of material from the continents (*18*, *19*), enough to erase most existing kimberlite pipes and impact craters (fig. S5A). The exceptions are the $D > 130$ km impact craters Sudbury (1850 Ma ago) and Vredefort (2023 Ma ago). Both craters were deep enough to survive, but each shows indications of multiple kilometers of erosion (*20*).

The change in the lunar and terrestrial impact flux may be due to the breakup of one or more large asteroids in the inner and/or central main asteroid belt (*21*). Those located near dynamical resonances may produce long-lived surges in the impact flux as the fragments are slowly driven to escape routes by nongravitational forces. Asteroid evolution models suggest that the contribution of kilometer-sized impactors from a large parent-body disruption would have reached their new level within a few tens of millions of years of the breakup event(s), with the wave of bodies perhaps receding after hundreds of millions of years (*21*, *22*).

REFERENCES AND NOTES

1. J. L. Bandfield *et al*., *J. Geophys. Res. Planets* **116**, E00H02 (2011).
2. R. R. Ghent *et al*., *Geology* **42**, 1059–1062 (2014).
3. Materials and methods are available as supplementary materials.
4. G. H. Heiken, D. T. Vaniman, B. M. French, *Lunar Sourcebook—A User's Guide to the Moon* (Cambridge Univ. Press, 1991).
5. R. J. Pike, *Geophys. Res. Lett.* **1**, 291–294 (1974).
6. T. S. Culler, T. A. Becker, R. A. Muller, P. R. Renne, *Science* **287**, 1785–1788 (2000).
7. N. Zellner, J. Delano, *Geochim. Cosmochim. Acta* **161**, 203–218 (2015).
8. C. I. Fassett, B. J. Thomson, *J. Geophys. Res. Planets* **119**, 2255–2271 (2014).
9. A. S. McEwen, J. M. Moore, E. M. Shoemaker, *J. Geophys. Res. Planets* **102** (E4), 9231–9242 (1997).
10. J. A. Grier, A. S. McEwen, P. G. Lucey, M. Milazzo, R. G. Strom, *J. Geophys. Res. Planets* **106** (E12), 32847–32862 (2001).
11. R. A. F. Greive, E. M. Shoemaker, The record of past impacts on Earth, in *Hazards Due to Comets and Asteroids* (Univ. Arizona Press, 1995), pp 417–462.
12. T. J. Blackburn *et al*., *Science* **335**, 73–76 (2012).
13. E. I. Smith, *J. Geophys. Res.* **76**, 5683–5689 (1971).
14. R. S. J. Sparks *et al*., *J. Volcanol. Geotherm. Res.* **155**, 18–48 (2006).
15. L. Wilson, J. W. Head Iii 3rd, *Nature* **447**, 53–57 (2007).
16. R. J. Brown, G. A. Valentine, *Geol. Soc. Am. Bull.* **125**, 1224–1238 (2013).
17. P. F. Hoffman, A. J. Kaufman, G. P. Halverson, D. P. Schrag, *Science* **281**, 1342–1346 (1998).
18. C. B. Keller *et al*., Neoproterozoic glacial origin of the Great Unconformity. *Proc. Natl. Acad. Sci. U.S.A.* 10.1073/pnas.1804350116 (2018).
19. M. S. DeLucia, W. R. Guenthner, S. Marshak, S. N. Thomson, A. K. Ault, *Geology* **46**, 167–170 (2017).
20. R. A. F. Grieve, W. U. Reimold, J. Morgan, U. Riller, M. Pilkington, *Meteorit. Planet. Sci.* **43**, 855–882 (2008).
21. W. F. Bottke, D. Vokrouhlický, D. Nesvorný, *Nature* **449**, 48–53 (2007).
22. D. Vokrouhlický, W. F. Bottke, D. Nesvorný, *Astron. J.* **153**, 172 (2017).
23. Paige *et al*., LRO DLRE LEVEL 5 GDR V1.0, NASA Planetary Data System, LRO-L-DLRE-5-GDR-V1.0 (2011); https://pds.nasa.gov/ds-view/pds/viewDataset.jsp?dsid=LRO-L-DLRE-5-GDR-V1.0; retrieved 22 July 2016.
24. "Earth Impact Database," Planetary and Space Science Centre (PASSC), University of New Brunswick; www.passc.net/EarthImpactDatabase; retrieved 22 July 2016.
25. S. Faure, CONSOREM Database (Version 3), Consortium de Recherche en Exploration Minérale CONSOREM, Université du Québec à Montréal; www.consorem.ca (2010); retrieved 22 July 2016.
26. M. Zanetti *et al*., *Icarus* **298**, 64–77 (2017).
27. H. Sato, M. S. Robinson, B. Hapke, B. W. Denevi, A. K. Boyd, *J. Geophys. Res. Planets* **119**, 1775–1805 (2014).
28. United States Geological Survey, Geologic Province Map; https://earthquake.usgs.gov/data/crust/type.html; retrieved 5 March 2018.
29. Geological Survey of Canada, "Generalized geological map of the world and linked databases," technical report 2915d (1995).

ACKNOWLEDGMENTS

We thank M. Schmeider and C. Koeberl for helpful discussions regarding ages of terrestrial craters, T. Hincks for her help generating the plots in Fig. 4 and fig. S5, and J. Husson for providing digital Precambrian bedrock outlines shown in Fig. 4. We thank P. F. Hoffman, C. B. Keller, and R. N. Mitchell for stimulating discussions concerning Cryogenian erosion. We also thank the anonymous referees for their useful and constructive comments. **Funding:** S.M.'s and R.R.G.'s work on this study were funded by a Discovery grant from the National Science and Engineering Research Council of Canada to R.R.G.; W.F.B.'s participation was supported by NASA's SSERVI program "Institute for the Science of Exploration Targets (ISET)" through institute grant NNA14AB03A. A.H.P.'s participation was supported in part by NASA's SSERVI program "Project for Exploration Science Pathfinder Research for Enhancing Solar System Observations (Project ESPRESSO)" through institute grant 80ARC0M0008. T.M.G. acknowledges funding from the UK Natural Environment Research Council, grant NE/R004978/1. **Author contributions:** R.R.G. conceived the lunar crater experiments and supervised data collection. S.M. collected lunar crater data. Statistical tests were performed by A.H.P. Expertise on asteroid evolution and impact probabilities was provided by W.F.B. Expertise on kimberlite pipes was provided by T.M.G. All authors (S.M, R.R.G., W.F.B, A.H.P., and T.M.G.) analyzed the results and wrote the manuscript. **Competing interests.** The authors have no competing interests. **Data and materials availability:** The LRO Diviner data used in this paper can be obtained from (*23*). The derived lunar crater data are provided in table S1, and the terrestrial crater data used [updated from (*24*)] are provided in table S2. The kimberlite database [updated from (*25*)] used to generate Fig. 4 and fig. S5 is provided in supplementary data file S1 (aar4058_s1). The Approximate Bayesian Computation rejection (ABCr) code and the counting area simulation code (used to generate fig. S4) are available at https://github.com/ghentr/Earth-Moon_flux.

SUPPLEMENTARY MATERIALS

www.sciencemag.org/content/363/6424/253/suppl/DC1
Materials and Methods
Supplementary Text
Figs. S1 to S6
Tables S1 and S2
References (*30*–*73*)
Data File S1

3 November 2017; resubmitted 5 June 2018
Accepted 5 December 2018
10.1126/science.aar4058

Downloaded from http://science.sciencemag.org/ on January 17, 2019

PHOTOSYNTHESIS

Structural adaptations of photosynthetic complex I enable ferredoxin-dependent electron transfer

Jan M. Schuller[1]*, James A. Birrell[2], Hideaki Tanaka[3,4], Tsuyoshi Konuma[5], Hannes Wulfhorst[6,7]†, Nicholas Cox[2,8], Sandra K. Schuller[9], Jacqueline Thiemann[6], Wolfgang Lubitz[2], Pierre Sétif[10], Takahisa Ikegami[5], Benjamin D. Engel[11], Genji Kurisu[3,4]*, Marc M. Nowaczyk[6]*

Photosynthetic complex I enables cyclic electron flow around photosystem I, a regulatory mechanism for photosynthetic energy conversion. We report a 3.3-angstrom-resolution cryo–electron microscopy structure of photosynthetic complex I from the cyanobacterium *Thermosynechococcus elongatus*. The model reveals structural adaptations that facilitate binding and electron transfer from the photosynthetic electron carrier ferredoxin. By mimicking cyclic electron flow with isolated components in vitro, we demonstrate that ferredoxin directly mediates electron transfer between photosystem I and complex I, instead of using intermediates such as NADPH (the reduced form of nicotinamide adenine dinucleotide phosphate). A large rate constant for association of ferredoxin to complex I indicates efficient recognition, with the protein subunit NdhS being the key component in this process.

Two light-driven electron transport pathways operate in all organisms that perform oxygenic photosynthesis: linear and cyclic electron flow. In linear electron flow (LEF), two photochemical reaction centers (photosystems I and II) act in series to drive the synthesis of adenosine triphosphate (ATP) and the reduced form of nicotinamide adenine dinucleotide phosphate (NADPH), whereas cyclic electron flow (CEF), powered by only photosystem I (PSI), leads solely to the formation of ATP. The contribution of each pathway varies in response to the environment (e.g., light quality), and organisms in which CEF is inactivated are functionally impaired (*1*).

Photosynthetic complex I of plant chloroplasts and cyanobacteria (*2*, *3*) has been implicated in CEF, taking electrons from and indirectly reinjecting them into PSI. It is structurally and functionally related to respiratory complex I from mitochondria and bacteria (*4*–*6*), but it lacks the peripheral dehydrogenase module (N-module), comprising subunits NuoE, NuoF, and NuoG (see table S1 for nomenclature in different organisms). This module catalyzes NADH (the reduced form of nicotinamide adenine dinucleotide) oxidation and contains five out of eight iron-sulfur (Fe-S) clusters. Biochemical and proteomic analyses of photosynthetic complexes have discovered at least eight distinct subunits required to assemble fully functional photosynthetic complex I (*7*–*13*). There is evidence that ferredoxin (Fd) likely mediates electron transfer between photosynthetic complex I and PSI (*14*), probably within a large supercomplex (*15*), but this process has not been directly observed. Furthermore, the structural adaptions that enable the photosynthetic complex to perform its distinct role remain uncharacterized.

We purified photosynthetic complex I from the thermophilic cyanobacterium *Thermosynechococcus elongatus* (fig. S1 and tables S2 and S3) and determined the structure by cryo–electron microscopy (cryo-EM) single-particle analysis to an overall resolution of 3.3 Å (Fig. 1; figs. S2 and S3; and table S4). We constructed models from homologous subunits or de novo where no model was available (fig. S4), except for NdhV, which binds transiently (*7*) and was not observed.

Photosynthetic complex I transfers electrons to the terminal acceptor plastoquinone. The quinone-binding site is coupled to the proton-pumping machinery in the membrane by a highly conserved charge-redistribution cascade (figs. S5 and S6), but the exact coupling mechanism remains elusive (*16*–*19*).

The photosynthesis-specific single-spanning membrane proteins NdhQ and NdhP (*8*) bind to either side of the NdhD protein, with NdhQ fixing the very long horizontal helix of NdhF (fig. S7). NdhP forms a small hydrophobic cavity to which a molecule of β-carotene is bound. A lipid molecule (monogalactosyldiacylglycerol) binds between the NdhD and NdhF proton channels and appears to be stabilized by the β-carotene molecule. Both molecules probably serve as "molecular glue," similar to lipids found in complex I of other species (*18*, *20*), to help assemble the proton-pumping membrane arm of the complex and to stabilize the NdhF binding interface. A third photosynthesis-specific membrane subunit, NdhL, binds to the N terminus of NdhA to form an extended heel under the peripheral arm (fig. S5).

The N-module subunits responsible for NADH oxidation are not present in photosynthetic complex I. Instead, the peripheral arm of the cyanobacterial complex (Q-module) contains photosynthesis-specific subunits (NdhM, NdhN, NdhO, and NdhS) (figs. S8 and S9), which bind to the conserved, nonmembrane subunits of complex I (NdhH, NdhI, NdhJ, and NdhK). The latter four subunits harbor three [4Fe-4S] clusters in addition to the quinone-binding site and have elongated termini that are conserved within the green linage (figs. S10 to S12). NdhM and NdhN are located at one side of the peripheral arm and form multiple interactions with the conserved [4Fe-4S]-carrying complex I subunits by binding to their elongated termini and covering otherwise solvent-exposed hydrophobic patches. NdhO has a globular fold and packs tightly to the side of NdhJ via a hydrophobic binding interface, covering the same space that is occupied by the species-specific protein TTHA1528 in *T. thermophilus* respiratory complex I (*21*). Furthermore, the photosynthesis-specific NdhS subunit, previously implicated in Fd binding (*22*), is located in a V-shaped groove formed by the NdhI protein, at a similar location to subunit Nqo15 within the N-module.

Our cryo-EM structure resolves the positions and conserved coordination of three [4Fe-4S] clusters, corresponding to the previously identified clusters N6a, N6b, and N2 in respiratory complex I (Fig. 2A). Electron paramagnetic resonance (EPR) measurements on chemically reduced samples quantitatively identify all three clusters (components 1, 2, and 3 in Fig. 2B). Components 1 and 2 are similar to the respiratory complex I signals of N2 and N6b (*23*, *24*), whereas component 3 bears little resemblance to N6a, in terms of width and structure (tables S6 and S13). The difference is due to either the proximity of N6a to N6b or the fact that N6a is surface exposed in photosynthetic complex I, as opposed to being buried in the protein, allowing it to act as the site of electron injection (see supplementary text).

To test the hypothesis that reduced Fd can inject electrons into photosynthetic complex I to enable CEF, we used absorption kinetics in

[1]Department of Structural Cell Biology, Max Planck Institute of Biochemistry, 82152 Martinsried, Germany. [2]Max Planck Institute for Chemical Energy Conversion, 45470 Mülheim an der Ruhr, Germany. [3]Institute for Protein Research, Osaka University, Suita, Osaka 565-0871, Japan. [4]Department of Macromolecular Science, Graduate School of Science, Osaka University, Toyonaka 560-0043, Japan. [5]Graduate School of Medical Life Science, Yokohama City University, 1-7-29 Suehiro-cho, Tsurumi-ku, Yokohama 230-0045, Japan. [6]Plant Biochemistry, Faculty of Biology and Biotechnology, Ruhr University Bochum, 44780 Bochum, Germany. [7]Daiichi Sankyo Deutschland GmbH, Zielstattstr. 48, 81379 München, Germany. [8]Research School of Chemistry, Australian National University, Canberra, ACT 2601, Australia. [9]Gene Center and Department of Biochemistry, Ludwig-Maximilians-Universität München, Feodor-Lynen-Str. 25, 81377 Munich, Germany. [10]Institut de Biologie Intégrative de la Cellule (I2BC), IBITECS, CEA, CNRS, Université Paris-Saclay, F-91198 Gif-sur-Yvette, France. [11]Department of Molecular Structural Biology, Max Planck Institute of Biochemistry, 82152 Martinsried, Germany.

***Corresponding author. Email: janschu@biochem.mpg.de (J.M.S.); gkurisu@protein.osaka-u.ac.jp (G.K.); marc.m.nowaczyk@rub.de (M.M.N.)** †Present address: Daiichi Sankyo Deutschland GmbH, Zielstattstr. 48, 81379 Munich, Germany.

Downloaded from http://science.sciencemag.org/ on January 19, 2019

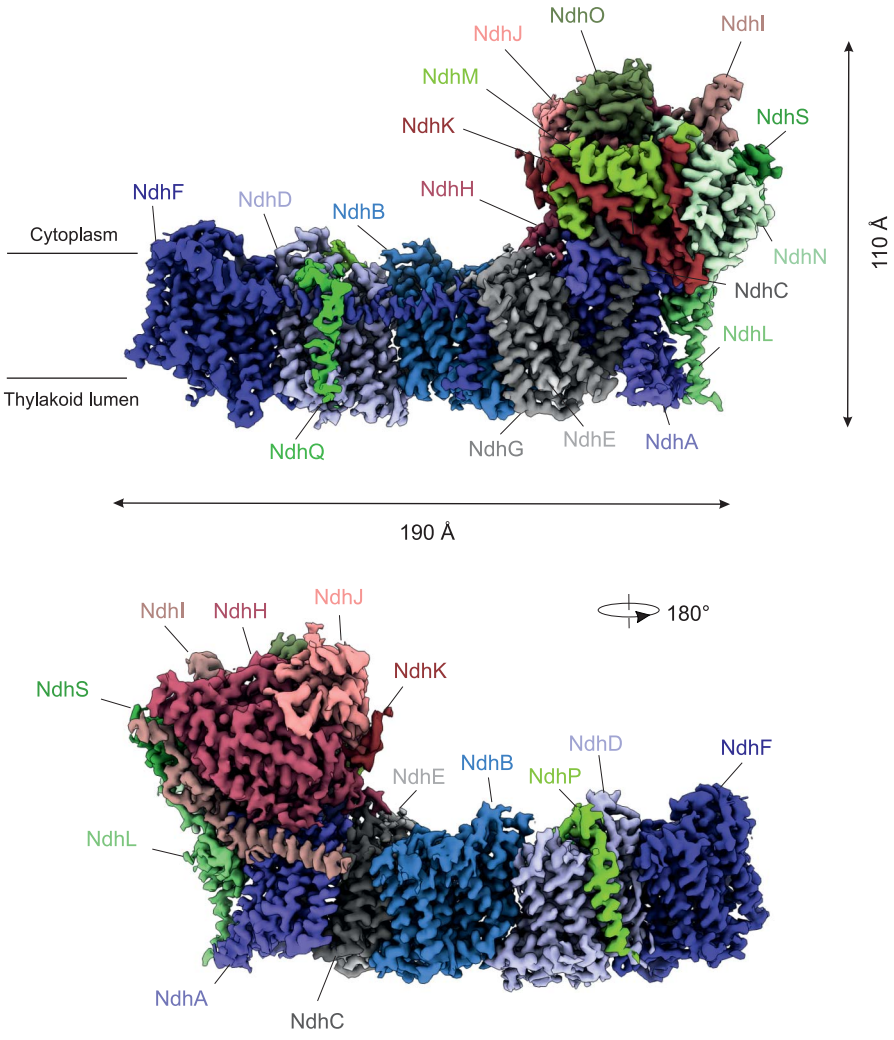


Fig. 1. Cryo-EM map of photosynthetic complex I from *T. elongatus* segmented by subunit. Eighteen subunits are colored and named accordingly (photosynthesis-specific subunits NdhL, NdhM, NdhN, NdhO, NdhP, NdhQ, and NdhS; other nonmembrane subunits NdhH, NdhI, NdhJ, and NdhK; and other membrane subunits NdhA, NdhB, NdhC, NdhD, NdhE, NdhF, and NdhG).

the submillisecond time range. Electron transfer reactions were monitored in vitro with samples containing purified PSI, Fd, and photosynthetic complex I (Fig. 2, C and D). Single PSI turnover was triggered with a short laser flash (Fig. 2C), and subsequent electron transfer was monitored by ultraviolet-visible light absorption (see supplementary text). Submicrosecond PSI charge separation and stabilization (fig. S14) was followed by Fd reduction by the terminal [4Fe-4S] cluster of PSI, dissociation of reduced Fd (Fd_{red}) from PSI, and reduction of a [4Fe-4S] cluster in photosynthetic complex I by Fd_{red} (Fig. 2C). The kinetics of the latter reaction were fitted to a biexponential function with rates of 245 and 1280 s^{-1} (Fig. 2C). With the conservative assumption that the slowest component (245 s^{-1}) corresponds to the association of Fd_{red} to the photosynthetic complex I, we calculated a lower limit of $k_{2FdComplexI} = 1.0 \times 10^9\ M^{-1}\ s^{-1}$ for binding. This association constant is clearly larger than values previously measured for other Fd partner proteins (*25*–*27*). We conclude that Fd participates in CEF via photosynthetic complex I and that Fd recruitment to complex I is very efficient.

The above analyses converge upon the hypothesis that the surface of the peripheral arm near the N6a cluster of photosynthetic complex I is responsible for Fd binding (Fig. 3A). We identified a putative Fd binding site in this region, guided by the surface charge at a tripartite interface formed by NdhK, NdhI, and NdhS (Fig. 3B). This surface area faces toward the missing [4Fe-4S] cluster N5 of the N-module of respiratory complex I (Fig. 2D).

Recent functional studies suggested that the photosynthesis-specific subunit NdhS plays an important role in CEF of *Arabidopsis thaliana* (*22*, *28*) and *Synechocystis* sp. PCC 6803 (*13*). However, because NdhS has no prosthetic group such as an Fe-S cluster or flavin, it is still elusive how it is involved in electron transfer of photosynthetic complex I. We confirmed that unbound NdhS adopts the same overall structure as in the full complex I by solving the x-ray crystal structure of recombinant NdhS at 1.90-Å resolution (table S5 and figs. S15 and S16). To assess the sites and mode of interaction between Fd and NdhS, we performed nuclear magnetic resonance (NMR) chemical shift perturbation experiments using ^{15}N-labeled Fd or NdhS with the nonlabeled counterpart, and vice versa (Fig. 3D and figs. S16 to S18). The NMR chemical shift perturbation indicated that the interaction site on NdhS was primarily located in its C-terminal region, from Glu^{104} (E104) to the C terminus, a domain that was not resolved in either the x-ray or cryo-EM structure owing to its high flexibility (Fig. 3, C and D). A similar "fly-casting" mechanism leads to fast electron transfer between Fd and ferredoxin:$NADP^+$ reductase (*25*, *29*), and it might be also responsible for the fast association between Fd and photosynthetic complex I. The C-terminal segment of NdhS contains five positively charged Lys residues, which likely "catch" the negatively charged patch of Fd through an electrostatic interaction. We propose that NdhS serves as a foothold for Fd binding by tuning the binding angle of Fd toward NdhI, the catalytic subunit with a redox center next to NdhS (Fig. 3C and fig. S19), as is the case for the variable subunit of ferredoxin:thioredoxin reductase and for the PsaE subunit of PSI.

Our structure of photosynthetic complex I suggests that adaptation of modular domains and interfaces contributes to functional differences between it and homologous complexes. The minimal functional unit of the Q-module for Fd-dependent electron transfer is shared with membrane-bound hydrogenase from Archaea (*30*), thus suggesting that they also share the minimal required interaction site for Fd binding. In respiratory complex I, the N-module is attached to the Q-module to enable NADH oxidation (*21*), whereas in photosynthetic complex I, extensions and accessory subunits (including NdhS) facilitate highly efficient electron transfer from Fd. The photosynthesis-specific structural elements may also mediate supercomplex formation with PSI, which is proposed to further optimize CEF in cyanobacteria and plants (*15*).

REFERENCES AND NOTES

1. Y. Munekage *et al.*, *Nature* **429**, 579–582 (2004).
2. G. Peltier, E.-M. Aro, T. Shikanai, *Annu. Rev. Plant Biol.* **67**, 55–80 (2016).
3. N. Battchikova, M. Eisenhut, E.-M. Aro, Cyanobacterial NDH-1 complexes: Novel insights and remaining puzzles *Biochim. Biophys. Acta* **1807**, 935–944 (2011).
4. L. A. Sazanov, *Nat. Rev. Mol. Cell Biol.* **16**, 375–388 (2015).
5. J. Hirst, M. M. Roessler, Energy conversion, redox catalysis and generation of reactive oxygen species by respiratory complex *I. Biochim. Biophys. Acta* **1857**, 872–883 (2016).
6. C. Wirth, U. Brandt, C. Hunte, V. Zickermann, Structure and function of mitochondrial complex *I. Biochim. Biophys. Acta* **1857**, 902–914 (2016).

Downloaded from http://science.sciencemag.org/ on January 19, 2019

Fig. 2. Assignment of Fe-S clusters by EPR spectroscopy and in vitro electron transfer kinetics from PSI via Fd toward complex I. (**A**) [4Fe-4S] clusters N6a, N6b, and N2 with coordinating subunits NdhI (dark salmon) and NdhK (ruby) compared with the corresponding *T. thermophilus* subunits Nqo9 and Nqo6 [gray, Protein Data Bank (PDB) 4HEA (*21*)]. (**B**) An EPR spectral simulation (red dashed line) of the spectrum at 10 K (black line), along with simulated spectra for the individual components (green, blue, and pink lines) and their associated *g*-values. (**C**) Changes in flash-induced absorption at 580 nm ($\Delta A_{580\ nm}$), attributed to Fd reduction by PSI (left) and complex I reduction by Fd_{red} (right). These changes correspond to differences between signals 1, 2, and 3, recorded in three different cuvettes containing PSI, PSI-Fd, and PSI-Fd-complex I, respectively (see individual measurements in fig. S14). The left graph shows the difference between signals 2 and 1. The slow component after 0.2 ms was fitted by a single rising exponential function (black curve; rate, 1379 s^{-1}). The difference is due to oxidized Fd (Fd_{ox}) binding to PSI (which follows Fd_{red} dissociation) with a second-order rate constant of 2.8×10^8 M^{-1} s^{-1} (see materials and methods). The downward arrow corresponds to the reduction of Fd by the PSI terminal acceptor. The right graph shows the difference between signals 3 and 2. To account for the lag preceding the signal rise due to complex I reduction by Fd_{red}, the kinetics were fitted by a biexponential function with rates of 245 and 1280 s^{-1} (black curve). The upward arrow corresponds to the reduction of a [4Fe-4S] cluster in photosynthetic complex I by Fd. The PSI, Fd, and complex I concentrations were 0.08, 5.0, and 0.24 μM, respectively. (**D**) Superposition of photosynthetic complex I (green) with the *T. thermophilus* complex I [gray, PDB 4HEA (*21*)]. The N-module—which contains the NADH binding site, the flavin mononucleotide (FMN) cofactor, and the six Fe-S clusters N1a, N1b, N3, N4, N5, and N7 that transfer electrons from NADH (light blue arrows)—is missing from photosynthetic complex I. In vitro, electrons are transferred after light-induced charge separation from PSI [PDB 5ZF0 (*31*)] via Fd [PDB 5AUI (*32*)] toward the Q-module of photosynthetic complex I, as indicated by the red and dark blue arrows. The lightning bolt indicates application of a laser flash to excite PSI. PQ, plastoquinone.

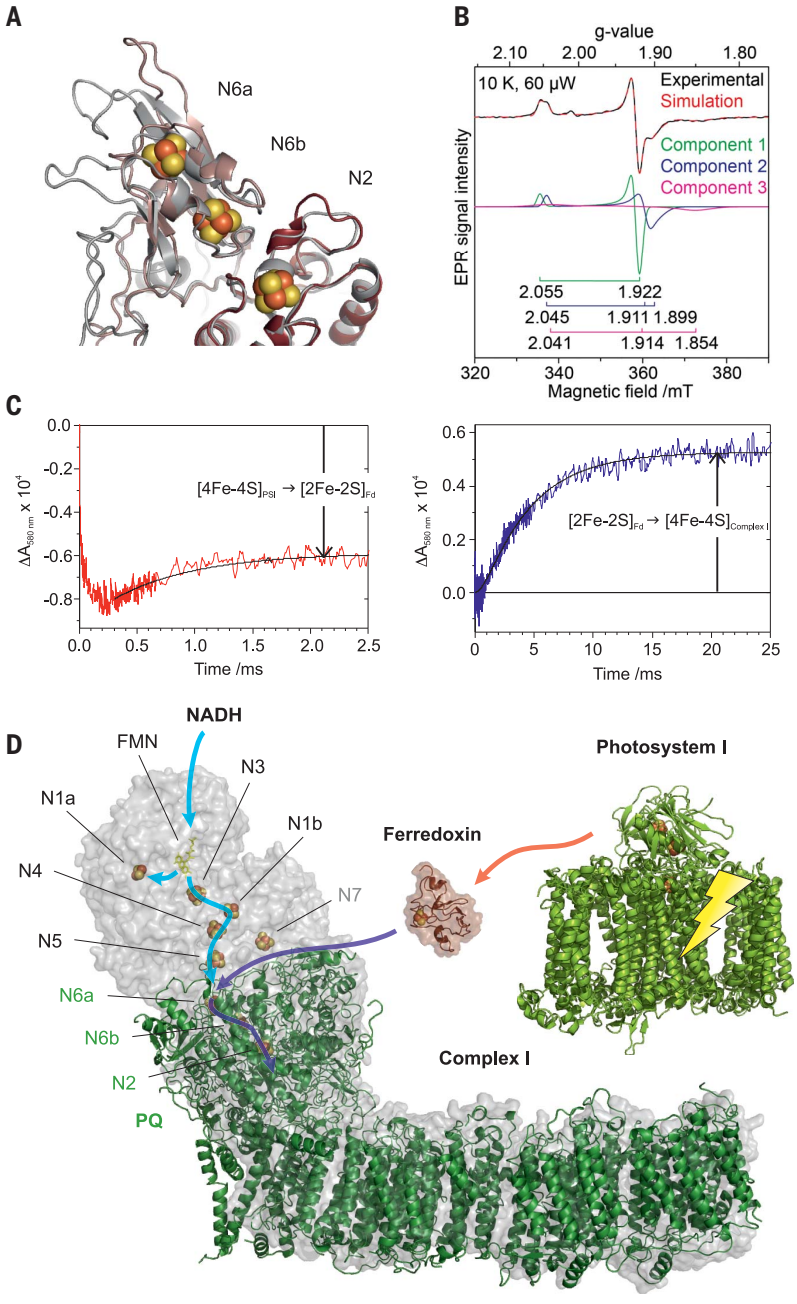
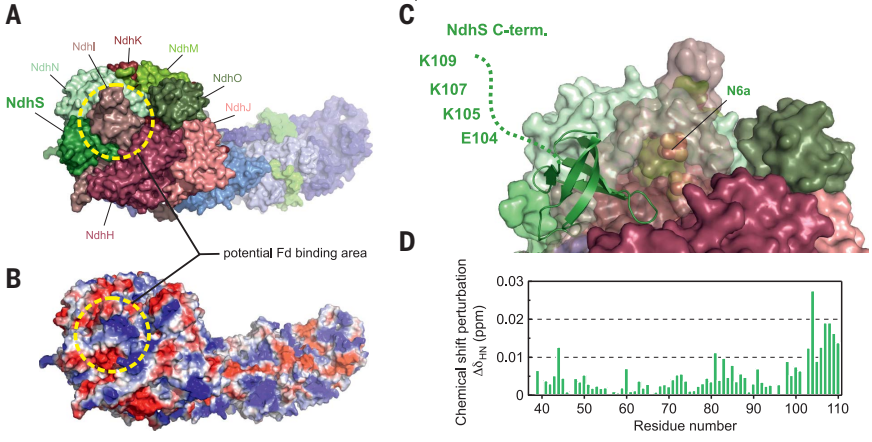


Fig. 3. Adaptation of the Q-module to Fd binding and the role of the NdhS C terminus. (**A**) Top view of the complex I surface with colored subunits. The potential Fd binding area is indicated by the yellow dashed circle. (**B**) Electrostatic potential surfaces on complex I (red for negative, white for neutral, and blue for positive) were calculated with the Adaptive Poisson-Boltzmann Solver (APBS) plug-in in PyMOL. (**C**) The C-terminal segment of NdhS (green ribbon structure) that was not resolved in the x-ray and cryo-EM structures is drawn as a dotted line in an arbitrary position. K, Lys. (**D**) Weighted $^1H/^{15}N$ chemical shift perturbations observed in [^{15}N]-NdhS upon binding to non-labeled Fd. ppm, parts per million.



Downloaded from http://science.sciencemag.org/ on January 19, 2019

7. X. Fan, J. Zhang, W. Li, L. Peng, *Plant J.* **82**, 221–231 (2015).
8. M. M. Nowaczyk *et al.*, *Biochemistry* **50**, 1121–1124 (2011).
9. T. Ogawa, *Plant Physiol.* **99**, 1604–1608 (1992).
10. N. Battchikova, P. Zhang, S. Rudd, T. Ogawa, E.-M. Aro, *J. Biol. Chem.* **280**, 2587–2595 (2005).
11. P. Prommeenate, A. M. Lennon, C. Markert, M. Hippler, P. J. Nixon, *J. Biol. Chem.* **279**, 28165–28173 (2004).
12. D. Rumeau *et al.*, *Plant Cell* **17**, 219–232 (2005).
13. N. Battchikova *et al.*, *J. Biol. Chem.* **286**, 36992–37001 (2011).
14. T. Friedrich, K. Steinmüller, H. Weiss, *FEBS Lett.* **367**, 107–111 (1995).
15. L. Peng, H. Shimizu, T. Shikanai, *J. Biol. Chem.* **283**, 34873–34879 (2008).
16. V. R. I. Kaila, *J. R. Soc. Interface* **15**, 20170916 (2018).
17. V. Zickermann *et al.*, *Science* **347**, 44–49 (2015).
18. A. A. Agip *et al.*, *Nat. Struct. Mol. Biol.* **25**, 548–556 (2018).
19. L. A. Sazanov, *J. Bioenerg. Biomembr.* **46**, 247–253 (2014).
20. K. Fiedorczuk *et al.*, *Nature* **538**, 406–410 (2016).
21. R. Baradaran, J. M. Berrisford, G. S. Minhas, L. A. Sazanov, *Nature* **494**, 443–448 (2013).
22. H. Yamamoto, L. Peng, Y. Fukao, T. Shikanai, *Plant Cell* **23**, 1480–1493 (2011).
23. M. Narayanan *et al.*, *J. Biol. Chem.* **288**, 14310–14319 (2013).
24. T. Yano, S. Magnitsky, V. D. Sled', T. Ohnishi, T. Yagi, *J. Biol. Chem.* **274**, 28598–28605 (1999).
25. N. Cassan, B. Lagoutte, P. Sétif, *J. Biol. Chem.* **280**, 25960–25972 (2005).
26. P. Sétif *et al.*, *Biochemistry* **48**, 2828–2838 (2009).
27. A. P. Srivastava, D. B. Knaff, P. Sétif, *Biochemistry* **53**, 5092–5101 (2014).
28. H. Yamamoto, T. Shikanai, *J. Biol. Chem.* **288**, 36328–36337 (2013).
29. M. Maeda *et al.*, *Biochemistry* **44**, 10644–10653 (2005).
30. H. Yu *et al.*, *Cell* **173**, 1636–1649.e16 (2018).
31. H. Kubota-Kawai *et al.*, *Nat. Plants* **4**, 218–224 (2018).
32. R. Mutoh *et al.*, *Biochemistry* **54**, 6052–6061 (2015).

ACKNOWLEDGMENTS

We thank F. Hara, K. Umeno, N. Hamaoka, Y. Misumi, J. Y. Kim, C. König, M. Völkel, and R. Oworah-Nkruma for excellent technical assistance and Y. Miyanoiri, E. Yamashita, and A. Nakagawa for support during data collection by x-ray and NMR analysis. J.M.S. is grateful to E. Conti for scientific independence and great mentorship and to J. M. Plitzko and W. Baumeister for access to the cryo-EM infrastructure and early career support. P.S. thanks A. Boussac and B. Lagoutte for purification of PSI and Fd. M.M.N. is grateful to his mentor M. Rögner for generous support. Synchrotron radiation experiments were performed at BL44XU of SPring-8, Japan (proposal no. 2017B6500). **Funding:** Financial support was provided by the Max Planck Society, the Cluster of Excellence RESOLV (EXC 1069 to W.L., N.C., and M.M.N.) funded by the German Research Council (DFG), the DFG research unit FOR2092 (EN 1194/1-1 to B.D.E. and NO 836/3-2 to M.M.N.), the DFG priority program 2002 (NO 836/4-1 to M.M.N.), DFG grant NO 836/1-1 (to M.M.N.), the Australian Research Council (FT140100834 to N.C.), JST-CREST (JPMJCR13M4 to G.K.), MEXT-KAKENHI (16H06560 to G.K.), the French Infrastructure for Integrated Structural Biology/FRISBI ANR-10-INSB-05 (P.S.), and the International Joint Research Promotion Program, Osaka University (G.K. and M.M.N.). **Author contributions:** J.M.S., J.A.B., N.C., W.L., P.S., B.D.E., G.K., and M.M.N. conceived the research, prepared the figures, and wrote the manuscript with the contributions of all other authors.
M.M.N. coordinated the activities. Preparation of complex I, biochemical analysis, and mass spectrometry were done by H.W., J.T., and M.M.N. J.M.S. and B.D.E. performed the cryo-EM analysis and built the structural model with the help of S.K.S. and G.K. Flash-absorption spectroscopy was carried out by P.S. EPR experiments were conducted by J.A.B. and N.C. and NMR and x-ray analysis by H.T., T.K., T.I., and G.K. All authors approved the final version of the manuscript. **Competing interests**: The authors declare no competing interests. **Data and materials availability:** The cryo-EM density map is deposited in the Electron Microscopy Data Bank under accession number EMD-0281. The atomic models of the cryo-EM and x-ray structures are deposited in the worldwide Protein Data Bank under accession numbers 6HUM and 6A7K, respectively. All other data are available in the manuscript or the supplementary materials.

SUPPLEMENTARY MATERIALS

www.sciencemag.org/content/363/6424/257/suppl/DC1
Materials and Methods
Supplementary Text
Figs. S1 to S19
Tables S1 to S6
References (*33*–*88*)

20 September 2018; accepted 6 December 2018
Published online 20 December 2018
10.1126/science.aau3613

Downloaded from http://science.sciencemag.org/ on January 19, 2019

CHEMICAL PHYSICS

Observation of magnetically tunable Feshbach resonances in ultracold $^{23}Na^{40}K + ^{40}K$ collisions

Huan Yang[1,2]*, De-Chao Zhang[1,2]*, Lan Liu[1,2]*, Ya-Xiong Liu[1,2], Jue Nan[1,2], Bo Zhao[1,2]†, Jian-Wei Pan[1,2]†

Resonances in ultracold collisions involving heavy molecules are difficult to simulate theoretically and have proven challenging to detect. Here we report the observation of magnetically tunable Feshbach resonances in ultracold collisions between potassium-40 (^{40}K) atoms and sodium-23–potassium-40 ($^{23}Na^{40}K$) molecules in the rovibrational ground state. We prepare the atoms and molecules in various hyperfine levels of their ground states and observe the loss of molecules as a function of the magnetic field. The atom-molecule Feshbach resonances are identified by observing an enhancement of the loss. We have observed 11 resonances in the magnetic field range of 43 to 120 gauss. The observed atom-molecule Feshbach resonances at ultralow temperatures probe the three-body potential energy surface with exceptional resolution and will help to improve understanding of ultracold collisions.

Understanding collisions involving molecules at the quantum level has been a long-standing goal in chemical physics (*1*). Scattering resonances are among the most remarkable quantum phenomena and play a critically important role in the study of collisions. They are sensitive to both the long-range and short-range portions of the molecule interaction potential and thus offer an ideal probe of the potential energy surface (PES) governing the collision dynamics. In theory, describing the PES requires solving the Schrödinger equation involving many electrons and nuclei, which is notoriously difficult owing to the electron correlations. Therefore, measurement of scattering resonances not only provides a global and accurate probe of the PES but also helps provide understanding of the complicated quantum many-body problem.

Although scattering resonances are well known and have been the main features studied in ultracold atomic gases and nuclear collisions (*2*), they have proven challenging to observe in molecular systems. Recently, major progress has been achieved in the experimental study of resonances in cold molecular collisions involving light particles—for example, H_2, HD molecules, or He atoms—by means of molecular beam techniques. In crossed-beam or merged-beam experiments, shape resonances or Feshbach resonances have been observed in atom-molecule chemical reactions (*3*–*8*), atom-molecule inelastic collisions (*9*–*11*), and molecule-molecule inelastic collisions (*12*, *13*). However, in these experiments, the collision energies are still high (at kelvin or subkelvin), and thus a few partial waves contribute to the scattering cross sections.

Ultracold molecules offer great opportunities to study molecular collisions in the quantum regime. At ultralow temperatures, the de Broglie wavelength of the collision partners is much larger than the range of molecular interaction potential, and only the lowest possible partial wave of relative orbital angular momentum dominates the collision process (*14*, *15*). Consequently, the collisions at ultracold temperatures are highly quantum mechanical. Owing to the anisotropy of the PES, the collisions involving ultracold molecules may support many resonances that are contributed by the rotational and vibrational excited states (*16*, *17*). Therefore, it is expected that scattering resonances should be routinely observed in ultracold molecular systems. For ultracold collisions involving light molecules, the low density of resonant states allows calculations of the scattering resonances, and many Feshbach resonances in atom-molecule collisions (*18*–*20*) and molecule-molecule collisions (*16*, *21*) have been predicted. However, owing to the experimental difficulties of preparing the ultracold colliding particles, these predictions have not been tested.

The situation is much more complicated for ultracold collisions involving heavy molecules, such as the alkali-metal-diatomic molecules in the rovibrational ground state created from ultracold atomic gases (*22*–*28*). The scattering resonances involving these heavy molecules are difficult to calculate and are highly challenging to observe. For reactive collisions, the reactions are universal, and the short-range losses with a near-unity probability suppress any possible resonances (*15*, *29*). For nonreactive atom-molecule collisions, the PES is so deep that thousands of rovibrational states may contribute to the resonances. As a consequence, the density of resonant states near the threshold of the collision channel is quite high, and it is not clear whether the individual resonances are resolvable (*17*). In this case, the theoretical calculation of the Feshbach resonances is extremely difficult, especially when nuclear spins and external fields are considered (*30*). Instead, a statistical model has been adopted to explore such highly resonant scattering (*17*), which predicts that at a temperature below 1 μK, for atom-diatomic-molecule collisions, many s-wave Feshbach resonances with an average spacing of less than 1 gauss should be observable. However, the experimental observation of these resonances remains elusive.

Here we report the observation of magnetic Feshbach resonances between ultracold $^{23}Na^{40}K$ ground-state molecules and ^{40}K atoms. The binding energies of $^{23}Na^{40}K$ [vibrational quantum number (v) = 0] and $^{40}K_2$ (v = 0) are about 5212 cm^{-1} (*25*) and 4405 cm^{-1} (*29*), respectively. Therefore, $^{23}Na^{40}K$ (v = 0, N = 0) + ^{40}K collisions with N the rotational quantum number are nonreactive: The reaction $^{23}Na^{40}K$ (v = 0) + $^{40}K \rightarrow {}^{40}K_2$ (v = 0) + ^{23}Na is highly endothermic and is forbidden at ultracold temperatures. The atomization energy of NaK_2 is estimated to be 7125 cm^{-1} (*31*), which gives rise to a deep PES. As illustrated in Fig. 1, the channels that are asymptotically closed support many triatomic bound states, which may lead to a high density of resonant states near the threshold. We prepared $^{23}Na^{40}K$ molecules and ^{40}K atoms in various hyperfine levels of their ground states and searched for the resonances by measuring the loss rate of the molecules due to atom-molecule inelastic collisions as a function of the magnetic field. The appearance of a Feshbach resonance is identified by observing a resonantly enhanced loss. We have observed 11 resonances in the magnetic field range $43 < B < 120$ G, where B is the magnetic field.

We first searched for the atom-molecule Feshbach resonances in the magnetic field range $99.3 < B < 103.8$ G, which is close to a broad atomic Feshbach resonance at 110 G. We created weakly bound Feshbach molecules in an ultracold ^{23}Na and ^{40}K atomic mixture at a temperature of about 500 nK by Raman photoassociation. The remaining ^{23}Na atoms were removed immediately after the Feshbach molecules were formed. We then transferred the molecules from the Feshbach state to the rovibrational ground state by means of stimulated Raman adiabatic passage (STIRAP). The details of the association and the STIRAP are given in the supplementary materials (*32*). The hyperfine levels of the ground states of the $^{23}Na^{40}K$ molecule are labeled by $|v, N, m_{I_{Na}}, m_{I_K}\rangle$, where the vibrational and rotational quantum numbers are $v = N = 0$ and $m_{I_{Na}}$

[1]Hefei National Laboratory for Physical Sciences at Microscale and Department of Modern Physics, University of Science and Technology of China, Hefei, Anhui 230026, China. [2]Shanghai Branch, CAS Center for Excellence and Synergetic Innovation Center in Quantum Information and Quantum Physics, University of Science and Technology of China, Shanghai 201315, China.
*These authors contributed equally to this work.
†Corresponding author. Email: bozhao@ustc.edu.cn (B.Z.); pan@ustc.edu.cn (J.-W.P.)

Downloaded from http://science.sciencemag.org/ on January 17, 2019

and m_{I_K} are the nuclear spin projections of ^{23}Na and ^{40}K, respectively. In our experiment, the hyperfine states $|0,0,-3/2,-2\rangle$, $|0,0,-3/2,-1\rangle$, $|0,0,-1/2,-3\rangle$, and $|0,0,-1/2,-2\rangle$ could be populated by choosing proper intermediate states and laser polarizations. The hyperfine structure of the ground-state molecule is shown in Fig. 1. After the ground-state molecules were prepared, the ^{40}K atoms were transferred to different hyperfine states $|f,m_f\rangle_K$ by radio frequency pulses, with the atomic angular momentum $f = 9/2$ and the projection quantum number $m_f = -9/2, \ldots, -1/2$. In this way, 20 different combinations of the atom and molecule hyperfine states could be prepared.

The ^{23}Na^{40}K molecules decay owing to two-body hyperfine-changing inelastic collisions with the ^{40}K atoms because the atoms and molecules are in excited hyperfine states. The hyperfine change may be caused by the interaction between the nuclear spins of the molecules and the unpaired electron spin of the atoms during the collision process (*17*). We recorded the time evolution of the number of the molecules, as shown in Fig. 2. After a certain hold time, the number of the remaining ground-state molecules was measured by transferring the molecules back to the Feshbach states, which were detected by absorption imaging. The typical lifetime of the molecules in the atom-molecule mixture is on the order of 10 ms. This is much shorter than the lifetime of the pure molecule gas, which is longer than 100 ms in the whole magnetic field window. Therefore, the decay of the molecule in the mixture is dominantly caused by atom-molecule inelastic collisions.

The decay of the molecules may be described by $dN_m/dt = -\gamma N_m$, where N_m is the number of molecules, t is time, and $\gamma = \beta\bar{n}_a$ is the decay rate, with β and $\bar{n}_a$ being the loss rate coefficient and the mean density of the ^{40}K atoms, respectively. The mean atomic density may be calculated by $\bar{n}_a = [(m_K\bar{\omega}^2)/(4\pi k_B T_K)]^{3/2} N_a$, where $\bar{\omega}$ is the geometric mean trapping frequencies of the ^{40}K atoms, k_B is the Boltzmann constant, T_K is the temperature, and N_a is the number of ^{40}K atoms. In our experiment, the number of ^{40}K atoms is about one order of magnitude larger than that of the molecules, and thus the mean density $\bar{n}_a$ is approximately a constant. In this case, the loss rate coefficient β may be extracted from the measured decay rate γ and the atomic mean density $\bar{n}_a$.

We searched for the atom-molecule Feshbach resonances in 20 different incoming collision channels. For each channel, we measured the loss rate coefficient as a function of the magnetic field. By varying the magnetic field, we expected to change the energy differences between the triatomic bound states and the threshold of the incoming scattering channel. If a triatomic bound state intersects the threshold of the scattering channel and the coupling between the bound state and the scattering state is strong, a Feshbach resonance may occur. The Feshbach resonances are identified through the strongly enhanced loss rate coefficients (*2*, *17*).

In the experiment, we found that the loss rate coefficients were different for various collision channels. For each channel, in most cases, the loss rate coefficients did not change considerably in the magnetic field range (*32*). However, in the $|0,0,-3/2,-2\rangle + |9/2,-3/2\rangle$, $|0,0,-3/2,-2\rangle + |9/2,-7/2\rangle$, and $|0,0,-1/2,-3\rangle + |9/2,-7/2\rangle$ collision channels, the loss rate coefficients show prominent features at about 101 G (Fig. 3). We attribute these loss features to the resonant enhancement of the inelastic collisions due to the s-wave atom-molecule Feshbach resonance. The resonance positions and widths obtained by the Gaussian fits are listed in Table 1.

It is valuable to compare the measured loss rate coefficients with the universal rate coefficient (*15*, *29*), which assumes short-range loss with unity probability. Using the parameters in (*17*), the s-wave universal rate coefficient is estimated to be about 1.3×10^{-10} cm^3/s. The background loss rate coefficients are usually smaller than the universal rate coefficient, except in the $|0,0,-1/2,-3\rangle + |9/2,-5/2\rangle$ channel. The resonantly enhanced loss rate coefficients in the three collision channels are larger than the universal rate coefficient by a factor of about 2 to 3.

We used a similar method to measure the loss rate coefficients in the magnetic field range of 89.4 to 89.9 G, close to an atomic Feshbach resonance at about 90.3 G (*32*). In this magnetic field window, we found that for the $|0,0,-3/2,-2\rangle + |9/2,-9/2\rangle$ channel, the loss rate coefficients in the range of 89.4 to 89.9 G are notably larger than the coefficients in the range of 99.3 to 103.8 G, which indicates that a loss feature may exist near 90 G. We also performed similar measurements in the magnetic field range of 84.4 to 85.6 G, where the atom and molecule can both be prepared in the lowest hyperfine states. In this

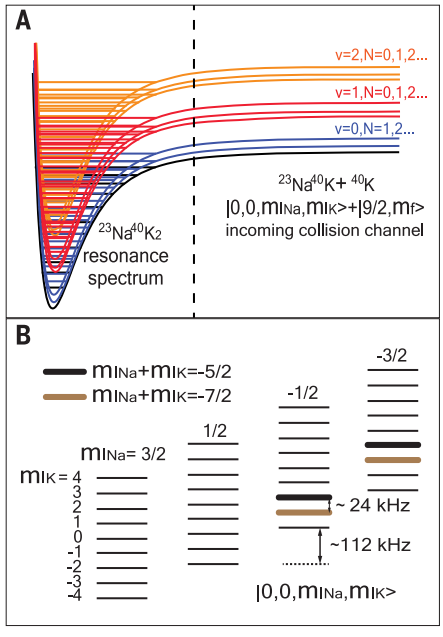


Fig. 1. Illustration of the atom-molecule Feshbach resonances between the ground-state ^{23}Na^{40}K molecule and ^{40}K atom. (**A**) The PES is very deep, and thus a large number of channels that are asymptotically closed can support the triatomic bound states, which give rise to a high density of resonant states near the threshold. The incoming channel is ^{23}Na^{40}K (v = 0, N = 0) + ^{40}K in a specific combination of hyperfine states. The atom-molecule Feshbach resonances probe the short-range resonance spectrum. The energy of the collision channels can be magnetically tuned. A Feshbach resonance occurs once the energy of the incoming channel coincides with the energy of a bound state. (**B**) Hyperfine structure of the ^{23}Na^{40}K ground-state molecule at a magnetic field of 100 G. The hyperfine levels of the ^{23}Na^{40}K molecule in the rovibrational ground state of the $^1\Sigma$ singlet potential are split owing to the nuclear Zeeman effects. The nuclear spin projections $m_{I_{Na}}$ and m_{I_K} are approximately good quantum numbers. The hyperfine levels that are used in the experiment are marked by thick black and brown lines.

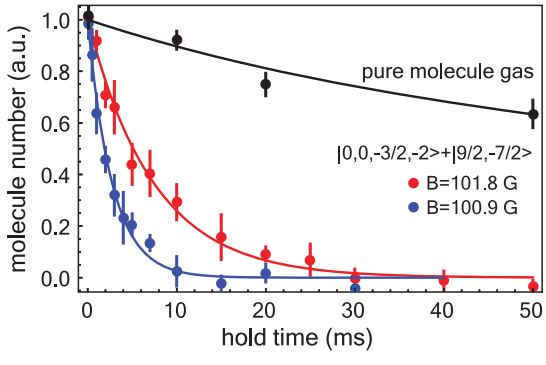


Fig. 2. The decay of the ^{23}Na^{40}K molecule in the atom-molecule mixture. The time evolutions of the number of the molecules are recorded. The solid curves are exponential fits with reduced chi-square values of 0.86 (red line) and 2.8 (blue line). The fits are not weighted to error bars. The loss rate coefficients are extracted from the measured decay rate. As a reference, the decay of the pure molecule gas in the $|0,0,-3/2,-2\rangle$ state at a magnetic field of 100.9 G is also shown. For the $|0,0,-3/2,-2\rangle + |9/2,-7/2\rangle$ collision, it can be clearly seen that the loss rates are dependent on the magnetic field. Each data point represents the average of three to five measurements, and the error bars represent 1 SD of the molecule number. a.u., arbitrary units.

Downloaded from http://science.sciencemag.org/ on January 17, 2019

magnetic field range, we did not observe an enhanced loss feature. We might expect that preparing both the molecule and atom in the lowest hyperfine states would largely suppress the loss rate. However, compared with the case in which the atom is prepared in the $|9/2, -7/2\rangle$ state, we do not observe a notable suppression of the loss rate. More theoretical and experimental studies are needed to understand these loss rate coefficients.

The observation of the three resonant loss features indicates that the resonance is resolvable. However, the magnetic field range that can be studied is limited close to the atomic Feshbach resonance, because the experiments are performed at fixed magnetic fields. This has hindered us from locating the possible resonance between $|0, 0, -3/2, -2\rangle$ and $|9/2, -9/2\rangle$ at about 90 G. To observe more resonances, the magnetic field range was expanded to $43 < B < 120$ G as follows. We first prepared the atom-molecule mixture at 102.3 G. After that, we swept the magnetic field to a desired strength in 2.5 to 4 ms. We have used the pre-emphasis method (*32*–*34*) to compensate for the magnetic fields created by the eddy currents induced by the stainless chamber or large coils. The atom-molecule mixture was held at the desired magnetic field for about 7 ms. During the hold time, the realistic magnetic field was within 100 to 400 mG of the desired magnetic field. The hold time was chosen in such a way that the resonantly enhanced loss could be clearly distinguished from the background loss. The ^{40}K atoms were then removed and the magnetic field swept back to 102.3 G in 3 ms, where the remaining molecules were transferred back to Feshbach state for detection. The Feshbach resonances manifest as the loss features of the remaining molecule number versus the magnetic field. Using this method, we have studied the collisions between the molecule state $|0, 0, -3/2, -2\rangle$ and the atom states $|9/2, -9/2\rangle$, $|9/2, -7/2\rangle$, and $|9/2, -5/2\rangle$, with a step of about 0.5 G. As shown in Fig. 4, we have observed eight new resonantly enhanced loss features. The resonance positions and widths obtained by the Gaussian fits are listed in Table 1. The resonance between $|0, 0, -3/2, -2\rangle$ and $|9/2, -9/2\rangle$ at about 90 G is clearly localized. The resonance between $|0, 0, -3/2, -2\rangle$ and $|9/2, -7/2\rangle$ at 101 G is also observed with this method.

The observation of the Feshbach resonances allows us to compare these values with the density of resonant states estimated from the statistical model. For the ^{23}Na^{40}K + ^{40}K collision studied in our experiment, neglecting the nuclear spins, the density of resonant states is estimated to be about 1.22 per mK (*17*). If the nuclear spins are considered, the density of resonant states is multiplied by the number of spin states that conserve the total magnetic quantum number. Assuming that the short-range physics does not change with the magnetic field, the resonance spectrum is probed with a rate of the Zeeman shift of the scattering channel (*17*). These arguments predict many s-wave resonances with an average spacing of about 1 G. However, in the approximate 70-G-wide magnetic field range, we observe only 11 resonantly enhanced loss features. This indicates that the density of resonant states may be not as large as the statistical model predicts. We cannot exclude the possibility that there are some narrow resonances that are not observed in our experiment.

In conclusion, we have observed magnetically tunable Feshbach resonances in ultracold collisions between ^{23}Na^{40}K ground-state molecules and ^{40}K atoms. In such a heavy and ultracold system, there may be many resonances in a magnetic field range of a few hundred gauss. The observation of more resonances may enable the study of the quantum chaos in ultracold molecular collisions (*17*).

The observed ultracold atom-molecule scattering resonances probe the short-range resonance spectrum with exceptional resolution and provide valuable information about the PES. So far, the accuracy of the PES calculated by solving the electronic Schrödinger equation is on the order of cm^{-1}, which is too low to be used to quantitatively understand these resonances. Therefore, the experimental observation of ultracold atom-molecule resonances challenges the accuracy of quantum chemistry simulations. In this sense, the observation of ultracold resonances provides a well-controlled and powerful tool to accurately simulate the quantum many-body problem in quantum chemistry. The observation of Feshbach resonances also opens up

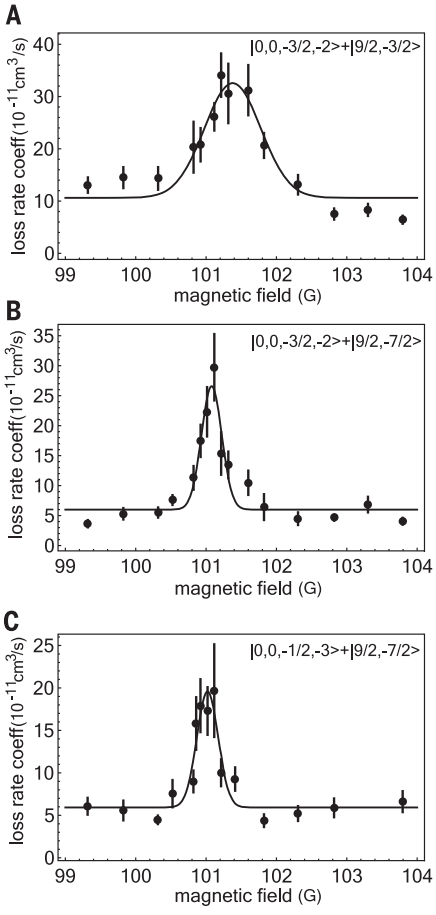


Fig. 3. Observations of the atom-molecule Feshbach resonances in the loss rate coefficients. (**A** to **C**) The loss rate coefficients are plotted as a function of the magnetic field. The collision channels are $|0, 0, -3/2, -2\rangle + |9/2, -3/2\rangle$ (A), $|0, 0, -3/2, -2\rangle + |9/2, -7/2\rangle$ (B), and $|0, 0, -1/2, -3\rangle + |9/2, -7/2\rangle$ (C). For these three channels, the resonantly enhanced loss rate coefficients at about 101 G provide clear evidence of the atom-molecule Feshbach resonances. The solid lines are phenomenological Gaussian fits with reduced chi-square values of 5.4 (A), 4.2 (B), and 2.4 (C). The fits are not weighted to error bars. The error bars represent 1 SD of the loss rate coefficients arising from the fitting uncertainty of decay rates and uncertainty of atomic densities.

Table 1. The Feshbach resonance position B_0 and width ΔB obtained by the Gaussian fits. The first three resonances are observed by measuring the loss rates at fixed magnetic fields. The other resonances are observed by sweeping the magnetic field. The resonance between $|0, 0, -3/2, -2\rangle$ and $|9/2, -7/2\rangle$ at 101 G is observed by both methods, and the second method gives a larger width.

Method	Collision channel	B_0 (G)	ΔB (G)
I	$\|0, 0, -3/2, -2\rangle + \|9/2, -3/2\rangle$	101.4	0.6
	$\|0, 0, -3/2, -2\rangle + \|9/2, -7/2\rangle$	101.1	0.2
	$\|0, 0, -1/2, -3\rangle + \|9/2, -7/2\rangle$	101.0	0.2
II	$\|0, 0, -3/2, -2\rangle + \|9/2, -5/2\rangle$	68.0	1.6
		74.2	3.5
		83.2	2.0
	$\|0, 0, -3/2, -2\rangle + \|9/2, -7/2\rangle$	54.5	0.6
		59.1	3.7
		101.0	0.6
		106.7	1.7
	$\|0, 0, -3/2, -2\rangle + \|9/2, -9/2\rangle$	48.1	2.6
		89.8	2.9

Downloaded from http://science.sciencemag.org/ on January 17, 2019

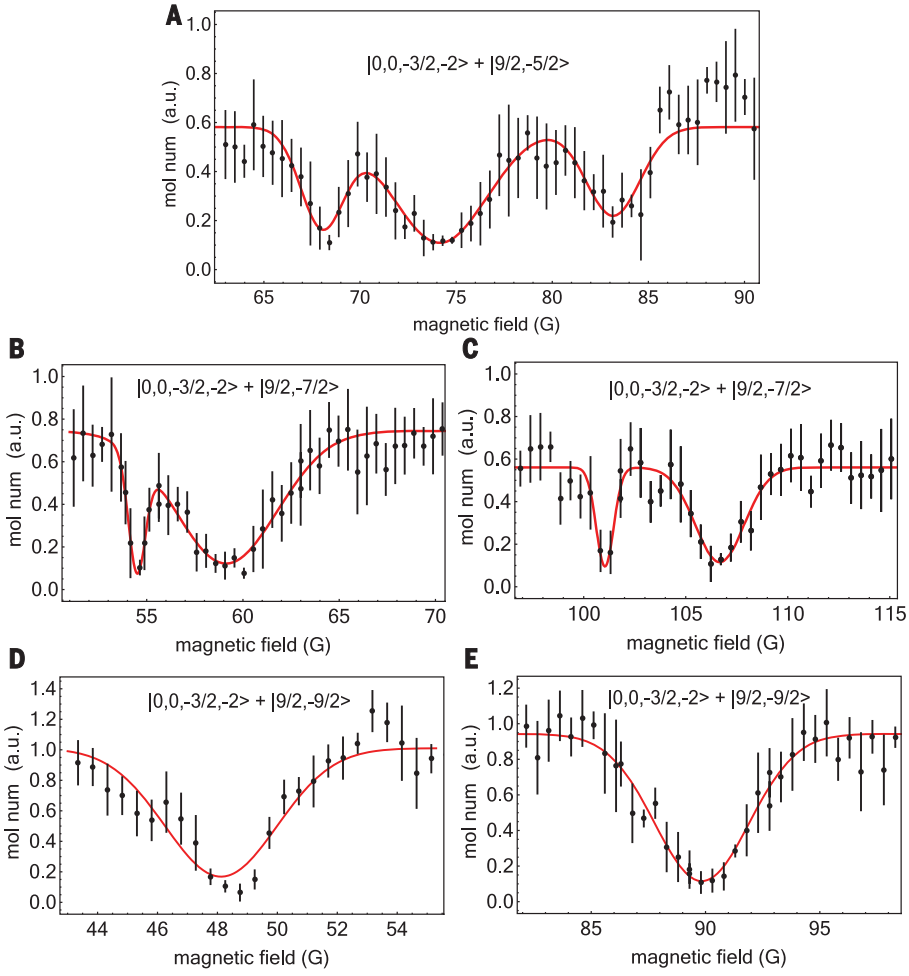


Fig. 4. The resonantly enhanced loss features observed by sweeping the magnetic field. (**A** to **E**) The remaining molecule numbers are plotted as a function of the magnetic field. The loss features provide clear evidence of the atom-molecule Feshbach resonances. The resonance between $|0,0,-3/2,-2\rangle$ and $|9/2,-7/2\rangle$ at about 101 G is also observed using this method. The solid red lines are phenomenological Gaussian fits with reduced chi-square values of 1.2 (A), 0.81 (B), 0.66 (C), 1.4 (D), and 0.56 (E). The fits are not weighted to error bars. Each data point represents the average of five to eight measurements, and the error bars represent 1 SD of the molecule number.

the exciting possibility of studying resonantly interacting atom-molecule mixtures and may allow creation of ultracold triatomic molecules using magnetic association (*2*).

REFERENCES AND NOTES

1. D. Herschbach, *Faraday Discuss.* **142**, 9–23 (2009).
2. C. Chin, R. Grimm, P. Julienne, E. Tiesinga, *Rev. Mod. Phys.* **82**, 1225–1286 (2010).
3. R. T. Skodje *et al.*, *Phys. Rev. Lett.* **85**, 1206–1209 (2000).
4. M. Qiu *et al.*, *Science* **311**, 1440–1443 (2006).
5. A. B. Henson, S. Gersten, Y. Shagam, J. Narevicius, E. Narevicius, *Science* **338**, 234–238 (2012).
6. T. Wang *et al.*, *Science* **342**, 1499–1502 (2013).
7. J. B. Kim *et al.*, *Science* **349**, 510–513 (2015).
8. T. Yang *et al.*, *Science* **347**, 60–63 (2015).
9. S. N. Vogels *et al.*, *Science* **350**, 787–790 (2015).
10. A. Bergeat, J. Onvlee, C. Naulin, A. van der Avoird, M. Costes, *Nat. Chem.* **7**, 349–353 (2015).
11. A. Klein *et al.*, *Nat. Chem.* **13**, 35–38 (2017).
12. S. Chefdeville *et al.*, *Science* **341**, 1094–1096 (2013).
13. W. E. Perreault, N. Mukherjee, R. N. Zare, *Science* **358**, 356–359 (2017).
14. L. D. Carr, D. DeMille, R. V. Krems, J. Ye, *New J. Phys.* **11**, 055049 (2009).
15. G. Quéméner, P. S. Julienne, *Chem. Rev.* **112**, 4949–5011 (2012).
16. J. L. Bohn, A. V. Avdeenkov, M. P. Deskevich, *Phys. Rev. Lett.* **89**, 203202 (2002).
17. M. Mayle, B. P. Ruzic, J. L. Bohn, *Phys. Rev. A* **85**, 062712 (2012).
18. T. V. Tscherbul, R. V. Krems, *Phys. Rev. Lett.* **97**, 083201 (2006).
19. M. T. Hummon *et al.*, *Phys. Rev. Lett.* **106**, 053201 (2011).
20. M. D. Frye, M. Morita, C. L. Vaillant, D. G. Green, J. M. Hutson, *Phys. Rev. A* **93**, 052713 (2016).
21. T. V. Tscherbul, Y. V. Suleimanov, V. Aquilanti, R. V. Krems, *New J. Phys.* **11**, 055021 (2009).
22. K.-K. Ni *et al.*, *Science* **322**, 231–235 (2008).
23. T. Takekoshi *et al.*, *Phys. Rev. Lett.* **113**, 205301 (2014).
24. P. K. Molony *et al.*, *Phys. Rev. Lett.* **113**, 255301 (2014).
25. J. W. Park, S. A. Will, M. W. Zwierlein, *Phys. Rev. Lett.* **114**, 205302 (2015).
26. M. Guo *et al.*, *Phys. Rev. Lett.* **116**, 205303 (2016).
27. T. M. Rvachov *et al.*, *Phys. Rev. Lett.* **119**, 143001 (2017).
28. F. Seeßelberg *et al.*, *Phys. Rev. A* **97**, 013405 (2018).
29. S. Ospelkaus *et al.*, *Science* **327**, 853–857 (2010).
30. J. F. E. Croft, N. Balakrishnan, B. K. Kendrick, *Phys. Rev. A* **96**, 062707 (2017).
31. P. S. Żuchowski, J. M. Hutson, *Phys. Rev. A* **81**, 060703 (2010).
32. Materials and methods are available as supplementary materials.
33. M. L. Olsen, "Experiments with Feshbach molecules in a Bose-Fermi mixture," thesis, University of Colorado (2008).
34. C.-L. Hung, "In situ probing of two-dimensional quantum gases," thesis, University of Chicago (2011).

ACKNOWLEDGMENTS

Funding: This work was supported by the National Key R&D Program of China (under grant no. 2018YFA0306502), the National Natural Science Foundation of China (under grant no.11521063), the Chinese Academy of Sciences, and the Anhui Initiative in Quantum Information Technologies. **Author contributions:** B.Z. and J.-W.P. conceived the experiment. H.Y., D.-C.Z., and L.L. carried out the experiments. All authors contributed to the analysis of the data and to the writing of the manuscript. B.Z. and J.-W.P. supervised the work. **Competing interests:** The authors declare no competing interests. **Data and materials availability:** All data are available in the main text or the supplementary materials.

SUPPLEMENTARY MATERIALS

www.sciencemag.org/content/363/6424/261/suppl/DC1
Materials and Methods
Figs. S1 to S5
Table S1
References (*35*–*40*)
Data S1

20 June 2018; resubmitted 27 August 2018
Accepted 28 November 2018
10.1126/science.aau5322

Downloaded from http://science.sciencemag.org/ on January 17, 2019

SOLAR CELLS

A Eu^{3+}-Eu^{2+} ion redox shuttle imparts operational durability to Pb-I perovskite solar cells

Ligang Wang[1], Huanping Zhou[1]*, Junnan Hu[1], Bolong Huang[2], Mingzi Sun[2], Bowei Dong[1], Guanghaojie Zheng[1], Yuan Huang[1], Yihua Chen[1], Liang Li[1], Ziqi Xu[1], Nengxu Li[1], Zheng Liu[1], Qi Chen[3], Ling-Dong Sun[1]*, Chun-Hua Yan[1]*

The components with soft nature in the metal halide perovskite absorber usually generate lead $(Pb)^0$ and iodine $(I)^0$ defects during device fabrication and operation. These defects serve as not only recombination centers to deteriorate device efficiency but also degradation initiators to hamper device lifetimes. We show that the europium ion pair Eu^{3+}-Eu^{2+} acts as the "redox shuttle" that selectively oxidized Pb^0 and reduced I^0 defects simultaneously in a cyclical transition. The resultant device achieves a power conversion efficiency (PCE) of 21.52% (certified 20.52%) with substantially improved long-term durability. The devices retained 92% and 89% of the peak PCE under 1-sun continuous illumination or heating at 85°C for 1500 hours and 91% of the original stable PCE after maximum power point tracking for 500 hours, respectively.

Device lifetime and power conversion efficiency (PCE) are the key factors determining the final cost of the electricity that solar cells generate. The certified PCE of perovskite solar cells (PSCs) has rapidly reached 23.7% over the past few years (*1*–*9*), which is on par with that of polycrystalline silicon and $Cu(In,Ga)Se_2$ solar cells, but poor device stability (*10*–*12*) under operating conditions prevents the perovskite photovoltaics from occupying even a tiny market share (*13*, *14*). Generally, commercial solar cells come with a warranty of a 20- to 25-year lifetime with a less than 10% drop of PCE, which corresponds to an average degradation rate of ~0.5% per year (*15*). Compared with those inorganic photovoltaic materials—e.g., silicon (IV group) and CIGS (I-III-VI group) (*16*)—the elements or components are mostly large and more polarized in organic-inorganic halide perovskite materials, such as I^-, methylammonium (MA^+), and Pb^{2+}. They construct a soft crystal lattice prone to deform (*17*) and vulnerable to various aging stresses such as oxygen, moisture (*18*, *19*), and ultraviolet (UV) exposure (*20*, *21*). By encapsulation (*22*–*24*), interface modification (*13*, *25*–*29*), and UV filtration, the device lifetime can be prolonged by the temporary exclusion of these external environmental factors.

However, some aging stresses cannot be avoided during device operation, including light illumination, electric field, and thermal stress, upon which both I^- and Pb^{2+} in perovskites become chemically reactive to initiate the decomposition even if they are well encapsulated (*30*). Because of the soft nature of I^-, Pb^{2+} ions, and Pb-I bonding, intrinsic degradation would occur in perovskite materials upon various excitation stresses, which finally induce PCE deterioration. On one hand, I^- is easily oxidized to I^0, which not only serve as carrier recombination centers but also initiate chemical chain reactions to accelerate the degradation in perovskite layers (*31*). On the other hand, Pb^{2+} is prone to be reduced to metallic Pb^0 upon heating or illumination, which has been observed in Pb halide perovskite films (*32*, *33*).

Pb^0 is a primary deep defect state that severely degrades the performance of perovskite optoelectronic devices (*34*, *35*), as well as their long-term durability (*36*). Furthermore, most soft inorganic semiconductors are suffering similar instability, such as PbS (*37*), PbI_2 (*38*, *39*), and AgBr (*40*), among others. Several attempts have been reported to eliminate either Pb^0 or I^0 defects, like optimizing film processing (*41*) and additive engineering (*42*–*44*). To date, these additives are mostly sacrificial agents specific for one kind of defects, which diminish soon after they take effects. Long-term operational durability requires the simultaneous elimination of both Pb^0 and I^0 defects in perovskite materials in a sustainable manner.

We demonstrated constant elimination of Pb^0 and I^0 simultaneously in PSCs over their life span, which leads to exceptional stability improvement and high PCE through incorporation of the ion pair of Eu^{3+} (f^6) ↔ Eu^{2+} (f^7) as the redox shuttle. In this cyclic redox transition, Pb^0 defects could be oxidized by Eu^{3+}, while I^0 defects could be reduced by Eu^{2+} at same time. The Eu^{3+}-Eu^{2+} pair is not consumed during device operation, probably because of its nonvolatility and the suitable redox potential in this cyclic transition. Thus, the champion PCE of the corresponding device was promoted to 21.52% (certified, 20.52%) with negligible current density-voltage (*J*-*V*) hysteresis. Devices with the Eu^{3+}-Eu^{2+} ion pair exhibited excellent shelf lifetime and thermal and light stability, which suggests that this approach may provide a universal solution to the inevitable degradation issue during device operation.

The reaction between Pb^0 and I^0 is thermodynamically favored and has a standard molar Gibbs formation energy for PbI_2(s) of –173.6 kJ/mol (*45*), which provides the driving force for eliminating both defects. However, simply mixing metallic Pb and I_2 powder only led to limited formation of PbI_2, which suggests the presence of kinetic barriers at room temperature. To enable elimination of Pb^0 and I^0 defects in PSCs simultaneously across device life span, we propose the "redox shuttle" to oxidize Pb^0 and reduce I^0 independently, wherein they can be regenerated during the complete circle. It requires selectively oxidizing Pb^0 and reducing I^0 defects without introducing additional deep-level defects. After finely screening many possible redox shuttle additives, the rare earth ion pair of Eu^{3+}-Eu^{2+} was identified as the best candidate, mostly owing to their appropriate redox potentials. Eu^{3+} could easily be reduced to Eu^{2+} with the stable half-full f^7 electron configuration to form the naturally associated ion pair. The redox shuttle can transfer electrons from Pb^0 to I^0 defects in a cyclical manner, wherein the Eu^{3+} oxidizes Pb^0 to Pb^{2+} and the formed Eu^{2+} simultaneously reduces I^0 to I^- (Fig. 1F). Thus, each ion in this pair is mutually replenished during defects elimination.

The proposed redox shuttle eliminates corresponding defects on the basis of the following two chemical reactions:

$$2Eu^{3+} + Pb^0 \rightarrow 2Eu^{2+} + Pb^{2+} \quad (1)$$

$$Eu^{2+} + I^0 \rightarrow Eu^{3+} + I^- \quad (2)$$

We first explored the feasibility of the Eu^{3+}-Eu^{2+} ion pair to promote electron transfer from Pb^0 to I^0 in solution (Fig. 1A) by dispersing I_2 (25 mg) powder and metallic Pb powder (25 mg) in 2 ml of *N*,*N*-dimethylformamide (DMF) and isopropanol (IPA) that had a volume ratio of 1:10 as a reference solution. The Eu^{3+}-Eu^{2+} ion pair was incorporated by further adding europium acetylacetonate [$Eu(acac)_3$] (11 mg) into the 2-ml solution. Under continuous stirring at 100°C,

[1]Beijing National Laboratory for Molecular Sciences, State Key Laboratory of Rare Earth Materials Chemistry and Applications, PKU-HKU Joint Laboratory in Rare Earth Materials and Bioinorganic Chemistry, Key Laboratory for the Physics and Chemistry of Nanodevices, Beijing Key Laboratory for Theory and Technology of Advanced Battery Materials, Department of Materials Science and Engineering, College of Engineering, College of Chemistry and Molecular Engineering, Peking University, Beijing 100871, P.R. China. [2]Department of Applied Biology and Chemical Technology, The Hong Kong Polytechnic University, Hung Hom, Kowloon, Hong Kong SAR. [3]Department of Materials Science and Engineering, Beijing Institute of Technology, Beijing 100081, P.R. China.
*Corresponding author. Email: happy_zhou@pku.edu.cn (H.Z.); yan@pku.edu.cn (C.-H.Y.); sun@pku.edu.cn (L.-D.S.)

Downloaded from http://science.sciencemag.org/ on January 17, 2019

the sample solution gradually turned from black to colorless with a large amount of yellow precipitates after 60 min, whereas the reference solution remained dark brown with little evidence of yellow precipitates.

UV-visible (UV-vis) spectra of the reference solution exhibited an absorption peak at ~370 nm (Fig. 1B), which we attributed to the presence of an I^0 species (*36*) that was absent in the sample solution, which had an absorption peak at ~290 nm that we attributed to a PbI_x species. Both the I^0 and Pb^0 species were effectively converted to I^- and Pb^{2+} upon Eu^{3+} addition. An x-ray diffraction (XRD) measurement on the precipitates revealed both PbI_2 (12.7°, 25.9°, 39.5°) and metallic Pb (31.3°, 36.2°, 52.2°) species in both cases (Fig. 1C). In the sample, the characteristic peak intensity ratio of PbI_2 to metallic Pb was larger than that of the reference. This result further confirmed that Eu^{3+} could accelerate the conversion of Pb^0 and I^0 to Pb^{2+} and I^-, respectively.

When we added $Eu(acac)_3$ to the CH_3NH_3I solution of water/chloroform, we observed no I^0 species absorption peak in the corresponding UV-vis spectrum (Fig. 1D), showing that Eu^{3+} selectively oxidizes Pb^0 rather than I^-. The stronger oxidizing agent of Fe^{3+} oxidized I^- species, and the absorption peak of I^0 was present. We verified that Eu^{3+} was reduced to paramagnetic Eu^{2+} in $CH_3NH_3PbI_3$ ($MAPbI_3$) perovskite films with 1% (Eu/Pb, molar ratio) Eu^{3+} incorporated, which showed a strong signal in electron paramagnetic resonance (EPR) measurements (Fig. 1E) that was absent in Eu_2O_3 and in the reference $MAPbI_3$ film.

We compared the effect of Eu^{3+} by studying other ions, including redox-inert Y^{3+} and strong oxidizing Fe^{3+}, by preparing film samples incorporated with 1% metal ions (M/Pb, molar ratio) and performed high-resolution x-ray photoelectron spectroscopy (XPS) analysis to elucidate the potential effects on both Pb^0 and I^0 defects. As shown in Fig. 2A, the binding energy (BE) at 142.8 and 137.9 eV were assigned to $4f_{5/2}$, $4f_{7/2}$ of divalent Pb^{2+}, respectively, and the two shoulder peaks at 141.3 and 136.4 eV around lower BE were associated with metallic Pb^0. We calculated the intensity ratio of $Pb^0/(Pb^0 + Pb^{2+})$ for three metal-incorporated samples and the reference to observe a notable tendency (Fig. 2, A and D, and table S1). The Pb^0 intensity ratio in reference reached 5.4%, which is comparable to that of Y^{3+}-incorporated film. This ratio in the perovskite film with oxidative Eu^{3+} and Fe^{3+} additives was reduced to nearly 1.0%, indicating that metallic Pb^0 was successfully oxidized.

With respect to I^0 species, it is difficult to obtain $I^0/(I^0 + I^-)$ ratio by peak fitting accurately

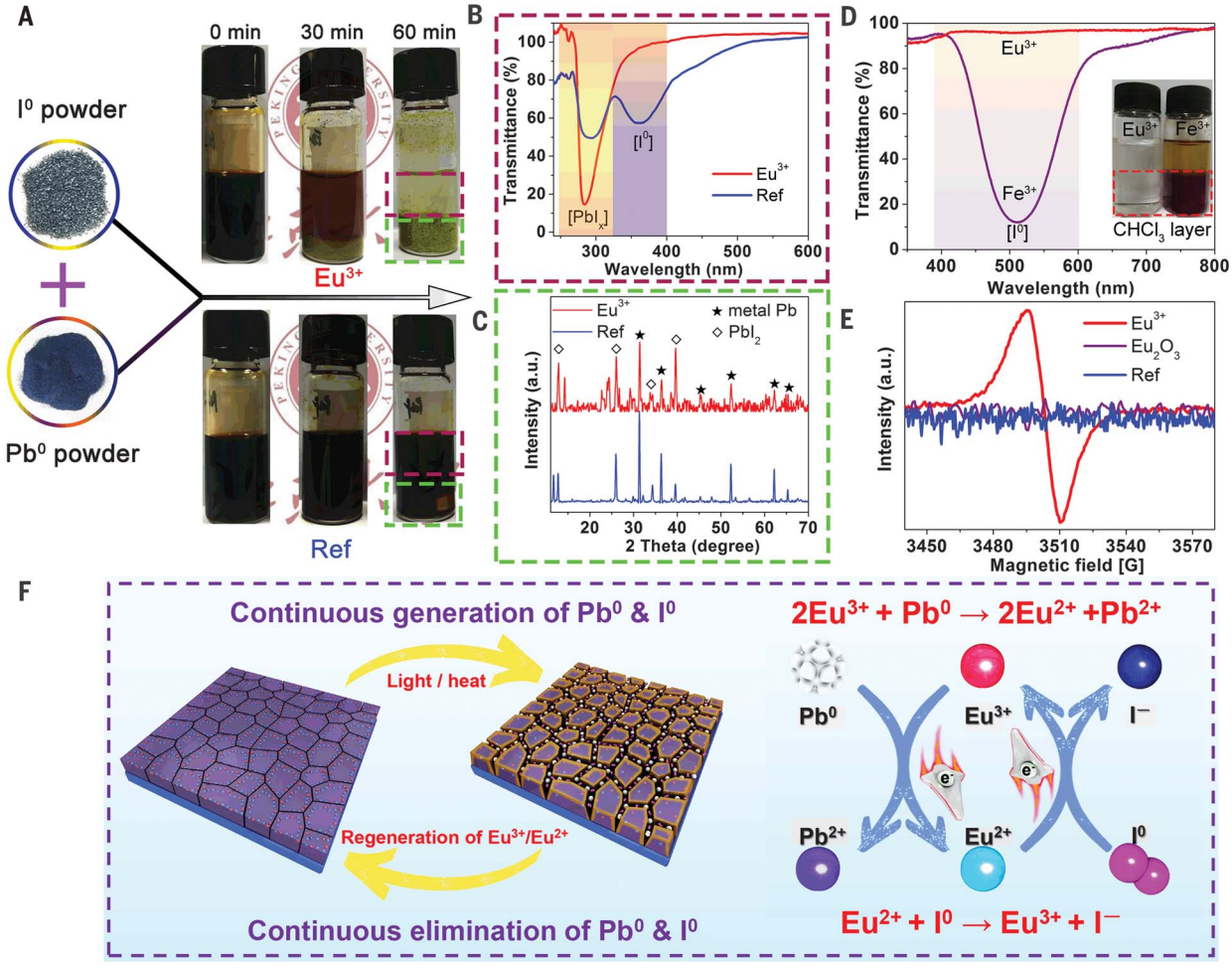


Fig. 1. Eu^{3+}-Eu^{2+} ion pair promotes the conversion of Pb^0 and I^0 to Pb^{2+} and I^- in solution and perovskite film. (**A**) I^0 and Pb^0 powder dispersed in mixed DMF/IPA solvent (volume ratio 1:10) with or without Eu^{3+} [$Eu(acac)_3$], and the solutions were stirred at 100°C. (**B**) The UV-vis absorption spectra of the upper solution and (**C**) XRD patterns of the bottom precipitation from the sample and reference solutions (after 60 min) shown in (A). (**D**) The representative solution and the absorption spectra of bottom layer in which MAI mixed with Eu^{3+} or Fe^{3+} dissolved in water/chloroform. (**E**) EPR spectra of $MAPbI_3$ film with or without Eu^{3+} incorporation and Eu_2O_3 sample, for which the value of proportionality factor (g-factor) is 2.0023. (**F**) Proposed mechanism diagram of cyclically elimination of Pb^0 and I^0 defects and regeneration of Eu^{3+}-Eu^{2+} metal ion pair. a.u., arbitrary units; Ref, reference.

Downloaded from http://science.sciencemag.org/ on January 17, 2019

because I^0 species are volatile during the annealing process of perovskite film preparation. Thus, we examined the ratio of I/Pb and BE shift to monitor the iodine evolution indirectly. As shown in Fig. 2, B and E, and table S1, we observed the similar I/Pb ratio in the reference and the Y^{3+}-incorporated sample but a much lower ratio in the Fe^{3+} sample. Incorporation of Fe^{3+} likely generated I^0 species that were released. A higher I/Pb ratio was observed in the Eu^{3+} sample compared with the reference, possibly indicating less volatile I^0 species produced in the corresponding film. Furthermore, the BE of I $3d_{3/2}$ further confirmed the argument, wherein it shifted toward a higher value of 0.3 eV in Fe^{3+} sample but lower 0.2 eV in Eu^{3+} sample as compared with the reference. Given the lower BE of I^-, it clearly showed that I^- was well preserved in the Eu^{3+} sample. In addition, Eu^{2+} was 36% of the total Eu content, which further confirmed the Eu^{3+}-Eu^{2+} ion pair working as a redox shuttle (Fig. 2C).

According to the charge conservation rule, the amount of I^0 should be twice that of Pb^0 involved in the entire redox reaction. Iodine species (HI and I_2) are all volatile, which follows the 1:2 molar ratio (*33*). We checked the total change in the amount of iodine (ΔI) and lead (ΔPb^0) in the film upon the addition of $Eu(acac)_3$, wherein $\Delta I/\Delta Pb^0$ was calculated to be 3.5 (see table S1 and supplementary text). The change in the amount of iodine (ΔI) was about three times that of lead (ΔPb^0) during the degradation process, indicating that the amount of I^0 species preserved was twice that of Pb^0 species consumed upon redox shuttle addition. In the context of a redox reaction, the standard electrode potential (E^θ) is often used as a reference point to rationally predict the occurrence of the reaction. According to the E^θ of each half reaction involved (which may deviate in solid materials) (table S2), Fe^{3+} is too oxidative and oxidizes Pb^0 and I^- simultaneously. On the contrary, Eu^{3+} exhibited the suitable E^θ to selectively oxidize Pb^0 without I^- oxidation, while the reduction product of Eu^{2+} reduced I^0 to I^- at same time. Thus, the constant elimination of Pb^0 and I^0 defects still preserved the Eu^{3+}-Eu^{2+} ion pair.

We examined the effectiveness of Eu^{3+}-Eu^{2+} redox shuttle in the film. Metallic Pb^0 is the major accumulated defect in aged perovskite films because of its nonvolatility (*33*). The content of Pb^0 is a measure of the extent of decomposition in the perovskite film. When the sample was subjected to 1 sun illumination or 85°C aging condition for more than 1000 hours, the $Pb^0/(Pb^0 + Pb^{2+})$ ratio in films with redox shuttle were 2.5% or 2.7%, compared with 7.4% or 11.3% in the reference film, respectively, as shown in fig. S1 and table S3. The redox shuttle can preserve the I/Pb ratio in the aged film. Meanwhile, the corresponding I/Pb ratio in Eu^{3+}-incorporated film was 2.68 or 2.57 as compared with that of reference 2.30 or 2.13, indicating the perovskite film was well preserved.

We also examined the crystallographic and optoelectronic properties perovskite films with the redox shuttle. According to XRD results, the phase structure was retained in the perovskite films with improved crystallinity upon Eu^{3+} addition (figs. S2 to S4). No residual acetylacetonate anion was detected by XPS and Fourier transform infrared spectroscopy measurement (figs. S5 and S6). The Eu^{3+}-Eu^{2+} ions were concentrated near the film surface, wherein the detected Eu/Pb ratio was much higher than the precursor ratio (table S1). When the $Eu(acac)_3$ was introduced from 0.15 to 4.8%, we observed neither extra diffraction peaks nor an obvious shift of diffraction peaks in the XRD patterns (figs. S2 to S4), which indicates that Eu^{3+}-Eu^{2+} ions may not necessarily accommodate in the crystal lattice.

Given the similar radius of Eu^{2+} [117 pm (*46*)] and Pb^{2+} (119 pm), however, we cannot confidently rule out the possibility that Eu^{2+} replaces Pb^{2+} at B site, wherein direct evidence is expected. In addition, europium-iodine–based organic-inorganic perovskite (*47*) and lanthanide ions doped $CsPbX_3$ perovskite nanocrystals were found in previous reports (*48*). The morphology and grain size of the perovskite film with the tiny amount redox shuttle remained similar to the reference (Fig. 3A and fig. S7). Also, we did not

Downloaded from http://science.sciencemag.org/ on January 17, 2019

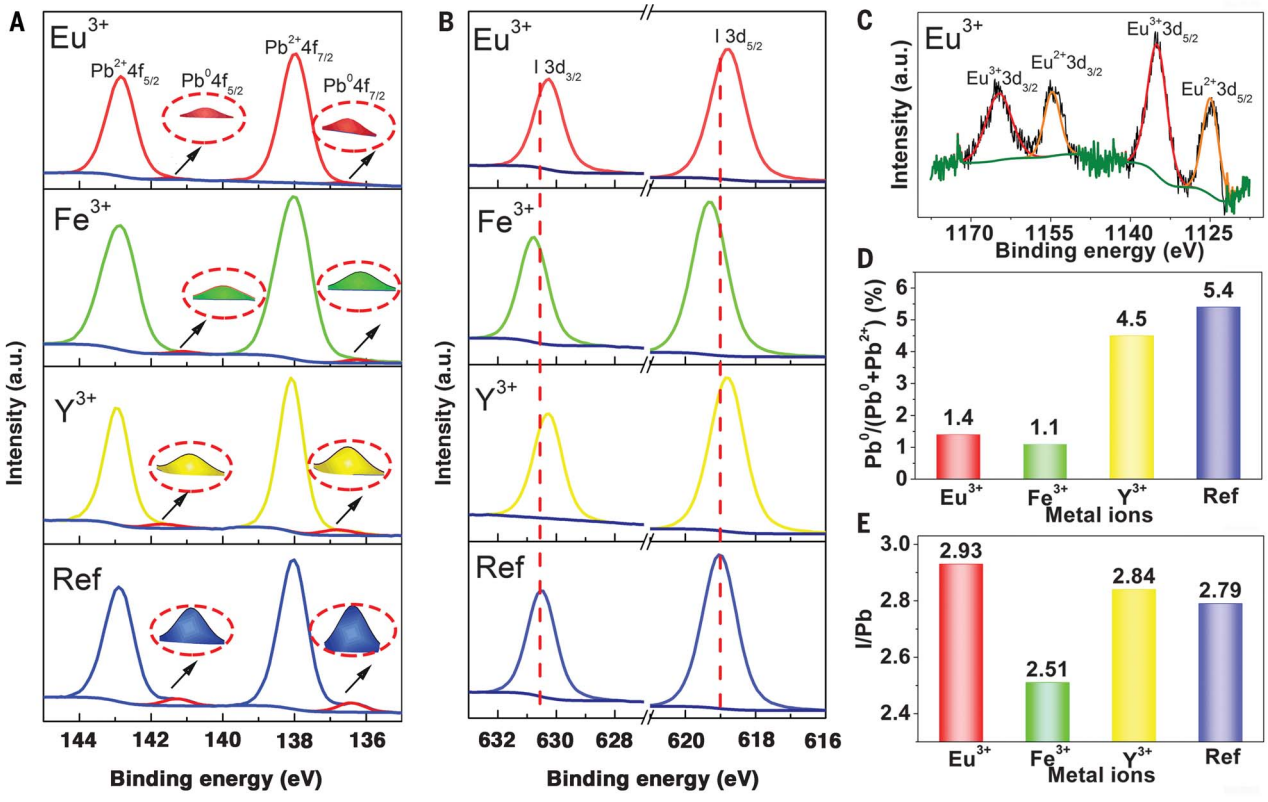


Fig. 2. High-resolution XPS spectra of Pb 4f, I 3d, and the Eu 3d of perovskite films with the incorporation of 1% M/Pb different acetylacetonate metal salts [$M(acac)_3$, M = Eu^{3+}, Y^{3+}, Fe^{3+}]. (**A**) Pb 4f spectra, the insertions are the enlarged spectra of Pb^0 4f. (**B**) I 3d spectra. (**C**) Eu 3d spectra. (**D**) Fitted results of the $Pb^0/(Pb^0+Pb^{2+})$ ratio. (**E**) Fitted results of I/Pb ratio.

observe obvious orientation variation by synchrotron grazing-incidence wide-angle x-ray scattering (GIWAXS) analysis (Fig. 3B and fig. S8).

In addition, the optical bandgap of the perovskite film upon Eu^{3+} addition was calculated to be 1.55 eV, similar to that of the reference (fig. S9). The photoluminescence (PL) intensity (fig. S10) and carrier lifetime (Fig. 3C) increased in the perovskite film with the incorporation of Eu^{3+}, indicating the decrease of nonradiative recombination centers from defects elimination. The improvement of the morphology and grain size could also lead to the increased PL lifetime, so the defects reduction should be further confirmed by other methods. We used the space charge–limited current (SCLC) measurement to quantify the defect density $N_{defects}$ of 5.1×10^{15} and 1.5×10^{16} cm^{-3} for Eu^{3+}-incorporated samples and the reference, respectively (Fig. 3D).

We studied the influence of the Eu^{3+}-Eu^{2+} ion pair on the formation energies of redox reaction, lattice stability, and energy band structure by density functional theory (DFT) calculations. To construct the model, a small fraction of metal ions (Eu^{3+}) was intercalated into two adjacent lattices (Fig. 3E), given the observation that Eu was concentrated at surfaces and grain boundaries. The formation energies for defects elimination (Eqs. 1 and 2) were calculated (Fig. 3F). For both reference and Eu^{3+}-incorporated systems, the half reactions related to Pb^0 elimination required a substantially high potential energy as the main barrier, whereas the I^0 elimination half reactions were comparably favorable. However, after introducing Eu species at the interface, the barrier in Pb^0 elimination half reactions was greatly decreased, but the barrier for I^0 elimination half reactions decreased only slightly. With the assistance of Eu species at the interface, the overall redox potential energy has been much lowered, representing an energetical stabilization trend for the charge-transfer reaction (Fig. 3F).

We also compared the thermodynamic properties for reference and Eu-incorporated systems. Figure 3G shows that the $MAPbI_3$ with Eu incorporation has a steeper slope in change of free energy ΔG than in that of reference, meaning that Eu-incorporated $MAPbI_3$ shows a more energetically favorable physicochemical trend than pure $MAPbI_3$ does. Additionally, it reveals Eu incorporation in $MAPbI_3$ materials did not bring in obvious electronic disorders as extra traps (fig. S11).

We incorporated the perovskite absorber equipped with the redox shuttle in two device configurations. One is based on ITO/TiO_2/perovskite/spiro-OMeTAD/Au, wherein spiro-OMeTAD refers to 2,2′,7,7′-tetrakis-(*N*,*N*-di-*p*-methoxyphenylamine)-9,9′-spirobifluorene, with $MAPbI_3$(Cl). The other is based on ITO/SnO_2/perovskite/spiro-OMeTAD (modified)/Au for higher PCE and stability, with (FA,MA,Cs)Pb(I,Br)$_3$(Cl), in which FA is formamidinium. Both perovskites were deposited by means of a traditional two-step method, during which Eu(acac)$_3$ or other additives were added in PbI_2/DMF precursor solution. The two devices showed similar trends (Fig. 4A and fig. S12). The Eu^{3+}-incorporated devices exhibited the best PCE, whereas the Fe^{3+}-incorporated devices suffered from the markedly decreased PCE. The average PCE increased from 18.5 to 20.7% in the mixed perovskite upon Eu^{3+} addition (Fig. 4A),

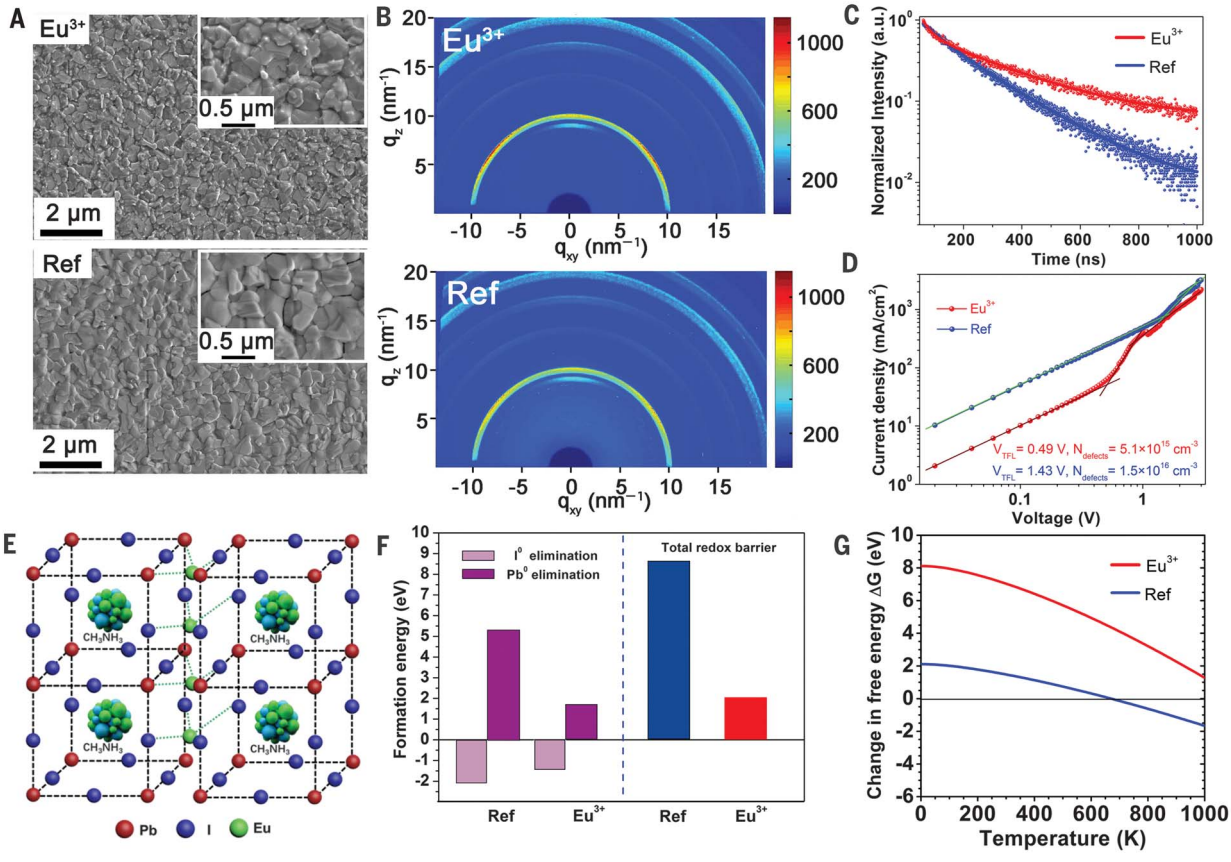


Fig. 3. Influence of morphology, orientation, electronic structure, carrier behaviors of Eu^{3+}-incorporated perovskite film, and results of DFT calculations. The characterization of reference and 0.15% Eu^{3+}-incorporated perovskite film: (**A**) scanning electron microscopy images; (**B**) GIWAXS data; (**C**) time-resolved photoluminescence spectra; (**D**) *J*-*V* characteristics of devices (ITO/perovskite/Au), used for estimating the SCLC defects concentration ($N_{defects} = 2\varepsilon\varepsilon_0 V_{TFL}/eL^2$, ε and ε_0 are the dielectric constants of perovskite and vacuum permittivity, *L* is the thickness of the perovskite film, and e is the elementary charge). (**E**) The interface ultrathin Eu clustering-layer-incorporated structural model. (**F**) Left: half-reaction potential barriers; right: overall redox charge-transfer reaction barrier for Eu incorporated at the interface. (**G**) The summary of ΔG between $MAPbI_3$ and $MAPbI_3$ incorporated with Eu at the interface.

Downloaded from http://science.sciencemag.org/ on January 17, 2019

which is attributed to the effective defects elimination. We attributed the decreased PCE in Fe^{3+}-incorporated devices to the additional I^0 defects introduced by oxidation.

One of the optimized devices achieved the PCE of 21.52% (reverse 21.89%, forward 21.15%) (Fig. 4B) with negligible hysteresis (certified reverse 20.73%, forward 20.30%, average 20.52%, certificate attached in fig. S13). The measured stable output at maximum point (0.97 V) was 20.9%. Integrating the overlap of the incident-photon-to-current-efficiency spectrum of Eu^{3+}-incorporated PSCs under the AM 1.5-G solar photon flux generated the current density of 23.2 $mA{\cdot}cm^{-2}$ (fig. S14). The stabilized *J-V* performance of PSCs was evaluated as follows (*49*): parameters are measured under a 13-point IV sweep configuration wherein the bias voltage (current for open circuit voltage V_{OC} determination) is held constant until the measured current (voltage for V_{OC}) was determined to be unchanging at the 0.05% level. The original, stabilized, and poststabilized efficiency of Eu^{3+}-incorporated PSCs tested by third-party certification institution were similar, which indicates the stable characteristics of the devices (fig. S15).

The shelf lifetime of the corresponding devices was investigated, wherein the PCE evolution was descripted for solar cells stored in an inert environment (Fig. 4C). With the Eu^{3+}-Eu^{2+} redox shuttle incorporated, the devices maintained 90% of the original PCE even after 8000 hours storage because of improved long-term V_{OC}, short-circuit current density (J_{SC}) and fill factor (FF) stability (fig. S16). Although the stability of Y^{3+}-incorporated PSCs was comparable to the reference, Fe^{3+}-incorporated PSC showed severely deteriorated stability, which lost the photoelectric conversion capability completely after merely 2000 hours of storage.

To estimate the stability of Eu^{3+}-incorporated PSCs under operational conditions, half solar cells were subjected to either continuous 1 sun illumination or 85°C aging condition, respectively (Fig. 4D), in which the top charge-transfer materials and electrode were deposited after aging test. Improved long-term V_{OC} and FF stability (fig. S17) allowed the devices, after 1000 hours, to retain 93% of the original PCE continuous 1 sun illumination or 91% after heating at 85°C. Several previous studies showed that small-molecule spiro-OMeTAD would crystallize under thermal stress and create pathways that allow for an interaction of the perovskite and the metal electrode (*50*, *51*). By modifying the hole-transport materials (spiro-OMeTAD) with conductive polymer poly(triarylamine), the full devices incorporated with the Eu^{3+}-Eu^{2+} ion pair maintained 92% and 89% of the original PCE because of obvious long-term V_{OC} and FF stability improvement (fig. S18) under the same light or thermal stress for 1500 hours, respectively (Fig. 4E). Furthermore, the Eu^{3+}-incorporated full devices could maintain 91% of the original stable PCE tracked at maximum power point (MPP) for 500 hours (Fig. 4F).

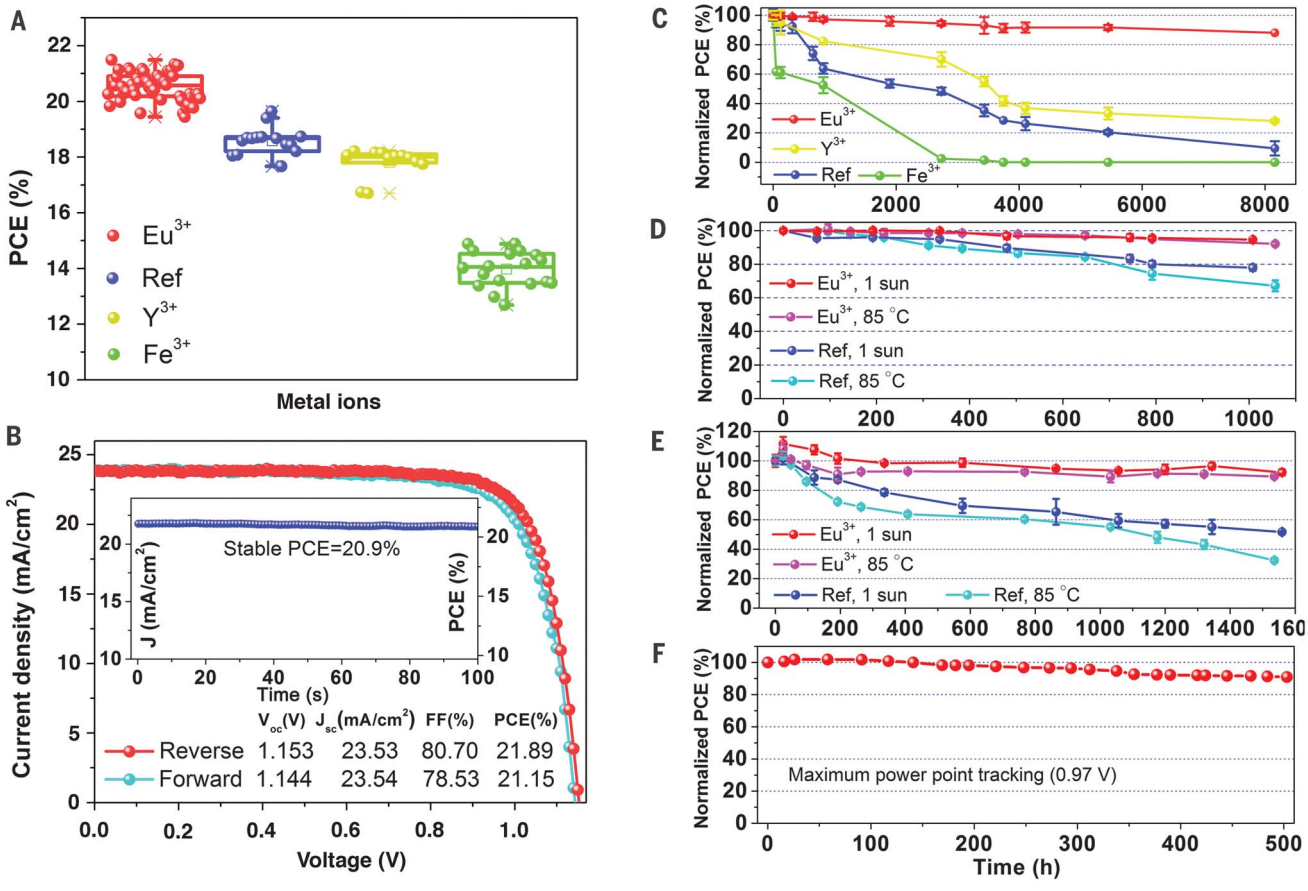


Fig. 4. Long-term stability and original performance evolution of PSCs. (**A**) Original performance evolution based on (FA,MA,Cs)Pb(I,Br)$_3$(Cl) perovskite with the incorporation of 0.15% different M(acac)$_3$ (M = Eu^{3+}, Y^{3+}, Fe^{3+}). (**B**) The J-V curve, stable output (measured at 0.97 V), and parameters of 0.15% Eu^{3+}-incorporated champion devices. (**C**) Long-term stability of PSCs based on $MAPbI_3$(Cl) perovskite absorber with the incorporation of 0.15% different [M(acac)$_3$ (M = Eu^{3+}, Y^{3+}, Fe^{3+})], stored in inert condition. The PCE evolution of Eu^{3+}-Eu^{2+}-incorporated and reference devices under 1 sun illumination or 85°C aging condition: (**D**) half PSCs (original PCE: 0.15% Eu^{3+} incorporated PSCs, 19.21 ± 0.54%; reference PSCs, 18.05 ± 0.38%) and (**E**) full PSCs (original PCE: 0.15% Eu^{3+} incorporated PSCs, 19.17 ± 0.42%; reference PSCs, 17.82 ± 0.30%). Scanning speed is 20 mV/s. (**F**) The MPP tracking of 0.15% Eu^{3+}-incorporated device, measured at 0.97 V and 1-sun illumination.

Downloaded from http://science.sciencemag.org/ on January 17, 2019

REFERENCES AND NOTES

1. A. Kojima, K. Teshima, Y. Shirai, T. Miyasaka, *J. Am. Chem. Soc.* **131**, 6050–6051 (2009).
2. M. M. Lee, J. Teuscher, T. Miyasaka, T. N. Murakami, H. J. Snaith, *Science* **338**, 643–647 (2012).
3. H. Zhou *et al*., *Science* **345**, 542–546 (2014).
4. J.-H. Im, I.-H. Jang, N. Pellet, M. Grätzel, N.-G. Park, *Nat. Nanotechnol.* **9**, 927–932 (2014).
5. M. Yang *et al*., *Adv. Mater.* **27**, 6363–6370 (2015).
6. O. Malinkiewicz *et al*., *Nat. Photonics* **8**, 128–132 (2014).
7. W. S. Yang *et al*., *Science* **348**, 1234–1237 (2015).
8. W. S. Yang *et al*., *Science* **356**, 1376–1379 (2017).
9. National Renewable Energy Laboratory (NREL) Efficiency chart (2018); www.nrel.gov/pv/assets/pdfs/pv-efficiency-chart.20181214.pdf.
10. N. H. Tiep, Z. Ku, H. J. Fan, *Adv. Energy Mater.* **6**, 1501420 (2016).
11. Y. Rong, L. Liu, A. Mei, X. Li, H. Han, *Adv. Energy Mater.* **5**, 1501066 (2015).
12. T. A. Berhe *et al*., *Energy Environ. Sci.* **9**, 323–356 (2016).
13. G. Grancini *et al*., *Nat. Commun.* **8**, 15684 (2017).
14. J. P. Correa-Baena *et al*., *Science* **358**, 739–744 (2017).
15. D. C. Jordan, S. R. Kurtz, *Prog. Photovolt. Res. Appl.* **21**, 12–29 (2013).
16. Q. Cao *et al*., *Adv. Energy Mater.* **1**, 845–853 (2011).
17. F. De Angelis *et al*., *ACS Energy Lett.* **2**, 857–861 (2017).
18. J. M. Frost *et al*., *Nano Lett.* **14**, 2584–2590 (2014).
19. Z. Yu, L. Sun, *Adv. Energy Mater.* **5**, 1500213 (2015).
20. W. Li, J. Li, G. Niu, L. Wang, *J. Mater. Chem. A* **4**, 11688–11695 (2016).
21. W. Li *et al*., *Energy Environ. Sci.* **9**, 490–498 (2016).
22. M. Saliba *et al*., *Science* **354**, 206–209 (2016).
23. M. Hösel, R. R. Søndergaard, M. Jørgensen, F. C. Krebs, *Adv. Eng. Mater.* **15**, 1068–1075 (2013).
24. Y. Han *et al*., *J. Mater. Chem. A* **3**, 8139–8147 (2015).
25. Y. Li *et al*., *J. Am. Chem. Soc.* **137**, 15540–15547 (2015).
26. H. Azimi *et al*., *Adv. Energy Mater.* **5**, 1401692 (2015).
27. J. Cao *et al*., *Nanoscale* **7**, 9443–9447 (2015).
28. X. Li *et al*., *Nat. Chem.* **7**, 703–711 (2015).
29. W. Peng *et al*., *Angew. Chem. Int. Ed.* **55**, 10686–10690 (2016).
30. R. K. Gunasekaran *et al*., *ChemPhysChem* **19**, 1507–1513 (2018).
31. S. Wang, Y. Jiang, E. J. Juarez-Perez, L. K. Ono, Y. Qi, *Nat. Energy* **2**, 16195 (2016).
32. S. R. Raga *et al*., *Chem. Mater.* **27**, 1597–1603 (2015).
33. Y. Li *et al*., *J. Phys. Chem. C* **121**, 3904–3910 (2017).
34. B. Philippe *et al*., *J. Phys. Chem. C* **121**, 26655–26666 (2017).
35. H. Cho *et al*., *Science* **350**, 1222–1225 (2015).
36. V. Adinolfi *et al*., *Adv. Mater.* **28**, 3406–3410 (2016).
37. G. W. Hwang *et al*., *Adv. Mater.* **27**, 4481–4486 (2015).
38. A. Friedenberg, Y. Shapira, *Surf. Sci.* **115**, 606–622 (1982).
39. X. Tang *et al*., *J. Mater. Chem. A* **4**, 15896–15903 (2016).
40. R. Purbia, S. Paria, *Dalton Trans.* **46**, 890–898 (2017).
41. H. Xie *et al*., *J. Phys. Chem. C* **120**, 215–220 (2016).
42. C. Qin, T. Matsushima, T. Fujihara, C. Adachi, *Adv. Mater.* **29**, 1603808 (2017).
43. W. Zhang *et al*., *Nat. Commun.* **6**, 10030 (2015).
44. Z. Liu *et al*., *Adv. Mater.* **29**, 1606774 (2017).
45. D. R. Lide, *CRC Handbook of Chemistry and Physics*, vol. 5 (CRC Press, ed. 84, 2003).
46. P. Jakubcová, F. M. Schappacher, R. Pöttgen, D. Johrendt, *Z. Anorg. Allg. Chem.* **635**, 759–763 (2009).
47. D. B. Mitzi, K. Liang, *Chem. Mater.* **9**, 2990–2995 (1997).
48. G. Pan *et al*., *Nano Lett.* **17**, 8005–8011 (2017).
49. ASTM E948-16, Standard Test Method for Electrical Performance of Photovoltaic Cells Using Reference Cells Under Simulated Sunlight. *ASTM International* (2016).
50. T. Malinauskas *et al*., *ACS Appl. Mater. Interfaces* **7**, 11107–11116 (2015).
51. K. Domanski *et al*., *ACS Nano* **10**, 6306–6314 (2016).

ACKNOWLEDGMENTS

The manuscript was improved by the insightful reviews of anonymous reviewers. We thank Y. Yang (University of California, Los Angeles), Y. Li (Beijing Institute of Technology), H. Xie (Central South University), Q. Bao (East China Normal University), and J. Xiao (Beijing Institute of Technology) for insightful data analysis and valuable discussion. We also thank the third certification institutions National Institute of Metrology (China) and Newport Technology and Application Center PV Lab (USA) for authentication tests; beamline BL14B1 (Shanghai Synchrotron Radiation Facility, SSRF) for providing beam time and help during the experiments; and Enli technology Co., Ltd. for help with PV efficiency and EQE measurement. **Funding:** This work was supported by National Natural Science Foundation of China (nos. 91733301, 51672008, 51722201, 21425101, 21331001, and 21621061), MOST of China (2014CB643800), National Key Research and Development Program of China (grant nos. 2017YFA0206701 and 2017YFA0205101), Beijing Natural Science Foundation (4182026), National Key Research and Development Program of China (grant no. 2016YFB0700700), National Natural Science Foundation of China (51673025), Beijing Municipal Science and Technology Project (no. Z181100005118002), and Young Talent Thousand Program. **Author contributions:** L.W. and H.Z. conceived the idea and designed the project. H.Z., C.-H.Y., and L.-D.S. directed and supervised the research. L.W. fabricated and characterized devices. Y.H., Y.C., L.L., Z.X., and N.L. also contributed to device fabrication. L.W. performed the SEM, PL, UPS, UV-vis, XPS, and XRD measurements. GIWAXS was performed and analyzed by G.Z., supported by BL14B1 beamline of SSRF. B.D. and Z.L. performed EPR. M.S. and B.H. carried out DFT calculation. L.W. drafted the manuscript; Q.C. and H.Z. revised and finalized the manuscript. **Competing interests:** The authors have no competing interests. **Data and materials availability:** All data are available in the main text or the supplementary materials.

SUPPLEMENTARY MATERIALS

www.sciencemag.org/content/363/6424/265/suppl/DC1
Materials and Methods
Supplementary Text
Figs. S1 to S18
Tables S1 to S3
References (*52*–*57*)

24 June 2018; resubmitted 25 September 2018
Accepted 28 November 2018
10.1126/science.aau5701

Downloaded from http://science.sciencemag.org/ on January 17, 2019

ORGANIC CHEMISTRY

Concise total syntheses of (–)-jorunnamycin A and (–)-jorumycin enabled by asymmetric catalysis

Eric R. Welin[1], Aurapat Ngamnithiporn[1], Max Klatte[1], Guillaume Lapointe[1], Gerit M. Pototschnig[1], Martina S. J. McDermott[2], Dylan Conklin[2], Christopher D. Gilmore[1], Pamela M. Tadross[1], Christopher K. Haley[1], Kenji Negoro[1], Emil Glibstrup[1], Christian U. Grünanger[1], Kevin M. Allan[1], Scott C. Virgil[1], Dennis J. Slamon[2]*, Brian M. Stoltz[1]*

The bis-tetrahydroisoquinoline (bis-THIQ) natural products have been studied intensively over the past four decades for their exceptionally potent anticancer activity, in addition to strong Gram-positive and Gram-negative antibiotic character. Synthetic strategies toward these complex polycyclic compounds have relied heavily on electrophilic aromatic chemistry, such as the Pictet–Spengler reaction, that mimics their biosynthetic pathways. Herein, we report an approach to two bis-THIQ natural products, jorunnamycin A and jorumycin, that instead harnesses the power of modern transition-metal catalysis for the three major bond-forming events and proceeds with high efficiency (15 and 16 steps, respectively). By breaking from biomimicry, this strategy allows for the preparation of a more diverse set of nonnatural analogs.

The bis-tetrahydroisoquinoline (bis-THIQ) natural products have been studied intensively by chemists and biologists alike during the 40+ years since their initial discovery because of their intriguing chemical structures, potent biological activities, and unique mechanisms of action (*1*, *2*). Jorumycin (**1**) (Fig. 1) and its congeners ecteinascidin 743 (Et 743, **2**) and jorunnamycin A (**3**) have a pentacyclic carbon skeleton, highly oxygenated ring termini, and a central pro-iminium ion (manifested either as a carbinolamine or an α-aminonitrile motif). This latter functionality serves as an alkylating agent in vivo, resulting in covalent modification of DNA in a process that ultimately leads to cell death (*3*). The promise of these natural products as anticancer agents has been realized in the case of Et 743 (Yondelis, trabectedin), which has been approved in the United States, Europe, and elsewhere for the treatment of a variety of drug-resistant and unresectable soft-tissue sarcomas and ovarian cancer (*3*). Although **2** is available from nature, isolation of 1 g of the drug would require more than one ton of biological material. For this reason, the successful application of **2** as an antitumor agent has necessitated its large-scale chemical synthesis, a 21-step process that begins with cyanosafracin A, a fermentable and fully functionalized bis-THIQ natural product (*4*). This has restricted medicinal chemistry endeavors through this route to the production of only compounds with a high degree of similarity to the natural products themselves.

Although **1** and **3** have quinone rings, these moieties are rapidly reduced in cells to their hydroquinone oxidation states, more closely resembling those of **2** (*5*). These highly electron-rich functional groups are key components in the biosynthetic pathways of the bis-THIQs, which are forged by the action of Pictet–Spenglerase enzymes (*6*, *7*). Previously reported chemical syntheses of bis-THIQ natural products feature elegant and creative application of electrophilic aromatic substitution (EAS) chemistry for the construction of one or more of the THIQ motifs. Though highly enabling, this approach has also limited the synthesis of nonnatural analogs to highly natural product–like derivatives. As a key example, despite the scores of analogs produced over the past few decades (*8*–*11*), the majority of the derivatives focus on substitution of the heteroatom moiety appended to the B-ring (compare structure **4**) (Fig. 1), and only a select few have substantial structural and substitutional variation around the aromatic or quinone A- and E-rings (*8*–*11*). Furthermore, derivatives possessing electron-withdrawing groups on these rings are inaccessible using biomimetic approaches, as these would inhibit the EAS chemistry used to construct the THIQs. This latter point is important, as studies have indicated that the smaller bis-THIQ natural products such as **1** and **3** are more susceptible to metabolic degradation than Et 743 and other larger bis-THIQs (*12*, *13*), and the installation of electron-withdrawing groups is a commonly employed strategy to improve a drug molecule's metabolic stability (*14*).

Jorumycin has been the target of four total syntheses (*15*–*18*) and two semisyntheses (*19*, *20*) since its isolation in 2000 (*21*), and jorunnamycin A has frequently been prepared en route. Jorumycin displays median inhibitory concentrations (IC_{50}s) of 0.24 nM versus A549 lung cancer, 0.49 nM versus DU145 prostate cancer, and 0.57 nM versus HCT116 colon cancer (*17*, *19*, *21*), among others, thus offering immense therapeutic potential. Furthermore, jorumycin and jorunnamycin A are appealing targets for further synthetic elaboration: the oxygen substitution appended to the B-ring (compare structure **4**, X = OH, Fig. 1) could allow rapid diversification to the ecteinascidin, saframycin, safracin, and renieramycin scaffolds (*1*). To overcome the limitations of the current state of the art with respect to analog diversity, we sought an alternative, nonbiomimetic route to these natural products.

Specifically, we envisioned the retrosynthetic strategy shown in Fig. 2A. We posited that a late-stage oxygenation event to provide jorumycin (**1**) would greatly simplify the construction of the precursor, pentacycle **6**. We then considered disconnection of the central C-ring (compare Fig. 1) through cleavage of the lactam moiety in **6**, providing bis-THIQ compound **7**. Critically, bis-THIQ structure **7** was recognized as a potential product of an enantioselective hydrogenation of bis-isoquinoline **8**. The central biaryl bond of **8** could be formed through a C–H cross-coupling reaction, leading to isoquinoline monomers **9** and **10**, thus greatly simplifying the synthetic challenge. As a key advantage, isoquinolines **9** and **10** could be prepared through the application of any known method, not limited only to those requiring highly electron-rich and π-nucleophilic species. Crucially, this approach would allow access to the natural products themselves, as well as derivatives featuring substantial structural and/or electronic variation.

As shown in Fig. 2B, we initiated our synthetic studies with the Sonogashira coupling of aryl bromide **11** (available in two steps from 3,5-dimethoxybenzaldehyde, see supplementary materials) with *tert*-butyldimethylsilyl propargyl ether (**12**); simply adding solid hydroxylamine hydrochloride to the reaction mixture after the coupling provided oxime-bearing alkyne **13** in 99% yield. Catalytic silver(I) triflate activated the alkyne toward nucleophilic attack by the oxime, directly generating isoquinoline *N*-oxide **9** in 77% yield on up to a 12-g scale (*22*). Next, we began our synthesis of isoquinoline triflate **10** by using aryne-based methodology developed in our laboratories (*23*). Silyl aryl triflate **14** (available in three steps from 2,3-dimethoxytoluene, see supplementary materials) was treated with cesium fluoride to generate the corresponding aryne intermediate in situ, which underwent aryne acyl-alkylation with in situ condensation to provide 3-hydroxy-isoquinoline **16** in 45% yield. Reaction with trifluoromethanesulfonic anhydride provided electrophilic coupling partner **10** in 94% yield.

[1]Warren and Katharine Schlinger Laboratory of Chemistry and Chemical Engineering, California Institute of Technology, Pasadena, CA 91125, USA. [2]Division of Hematology/Oncology, Department of Medicine, Geffen School of Medicine at UCLA, Los Angeles, CA, USA.
*Corresponding author. Email: dslamon@mednet.ucla.edu (D.J.S.); stoltz@caltech.edu (B.M.S.)

Downloaded from http://science.sciencemag.org/ on January 22, 2019

With working routes to both isoquinoline monomers in hand, we turned our attention to the palladium-catalyzed cross-coupling reaction that would be used to construct the carbon skeleton of jorumycin. We were pleased to find that isoquinolines **9** and **10** were efficiently coupled under modified conditions developed by Fagnou and co-workers to provide bis-isoquinoline **18** in 94% yield on a 7-g scale (*24*). This large-scale application of C–H activation likely proceeds through a transition state similar to **17** and allows for the direct construction of **18** without the need for prefunctionalization (*25*). The excess of *N*-oxide **9** required to achieve maximum levels of efficiency appears to be due only to kinetic factors, as all excess **9** was recovered after the reaction.

At this stage, we sought to install the level of oxidation necessary to initiate our hydrogenation studies (Fig. 2C). Specifically, this required selective oxidation of the nitrogen-adjacent methyl and methylene groups on the B- and D-rings, respectively. We attempted a double-Boekelheide rearrangement to transpose the *N*-oxidation to both *C*-positions simultaneously, effecting formal C–H oxidation reactions (*26*). However, after oxidation to intermediate bis-*N*-oxide **19**, only the B-ring azine underwent rearrangement. Despite this setback, we found that it was possible to parlay this reactivity into a one-pot protocol by adding acetic anhydride upon complete oxidation, providing differentially protected diol **20** in 62% yield. N–O bond cleavage and oxyl-mediated oxidation provided bis-isoquinoline **8** in two additional steps. To date, we have produced more than 5 g of bis-isoquinoline **8**.

With a scalable route to isoquinoline **8** in hand, we turned our attention to the key hydrogenation event. If successful, this strategic disconnection would add four molar equivalents of hydrogen, create four new stereocenters, and form the central C-ring lactam. Although the enantioselective hydrogenation of nitrogen-based heterocycles is a well-studied reaction, isoquinolines are possibly the most challenging and least investigated substrates (*27*). To our knowledge, only four reports existed before our studies that described asymmetric isoquinoline hydrogenation, and only one appeared to tolerate 1,3-disubstitution patterns (*28*–*31*).

We nonetheless noted that metal-catalyzed imine and carbonyl reduction is a comparatively successful and well-studied transformation (*32*, *33*). We were drawn to the iridium catalyst developed by scientists at Ciba-Geigy (now Syngenta) for asymmetric ether-directed imine reduction in the preparation of metolachlor (*34*). Considering the positioning of the hydroxymethyl group appended to the B-ring of **8** and the electronic similarity of the adjacent C1–N π-bond to that of an imine, we posited that a similar catalytic system might be used to direct the initial reduction to this position (Fig. 3). Furthermore, the chelation mode was attractive as a scaffolding element to enable enantioselective *Si*-face reduction. In keeping with previous observations (*28*–*31*), we anticipated that full B-ring reduction would provide *cis*-mono-THIQ **22** as the major product. We believed that **22** would then act as a tridentate ligand for a metal ion (although not necessarily the catalytically active species), and that the three-dimensional coordination environment of metal-bound **22•M** would direct D-ring hydrogenation from the same face. Finally, the all-*syn* nature of **7** places the ester moiety in proximity to

Downloaded from http://science.sciencemag.org/ on January 22, 2019

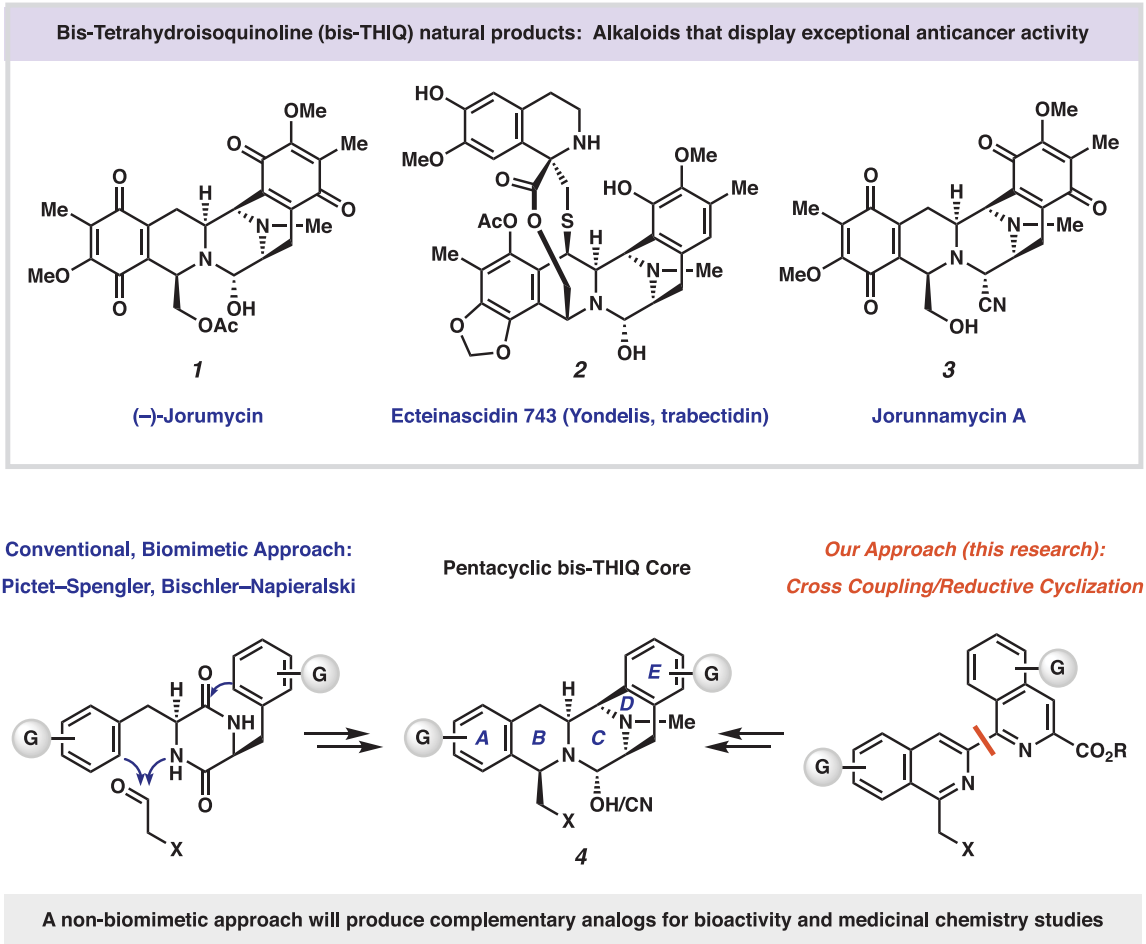


Fig. 1. bis-THIQ natural products. Jorumycin (**1**), ecteinascidin 743 (**2**), and jorunnamycin A (**3**). Ac, acetyl; G, oxygen or carbon substitution; Me, methyl; R, generic alkyl substitution; X, oxygen or nitrogen substitution.

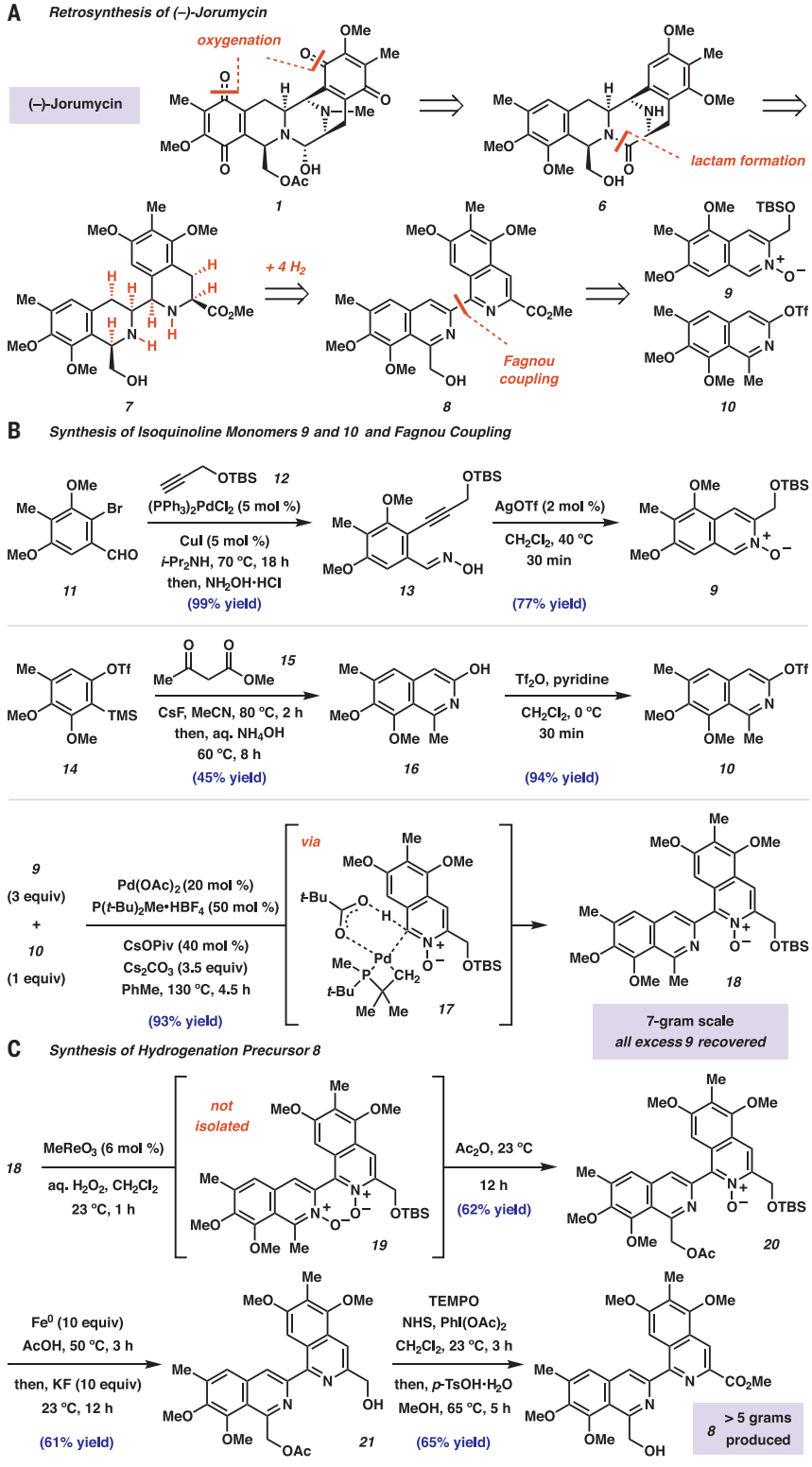


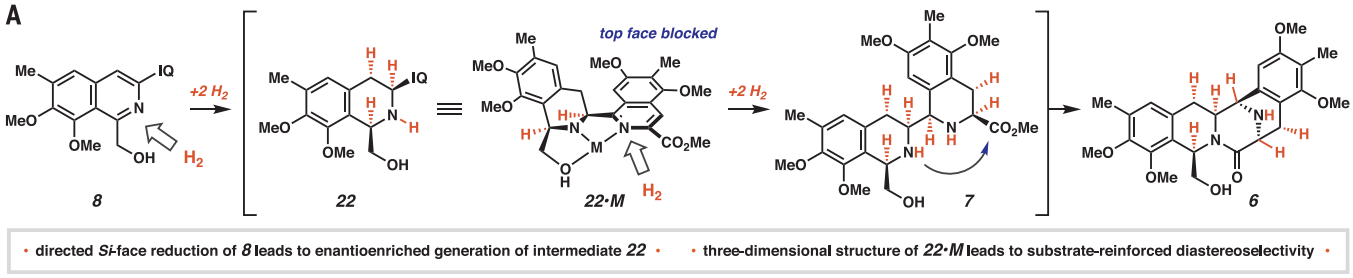
Fig. 2. Considerations for an orthogonal synthesis of jorunnamycin A and jorumycin. (**A**) Retrosynthetic analysis leading to a synthesis of jorumycin that deviates from previous synthetic strategies. (**B**) Isoquinoline **9** and **10** were synthesized in two steps each from aryl bromide **11** and *ortho*-silyl aryl triflate **14**, respectively. (**C**) Boekelheide rearrangement provided an efficient and scalable route to bis-isoquinoline **8** under mild conditions. aq., aqueous; equiv, molar equivalent; *i*-Pr, isopropyl; MeCN, acetonitrile; NHS, *N*-hydroxysuccinimide; Ph, phenyl; Piv, trimethyl-acetyl; *p*-TsOH•H_2O, *para*-toluenesulfonic acid monohydrate; TBS, *tert*-butyldimethylsilyl; *t*-Bu, *tert*-butyl; TEMPO, 2,2,6,6-tetramethylpiperidine-*N*-oxyl; Tf, trifluoromethanesulfonyl; TMS, trimethylsilyl.

B-ring secondary amine, and we expected lactamization to be rapid. If successful, this self-reinforcing diastereoselectivity model would allow for control over the four new stereocenters and produce the bis-THIQ core in a single step.

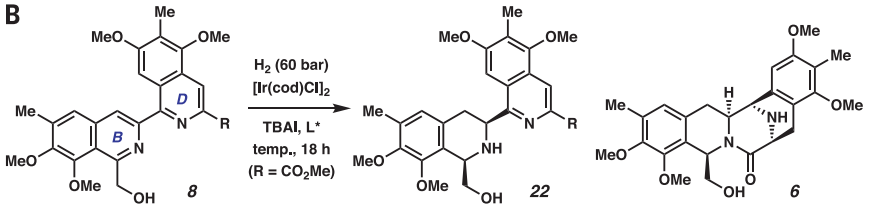
Upon beginning our enantioselective hydrogenation studies, we found that we could identify trace amounts of conversion to mono-THIQ product **22** by using the catalyst mixture developed at Ciba-Geigy (*34*), thus confirming the accelerating effects of the pendent hydroxy directing group. Under these general conditions, we then performed a broad evaluation of more than 60 chiral ligands commonly used in enantioselective catalysis protocols (see supplementary materials). From this survey, we identified three ligands that provided **22** in at least 80% enantiomeric excess (ee) and with uniformly excellent diastereoselectivity [all >20:1 diastereomeric ratio (dr)]: (*S*)-(CF_3)-*t*-BuPHOX (**23**, Entry 2, 22% yield, –82% ee), (*S,S*)-Et-FerroTANE (**24**, Entry 3, 26% yield, –87% ee), and (*S,*R_P)-Xyliphos (**25**, Entry 4, 30% yield, 80% ee). After evaluating these ligand classes further, we identified (*S,*R_P)-BTFM-Xyliphos (**26**) (*35*) as a strongly activating ligand that provided mono-THIQ **22** in 83% yield, >20:1 dr, and in a remarkable 94% ee (Entry 5). Moreover, we found that ligand **26** formed a catalyst that provided pentacycle **6** as a single diastereomer in 10% yield. Further evaluation of the reaction parameters revealed that increasing temperature provided higher levels of reactivity, albeit at the expense of enantioselectivity (Entry 6, 31% yield of **22**, 87% ee, 43% yield of **6**). The best results were achieved by performing the reaction at 60°C for 18 hours and then increasing the temperature to 80°C for 24 hours. Under these conditions, **6** was isolated in 59% yield with >20:1 dr and 88% ee (Entry 7) (*36*). In the end, doubling the catalyst loading allowed us to isolate **6** in 83% yield, also with >20:1 dr and 88% ee (Entry 8) on greater than 1-mmol scale. bis-THIQ **6** could be easily accessed in enantiopure form [>99% ee by high-performance liquid chromatography (HPLC)] by crystallization from a slowly evaporating acetonitrile solution, and we were able to confirm the relative and absolute stereochemistry by obtaining an x-ray crystal structure on corresponding 4-bromophenyl sulfonamide **27**. In the context of this synthesis, the relatively high catalyst loading [20 mole % (mol %) Ir] is mitigated by the substantial structural complexity generated in this single transformation.

At this stage, we were poised to investigate the third and final key disconnection from our retrosynthetic analysis, namely, late-stage C–H oxidation of the arenes (Fig. 4). To set up this chemistry, the piperazinone N–H of **6** was methylated under reductive amination conditions in quantitative yield. Despite numerous attempts to effect catalytic C–H oxidation on this advanced intermediate, we found that a two-step procedure was necessary instead. We were able to chlorinate both of the remaining aromatic positions, providing bis-THIQ **28** in 68% yield.

Downloaded from http://science.sciencemag.org/ on January 22, 2019



B



entry	catalyst loading	ligand	temperature	yield 22*	ee 22†	yield 6*	dr 6‡	ee 6†
1	5 mol %	25	23 °C	2%	ND	0%	–	–
2	5 mol %	23	60 °C	22%	–82%	0%	–	–
3	5 mol %	24	60 °C	26%	–87%	0%	–	–
4	5 mol %	25	60 °C	30%	80%	0%	–	–
5	5 mol %	26	60 °C	83%	94%	10%	>20:1	ND
6	5 mol %	26	80 °C	31%	87%	43%	>20:1	ND
7	5 mol %	26	60 °C → 80 °C§	7%	94%	59%¶	>20:1	88%
8	10 mol %	26	60 °C → 80 °C§	3%	94%	83%¶	>20:1	88% (>99%)#

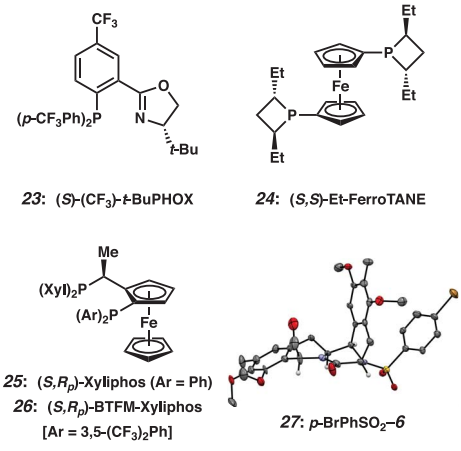


Fig. 3. Development of the enantioselective hydrogenation. (**A**) Stereochemical rationale for the enantio- and diastereoselective hydrogenation of bis-isoquinoline **8**. (**B**) Optimization of the hydrogenation reaction. Unless otherwise noted, all reactions were performed in 9:1 toluene:acetic acid (0.02 M) by using a 1.2:1 ligand:metal ratio and a 3:1 iodide:metal ratio under a hydrogen atmosphere (60 bar) for 18 hours. *Measured by ultra-HPLC–mass spectrometry ultraviolet absorption versus 1,3,5-trimethoxybenzene internal standard unless otherwise noted. †Measured by chiral HPLC analysis. ‡Measured by ^{1}H-NMR analysis of the crude reaction mixture. §Reaction performed at 60°C for 18 hours; then the temperature (temp.) was raised to 80°C and maintained at that temperature for 24 hours. ¶Yield of isolated product after column chromatography using 10.5 mol % **26** in entry 7 and 21 mol % **26** in entry 8. #After one recrystallization. Ar, aryl; BTFM, 3,5-bis-trifluoromethylphenyl; cod, 1,5-cyclooctadiene; dr, diastereomeric ratio (major isomer versus all others); Et, ethyl; IQ, 3-carbomethoxy-5,7-dimethoxy-6-methylisoquinolin-1-yl; ND, not determined; TBAI, tetra-*n*-butylammonium iodide; Xyl, 3,5-dimethylphenyl.

From here, we once again turned to catalysis, this time for the oxygenation of aryl halides. After extensive investigation, we found that Stradiotto and co-workers' recently developed protocol for the hydroxylation of aryl halides was uniquely effective (*37*). Further optimization revealed that the combination of adamantyl BippyPhos ligand with Buchwald's cyclometalated palladium(II) dimer was ideal (*38*), providing dihydroxylated bis-THIQ **29** in 46% yield, an impressive result for such a challenging coupling reaction on a sterically large, electron-rich, and Lewis-basic substrate in the final stages of the synthesis. Partial lactam reduction with cyanide trapping proceeded in 50% yield, and oxidation of the phenols provided jorunnamycin A (**3**) in only 15 linear steps. We isolated hemiacetal **30** in 33% yield, which was surprising given the generally low stability of acyclic hemiacetals. Finally, we developed conditions for the conversion of jorunnamycin A into jorumycin in a single step, providing **1** in 68% yield in 16 linear steps (*1*). Jorunnamycin A (**3**) and jorumycin (**1**) are produced in 0.24% and 0.17% yield, respectively, from commercially available materials, but key bis-THIQ **6**, the branching point for derivative synthesis, is accessed over 10 steps in 5.0% overall yield on greater than 500-mg scale. These efforts are similar to Zhu and co-workers' elegant synthesis of jorumycin with regard to brevity (*16*).

Central to the anticancer activity of the bis-THIQ natural products is the capacity to alkylate DNA upon loss of water or cyanide from the central carbinolamine or α-cyanoamine, respectively (*39*). After alkylation, compelling evidence suggests formation of reactive oxygen species (*5*) or DNA-protein cross-links (*8*, *40*) leads to cell-cycle arrest or cell death. We therefore synthesized analogs **31** to **34**, which feature the nonoxygenated framework as well as all permutations of partial and full oxygenation. The activity of this series would allow us to determine the relative importance of the location and degree of oxygenation on the A- and E-rings, the structure-activity relationships of which have not previously been explored.

With the backdrop that preclinical efficacy studies are complex and demanding, we conducted very preliminary studies to probe the relative cytotoxicity of synthetic analogs **31** to **34** and established that modifying one site on the scaffold greatly diminishes cytotoxicity, whereas other modifications conserved cytotoxicity. The cytostatic and cytotoxic properties of **31** to **34** were determined using long-term, growth-maximizing assay conditions against 29 cancer cell lines known to be responsive in vitro to other general cytotoxics (Fig. 5, see also table S12) (*41*, *42*). Cells were routinely assessed for mycoplasma contamination by using a multiplex polymerase chain reaction (PCR) method and short tandem repeat profiling for cell-line authentication. This methodology differs markedly from the standard 72-hour, luminescence-based cytotoxicity assays employed most commonly for in vitro quantification of drug response. This approach was chosen because it is specifically well suited to determine the activity of compounds wherein antiproliferative effects occur over a longer time period than standard cytotoxic agents. Removal of both phenolic oxygens resulted in a complete loss in activity (i.e., **31,** all IC_{50}s > 1 μM), whereas fully oxygenated bis-THIQ **34** showed cytotoxicity. The most notable results were provided by **32** and **33**, which have A- and E-ring monohydroxylation, respectively. Whereas compound **32**, which is devoid of E-ring oxygenation, showed

Downloaded from http://science.sciencemag.org/ on January 22, 2019

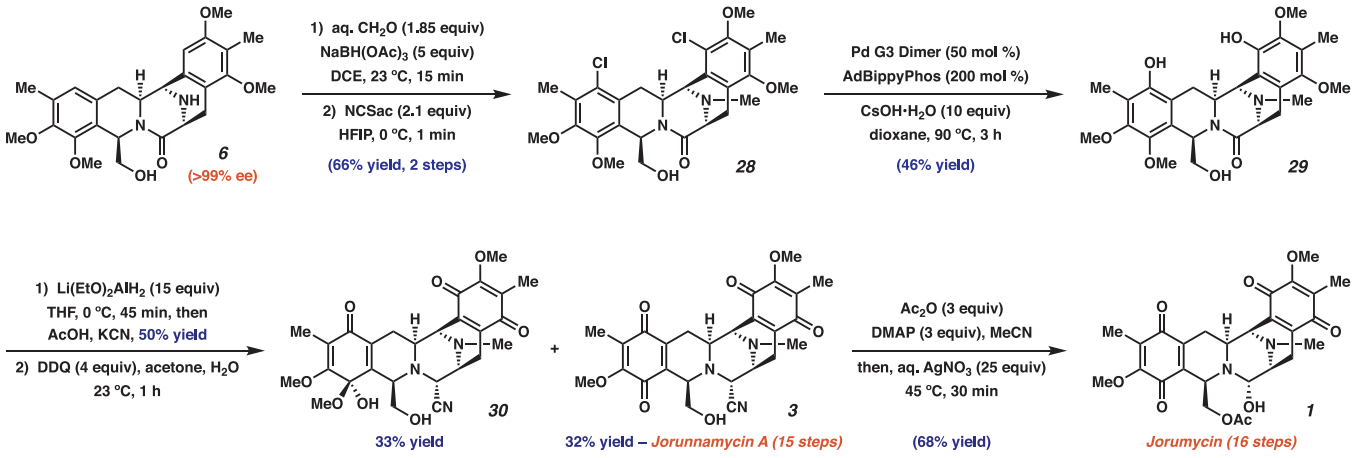
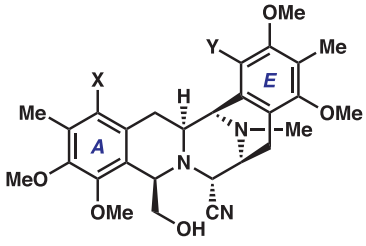


Fig. 4. Completion of jorunnamycin A and jorumycin. After the reductive cyclization, five and six steps, including a palladium-catalyzed hydroxylation event, were required for the complete synthesis of jorunnamycin A (**3**) and jorumycin (**1**), respectively. Ad, 1-adamantyl; DCE, 1,2-dichloroethane; DDQ, 2,3-dichloro-5,6-dicyano-1,4-benzoquinone; DMAP, 4-dimethylaminopyridine; HFIP, 1,1,1,3,3,3-hexafluoroisopropanol; NCSac, *N*-chlorosaccharine; Pd G3 Dimer, (2'-Amino-1,1'-biphenyl-2-yl) methanesulfonatopalladium(II) dimer; THF, tetrahydrofuran.



31: X = Y = H → both rings partially deoxygenated
32: X = OH, Y = H → E-ring partially deoxygenated
33: X = H, Y = OH → A-ring partially deoxygenated
34: X = Y = OH → both rings fully oxygenated

Selective, partial oxygenation allows basic SAR development

Compound	Mean IC_{50} (nM)	Description
31	≥1000	full deoxygenation
32	708	partial (E-ring) deoxygenation
33	233	partial (A-ring) deoxygenation
34	397	full oxygenation
Carfilzomib	4	Proteosome inhibitor
Cisplatin	202	DNA binder
MK8745	360	Aurora kinase inhibitor
MMAE	438	tubulin binder

• Cytotoxicity diminished upon E-ring deoxygenation • • Cytotoxicity maintained upon A-ring deoxygenation •

Fig. 5. Biological evaluation of nonnatural analogs. Leveraging the nonbiomimetic approach to A- and E-ring construction allows for the production of previously inaccessible bis-THIQ analogs. Data reported are IC_{50}s measured from whole cells treated for 6 days using a 1:5 dilution series to cover a range of concentrations from 0 to 1 μM from an initial 10 mM dimethyl sulfoxide stock solution of the analog in question. The IC_{50} of each compound was calculated as a function of population doublings from baseline. MMAE, monomethyl auristatin E; SAR, structure-activity relationship.

diminished activity, we were surprised to find that compound ***33*** featuring only E-ring oxygenation maintained a similar activity profile to fully oxygenated ***34*** (see supplementary materials). At the moment, we believe these data to be the result of general cytotoxicity, as opposed to cancer cell–specific activity. As a reference, three out of four previously known anticancer agents that function through general cytotoxicity showed similar levels of activity in our model. Though more sophisticated studies are necessary to determine actual efficacy, the capacity to delete one oxygen atom and retain activity is both intriguing and unexpected.

The use of catalysis, rather than native reactivity, is a key advantage to our synthesis, allowing us to expedite access to both the natural products themselves and also biologically relevant derivatives.

REFERENCES AND NOTES

1. M. Chrzanowska, A. Grajewska, M. D. Rozwadowska, *Chem. Rev.* **116**, 12369–12465 (2016).
2. D. J. Newman, G. M. Cragg, *J. Nat. Prod.* **79**, 629–661 (2016).
3. C. Cuevas, A. Francesch, *Nat. Prod. Rep.* **26**, 322–337 (2009).
4. C. Cuevas *et al.*, *Org. Lett.* **2**, 2545–2548 (2000).
5. J. W. Lown, A. V. Joshua, J. S. Lee, *Biochemistry* **21**, 419–428 (1982).
6. C. M. Rath *et al.*, *ACS Chem. Biol.* **6**, 1244–1256 (2011).
7. L.-Q. Song *et al.*, *Angew. Chem. Int. Ed.* **56**, 9116–9120 (2017).
8. E. J. Martinez, T. Owa, S. L. Schreiber, E. J. Corey, *Proc. Natl. Acad. Sci. U.S.A.* **96**, 3496–3501 (1999).
9. A. G. Myers, A. T. Plowright, *J. Am. Chem. Soc.* **123**, 5114–5115 (2001).
10. A. G. Myers, B. A. Lanman, *J. Am. Chem. Soc.* **124**, 12969–12971 (2002).
11. E. M. Ocio *et al.*, *Blood* **113**, 3781–3791 (2009).
12. N. J. Carter, S. J. Keam, *Drugs* **70**, 355–376 (2010).
13. J. R. Spencer *et al.*, *Bioorg. Med. Chem. Lett.* **16**, 4884–4888 (2006).
14. H. Gunaydin *et al.*, *ACS Med. Chem. Lett.* **9**, 528–533 (2018).
15. J. W. Lane, Y. Chen, R. M. Williams, *J. Am. Chem. Soc.* **127**, 12684–12690 (2005).
16. Y.-C. Wu, J. Zhu, *Org. Lett.* **11**, 5558–5561 (2009).

Downloaded from http://science.sciencemag.org/ on January 22, 2019

17. W. Liu *et al*., *Tetrahedron* **68**, 2759–2764 (2012).
18. R. Chen, H. Liu, X. Chen, *J. Nat. Prod.* **76**, 1789–1795 (2013).
19. N. Saito *et al*., *Tetrahedron* **60**, 3873–3881 (2004).
20. S. Xu *et al*., *Eur. J. Org. Chem.* **2017**, 975–983 (2017).
21. A. Fontana, P. Cavaliere, S. Wahidulla, C. G. Naik, G. Cimino, *Tetrahedron* **56**, 7305–7308 (2000).
22. H.-S. Yeom, S. Kim, S. Shin, *Synlett* **2008**, 924–928 (2008).
23. K. M. Allan, B. D. Hong, B. M. Stoltz, *Org. Biomol. Chem.* **7**, 4960–4964 (2009).
24. L.-C. Campeau, D. J. Schipper, K. Fagnou, *J. Am. Chem. Soc.* **130**, 3266–3267 (2008).
25. Y. Tan, F. Barrios-Landeros, J. F. Hartwig, *J. Am. Chem. Soc.* **134**, 3683–3686 (2012).
26. V. Boekelheide, W. J. Linn, *J. Am. Chem. Soc.* **76**, 1286–1291 (1954).
27. D.-S. Wang, Q.-A. Chen, S.-M. Lu, Y.-G. Zhou, *Chem. Rev.* **112**, 2557–2590 (2012).
28. S.-M. Lu, Y.-Q. Wang, X.-W. Han, Y.-G. Zhou, *Angew. Chem. Int. Ed.* **45**, 2260–2263 (2006).
29. L. Shi *et al*., *Angew. Chem. Int. Ed.* **51**, 8286–8289 (2012).
30. A. Iimuro *et al*., *Angew. Chem. Int. Ed.* **52**, 2046–2050 (2013).
31. J. Wen, R. Tan, S. Liu, Q. Zhao, X. Zhang, *Chem. Sci.* **7**, 3047–3051 (2016).
32. R. Noyori, S. Hashiguchi, *Acc. Chem. Res.* **30**, 97–102 (1997).
33. J.-H. Xie, S.-F. Zhu, Q.-L. Zhou, *Chem. Rev.* **111**, 1713–1760 (2011).
34. R. Dorta *et al*., *Chem. Eur. J.* **10**, 267–278 (2004).
35. *S*,R_P-BTFM-Xyliphos (**27**) is produced and sold by Solvias AG and is licensed to Sigma-Aldrich Co. and Strem Chemicals under the name SL-J008-2.
36. The lower ee measured on isolated **6** as compared with isolated **22** can be rationalized by competitive (although minor), nonselective D-ring reduction leading to the same major diastereomer. See supplementary materials.
37. C. B. Lavery, N. L. Rotta-Loria, R. McDonald, M. Stradiotto, *Adv. Synth. Catal.* **355**, 981–987 (2013).
38. N. C. Bruno, M. T. Tudge, S. L. Buchwald, *Chem. Sci.* **4**, 916–920 (2013).
39. Y. Pommier *et al*., *Biochemistry* **35**, 13303–13309 (1996).
40. C. Xing, J. R. LaPorte, J. K. Barbay, A. G. Myers, *Proc. Natl. Acad. Sci. U.S.A.* **101**, 5862–5866 (2004).
41. N. A. O'Brien *et al*., *Clin. Cancer Res.* **20**, 3507–3520 (2014).
42. R. S. Finn *et al*., *Breast Cancer Res.* **11**, R77–R89 (2009).

ACKNOWLEDGMENTS

We thank S. H. Christensen for experimental assistance and M. Takase and L. Henling for assistance with x-ray structure determination. **Funding:** Research reported in this publication was supported by the NIH National Institute of General Medical Sciences (R01 127972), the Margaret E. Early Medical Research Trust, the NSF under the CCI Center for Selective C–H Functionalization (CHE-1700982), the Teva Pharmaceuticals Marc A. Goshko Memorial Grant Program, and the California Institute of Technology RI2 Program. E.R.W. was supported by a postdoctoral fellowship (PF-16-011-01-CDD) from the American Cancer Society. A.N. was supported by the Royal Thai Government Scholarship program. M.K. was supported by a postdoctoral fellowship from the German Academic Exchange Service. G.L. was supported by the Swiss National Science Foundation. G.M.P. was supported by an Erwin Schroedinger Fellowship, J 3893–N34, from the Austrian Science Fund (FWF). P.M.T. was supported by a graduate fellowship from the California HIV/AIDS Research Program. E.G. was supported by Knud Højgaards Fond and Oticon Fonden. C.U.G. was supported by a Feodor Lynen Research Fellowship from the Alexander von Humboldt Foundation. **Author contributions:** B.M.S. conceived and directed the project. E.R.W., C.D.G., P.M.T., K.M.A., and B.M.S. conceptualized and designed the synthetic strategy. E.R.W., A.N., M.K., G.L., G.M.P., C.D.G., P.M.T., C.K.H., K.N., E.G., and C.U.G. designed, performed, and analyzed the synthetic chemistry experiments. E.R.W., A.N., and G.M.P. designed and synthesized bis-THIQ analogs **31**–**34**. D.J.S., M.S.J.M., and D.C. designed, performed, and analyzed biological activity experiments. S.C.V. assisted with experimental design and purification and obtained x-ray quality crystals of bis-THIQ **27**. E.R.W., A.N., G.M.P., and B.M.S. prepared the manuscript. D.J.S. and B.M.S. acquired funding for the project. **Competing interests:** B.M.S. has received financial support unrelated to the current science from 1200 Pharma, LLC, Novartis, Holoclara, and Amgen. B.M.S. is a cofounder of 1200 Pharma, LLC. D.J.S. has received financial support unrelated to the current science from Pfizer, Novartis, Eli Lilly and Company, and BioMarin Pharmaceutical. D.J.S. is a paid consultant to Novartis and Eli Lilly and Company. The California Institute of Technology holds a patent application on methods for preparing bis-THIQ-containing compounds (U.S. patent application 16/038,968; international patent application PCT/US18/42710), on which E.R.W., A.N., M.K., G.L., G.M.P., C.D.G., P.M.T., C.K.H., K.N., E.G., C.U.G., K.M.A., S.C.V., and B.M.S. are named as inventors. **Data and materials availability:** Crystallographic parameters for compound **27** are available free of charge from the Cambridge Crystallographic Data Centre under CCDC 1875455. Data are available in the supplementary materials. The molecular characterization of the cell lines used in this Report has been deposited in the GEO public database (GEO:GSE18496).

SUPPLEMENTARY MATERIALS

www.sciencemag.org/content/363/6424/270/suppl/DC1
Materials and Methods
Tables S1 to S13
Figs. S1 to S4
NMR Spectra
References (*43*–*52*)

6 September 2018; accepted 26 November 2018
Published online 20 December 2018
10.1126/science.aav3421

Downloaded from http://science.sciencemag.org/ on January 22, 2019

NEUROSCIENCE

An amygdalar neural ensemble that encodes the unpleasantness of pain

Gregory Corder[1,2,3,4]*†, Biafra Ahanonu[5,6,7]*, Benjamin F. Grewe[5,7]‡, Dong Wang[1], Mark J. Schnitzer[5,6,7,8]§, Grégory Scherrer[1,2,3,4,9]§

Pain is an unpleasant experience. How the brain's affective neural circuits attribute this aversive quality to nociceptive information remains unknown. By means of time-lapse in vivo calcium imaging and neural activity manipulation in freely behaving mice encountering noxious stimuli, we identified a distinct neural ensemble in the basolateral amygdala that encodes the negative affective valence of pain. Silencing this nociceptive ensemble alleviated pain affective-motivational behaviors without altering the detection of noxious stimuli, withdrawal reflexes, anxiety, or reward. Following peripheral nerve injury, innocuous stimuli activated this nociceptive ensemble to drive dysfunctional perceptual changes associated with neuropathic pain, including pain aversion to light touch (allodynia). These results identify the amygdalar representations of noxious stimuli that are functionally required for the negative affective qualities of acute and chronic pain perception.

Pain is both a sensory and affective experience (*1*). The unpleasant percept that dominates the affective dimension of pain is coupled with the motivational drive to engage protective behaviors that limit exposure to noxious stimuli (*2*). Although previous work has uncovered detailed mechanisms underlying the sensory detection of noxious stimuli and spinal processing of nociceptive information (*3*), how brain circuits transform emotionally inert information ascending from the spinal cord into an affective pain percept remains unclear (*4*). Attaining a better understanding of the mechanisms underlying pain affect is important, because it could lead to novel therapeutic strategies to limit the suffering of chronic pain patients.

The amygdala critically contributes to the emotional and autonomic responses associated with valence coding of neural information, such as responses during fear or pain (*5*). Damage to the basolateral amygdala (BLA) can induce a rare phenomenon in which noxious stimuli remain detected and discriminated but are devoid of perceived unpleasantness and do not motivate avoidance (*6*, *7*). Conversely, impairment of somatosensory cortex function reduces the ability to both localize noxious stimuli and describe their intensity, without altering aversion or avoidance (*8*, *9*). Thus, BLA affective neural circuits might link nociceptive inputs to aversive perceptions and behavior selection.

Patients with chronic pain often suffer allodynia, a pathological state in which an intense unpleasant percept arises in response to innocuous stimuli such as light touch (*10*). Notably, the BLA displays heightened activity during chronic pain (*11*), and longitudinal functional magnetic resonance imaging studies in humans and rodents show that neural hyperactivity and altered functional connectivity in the amygdala parallel the onset of chronic pain, suggesting that the BLA might play a critical role in shaping pathological pain perceptions (*12*–*14*). However, it remains unclear how the BLA influences the unpleasant aspects of innate acute and chronic pain perceptions (*15*), while the role of nociceptive circuits in the central amygdala are better understood (*16*, *17*). Previous studies attempting to define pain affect mechanisms recorded the acute nociceptive responses of single amygdalar neurons in anesthetized animals (*11*, *18*). However, recent work has shown that the BLA encodes information via the coordinated dynamics of neurons within large ensembles (*19*); it is therefore important to resolve how the BLA processes pain affect at the neural ensemble level in awake, freely behaving animals.

We first performed fluorescence in situ hybridization studies and used the immediate-early gene marker of neural activity, *c-Fos*, to determine that *c-Fos*$^+$ neurons activated by nociceptive stimuli comprised a population of mid-anterior BLA *Camk2a*$^+$ principal neurons (fig. S1). To identify how the BLA encodes nociceptive information, we used a head-mounted miniature microscope to track the somatic Ca^{2+} dynamics of individual BLA *Camk2a*$^+$ principal neurons in freely behaving mice presented with diverse noxious and innocuous stimuli (Fig. 1, A to D, and figs. S2 and S3) (*20*). We monitored pain-related behaviors by measuring each animal's locomotor acceleration, which allowed us to track both reflexive withdrawal and affective-motivational behaviors that include attendance to the stimulated tissue and escape (Fig. 1, A and E, and fig. S4).

Noxious heat, cold, and pin prick stimuli elicited significant Ca^{2+} responses in 15 ± 2% (SEM), 13 ± 2%, and 13 ± 2% of active BLA neurons, respectively [3397 neurons (117 ± 8 neurons per session)] (Fig. 1, F to H, and table S1). Innocuous light touch induced Ca^{2+} activity in a smaller subset of neurons (7 ± 1%) (Fig. 1, F and I, and fig. S5E). Alignment of all stimulus-evoked ensemble responses to the noxious heat trials revealed an overlapping population of principal neurons that encoded nociceptive information across pain modalities (i.e., noxious heat, cold, pin), which we refer to here as the BLA nociceptive ensemble (24 ± 2% of active BLA neurons) (Fig. 1, F to I).

This ensemble was composed of multimodal responsive neurons, as well as a unique population that appeared to encode nociception selectively and no other sensory information (6 ± 1% of all imaged neurons) (Fig. 1K and fig. S5G). Pain behavioral responses evoked by noxious stimuli closely mirrored the activity of this nociceptive neural ensemble (Fig. 1, E and G, and fig. S4, D and E). The nociceptive ensemble contained a subset of neurons that maintained their noxious stimulus response properties for more than a week (11% of 3223 cross-day–aligned neurons) (fig. S6). Increasingly salient stimuli, from light touch (18 ± 3% of the nociceptive ensemble) to mild touch (31 ± 4%), activated larger subsets of the nociceptive ensemble (Fig. 1, G and I, fig. S5, D and E, and table S1) and induced heightened behavior (Fig. 1E and fig. S4). Expectation of stimulus contact ("approach/no contact" trials) also evoked sparse BLA activity (7 ± 2% of the total population) (fig. S5, A to E, and table S1). BLA activity did not correlate with exploratory locomotion (fig. S7, A to E) (*21*).

To determine whether the BLA nociceptive ensemble broadly encodes stimulus valence (*22*, *23*), we presented mice with an appetitive stimulus (10% sucrose). Sucrose consumption was encoded by a distinct ensemble (18 ± 3% of all neurons) that only overlapped with a subset of neurons in the nociceptive ensemble (7% of total neurons) (Fig. 1J and fig. S5E) (*19*). Similar to conditioned responsive valence networks (*23*), neurons encoding unconditioned nociceptive and appetitive information were spatially intermingled (fig. S5, F, H, and I). Consistent with these results, nociceptive *c-Fos*$^+$ neurons

[1]Department of Anesthesiology, Perioperative, and Pain Medicine, Stanford University School of Medicine, Stanford, CA 94305, USA. [2]Department of Molecular and Cellular Physiology, Stanford University School of Medicine, Stanford, CA 94305, USA. [3]Department of Neurosurgery, Stanford University School of Medicine, Stanford, CA 94305, USA. [4]Stanford Neurosciences Institute, Stanford University, Stanford, CA 94305, USA. [5]Department of Biology, Stanford University, Stanford, CA 94305, USA. [6]Howard Hughes Medical Institute, Stanford University, Stanford, CA 94305, USA. [7]CNC Program, Stanford University, Stanford, CA 94305, USA. [8]Department of Applied Physics, Stanford University, Stanford, CA 94305, USA. [9]New York Stem Cell Foundation—Robertson Investigator, Stanford University, Stanford, CA 94305, USA.
*These authors contributed equally to this work. †Present address: Department of Psychiatry and Department of Neuroscience, Perelman School of Medicine, University of Pennsylvania, Philadelphia, PA 19104, USA. ‡Present address: Institute of Neuroinformatics, ETH and University of Zurich, Zurich 8057, Switzerland.
§Corresponding author. Email: mschnitz@stanford.edu (M.J.S.); gs25@stanford.edu (G.S.)

Downloaded from http://science.sciencemag.org/ on January 17, 2019

expressed the negative valence marker gene *Rspo2* but not the positive valence marker gene *Pppr1b* (*24*) (fig. S1, D and E).

We next determined if the nociceptive ensemble was engaged during aversive experiences other than pain by presenting a panel of sensory, but nonsomatosensory or nonnaturalistic, aversive stimuli, including repulsive odor, bitter taste, loud tone, facial air puff, and electric shock. We found that while there was overlap between the neural ensembles that encode nociceptive, aversive, and electric shock stimuli (~10% of all imaged neurons), there remained a subset of BLA neurons (~6% of imaged neurons) that responded only to naturalistic nociceptive stimuli (Fig. 1K and fig. S8).

By analyzing the neural ensemble dynamics with pattern classification methods, we were able to classify and distinguish with high accuracy noxious stimuli from other aversive stimuli (fig. S8E), supporting the finding that noxious stimuli induce a distinct mode of BLA activation (supplementary text S1). Moreover, sensory stimuli of different valences, intensities, and modalities are represented by unique activity codes. Noxious stimuli were encoded distinctly from one another and could be distinguished

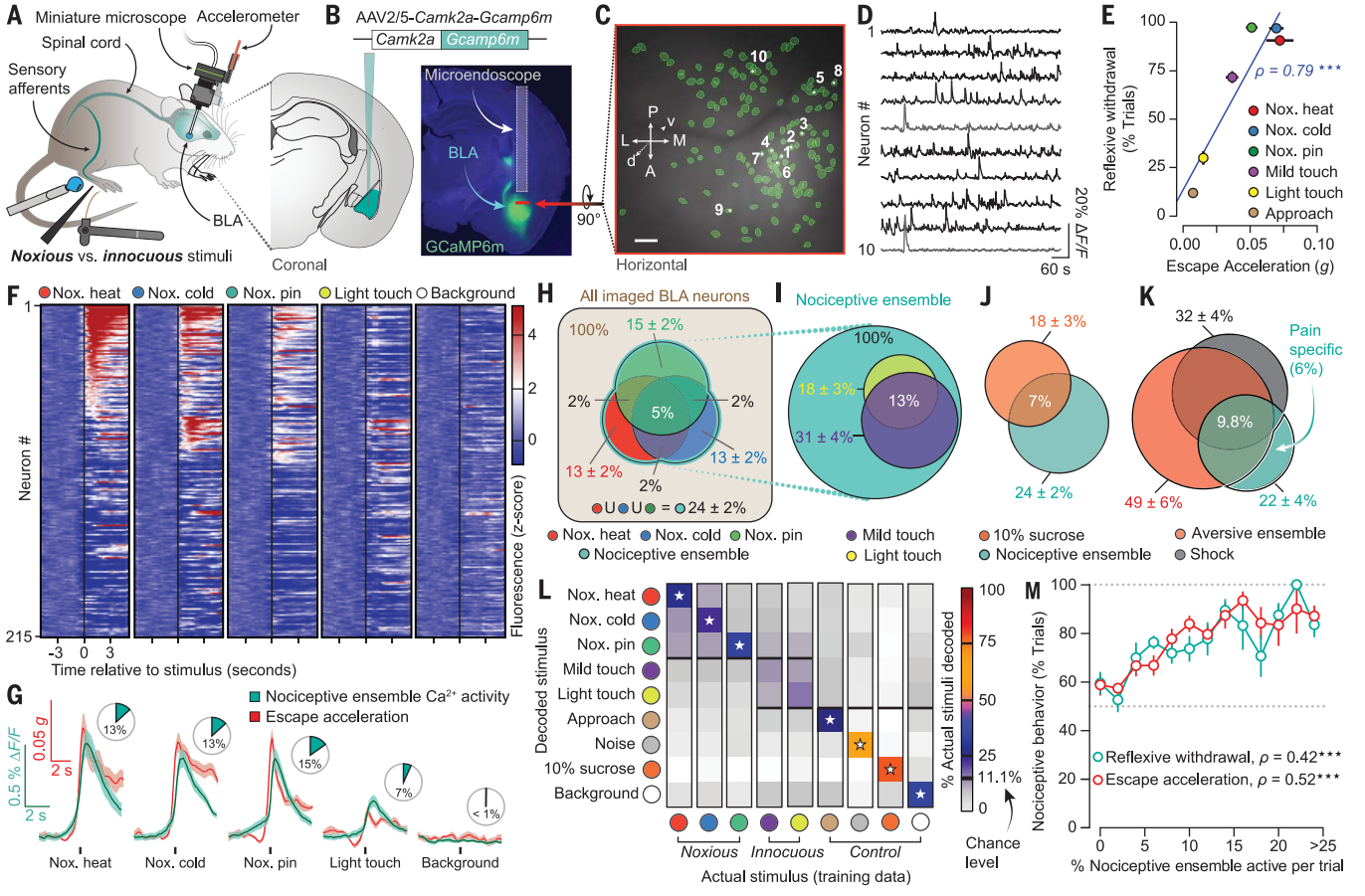


Fig. 1. A distinct nociceptive neural ensemble in the BLA represents diverse painful stimuli. (**A**) BLA neural activity was imaged in freely behaving mice with a microendoscope and the virally expressed fluorescent Ca^{2+} indicator GCaMP6m. Noxious mechanical (pin prick) and thermal (55°C H_2O and 5°C H_2O or acetone) stimuli were delivered to the left hindpaw, while reflexive and affective-motivational behavior were monitored via a scope-mounted accelerometer. (**B**) Microendoscope placement and GCaMP6m expression in the right, contralateral BLA. The red line marks the focal plane and is also a 1.0-mm scale bar. (**C** and **D**) Map of active BLA neurons (n = 131 neurons) with numbers in (C) matching independent component analysis–derived neuron activity traces in (D). Scale bar, 100 μm. (**E**) Spearman's correlation between reflexive withdrawal and affective-motivational escape acceleration. (**F**) Mean Ca^{2+} response (Z-scored $\Delta F/F$ per trial) across all trials for all BLA neurons imaged during a single session (n = 215 neurons) from the same animal. Neurons are aligned from high to low Ca^{2+} responses in the noxious heat trials. Individual neuron identifications between different stimuli are consistent across the trial rows. (**G**) Stimulus-locked mean Ca^{2+} activity within the nociceptive ensemble (cyan) and mean affective-motivational escape acceleration (red). Shaded region, ±SEM. Pie charts indicate the percentages of significantly responding neurons. (**H**) Venn diagram of neural populations encoding nociceptive information in response to noxious heat, cold, and pin stimuli. Numbers show means ± SEM of percentages of significantly responding neurons across imaging sessions (see fig. S5E). (**I**) Neural populations within the nociceptive ensemble that encode innocuous light touch (0.07-g filament) and mild touch (a 1.4- or 2.0-g filament). (**J**) Divergent neural populations (versus the nociceptive ensemble) encoding appetitive stimuli (10% sucrose consumption). (**K**) Overlapping BLA populations between the nociceptive ensemble, electric footshock, and aversive stimuli (isopentylamine odor, facial air puff, 85-dB noise, and quinine consumption). A subset of nociceptive ensemble neurons were pain specific (~6% of the BLA neurons). (**L**) Accuracies of a nine-way Naïve Bayes decoder that distinguishes the ensemble activities for noxious, innocuous, aversive, anticipatory, and appetitive stimuli. The percentage of decoder accuracy to output for the actual stimuli (diagonal) was compared to that for the incorrect stimuli (off the diagonal) and normalized so that each actual stimuli column added up to 100%. Stars on the diagonal indicate the correct prediction of said stimulus was significantly greater than all off-diagonal stimuli within the same column (Wilcoxon sign-rank, Benjamini-Hochberg corrected). (**M**) Spearman's correlation (ρ) between per trial pain behavioral responses and nociceptive ensemble activation. Error bars, ±SEM per session animal responses; n = 9 mice, 3 to 4 sessions each.

Downloaded from http://science.sciencemag.org/ on January 17, 2019

with even higher fidelity from innocuous, non-nociceptive aversive, and appetitive stimuli (Fig. 1L and fig. S9, A and B), indicating that there is a core set of BLA neurons that encodes nociceptive stimuli via specific dynamic neural codes. One crucial finding was that greater activation of this BLA nociceptive ensemble was predictive of increased pain behaviors, suggesting that BLA nociceptive processing influences the magnitude of pain behaviors (Fig. 1M and fig. S7, H and I).

To test the causal role of the BLA nociceptive ensemble for pain behaviors, we expressed a Cre-dependent inhibitory DREADD neuromodulator (hM4-mCherry) in mutant TRAP mice (*Fos*^{CreERT2}) by applying noxious pin pricks that induced activity-dependent, spatially, and temporally controlled DNA recombination and hM4-mCherry expression (noci-TRAP^{hM4} mice) (Fig. 2, A to C, and fig. S10) (*25*, *26*). Since the BLA encodes multiple modalities of nociceptive stimuli within a core ensemble (Fig. 1H), we hypothesized that silencing the neurons activated by noxious pin prick would alter behavioral responses to all types of noxious stimuli. Indeed, the hM4 agonist clozapine-*N*-oxide (CNO; 10 mg/kg) significantly reduced both attending and escape behaviors, but not stimulus detection and withdrawal, for both mechanical and thermal noxious stimuli (Fig. 2, D to G, and fig. S11, A and B). CNO alone had no effect on pain behaviors in control mice (fig. S11C) (*27*). To test operant pain behavior, we next allowed noci-TRAP^{hM4} mice to explore a thermal gradient track in which the polar ends were set at noxious cold (5 to 17°C) and hot (42 to 48°C) temperatures (Fig. 2H). The noci-TRAP^{hM4} mice injected with control saline rapidly acquired an adaptive avoidance strategy of the noxious zones. In contrast, noci-TRAP^{hM4} mice treated with CNO visited the noxious zones more frequently and for prolonged periods (Fig. 2, H to J, and fig. S12). Similarly, inhibition of the BLA nociceptive ensemble eliminated pain affective-motivational behaviors induced by the optogenetic activation of peripheral primary afferent nociceptors (fig. S13).

Whether pain and anxiety rely on common or distinct BLA ensembles is unknown; therefore, we placed noci-TRAP^{hM4} mice within an elevated plus maze, in which anxiety drives avoidance of the open arms (Fig. 2K). The noci-TRAP^{hM4} mice given either saline or CNO displayed equivalent visits to and occupancy of the open arms (fig. S14, A and B). Since nociceptive and

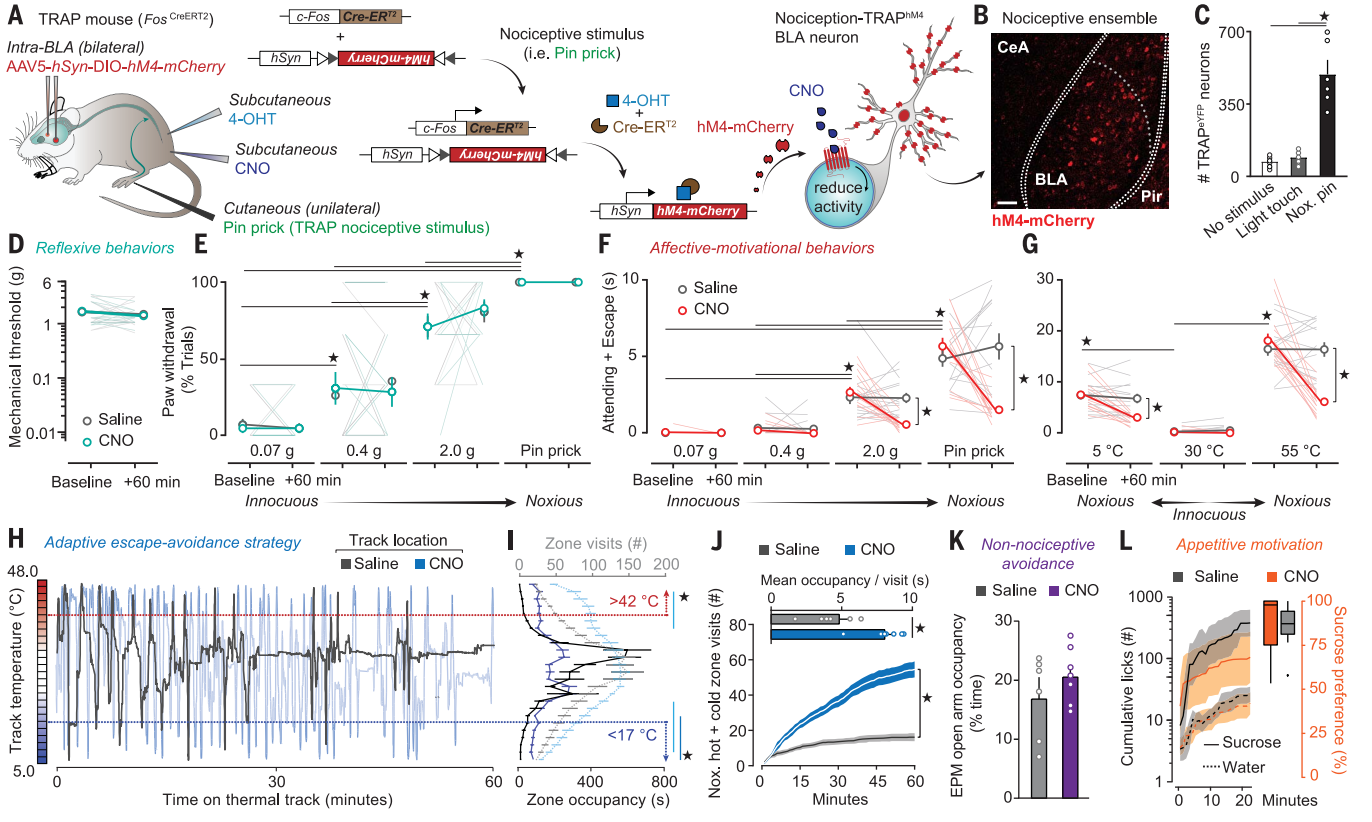


Fig. 2. The BLA nociceptive ensemble is necessary for generating protective and avoidance behavioral responses to painful stimuli. (**A**) Experimental strategy for inhibiting BLA nociceptive ensemble activity. Nociception-mediated targeted recombination in activity neural populations (noci-TRAP) of the inhibitory DREADD(hM4) receptor. CNO, clozapine N-oxide; 4-OHT, 4-hydroxytamoxifen. (**B**) noci-TRAP^{hM4} expression in the BLA nociceptive ensemble. CeA, central amygdala; ITC, intercalated neurons; Pir, piriform cortex. Scale bar, 50 μm. (**C**) Quantification of BLA noci-TRAP^{eYFP} neurons following either no stimulus, innocuous touch (0.07-g filament), or noxious pin prick stimulation; *n* = 6 mice/group. (**D** and **E**) Effect of inhibiting the BLA nociceptive ensemble against reflexive behaviors, demonstrated by a von Frey mechanical threshold assay (D) and reflexive withdrawal frequency to increasing noxious mechanical stimuli (E). *n* = 14 mice per group. (**F** and **G**) Effect of inhibiting the BLA nociceptive ensemble against pain affective-motivational behaviors in response to increasingly noxious mechanical (F) and thermal stimuli (G). *n* = 14 mice per group. (**H**) Effect of inhibiting the BLA nociceptive ensemble on adaptive avoidance behavior to noxious thermal environments. The kymograph displays mouse location on a thermal gradient track over a 60-min trial following administration of saline (*n* = 6 mice) or CNO (*n* = 7 mice). Noxious temperature zones were areas at <17°C and >42°C. (**I**) Total number of visit entries (gray and light blue lines) and the occupancy time (black and dark blue lines) in the track's 25 thermal zones. (**J**) Temporal cumulative visits and the mean occupancy time per visit (inset) to the noxious hot and cold zones. (**K**) Occupancy time within the open arms of an elevated plus maze (EPM). (**L**) The 10% sucrose spout lick rates and preference over a water choice. Overlaid dots and lines represent individual animals. Error bars, ± SEM. For (C) and (E) to (G) (CNO group baseline time points only), one-way analysis of variance (ANOVA; Friedman's) plus Dunn's correction. For (D) to (G) and (I), two-way repeated measures ANOVA with Bonferroni correction. For (J) and (K), data on left analyzed with Kolmogorov-Smirnov test; data on right analyzed with Student's *t* test. Star, $P < 0.05$.

Downloaded from http://science.sciencemag.org/ on January 17, 2019

sucrose reward-related information were encoded in divergent networks (Fig. 1J), we tested the contribution of the nociceptive ensemble to appetitive motivational drive during sucrose preference training. CNO enhanced sucrose reward in sucrose-naïve conditions (*28*) but had no retarding effects on preference development or on lick rates, relative to controls (Fig. 2L and fig. S14C). Thus, this BLA nociceptive ensemble transforms emotionally inert nociceptive information into an affective signal that is necessary for the selection and learning of motivational protective pain behaviors.

We next investigated the contribution of BLA neural ensemble activity to chronic pain. A hallmark of chronic neuropathic pain is the appearance of allodynia and hyperalgesia, both pathological perceptual states in which aversion is ascribed to innocuous somatosensory stimuli and exacerbated in response to noxious stimuli, respectively (Fig. 3A) (*29*). We hypothesized that this pathological perceptual switch might result from maladaptive transformations in BLA coding. We tracked the longitudinal dynamics of BLA ensembles before and after the development of neuropathic pain induced by sciatic nerve injury (17,396 neurons, n = 17 mice) (Fig. 3). Throughout the development of chronic neuropathic pain, a subset of neurons stably encoded the nociceptive ensemble for both noxious mechanical and cold stimuli (fig. S6). Nerve injury did not significantly increase the spontaneous activity of the nociceptive ensemble and overall BLA population (fig. S15, A and B). However, BLA neural activity elicited in response to light touch displayed a significant expansion within the nociceptive ensemble in neuropathic (291 ± 88% increase) but not in uninjured mice (38 ± 14% decrease) (Fig. 3, D to G, and fig. S15, C to E). The emergence of this neuropathic coding schema was accompanied by the development of reflexive paw withdrawal hypersensitivity and by enhanced affective-motivational pain behaviors (Fig. 3, B and C, and fig. S4, C to F). The magnitudes of

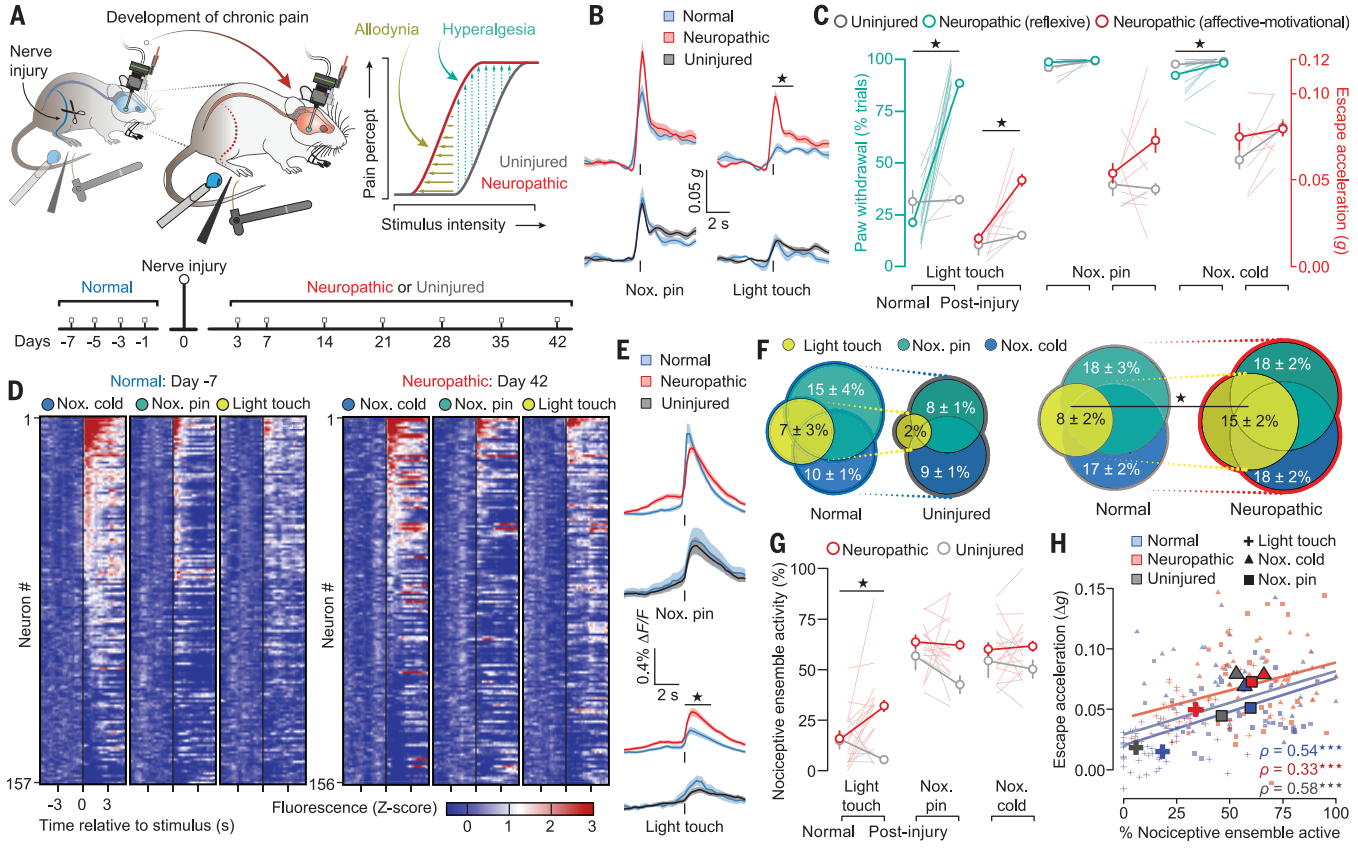


Fig. 3. Convergence of BLA neural ensemble representations of innocuous and noxious information during chronic pain. (**A**) Long-term tracking of BLA neural activity with microendoscopes throughout the development of chronic neuropathic pain. Peripheral nerve injury results in an increased sensitivity and perceived aversion to innocuous (allodynia) and noxious (hyperalgesia) stimuli. (**B**) Affective-motivational escape acceleration for neuropathic (top row; n = 5 mice) and uninjured (bottom row; n = 4 mice) animals in response to noxious pin or light touch stimuli before and after nerve injury. Dark lines, means; shaded regions, ±SEM. (**C**) Hyperalgesic and allodynic behavioral responses in neuropathic (n = 13 mice for paw withdrawal, n = 5 mice for escape acceleration) or uninjured (n = 4 mice for both measures) animals after application of light touch (0.07-g filament), noxious pin, or noxious cold (acetone or 5°C H_2O drop) stimuli, respectively. Data were quantified by reflexive hypersensitivity (left axis) and affective-motivational escape acceleration (right axis). (**D**) Mean Ca^{2+} activity (Z-scored $\Delta F/F$ per trial) of all neurons from the same animal for that imaging session, before and after nerve injury, in response to noxious pin prick, noxious cold, and light touch stimuli. Neuron identifications were consistent between stimuli within a day, but not across days (n = 157 and 156 neurons, for days −7 and 42, respectively). (**E**) Mean Ca^{2+} response within the nociceptive ensemble for neuropathic (top row; n = 13 mice, 12,026 total neurons imaged) and uninjured (bottom row; n = 4 mice, 5370 total neurons imaged) animals in response to noxious pin or light touch stimuli. (**F**) Venn diagrams of percentages of significantly responding neurons to noxious pin, noxious cold, and light touch before and after nerve injury. (**G**) Overlapping neural populations responsive to light touch within the nociceptive ensemble (pin prick and 5°C water or acetone responsive neurons) after nerve injury (n = 13 mice) or in uninjured animals (n = 4 mice). Numbers indicate means ± SEM. (**H**) Percentages of nociceptive ensemble activated and escape acceleration per imaging session (light-colored points) and across animal groups and conditions (dark, larger points) show significant correlations [Spearman's ρ = 0.54 (normal), 0.33 (Neuropathic), and 0.58 (Uninjured) groups]. All tests results in the figure were analyzed via Wilcoxon rank-sum with Benjamini-Hochberg correction unless otherwise noted. Stars, P < 0.01.

Downloaded from http://science.sciencemag.org/ on January 17, 2019

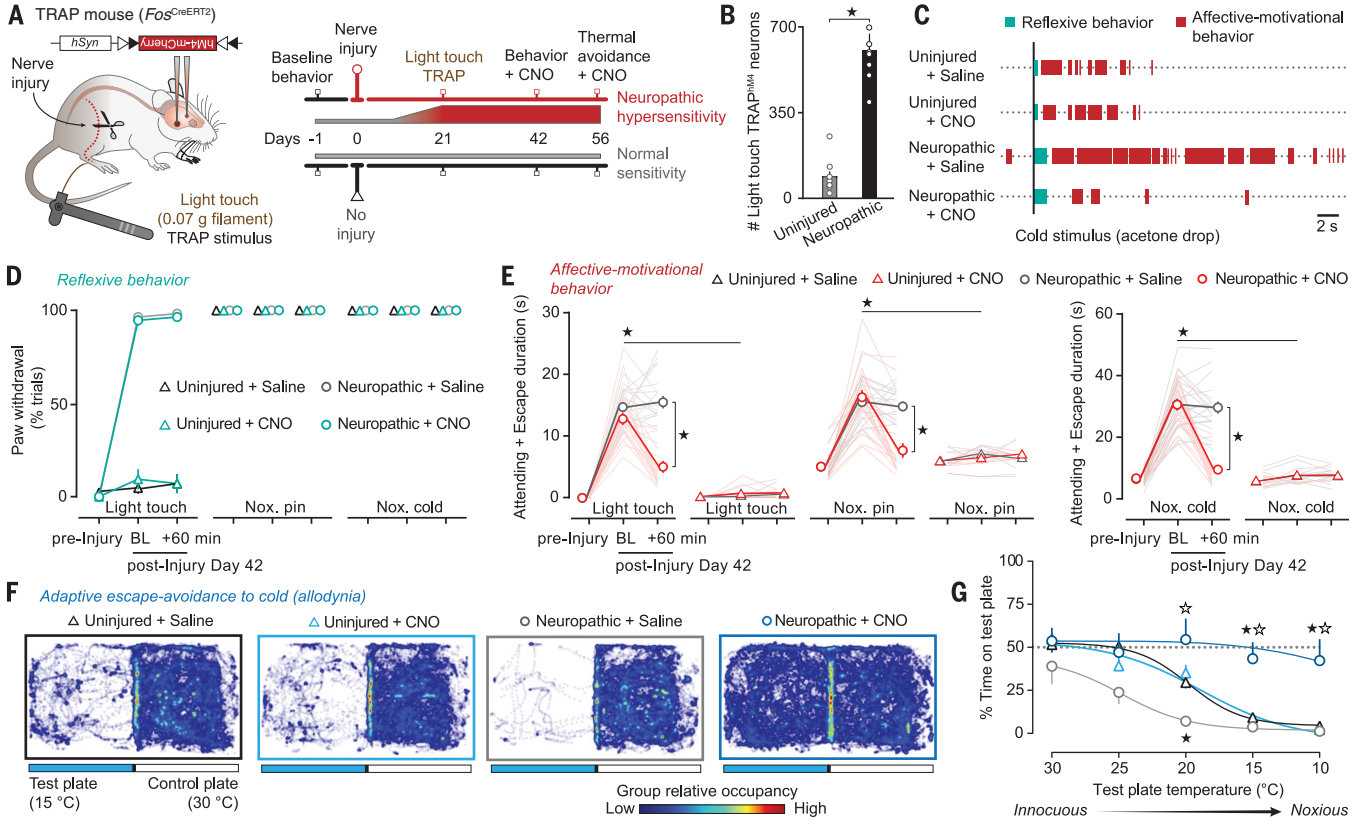


Fig. 4. Inhibition of neuropathic BLA ensemble activity reduces the aversive quality of chronic pain. (**A**) Utilization of light touch to gain genetic access to, and manipulate, the neuropathic nociceptive ensemble. (**B**) Quantification of light touch TRAP neurons in the BLA of neuropathic mice compared to uninjured mice; $n = 7$ per group. (**C**) Behavioral raster plots from neuropathic mice showing the effects of inhibiting the BLA nociceptive ensemble on reflexive and affective-motivational pain behaviors associated with cold allodynia. (**D** and **E**) Summary of the effects of ensemble inhibition against reflexive (D) and affective-motivational (E) pain behaviors in response to noxious pin prick, noxious cold (acetone drop), or formerly innocuous touch stimuli (0.07-g filament). Behavior was assessed before and 42 days after nerve injury and again at 60 min after CNO or saline administration on day 42; $n = 14$ per group. (**F** and **G**) Effects of neuropathic ensemble inhibition on adaptive avoidance during a cold place aversion assay. (F) Group mean exploration paths, color coded for the relative occupancy time, following CNO or saline treatments; (G) summary of the effects in response to decreasing floor plate temperatures; $n = 6$ per group. Stars, $P < 0.05$ for all panels. In (G), the black star indicates $P < 0.05$ versus the uninjured + saline group; open star, $P < 0.05$ versus the neuropathic + saline group. Overlaid dots and lines represent individual subjects. Error bars, ±SEM. For (B), Student's *t* test; (D and E), two-way ANOVA with Bonferroni correction; (G) three-way ANOVA with Bonferroni correction.

the behavioral responses and the BLA nociceptive ensemble Ca^{2+} activity were significantly correlated before and after injury (Fig. 3H and fig. S15F). These results suggest a role for the BLA in the emergence of allodynia in chronic pain states.

We next asked if we could prevent the neural transformation of light touch sensory information into an aversive signal and eliminate chronic pain unpleasantness by gaining genetic access to the nociceptive ensemble with innocuous stimuli in neuropathic TRAP mice. At 21 days post–nerve injury, when allodynia had fully developed (fig. S16, B to E), we delivered a light touch TRAP protocol to express hM4-mCherry in the BLA nociceptive ensemble (neuropathic $TRAP^{hM4}$ mice) (Fig. 4, A and B, and fig. S16). At day 42 postinjury, neuropathic $TRAP^{hM4}$ mice displayed significant allodynia and hyperalgesia, for both reflexive and affective-motivational pain responses, relative to uninjured mice (Fig. 4, C to E). While the injection of CNO in neuropathic $TRAP^{hM4}$ mice did not alter reflexive hypersensitivity (Fig. 4D), we observed a profound decrease in neuropathic affective-motivational behaviors, regardless of stimulus intensity or modality (Fig. 4E and fig. S17, A and B). Uninjured $TRAP^{hM4}$ mice given the light touch TRAP protocol expressed levels of hM4-mCherry in the BLA that were similar to those of nonstimulated control mice (Fig. 4B and fig. 2C), presumably because the nociceptive ensemble does not strongly encode innocuous information under normal conditions (Fig. 1I). We observed neither CNO-mediated changes in affective-motivational pain behaviors in these uninjured mice nor CNO effects on neuropathic reflexive or affective-motivational behaviors in the absence of hM4 expression (Fig. 4, C to E, and fig. S17, A and B). In addition to tactile allodynia, patients with neuropathic pain often report intense pain in response to cold temperatures (cold allodynia). We therefore ran neuropathic $TRAP^{hM4}$ mice through a two-chamber thermal escape-avoidance assay in which the floor of one chamber was cooled (from 30° to 10°C) (Fig. 4F). Uninjured $TRAP^{hM4}$ mice avoided the cold chamber, while mice with nerve injury showed enhanced avoidance, consistent with allodynia (Fig. 4, F and G). Notably, CNO administration to neuropathic $TRAP^{hM4}$ mice generated a near-total indifference between cold and neutral temperature chambers (Fig. 4, F and G). Together, these results indicate that the BLA nociceptive ensemble is also necessary for the pain aversion associated with allodynia and hyperalgesia during chronic pain states.

Thus, disrupting neural activity in a nociceptive ensemble in the BLA is sufficient to reduce the affective dimension of pain experiences, without altering their sensory component. The unconditioned nociceptive ensemble described here is a stable network of amygdalar principal neurons that is responsive to a diverse array of noxious stimuli. Within this ensemble, combinatorial neural ensemble codes distinguish the

Downloaded from http://science.sciencemag.org/ on January 17, 2019

various thermal and mechanical nociceptive stimuli. These codes likely represent stimulus modality, intensity, salience, and valence to provide additional qualitative information that enriches individual pain affect percepts (*30*). The presence of a purely nociceptive-specific subpopulation of neurons within the larger BLA nociceptive ensemble, distinct from general aversion-encoding populations, suggests the capacity for computing and assigning an accompanying "pain tag" to valence information. This categorical signal could prioritize the negative valence of intense noxious stimuli and scale the selection of conative pain protective behaviors. It is thought that hierarchical pathways transform low-level sensory inputs into higher-order affective responses (*5*, *31*). Our chemogenetic manipulations suggest that this critical node in the nociceptive brain circuitry plays a critical role in shaping pain experiences, by providing an evaluation of nociceptive information that, in turn, intrinsically motivates protective behaviors associated with pain (*32*).

The phenomenological description of a pain experience is normally that of a complex but unified sensory and emotional perception that can neither exist alone as an unanchored aversive state nor stand merely on its emotionally inert sensory qualities (*33*, *34*). Though activity within the BLA nociceptive ensemble cannot account for the instantiation of the entire pain experience, we propose that the BLA nociceptive ensemble transmits abstracted valence information to the central amygdala, striatal, and cortical networks (*35*–*37*). For example, BLA neurons projecting to the CeA may send a "pain tag" that helps select for appropriate defensive responses to impending or immediate threats (*23*) (supplementary text S2). In parallel, connected cortical regions might coalesce BLA affective signals with sensory-discriminative information to process them against prior experiences and internal states for further evaluation at cognitive levels, all of which contribute to the construction of a pain experience (*4*, *38*).

During chronic pain states, BLA ensemble coding of innocuous somatosensory information changes to engage the nociceptive ensemble, leading to perceived aversion and protective behavioral responses when encountering normally nonpainful stimuli, such as light touch. Whether this change in ensemble activity results from peripheral or central sensitization (*3*, *39*), amygdalar input, or intra-amygdala plasticity (*11*) remains an open question. Chronic pain is not simply a sensory disorder but a neurological disease with affective dysfunction that profoundly impacts the mental state of millions of pain patients (*40*). Clinical management of chronic pain remains a staggering challenge, given the heterogeneity of underlying causes, and the overreliance on opioid analgesics has contributed to the opioid epidemic (*41*, *42*). Comprehensive strategies that provide substantive relief across pain types are urgently needed (*43*). To make progress along this translational path, we have identified in the BLA a critical neural ensemble target that mediates chronic pain unpleasantness. This finding may enable the development of chronic pain therapies that could selectively diminish pain unpleasantness, regardless of etiology, without influencing reward, and importantly, preserving reflexes and sensory-discriminative processes necessary for the detection and localization of noxious stimuli (*44*, *45*). Collectively, our findings begin to refine the neural basis and coding principles underlying the multiple dimensions and complexity of the pain experience for developing more effective analgesic therapies.

REFERENCES AND NOTES

1. D. D. Price, *Science* **288**, 1769–1772 (2000).
2. M. N. Baliki, A. V. Apkarian, *Neuron* **87**, 474–491 (2015).
3. C. Peirs, R. P. Seal, *Science* **354**, 578–584 (2016).
4. L. Garcia-Larrea, H. Bastuji, *Prog. Neuropsychopharmacol. Biol. Psychiatry* (2017).
5. P. H. Janak, K. M. Tye, *Nature* **517**, 284–292 (2015).
6. N. Hebben, S. Corkin, H. Eichenbaum, K. Shedlack, *Behav. Neurosci.* **99**, 1031–1039 (1985).
7. N. Neimann *et al*., *Bull. Soc. Fr. Dermatol. Syphiligr.* **71**, 292–294 (1964).
8. M. Ploner, H. J. Freund, A. Schnitzler, *Pain* **81**, 211–214 (1999).
9. M. L. Uhelski, M. A. Davis, P. N. Fuchs, *Pain* **153**, 885–892 (2012).
10. M. Costigan, J. Scholz, C. J. Woolf, *Annu. Rev. Neurosci.* **32**, 1–32 (2009).
11. V. Neugebauer, Amygdala Pain Mechanisms. *Handb. Exp. Pharmacol.* **227**, 261–284 (2015).
12. P. C. Chang, M. V. Centeno, D. Procissi, A. Baria, A. V. Apkarian, *Pain* **158**, 488–497 (2017).
13. L. E. Simons *et al*., The responsive amygdala: Treatment-induced alterations in functional connectivity in pediatric complex regional pain syndrome. *Pain* **155**, 1727–1742 (2014).
14. J. A. Hashmi *et al*., *Brain* **136**, 2751–2768 (2013).
15. F. Gore *et al*., *Cell* **162**, 134–145 (2015).
16. V. Neugebauer, W. Li, G. C. Bird, G. Bhave, R. W. Gereau 4th, *J. Neurosci.* **23**, 52–63 (2003).
17. S. Han, M. T. Soleiman, M. E. Soden, L. S. Zweifel, R. D. Palmiter, *Cell* **162**, 363–374 (2015).
18. G. Ji *et al*., *J. Neurosci.* **30**, 5451–5464 (2010).
19. B. F. Grewe *et al*., *Nature* **543**, 670–675 (2017).
20. Y. Ziv *et al*., *Nat. Neurosci.* **16**, 264–266 (2013).
21. J. G. Parker *et al*., *Nature* **557**, 177–182 (2018).
22. W. Zhang *et al*., *J. Neurosci.* **33**, 722–733 (2013).
23. P. Namburi *et al*., *Nature* **520**, 675–678 (2015).
24. J. Kim, M. Pignatelli, S. Xu, S. Itohara, S. Tonegawa, Antagonistic negative and positive neurons of the basolateral amygdala. *Nat. Neurosci.* **19**, 1636–1646 (2016).
25. C. J. Guenthner, K. Miyamichi, H. H. Yang, H. C. Heller, L. Luo, *Neuron* **78**, 773–784 (2013).
26. B. L. Roth, *Neuron* **89**, 683–694 (2016).
27. J. L. Gomez *et al*., *Science* **357**, 503–507 (2017).
28. G. G. Calhoon *et al*., Acute food deprivation rapidly modifies valence-coding microcircuits in the amygdala. *bioRxiv* 285189 [Preprint]. 19 March 2018.
29. C. A. von Hehn, R. Baron, C. J. Woolf, *Neuron* **73**, 638–652 (2012).
30. B. W. Balleine, S. Killcross, *Trends Neurosci.* **29**, 272–279 (2006).
31. C. D. Salzman, S. Fusi, *Annu. Rev. Neurosci.* **33**, 173–202 (2010).
32. J. E. LeDoux, R. Brown, *Proc. Natl. Acad. Sci. U.S.A.* **114**, E2016–E2025 (2017).
33. N. Grahek, *Feeling Pain and Being in Pain* (MIT Press, 2007).
34. R. Melzack, K. Casey, in *The Skin Senses* (Charles C. Thomas, 1968), pp. 432–439.
35. F. Ramirez, J. M. Moscarello, J. E. LeDoux, R. M. Sears, *J. Neurosci.* **35**, 3470–3477 (2015).
36. A. Burgos-Robles *et al*., Amygdala inputs to prefrontal cortex guide behavior amid conflicting cues of reward and punishment. *Nat. Neurosci.* **20**, 824–835 (2017).
37. A. Beyeler *et al*., *Cell Reports* **22**, 905–918 (2018).
38. K. Wiech, *Science* **354**, 584–587 (2016).
39. C. Torsney, A. B. MacDermott, *J. Neurosci.* **26**, 1833–1843 (2006).
40. P. A. Pizzo, N. M. Clark, O. Carter Pokras, *Relieving Pain in America: A Blueprint for Transforming Prevention, Care, Education, and Research* (National Academies Press, 2011).
41. N. D. Volkow, F. S. Collins, *N. Engl. J. Med.* **377**, 391–394 (2017).
42. G. Corder, D. C. Castro, M. R. Bruchas, G. Scherrer, Endogenous and exogenous opioids in pain. *Annu. Rev. Neurosci.* **41**, 453–473 (2018).
43. P. Skolnick, N. D. Volkow, *Neuron* **92**, 294–297 (2016).
44. F. Jelasić, *Confin. Neurol.* **27**, 53–55 (1966).
45. T. Grosser, C. J. Woolf, G. A. FitzGerald, *Science* **355**, 1026–1027 (2017).
46. B. Ahanonu, calciumImagingAnalysis: A software package for analyzing one- and two-photon calcium imaging datasets. GitHub (2018); https://doi.org/10.5281/zenodo.2222295.

ACKNOWLEDGMENTS

We thank Y. Zhang and J. Z. Li (Stanford) for viral preparations, J. Dickinson and C. Sotoudeh (Stanford) for technical support and help with data analysis, S. Low (Stanford) for construction of the optical place avoidance chambers, L. Luo (Stanford) for providing TRAP mice, and K. T. Creasy (U.C. San Francisco), N. Corder (Mills College), and D. C. Dennett (Tufts University) for critical discussions and editing. **Funding:** This work was supported by U.S. National Institutes of Health (NIH) grants R00DA031777 (G.S.), R01NS106301 (G.S.), K99DA043609 (G.C.), F32DA041029 (G.C), and T32DA35165 (G.C.), the New York Stem Cell Foundation (G.S.), a Rita Allen Foundation and American Pain Society Award (G.S.), a Stanford School of Medicine Dean's Fellowship (G.C.), a National Science Foundation fellowship DGE-114747 (B.A.), HHMI Gilliam Fellowships for Advanced Study (B.A.), Gates Millennium Scholarship (B.A.), the Swiss National Science Foundation (B.F.G.), and the Howard Hughes Medical Institute (M.J.S.). G.S. is a New York Stem Cell Foundation—Robertson Investigator.

This work is licensed under a Creative Commons Attribution 4.0 International (CC BY 4.0) license, which permits unrestricted use, distribution, and reproduction in any medium, provided the original work is properly cited. To view a copy of this license, visit http://creativecommons.org/licenses/by/4.0/. This license does not apply to figures/photos/artwork or other content included in the article that is credited to a third party; obtain authorization from the rights holder before using such material.

Author contributions: G.C., B.A., and B.F.G. designed, performed, and analyzed all imaging studies. G.C. and B.A. designed, performed, and analyzed all behavioral experiments. G.C., B.A., and D.W. performed and analyzed histology. M.J.S. and G.S. supervised all studies. G.C., B.A., M.J.S., and G.S. wrote the manuscript. All authors edited and finalized the manuscript and figures. **Competing interests:** M.J.S. is a consultant and scientific cofounder of Inscopix Inc., which makes the miniature microscope used for Ca^{2+} imaging in this study. **Data and materials availability:** Additional data relating to this paper are available upon request, because of the size (43 TB) of the data. Code used in this analysis is available at (*46*).

SUPPLEMENTARY MATERIALS

www.sciencemag.org/content/363/6424/276/suppl/DC1
Supplementary Text
Materials and Methods
Figs. S1 to S17
Table S1
References (*47*–*94*)

19 November 2017; accepted 13 December 2018
10.1126/science.aap8586

Downloaded from http://science.sciencemag.org/ on January 17, 2019

BIODIVERSITY

Agriculturally dominated landscapes reduce bee phylogenetic diversity and pollination services

Heather Grab[1]*, Michael G. Branstetter[2], Nolan Amon[1,3], Katherine R. Urban-Mead[1], Mia G. Park[4], Jason Gibbs[5], Eleanor J. Blitzer[6], Katja Poveda[1], Greg Loeb[7], Bryan N. Danforth[1]

Land-use change threatens global biodiversity and may reshape the tree of life by favoring some lineages over others. Whether phylogenetic diversity loss compromises ecosystem service delivery remains unknown. We address this knowledge gap using extensive genomic, community, and crop datasets to examine relationships among land use, pollinator phylogenetic structure, and crop production. Pollinator communities in highly agricultural landscapes contain 230 million fewer years of evolutionary history; this loss was strongly associated with reduced crop yield and quality. Our study links landscape–mediated changes in the phylogenetic structure of natural communities to the disruption of ecosystem services. Measuring conservation success by species counts alone may fail to protect ecosystem functions and the full diversity of life from which they are derived.

A preponderance of evidence supports the positive relationship between biodiversity and ecosystem functioning (*1*–*3*), particularly the link between trait diversity and ecosystem function (*4*–*6*). In communities where species have high functional trait overlap, often owing to recent shared evolutionary history, each individual species contributes less to overall community function and potentially less to the many ecosystem services derived from the functioning of healthy ecosystems (*7*, *8*). Alternatively, closely related species may provide redundancy that ensures resilience of function under variable environmental conditions, or they may diverge in their traits through strong competition resulting in high function even among communities consisting of closely related species. Currently, it is unclear whether losses of more closely or distantly related species will have a greater affect on the magnitude of ecosystem functions. Phylogenetic diversity is a measure of the evolutionary history represented within a community. It not only captures similarities in traits that mediate responses to the environment (*9*) but also reflects similarities among taxa in the traits that contribute to ecosystem function (*10*). Understanding the role of nonrandom species loss with respect to phylogeny is essential for effectively prioritizing the conservation of either functionally important or evolutionarily diverse lineages and maintaining ecosystem function and associated ecosystem services.

Land-use change, associated with the transition from natural to agricultural lands, is a primary driver of biodiversity loss worldwide (*11*), threatening even those organisms that deliver essential ecosystem services to agriculture (*12*, *13*). Bees are responsible for pollinating the majority of our most valuable and nutritious crops (*14*, *15*). Diverse bee communities ensure high and stable delivery of pollination services (*16*), but habitat loss and agricultural intensification have been implicated in recent bee declines (*17*). The suite of traits exhibited by different bee species mediates their ability to persist in agricultural landscapes (*18*). These traits may be conserved among closely related taxa. Because lineages vary in their response to land-use change (*18*), loss of taxonomic diversity is not expected to be uniform across the phylogeny (*9*, *19*, *20*). However, the extent and pattern by which landscape simplification prunes the evolutionary history represented within pollinator communities remain poorly studied. Furthermore, we know little about the consequences of lost evolutionary history for ecosystem function, including pollination services.

To examine interactions among land-use change, phylogenetic diversity, and ecosystem function, we quantify changes in bee phylogenetic diversity across a landscape gradient. Specifically, we combine a time-calibrated genomic phylogeny (Fig. 1 and fig. S1) with extensive pollinator community and pollination datasets. The pollinator community data are derived from sampling in 27 apple orchards over 10 years (8700 records of 88 species). Landscape composition in a 750-m radius surrounding each orchard varied from a heterogeneous mix of forest, urban, old-field, and agricultural land to homogeneous landscapes dominated by agriculture (fig. S2). Our analyses focused on two unresolved questions: (i) How does land-use change influence the phylogenetic structure of pollinator communities in agroecosystems? (ii) What are the consequences of phylogenetic diversity loss on pollination services and crop yield?

We found that species loss due to agriculturally driven land-use change is not random across the bee phylogeny. Rather, some branches of the bee tree of life are "pruned" more heavily than others, resulting in communities that contain more closely related species in highly agricultural landscapes compared with those found in landscapes with less agricultural cover [$F_{(1,48)}$ = 10.25, P = 0.002] (Fig. 2A). Although species richness was 55% lower in orchards with the highest proportion of agriculture in the landscape [$F_{(1,48)}$ = 8.19, P = 0.006] (Fig. 2B), the loss of phylogenetic diversity was greater than would be expected as a result of changes in species richness alone [$F_{(1,48)}$ = 8.60, P = 0.005] (fig. S3). We estimate that pollinator communities lose 35 million years of evolutionary history for every 10% increase in agricultural cover within the landscape [$F_{(1,48)}$ = 13.41, P = 0.001] (Fig. 2C), which represents a 49% reduction in total evolutionary history compared with communities in landscapes with low agricultural cover.

Loss of phylogenetic diversity from pollinator communities along the land-use gradient could occur in two different ways. First, clades may be pruned from the full set of species present in landscapes with low agricultural cover. Alternatively, agricultural landscapes may favor particular clades, whereas other, perhaps more diverse, branches of the tree are favored in more complex landscapes, as has recently been shown (*21*). The first scenario would generate a pattern in which communities along the land-use gradient exhibit a nested structure, and the second scenario would lead to a pattern of strong species turnover, as the clades present in highly agricultural landscapes are not those favored in more diverse landscapes and vice versa (fig. S4). Here, we find that bee communities ordered along the agricultural gradient exhibit greater nestedness (t = −105.59, df = 99, P < 0.05) (fig. S5) and lower turnover (t = 96.63, df = 99, P < 0.05) than would be expected by chance, which suggests that land-use changes are pruning lineages from the more complete communities present in landscapes with low agricultural cover.

Although individual taxa varied in their response to increasing agricultural land cover,

[1]Department of Entomology, Cornell University, Ithaca, NY 14853, USA. [2]U.S. Department of Agriculture–Agricultural Research Service (USDA-ARS) Pollinating Insects Research Unit, Utah State University, Logan, UT 84322, USA. [3]Department of Entomology, University of Wisconsin–Madison, Madison, WI 53706, USA. [4]Department of Biological Sciences, North Dakota State University, Fargo, ND 58102, USA. [5]Department of Entomology, University of Manitoba, Winnipeg, MB R3T 2N2, Canada. [6]Department of Biology, Carroll College, Helena, MT 56901, USA. [7]Department of Entomology, Cornell AgriTech, New York State Agricultural Experiment Station, Cornell University, Geneva, NY 14456, USA.
*Corresponding author. Email: heathergrab@cornell.edu

Downloaded from http://science.sciencemag.org/ on January 17, 2019

closely related species responded more similarly than species pairs selected at random (Blomberg's K = 0.23, P = 0.049) (Fig. 1). The clades most resilient to land-use change included *Bombus* and *Lasioglossum* (*Dialictus*), which are among the most commonly collected wild bees in North America. Diversification rate analysis suggests that *L.* (*Dialictus*) has undergone a recent rapid radiation (fig. S6). This result indicates that agriculturally dominated landscapes favor more recent, less evolutionarily distinct species, a finding paralleled in neotropical birds (*22*). Our analyses reveal several clades sensitive to land-use change, including many *Andrena* species. The relative sensitivity of *Andrena* to land-use change compared with *Bombus* and *L.* (*Dialictus*) may be driven by their different life histories. *Andrena* are solitary and have a narrow flight phenology, whereas social species and those with longer flight phenology [e.g., *Bombus* and *L.* (*Dialictus*)] are favored in agricultural rather than more natural landscapes (*21*). Our results, therefore, underscore the utility of methods that account for shared evolutionary history for understanding how communities are altered in response to environmental stressors.

Clade loss may lead to a reduction in the suite of functional traits present in pollinator communities when these traits show phylogenetic signal. In this study, we found that closely

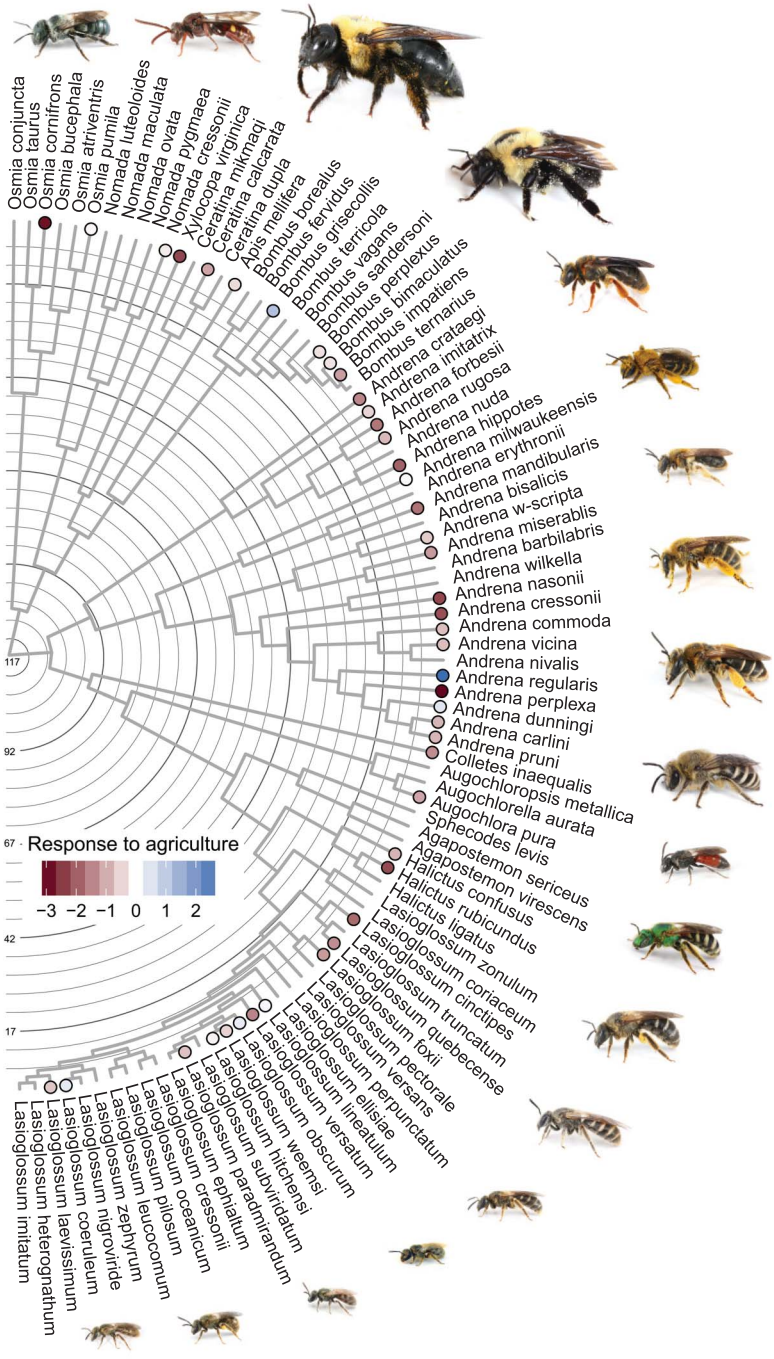


Fig. 1. Time-calibrated phylogeny of the apple bee community. Tip labels indicate species' response (*z*-score) to increasing agricultural land cover at the 750-m scale for the 44 taxa observed more than 10 times across all surveys. Color represents the magnitude of the response (dark red indicates strong negative, dark blue indicates strong positive). The root is at 117 million years (Ma) with 5 Ma increments to present. Posterior probabilities are 1.0 for all nodes. Communities in mixed-use landscapes are likely to contain species from across the entire tree, whereas those in agriculturally dominated landscapes will contain species with white or blue tip markers. [Bee images (copyright of Joseph Wilson) are used with permission.]

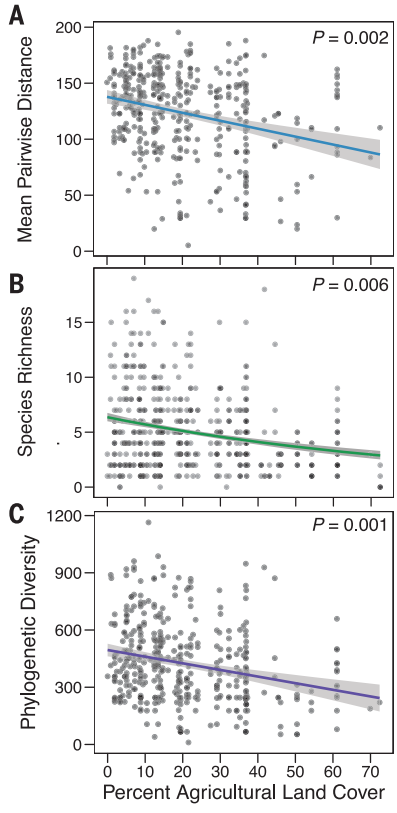


Fig. 2. Relationship between the percent agricultural cover in the surrounding landscape at a 750-m radius and per-transect community diversity metrics. In highly agricultural landscapes, (**A**) the mean pairwise phylogenetic distance separating individuals is lower, (**B**) fewer species are observed per transect, and (**C**) the evolutionary history represented by communities is lower. Points are semitransparent to aid in visualizing overlap. Solid lines indicate a significant relationship between variables at $P < 0.05$, shading represents 95% confidence interval.

Downloaded from http://science.sciencemag.org/ on January 17, 2019

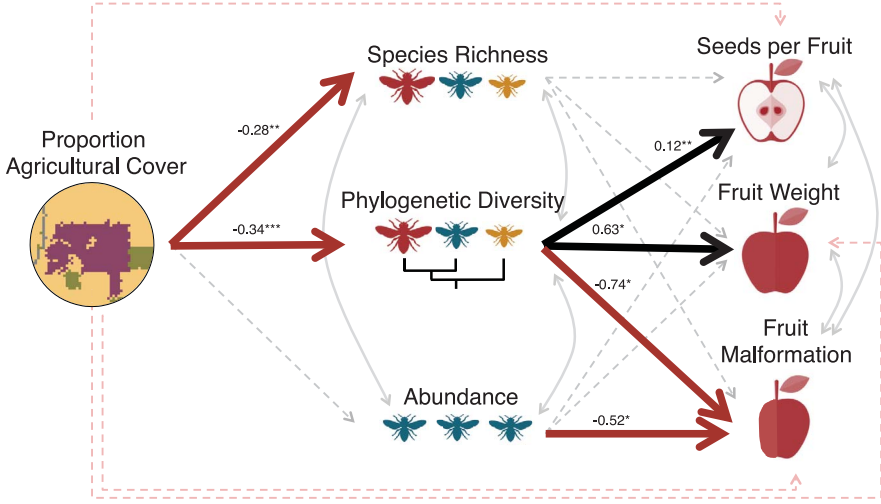


Fig. 3. Land-use change has an indirect impact on pollination services and crop production mediated by a reduction in observed mean pairwise phylogenetic distances separating individuals in a community. Community data include wild and managed bees and the following apple variables: the number of seeds per fruit, fruit weight, and fruit shape in the varieties Golden Delicious and McIntosh. Curved lines indicate correlated errors among variables. For straight lines, solid lines indicate a significant relationship between variables and their color indicates direction (black indicates positive, red indicates negative). Numbers above lines are the standardized coefficients, with asterisks indicating level of significance (*P < 0.05, **P < 0.01, ***P < 0.001).

related bee species share many behavioral and morphological traits including body size, plant fidelity, and visitation rate but not flower-handling behavior (fig. S7), which may influence their effectiveness as crop pollinators. To assess the impact of phylogenetic diversity loss on pollination services, we quantified seed set, fruit weight, and shape (a measure of fruit quality) in two apple varieties, Golden Delicious and McIntosh, at 12 orchards. We employed a structural equation modeling approach to evaluate the importance of phylogenetic diversity, species richness, and abundance, which allowed us to explicitly model the covariation between these predictor variables and to evaluate the direct and indirect effects of landscape structure on pollination services. Land-use change had an indirect impact on pollination services and crop production mediated by a reduction in mean pairwise phylogenetic distances separating individuals in a community (Fig. 3 and fig. S8). In both varieties, fruit weight and seed set were best predicted by the observed pairwise phylogenetic distances separating individuals in a community as compared to either abundance or species richness, whereas fruit shape was best predicted by both phylogenetic diversity and abundance (tables S1 to S3).

Our findings reveal that landscape-mediated loss of evolutionary history from bee communities has consequences for current ecosystem functioning and the delivery of ecosystem services to agriculture (Fig. 3). Specifically, we show that loss of phylogenetic diversity from pollinator communities has a negative effect on pollination services. In light of ongoing land-use change worldwide (*23*), our results have clear implications for the functional and evolutionary potential of bee communities to respond to future challenges. Conservation practices that measure their success only by the number of species conserved may fail to protect the full diversity of life impacted by these stressors (*24*). Greater understanding of how shared evolutionary history shapes responses to environmental stressors is essential for assessing the potential mechanisms driving biodiversity declines in agricultural landscapes and their effects on ecosystem functions and services.

REFERENCES AND NOTES

1. B. J. Cardinale *et al.*, *Nature* **486**, 59–67 (2012).
2. S. A. Wood *et al.*, *Trends Ecol. Evol.* **30**, 531–539 (2015).
3. R. Winfree *et al.*, *Science* **359**, 791–793 (2018).
4. M. W. Cadotte, K. Carscadden, N. Mirotchnick, *J. Appl. Ecol.* **48**, 1079–1087 (2011).
5. V. Gagic *et al.*, *Proc. Biol. Sci.* **282**, 20142620 (2015).
6. J. Fründ, C. F. Dormann, A. Holzschuh, T. Tscharntke, *Ecology* **94**, 2042–2054 (2013).
7. D. Tilman *et al.*, *Science* **277**, 1300–1302 (1997).
8. D. S. Srivastava, M. W. Cadotte, A. A. M. MacDonald, R. G. Marushia, N. Mirotchnick, *Ecol. Lett.* **15**, 637–648 (2012).
9. M. R. Helmus *et al.*, *Ecol. Lett.* **13**, 162–174 (2010).
10. S. Díaz *et al.*, *Ecol. Evol.* **3**, 2958–2975 (2013).
11. T. Newbold *et al.*, *Nature* **520**, 45–50 (2015).
12. C. Kremen, N. M. Williams, R. W. Thorp, *Proc. Natl. Acad. Sci. U.S.A.* **99**, 16812–16816 (2002).
13. T. Tscharntke, A. M. Klein, A. Kruess, I. Steffan-Dewenter, C. Thies, *Ecol. Lett.* **8**, 857–874 (2005).
14. A. M. Ellis, S. S. Myers, T. H. Ricketts, *PLOS ONE* **10**, e114805 (2015).
15. R. Winfree, B. J. Gross, C. Kremen, *Ecol. Econ.* **71**, 80–88 (2011).
16. P. Hoehn, T. Tscharntke, J. M. Tylianakis, I. Steffan-Dewenter, *Proc. Biol. Sci.* **275**, 2283–2291 (2008).
17. D. Goulson, E. Nicholls, C. Botías, E. L. Rotheray, *Science* **347**, 1255957 (2015).
18. S. Gámez-Virués *et al.*, *Nat. Commun.* **6**, 8568 (2015).
19. A. De Palma *et al.*, *Divers. Distrib.* **23**, 1435–1446 (2017).
20. M. P. Arbetman, G. Gleiser, C. L. Morales, P. Williams, M. A. Aizen, *Proc. Biol. Sci.* **284**, 20170204 (2017).
21. T. Harrison, J. Gibbs, R. Winfree, *Global Change Biol.* **24**, 287–296 (2018).
22. L. O. Frishkoff *et al.*, *Science* **345**, 1343–1346 (2014).
23. T. K. Rudel *et al.*, *Proc. Natl. Acad. Sci. U.S.A.* **106**, 20675–20680 (2009).
24. A. Purvis, P.-M. Agapow, J. L. Gittleman, G. M. Mace, *Science* **288**, 328–330 (2000).
25. H. Grab *et al.*, Data from: Agriculturally dominated landscapes reduce bee phylogenetic diversity and pollination services, Dryad Digital Repository (2019); https://doi.org/10.5061/dryad.3df2q0k.

ACKNOWLEDGMENTS

We thank A. Agrawal for comments on the manuscript and J. Wilson for use of photographs in Fig. 1. We also thank E. Murray, S. Bossert, and C. Edwards for advice on analyses. **Funding:** Data collection was funded by USDA-AFRI (project 2010-03689) to B.N.D., USDA-ARS (project 2080-21000-015-00-D) to M.G.B., and an Atkinson Center for a Sustainable Future grant to H.G. USDA is an equal opportunity provider and employer. **Author contributions:** H.G. conceived of the study, led the conceptual development, conducted analyses, and wrote the manuscript draft. M.G.B. conducted the molecular work and phylogenomic analyses. N.A. contributed to molecular work. K.R.U.-M. contributed to data analysis and fieldwork. M.G.P., J.G., B.N.D., and E.J.B. conducted the fieldwork. K.P., G.L., and B.N.D. contributed to study design. All authors contributed to the final manuscript. **Competing interests:** None declared. **Data and materials availability:** The data and R script files used in this study are available in Dryad (*25*). Raw sequence data and contigs representing ultraconserved element loci are available in the NCBI Sequence Read Archive and GenBank, respectively, under BioProject accession PRJNA454902. The bee specimens are housed in the Cornell University Insect Collection.

SUPPLEMENTARY MATERIALS

www.sciencemag.org/content/363/6424/282/suppl/DC1
Materials and Methods
Figs. S1 to S8
Tables S1 to S6
References (*26*–*70*)

30 March 2018; accepted 12 December 2018
10.1126/science.aat6016

Downloaded from http://science.sciencemag.org/ on January 17, 2019

CILIA

Flagellar microtubule doublet assembly in vitro reveals a regulatory role of tubulin C-terminal tails

M. Schmidt-Cernohorska[1]*, I. Zhernov[2,3], E. Steib[1], M. Le Guennec[1], R. Achek[4], S. Borgers[1], D. Demurtas[5], L. Mouawad[4], Z. Lansky[2], V. Hamel[1]†, P. Guichard[1]†

Microtubule doublets (MTDs), consisting of an incomplete B-microtubule at the surface of a complete A-microtubule, provide a structural scaffold mediating intraflagellar transport and ciliary beating. Despite the fundamental role of MTDs, the molecular mechanism governing their formation is unknown. We used a cell-free assay to demonstrate a crucial inhibitory role of the carboxyl-terminal (C-terminal) tail of tubulin in MTD assembly. Removal of the C-terminal tail of an assembled A-microtubule allowed for the nucleation of a B-microtubule on its surface. C-terminal tails of only one A-microtubule protofilament inhibited this side-to-surface tubulin interaction, which would be overcome in vivo with binding protein partners. The dynamics of B-microtubule nucleation and its distinctive isotropic elongation was elucidated by using live imaging. Thus, inherent interaction properties of tubulin provide a structural basis driving flagellar MTD assembly.

The cilium is an organelle crucial for motility, as well as for sensing environmental cues such as signaling molecules, light, and mechanical stimuli (*1*). The core structure of the cilium is characterized by nine microtubule doublets (MTDs) (*2*). In *Chlamydomonas*, MTDs form a double-track railway for intraflagellar transport trains (*3*), which carry ciliary building blocks along microtubules during the assembly and disassembly of the cilium (*4*). These MTDs display distinctive structural features and are formed by a complete A-microtubule composed of 13 protofilaments and an incomplete B-microtubule of 10 protofilaments, which starts from the outer junction (OJ) between protofilaments A10 and A11 of the A-microtubule (Fig. 1A and fig. S1A) (*5*–*8*). Cryo–electron microscopy (cryo-EM) analysis of the *Tetrahymena* ciliary MTD reveals that this OJ involves noncanonical, surface-to-side tubulin-tubulin contacts (*9*). It also reveals an inner sheath composed of microtubule inner proteins (MIPs) inside the MTD.

MTD assembly occurs at the centriolar level, with the B-microtubule nucleating and elongating bidirectionally onto the surface of the A-microtubule, as assessed by cryo–electron tomography (cryo-ET) in human centrosomes (*10*). However, the molecular mechanism enabling B-microtubule nucleation at the surface of the A-microtubule is unclear. C-terminal tails of tubulin may play a role (*11*) because their limited proteolytic digestion by subtilisin induces the nucleation of hooked microtubules and protofilament bundles (fig. S1, B and C).

We hypothesized that B-microtubule assembly could be mediated solely through tubulin-tubulin interactions. We first set out to address whether tubulin devoid of the C termini alone could assemble MTDs. We developed an in vitro assay to mimic the sequential assembly of MTDs by A-microtubule formation followed by B-microtubule nucleation. First, stable microtubules (*12*) were assembled (Fig. 1B) and subsequently incubated with subtilisin-treated tubulin without C-terminal tails (Tub_S) (*11*, *13*) (materials and methods in the supplementary materials). This did not result in MTD formation (Fig. 1C). We next assessed whether the removal of C-terminal tails of the A-microtubule would promote MTD formation. Microtubules treated with subtilisin (MT_S) (*13*, *14*) (fig. S1D) looked identical to untreated microtubules (Fig. 1, B and D). When we added free tubulin to subtilisin-treated microtubules, 72% of these microtubules formed assemblies that resembled MTDs (Fig. 1, E and F), reaching a median length of 0.66 ± 0.5 μm after 15 min (fig. S1E). By contrast, only ~7.5% of MTD-like structures were observed among microtubules treated with subtilisin alone. This possibly reflects some depolymerization of the tubulin lacking C-terminal tails; this tubulin would reattach at the surface of the A-microtubule and nucleate efficiently because of having a lower critical concentration than untreated tubulin (*15*) (Fig. 1F). Thus, C-terminal tails of the A-microtubule negatively regulate a noncanonical, surface-to-side tubulin interaction, allowing microtubule branching.

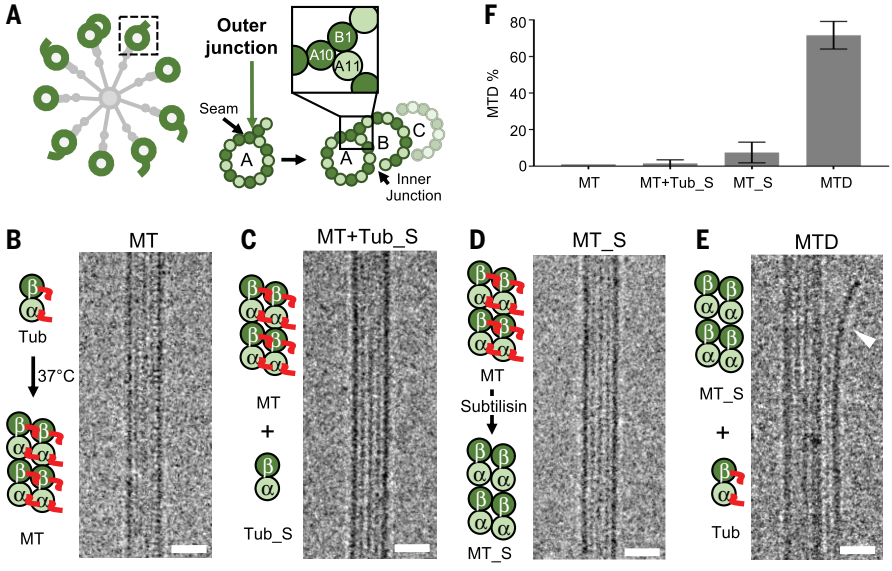


Fig. 1. MTD assembly in vitro. (**A**) Schematic of a procentriole with A- and B-microtubules (green) and the procentriole cartwheel structure (gray). B-microtubule branching occurs at the OJ, highlighting the protofilaments A10, A11, and B1. The dashed box corresponds to the closer view to the right. Black arrows, seam of the A-microtubule and inner junction. (**B** to **E**) Representative cryo-EM images of microtubules (MT) (B), microtubules supplemented with tubulin pretreated with subtilisin (MT+Tub_S) (C), subtilisin-treated microtubules (MT_S) (D), and MT_S incubated with tubulin (MTD) (E) with their corresponding schematics. Arrowhead, MTD. Tub, tubulin. Scale bars, 25 nm. (**F**) Percentage of MTD formation (three independent experiments): 0% for MT (n = 825 microtubules), 3 ± 2% for MT+Tub_S (n = 729), 8 ± 6% for MT_S (n = 1515), and 72 ± 8% for MTDs (n = 2341). Errors bars represent SD.

[1]Department of Cell Biology, Sciences III, University of Geneva, Geneva, Switzerland. [2]Institute of Biotechnology of the Czech Academy of Sciences, BIOCEV, Vestec, Czech Republic. [3]Faculty of Mathematics and Physics, Charles University in Prague, Prague, Czech Republic. [4]Institut Curie, PSL Research University, CNRS UMR 9187 – INSERM U1196, Paris-Saclay University, F-91405 Orsay, France. [5]Interdisciplinary Centre for Electron Microscopy, Swiss Federal Institute of Technology (EPFL), Lausanne, Switzerland.
*Present address: Laboratory of Adaptive Immunity, Institute of Molecular Genetics, Academy of Sciences of the Czech Republic, Prague, Czech Republic.
†Corresponding author. Email: virginie.hamel@unige.ch (V.H.); paul.guichard@unige.ch (P.G.)

Downloaded from http://science.sciencemag.org/ on January 17, 2019

By using cryo-EM, we next investigated whether branching occurs at the tip or on the main body of the A-microtubule and found that B-microtubules assembled mainly on the body of the A-microtubule (fig. S2A), corroborating previous in vivo findings (*10*). Cryo-ET of these reconstituted MTDs showed structural similarity to the ciliary MTDs (Fig. 2, A and B; movie S1; and fig. S2B), with 23% of multiple MTDs surrounding a single A-microtubule (Fig. 2C and fig. S2C). This indicates that B-microtubule nucleation in vitro was not restricted to one protofilament of the A-microtubule and that, in vivo, additional proteins may be needed to provide positional information. By using subtomogram averaging to improve the resolution of the OJ to 17.2 Å (fig. S2D), we confirmed the typical triangular junction formed among protofilaments A10 and A11 of the A-microtubule and protofilament B1 of the B-microtubule in the reconstituted MTDs (Fig. 2, D to G, and fig. S2E) (*9*). Additionally, inspecting the curvature of the B-microtubule junction from individual MTDs in cryo-ET (fig. S3A) revealed a curvature similar to that observed in in vivo MTDs (Fig. 2F). This suggested that the surface-to-side tubulin-tubulin interaction at the OJ is sufficient to drive the correct angle for MTD assembly. We noticed an important mobility of the B-microtubule at the MTD inner junction, possibly because of the lack of MIPs or because of a protein such as FAP20, which closes the MTDs in cilia (Figs. 1A and 2, I to J) (*16*).

By using an in silico approach, we explored how the C-terminal tails of the A-microtubule hinder MTD assembly. In our simulations, the A-microtubule was composed of 13 protofilaments of three αβ-tubulin dimers each, where all atoms were taken into account. Because tubulin tails are unstructured, they may adopt random conformations. To obtain a representative sample of these conformations, we used molecular dynamics simulations (see materials and methods). The first protofilament from the B-microtubule, B1, was added to the A-microtubule between A10 and A11 according to the method of (*9*) (fig. S3, B to D). To capitalize on all the A-microtubule sampled tails, every two successive protofilaments of the A-microtubule (A1-A2, A2-A3, A3-A4, ... A12-A13) were superimposed on A10-A11 of the same microtubule in order to obtain a variety of tail positions at the OJ (Fig. 2K and fig. S3C). Then, for each of these couples of protofilaments, the tails were relaxed and their interaction energy with the entire protofilament B1 was calculated. For the A10 tails, this energy was distributed around 0 kcal/mol, indicating that these tails did not play a role in the insertion of B1 (Fig. 2M). By contrast, for A11 tails, the interaction energy was highly repulsive in 11% of the cases, with an energy value of several thousands of kilocalories per mole, which is sufficient to strongly hinder the insertion of B1 (Fig. 2N). Visual inspection of the constructed junctions confirmed that A11 tails did interpenetrate the core of B1, whereas A10 tails did not (Fig. 2L). This provides an explanation for the results of the in vitro experiments but not for the formation of MTDs in vivo despite the presence of these tails. Observation of the in vivo MTD structure isolated from flagella (*9*) showed the presence of an unidentified MIP (MIP7) at the junction between A11 and B1, at the same location as the tails of A11 in our model. This MIP7 has been proposed to stabilize the interaction between B1 and A10-A11 (*9*). We hypothesized that MIP7 action is not in stabilizing the interaction but rather in binding A11 protofilament tubulin tails to enable the B1 insertion.

Next, we monitored the assembly dynamics of MTDs. We immobilized subtilisin-treated Alexa 488–labeled A-microtubules on a glass slide. Rhodamine-labeled free tubulin was added to the reaction mixture to trigger B-microtubule

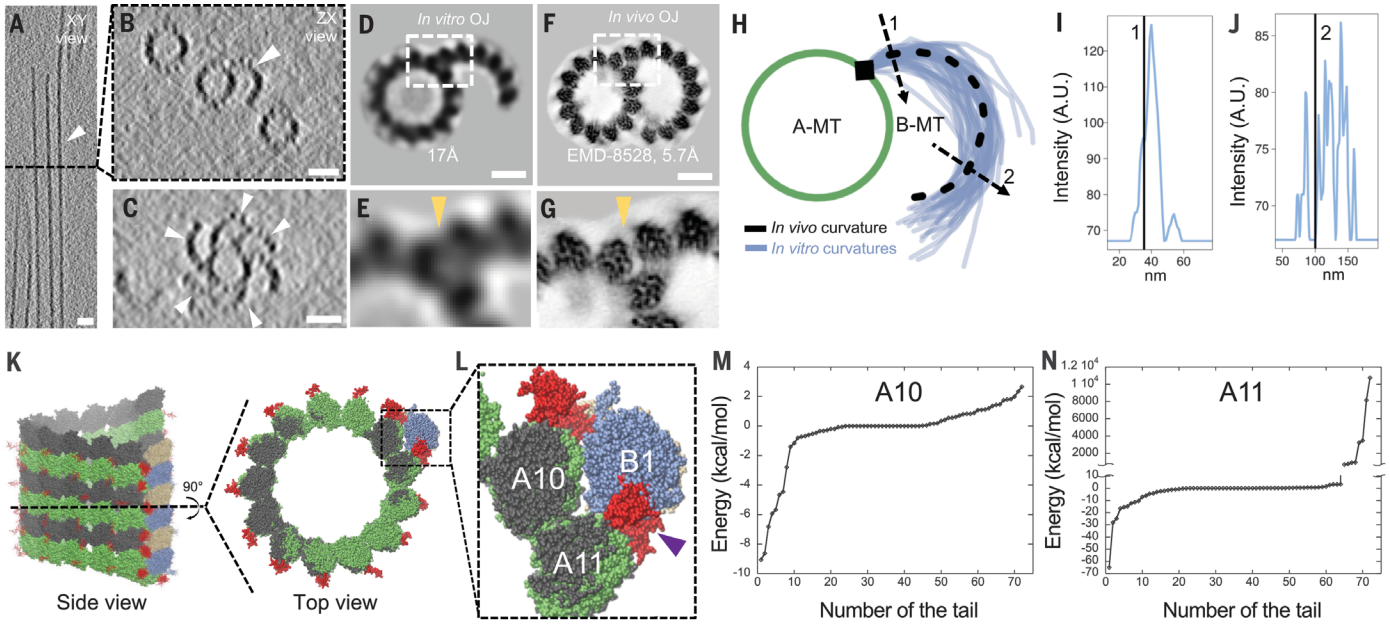


Fig. 2. Cryo-EM reconstruction of in vitro MTDs. (**A**) Representative image of a cryo-ET section. Scale bar, 25 nm. (**B**) *zx* view of a cryo-ET section. Scale bar, 25 nm. (**C**) *zx* view of a cryo-ET section showing an MTD flower. Scale bar, 25 nm. Arrowheads in (A) to (C) indicate B-microtubules. (**D** and **F**) Subtomogram averaging of in vitro MTDs at 17-Å resolution (D) and of *Tetrahymena* ciliary MTDs at 5.7 Å (EMD-8528 map from the Electron Microscopy Data Bank) (F). Scale bars, 25 nm. (**E** and **G**) Closer view of the OJ for the in vitro MTD (E) and the OJ of the ciliary MTD (G). Arrowheads indicate the triangular shape of the A10, A11, and B1 protofilaments. (**H**) Traces of the B-microtubules starting at the OJ and highlighting the curvatures of the B-microtubules in vitro compared with those of the in vivo ciliary MTDs (n = 44 microtubules). (**I** and **J**) Plot profiles at the positions indicated by the arrows in (H) showing that the curvature of the OJ is stable (I) whereas the end of the B-microtubule is more flexible (J). The black line indicates the position of the B-microtubule in vivo. A.U., arbitrary units. (**K**) Side and top views of an MTD model with the A-microtubule in green and gray (α-tubulin, gray; β-tubulin, green), the tubulin C-terminal tails of the A-microtubule in red, and the protofilament B1 in blue and beige (α-tubulin, blue; β-tubulin, beige). Atoms are represented as spheres. (**L**) Closer view of the OJ highlighting the interactions of the tubulin C-terminal tails of the protofilaments A10 and A11 with B1. The arrowhead indicates the conflict between the C-terminal tails of A11 and B1. (**M** and **N**) Plots of the interaction energy between tubulin C-terminal tails of A10 and the protofilament B1 (M) or A11 and the protofilament B1 (N).

Downloaded from http://science.sciencemag.org/ on January 17, 2019

assembly (Fig. 3A), and we monitored the reaction by using total internal reflection fluorescence (TIRF) microscopy. With either guanosine triphosphate or guanosine-5′-[(α,β)-methyleno] triphosphate (GMPCPP) in solution, we observed the usual elongation of template A-microtubules at both tips. However, we observed nucleation and elongation of patches of fluorescent rhodamine signal on the A-microtubule only in the presence of GMPCPP (movies S2 and S3), the same condition used in our cryo-EM experiments. We thus interpreted these patches as B-microtubules (Fig. 3B and fig. S4A). This result suggests that MTD formation requires a certain level of stabilization, mediated in our experiments by GMPCPP and in vivo possibly by the presence of MIPs. Investigating the growth rates of A- and B-microtubule tips showed that, unlike the plus and minus tips of the A-microtubules, which are known to grow at different rates (*17*), B-microtubules grow at the same rate in both directions (Fig. 3, C and D, and fig. S4, A to D). The isotropic B-microtubule growth rate was faster than the growth rate of the plus tip of the A-microtubule (Fig. 3D), and this rate correlated with increasing tubulin concentration (Fig. 3D and fig. S4D). Thus, B-microtubules are dynamic structures nucleating on the lattice of the A-microtubule and elongating in both directions without apparent anisotropy. To estimate the protofilament number in B-microtubules, we compared the rhodamine fluorescent signal in the center of the B-microtubules with the steady-state rhodamine fluorescent signal at the tips of the template A-microtubules, which are formed by 14 protofilaments because of the presence of GMPCPP (*18*). This quantification suggested that after 40 min, B-microtubules were assembled, with on average (±SD) 5.7 ± 2.6 and 13.8 ± 3.8 protofilaments at the free tubulin concentrations of 1 and 2 μM, respectively (fig. S4E and movies S2 and S4). Finally, we repeated the experiment with A-microtubules treated with decreasing subtilisin:tubulin ratios (1:1, 1:50; 1:100, and 1:1000), leading to predominant β-tubulin C-terminal tail removal (fig. S5) (*13*). We found that MTD nucleation decreased markedly (fig. S5 and movie S5), suggesting that the removal of C-terminal tails from both α- and β-tubulin is necessary for the MTD nucleation.

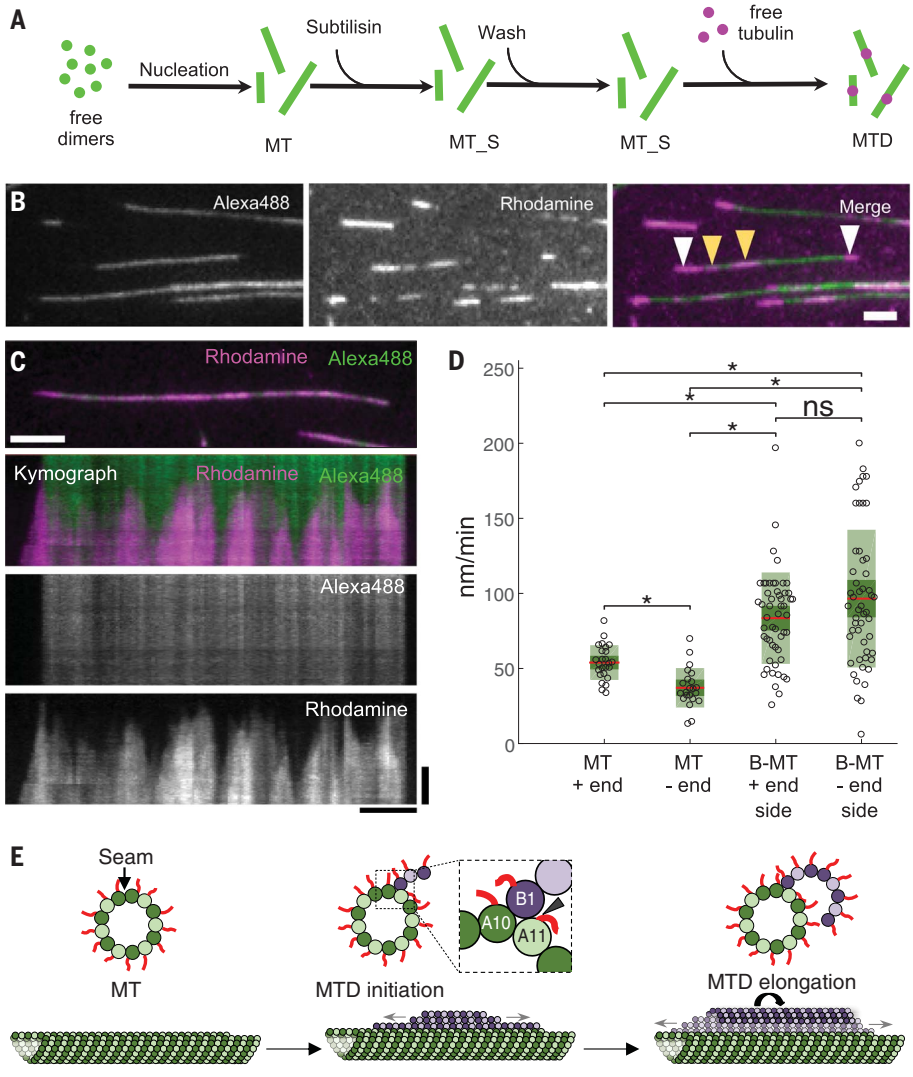


Fig. 3. Dynamics of MTD assembly. (**A**) Protocol to visualize MTD assembly by using TIRF microscopy. (**B**) Montage showing MTDs. Subtilisin-treated A-microtubules are in green; A-microtubule tips and B-microtubules formed by rhodamine-labeled tubulin are depicted in magenta. White arrowheads indicate the tip elongation of the A-microtubule. Yellow arrowheads point to the B-microtubule assembling on the surface of the A-microtubule. Scale bar, 1 μm. (**C**) Montage showing MTDs and the corresponding multichannel kymograph. Scale bars: horizontal, 5 μm; vertical, 15 min. (**D**) Polymerization rate of B-microtubules at 2 μM free tubulin. ns, not significant, *P < 0.0001, determined by the Mann-Whitney test. Plus and minus tips of A-microtubules polymerize at 53.93 ± 11.56 nm/min (n = 25 tips) and 37.13 ± 13.13 nm/min (n = 22 tips), respectively. The polymerization rates of B-microtubules toward plus and minus tips of the A-microtubules are 83.51 ± 30.44 nm/min (n = 53 tips) and 96.52 ± 45.87 nm/min (n = 52 tips) [values are averages (represented by red lines) ± SD]. (**E**) Model of MTD formation. In vitro, MTD assembly initiates on the surface of an A-microtubule (green) deprived of tubulin C-termini (red tails) by the addition of a protofilament owing to a noncanonical surface-to-side tubulin interaction. Protofilaments in the B-microtubule (purple) continue to assemble to ultimately lead to a near-complete MTD.

In vivo, MTDs are composed of heterodimers of α- and β-tubulin and dozens different MIPs. Our work establishes that the C-terminal tail of tubulin exhibits an inhibitory effect that, in vivo, may prevent uncontrolled MTD formation. Molecular simulations suggested that the C-terminal tails of one specific protofilament hinder the attachment of protofilament B1 at the internal side of the OJ. We propose that in vivo, specific MIPs bind and displace the C-terminal tails of A11 and allow for the formation of a B-microtubule that elongates bidirectionally (Fig. 3E). Moreover, such proteins may be needed to precisely position the MTD branching to a specific protofilament on the A-microtubule, as well as to stabilize the entire MTD. The requirement for such protein is alleviated in our in vitro minimal system by providing GMPCPP.

In summary, our work highlights the crucial role of tubulin C-terminal tails in regulating MTDs, which are key to the assembly and function of centrioles, cilia, and flagella.

REFERENCES AND NOTES

1. J. J. Malicki, C. A. Johnson, *Trends Cell Biol.* **27**, 126–140 (2017).
2. S. C. Goetz, K. V. Anderson, *Nat. Rev. Genet.* **11**, 331–344 (2010).
3. L. Stepanek, G. Pigino, *Science* **352**, 721–724 (2016).
4. J. L. Rosenbaum, G. B. Witman, *Nat. Rev. Mol. Cell Biol.* **3**, 813–825 (2002).
5. D. Nicastro *et al.*, *Science* **313**, 944–948 (2006).
6. R. V. Dippell, *Proc. Natl. Acad. Sci. U.S.A.* **61**, 461–468 (1968).
7. I. V. Nechipurenko, C. Berciu, P. Sengupta, D. Nicastro, *eLife* **6**, e25686 (2017).

Downloaded from http://science.sciencemag.org/ on January 17, 2019

8. P. Guichard *et al*., *Nat. Commun.* **8**, 14813 (2017).
9. M. Ichikawa *et al*., *Nat. Commun.* **8**, 15035 (2017).
10. P. Guichard, D. Chrétien, S. Marco, A.-M. Tassin, *EMBO J.* **29**, 1565–1572 (2010).
11. L. Serrano, J. de la Torre, R. B. Maccioni, J. Avila, *Proc. Natl. Acad. Sci. U.S.A.* **81**, 5989–5993 (1984).
12. A. A. Hyman, S. Salser, D. N. Drechsel, N. Unwin, T. J. Mitchison, *Mol. Biol. Cell* **3**, 1155–1167 (1992).
13. Y. Saoudi, I. Paintrand, L. Multigner, D. Job, *J. Cell Sci.* **108**, 357–367 (1995).
14. V. Redeker, R. Melki, D. Promé, J. P. Le Caer, J. Rossier, *FEBS Lett.* **313**, 185–192 (1992).
15. D. L. Sackett, B. Bhattacharyya, J. Wolff, *J. Biol. Chem.* **260**, 43–45 (1985).
16. H. A. Yanagisawa *et al*., *Mol. Biol. Cell* **25**, 1472–1483 (2014).
17. G. J. Brouhard, L. M. Rice, *Nat. Rev. Mol. Cell Biol.* **19**, 451–463 (2018).
18. A. A. Hyman, D. Chrétien, I. Arnal, R. H. Wade, *J. Cell Biol.* **128**, 117–125 (1995).

ACKNOWLEDGMENTS

We thank N. Klena for critical reading of the manuscript and M. Braun for helpful discussions. We thank N. Olieric for initially providing the subtilisin enzyme. We thank the BioImaging Center of the University of Geneva. **Funding:** This work was supported by ERC StG 715289 (ACCENT), granted to P.G., and V.H., P.G., and M.L.G. are supported by Swiss National Science Foundation (SNSF) PP00P3_157517. E.S. and S.B. are supported by the University of Geneva. Z.L. is supported by the Czech Science Foundation (18-08304S), the project BIOCEV (CZ.1.05/1.1.00/02.0109) from the ERDF, and CAS (RVO: 86652036). I.Z. is supported by GAUK (1372218). We acknowledge the Centre of Imaging Methods core facility, Faculty of Science, Charles University, supported by the MEYS CR (LM2015062 Czech-BioImaging).
Author contributions: M.S.-C. prepared the samples, analyzed the cryo-EM data, and set up the immunofluorescence, Coomassie, and Western blot experiments. M.L.G. performed subtomogram averaging. I.Z. and Z.L. performed and analyzed the TIRF experiments. R.A. and L.M. performed the molecular modeling analysis. D.D. provided access and assistance with the cryo-EM F20 microscope. E.S. prepared samples for the cryo-EM session and performed immunofluorescence experiments. S.B. prepared the SDS–polyacrylamide gel electrophoresis gels and Western blots. P.G. performed the cryo-EM. P.G., Z.L., L.M., and V.H. designed, analyzed, and supervised the work, and P.G., V.H., L.M., M.S.-C., and Z.L. wrote the manuscript. **Competing interests:** The authors declare no competing interests. **Data and materials availability:** All data are available in the main text or the supplementary materials.

SUPPLEMENTARY MATERIALS

www.sciencemag.org/content/363/6424/285/suppl/DC1
Materials and Methods
Figs. S1 to S5
References (*19*–*32*)
Movies S1 to S5

30 August 2018; accepted 19 December 2018
10.1126/science.aav2567

Downloaded from http://science.sciencemag.org/ on January 17, 2019

IMMUNOTHERAPY

Strain-specific antibody therapy prevents cytomegalovirus reactivation after transplantation

Jose Paulo Martins[1,2]*, Christopher E. Andoniou[3,4,5]*, Peter Fleming[3,4]*, Rachel D. Kuns[1], Iona S. Schuster[3,4,5], Valentina Voigt[3,4], Sheridan Daly[3,4], Antiopi Varelias[1], Siok-Keen Tey[1], Mariapia A. Degli-Esposti[3,4,5]†‡, Geoffrey R. Hill[1,6,7]†‡

Cytomegalovirus infection is a frequent and life-threatening complication that significantly limits positive transplantation outcomes. We developed preclinical mouse models of cytomegalovirus reactivation after transplantation and found that humoral immunity is essential for preventing viral recrudescence. Preexisting antiviral antibodies decreased after transplant in the presence of graft-versus-host disease and were not replaced, owing to poor reconstitution of donor B cells and elimination of recipient plasma cells. Viral reactivation was prevented by the transfer of immune serum, without a need to identify and target specific antigenic determinants. Notably, serotherapy afforded complete protection, provided that the serum was matched to the infecting viral strain. Thus, we define the mechanisms for cytomegalovirus reactivation after transplantation and identify a readily translatable strategy of exceptional potency, which avoids the constraints of cellular therapies.

Cytomegalovirus (CMV) infection and reactivation are associated with significantly reduced survival after bone marrow or hematopoietic stem cell transplantation (BMT) (*1*–*3*). The development of an effective CMV vaccine has proved problematic, and antiviral therapies are limited by toxicity and the emergence of drug-resistant CMV strains (*1*, *4*). Efforts to improve the outcome of CMV infection have focused primarily on developing improved antiviral drugs (*5*, *6*) or using adoptive T cell immunotherapy to mitigate the impact of infection and reduce disease (*5*, *7*).

The risk factors that contribute to CMV reactivation in BMT have been examined in clinical trials but are associative in nature. A major limitation to improving CMV infection outcomes in transplant recipients is the paucity of preclinical animal models that faithfully represent the clinical situation in which CMV reactivation occurs post-latency. To address this unmet need, we developed mouse models of CMV reactivation after BMT. As in the clinical setting, we defined CMV reactivation functionally. Functional reactivation occurs after a period of latency and results in plasma viremia, as well as viral replication in target organs.

We used mice that were latently infected with murine CMV (MCMV) (Fig. 1A) as recipients in a major histocompatibility complex–disparate BMT model to investigate the role of conditioning and BMT on viral reactivation. Latently infected mice transplanted with T cell–replete grafts [graft-versus-host disease (GVHD) group] showed reduced survival compared with those that received bone marrow (BM) alone (non-GVHD group) (Fig. 1B). Mice that developed GVHD (Fig. 1C) demonstrated MCMV reactivation post-transplant (Fig. 1D). At 4 weeks post-transplant, reactivation occurred in 10 of 16 mice (63%) versus 2 of 12 mice (17%) in the GVHD and non-GVHD groups, respectively (Fig. 1E). Viral loads were detected in target organs and were significantly higher in recipients with GVHD (Fig. 1F). The lack of reactivation in the non-GVHD group suggested that conditioning and relative immunosuppression, modeled in this study by the absence of donor T cells, were insufficient to permit MCMV reactivation.

In clinical settings, the increasing use of rigorously T cell–depleted grafts in haploidentical stem cell transplantation has led to the reemergence of CMV as a major problem (*8*). This type of transplant requires intensive chemoradiotherapy combined with the administration of T and B cell–depleting antibodies, which results in the sustained loss of these lymphocyte populations (*9*). To model this clinical scenario, we used a haploidentical transplant system. In this system, conditioning and the GVHD response result in the loss of host B, T, and natural killer (NK) cells, as well as the poor reconstitution of donor B, T, and NK cells owing to profound type 1 inflammation (*10*, *11*). Post-transplant, in the presence of GVHD, latently infected recipients (Fig. 1G) displayed significant viremia (Fig. 1H) and high viral loads in target organs (Fig. 1I). GVHD severity and survival during this period were not affected by latent infection (fig. S1). Using recipients latently infected with a recombinant MCMV carrying a LacZ reporter, reactivation was first detected at 3 weeks post-transplant (Fig. 1J). By week 4, replicating virus was present in multiple tissues (Fig. 1, K and L), including the lung and gut, which are common sites of clinical disease in patients.

During GVHD, immune reconstitution from the donor graft is compromised. Alloreactive T cells impair thymopoiesis, and peripheral expansion of T cells is also affected, as alloreactive T cells are more prone to apoptosis (*12*, *13*). The B cell compartment is generally very slow to reconstitute because lymphopoiesis is also impaired (*14*). Consequently, the pathobiology of GVHD, combined with the immunosuppression required to treat GVHD, results in delayed immune reconstitution and long-term immunodeficiency (*10*).

CMV reactivation is thought to be largely controlled by antiviral $CD8^+$ T cell responses, with NK cells further contributing to protection (*15*–*19*). Virus-specific $CD8^+$ T cells were examined in a BALB/c→B6 transplant using tetramers that recognize recipient H-$2K^b$ m38– and donor H-$2L^d$ IE1–restricted responses. Early after BMT, recipient $m38^+$ $CD8^+$ T cells were detected only in non-GVHD conditions (Fig. 2A), whereas donor-derived $IE1^+$ $CD8^+$ T cells were not detected in either GVHD or non-GVHD groups (Fig. 2B). In the B6→B6D2F1 haploidentical transplant model, significantly lower numbers of both H-$2K^b$ m38 (recipient and donor) and H-$2L^d$ IE1 (recipient) $CD8^+$ T cells were present in mice with GVHD (Fig. 2C). Thus, in the absence of donor T cell–mediated alloreactivity, recipient MCMV-specific T cells persist, potentially providing adequate protection against reactivation. We investigated this potential protection by imposing sustained immunodepletion to remove residual host and donor T and NK cells. $TCR\delta^{-/-}$ grafts were used to examine protection conferred by γδ T cells. In transplanted mice without GVHD, despite the complete absence of T and NK cells (fig. S2), MCMV was not detected (Fig. 2D). Thus, in the absence of GVHD, T and NK cells (either recipient or donor-derived) and donor-derived γδ T cells are not essential for protection against MCMV reactivation. The lack of reactivation in mice without GVHD and depleted of all T cell subsets also indicates that conditioning and immunosuppressive therapy (the latter modeled here by profound immunodepletion) were insufficient to permit MCMV reactivation.

Our data suggest that humoral immunity may be sufficient to protect from viral reactivation in the absence of GVHD. Latently infected B6.μMt (μMt) mice, which lack mature B cells, were transplanted with T cell–depleted BM (TCD-BM) and depleted of $CD4^+$, $CD8^+$, and $NK1.1^+$ cells. MCMV reactivation was detected in all μMt recipients, with high-level viremia in plasma (Fig. 2E) at day 14 post-transplant and substantial

[1]QIMR Berghofer Medical Research Institute, Brisbane, Queensland, Australia. [2]School of Medicine, University of Queensland, Brisbane, Queensland, Australia. [3]Immunology and Virology Program, Centre for Ophthalmology and Visual Science, University of Western Australia, Perth, Western Australia, Australia. [4]Centre for Experimental Immunology, Lions Eye Institute, Perth, Western Australia, Australia. [5]Infection and Immunity Program and Department of Microbiology, Biomedicine Discovery Institute, Monash University, Clayton, Victoria, Australia. [6]Clinical Research Division, Fred Hutchinson Cancer Research Center, Seattle, WA, USA. [7]Division of Medical Oncology, University of Washington, Seattle, WA, USA.
*These authors contributed equally to this work.
†These authors contributed equally to this work.
‡Corresponding author. Email: mariapia@lei.org.au (M.A.D.-E.); grhill@fredhutch.org (G.R.H.)

Downloaded from http://science.sciencemag.org/ on January 17, 2019

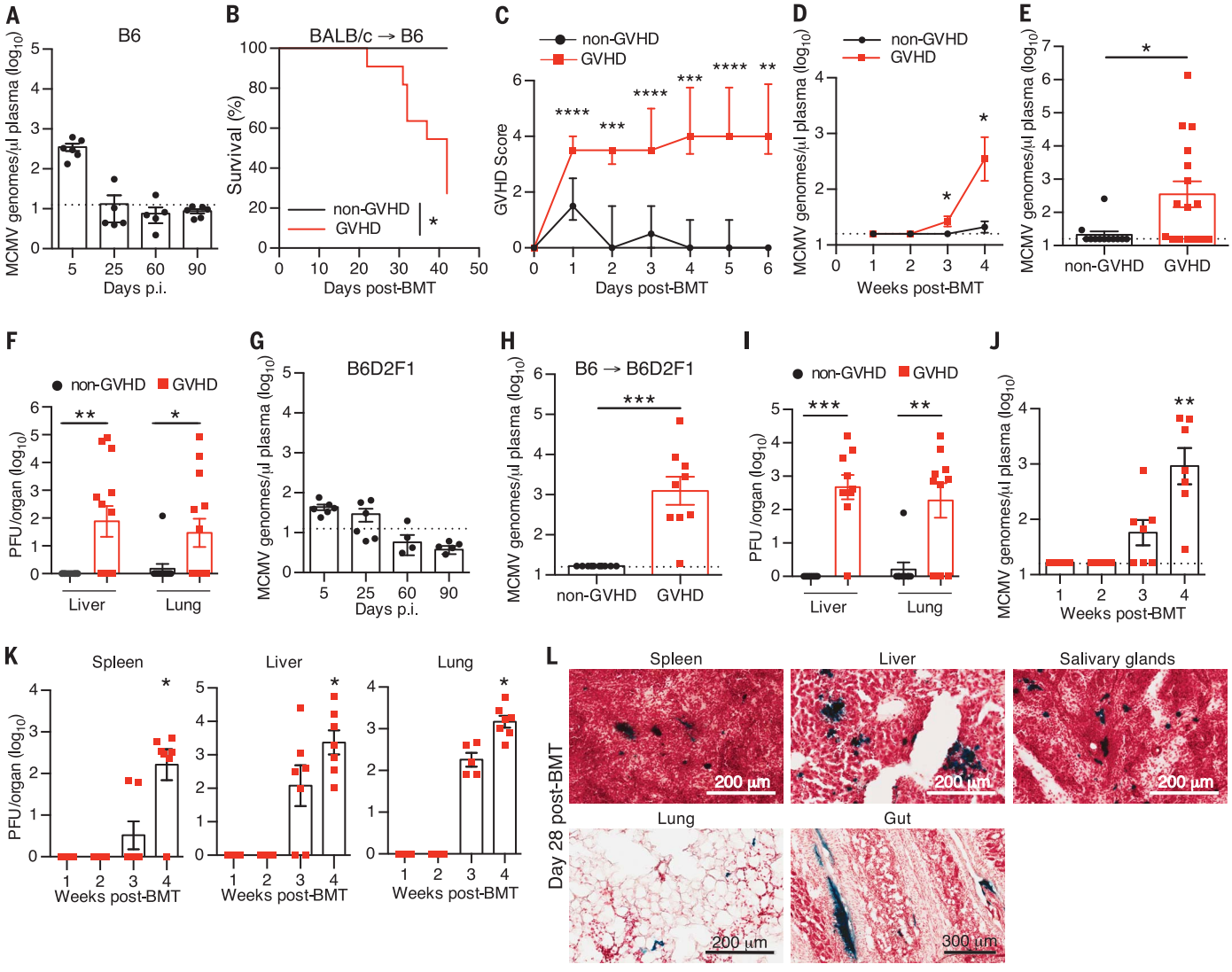


Fig. 1. MCMV reactivation after BMT. (**A**) B6 (H-2^{b}) mice were infected with MCMV-K181^{Perth}; viremia (virus in plasma) measured by quantitative polymerase chain reaction at the indicated time points post-infection (p.i.) is shown (n = 6). (**B** to **F**) Latently infected (>90 days p.i.) B6 mice were lethally irradiated and transplanted with TCD-BM (non-GVHD) or BM + T cells (GVHD) from naïve BALB/c (H-2^{d}) mice. (B) Survival outcome (Kaplan-Meier analysis compared by log-rank analysis) and (C) GVHD clinical scores (median and interquartile range) are shown. Data are combined from two experiments with 3 to 6 mice per group per experiment (non-GVHD, n = 7; GVHD, n = 11). (D) Viremia over time; (E) viremia for individual mice at 4 weeks post-transplant (non-GVHD, n = 12; GVHD, n = 17); and (F) viral titers in target organs at weeks 4 to 5 post-transplant (non-GVHD, n = 12; GVHD, n = 13) are shown. PFU, plaque-forming units. Data in (D) to (F) are combined from three experiments with 3 to 6 mice per group per experiment. (**G**) Viremia in B6D2F1 mice at the indicated time points p.i. is shown (n = 6). (**H** to **L**) Latently infected B6D2F1 (H-2$^{b/d}$) mice were lethally irradiated and transplanted with TCD-BM (non-GVHD) or BM + T cells (GVHD) from naïve B6 (H-2^{b}) mice. (H) Viremia (non-GVHD, n = 10; GVHD, n = 9) and (I) viral titers in the indicated organs (non-GVHD, n = 9; GVHD, n = 10) at week 4 post-transplant are shown. Data are combined from two experiments with 4 to 6 mice per group per experiment. Kinetics of viral reactivation in B6D2F1 mice, assessed by measuring (J) viremia and (K) viral loads in target organs after transplant, are shown (n = 7 per time point). Data are combined from two experiments with 3 or 4 mice per group per experiment. (L) Tissue sections from transplanted B6D2F1 mice with GVHD. MCMV-infected cells in various organs are identified by X-gal staining. Data in (D) to (K) represent mean ± SEM. *P < 0.05, **P < 0.01, ***P < 0.001, ****P < 0.0001 (Mann-Whitney U test). A dotted line represents the limit of detection.

viral loads in target organs (Fig. 2F) at day 16 post-transplant. µMt mice lacked MCMV-neutralizing antibodies pre-transplant (Fig. 2G). After transplant, they had low levels of MCMV-specific immunoglobulin M (IgM) and lacked MCMV-specific immunoglobulin G (IgG) antibodies (Fig. 2H). In addition to antibodies, T and NK cells may limit CMV reactivation. Indeed, MCMV reactivation occurred only in immunodepleted µMt recipients (Fig. 2, I and J), and donor-derived humoral responses did not participate in protection (Fig. 2, K and L). Thus, humoral immunity is sufficient to limit viral reactivation after transplantation, with MCMV reactivation requiring the combined lack of antibodies, T cells, and NK cells.

Next, we defined the contribution of humoral immunity to CMV reactivation during GVHD. Serum from latently infected mice neutralized MCMV in vitro and contained high levels of MCMV-specific IgG pre-transplant (Fig. 3A). In transplanted mice with GVHD, MCMV-specific IgG levels were significantly reduced by day 28 post-transplant (Fig. 3B and fig. S3). MCMV-specific

Downloaded from http://science.sciencemag.org/ on January 17, 2019

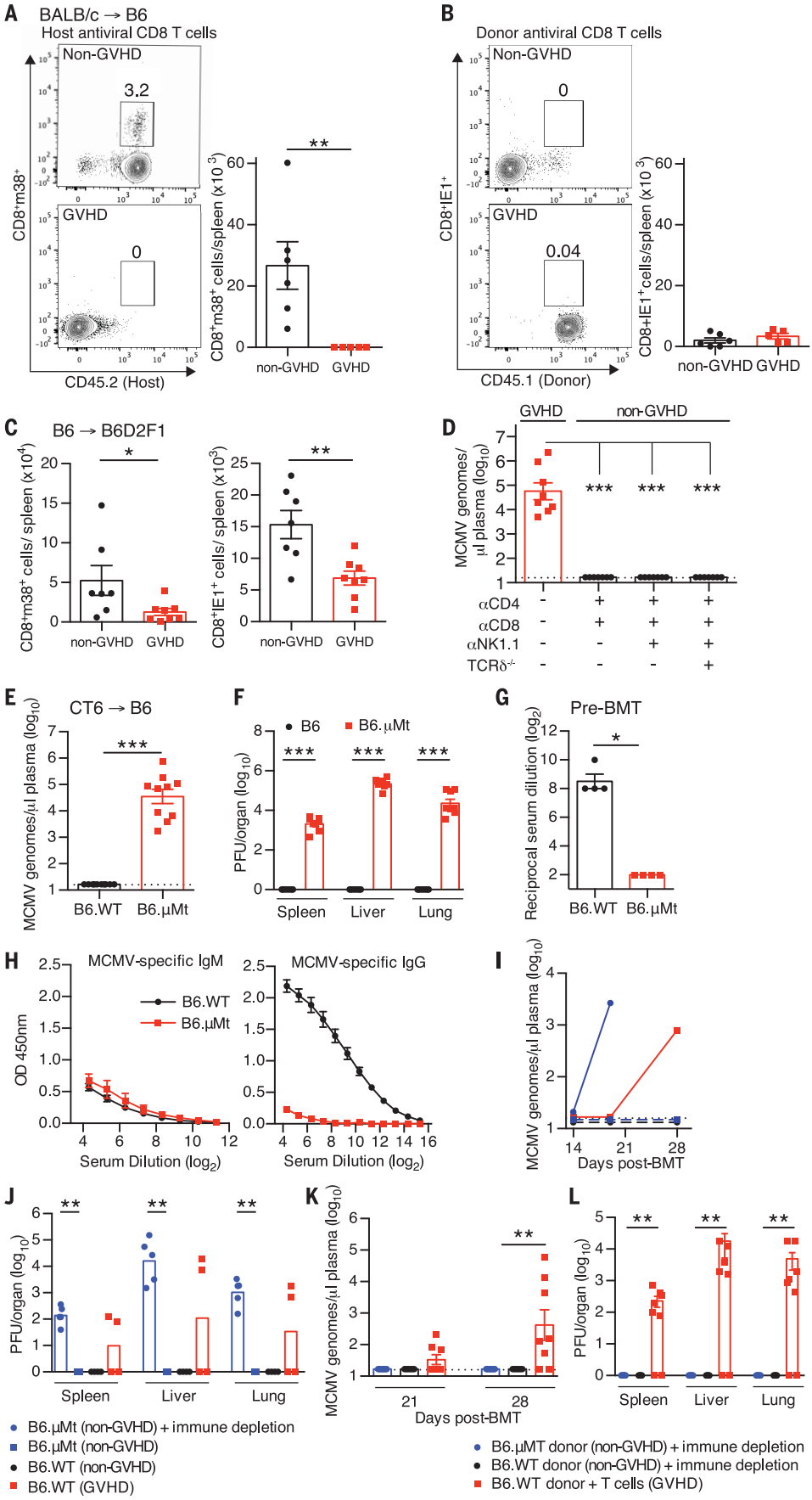


Fig. 2. Humoral immunity is required to prevent MCMV reactivation. Latently infected B6.CD45.2 mice were transplanted with BALB/c.CD45.1 TCD-BM (non-GVHD) or BM + T cells (GVHD). On day 14 post-transplant, the frequency and number of antiviral $CD8^+$ T cells were assessed by flow cytometry. Representative flow plots and total number of (**A**) recipient-derived, virus-specific $m38^+$ $CD8^+$ T cells or (**B**) donor-derived virus-specific $IE1^+$ $CD8^+$ T cells (non-GVHD, $n = 6$; GVHD, $n = 5$) are shown. The data are representative of two experiments. (**C**) Latently infected B6D2F1 mice were transplanted with TCD-BM (non-GVHD) or BM + T cells (GVHD) from B6 mice. Virus-specific $m38^+$ and $IE1^+$ $CD8^+$ T cells enumerated at day 14 post-transplant (non-GVHD, $n = 7$; GVHD, $n = 7$) are shown. Data are combined from two experiments with 3 or 4 mice per group per experiment. (**D**) Latently infected B6D2F1 mice were transplanted with TCD-BM from B6.WT or B6.TCR$\delta^{-/-}$ mice. The indicated depleting antibodies were administered after transplant. Viremia at 4 weeks (GVHD) or 6 weeks (non-GVHD) post-transplant (non-GVHD, $n = 7$; GVHD, $n = 8$) is shown. Data are pooled from two experiments with 3 or 4 mice per group per experiment. (**E** to **H**) Latently infected B6.WT or B6.µMt mice were transplanted with TCD-BM from CT6 mice (BALB/c $NK1.1^+$). CD4-, CD8-, and NK1.1-depleting antibodies were administered to all groups post-transplant. (E) Viremia at day 14 post-transplant (B6.WT, $n = 10$; B6.µMt, $n = 9$) and (F) viral titers in target organs at day 16 post-transplant (B6.WT, $n = 10$; B6.µMt, $n = 8$) are shown. Data are pooled from two experiments with 3 to 5 mice per group per experiment. (G) MCMV-specific antibody titer pre-transplant was measured using a complement-dependent neutralization assay. (H) MCMV-specific IgM and IgG antibodies were measured by enzyme-linked immunosorbent assay at day 16 post-transplant (B6.WT, $n = 5$; B6.µMt, $n = 3$). OD, optical density. (**I** and **J**) Latently infected B6.WT or B6.µMt mice were transplanted with CT6 TCD-BM or BM + T cells and treated with CD4-, CD8-, and NK1.1-depleting antibodies post-transplant, as indicated. (I) Viremia at the indicated time points p.i. and (J) viral titers in target organs ($n = 4$ or 5 per time point). Data are representative of two individual experiments. (**K** and **L**) Latently infected B6D2F1 mice were transplanted with TCD-BM from B6.WT or B6.µMt mice and depleted of T cells and NK cells post-transplant. One group received B6.WT BM + T cells to induce GVHD. (K) Viremia at days 21 and 28 post-transplant and (L) viral loads in target organs at day 28 post-transplant are shown ($n = 7$ or 8 per time point). Data are combined from two experiments with 3 or 4 mice per group per experiment. The mean is plotted for (I) and (J). All other data represent mean ± SEM. $^*P < 0.05$, $^{**}P < 0.01$, $^{***}P < 0.001$ (Mann-Whitney U test). A dotted line represents the limit of detection.

Downloaded from http://science.sciencemag.org/ on January 17, 2019

IgM antibodies were scant or absent in both GVHD and non-GVHD mice (Fig. 3B). The neutralizing capacity of antibodies present in the serum at day 28 post-transplant was not significantly different between GVHD and non-GVHD groups (Fig. 3C). In contrast, serum isolated from mice with GVHD at day 28 post-transplant showed a complete inability to inhibit cell-to-cell spread of MCMV in vitro (table S1 and fig. S4). Thus, inhibition of cell-to-cell spread in vitro is the best indicator of protective capacity in vivo, suggesting that this is a major mechanism by which antibodies inhibit viral reactivation and spread after transplantation.

Mechanistically, antibody-mediated protection can also operate via antibody-dependent cell-mediated cytotoxicity (ADCC), which requires an interaction with Fc-receptor–expressing cells. No reactivation was observed in latently infected mice that received FcγRIII-deficient grafts and immunodepletion (Fig. 3D). Thus, the protection mediated by MCMV antibodies occurs independently of donor FcγRIII-mediated ADCC.

GVHD results in long-term cellular immunodeficiency and impaired pathogen-specific immunity (*20*). The B cell compartment is slow to reconstitute and B cell numbers can take several years to return to normal, leaving recipients with impaired humoral immunity (*14*, *21*). Mature splenic B cells (Fig. 3E) and plasma cells in BM (Fig. 3F) were significantly reduced in latently infected recipients with GVHD, as compared with non-GVHD mice. Plasma cells are long-lived and reported to be radiation-resistant (*22*). However, plasma cell numbers were greatly reduced

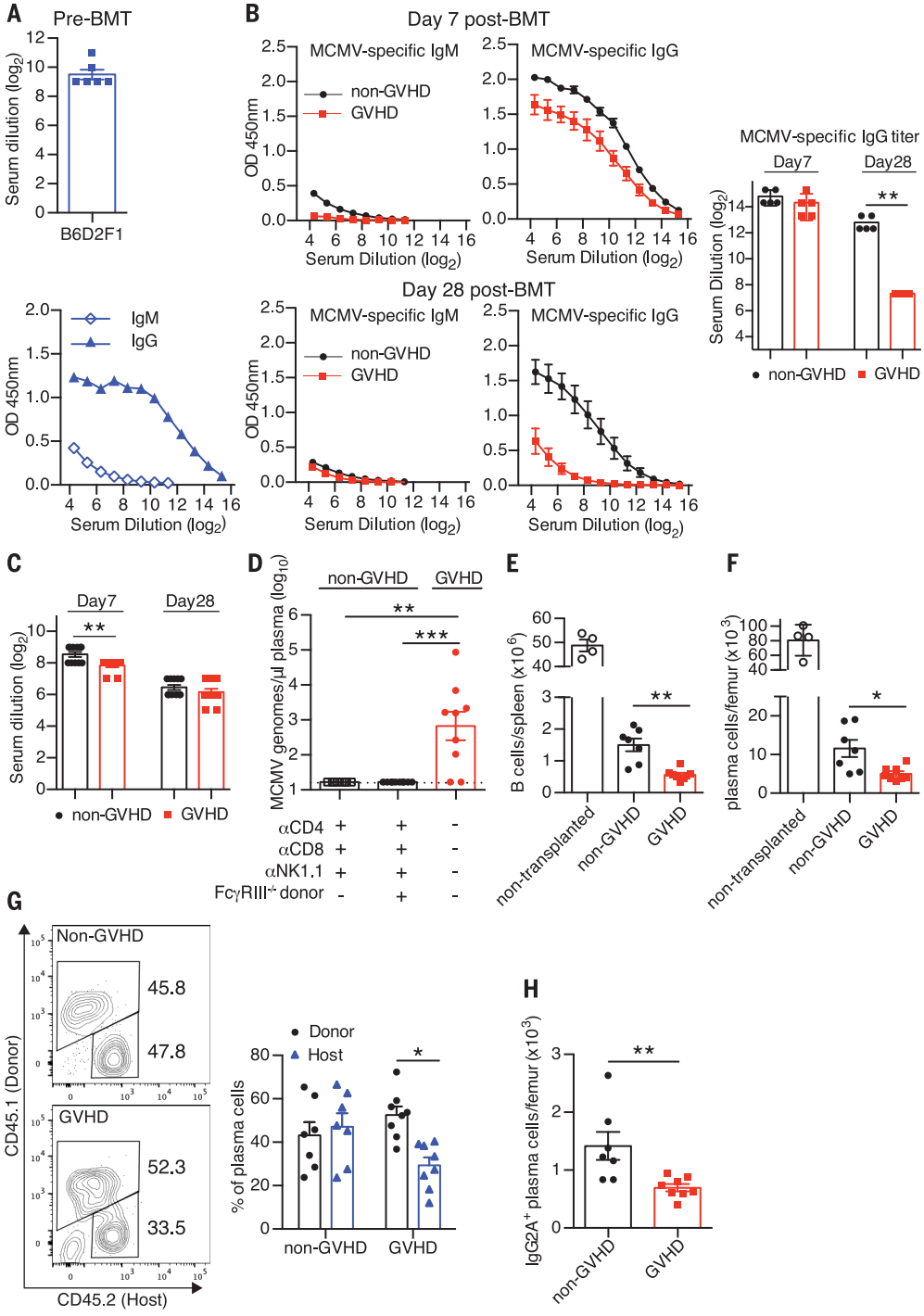


Fig. 3. MCMV reactivation in GVHD correlates with reduced levels of MCMV-specific antibodies. (**A**) MCMV-specific neutralizing antibodies (top) and MCMV-specific IgM and IgG quantification (bottom) in latently infected B6D2F1 mice pre-transplant (n = 6 per group) are shown. (**B** to **H**) Latently infected B6D2F1 mice were transplanted with B6 TCD-BM (non-GVHD) or BM + T cells (GVHD). (B) MCMV-specific IgM and IgG quantification at days 7 and 28 post-transplant (n = 6 per group) is shown. MCMV-specific IgG titers, calculated as described in the supplementary materials and methods, together with statistical analysis, are shown in the far right graph. Data are representative of two experiments where n = 4 mice per group. (C) Levels of neutralizing antibodies at days 7 and 28 post-transplant (non-GVHD, n = 11; GVHD, n = 12) are shown. Data are combined from two experiments with 5 or 6 mice per group per experiment. (D) Latently infected B6D2F1 hosts were transplanted with B6.WT or B6.FcγRIII$^{-/-}$, TCD-BM (non-GVHD), or BM + T cells (GVHD), and treated with the anti-CD4, -CD8, and -NK1.1 depleting antibodies, as indicated. Viremia at 4 weeks post-transplant is shown. n > 8 per group from two experiments with 4 or 5 mice per group per experiment. The number of (E) mature B cells in the spleen and (F) plasma cells in BM of latently infected B6D2F1 mice 14 days post-transplant (non-GVHD, n = 7; GVHD, n = 8) is shown. Data are combined from two experiments with 3 or 4 mice per group per experiment. Nontransplanted controls are shown for comparison. (G) The relative contributions of host and donor cells to the plasma cell pool are shown. (H) The number of IgG2A$^+$ plasma cells in BM is shown (non-GVHD, n = 7; GVHD, n = 8). Data are combined from two experiments with 3 or 4 mice per group per experiment. Data represent mean ± SEM. *P < 0.05, **P < 0.01, ***P < 0.001 (Mann-Whitney U test).

Downloaded from http://science.sciencemag.org/ on January 17, 2019

post-transplant in both non-GVHD and GVHD recipients (Fig. 3F). The relative contribution of donor and host to the plasma cell pool in BM demonstrated that there was a significant enhancement of recipient plasma cell loss under GVHD conditions (Fig. 3G). Host IgG2A$^+$ plasma cell numbers were also reduced by GVHD (Fig. 3H). Thus, although recipient plasma cells can persist post-transplant, they are actively eliminated by the GVHD reaction.

Next, we examined whether passively acquired antibodies could limit MCMV reactivation in recipients with GVHD. The adoptive transfer of immune serum did not affect the development of GVHD (Fig. 4A), but it did protect mice from

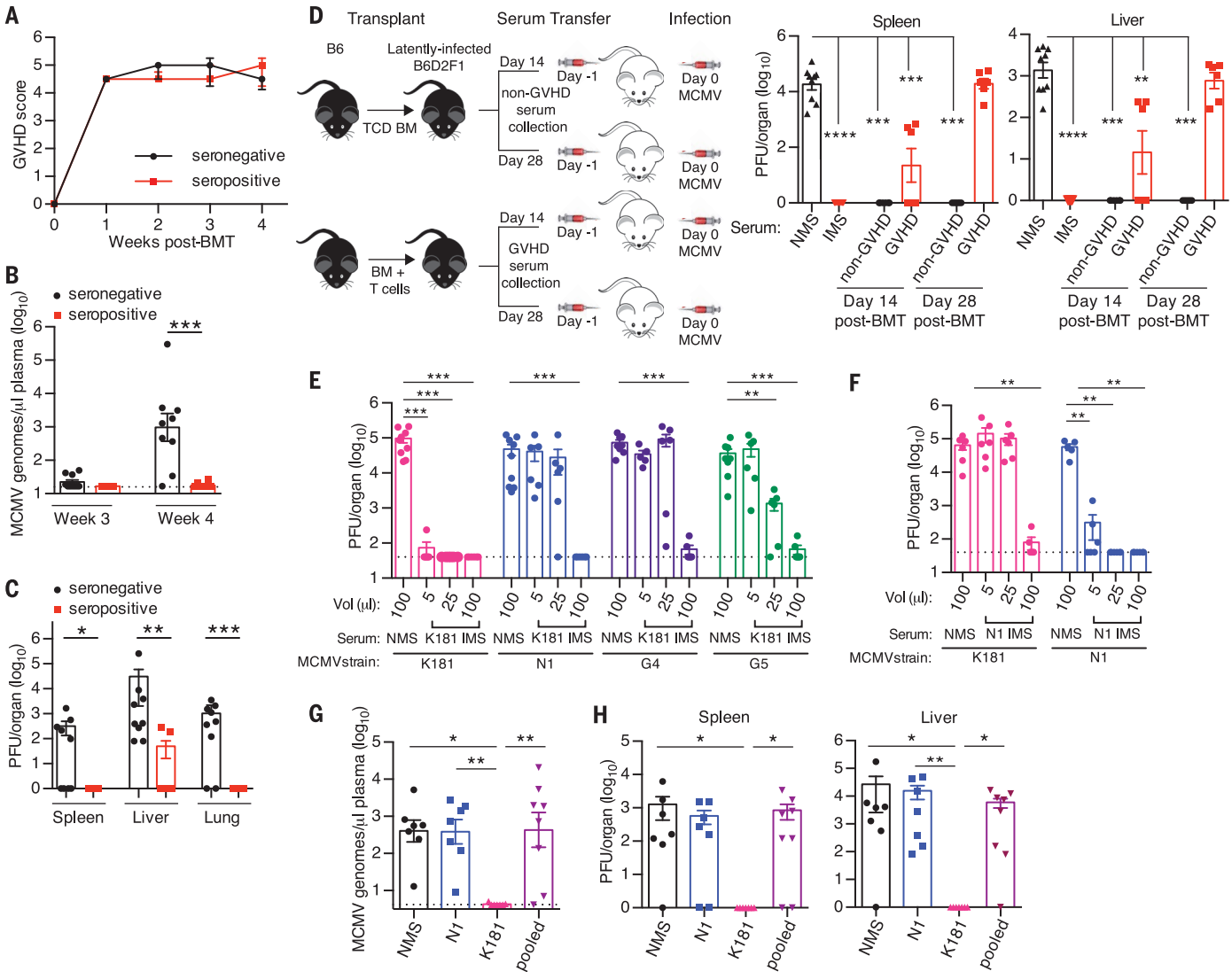


Fig. 4. Strain-specific serotherapy prevents MCMV reactivation. Latently infected B6D2F1 mice were transplanted with B6 BM + T cells. Serum from latently infected (seropositive) or uninfected (seronegative) BALB/c mice was injected twice weekly post-transplant. (**A**) GVHD scores of mice that received serum from seronegative (black) and seropositive (red) donors (median and interquartile range) are shown. (**B**) Viremia at 3 and 4 weeks post-transplant and (**C**) viral titers in organs at 4 weeks post-transplant (seronegative, n = 9; seropositive, n = 10) are shown. Data are pooled from two experiments with 4 to 6 mice per group per experiment. (**D**) Serum collected from non-GVHD or GVHD mice at day 14 or 28 post-BMT (as per schema), naïve mouse serum (NMS), or serum from latently infected mice (IMS) was injected into BALB/c 3-week-old weaners. Mice were infected with MCMV 24 hours later. Viral titers quantified 4 days p.i. are shown. Data are combined from two experiments with 3 mice per group per experiment, except for NMS and IMS, where n = 9 from three experiments. (**E**) NMS or immune serum collected from BALB/c mice latently infected with K181 (K181 IMS) was injected into BALB/c weaners before infection with K181, N1, G4, or G5 viral isolates. The transferred serum volumes are indicated. Viral titers in the spleen 4 days p.i. are shown. Data are combined from two experiments with 3 to 6 mice per group per experiment. (**F**) NMS or serum collected from BALB/c mice latently infected with the N1 strain (N1 IMS) was transferred to BALB/c weaners before infection with the K181 or N1 viral strains. Viral titers in the spleen 4 days p.i. are shown. Data are combined from two experiments with 2 or 3 mice per group per experiment. (**G** and **H**) B6D2F1 mice latently infected with K181 were transplanted with B6 BM + T cells to induce GVHD. NMS or serum from mice latently infected with K181, N1, or sera pooled from mice individually infected with one of eight different MCMV isolates (including K181) was injected twice weekly from day 14 post-transplant. (G) Viremia and (H) viral titers in the indicated organs at 4 weeks post-transplant are shown. Data are combined from two experiments with 3 or 4 mice per group per experiment. Data represent mean ± SEM. *P < 0.05, **P < 0.01, ***P < 0.001 [Mann-Whitney U test used for all analyses, except for those represented in (G) and (H), where the Kruskal-Wallis H test was used].

Downloaded from http://science.sciencemag.org/ on January 17, 2019

reactivation (Fig. 4, B and C). Because MCMV antibody levels were compromised by GVHD, we investigated whether antibody present under such conditions was able to limit MCMV infection. Serum collected at days 14 and 28 post-transplant from latently infected mice, with or without GVHD, was transferred to highly susceptible 3-week-old mice (*18*) before primary MCMV infection (Fig. 4D). Serum from transplanted mice without GVHD limited viral replication to the same extent as treatment with immune serum (Fig. 4D and fig. S5). In contrast, serum collected from mice with GVHD showed incomplete protection, which diminished over the course of GVHD, such that serum collected at day 28 post-transplant showed no protection (Fig. 4D and fig. S5). Thus, the loss of preexisting antibodies and elimination of recipient plasma cells lead to MCMV reactivation in recipients with GVHD.

Previous attempts to ameliorate CMV disease in transplant recipients with immunoglobulins, purified from either normal donors (intravenous immunoglobulin) or donors with high CMV antibody titers (CMV-IG), have provided ambiguous results (*1*, *23*, *24*). We tested the potential requirement for virus-strain–specific antibodies in 3-week-old mice by examining whether immune serum from mice infected with MCMV-K181 afforded protection against infection with unrelated MCMV strains. As little as 5 μl of K181 immune serum provided complete protection against infection with the same viral isolate (Fig. 4E and fig. S6). In comparison, protection against infection with three unrelated MCMV isolates (N1, G4, and G5) required immune serum to be administered in significantly larger quantities (5- to 20-fold) (Fig. 4E and fig. S6). Similar findings were obtained when immune serum from mice latently infected with the N1 isolate was tested in a reverse experimental setting (Fig. 4F and fig. S7). Finally, the capacity of antibodies to protect against reactivation of an antigenically mismatched MCMV strain was tested. Treatment of transplant recipients with K181 serum prevented reactivation of K181 (Fig. 4, G and H, and fig. S8). In contrast, neither the serum that was specific for the N1 isolate nor pooled sera generated by combining serum from mice individually infected with eight different MCMV isolates (including K181) were able to prevent K181 reactivation (Fig. 4, G and H, and fig. S8). Thus, CMV serotherapy is effective and confers high-level protection, even during GVHD, provided that the antibodies are specific for the infecting CMV isolate. Conversely, the dilution of strain-specific antibodies in polyclonal preparations renders them ineffective. This may explain the poor efficacy of polyclonal CMV immunoglobulin therapy observed in clinical studies.

The importance of strain-specific antibodies is consistent with the fact that superinfection with multiple genetic variants of HCMV is common (*25*). Furthermore, preexisting immunity to one HCMV strain does not inevitably confer protection against other strains (*26*, *27*). Although significant variability in the capacity of human sera to neutralize heterologous HCMV isolates in vitro has been noted (*28*), strain-specific neutralization has not been extensively examined. Our study provides the basis for validation in clinical settings of HCMV infection.

The identification of potently neutralizing antibodies against a viral pentameric complex has sparked renewed interest in antibody therapy for HCMV (*29*–*31*). Thus, patient-derived serotherapy after transplant or the use of broadly neutralizing monoclonal antibodies emerge as potential strategies likely to meet the urgent need for inexpensive, nontoxic therapies to prevent and treat CMV reactivation and improve transplantation outcomes.

REFERENCES AND NOTES

1. P. Ljungman, M. Hakki, M. Boeckh, *Hematol. Oncol. Clin. North Am.* **25**, 151–169 (2011).
2. P. Teira *et al.*, *Blood* **127**, 2427–2438 (2016).
3. M. L. Green *et al.*, *Lancet Haematol.* **3**, e119–e127 (2016).
4. F. El Chaer, D. P. Shah, R. F. Chemaly, *Blood* **128**, 2624–2636 (2016).
5. M. Boeckh, W. J. Murphy, K. S. Peggs, *Biol. Blood Marrow Transplant.* **21**, 24–29 (2015).
6. F. M. Marty *et al.*, *N. Engl. J. Med.* **377**, 2433–2444 (2017).
7. C. Roddie, K. S. Peggs, *J. Clin. Invest.* **127**, 2513–2522 (2017).
8. M. Boeckh *et al.*, *Biol. Blood Marrow Transplant.* **9**, 543–558 (2003).
9. F. Locatelli *et al.*, *Blood* **130**, 677–685 (2017).
10. K. A. Markey, K. P. MacDonald, G. R. Hill, *Blood* **124**, 354–362 (2014).
11. M. D. Bunting *et al.*, *Blood* **129**, 630–642 (2017).
12. S. Brochu, B. Rioux-Massé, J. Roy, D. C. Roy, C. Perreault, *Blood* **94**, 390–400 (1999).
13. K. Weinberg *et al.*, *Blood* **97**, 1458–1466 (2001).
14. J. Storek, D. Wells, M. A. Dawson, B. Storer, D. G. Maloney, *Blood* **98**, 489–491 (2001).
15. C. A. Biron, K. S. Byron, J. L. Sullivan, *N. Engl. J. Med.* **320**, 1731–1735 (1989).
16. E. A. Walter *et al.*, *N. Engl. J. Med.* **333**, 1038–1044 (1995).
17. M. J. Reddehase, *Nat. Rev. Immunol.* **2**, 831–844 (2002).
18. N. Sumaria *et al.*, *Immunol. Cell Biol.* **87**, 559–566 (2009).
19. M. Boeckh, A. P. Geballe, *J. Clin. Invest.* **121**, 1673–1680 (2011).
20. R. Zeiser, B. R. Blazar, *N. Engl. J. Med.* **377**, 2167–2179 (2017).
21. E. Corre *et al.*, *Haematologica* **95**, 1025–1029 (2010).
22. G. Cassese *et al.*, *J. Immunol.* **171**, 1684–1690 (2003).
23. P. Raanani *et al.*, *J. Clin. Oncol.* **27**, 770–781 (2009).
24. A. J. Ullmann *et al.*, *Ann. Hematol.* **95**, 1435–1455 (2016).
25. C. Smith *et al.*, *J. Virol.* **90**, 7497–7507 (2016).
26. S. W. Chou, *N. Engl. J. Med.* **314**, 1418–1423 (1986).
27. S. B. Boppana, L. B. Rivera, K. B. Fowler, M. Mach, W. J. Britt, *N. Engl. J. Med.* **344**, 1366–1371 (2001).
28. M. Klein, K. Schoppel, N. Amvrossiadis, M. Mach, *J. Virol.* **73**, 878–886 (1999).
29. A. Macagno *et al.*, *J. Virol.* **84**, 1005–1013 (2010).
30. A. Lanzavecchia, A. Frühwirth, L. Perez, D. Corti, *Curr. Opin. Immunol.* **41**, 62–67 (2016).
31. S. Ha *et al.*, *J. Virol.* **91**, e02033-16 (2017).

ACKNOWLEDGMENTS

We thank J. Mauclair, L. Attwood, and S. Ross for support with animal maintenance and S. Pervan for histology assistance. **Funding:** This work was supported by fellowships (1119298 and 1107797) and grants (1071822, 1125357, and 1065939) from the National Health and Medical Research Council of Australia (NHMRC) and by the Stan Perron Charitable Foundation. G.R.H. is a NHMRC Senior Principal Research Fellow, M.A.D.-E. is a NHMRC Principal Research Fellow, and C.E.A. holds the John Forrester Senior Research Fellowship. **Author contributions:** J.P.M., C.E.A., and P.F. designed experiments; J.P.M., C.E.A., P.F., R.D.K., S.D., I.S.S., V.V., and A.V. performed experiments; J.P.M., C.E.A., P.F., I.S.S., and S.-K.T. analyzed data; and M.A.D.-E. and G.R.H. conceived the project, designed the studies, interpreted data, and wrote the manuscript. Results were discussed and the manuscript was critically commented on and edited by all authors. **Competing interests:** The authors have submitted a provisional patent application for strain-specific antibody therapy to prevent CMV reactivation. **Data and materials availability:** All data are available in the main text or the supplementary materials. Viruses are available from M.A.D.-E. under a material agreement with the Lions Eye Institute.

SUPPLEMENTARY MATERIALS

www.sciencemag.org/content/363/6424/288/suppl/DC1
Materials and Methods
Supplementary Text
Figs. S1 to S8
Table S1
References (*32*–*41*)

15 January 2018; resubmitted 19 August 2018
Accepted 15 November 2018
10.1126/science.aat0066

Downloaded from http://science.sciencemag.org/ on January 17, 2019

CELL DIFFERENTIATION

H3K9me3-heterochromatin loss at protein-coding genes enables developmental lineage specification

Dario Nicetto[1,2,3], Greg Donahue[1,2,3], Tanya Jain[1,2,3], Tao Peng[4,5], Simone Sidoli[2,6], Lihong Sheng[2,3], Thomas Montavon[7], Justin S. Becker[1,2,3], Jessica M. Grindheim[1,2,3], Kimberly Blahnik[1,2,3], Benjamin A. Garcia[2,6], Kai Tan[3,4,5,8], Roberto Bonasio[2,3], Thomas Jenuwein[7], Kenneth S. Zaret[1,2,3]*

Gene silencing by chromatin compaction is integral to establishing and maintaining cell fates. Trimethylated histone 3 lysine 9 (H3K9me3)–marked heterochromatin is reduced in embryonic stem cells compared to differentiated cells. However, the establishment and dynamics of closed regions of chromatin at protein-coding genes, in embryologic development, remain elusive. We developed an antibody-independent method to isolate and map compacted heterochromatin from low–cell number samples. We discovered high levels of compacted heterochromatin, H3K9me3-decorated, at protein-coding genes in early, uncommitted cells at the germ-layer stage, undergoing profound rearrangements and reduction upon differentiation, concomitant with cell type–specific gene expression. Perturbation of the three H3K9me3-related methyltransferases revealed a pivotal role for H3K9me3 heterochromatin during lineage commitment at the onset of organogenesis and for lineage fidelity maintenance.

The phylotypic period of embryologic development occurs at the onset of organogenesis, when morphological development is most conserved between different species (*1*–*3*). The "hourglass" model suggests that cell fate decisions are restricted during the phylotypic period by evolutionarily conserved transcription factor and signaling activities (*1*–*3*). Limited assay sensitivity and small numbers of cells have made it difficult to investigate chromatin dynamics during the phylotypic period, when cell differentiation initiates extensively in embryos. Current thinking from the embryonic stem (ES) cell model (*4*) suggests that compacted heterochromatic domains expand as cells mature, helping to establish cell identity (*5*–*11*). However, these studies did not examine the dynamic events occurring during natural lineage commitment at organogenesis.

Regions of trimethylated histone 3 lysine 9 (H3K9me3)–marked heterochromatin can have a physically condensed structure (*12*–*14*) that serves to repress repeat-rich regions of the genome (*7*, *15*–*17*), including centromeric and telomeric regions (*18*, *19*), and silence protein-coding genes at facultative heterochromatin (*20*, *21*). The early lethal in vivo developmental phenotypes associated with the depletion of H3K9me3-related histone methyltransferases (HMTases) (*15*, *22*, *23*) support the idea that H3K9me3 controls genome stability and differentiation. Recently, H3K9me3 dynamics at repetitive elements and promoters have been characterized at pregastrula stages (*24*). The global heterochromatin reorganization at germ-layer stages and during lineage commitment in vivo has not been addressed, and prior studies did not distinguish H3K9me3-decorated regions that are euchromatic from those that are heterochromatic (*25*). H3K9me3-enriched domains also impede cell reprogramming and somatic cell nuclear transfer (*17*, *25*–*27*), underscoring the importance of understanding the natural dynamics by which heterochromatic domains restrict cell fates during normal development.

We globally assessed the dynamics of compacted, sonication-resistant heterochromatin (srHC) (*25*) and H3K9me3 deposition at critical developmental time points in the murine endoderm germ layer and in cells along the descendent hepatic and pancreatic lineages (Fig. 1A and figs. S1, A and B; S2, A to H; and S3, A to F). Because the embryonic starting material has low cell numbers, we developed a sonication-resistant heterochromatin sequencing (srHC-seq) method that is sucrose gradient–independent (*25*) to detect regions of srHC (fig. S4, A to E). We performed srHC-seq in definitive endodermal cells, hepatocytes, and mature beta cells and found similar fractions of the genome in srHC in the three cell types (fig. S4, F and G). In all stages, gene expression was anticorrelated with sonication resistance (fig. S4H). Analysis of Hi-C–identified closed compartments revealed a 40% overlap with srHC in adult hepatocytes and mature beta cells (fig. S4I), whereas no significant correlation with open compartments was detected. We observed extensive dynamics of srHC upon definitive endoderm differentiation (Fig. 1B and table S7), including 5979 and 4879 genes that lose compaction, whereas 1630 and 5632 genes gain srHC, during hepatocyte and mature beta cell development, respectively. Gene Ontology (GO) analysis revealed that srHC is removed in adult function genes (table S7).

We mapped H3K9me3 in cells sorted from embryos at different developmental stages (fig. S5, A to D). Unsupervised hierarchical clustering revealed a high correlation between individual replicates, with definitive endoderm cells clustering separately from the hepatic and pancreatic lineages (fig. S5E). To compare H3K9me3 landscapes across the three germ layers, we included mesoderm progenitors and ectoderm-derived, already specified midbrain neuroepithelial cells isolated at embryonic day 8.25 (e8.25) (fig. S6, A to H) and compared their H3K9me3 profiles to those of definitive endodermal cells, as well as to postnatal day 0 (P0) heart and adult nucleus accumbens (Fig. 1A). Concordant with the heterochromatin analysis, H3K9me3 marked more gene bodies, promoters, and termination transcription sites (TTSs) in endoderm and mesoderm germ layer than in pregastrula stages or differentiating cells (Fig. 1C; fig. S7, A to E; and tables S8 and S9). A stepwise developmental transition analysis of H3K9me3 revealed a substantial loss of H3K9me3 when definitive endodermal cells differentiate into hepatic and pancreatic progenitors (Fig. 1D and tables S10 and S11). A similar process is detected in the mesoderm lineage, but not upon differentiation of midbrain neuroepithelium, which is already past the ectoderm stage, into neurons (fig. S7F and tables S10 and S11).

H3K9me3 and H3K27me3 reside both in srHC and open chromatin, where they decorate regions independently or in combination (*25*) (fig. S8, A to C). However, unlike H3K9me3, heterochromatin marked by H3K27me3 was similarly distributed over genes and intergenic regions in definitive endoderm, hepatocytes, and mature beta cells (fig. S9, A to E).

We assessed the acquisition of stage-specific transcriptional signatures along the hepatic and pancreatic lineages (fig. S10, A to C, and table S12). Combined analysis of srHC, H3K9me3, and transcriptional profiles revealed that gene bodies, transcription start sites (TSSs), or TTSs marked by H3K9me3 are more repressed when present in srHC than in open chromatin (fig. S11, A and B). K-means cluster analysis of six developmental stages (fig. S12A and table S13) identified 15 patterns of gene expression. Notably, cell type–specific genes that acquire expression in terminally differentiated cells showed a net loss of srHC and H3K9me3 along both the hepatic and pancreatic lineages (Fig. 2, A and C

[1]Institute for Regenerative Medicine, University of Pennsylvania, Philadelphia, PA, USA. [2]Penn Epigenetics Institute, University of Pennsylvania, Philadelphia, PA, USA. [3]Department of Cell and Developmental Biology, University of Pennsylvania, Philadelphia, PA, USA. [4]Department of Biomedical and Health Informatics, Children's Hospital of Philadelphia, Philadelphia, PA, USA. [5]Division of Oncology and Center for Childhood Cancer Research, Children's Hospital of Philadelphia, Philadelphia, PA, USA. [6]Department of Biochemistry and Molecular Biophysics, University of Pennsylvania, Philadelphia, PA, USA. [7]Max Planck Institute of Immunobiology and Epigenetics, Freiburg, Germany. [8]Department of Pediatrics, Perelman School of Medicine, University of Pennsylvania, Philadelphia, PA, USA.
*Corresponding author. Email: zaret@upenn.edu

Downloaded from http://science.sciencemag.org/ on January 22, 2019

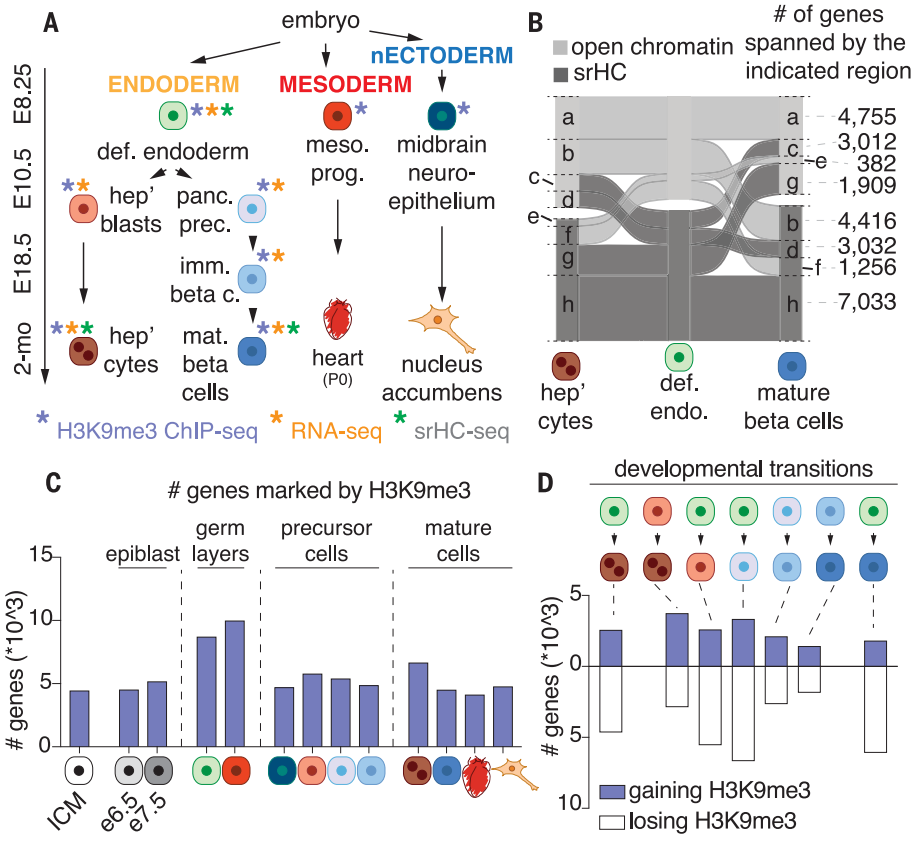


Fig. 1. Chromatin compaction and H3K9me3 landscape upon germ-layer differentiation. (**A**) Schematic of the cell types and embryonic developmental stages considered in this study. Purple, orange, and green asterisks next to the represented cell types indicate samples processed for H3K9me3 ChIP-seq, RNA-seq, and srHC-seq, respectively. (**B**) Alluvial plot showing dynamics in definitive endoderm srHC (dark gray) and open chromatin (light gray) patches upon differentiation into adult hepatocytes and insulin-producing cells; a to h indicate distinct categories or alluvia, characterized by a specific dynamic in srHC and open chromatin; the number of genes in each alluvium is indicated. (**C**) Number of genes marked by H3K9me3 in each indicated stage, along the hepatic and pancreatic lineages. Inner cell mass (ICM), e6.5, and e7.5 data from (*25*). (**D**) Number of genes gaining (purple) or losing (white) H3K9me3 upon stepwise transition in successive developmental stages. Each transition is indicated above the corresponding gene number bar.

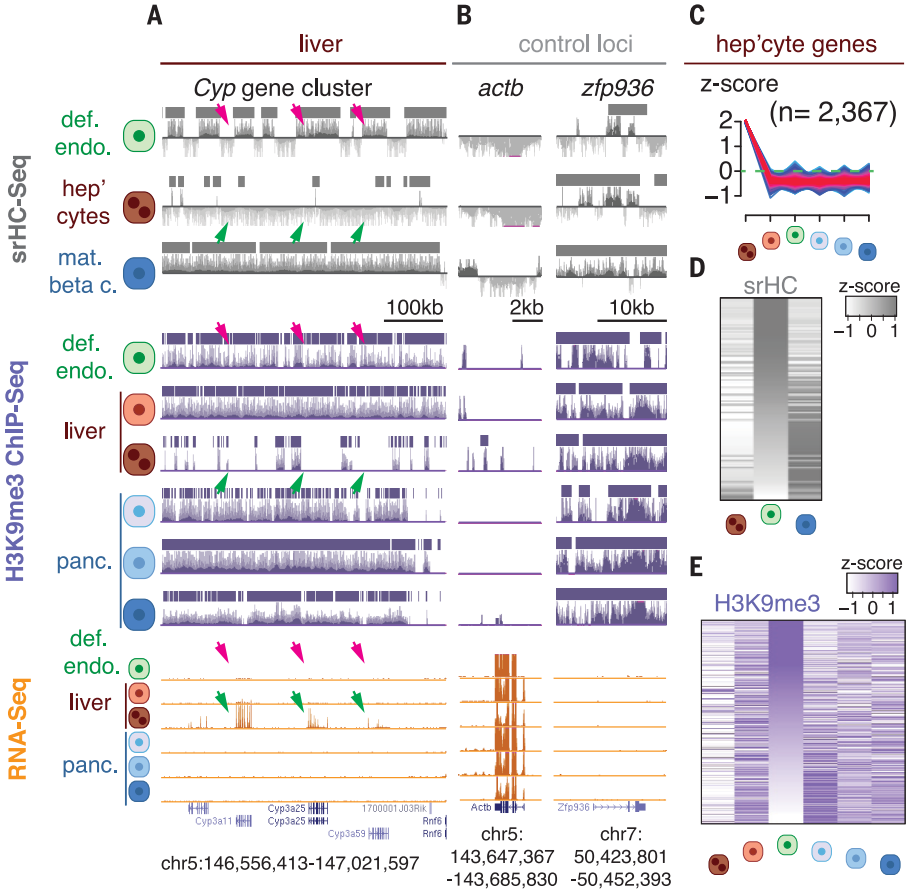


Fig. 2. Loss of srHC and H3K9me3 correlates with gene expression of hepatic-specific markers upon differentiation. (**A**) Representative UCSC genome browser tracks of srHC-seq (gray), input-divided H3K9me3 (purple), and RNA-seq profiles (orange) upon definitive endoderm differentiation into adult hepatocytes. srHC and H3K9me3 patches are shown as gray and purple bars above each profile, respectively. Cytochrome P450 (*Cyp*) genes on chromosome 5 (A) are shown. The constitutive H3K9me3-undecorated and active *Actin b* (*Actb*) and the permanently H3K9me3-enriched and silenced *zinc finger protein (Zfp) 936* (**B**) have been included as examples of genes whose expression inversely correlates to H3K9me3 presence. Magenta arrows indicate presence of srHC and H3K9me3 and absence of expression. Green arrows indicate absence of srHC, H3K9me3, and gene expression. (**C**) Z-score cluster representations for genes expressed in adult hepatocytes. (**D** and **E**) Heatmaps showing levels of srHC (D) and H3K9me3 (E) in the indicated stages. For both srHC and H3K9me3 heatmaps, definitive endodermal cell values have been ordered in a descendent manner.

Downloaded from http://science.sciencemag.org/ on January 22, 2019

to E; figs. S13A and S14, A to D; and table S14), whereas constitutively expressed or repressed genes were depleted or decorated by the mark, respectively (Fig. 2B and fig. S13, B and C). H3K27me3 dynamics at both hepatic and pancreatic-specific genes were also detected, showing loss in development (fig. S14E). Of the 1008 and 1249 genes in adult hepatocytes and mature beta cells that fail to be expressed at a higher level in differentiated versus uncommitted cells, but lose H3K9me3, 71% and 74%, respectively, showed increased H3K27me3 levels compared to definitive endoderm (fig S15A), indicating a compensatory mechanism for maintaining heterochromatin at a subset of genes that remain developmentally silent. Overall, the results show that H3K9me3-marked heterochromatin is transiently deployed in germ-layer cells to repress genes associated with mature cell function and is removed at many sites during differentiation to allow tissue-specific gene expression.

H3K9me3 is established by three main HMTases: Setdb1, Suv39h1, and Suv39h2 (*15*, *22*, *23*). *Setdb1* single and *Suv39h1/h2* double germline knockouts are associated with early lethal phenotypes (*15*, *17*, *22*). We used *FoxA3-Cre* to generate endoderm-specific (*28*, *29*), conditional knockout (KO) mice for *Setdb1* (*30*) (fig. S16A) and analyzed e11.5 livers. H3K9me3 was modestly reduced in mutant embryos (fig. S16B), which showed bleeding in different body regions but no gross morphological differences in the liver structure and cell composition (fig. S16C). Single-cell RNA-seq on wild-type (wt) e11.5 hepatoblasts revealed three clusters of cell types (clusters 1 to 3, table S15), whose differentially expressed genes were associated with developmental processes, hepatic metabolism, and hematopoiesis, respectively (Fig. 3A and fig. S17, A to E). Expressed genes in *Setdb1* mutant cells more than doubled in cluster 1 compared to wt cells but were reduced in cluster 2 (Fig. 3A). *Setdb1* mutant *albumin*-positive (*Alb*+) cells from cluster 2 fail to induce hepatic markers and separate into a distinct subcluster from that of wt *Alb*+ cells (Fig. 3B and table S15). Adult, conditional *Setdb1* mutant livers show occasional hypertrophic hepatocytes (fig. S16, D and E) that maintain nuclear Setdb1 and H3K9me3 levels, as well as expression of major urinary proteins (MUPs) (fig. S16D). However, the bulk of *Setdb1*-negative cells show lower levels of H3K9me3 and no expression of MUPs, in stark contrast to wt livers that uniformly express pericentral MUPs (fig. S16D). Thus, *Setdb1* modulates hepatocyte differentiation.

The persistence of low-level H3K9me3 in the conditional *Setdb1* mutants and *Suv39h1* and *Suv39h2* double mutants (fig. S16B and S18A), the appearance of escaper cells (fig. S16D, arrows), and the expression of H3K9me3-related HMTases being higher in definitive endoderm, compared to more specified cells (fig. S18B), prompted us to generate an endoderm-specific conditional triple-knockout mutant (TKO) murine strain of all three H3K9me3-related HMTases (fig. S19, A to F). Protein analysis showed a clear reduction in Setdb1, Suv39h1 (fig. S20A), and Suv39h2 (fig. S20B), leading to a marked decrease in H3K9me3, but not in H3K27me3 and H3K9me2 (fig. S20, A and C). Single-cell RNA-seq on e11.5 Liv2+ cells revealed that TKO hepatoblasts clustered into a separate group compared to wt and *Setdb1* mutant cells (Fig. 4A), with an overlap of only 43 genes, of nonliver types, up-regulated in common between TKO and *Setdb1* mutant cells (table S15). Indeed, despite expressing *albumin* (fig. S20D), TKO cells did not gain a clear hepatic transcriptional profile (fig. S20E and table S15). One-month-old triple-mutant animals (n = 5) appeared smaller in size compared to control littermates (Fig. 4B), showing up to a threefold reduction in body weight (fig. S21A). TKO livers display inflammatory phenotypes, characterized by a ductular reaction (Fig. 4C). Genomic analysis (fig. S21, B and C) confirmed a substantial loss in srHC and H3K9me3 (Fig. 4D), which was validated by a global loss of condensed chromatin as seen by electron microscopy (Fig. 4E). RNA-seq data on 1-month-old livers (fig. S21, D and E) revealed a marked derepression of nonhepatic genes in TKO livers and a failure to induce mature hepatocyte genes such as MUPs (fig. S22, A and B, and table S16). The latter phenotype, seen also in adult *Setdb1* KO livers (fig. S16D), indicates secondary effects upon depletion of H3K9me3-related HMTases. Notably, markers associated with chromosomal instability were mostly unaffected (fig. S22, C to E). Thus, failure to establish H3K9me3-marked heterochromatin during early development leads to a failure of hepatocyte maturation, even 1 month after birth, and results in expression of inappropriate lineage genes.

Heterochromatin has been defined by biophysical properties more than by repressive histone modifications (*25*). We employed an

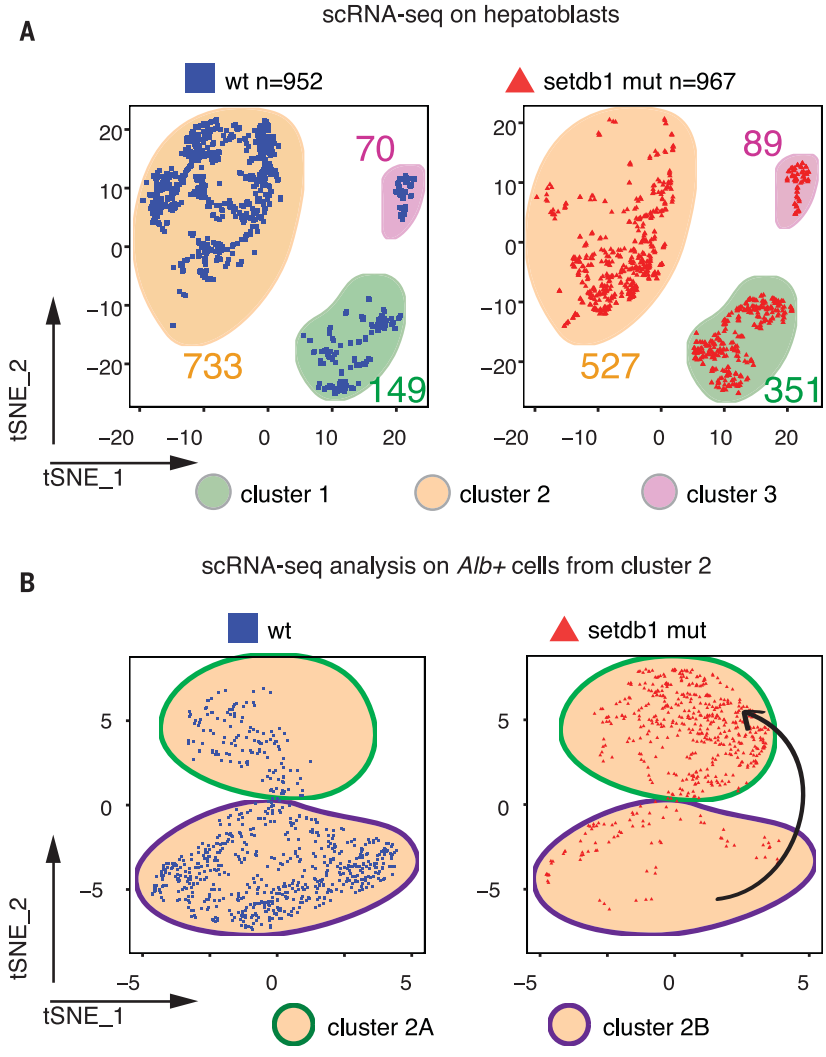


Fig. 3. Setdb1 mutant hepatoblasts up-regulate lineage-nonspecific genes. (**A**) t-Distributed stochastic neighbor embedding (tSNE) plots of single-cell RNA-seq data showing wt (cells from n = 7 embryos; left, blue squares) and Setdb1 mutant (cells from n = 3 embryos; right, red triangles) cells in the three identified clusters. (**B**) tSNE plots of single cell RNA-seq data showing wt (top, blue squares) and Setdb1 mutant (bottom, red triangles) Albumin-positive cells from cluster 2. The black arrow indicates transition of Setdb1 mutant cells (red triangles) to a different cluster from that of the wt cells (blue squares).

Downloaded from http://science.sciencemag.org/ on January 22, 2019

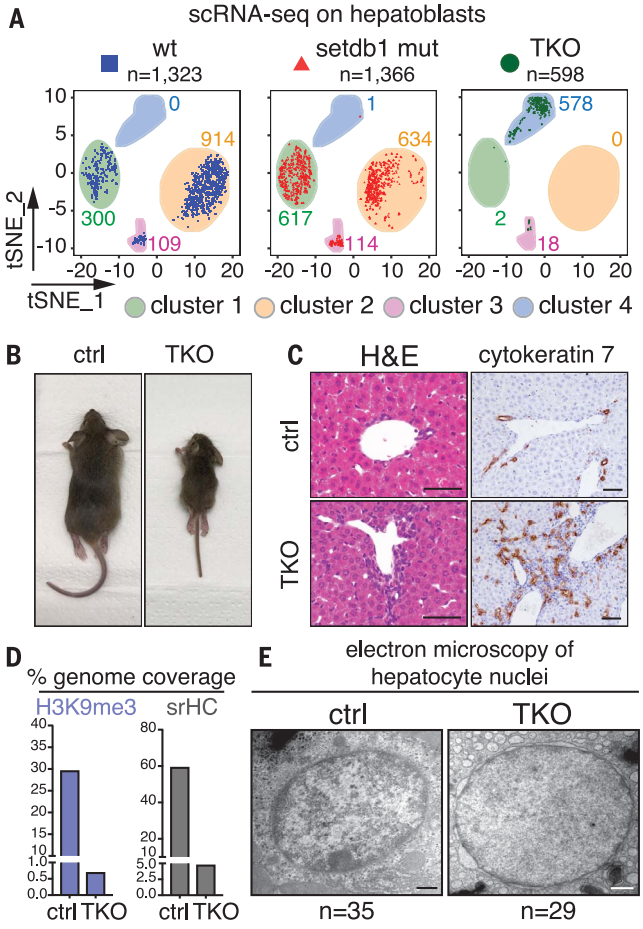


Fig. 4. TKO mutant cells lose hepatic identity and show developmental phenotypes associated with decreased H3K9me3 and srHC levels. (**A**) tSNE plots of e11.5 single-cell RNA-seq data showing wt, Setdb1 mutant (same as in Fig. 3), and TKO (cells from n = 7 embryos; right, dark green circles) cells in the four identified clusters. (**B**) Representative morphological phenotype of 1-month-old control (ctrl) (n = 3) and FoxA3-cre; Setdb1 fl/fl; Suv39h1 fl/fl, Suv39h2 KO KO triple-knockout (TKO) mutants (n = 5). (**C**) Hematoxylin and eosin (H&E) staining and cytokeratin 7 immunohistochemistry in 1-month-old ctrl and TKO livers. Scale bar: 50 μm. (**D**) Percentage of genome covered by H3K9me3 and srHC domains in ctrl and TKO livers. (**E**) Representative electron microscopy images for ctrl and TKO 1-month-old hepatocytes. Scale bar: 600 nm. The number of cells recorded in the two groups is indicated at the bottom.

approach whereby srHC is isolated and characterized independently and in correlation with H3K9me3. We found higher levels of heterochromatin at gene bodies in early, uncommitted endodermal and mesodermal cells and observed a developmental loss of H3K9me3 and srHC during cell differentiation in vivo (fig. S23A). Genetics of H3K9me3-related HMTase mutant mice highlighted the importance of proper heterochromatin establishment to promote cell differentiation. These findings underscore how epigenetic regulation of chromatin structure controls cell identity in embryogenesis. We propose a role for H3K9me3-marked heterochromatin as an epigenetic contributor to the hourglass model (*1*–*3*), working in concert with homeobox proteins (*1*) and signaling (*2*) influences, to constrain gene activity during the phylotypic period of embryonic development and guarantee establishment of cell identity.

REFERENCES AND NOTES

1. D. Duboule, *Dev. Suppl.*, 135–142 (1994).
2. R. A. Raff, *The Shape of Life: Genes, Development, and the Evolution of Animal Form* (University of Chicago Press, IL, 1996).
3. N. Irie, S. Kuratani, *Development* **141**, 4649–4655 (2014).
4. E. Meshorer, T. Misteli, *Nat. Rev. Mol. Cell Biol.* **7**, 540–546 (2006).
5. B. Wen, H. Wu, Y. Shinkai, R. A. Irizarry, A. P. Feinberg, *Nat. Genet.* **41**, 246–250 (2009).
6. K. Ahmed *et al.*, *PLOS ONE* **5**, e10531 (2010).
7. R. D. Hawkins *et al.*, *Cell Stem Cell* **6**, 479–491 (2010).
8. J. Zhu *et al.*, *Cell* **152**, 642–654 (2013).
9. F. Ugarte *et al.*, *Stem Cell Reports* **5**, 728–740 (2015).
10. M. J. Vogel *et al.*, *Genome Res.* **16**, 1493–1504 (2006).
11. T. Chen, S. Y. R. Dent, *Nat. Rev. Genet.* **15**, 93–106 (2014).
12. L. L. Wallrath, S. C. Elgin, *Genes Dev.* **9**, 1263–1277 (1995).
13. N. Gilbert *et al.*, *Cell* **118**, 555–566 (2004).
14. E. Fussner *et al.*, *EMBO J.* **30**, 1778–1789 (2011).
15. A. H. Peters *et al.*, *Cell* **107**, 323–337 (2001).
16. C. Beisel, R. Paro, *Nat. Rev. Genet.* **12**, 123–135 (2011).
17. J. S. Becker, D. Nicetto, K. S. Zaret, *Trends Genet.* **32**, 29–41 (2016).
18. G. Almouzni, A. V. Probst, *Nucleus* **2**, 332–338 (2011).
19. P. Martínez, M. A. Blasco, *Nat. Rev. Cancer* **11**, 161–176 (2011).
20. S. J. Nielsen *et al.*, *Nature* **412**, 561–565 (2001).
21. A. H. F. M. Peters *et al.*, *Nat. Genet.* **30**, 77–80 (2002).
22. J. E. Dodge, Y.-K. Kang, H. Beppu, H. Lei, E. Li, *Mol. Cell. Biol.* **24**, 2478–2486 (2004).
23. M. Tachibana, M. Nozaki, N. Takeda, Y. Shinkai, *EMBO J.* **26**, 3346–3359 (2007).
24. C. Wang *et al.*, *Nat. Cell Biol.* **20**, 620–631 (2018).
25. J. S. Becker *et al.*, *Mol. Cell* **68**, 1023–1037.e15 (2017).
26. A. Soufi, G. Donahue, K. S. Zaret, *Cell* **151**, 994–1004 (2012).
27. S. Matoba *et al.*, *Cell* **159**, 884–895 (2014).
28. C. S. Lee, J. R. Friedman, J. T. Fulmer, K. H. Kaestner, *Nature* **435**, 944–947 (2005).
29. A. Calmont *et al.*, *Dev. Cell* **11**, 339–348 (2006).
30. T. Matsui *et al.*, *Nature* **464**, 927–931 (2010).

ACKNOWLEDGMENTS

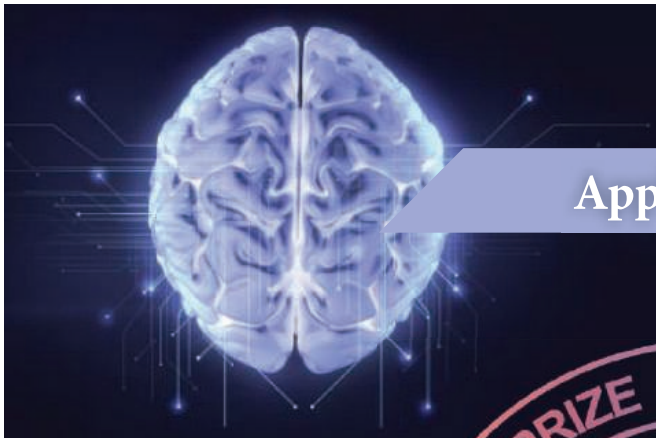
We thank K. Kaeding and R. McCarthy for comments on the manuscript; Y. Shinkai (RIKEN) for the *Setdb1* floxed/floxed strain; the Molecular Pathology and Imaging Core at The University of Pennsylvania (UPenn); T. D. Raabe, J. Henao-Mejia, and J. Richa and the Transgenic and Chimeric Mouse Core (NIH/NIDDK Digestive Diseases Research Center; NIH-P30-DK050306); and the Flow Cytometry and Cell Sorting Facility and the Electron Microscopy Biomedical Research Core Facilities at UPenn. **Funding:** DFG grant NI-1536 to D.N.; NIH grant GM036477 to K.S.Z.; NIH grant GM110174 to B.A.G; NIH grant DP2MH107055 and the Charles E. Kaufman Foundation (KA2016-85223) to R.B. **Author contributions:** D.N. and K.S.Z. designed this study and wrote the manuscript; D.N., T.J., L.S., T.M., and J.M.G. conducted the experiments; G.D., T.P., and J.S.B. performed the bioinformatic analysis; S.S. performed the K-mean clustering analysis of RNA-seq data; K.B. helped with small cell number ChIP protocol; and T.M. and T.J. provided Suv39h dn samples. B.A.G., K.T., and R.B. helped with proteomic and single-cell RNA seq analysis. **Competing interests:** The authors declare no competing interests. **Data and materials availability:** All genomic data are being made accessible at the Gene Expression Omnibus (GEO) database repository GSE114198.

SUPPLEMENTARY MATERIALS

www.sciencemag.org/content/363/6424/294/suppl/DC1
Materials and Methods
Figs. S1 to S23
Tables S1 to S16
References (*31*–*47*)

2 May 2018; resubmitted 23 October 2018
Accepted 20 December 2018
Published online 3 January 2019
10.1126/science.aau0583

Downloaded from http://science.sciencemag.org/ on January 22, 2019



Apply for our exciting research Prize!

SCIENCE-PINS PRIZE FOR NEUROMODULATION

SCIENCE-PINS

$25, 000 Grand Prize!

Get published in *Science*!

The Science & PINS Prize is awarded for innovative research that modulates neural activity through physical (electrical, magnetic, optical) stimulation of targeted sites in the nervous system with implications for translational medicine.

For full details, judging criteria and eligibility requirements, visit:

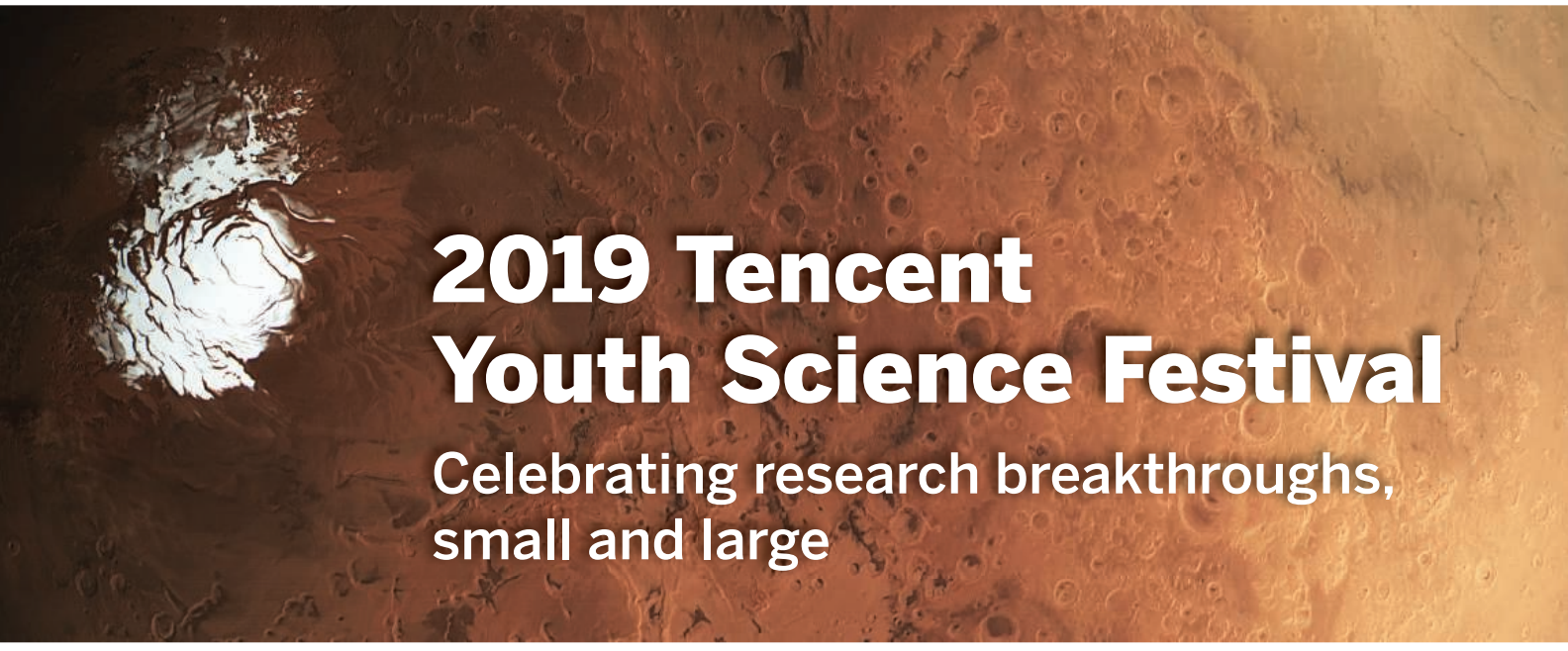
www.sciencemag.org/prizes/pins

Submission Deadline: March 15, 2019

Science AAAS

PINS 品驰

Science Translational Medicine AAAS



2019 Tencent Youth Science Festival

Celebrating research breakthroughs, small and large

Close-up of Mars' south polar ice cap where liquid water was discovered under its surface, pointing to the possibility of life forms and future colonization.

For almost 30 years, *Science* and its Breakthrough of the Year issues have been observing and commemorating the essence of humanity: our innate hunger to understand and document the world around us. These issues serve us in two ways: They celebrate moments of success in science and engineering, and act as a prompt, encouraging us to ask even more questions.

To encourage adolescents to inquire more about science, the Tencent Youth Science Festival—a forum targeting the youth in China and cosponsored by *Science*/AAAS and Tencent, a China-based tech giant and artificial intelligence (AI) leader—will be launched in January 2019. A shortlist of breakthrough topics was collated by the News team at *Science* and provided to Tencent, which leveraged its social, data, and analysis services to gauge the interests of more than 100,000 young users, providing the final 10 breakthrough topics that will be discussed at the forum and also published online on the *Science* website on January 20.

Although the breakthroughs reported are diverse, spanning all fields of science, technology, engineering, and math (STEM), they can all be defined according to their scale. For example, some of these achievements deal with the macroworlds of our solar system and our planet, such as the discovery of liquid water on Mars, and an examination of samples from the Earth's oldest ice cores, which has given us a clearer picture of Earth's atmosphere 2.7 million years ago. Some breakthroughs have expanded the scale of human history, such as a skull found in a Moroccan cave that astonishingly turned back the clock for the emergence of the first *Homo sapiens* to 300,000 years ago—100,000 years earlier than previously thought!

Other breakthroughs demonstrate the ability to examine our universe on a smaller scale. For instance, we are now uncovering increasingly detailed information about our cells and our enigmatic brains. And recently, scientists have started to better understand and even tinker with memory's physical framework, discovering ways to manipulate specific memories in mice using optogenetics, a powerful technique that harnesses laser light to trigger nerve cells in animals' brains. In addition, we have begun to unravel the mystery of sleep and the fact that it serves not just as a way to rest, but as a mechanism to flush out debris from our cells that could cause plaques associated with Alzheimer's disease.

Groundbreaking techniques such as CRISPR, which can be used to edit genes, and new interdisciplinary fields like synthetic biology, which integrates innovations in engineering and the life sciences, are helping us comprehend our lives at even smaller scales. For example, new knowledge concerning the human microbiome, and the body's role as a vast "apartment complex" that serves as home to trillions of microbes, will help us appreciate how these tiny "tenants" impact human health.

The more we understand about ourselves at the cellular level and below, the more we can influence systems on much larger scales. Our knowledge of how neurons work has led to the first large-scale neuromorphic chips, designed to process information in ways similar to human brains. And our increasing comprehension of human cognition has enabled scientists to show that autonomous robot–robot communication is possible, and will allow these devices to "think" and act together, improving their efficiency and capacity to "learn." Advances in artificial intelligence have also made it possible for the newest robots to navigate unmapped environments.

A lot of uncharted territory remains in science. But make no mistake: Each new discovery, while seemingly small, is a thread woven together with all our previous knowledge into an extremely strong cord. And it is this cord that unites us, inspires us, guides us, and defines us as human beings in our quest for greater understanding.

For an expanded version of this advertorial go to **scim.ag/BTYouthForum**.

Tencent 腾讯

IMAGE: © ESA/DLR/FU Berlin, CC BY-SA 3.0 IGO

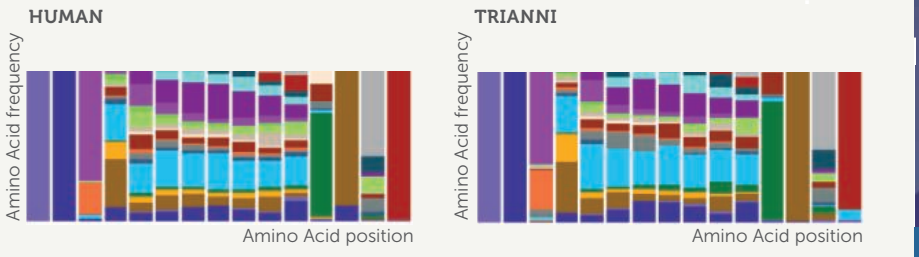
The Best Antibody Discovery Technology Is Now at Your Fingertips

Trianni Mouse Antibodies are a Match for Humans

The Trianni Mouse™ platform is the only transgenic antibody discovery platform ever developed that offers the entirety of human antibody variable gene diversity in a single organism.

The V-gene segments in The Trianni Mouse are chimeric, but the variable domains of antibodies made by the mouse are entirely human. The result is human antibody leads generated from antibody genes optimized for function in the mouse. Or, in the simplest terms, **The Trianni Mouse is a more human mouse.**

To learn more about this innovative platform, visit **Trianni.com**



CDR-H3 residue utilization in antibodies derived from human samples and the Trianni transgenic Ig Mouse. In the naive Trianni Mouse, heavy chain CDR3 (CDR-H3) aa utilization frequency is effectively the same in humans and in The Trianni Mouse.

TRIANNI

Exceptional Human Antibody Discovery Technology





Eye Wash

Aero Emergency Eye Wash Solution is an all-in-one eye wash that combines sterile saline with a buffered, pH-neutralizing solution to not only rinse impurities and irritants from the eyes, but also help the eye return to a normal 7.4-pH level by quickly neutralizing corrosive chemicals. Along with the 16-oz. and 32-oz. sizes, we also offer 5-oz. and ½-oz. sizes that can be easily included in portable workstations or in pockets for high-risk situations. All bottles have easy-to-open quick twist tops for immediate access. A wall-mounting station that contains two 16-oz. bottles is also available. Aero Eye Wash has an expiration date of four years from the date of manufacture. It meets all FDA requirements for eye wash as per 21 CFR Part 349, and also meets the ANSI Z358.1-2009 standard (as a personal eye wash only).
Bel-Art–SP Scienceware
For info: 800-423-5278
www.belart.com

Automation-Friendly Cell Growth Microplates

BactiGrowth is a range of specially packaged plates designed to enable high-yield growth of bacteria, yeast, mammalian, or insect cell lines. Precisely manufactured to conform to the automation-friendly ANSI/SBS format, BactiGrowth plates are available in formats from 24-well to 384-well and well volumes from 300 µL to 10 mL per well, to suit most cellular-growth applications. Produced under Class 10,000 cleanroom conditions from ultrapure-grade polypropylene, every batch of plates is rigorously tested to validate their contamination-free status, ensuring reproducibility and maintaining customer confidence in the cells you grow. BactiGrowth plates are supplied in packs of five with tight-fitting lids and sealed in a sterile polymer bag.
Porvair Sciences
For info: 800-552-3696
www.porvair-sciences.com/bacti-growth-plates

Chromatography Resin

CHT Ceramic Hydroxyapatite XT Media (CHT XT) is a calcium-affinity, cation-exchange chromatography media. It is engineered with advanced technology, resulting in unique selectivity and robust, uniformly sized beads with excellent pressure-flow properties. The chemical composition of CHT XT is $Ca_{10}(PO_4)_6(OH)_2$, and it is a mixed-mode media. CHT XT provides unparalleled separation properties and resolution. It can be used in applications such as purification of enzymes, monoclonal and polyclonal antibodies of various classes, antibody fragments, and bispecific antibodies; efficient isolation and purification of viruses and virus-like particles; and separation of supercoiled DNA from linear duplexes as well as separation of single-stranded from double-stranded DNA. It is ideal for large-scale bioprocess applications. CHT XT Media delivers unique selectivity, efficient single-step clearance of aggregates and other impurities, high physical and chemical stability, and straightforward column packing.
Bio-Rad
For info: 800-424-6723
www.bio-rad.com

Automated Western Blot Processor

BlotCycler by Precision Biosystems is designed to perform automatic blocking, addition, and incubation of primary and secondary antibodies as well as automatic washing steps. It features trays that can be configured to process up to 24 blots with six different primary and secondary antibodies simultaneously. Users simply add their antibodies and fill the BlotCycler tank with buffer solution, add blot membranes to processing trays, and select the protocol for blocking, incubation, and washing. With precise timing, BlotCycler distributes buffers and antibodies, and performs controlled agitation for consistent processing. When blots are removed, the automatic-cleaning protocol is employed for thorough cleaning. The system accommodates most blocking and incubation protocols, and laboratories can continue using the same reagents. BlotCycler can run multiple Western blots using two different protocols at once, performing all steps in precise, reproducible fashion to yield uniform assay results unattended by an operator.
Precision Biosystems
For info: 888-490-4443
www.blotcycler.com

sCMOS Camera for Astronomy and Physical Sciences

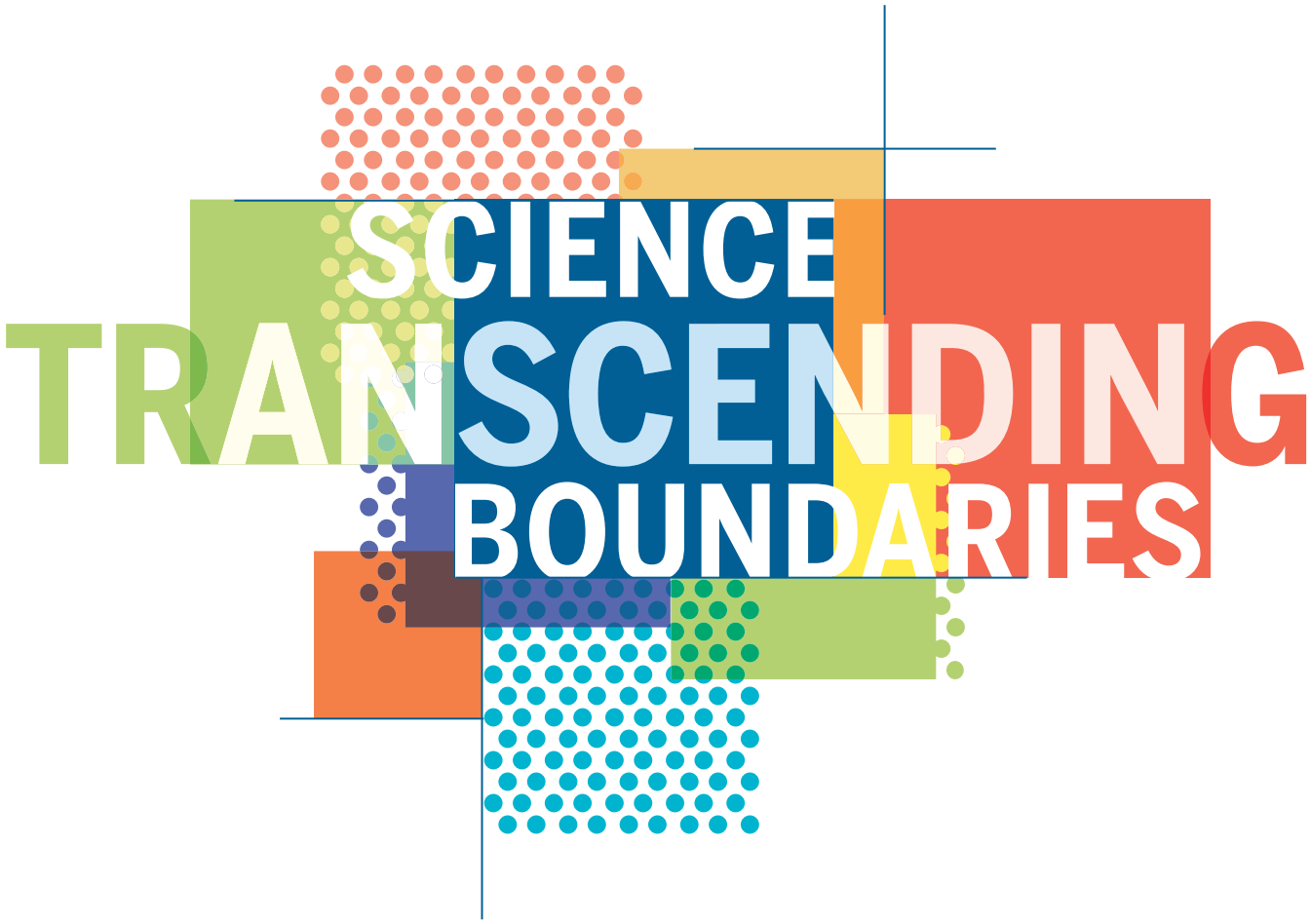
The Marana 4.2B-11 back-illuminated scientific complementary metal-oxide semiconductor (sCMOS) camera for astronomy and physical sciences features 95% quantum efficiency (QE) and market-leading vacuum cooling down to –45°C. It delivers up to 48 fps, perfectly suited to "dynamic astronomy" applications such as space-debris tracking, near-Earth-object detection, and solar astronomy. Marana 4.2B-11 combines a 4.2-megapixel-array format with 11-µm pixels, enabling an impressive 32-mm sensor diagonal. The full 2,048 × 2,048 array is accessed through implementation of Andor's unique Anti-Glow technology, meaning the full sensor area is usable across a wide range of exposure durations. A UV-enhanced option maximizes response across the wavelength region between 200 nm and 400 nm, enveloping both 266-nm and 355-nm laser lines and presenting a strong solution for applications such as wafer inspection and ultracold ion measurements. The hermetically sealed vacuum enclosure also uniquely protects the delicate and exposed sensor from attack by moisture and other gas contaminants, thus preserving both QE and cooling performance year after year.
Andor
For info: 847-212-0500
www.andor.com/marana

Anti-Idiopathic Reagents

Avacta has expanded its catalog of anti-idiotypic (ID) reagents to include the therapeutic targets adalimumab, ipilimumab, and rituximab. All anti-ID Affimer reagents have been developed in collaboration with leading clinical research organizations and pharmaceutical companies. They offer several benefits, including (1) highly specific and sensitive recognition of your therapeutic antibody with a generic detection system to overcome the need for bridging assays and to simplify assay setup; (2) low matrix effect to ensure assay performance within a range of complex samples; and (3) batch-to-batch consistency assuring security of supply. Avacta's custom anti-ID development service offers rapid development of reagents, with no affinity maturation needed.
Avacta
For info: +44-(0)-1904-21-7070
https://www.avacta.com

Electronically submit your new product description or product literature information! Go to www.sciencemag.org/about/new-products-section for more information.

Newly offered instrumentation, apparatus, and laboratory materials of interest to researchers in all disciplines in academic, industrial, and governmental organizations are featured in this space. Emphasis is given to purpose, chief characteristics, and availability of products and materials. Endorsement by *Science* or AAAS of any products or materials mentioned is not implied. Additional information may be obtained from the manufacturer or supplier.



BE PART OF THE CONVERSATION

Artificial Intelligence | Astrophysics | Genomics | Sustainability
Science Diplomacy | Food Security | Digital Privacy | Infection Control
Public Engagement | Climate Change | Diversity | Big Data

AAAS
ANNUAL MEETING
Washington, DC | Feb. 14–17, 2019

SEE INSIDE FOR DETAILS:

Plenary Sessions | Topical Sessions
Milestone Celebrations | Scientific Sessions
Career Workshops | Flash Talk Program

Plenary Sessions



President's Address

MARGARET A. HAMBURG
AAAS President
Foreign Secretary, National Academy of Medicine



Fundamental Research at CERN and International Collaboration

FABIOLA GIANOTTI
Director-General, CERN, European Organization for Nuclear Research



Science Activation: How Do We Get Our Science Used by Those in Power?

LUCY JONES
Founder and Chief Scientist, Dr. Lucy Jones Center for Science and Society

INTERNATIONAL PANEL: Responding Faster and Smarter to New Problems

MICHINARI HAMAGUCHI
President, Japan Science & Technology Agency

MARGARET A. HAMBURG
AAAS President

H.E. MMAMOLOKO KUBAYI-NGUBANE
Minister of Science and Technology, Ministry of Science & Technology, South Africa

JEAN ERIC PAQUET
Director-General Research and Innovation, European Commission

SIR MARK WALPORT
CEO, UK Research and Innovation

See the last page of this ad for information about **Celebrating Scientific Milestones** at the 2019 Annual Meeting!

Join us in Washington, DC

Learn about the many ways that scientific research and diplomacy overcome disciplinary and geographic limitations:

- Plenary and topical sessions by accomplished speakers
- Celebrations of scientific milestones
- 120+ scientific sessions in 11 disciplinary tracks covering exciting advances in research and policy
- 20+ flash talk sessions on current scientific projects and initiatives
- Opportunities to network with colleagues and attend workshops on career guidance
- E-poster presentations highlighting science research by students and professionals

CONNECT WITH US!

@AAASmeetings
#AAASmtg

facebook.com/AAAS.Science

aaas.org/meetings

REPORTERS

The AAAS Annual Meeting Newsroom is hosted on EurekAlert! at **eurekalert.org/aaasnewsroom**

MEETING APP

Download the meeting app for the most up to date program information: **aaas.org/app**

Sponsors As of December 2018

AAAS, publisher of *Science*, thanks the sponsors and supporters of the 2019 Annual Meeting.

Topical Sessions



Materials for the Future: Self-driving Laboratories

ALÁN ASPURU-GUZIK
University of Toronto



Plagues and Progress: Why the World is Getting Healthier in Worrisome Ways

THOMAS J. BOLLYKY
Council on Foreign Relations



Climate Change 2019: Finding the Accelerator Pedal

CHRISTOPHER B. FIELD
Stanford University



Organs-on-Chips Technology: Drug Discovery and Development Beyond Animal Models

GERALDINE HAMILTON
Emulate, Inc.



Secrets of Spider Webs: Unraveling the Complexity of Spider Silk Genes

CHERYL Y. HAYASHI
American Museum of Natural History



Critical Steps Toward Modernizing Graduate STEM Education

ALAN I. LESHNER
American Association for the Advancement of Science



Behave: The Biology of Humans at Our Best and Worst

ROBERT SAPOLSKY
Stanford Univeristy



Health Beyond Humanity: A Planetary Perspective On Our Past and Future

SABRINA SHOLTS
National Museum of Natural History, Smithsonian Institution



Heredity: Our Defining Mystery

CARL ZIMMER
New York Times



SARTON MEMORIAL LECTURE IN THE HISTORY AND PHILOSOPHY OF SCIENCE

Science for Grown-Ups: Assessing Past and Present Adult Informal Science Education

KAREN A. RADER
Virginia Commonwealth University



JOHN P. MCGOVERN AWARD LECTURE IN THE BEHAVIORAL SCIENCES

The Gestural Origins of Language and Thought

SUSAN GOLDIN-MEADOW
University of Chicago

PANEL: ## Societies' Next Steps to Combat Sexual Harassment in STEM

SPEAKERS:



DAVID ACOSTA
Association of American Medical Colleges



JAMIE LEWIS KEITH
EducationCounsel LLC



VICKI MAGLEY
University of Connecticut



SHIRLEY MALCOM
American Association for the Advancement of Science



BILLY WILLIAMS
American Geophysical Union

MODERATOR:

ANDREW BLACK
American Association for the Advancement of Science

Download the Annual Meeting app for the most up-to-date program information: **aaas.org/app**

Scientific Sessions

Keep up with cutting edge developments in science and policy

Controlling Contagion

ANTIBIOTIC USE IN HUMANS AND ANIMALS: STRATEGIES FROM SOCIAL SCIENCE
Organized by Renata Ivanek Miojevic and Michelle Wemette, Cornell University, Ithaca, NY

EPIGENETICS IN INFECTION, DIETS, AND ENVIRONMENTS: RESPONSIBLE RESEARCH AND INNOVATION
Organized by Vittorio Colizzi, University of Rome—Tor Vergata, Italy; Maria S. Salvato, University of Maryland School of Medicine, Baltimore, MD

INFECTIOUS DISEASE CONTROL AND PREVENTION: THE FUTURE IS INTERDISCIPLINARY
Organized by Terry O'Connor, UK Research and Innovation, Swindon, United Kingdom

INFECTIOUS DISEASES: PUSHING THE BOUNDARIES OF PHYSIOLOGY
Organized by Isabelle Boscaro-Clarke, Diamond Light Source, Didcot, United Kingdom

MATHEMATICAL MODELING OF DISEASES: TRANSLATIONAL APPROACHES
Organized by Reinhard Laubenbacher, UConn Health, Farmington, CT; Mark Alber, University of California, Riverside, CA

OPENNESS ABOUT CLINICAL TRIAL RESULTS: LESSONS FROM COMPANIES ON THE FRONT LINE
Organized by Síle Lane, Sense about Science, London, United Kingdom

THE QUEST FOR A UNIVERSAL FLU VACCINE
Organized by Karen Chandross, Sanofi, Bridgewater, NJ

THE ROLE OF STEM CELLS IN THE FUTURE OF MEDICINE
Organized by Jens Wilkinson, RIKEN, Saitama, Japan; Ayaka Nakauchi, Kyoto University, Japan

THE SILENCE OF THE FROGS
Organized by Erin Heath, AAAS, Washington, DC; Julia Smith, Association of American Universities, Washington, DC

UNDERSTANDING ANTIBIOTIC RESISTANCE: REGULATION, QUALITY, AND ACCESS
Organized by Muhammad Zaman, Boston University, MA

VIRUSES, MICROBES, AND THEIR ENTANGLED FATES
Organized by Joshua Weitz, Georgia Institute of Technology, Atlanta, GA; Adrienne Correa, Rice University, Houston, TX

Cultivating Borderless Research

BEYOND OR DESPITE POLITICAL BORDERS: SCIENCE DIPLOMACY AND THE CONSTRUCTION OF EUROPE
Organized by Pascal Griset, Sorbonne Université, Paris, France; Elke Boers, Vrije Universiteit Brussel, Brussels, Belgium

BORDER WALLS: EXCLUSIONARY AND INEFFECTIVE
Organized by Dudley Poston, Texas A&M University, College Station, TX

BUILDING GLOBAL RELATIONSHIPS THROUGH DEFENSE DIPLOMACY AND SCIENTIFIC COOPERATION
Organized by Esha Mathew, AAAS, Washington, DC

COMPETITIVE ADVANTAGE: PROTECTING THE BALANCE IN AFRICA, ASIA, AND EUROPE
Organized by Aidan Gilligan, SciCom—Making Sense of Science, Brussels, Belgium; Daan du Toit, South African Department of Science and Technology, Pretoria, South Africa

COUNTDOWN TO AFRICA'S SCIENTIFIC LIFTOFF
Organized by Neil Turok, Perimeter Institute for Theoretical Physics, Waterloo, Canada

FUNDING AGENCIES AND RESEARCH: COPING WITH GEOGRAPHIC AND DISCIPLINARY CHALLENGES
Organized by Shaun Baron, Natural Sciences and Engineering Research Council of Canada, Ottawa, Canada; Rainer Gruhlich, German Research Foundation, Washington, DC

GLOBAL SCIENCE PARTNERSHIPS AND LOCAL OUTCOMES
Organized by Elizabeth Lyons, National Science Foundation, Alexandria, VA

GLOBAL SCIENTIFIC COLLABORATIONS: NEW TRENDS
Organized by David Cheney, Technology Policy international, LLC, Silver Spring, MD; Go Ohba, National Institute of Science and Technology Policy, Tokyo, Japan

GOING GLOBAL: TOWARD A TRULY INTERNATIONAL PROCESS FOR RESEARCH INFRASTRUCTURES
Organized by Terry O'Connor, UK Research and Innovation, Swindon, United Kingdom; Peggy Pan, Chinese Academy of Sciences, Beijing, China

KILLER ROBOTS: TECHNOLOGICAL, LEGAL, AND ETHICAL CHALLENGES
Organized by Toby Walsh, University of New South Wales, Kensington, Australia

SCIENCE DIPLOMACY: CONTRIBUTIONS TO THE RESOLUTION OF CONFLICTS AND GLOBAL INSECURITY
Organized by Karen Lips, University of Maryland, College Park, MD; Meredith Gore, Michigan State University, East Lansing, MI



SCIENCE IN AFRICA: NEW PROGRAMS AND CONTRIBUTIONS
Organized by Herman B White, Fermi National Accelerator Laboratory, Batavia, IL; Ketevi Assamagan, Brookhaven National Laboratory, Wading River, NY

SCIENCE IN THE NEW ARCTIC: THE CONVERGING OF NATURAL AND SOCIAL SCIENCES
Organized by Andrey Petrov, International Arctic Social Sciences Association, Cedar Falls, IA; Jack Kaye, NASA, Washington, DC

TREATING PEDIATRIC CANCER IN CRISIS: LESSONS FOR DELIVERING CARE
Organized by Sima Jeha, St. Jude Children's Research Hospital, Memphis, TN

Diversifying Scientific Contributions

HOW PEOPLE LEARN: A NEW LOOK
Organized by Nora Newcombe, Temple University, Philadelphia, PA; Zewelanji Serpell, Virginia Commonwealth University, Richmond, VA

ACADEMIC RESEARCH ASSESSMENT: REDUCING BIASES IN EVALUATION
Organized by Anna Hatch, American Society for Cell Biology, Bethesda, MD; Stephen Curry, Imperial College, London, United Kingdom

EFFECTIVE MENTORING: STRATEGIES AND EXPERIENCES
Organized by Maria Lund Dahlberg, National Academy of Sciences, Engineering, and Medicine, Washington, DC; Juan Gilbert, The University of Florida, Gainesville, FL

PRACTICAL REPRODUCIBLE RESEARCH: REPLICATING SCIENTIFIC DISCOVERIES
Organized by Susan Holmes, Stanford University, CA

PROMOTING GENDER EQUITY IN STEM: TOP DOWN AND BOTTOM UP APPROACHES
Organized by Christine O'Connell, Stony Brook University, NY; Merryn McKinnon, Australian National University, Canberra, Australia

REDUCING SOCIETAL POLARIZATION ABOUT SCIENCE-BASED ISSUES: PROPOSED STRATEGIES
Organized by Edward W. Maibach, George Mason University, Fairfax, VA

REFUGEES AND IMMIGRANTS: HISTORIC CONTRIBUTIONS TO STEM
Organized by Lynn Caporale, New York, NY

SCIENTIFIC LEADERSHIP PROGRAMS: PREPARING SCIENTISTS TO MAKE A DIFFERENCE
Organized by Giovanna Guerrero-Medina, Yale University & Ciencia Puerto Rico, New Haven, CT

SEXUAL MINORITIES IN THE STEM PIPELINE: FROM EDUCATION TO WORKFORCE
Organized by Rochelle Diamond, National Organization of Gay and Lesbian Scientists and Technical Professionals, Pasadena, CA

SUPPORTING UNDERGRADUATE RESEARCHERS TRANSITIONING BETWEEN 2 AND 4 YEAR COLLEGES
Organized by Linda M. Grisham, Massachusetts Bay Community College, Wellesley Hills, MA; Stacey Kiser, Lane Community College, Eugene, OR

USING ONLINE PLATFORMS TO CREATE CULTURALLY RELEVANT COMMUNITIES OF PRACTICE
Organized by Lou Woodley, AAAS, Washington, DC

WOMEN IN SCIENCE: UNDERSTANDING WHAT WORKS
Organized by Ashley Bear, National Academies of Sciences, Engineering, and Medicine, Washington, DC; Tom Rudin, Board on Higher Education and Workforce, Washington, DC

Engaging the Human Ecosystem

COMPUTATIONAL SOCIAL SCIENCE: THE NEXT DECADE
Organized by David Lazer, Northeastern University, Boston, MA

DRUG DEVELOPMENT: OVERCOMING OBSTACLES
Organized by Richard Neubig, Michigan State University, East Lansing, MI; William Beck, University of Illinois, Chicago, IL

GLOBAL NEUROSCIENCE: ACCELERATING BRAIN SCIENCE DISCOVERY
Organized by Stephanie Albin, The Kavli Foundation, Los Angeles, CA

HUMAN GENETIC RESEARCH: OVERCOMING RACE
Organized by Keegan Sawyer, National Academies of Sciences, Engineering, and Medicine, Washington, DC; Michael Yudell, Drexel University, Philadelphia, PA

MEDICINE, COMPUTER SCIENCE, AND ART: LEARNING THROUGH TECHNOLOGY
Organized by Francesca Casadio, Art Institute of Chicago, IL

MISSIONS TO MARS: UNDERSTANDING AND PREPARING TEAMS FOR THE FUTURE
Organized by Noshir Contractor, Northwestern University, Evanston, IL

NEUROBIOLOGICAL AND PUBLIC HEALTH PERSPECTIVES ON EARLY LIFE ADVERSITY
Organized by Rachel Anderson, AAAS, Washington, DC

NEURODEVELOPMENTAL DISORDERS: DEVELOPING MEDICAL TREATMENTS
Organized by Jacqueline Crawley, University of California, Davis School of Medicine, Sacramento, CA

NEUROLOGY AND PSYCHIATRY: MEETING IN THE AGING BRAIN
Organized by Irina Esterlis, National Center for Post-Traumatic Stress Disorder, West Haven, CT

NORDIC REGISTERS AND BIOBANKS: A GOLDMINE FOR PRECISION MEDICINE RESEARCH
Organized by Tor Martin Nilsen, NordForsk, Oslo, Norway

P7: A NEW PARADIGM FOR HEALTH CARE IN THE 21ST CENTURY
Organized by Ram D. Sriram, National Institute of Standards and Technology, Gaithersburg, MD; Ramesh Jain, University of California, Irvine, CA

PREVENTING SEXUAL HARASSMENT: NEXT STEPS FOR SCIENCE, ENGINEERING, AND MEDICINE
Organized by Frazier Benya, National Academies of Sciences, Engineering, and Medicine, Washington, DC

RACE, SEX, AND GENES: SHAPING BODIES, SHIFTING BOUNDARIES, CHALLENGING MYTHS
Organized by Agustín Fuentes, University of Notre Dame, IN

TEETH AS A BIOMARKER FOR ENVIRONMENTAL STRESS AND RISK OF DISEASE
Organized by Pamela Den Besten, University of California, San Francisco, CA

Expanding Tech Applications

BIG DATA: OVERCOMING CHALLENGES TO FACILITATE DATA RE-USE
Organized by Sabina Leonelli, University of Exeter, United Kingdom; Nancy J. Nersessian, Georgia Institute of Technology and Harvard University, Cambridge, MA

BLOCKCHAIN AND THE SCIENTIFIC METHOD
Organized by Kush Varshney, IBM Research, Yorktown Heights, NY; Lav Varshney, University of Illinois at Urbana-Champaign, IL

BUILDING QUANTUM COMPUTERS: WHY AND HOW
Organized by Charles Clark, Joint Quantum Institute, Gaithersburg, MD; Anice Anderson, Private Engineering Consulting, Carmel, IN

DRIVERLESS FUTURES: DISCIPLINES, SECTORS, AND GEOGRAPHIC CONSIDERATIONS
Organized by Mahmud Farooque and Jason Lloyd, Consortium for Science, Policy & Outcomes, Arizona State University, Washington, DC

EARTH'S MANTLE REVEALS EVIDENCE OF NORTH AMERICA'S STORIED GEOLOGICAL PAST
Organized by Beth Grassi and Elisabeth Nadin, EarthScope National Office, Fairbanks, AK

EARTH'S SURFACE RESPONSE TO EARTHQUAKES, VOLCANOES, AND GROUNDWATER: BULGE AND RUPTURE
Organized by Beth Grassi and Elisabeth Nadin, EarthScope National Office, Fairbanks, AK

ENABLING LONG-DURATION MANNED EXPLORATION OF SPACE: CHALLENGES AND NEW DEVELOPMENTS
Organized by Sigrid Reinsch and Sandra Dueck, NASA Ames Research Center, Moffett Field, CA

HOW NEW TECHNOLOGY AFFECTS SOCIETY
Organized by Giovanni Felici, European Research Council Executive Agency, Brussels, Belgium; Frank Kuhn, European Research Council Executive Agency, Saint-Josse-ten-Noode, Belgium

MULTI-MESSENGER ASTROPHYSICS: INSIGHTS FROM COMBINING GRAVITY AND RADIO WAVES
Organized by Eric Murphy, National Radio Astronomy Observatory, Charlottesville, VA

PUBLIC USE DATA PRODUCTS AND PRIVACY PROTECTION: EXPERIENCES FROM THE FRONT LINES
Organized by Jerome Reiter, Duke University, Durham, NC

SOLVING THE BIGGEST MYSTERIES WITH THE TINIEST PARTICLES
Organized by Kurt Riesselmann, Fermi National Accelerator Laboratory, Batavia, IL

SYNTHETIC BIOLOGY AND ADAPTIVE MANAGEMENT
Organized by Wayne Landis, Western Washington University, Bellingham, WA; Keegan Sawyer, The National Academies of Sciences, Engineering, and Medicine, Washington, DC

THE ORIGIN OF GOLD, PLATINUM, AND OTHER HEAVY ELEMENTS IN THE UNIVERSE
Organized by Reiner Kruecken and Jonathan Bagger, TRIUMF, Vancouver, Canada

THE SCIENCE OF QUANTUM INFORMATION: DISENTANGLING OPPORTUNITIES FROM THE HYPE
Organized by David Steuerman, The Kavli Foundation, Los Angeles, CA

Feeding Society

ADDRESSING HUNGER THROUGH AGRICULTURAL DISCOVERY
Organized by Elizabeth Ainsworth, USDA Agricultural Research Center, Urbana, IL

FOOD AND NUTRITION SECURITY: SCIENTIFIC PARTNERSHIPS AND OPPORTUNITIES
Organized by Volker ter Meulen, InterAcademy Partnership, Trieste, Italy; Robin Fears, European Academies Science Advisory Council, Halle (Saale), Germany

FOOD WASTE: A SOCIETAL CONCERN
Organized by Sheril Kirshenbaum, Michigan State University, East Lansing, MI; Michael E. Webber, University of Texas at Austin, TX

GENOME EDITED LIVESTOCK AND REGULATORY STALEMATES
Organized by Alison Van Eenennaam, University of California, Davis, CA

HUMAN INTERACTIONS, BIODIVERSITY, AND SOCIO-ECOLOGICAL DYNAMICS IN DEEP TIME, PARTS I AND II
Organized by Stefani Crabtree, The Pennsylvania State University, State College, PA; Jennifer A. Dunne, Santa Fe Institute, NM

SUSTAINABLY FEEDING TEN BILLION PEOPLE
Organized by Jim Ballingall, Industry-Academia Partnership, Los Gatos, CA

Forming Connections

(IN)JUSTICE BEFORE TRIAL: UNDERSTANDING EARLY STEPS IN THE CRIMINAL JUSTICE SYSTEM
Organized by Barbara Spellman, University of Virginia, Charlottesville, VA

APPLIED SYSTEMS ANALYSIS: BRIDGING EAST AND WEST
Organized by Jan Marco Müller, International Institute for Applied Systems Analysis, Laxenburg, Austria

CENSUS 2020: RECENT CHANGES AND IMPACTS
Organized by Robin Mejia, Carnegie Mellon University, Pittsburgh, PA

FUNDING SCIENCE IN CANADA: POLITICAL INITIATIVE MEETS GRASSROOTS SUPPORT
Organized by Mehrdad Hariri, Canadian Science Policy Centre, Toronto, Canada

GOVERNMENT SCIENTISTS: ROLES AND CHALLENGES
Organized by Margaret Taylor, Lawrence Berkeley National Laboratory, Berkeley, CA

INTERNATIONAL SCIENTIFIC PARTNERSHIPS: OPPORTUNITIES AND CHALLENGES
Organized by Caroline S. Wagner, Ohio State University, Columbus, OH; Rainer Asse, American Academy of Arts and Sciences, Cambridge, MA

LEGAL PROTECTION FOR SCIENTISTS: OVERCOMING REAL AND PERCEIVED BARRIERS
Organized by Joanne P. Carney and Theresa Harris, AAAS, Washington, DC

PARTICLE PHYSICS: FRONTIER SCIENCE AND INTERNATIONAL PARTNERSHIPS
Organized by Pushpalatha Bhat, Fermi National Accelerator Laboratory, Batavia, IL

POLICYMAKERS AND COMMUNICATING SCIENCE: OPPORTUNITIES AND BEST PRACTICES
Organized by Kei Koizumi, AAAS, Washington, DC; Karen Akerlof, George Mason University, Fairfax, VA

SCIENCE DIPLOMACY AND NORTH KOREA: THE DAWN OF A NEW ERA
Organized by Mijung Jung and Soyeon Shin, National Research Council of Science & Technology, Sejong, Korea, Republic of (South)

SCIENCE INFORMING POLICY: RESPONSIBLE DECISION MAKING
Erica Goldman, National Council for Science and the Environment, Washington, DC; Stephen Posner, COMPASS, Silver Spring, MD

SCIENCE MEETS PARLIAMENT: LESSONS LEARNED
Organized by Kylie Walker and Emma Johnston, Science & Technology Australia, Canberra, Australia

Navigating Technology

ACCESS TO PRIVATE AND PROPRIETARY DATA: THEOREMS AND WORKING PROTOTYPES
Organized by Daniel Goroff, Alfred P. Sloan Foundation, New York, NY

AI AND MACHINE LEARNING: INDUSTRIAL APPLICATIONS AND SOCIAL IMPLICATIONS
Organized by Sudarsan Rachuri, U.S. Department of Energy, Washington, DC; James Garrett, Carnegie Mellon University, Pittsburgh, PA

CYBERSECURITY: TRANSCENDING PHYSICS, TECHNOLOGY, AND SOCIETY
Organized by Kevin Fu, University of Michigan, Ann Arbor, MI

HOW AI AND KNOWLEDGE CENTERS ARE CHANGING SOCIETAL VIEWS OF CRITICAL EARTH RESOURCES
Organized by Suzanne A. Pierce, Texas Advanced Computing Center, Austin, TX; Vipin Kumar, University of Minnesota, Minneapolis, MN

INEQUALITY IN NETWORKS, MINDS, AND MACHINES
Organized by Keith Payne, University of North Carolina at Chapel Hill, NC

MACHINE LEARNING AND HUMAN LANGUAGE
Organized by Cecile McKee, University of Arizona, Tucson, AZ

MACHINE LEARNING AND STATISTICS: APPLICATIONS IN GENOMICS AND COMPUTER VISION
Organized by Hal Stern, University of California, Irvine, CA

MACHINE LEARNING FOR THE AUTOMATION OF SCIENTIFIC DISCOVERY ACROSS DISCIPLINES
Organized by Ben Wender, National Academies of Sciences, Engineering, and Medicine, Washington, DC

MASS SPECTROMETRY: NEW ADVANCES IN CHEMISTRY, ARCHEOLOGY, AND PALEONTOLOGY
Organized by Timothy Cleland and Caroline Solazzo, Smithsonian Institution, Suitland, MD

MICROGRAVITY RESEARCH: TIME, SPACE, AND MATERIALS
Organized by Lynnette D. Madsen, National Science Foundation, Alexandria, VA

SOCIO-TECHNICAL CYBERSECURITY: IT'S ALL ABOUT PEOPLE
Organized by Keith Marzullo, University of Maryland, College Park, MD

Reaching Sustainable Development

ADVANCING SUSTAINABLE DEVELOPMENT GOALS THROUGH CHEMISTRY
Organized by Mary M. Kirchhoff, American Chemical Society, Washington, DC

CLIMATE IMPACTS ANALYSIS: INTEGRATING SCIENTIFIC DISCIPLINES
Organized by Juan-Carlos Ciscar, European Commission, Seville, Spain; Marton Hajdu, European Commission, Brussels, Belgium

SUSTAINABLE DEVELOPMENT GOALS: NEW SCIENCE BALANCING A HYPERCONNECTED WORLD
Organized by Sue Nichols and Jianguo (Jack) Liu, Michigan State University, East Lansing, MI

SUSTAINABLE DEVELOPMENT: IMPLEMENTING SYSTEMIC DIMENSIONS
Organized by Jan Marco Müller, International Institute for Applied Systems Analysis, Laxenburg, Austria

SUSTAINABLE INVESTING: SCIENCE, ASSET MANAGEMENT AND SUSTAINABLE DEVELOPMENT
Organized by Brad Wible, *Science* magazine, Washington, DC; Charles Vorosmarty, The City College of New York, NY

SUSTAINABLE TRANSITIONS: LEADERSHIP MODELS FOR COMMUNITY COLLABORATION
Organized by Josh Tewksbury, University of Colorado and Colorado State University, Boulder, CO

THE CARBON CYCLE: CONDITIONS AND OPPORTUNITIES FOR CAPTURE AND UTILIZATION
Organized by Carmine Marzano, European Commission, Brussels, Belgium

THE RESEARCH CLOUD: SUPPORTING THE SUSTAINABLE DEVELOPMENT GOALS
Organized by Vinny Pillay, South African Department of Science and Technology, Brussels, Belgium

TO SAVE 1,000,000 CHILDREN A YEAR: DATA, SCIENCE, AND SUSTAINABLE DEVELOPMENT
Organized by Abraham Flaxman, Institute for Health Metrics and Evaluation, Seattle, WA

Rehabilitating Habitats

CARBON CYCLE PROCESSES, POLICIES, AND UNCERTAINTIES: NEW PERSPECTIVES
Organized by Maureen McCarthy, University of Nevada, Reno, NV; Gyami Shrestha, U.S. Global Change Research Program, Washington, DC

CLUTCHING AT STRAWS: SCIENCE ADVICE, UNCERTAINTY, AND GLOBAL MICROPLASTIC POLLUTION
Organized by Jeremy Bray, European Commission, Brussels, Belgium

EXTREME EVENT ATTRIBUTION IN THE CONTEXT OF CLIMATE CHANGE
Organized by Francis Zwiers, University of Victoria, Canada; Debbie J. Dupuis, HEC Montreal, Canada



CLIMATE CHANGE: UNDERSTANDING FEEDBACK FROM NATURE, CULTURE, AND SOCIETY
Organized by Marianne Lucien, ETH Zürich, Switzerland

COMMUNITY RESPONSES TO CLIMATE CHANGE
Organized by Emily Therese Cloyd and Elana Kimbrell, AAAS, Washington, DC

ECOLOGIES OF INNOVATION: THE POTENTIAL FOR BIOTECHNOLOGY TO ADDRESS FOREST HEALTH
Organized by Kara Laney, National Academies of Sciences, Engineering, and Medicine, Washington, DC

ENVIRONMENTAL AND TEXTILE SCIENTISTS COMBATING MICROPLASTIC POLLUTION
Organized by Margaret Murphy, Washington, DC; Judith Weis, Rutgers University, Newark, NJ

ENVIRONMENTAL HEALTH DATA INTEGRATION: MEASUREMENT AND IMPACT
Organized by Andrea Hodgson and Ben Wender, The National Academies of Sciences, Engineering, and Medicine, Washington, DC

ENVIRONMENTAL MICROBIOMES: BACTERIAL AND FUNGAL COMMUNITIES IN EXTREME ECOSYSTEMS
Organized by Barbara Illman, U.S. Forest Service, Madison, WI

HOMES AT THE CENTER OF CHEMICAL EXPOSURE: UNITING CHEMISTS, ENGINEERS AND HEALTH SCIENTISTS
Organized by Glenn Morrison, University of North Carolina at Chapel Hill, NC; Jon Abbatt, University of Toronto, Canada

PLASTICS IN THE OCEANS: SOURCES, SINKS, AND SOLUTIONS
Organized by Linsey Haram and Christina Simkanin, Smithsonian Environmental Research Center, Edgewater, MD

SUSTAINABILITY SCIENCE AND PUBLIC ENGAGEMENT: INVOLVING LAND OWNERS IN RESEARCH
Organized by Kimberly La Pierre, Smithsonian Environmental Research Center, Edgewater, MD; Sally Koerner, University of North Carolina, Greensboro, NC

THE FOURTH NATIONAL CLIMATE ASSESSMENT: ADVANCING SCIENCE, INFORMING DECISIONS
Organized by Katie Reeves, U.S. Global Change Research Program, Washington, DC; Donald J. Wuebbles, University of Illinois at Urbana-Champaign, IL

TRANSBOUNDARY AIR POLLUTION: THE IMPACT OF SCIENCE ON POLICY
Organized by Terry Keating, U.S. Environmental Protection Agency, Washington, DC; Barry Lefer, NASA, Washington, DC

Sharing Science

A FEMINIST AGENDA FOR SCIENCE COMMUNICATION: NECESSARY AND TIMELY
Organized by Megan Halpern, Michigan State University, East Lansing, MI

AGRICULTURAL INNOVATION AND UPTAKE: USING A MULTI-ACTOR APPROACH
Organized by Jean-Marc Gautier, Institut de l'Elevage, Castanet-Tolosan Cedex, France; Cathy Dwyer, Scotland's Rural College, Midlothian, United Kingdom

FIGHTING FAKE NEWS: VIEWS FROM SOCIAL AND COMPUTATIONAL SCIENCE
Organized by Stephan Lewandowsky, University of Bristol, United Kingdom; Edward W. Maibach, George Mason University, Fairfax, VA

GLOBALIZATION OF THE STEM WORKFORCE: IMPLICATIONS FOR CAREERS AND INSTITUTIONS
Organized by Julia E. Melkers, Georgia Institute of Technology, Atlanta, GA; Eric Welch, Arizona State University, Phoenix, AZ

HUMAN GENETIC VARIATION AND EDUCATION: NOT A SOCIALLY NEUTRAL ENDEAVOR
Organized by Jonathan Beckwith, Harvard Medical School, Boston, MA; Kostia Bergman, Northeastern University, Boston, MA

HUMAN RESOURCE DEVELOPMENT AND DIVERSITY: INSIGHTS FROM PUBLIC AND PRIVATE SECTORS
Organized by Takashi Inutsuka, Ministry of Education, Culture, Sports, Science and Technology, Tokyo, Japan

IMPROVING ATTITUDES TOWARDS CHEMISTRY THROUGH INFORMAL SCIENCE COMMUNICATION
Organized by Larry Bell and David Sittenfeld, Museum of Science, Boston, MA

SCIENCE ENGAGEMENT WITH FAITH COMMUNITIES
Organized by Robert O'Malley, AAAS, Washington, DC

SCIENTIFIC INTEGRITY: PRINCIPLES AND BEST PRACTICES
Organized by Alison Kretser, International Life Sciences Institute North America, Washington, DC

TALKING WITHOUT SPEAKING: OVERCOMING COMMUNICATION CHALLENGES WITH TECHNOLOGY
Organized by Nan Ratner, University of Maryland, College Park, MD

TECHNOLOGY TRANSFER AND INNOVATION: RESHAPING LABORATORY-MARKET RELATIONSHIPS
Organized by Heather Evans, National Institute of Standards and Technology, Gaithersburg, MD; Anice Anderson, Private Engineering Consulting, Carmel, IN

TECHNOLOGY TRANSFER FROM BLUE SKY SCIENCE: AVOIDING PITFALLS, MAXIMIZING RETURNS
Organized by Terry O'Connor, UK Research and Innovation, Swindon, United Kingdom; Ana Godinho, CERN, Geneva, Switzerland

THE BIOLOGY OF RESILIENCE: HOW SCIENCE AND FAITH COMMUNITIES CAN WORK TOGETHER
Organized by Se Y. Kim and Curtis Baxter, AAAS, Washington, DC

YOUTUBE: FRIEND OR FOE IN COMMUNICATING ABOUT SCIENCE AND HEALTH
Organized by Erik Bucy and Asheley Landrum, Texas Tech University, Lubbock, TX



Flash Talks

Brief presentations highlighting scientific findings and programs

A Balancing Act: Navigating Jargon Use When Communicating with Citizen Scientists

The Biology of Fatherhood: Adaptive Origins, Day-to-Day Functions, and Men's Health

Building a Seismic Network in Africa

Developing Engagement Through Early Career Science Policy Groups

Development of a Transdisciplinary Scale to Measure Household Water Insecurity

Drivers of Data Ecologies in Genomics and the Infrastructure Sciences

Engagement and the All of Us Research Program: Meeting People Where They Are

Environmental Perceptions and Migration Decisions Within the United States Gulf Coast

Football, Disabilities, and Engineering: Customer Centered Innovation

From Pipette to Pen: A Scientist's Summer in the Newsroom

Gut Microbiome of Bees and Wasps

Hard Lessons from the Soft Sciences on Gender in Engineering and Technology

International Partnerships and the Open Knowledge Africa Platform

Making Hands-on Biology Experiences Accessible for Everyone

March Mammal Madness: The Power of Science as Narrative

The Next NASA Golden Record Anchored in Science, Information, and Digital Literacies

Nonlinear Optical Study of Two-Dimensional Materials

Optical Markers and Biomarkers for the Risk Assessment of Oral Premalignant Lesions

Promising Genetic Research for Prognosis and Treatment of Many Cancers

Public Engagement Leadership: A Journey From Practitioner to Change Agent

Regenerative Medicine and Tissue Engineering: Transforming 21st Century Medicine

#ScientistsWhoSelfie: Instagramming the Way to Public Trust

The Second Quantum Revolution

The Shape of Human Evolution

Using Policy Analysis to Engage Policymakers and the Public with Research Results

Using Science to Engage Business

Virtual Scientific Communities: Choose Development! Takes Broadening Participation to the Next Level

Zika Virus Mediated Immunopathology: Defining Disease Damage to Infectious Agents

Career Workshops

Opportunities to gain advice and strategies from experienced STEM professionals

A Shared Vision: Overcoming the Barriers for Scientists to Communicate and Engage

Accessibility and Inclusion in STEM Education

Applying Negotiation Tools to Improve Communication and Address Conflict

Attract Recruiters and Jump-start Networking With an All Star LinkedIn Profile

Authorship Decisions: Advocating for Representation

Conducting Science Outreach Online: Social and Multimedia

Diversity + STEM = X: Solving the Equation for Higher Education and the Workforce

Exceptional Presentations in Spite of PowerPoint: How to Communicate Science in the Digital Age

Finding Your Voice: Storytelling Lessons for Scientists

Formulate to Communicate: Heroes, Improv, and Science Storytelling

From a Moment to a Movement: Building Infrastructure to Sustain Scientist Advocacy

Influencing Policy: Opportunities for Scientists and Engineers

LGBTQ+ in Academia and the Workplace: Rights and the Law

Making the Most of the First Two Years On the Tenure Track

Overcoming the STEM-Policy Divide with Fellowships in State Governments

Polish Pitches—For Scientists, Researchers, and Science Journalists

Research Funding: Exploring Programs in the European Union

Scholarly Publishing: Avoiding Pitfalls and Showing Impact

Scientists Engaged in Human Rights: Professional Societies Offer Opportunities

Scientists Who Draw Comics: The Double Life of Visual Science Communicators

YouTube as Outreach: How to Document Research Using Social Media and Video

The Gender Dimension of Science Advice

The Global Entrepreneur: How to Harness International Innovation

Celebrating Scientific Milestones

with the following special sessions and other exciting activities:

NEARLY DOUBLE PLATINUM:
150 YEARS OF THE PERIODIC TABLE



THE LEGACY OF THE APOLLO PROGRAM: 1969 TO 2069



ARPANET: CELEBRATING 50 YEARS SINCE "LO"



AAAS Film Showcase

presented in partnership with JACKSON HOLE WILD

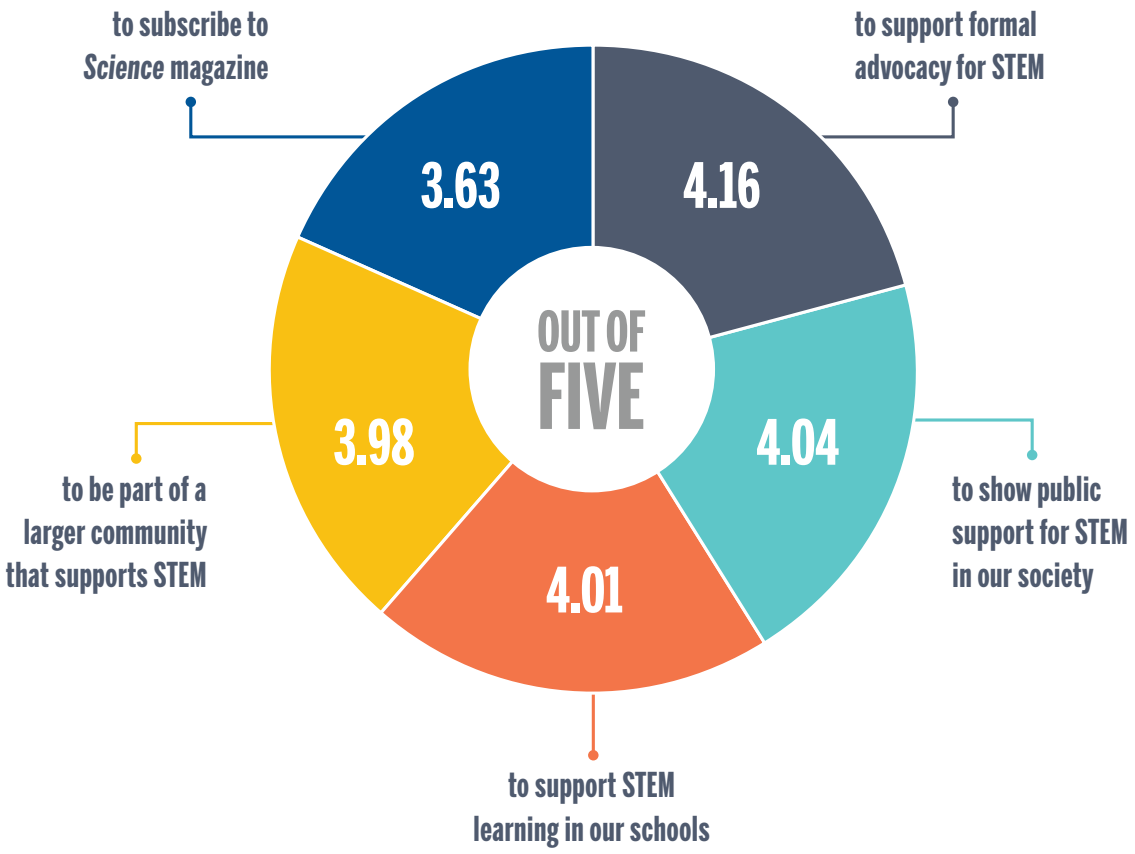
AlphaGo
Attenborough's Ant Mountain
The Kingdom—How Fungi Made Our World
Let There Be Light
Mosquito
Space's Deepest Secrets: Cassini's Grand Finale

Advance registration rates are available now through **January 22, 2019.**

	Advance Rates for AAAS Member for members in good standing	Advance Rates for Non-Member for all other attendees	On-site Rates after 1/22/2019 AAAS Member/Non-Member
General Attendee	$310	$440	$380/480
Postdoc	$135	$360	$135/380
K-12 Teacher	$135	$360	$135/380
Retired Professional	$250	$360	$295/380
Student	$65	$95	$75/105
One-Day	$175	$220	$200/240

AAAS IS THE FORCE FOR SCIENCE

According to the 2017 Member Survey, you joined AAAS ...





TELL US WHAT'S IMPORTANT TO YOU!

The 2018 Member Survey is launching in September. Look in your inbox for a link.

Your responses help us to better serve science, scientists, and the global community. Don't miss your chance to tell us what's most important to you!

BIOLOGY ■ EARTH ■ ENVIRONMENT ■ LIFE ■ INTERDISCIPLINARY ■ PHYSICAL ■ MATERIAL ■ SOCIAL SCIENCES

Science Advances | AAAS

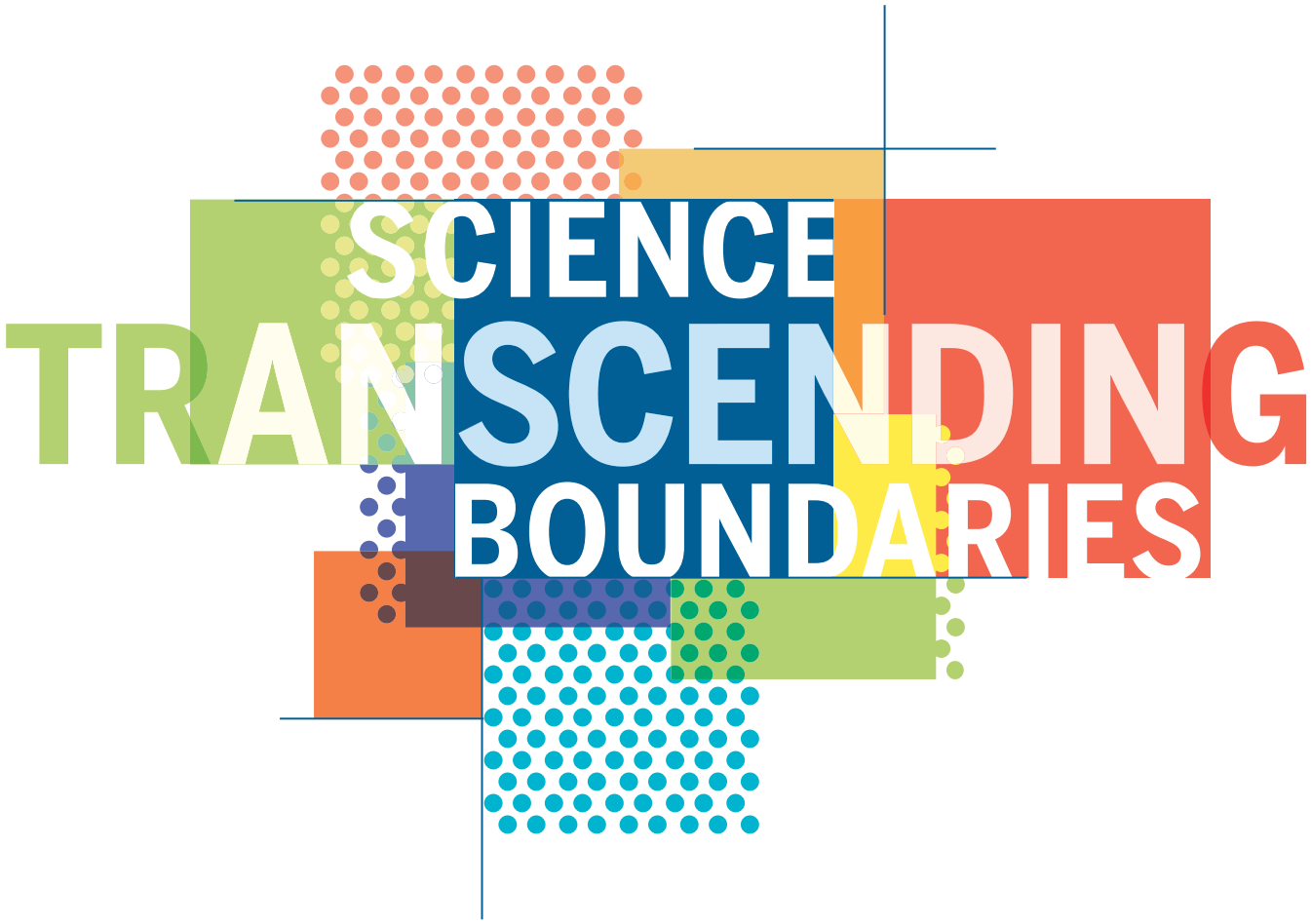
OPEN ACCESS, DIGITAL, AND FREE TO ALL READERS



OPEN ACCESS

Pushing the Boundaries of Knowledge

As AAAS's first multidisciplinary, open access journal, *Science Advances* publishes research that reflects the selectivity of high impact, innovative research you expect from the *Science* family of journals, published in an open access format to serve a vast and growing global audience. Check out the latest findings or learn how to submit your research: **ScienceAdvances.org**



BE PART OF THE CONVERSATION

Artificial Intelligence | Astrophysics | Genomics | Sustainability
Science Diplomacy | Food Security | Digital Privacy | Infection Control
Public Engagement | Climate Change | Diversity | Big Data

AAAS
ANNUAL MEETING
Washington, DC | Feb. 14–17, 2019

SEE INSIDE FOR DETAILS:

Plenary Sessions | Topical Sessions
Milestone Celebrations | Scientific Sessions
Career Workshops | Flash Talk Program

Downloaded from http://science.sciencemag.org/ on January 21, 2019

Plenary Sessions



President's Address

MARGARET A. HAMBURG
AAAS President
Foreign Secretary, National Academy of Medicine



Fundamental Research at CERN and International Collaboration

FABIOLA GIANOTTI
Director-General, CERN, European Organization for Nuclear Research



Science Activation: How Do We Get Our Science Used by Those in Power?

LUCY JONES
Founder and Chief Scientist, Dr. Lucy Jones Center for Science and Society

INTERNATIONAL PANEL: Responding Faster and Smarter to New Problems

MICHINARI HAMAGUCHI
President, Japan Science & Technology Agency

MARGARET A. HAMBURG
AAAS President

H.E. MMAMOLOKO KUBAYI-NGUBANE
Minister of Science and Technology, Ministry of Science & Technology, South Africa

JEAN ERIC PAQUET
Director-General Research and Innovation, European Commission

SIR MARK WALPORT
CEO, UK Research and Innovation

See the last page of this ad for information about **Celebrating Scientific Milestones** at the 2019 Annual Meeting!

Join us in Washington, DC

Learn about the many ways that scientific research and diplomacy overcome disciplinary and geographic limitations:

- Plenary and topical sessions by accomplished speakers
- Celebrations of scientific milestones
- 120+ scientific sessions in 11 disciplinary tracks covering exciting advances in research and policy
- 20+ flash talk sessions on current scientific projects and initiatives
- Opportunities to network with colleagues and attend workshops on career guidance
- E-poster presentations highlighting science research by students and professionals

CONNECT WITH US!

@AAASmeetings
#AAASmtg

facebook.com/AAAS.Science

aaas.org/meetings

REPORTERS

The AAAS Annual Meeting Newsroom is hosted on EurekAlert! at **eurekalert.org/aaasnewsroom**

MEETING APP

Download the meeting app for the most up to date program information: **aaas.org/app**

Sponsors As of December 2018

AAAS, publisher of *Science*, thanks the sponsors and supporters of the 2019 Annual Meeting.

European Commission · Johnson & Johnson INNOVATION · GREAT BRITAIN & NORTHERN IRELAND · Federal Ministry of Education and Research · Research in Germany Land of Ideas · ANALOG DEVICES AHEAD OF WHAT'S POSSIBLE™ · Bristol-Myers Squibb · SUBARU · 3M Science. Applied to Life. · Smithsonian · UC RIVERSIDE

Downloaded from http://science.sciencemag.org/ on January 21, 2019

Topical Sessions



Materials for the Future: Self-driving Laboratories

ALÁN ASPURU-GUZIK
University of Toronto



Plagues and Progress: Why the World is Getting Healthier in Worrisome Ways

THOMAS J. BOLLYKY
Council on Foreign Relations



Climate Change 2019: Finding the Accelerator Pedal

CHRISTOPHER B. FIELD
Stanford University



Organs-on-Chips Technology: Drug Discovery and Development Beyond Animal Models

GERALDINE HAMILTON
Emulate, Inc.



Secrets of Spider Webs: Unraveling the Complexity of Spider Silk Genes

CHERYL Y. HAYASHI
American Museum of Natural History



Critical Steps Toward Modernizing Graduate STEM Education

ALAN I. LESHNER
American Association for the Advancement of Science



Behave: The Biology of Humans at Our Best and Worst

ROBERT SAPOLSKY
Stanford Univeristy



Health Beyond Humanity: A Planetary Perspective On Our Past and Future

SABRINA SHOLTS
National Museum of Natural History, Smithsonian Institution



Heredity: Our Defining Mystery

CARL ZIMMER
New York Times



SARTON MEMORIAL LECTURE IN THE HISTORY AND PHILOSOPHY OF SCIENCE

Science for Grown-Ups: Assessing Past and Present Adult Informal Science Education

KAREN A. RADER
Virginia Commonwealth University



JOHN P. MCGOVERN AWARD LECTURE IN THE BEHAVIORAL SCIENCES

The Gestural Origins of Language and Thought

SUSAN GOLDIN-MEADOW
University of Chicago

PANEL: Societies' Next Steps to Combat Sexual Harassment in STEM

SPEAKERS:



DAVID ACOSTA
Association of American Medical Colleges



JAMIE LEWIS KEITH
EducationCounsel LLC



VICKI MAGLEY
University of Connecticut



SHIRLEY MALCOM
American Association for the Advancement of Science



BILLY WILLIAMS
American Geophysical Union

MODERATOR:

ANDREW BLACK
American Association for the Advancement of Science

Downloaded from http://science.sciencemag.org/ on January 21, 2019

Download the Annual Meeting app for the most up-to-date program information: **aaas.org/app**

Scientific Sessions

Keep up with cutting edge developments in science and policy

Controlling Contagion

ANTIBIOTIC USE IN HUMANS AND ANIMALS: STRATEGIES FROM SOCIAL SCIENCE
Organized by Renata Ivanek Miojevic and Michelle Wemette, Cornell University, Ithaca, NY

EPIGENETICS IN INFECTION, DIETS, AND ENVIRONMENTS: RESPONSIBLE RESEARCH AND INNOVATION
Organized by Vittorio Colizzi, University of Rome—Tor Vergata, Italy; Maria S. Salvato, University of Maryland School of Medicine, Baltimore, MD

INFECTIOUS DISEASE CONTROL AND PREVENTION: THE FUTURE IS INTERDISCIPLINARY
Organized by Terry O'Connor, UK Research and Innovation, Swindon, United Kingdom

INFECTIOUS DISEASES: PUSHING THE BOUNDARIES OF PHYSIOLOGY
Organized by Isabelle Boscaro-Clarke, Diamond Light Source, Didcot, United Kingdom

MATHEMATICAL MODELING OF DISEASES: TRANSLATIONAL APPROACHES
Organized by Reinhard Laubenbacher, UConn Health, Farmington, CT; Mark Alber, University of California, Riverside, CA

OPENNESS ABOUT CLINICAL TRIAL RESULTS: LESSONS FROM COMPANIES ON THE FRONT LINE
Organized by Síle Lane, Sense about Science, London, United Kingdom

THE QUEST FOR A UNIVERSAL FLU VACCINE
Organized by Karen Chandross, Sanofi, Bridgewater, NJ

THE ROLE OF STEM CELLS IN THE FUTURE OF MEDICINE
Organized by Jens Wilkinson, RIKEN, Saitama, Japan; Ayaka Nakauchi, Kyoto University, Japan

THE SILENCE OF THE FROGS
Organized by Erin Heath, AAAS, Washington, DC; Julia Smith, Association of American Universities, Washington, DC

UNDERSTANDING ANTIBIOTIC RESISTANCE: REGULATION, QUALITY, AND ACCESS
Organized by Muhammad Zaman, Boston University, MA

VIRUSES, MICROBES, AND THEIR ENTANGLED FATES
Organized by Joshua Weitz, Georgia Institute of Technology, Atlanta, GA; Adrienne Correa, Rice University, Houston, TX

Cultivating Borderless Research

BEYOND OR DESPITE POLITICAL BORDERS: SCIENCE DIPLOMACY AND THE CONSTRUCTION OF EUROPE
Organized by Pascal Griset, Sorbonne Université, Paris, France; Elke Boers, Vrije Universiteit Brussel, Brussels, Belgium

BORDER WALLS: EXCLUSIONARY AND INEFFECTIVE
Organized by Dudley Poston, Texas A&M University, College Station, TX

BUILDING GLOBAL RELATIONSHIPS THROUGH DEFENSE DIPLOMACY AND SCIENTIFIC COOPERATION
Organized by Esha Mathew, AAAS, Washington, DC

COMPETITIVE ADVANTAGE: PROTECTING THE BALANCE IN AFRICA, ASIA, AND EUROPE
Organized by Aidan Gilligan, SciCom—Making Sense of Science, Brussels, Belgium; Daan du Toit, South African Department of Science and Technology, Pretoria, South Africa

COUNTDOWN TO AFRICA'S SCIENTIFIC LIFTOFF
Organized by Neil Turok, Perimeter Institute for Theoretical Physics, Waterloo, Canada

FUNDING AGENCIES AND RESEARCH: COPING WITH GEOGRAPHIC AND DISCIPLINARY CHALLENGES
Organized by Shaun Baron, Natural Sciences and Engineering Research Council of Canada, Ottawa, Canada; Rainer Gruhlich, German Research Foundation, Washington, DC

GLOBAL SCIENCE PARTNERSHIPS AND LOCAL OUTCOMES
Organized by Elizabeth Lyons, National Science Foundation, Alexandria, VA

GLOBAL SCIENTIFIC COLLABORATIONS: NEW TRENDS
Organized by David Cheney, Technology Policy international, LLC, Silver Spring, MD; Go Ohba, National Institute of Science and Technology Policy, Tokyo, Japan

GOING GLOBAL: TOWARD A TRULY INTERNATIONAL PROCESS FOR RESEARCH INFRASTRUCTURES
Organized by Terry O'Connor, UK Research and Innovation, Swindon, United Kingdom; Peggy Pan, Chinese Academy of Sciences, Beijing, China

KILLER ROBOTS: TECHNOLOGICAL, LEGAL, AND ETHICAL CHALLENGES
Organized by Toby Walsh, University of New South Wales, Kensington, Australia

SCIENCE DIPLOMACY: CONTRIBUTIONS TO THE RESOLUTION OF CONFLICTS AND GLOBAL INSECURITY
Organized by Karen Lips, University of Maryland, College Park, MD; Meredith Gore, Michigan State University, East Lansing, MI



Downloaded from http://science.sciencemag.org/ on January 21, 2019

SCIENCE IN AFRICA: NEW PROGRAMS AND CONTRIBUTIONS
Organized by Herman B White, Fermi National Accelerator Laboratory, Batavia, IL; Ketevi Assamagan, Brookhaven National Laboratory, Wading River, NY

SCIENCE IN THE NEW ARCTIC: THE CONVERGING OF NATURAL AND SOCIAL SCIENCES
Organized by Andrey Petrov, International Arctic Social Sciences Association, Cedar Falls, IA; Jack Kaye, NASA, Washington, DC

TREATING PEDIATRIC CANCER IN CRISIS: LESSONS FOR DELIVERING CARE
Organized by Sima Jeha, St. Jude Children's Research Hospital, Memphis, TN

Diversifying Scientific Contributions

HOW PEOPLE LEARN: A NEW LOOK
Organized by Nora Newcombe, Temple University, Philadelphia, PA; Zewelanji Serpell, Virginia Commonwealth University, Richmond, VA

ACADEMIC RESEARCH ASSESSMENT: REDUCING BIASES IN EVALUATION
Organized by Anna Hatch, American Society for Cell Biology, Bethesda, MD; Stephen Curry, Imperial College, London, United Kingdom

EFFECTIVE MENTORING: STRATEGIES AND EXPERIENCES
Organized by Maria Lund Dahlberg, National Academy of Sciences, Engineering, and Medicine, Washington, DC; Juan Gilbert, The University of Florida, Gainesville, FL

PRACTICAL REPRODUCIBLE RESEARCH: REPLICATING SCIENTIFIC DISCOVERIES
Organized by Susan Holmes, Stanford University, CA

PROMOTING GENDER EQUITY IN STEM: TOP DOWN AND BOTTOM UP APPROACHES
Organized by Christine O'Connell, Stony Brook University, NY; Merryn McKinnon, Australian National University, Canberra, Australia

REDUCING SOCIETAL POLARIZATION ABOUT SCIENCE-BASED ISSUES: PROPOSED STRATEGIES
Organized by Edward W. Maibach, George Mason University, Fairfax, VA

REFUGEES AND IMMIGRANTS: HISTORIC CONTRIBUTIONS TO STEM
Organized by Lynn Caporale, New York, NY

SCIENTIFIC LEADERSHIP PROGRAMS: PREPARING SCIENTISTS TO MAKE A DIFFERENCE
Organized by Giovanna Guerrero-Medina, Yale University & Ciencia Puerto Rico, New Haven, CT

SEXUAL MINORITIES IN THE STEM PIPELINE: FROM EDUCATION TO WORKFORCE
Organized by Rochelle Diamond, National Organization of Gay and Lesbian Scientists and Technical Professionals, Pasadena, CA

SUPPORTING UNDERGRADUATE RESEARCHERS TRANSITIONING BETWEEN 2 AND 4 YEAR COLLEGES
Organized by Linda M. Grisham, Massachusetts Bay Community College, Wellesley Hills, MA; Stacey Kiser, Lane Community College, Eugene, OR

USING ONLINE PLATFORMS TO CREATE CULTURALLY RELEVANT COMMUNITIES OF PRACTICE
Organized by Lou Woodley, AAAS, Washington, DC

WOMEN IN SCIENCE: UNDERSTANDING WHAT WORKS
Organized by Ashley Bear, National Academies of Sciences, Engineering, and Medicine, Washington, DC; Tom Rudin, Board on Higher Education and Workforce, Washington, DC

Engaging the Human Ecosystem

COMPUTATIONAL SOCIAL SCIENCE: THE NEXT DECADE
Organized by David Lazer, Northeastern University, Boston, MA

DRUG DEVELOPMENT: OVERCOMING OBSTACLES
Organized by Richard Neubig, Michigan State University, East Lansing, MI; William Beck, University of Illinois, Chicago, IL

GLOBAL NEUROSCIENCE: ACCELERATING BRAIN SCIENCE DISCOVERY
Organized by Stephanie Albin, The Kavli Foundation, Los Angeles, CA

HUMAN GENETIC RESEARCH: OVERCOMING RACE
Organized by Keegan Sawyer, National Academies of Sciences, Engineering, and Medicine, Washington, DC; Michael Yudell, Drexel University, Philadelphia, PA

MEDICINE, COMPUTER SCIENCE, AND ART: LEARNING THROUGH TECHNOLOGY
Organized by Francesca Casadio, Art Institute of Chicago, IL

MISSIONS TO MARS: UNDERSTANDING AND PREPARING TEAMS FOR THE FUTURE
Organized by Noshir Contractor, Northwestern University, Evanston, IL

NEUROBIOLOGICAL AND PUBLIC HEALTH PERSPECTIVES ON EARLY LIFE ADVERSITY
Organized by Rachel Anderson, AAAS, Washington, DC

NEURODEVELOPMENTAL DISORDERS: DEVELOPING MEDICAL TREATMENTS
Organized by Jacqueline Crawley, University of California, Davis School of Medicine, Sacramento, CA

NEUROLOGY AND PSYCHIATRY: MEETING IN THE AGING BRAIN
Organized by Irina Esterlis, National Center for Post-Traumatic Stress Disorder, West Haven, CT

NORDIC REGISTERS AND BIOBANKS: A GOLDMINE FOR PRECISION MEDICINE RESEARCH
Organized by Tor Martin Nilsen, NordForsk, Oslo, Norway

P7: A NEW PARADIGM FOR HEALTH CARE IN THE 21ST CENTURY
Organized by Ram D. Sriram, National Institute of Standards and Technology, Gaithersburg, MD; Ramesh Jain, University of California, Irvine, CA

PREVENTING SEXUAL HARASSMENT: NEXT STEPS FOR SCIENCE, ENGINEERING, AND MEDICINE
Organized by Frazier Benya, National Academies of Sciences, Engineering, and Medicine, Washington, DC

RACE, SEX, AND GENES: SHAPING BODIES, SHIFTING BOUNDARIES, CHALLENGING MYTHS
Organized by Agustín Fuentes, University of Notre Dame, IN

TEETH AS A BIOMARKER FOR ENVIRONMENTAL STRESS AND RISK OF DISEASE
Organized by Pamela Den Besten, University of California, San Francisco, CA

Expanding Tech Applications

BIG DATA: OVERCOMING CHALLENGES TO FACILITATE DATA RE-USE
Organized by Sabina Leonelli, University of Exeter, United Kingdom; Nancy J. Nersessian, Georgia Institute of Technology and Harvard University, Cambridge, MA

Downloaded from http://science.sciencemag.org/ on January 21, 2019

BLOCKCHAIN AND THE SCIENTIFIC METHOD
Organized by Kush Varshney, IBM Research, Yorktown Heights, NY; Lav Varshney, University of Illinois at Urbana-Champaign, IL

BUILDING QUANTUM COMPUTERS: WHY AND HOW
Organized by Charles Clark, Joint Quantum Institute, Gaithersburg, MD; Anice Anderson, Private Engineering Consulting, Carmel, IN

DRIVERLESS FUTURES: DISCIPLINES, SECTORS, AND GEOGRAPHIC CONSIDERATIONS
Organized by Mahmud Farooque and Jason Lloyd, Consortium for Science, Policy & Outcomes, Arizona State University, Washington, DC

EARTH'S MANTLE REVEALS EVIDENCE OF NORTH AMERICA'S STORIED GEOLOGICAL PAST
Organized by Beth Grassi and Elisabeth Nadin, EarthScope National Office, Fairbanks, AK

EARTH'S SURFACE RESPONSE TO EARTHQUAKES, VOLCANOES, AND GROUNDWATER: BULGE AND RUPTURE
Organized by Beth Grassi and Elisabeth Nadin, EarthScope National Office, Fairbanks, AK

ENABLING LONG-DURATION MANNED EXPLORATION OF SPACE: CHALLENGES AND NEW DEVELOPMENTS
Organized by Sigrid Reinsch and Sandra Dueck, NASA Ames Research Center, Moffett Field, CA

HOW NEW TECHNOLOGY AFFECTS SOCIETY
Organized by Giovanni Felici, European Research Council Executive Agency, Brussels, Belgium; Frank Kuhn, European Research Council Executive Agency, Saint-Josse-ten-Noode, Belgium

MULTI-MESSENGER ASTROPHYSICS: INSIGHTS FROM COMBINING GRAVITY AND RADIO WAVES
Organized by Eric Murphy, National Radio Astronomy Observatory, Charlottesville, VA

PUBLIC USE DATA PRODUCTS AND PRIVACY PROTECTION: EXPERIENCES FROM THE FRONT LINES
Organized by Jerome Reiter, Duke University, Durham, NC

SOLVING THE BIGGEST MYSTERIES WITH THE TINIEST PARTICLES
Organized by Kurt Riesselmann, Fermi National Accelerator Laboratory, Batavia, IL

SYNTHETIC BIOLOGY AND ADAPTIVE MANAGEMENT
Organized by Wayne Landis, Western Washington University, Bellingham, WA; Keegan Sawyer, The National Academies of Sciences, Engineering, and Medicine, Washington, DC

THE ORIGIN OF GOLD, PLATINUM, AND OTHER HEAVY ELEMENTS IN THE UNIVERSE
Organized by Reiner Kruecken and Jonathan Bagger, TRIUMF, Vancouver, Canada

THE SCIENCE OF QUANTUM INFORMATION: DISENTANGLING OPPORTUNITIES FROM THE HYPE
Organized by David Steuerman, The Kavli Foundation, Los Angeles, CA

Feeding Society

ADDRESSING HUNGER THROUGH AGRICULTURAL DISCOVERY
Organized by Elizabeth Ainsworth, USDA Agricultural Research Center, Urbana, IL

FOOD AND NUTRITION SECURITY: SCIENTIFIC PARTNERSHIPS AND OPPORTUNITIES
Organized by Volker ter Meulen, InterAcademy Partnership, Trieste, Italy; Robin Fears, European Academies Science Advisory Council, Halle (Saale), Germany

FOOD WASTE: A SOCIETAL CONCERN
Organized by Sheril Kirshenbaum, Michigan State University, East Lansing, MI; Michael E. Webber, University of Texas at Austin, TX

GENOME EDITED LIVESTOCK AND REGULATORY STALEMATES
Organized by Alison Van Eenennaam, University of California, Davis, CA

HUMAN INTERACTIONS, BIODIVERSITY, AND SOCIO-ECOLOGICAL DYNAMICS IN DEEP TIME, PARTS I AND II
Organized by Stefani Crabtree, The Pennsylvania State University, State College, PA; Jennifer A. Dunne, Santa Fe Institute, NM

SUSTAINABLY FEEDING TEN BILLION PEOPLE
Organized by Jim Ballingall, Industry-Academia Partnership, Los Gatos, CA

Forming Connections

(IN)JUSTICE BEFORE TRIAL: UNDERSTANDING EARLY STEPS IN THE CRIMINAL JUSTICE SYSTEM
Organized by Barbara Spellman, University of Virginia, Charlottesville, VA

APPLIED SYSTEMS ANALYSIS: BRIDGING EAST AND WEST
Organized by Jan Marco Müller, International Institute for Applied Systems Analysis, Laxenburg, Austria

CENSUS 2020: RECENT CHANGES AND IMPACTS
Organized by Robin Mejia, Carnegie Mellon University, Pittsburgh, PA

FUNDING SCIENCE IN CANADA: POLITICAL INITIATIVE MEETS GRASSROOTS SUPPORT
Organized by Mehrdad Hariri, Canadian Science Policy Centre, Toronto, Canada

GOVERNMENT SCIENTISTS: ROLES AND CHALLENGES
Organized by Margaret Taylor, Lawrence Berkeley National Laboratory, Berkeley, CA

INTERNATIONAL SCIENTIFIC PARTNERSHIPS: OPPORTUNITIES AND CHALLENGES
Organized by Caroline S. Wagner, Ohio State University, Columbus, OH; Rainer Asse, American Academy of Arts and Sciences, Cambridge, MA

LEGAL PROTECTION FOR SCIENTISTS: OVERCOMING REAL AND PERCEIVED BARRIERS
Organized by Joanne P. Carney and Theresa Harris, AAAS, Washington, DC

PARTICLE PHYSICS: FRONTIER SCIENCE AND INTERNATIONAL PARTNERSHIPS
Organized by Pushpalatha Bhat, Fermi National Accelerator Laboratory, Batavia, IL

POLICYMAKERS AND COMMUNICATING SCIENCE: OPPORTUNITIES AND BEST PRACTICES
Organized by Kei Koizumi, AAAS, Washington, DC; Karen Akerlof, George Mason University, Fairfax, VA

SCIENCE DIPLOMACY AND NORTH KOREA: THE DAWN OF A NEW ERA
Organized by Mijung Jung and Soyeon Shin, National Research Council of Science & Technology, Sejong, Korea, Republic of (South)

SCIENCE INFORMING POLICY: RESPONSIBLE DECISION MAKING
Erica Goldman, National Council for Science and the Environment, Washington, DC; Stephen Posner, COMPASS, Silver Spring, MD

SCIENCE MEETS PARLIAMENT: LESSONS LEARNED
Organized by Kylie Walker and Emma Johnston, Science & Technology Australia, Canberra, Australia

Downloaded from http://science.sciencemag.org/ on January 21, 2019

Navigating Technology

ACCESS TO PRIVATE AND PROPRIETARY DATA: THEOREMS AND WORKING PROTOTYPES
Organized by Daniel Goroff, Alfred P. Sloan Foundation, New York, NY

AI AND MACHINE LEARNING: INDUSTRIAL APPLICATIONS AND SOCIAL IMPLICATIONS
Organized by Sudarsan Rachuri, U.S. Department of Energy, Washington, DC; James Garrett, Carnegie Mellon University, Pittsburgh, PA

CYBERSECURITY: TRANSCENDING PHYSICS, TECHNOLOGY, AND SOCIETY
Organized by Kevin Fu, University of Michigan, Ann Arbor, MI

HOW AI AND KNOWLEDGE CENTERS ARE CHANGING SOCIETAL VIEWS OF CRITICAL EARTH RESOURCES
Organized by Suzanne A. Pierce, Texas Advanced Computing Center, Austin, TX; Vipin Kumar, University of Minnesota, Minneapolis, MN

INEQUALITY IN NETWORKS, MINDS, AND MACHINES
Organized by Keith Payne, University of North Carolina at Chapel Hill, NC

MACHINE LEARNING AND HUMAN LANGUAGE
Organized by Cecile McKee, University of Arizona, Tucson, AZ

MACHINE LEARNING AND STATISTICS: APPLICATIONS IN GENOMICS AND COMPUTER VISION
Organized by Hal Stern, University of California, Irvine, CA

MACHINE LEARNING FOR THE AUTOMATION OF SCIENTIFIC DISCOVERY ACROSS DISCIPLINES
Organized by Ben Wender, National Academies of Sciences, Engineering, and Medicine, Washington, DC

MASS SPECTROMETRY: NEW ADVANCES IN CHEMISTRY, ARCHEOLOGY, AND PALEONTOLOGY
Organized by Timothy Cleland and Caroline Solazzo, Smithsonian Institution, Suitland, MD

MICROGRAVITY RESEARCH: TIME, SPACE, AND MATERIALS
Organized by Lynnette D. Madsen, National Science Foundation, Alexandria, VA

SOCIO-TECHNICAL CYBERSECURITY: IT'S ALL ABOUT PEOPLE
Organized by Keith Marzullo, University of Maryland, College Park, MD

Reaching Sustainable Development

ADVANCING SUSTAINABLE DEVELOPMENT GOALS THROUGH CHEMISTRY
Organized by Mary M. Kirchhoff, American Chemical Society, Washington, DC

CLIMATE IMPACTS ANALYSIS: INTEGRATING SCIENTIFIC DISCIPLINES
Organized by Juan-Carlos Ciscar, European Commission, Seville, Spain; Marton Hajdu, European Commission, Brussels, Belgium

SUSTAINABLE DEVELOPMENT GOALS: NEW SCIENCE BALANCING A HYPERCONNECTED WORLD
Organized by Sue Nichols and Jianguo (Jack) Liu, Michigan State University, East Lansing, MI

SUSTAINABLE DEVELOPMENT: IMPLEMENTING SYSTEMIC DIMENSIONS
Organized by Jan Marco Müller, International Institute for Applied Systems Analysis, Laxenburg, Austria

SUSTAINABLE INVESTING: SCIENCE, ASSET MANAGEMENT AND SUSTAINABLE DEVELOPMENT
Organized by Brad Wible, *Science* magazine, Washington, DC; Charles Vorosmarty, The City College of New York, NY

SUSTAINABLE TRANSITIONS: LEADERSHIP MODELS FOR COMMUNITY COLLABORATION
Organized by Josh Tewksbury, University of Colorado and Colorado State University, Boulder, CO

THE CARBON CYCLE: CONDITIONS AND OPPORTUNITIES FOR CAPTURE AND UTILIZATION
Organized by Carmine Marzano, European Commission, Brussels, Belgium

THE RESEARCH CLOUD: SUPPORTING THE SUSTAINABLE DEVELOPMENT GOALS
Organized by Vinny Pillay, South African Department of Science and Technology, Brussels, Belgium

TO SAVE 1,000,000 CHILDREN A YEAR: DATA, SCIENCE, AND SUSTAINABLE DEVELOPMENT
Organized by Abraham Flaxman, Institute for Health Metrics and Evaluation, Seattle, WA

Rehabilitating Habitats

CARBON CYCLE PROCESSES, POLICIES, AND UNCERTAINTIES: NEW PERSPECTIVES
Organized by Maureen McCarthy, University of Nevada, Reno, NV; Gyami Shrestha, U.S. Global Change Research Program, Washington, DC

CLUTCHING AT STRAWS: SCIENCE ADVICE, UNCERTAINTY, AND GLOBAL MICROPLASTIC POLLUTION
Organized by Jeremy Bray, European Commission, Brussels, Belgium

EXTREME EVENT ATTRIBUTION IN THE CONTEXT OF CLIMATE CHANGE
Organized by Francis Zwiers, University of Victoria, Canada; Debbie J. Dupuis, HEC Montreal, Canada



Downloaded from http://science.sciencemag.org/ on January 21, 2019

CLIMATE CHANGE: UNDERSTANDING FEEDBACK FROM NATURE, CULTURE, AND SOCIETY
Organized by Marianne Lucien, ETH Zürich, Switzerland

COMMUNITY RESPONSES TO CLIMATE CHANGE
Organized by Emily Therese Cloyd and Elana Kimbrell, AAAS, Washington, DC

ECOLOGIES OF INNOVATION: THE POTENTIAL FOR BIOTECHNOLOGY TO ADDRESS FOREST HEALTH
Organized by Kara Laney, National Academies of Sciences, Engineering, and Medicine, Washington, DC

ENVIRONMENTAL AND TEXTILE SCIENTISTS COMBATING MICROPLASTIC POLLUTION
Organized by Margaret Murphy, Washington, DC; Judith Weis, Rutgers University, Newark, NJ

ENVIRONMENTAL HEALTH DATA INTEGRATION: MEASUREMENT AND IMPACT
Organized by Andrea Hodgson and Ben Wender, The National Academies of Sciences, Engineering, and Medicine, Washington, DC

ENVIRONMENTAL MICROBIOMES: BACTERIAL AND FUNGAL COMMUNITIES IN EXTREME ECOSYSTEMS
Organized by Barbara Illman, U.S. Forest Service, Madison, WI

HOMES AT THE CENTER OF CHEMICAL EXPOSURE: UNITING CHEMISTS, ENGINEERS AND HEALTH SCIENTISTS
Organized by Glenn Morrison, University of North Carolina at Chapel Hill, NC; Jon Abbatt, University of Toronto, Canada

PLASTICS IN THE OCEANS: SOURCES, SINKS, AND SOLUTIONS
Organized by Linsey Haram and Christina Simkanin, Smithsonian Environmental Research Center, Edgewater, MD

SUSTAINABILITY SCIENCE AND PUBLIC ENGAGEMENT: INVOLVING LAND OWNERS IN RESEARCH
Organized by Kimberly La Pierre, Smithsonian Environmental Research Center, Edgewater, MD; Sally Koerner, University of North Carolina, Greensboro, NC

THE FOURTH NATIONAL CLIMATE ASSESSMENT: ADVANCING SCIENCE, INFORMING DECISIONS
Organized by Katie Reeves, U.S. Global Change Research Program, Washington, DC; Donald J. Wuebbles, University of Illinois at Urbana-Champaign, IL

TRANSBOUNDARY AIR POLLUTION: THE IMPACT OF SCIENCE ON POLICY
Organized by Terry Keating, U.S. Environmental Protection Agency, Washington, DC; Barry Lefer, NASA, Washington, DC

Sharing Science

A FEMINIST AGENDA FOR SCIENCE COMMUNICATION: NECESSARY AND TIMELY
Organized by Megan Halpern, Michigan State University, East Lansing, MI

AGRICULTURAL INNOVATION AND UPTAKE: USING A MULTI-ACTOR APPROACH
Organized by Jean-Marc Gautier, Institut de l'Elevage, Castanet-Tolosan Cedex, France; Cathy Dwyer, Scotland's Rural College, Midlothian, United Kingdom

FIGHTING FAKE NEWS: VIEWS FROM SOCIAL AND COMPUTATIONAL SCIENCE
Organized by Stephan Lewandowsky, University of Bristol, United Kingdom; Edward W. Maibach, George Mason University, Fairfax, VA

GLOBALIZATION OF THE STEM WORKFORCE: IMPLICATIONS FOR CAREERS AND INSTITUTIONS
Organized by Julia E. Melkers, Georgia Institute of Technology, Atlanta, GA; Eric Welch, Arizona State University, Phoenix, AZ

HUMAN GENETIC VARIATION AND EDUCATION: NOT A SOCIALLY NEUTRAL ENDEAVOR
Organized by Jonathan Beckwith, Harvard Medical School, Boston, MA; Kostia Bergman, Northeastern University, Boston, MA

HUMAN RESOURCE DEVELOPMENT AND DIVERSITY: INSIGHTS FROM PUBLIC AND PRIVATE SECTORS
Organized by Takashi Inutsuka, Ministry of Education, Culture, Sports, Science and Technology, Tokyo, Japan

IMPROVING ATTITUDES TOWARDS CHEMISTRY THROUGH INFORMAL SCIENCE COMMUNICATION
Organized by Larry Bell and David Sittenfeld, Museum of Science, Boston, MA

SCIENCE ENGAGEMENT WITH FAITH COMMUNITIES
Organized by Robert O'Malley, AAAS, Washington, DC

SCIENTIFIC INTEGRITY: PRINCIPLES AND BEST PRACTICES
Organized by Alison Kretser, International Life Sciences Institute North America, Washington, DC

TALKING WITHOUT SPEAKING: OVERCOMING COMMUNICATION CHALLENGES WITH TECHNOLOGY
Organized by Nan Ratner, University of Maryland, College Park, MD

TECHNOLOGY TRANSFER AND INNOVATION: RESHAPING LABORATORY-MARKET RELATIONSHIPS
Organized by Heather Evans, National Institute of Standards and Technology, Gaithersburg, MD; Anice Anderson, Private Engineering Consulting, Carmel, IN

TECHNOLOGY TRANSFER FROM BLUE SKY SCIENCE: AVOIDING PITFALLS, MAXIMIZING RETURNS
Organized by Terry O'Connor, UK Research and Innovation, Swindon, United Kingdom; Ana Godinho, CERN, Geneva, Switzerland

THE BIOLOGY OF RESILIENCE: HOW SCIENCE AND FAITH COMMUNITIES CAN WORK TOGETHER
Organized by Se Y. Kim and Curtis Baxter, AAAS, Washington, DC

YOUTUBE: FRIEND OR FOE IN COMMUNICATING ABOUT SCIENCE AND HEALTH
Organized by Erik Bucy and Asheley Landrum, Texas Tech University, Lubbock, TX



Downloaded from http://science.sciencemag.org/ on January 21, 2019

Flash Talks

Brief presentations highlighting scientific findings and programs

A Balancing Act: Navigating Jargon Use When Communicating with Citizen Scientists

The Biology of Fatherhood: Adaptive Origins, Day-to-Day Functions, and Men's Health

Building a Seismic Network in Africa

Developing Engagement Through Early Career Science Policy Groups

Development of a Transdisciplinary Scale to Measure Household Water Insecurity

Drivers of Data Ecologies in Genomics and the Infrastructure Sciences

Engagement and the All of Us Research Program: Meeting People Where They Are

Environmental Perceptions and Migration Decisions Within the United States Gulf Coast

Football, Disabilities, and Engineering: Customer Centered Innovation

From Pipette to Pen: A Scientist's Summer in the Newsroom

Gut Microbiome of Bees and Wasps

Hard Lessons from the Soft Sciences on Gender in Engineering and Technology

International Partnerships and the Open Knowledge Africa Platform

Making Hands-on Biology Experiences Accessible for Everyone

March Mammal Madness: The Power of Science as Narrative

The Next NASA Golden Record Anchored in Science, Information, and Digital Literacies

Nonlinear Optical Study of Two-Dimensional Materials

Optical Markers and Biomarkers for the Risk Assessment of Oral Premalignant Lesions

Promising Genetic Research for Prognosis and Treatment of Many Cancers

Public Engagement Leadership: A Journey From Practitioner to Change Agent

Regenerative Medicine and Tissue Engineering: Transforming 21st Century Medicine

#ScientistsWhoSelfie: Instagramming the Way to Public Trust

The Second Quantum Revolution

The Shape of Human Evolution

Using Policy Analysis to Engage Policymakers and the Public with Research Results

Using Science to Engage Business

Virtual Scientific Communities: Choose Development! Takes Broadening Participation to the Next Level

Zika Virus Mediated Immunopathology: Defining Disease Damage to Infectious Agents

Career Workshops

Opportunities to gain advice and strategies from experienced STEM professionals

A Shared Vision: Overcoming the Barriers for Scientists to Communicate and Engage

Accessibility and Inclusion in STEM Education

Applying Negotiation Tools to Improve Communication and Address Conflict

Attract Recruiters and Jump-start Networking With an All Star LinkedIn Profile

Authorship Decisions: Advocating for Representation

Conducting Science Outreach Online: Social and Multimedia

Diversity + STEM = X: Solving the Equation for Higher Education and the Workforce

Exceptional Presentations in Spite of PowerPoint: How to Communicate Science in the Digital Age

Finding Your Voice: Storytelling Lessons for Scientists

Formulate to Communicate: Heroes, Improv, and Science Storytelling

From a Moment to a Movement: Building Infrastructure to Sustain Scientist Advocacy

Influencing Policy: Opportunities for Scientists and Engineers

LGBTQ+ in Academia and the Workplace: Rights and the Law

Making the Most of the First Two Years On the Tenure Track

Overcoming the STEM-Policy Divide with Fellowships in State Governments

Polish Pitches—For Scientists, Researchers, and Science Journalists

Research Funding: Exploring Programs in the European Union

Scholarly Publishing: Avoiding Pitfalls and Showing Impact

Scientists Engaged in Human Rights: Professional Societies Offer Opportunities

Scientists Who Draw Comics: The Double Life of Visual Science Communicators

YouTube as Outreach: How to Document Research Using Social Media and Video

The Gender Dimension of Science Advice

The Global Entrepreneur: How to Harness International Innovation

Downloaded from http://sciencesignaling.org/ on January 21, 2019

Celebrating Scientific Milestones

with the following special sessions and other exciting activities:

NEARLY DOUBLE PLATINUM:
150 YEARS OF THE PERIODIC TABLE



THE LEGACY OF THE APOLLO PROGRAM: 1969 TO 2069



ARPANET: CELEBRATING 50 YEARS SINCE "LO"



AAAS Film Showcase

presented in partnership with JACKSON HOLE WILD

AlphaGo
Attenborough's Ant Mountain
The Kingdom—How Fungi Made Our World
Let There Be Light
Mosquito
Space's Deepest Secrets: Cassini's Grand Finale

Advance registration rates are available now through **January 22, 2019.**

	Advance Rates for AAAS Member for members in good standing	Advance Rates for Non-Member for all other attendees	On-site Rates after 1/22/2019 AAAS Member/Non-Member
General Attendee	$310	$440	$380/480
Postdoc	$135	$360	$135/380
K-12 Teacher	$135	$360	$135/380
Retired Professional	$250	$360	$295/380
Student	$65	$95	$75/105
One-Day	$175	$220	$200/240

Downloaded from http://science.sciencemag.org/ on January 21, 2019

SCIENCE CAREERS ADVERTISING



For full advertising details, go to ScienceCareers.org and click For Employers, or call one of our representatives.

AMERICAS
+1 (202) 326 6577
+1 (202) 326 6578
advertise@sciencecareers.org

EUROPE, INDIA, AUSTRALIA, NEW ZEALAND, REST OF WORLD
+44 (0) 1223 326527
advertise@sciencecareers.org

CHINA, KOREA, SINGAPORE, TAIWAN, THAILAND
+86 (131) 4114 0012
advertise@sciencecareers.org

JAPAN
+81 (3) 6459 4174
advertise@sciencecareers.org

JOB BOARD SUPPORT
support@sciencecareers.org

ScienceCareers
FROM THE JOURNAL SCIENCE AAAS

ScienceCareers.org

All ads submitted for publication must comply with applicable U.S. and non-U.S. laws. *Science* reserves the right to refuse any advertisement at its sole discretion for any reason, including without limitation for offensive language or inappropriate content, and all advertising is subject to publisher approval. *Science* encourages our readers to alert us to any ads that they feel may be discriminatory or offensive.

myIDP: A career plan customized for you, by you.



For your career in science, there's only one Science

my IDP ScienceCareers

Recommended by leading professional societies and the NIH

Features in myIDP include:

- Exercises to help you examine your skills, interests, and values.
- A list of 20 scientific career paths with a prediction of which ones best fit your skills and interests.
- A tool for setting strategic goals for the coming year, with optional reminders to keep you on track.
- Articles and resources to guide you through the process.
- Options to save materials online and print them for further review and discussion.
- Ability to select which portion of your IDP you wish to share with advisors, mentors, or others.
- A certificate of completion for users that finish myIDP.

Visit the website and start planning today!
myIDP.sciencecareers.org

ScienceCareers AAAS In partnership with:

advancing the life sciences 1912-2012 FASEB Federation of American Societies for Experimental Biology

Medical College of Wisconsin

UCSF University of California San Francisco

Burroughs Wellcome Fund

ScienceCareers online @sciencecareers.org

Marine Biological Laboratory
THE UNIVERSITY OF CHICAGO

Faculty Position in Evolutionary Genomics and Molecular Evolution

Josephine Bay Paul Center for Comparative Molecular Biology and Evolution, Marine Biological Laboratory



The Josephine Bay Paul Center at the Marine Biological Laboratory (MBL) invites applications for a faculty position at the Assistant Scientist level in the area of evolutionary and functional genomics. The successful candidate will apply experimental and computational approaches to research areas including but not limited to: microbiome interactions, functional studies of host-associated marine microbial communities, evolutionary and ecological changes in marine systems, or genomic and transcriptomic studies of marine organisms.

The Bay Paul Center and the MBL have strengths in molecular evolution, functional genomics, microbial diversity and ecology, advanced imaging, and marine animal husbandry. The Center maintains state-of-the-art facilities for high-throughput sequencing and computational analysis. The MBL, an affiliate of the University of Chicago, has a distinguished history in fundamental biological discovery, now with a renewed focus on marine organisms, microbiomes, and the impact of environmental change on coastal ecosystems.

Qualifications:
Applicants must hold a Ph.D. (or equivalent advanced degree) in a relevant field. The successful candidate will demonstrate strong potential for establishing a vigorous extramurally supported research program that can complement existing areas of strength across the institution's research and educational programs.

Applications:
The MBL is an Affirmative Action/Equal Opportunity/ Disabled/Veterans Employer and strongly encourages applications from candidates who would contribute to the diversity of its research community. Applications will be reviewed immediately upon receipt and will continue on a rolling basis until the position is filled. Those interested in the position should submit an application, including a CV, short summary of accomplishments and future research interests, and the names and contact information of at least three references to research@mbl.edu.

For full consideration applications should be submitted by **March 1, 2019**

The UNIVERSITY *of* OKLAHOMA
Health Sciences Center

POSITION DESCRIPTION CHAIR
Department of Biochemistry and Molecular Biology
College of Medicine

The University of Oklahoma College of Medicine, in conjunction with the Oklahoma Center for Geroscience, seeks a distinguished academic leader in Aging research for the position of Chair of Biochemistry and Molecular Biology. Appointment will be at the level FULL PROFESSOR with TENURE-ELIGIBILITY. A qualified applicant for this ENDOWED position must have a PhD, MD or MD/PhD.

The Department of Biochemistry and Molecular Biology has a diverse faculty with interests in biochemical mechanisms of neuro-degeneration, aging, metabolic regulation or structural biology. The University of Oklahoma Health Sciences Center is an actively growing campus with 7 colleges and three (3) hospitals (OU Medical Center, OU Children's Hospital and the Veteran's Affairs Medical Center). The environment to conduct scientific research and interact with colleagues is excellent.

Over the past decade, OUHSC has developed a nationally recognized program in aging, which includes a P-30 Nathan Shock Center of Excellence, GeroScience CoBRE, and a T32 Training program in Geroscience. The Chair of the Department of Biochemistry and Molecular Biology is expected to play a major role in developing the newly developed GeroScience Center but to also integrate into OUHSC's research strategic plan to expand the relationship between the NCI-Designated Stephenson Cancer Center and the Harold Hamm Diabetes Center as well as other departments on campus.

Interested candidates should send a CV and cover letter describing academic accomplishments and leadership vision to: **Ann Louise Olson, PhD, Chair, Search Committee, Department of Biochemistry and Molecular Biology, University of Oklahoma Health Sciences Center, Oklahoma City, OK 73104 (ann-olson@ouhsc.edu)**.

University of Oklahoma Health Sciences Center is an Equal Employment Opportunity and Affirmative Action Institution http://www.ou.edu/eoo/. Individuals with disabilities and protected veterans are encouraged to apply.

Advance your career with expert advice from *Science* Careers.



Download Free Career Advice Booklets!
ScienceCareers.org/booklets

Featured Topics:
- Networking
- Industry or Academia
- Job Searching
- Non-Bench Careers
- And More



ScienceCareers
FROM THE JOURNAL SCIENCE AAAS



Shenzhen Technology University Seeks Talents Globally: Shenzhen, China

Shenzhen Technology University

Funded by the Municipal Government of Shenzhen, Shenzhen Technology University (SZTU) was established in Pingshan District of Shenzhen. With the strong financial support and favorable policies from Shenzhen government, Shenzhen Technology University (SZTU) aims to be a high degree university of applied sciences and technologies. The total campus area will be 150 hectares.

Mission

To meet the urgent demand from the advanced manufacturing industry locally and nationally, the future SZTU is obligated to produce talent with spirit of craftsmanship such as senior engineers and architects. SZTU aims to establish itself as an open and innovative international university with Chinese characteristic and global outlook.

Education Mode

By learning from the dual system of Germany, SZTU will implement a modern apprenticeship system in teaching. The university is geared to meet the demands of high-end manufacturing industry with the orientation of employment and entrepreneurship. It is based on enhancing the capacity of engineering, practice and innovation. SZTU will explore a new education mode of applied sciences by joining efforts between industries and universities, between production and teaching, between practice and learning.

Talent Cultivation

In terms of talents training, SZTU is exploring a new mode of "university education +enterprise internship+engineering projects". In accordance with the principle of producing talents in applied sciences with market orientation, SZTU will push the cooperation between industries and universities to a new height; put more focus on the assessment of practical capability and undergo small-sized teaching; promote the integration among teaching, learning and practical training; recruit students from diversified sources. SZTU will try to realize Five Connections: connection between specialty setup and industry needs, connection between curriculum setting and professional criteria, connection between teaching processing and production processing, connection between diploma and professional certificate, and connection between vocational education and lifelong study.

Specialty Setup

SZTU sets up specialties and courses according to the needs of industrial chain and innovative chain. To meet the demand of pillar industry , strategic emerging industry and future industry in Shenzhen, the newly issued Shenzhen Action on Made in China 2025 defines eleven strategic key areas for the advanced manufacturing industry of Shenzhen (Digitalized Network Equipment, New-type Display, Integrated Circuit, New-type Components and parts, Robots, Precision Manufacturing Equipment, New Material, New Energy Automobile, Aeronautics and Space, Marine Engineering Equipments, Gene Engineering equipment), based on this, SZTU has set up six colleges in the first period: Intelligent Manufacturing, Big Data and Internet, Urban Transportation and Logistics, New Materials and New Energies, Health Science and Environmental Engineering and Creative Design.

Recruitment Disciplines and Majors:

Sino-German College of Intelligent Manufacturing

Control Science and Engineering, Electronic Science and Technology, Automatic Control, Mechanical Engineering, Control Science or Electromechanical, Optical Engineering, Physics and other related majors.

College of Big Data and Internet

Computer Science and Technology, Electronic Science and Technology, Information and Communication Engineering, Information Security.

College of Urban Transportation and Logistics

Vehicle Engineering, Vehicle Operation Engineering, Electrical Engineering, Mechanical Engineering, Control Engineering, Combustion Engine, Energy and Control Engineering, Transportation Engineering, Civil Engineering, Transportation, Microcontrollers and Computer Science, Instrumentation and Measurement, Business and Management, Surveying and Mapping, Urban Planning, Logistics, Supply Chain Management, Transportation Management, Transport Policy and Economics.

College of New Materials and New Energies

Mechanical Engineering (Renewable Energy area), Communication Engineering, Measurement, Control Technology and Instruments, Electrical Engineering and Automation, Optic Engineering, Electronic Information, Energy and Power Physics, Material and Condensed Matter Physics, Physics, Material Science and other related majors.

College of Health Science and Environmental Engineering

Biology-related majors (i.e. Biochemistry, Molecular Biology, Cell Biology, etc.), Medical Apparatus Engineering, Biomedical Engineering (Biophysics, Bioinformatics-oriented majors).

College of Creative Design

Environment Design(Environment Design, Architectural design and its theory, Landscape Design ,Sight Design or Interior Design); Industrial Design(Product Design, Jewelry Design or Interactive Design); Digital Media Arts; Fine Art(Chinese Painting, Sculpture arts, Arts and Crafts or Art theory).

Faculty of Arts and Sciences

English (English Language Teacher – Native/Chinese speakers), German (German Language Teacher –Native/ Chinese speakers), Computer Science or related, Mathematics or related, Physics.

How to apply

Qualified applicants are strongly encouraged to submit their application documents electronically to **recruitment@sztu.edu.cn**. Please title your email as "Full Name of Applicant + Job Title + Science" (for example: James + Z01 + Science).

Please scan the QR code of recruitment information below to get more details about Job Title.

※Application materials sent inconsistently with our requirements will be considered as invalid. ※

Application Documents should include:

(1) A comprehensive curriculum vitae with a list of publications {Work experience (full-time), Education experience (fill in from undergraduate stage), overseas exchange program experience (for example: visiting scholar experience) must be included also};

(2) Copies of highest academic degree and related qualification certificates;

(3) A statement of future teaching & research plan;

(4) Application form (Please download the application form by scanning the QR code below, for Chinese-speaking applicants please fill out both Chinese and English application forms).

Application Form | SZTU Website | Recruitment Information

Human Resources Office
Shenzhen Technology University
Email: recruitment@sztu.edu.cn
Tel: +86-755-23256280
University Website: http://www.sztu.edu.cn/ (Chinese)
http://english.sztu.edu.cn/ (English)
Recruitment Website: http://ohr.sztu.edu.cn/zp/



10 ways that *Science* Careers can help advance your career

1. Register for a free online account on **ScienceCareers.org**.
2. Search thousands of job postings and find your perfect job.
3. Sign up to receive e-mail alerts about job postings that match your criteria.
4. Upload your resume into our database and connect with employers.
5. Watch one of our many webinars on different career topics such as job searching, networking, and more.
6. Download our career booklets, including Career Basics, Careers Beyond the Bench, and Developing Your Skills.
7. Complete an interactive, personalized career plan at "my IDP."
8. Visit our Career Forum and get advice from career experts and your peers.
9. Research graduate program information and find a program right for you.
10. Read relevant career advice articles from our library of thousands.



Visit **ScienceCareers.org** today — all resources are free

ScienceCareers
FROM THE JOURNAL SCIENCE AAAS

SCIENCECAREERS.ORG

UPMC | HILLMAN CANCER CENTER

Affiliated with the University of Pittsburgh School of Medicine

Assistant Director / Associate Director for Research Administration

UPMC Hillman Cancer Center (Hillman) seeks a talented and experienced individual to step into a highly supportive environment as Assistant/Associate Director (AD) for Research Administration. This is a very exciting time for a new AD for Administration to join Hillman. Hillman is strongly supported by UPMC and the University of Pittsburgh School of Medicine. The Hillman Foundation recently committed a large amount of continued support for our Center over the next 10 years. The new AD will collaborate with Hillman CC members to promote and invest these funds in strategic new projects, recruits, shared resources, and pilot programs. With our re-naming as UPMC Hillman Cancer Center, a new Director, and upcoming expansion of space for Hillman researchers, Hillman is unified and supportive of cancer research, prevention and therapy.

The AD for Research Administration reports directly to the Deputy Director for Research Administration and is a member of Hillman's leadership team. Primary duties and responsibilities include: oversight and management of Hillman facilities, scientific shared resources, development, facilitation and support of multi-component team science cancer research programs as well as spearheading internal and external collaborative research endeavors. To meet the position requirements, the AD for Research Administration will collaborate with a team of administrators and PhD-level scientists, coordinate vision setting and strategic planning; support and participate in CCSG Research Program and Shared Resource activates; develop operational and administrative policies and procedures; work with the Hillman Fiscal Office to develop budgets and monitor spending; develop staff and space utilization plans; oversee facility operations; and communicate research outcomes to Hillman investigators, the NCI, and the public. To facilitate and advance Hillman science, the AD will also: coordinate CCSG preparation and submission; grow the funded research base, with emphasis on multi-disciplinary collaboration with internal and external investigators; work with the Hillman Development Office to promote and increase philanthropic donations; assist in recruitment of faculty.

Located in the City of Pittsburgh's Shadyside neighborhood, (Pittsburgh is routinely ranked as one of the top-most livable and affordable U.S. cities), Hillman is a National Cancer Institute (NCI)-designated matrix cancer center focused on state-of-the-art cancer research, training the next generation of cancer researchers, and community outreach. In 2015, Hillman celebrated its 30th anniversary and the renewal of its 5-year NCI Cancer Center Support Grant (CCSG). Hillman has over 330 members, 10 scientific programs, 13 CCSG-supported shared resources, and an FY17 institutional funding base of nearly $157 million. In FY16 the University of Pittsburgh ranked #5 in overall NIH funding. During its 2015 CCSG review, Hillman Research Administration scored exceptional.

Candidates for the position must have a PhD or master's degree in business, administration, policy, or other research administration-relevant field. Candidates also must have 5+ years in research administration, which includes an understanding of the regulatory requirements and complexities pertaining to animal and clinical research; familiarity with NCI CCSG requirements; experience with NCI-funded cancer centers; and excellent written and oral communication, computer, people management, and interpersonal skills. Candidate will be an Assistant or Associate Professor commiserate with experience.

The successful candidate will be hired as an employee of the University of Pittsburgh, with a very competitive salary and benefits package (see www.hr.pitt.edu/benefits). The University of Pittsburgh is an equal opportunity employer. EEO/AA/M/F/Vets/Disabled.

To apply for the position of Associate Director for Research Administration at UPMC Hillman Cancer Center, please send a 1-page personal statement highlighting your qualifications and experience, along with your CV or resume, to Hillman Director Robert L. Ferris, MD, PhD (care of thompsonla3@upmc.edu).

Robert L. Ferris., MD, PhD, Director, UPMC Hillman Cancer Center
C/O Lola Thompson, 5150 Centre Avenue, Suite 500
Pittsburgh, PA 15232



TEXAS TECH UNIVERSITY
HEALTH SCIENCES CENTER.

School *of* Medicine
Department of Cell Biology and Biochemistry

ENDOWED CHAIR IN CANCER RESEARCH
TEXAS TECH UNIVERSITY HEALTH SCIENCES CENTER, LUBBOCK

The Department of Cell Biology and Biochemistry in the TTUHSC School of Medicine seeks to recruit an established investigator to fill the Weitlauf Endowed Chair in Cancer Biology. This endowed position, together with potential for considerable state recruitment and ongoing research funding from the Cancer Prevention Research Institute of Texas (CPRIT) (http://www.cprit.state.tx.us), represents an outstanding opportunity for a senior or rising mid-career investigator. The successful candidate will have established a strong track record of discovery with a primary interest in cancer biology. The position is otherwise not restricted with respect to research area within cancer biology, so we invite applications from investigators with any such interests, from the basic scientific underpinnings of cancer to translational research in cancer therapies.

The department (https://www.ttuhsc.edu/medicine/cell-biology-biochemistry/default.aspx) is currently comprised of fourteen full-time faculty. Current faculty study biochemistry and cellular and molecular biology of widely ranging topics in medicine and biology, including cancer, reproduction, diabetes, metabolism, development, and genetic and neurodegenerative diseases. We enjoy a collegial and cooperative research environment both within and between departments that is especially conducive to collaboration and scientific discourse.

This endowed position will be a primary appointment in the School of Medicine, with state-supported salary, and a concurrent appointment in the Graduate School of Biomedical Sciences that affords opportunity to recruit and advise excellent graduate students from the Biomedical Sciences and Biotechnology graduate programs. Salary and lab set-up package are nationally competitive. Applicants must have a terminal degree (Ph.D., M.D. or US Equivalent) and a commitment to sustained research in cancer biology. Ability and enthusiasm for teaching will be a consideration but not a requirement. The Department of Cell Biology and Biochemistry is committed to diversity in education and employment, and strongly encourages applications from women and minorities.

TTUHSC is in Lubbock, Texas, a family-friendly city of more than 250,000 residents on the South Plains of West Texas. Our region boasts a diverse economy with strengths in agriculture, heath care, and higher education. Lubbock is home to Texas Tech University providing educational and entertainment opportunities in collegiate athletics and the performing arts. The city's K-12 school system provides a solid education for children to achieve at the highest levels, including magnet, AP, and International Baccalaureate programs. Lubbock weather is mild, with an average of 262 days of sunshine per year.

Interested candidates must apply online at **https://www.ttuhsc.edu/medicine/cell-biology-biochemistry/positions.aspx**. Requisition ID: 16300BR. Candidates should submit a single PDF that includes a cover letter describing their interest in the position (including possible collaborations with current faculty), curriculum vitae, and a brief summary of research interests. Candidates should also provide names of three individuals from whom recommendation letters may be requested.

3601 4th Street STOP 6540 | Lubbock, TX 79430-6540 | T 806.743.2700 | F 806.743.2990

An EEO/Affirmative Action Institution.

ScienceCareers online @sciencecareers.org

By **Victor S. C. Wong**

Lessons from a postdoc gone wrong

I sat hunched over my computer screen, analyzing data, when a university administrator walked into our lab and handed out a series of sealed envelopes. Puzzled, I opened the letter addressed to me: "It has become necessary for the University to effect a layoff of your position as a Postdoctoral Scholar." In silence, my labmates opened their own letters, all of which said essentially the same thing. I knew that our lab was under investigation, but I had no inkling that my job was in jeopardy, so the news came as a huge shock. My mind raced from concerns about my personal finances—"How will I pay rent?"—to questions about my future in science: "How will we finish our experiments? Will this mark the end of my research career?"

Three years earlier, I had started my postdoc brimming with enthusiasm, excited to work for a brilliant scientist on a project that, we hoped, would help people with hearing loss—a group that includes me. My enthusiasm was short-lived. Almost as soon as I arrived, it became clear that the lab had problems. For one, my supervisor had been receiving animal care violation warnings for the lab's work with mice for years. They continued to pile up during my tenure, at times forcing us to suspend our experiments. Eventually, our funding was cut off entirely and the lab was shut down.

I ended up digging out of the mess and moving on to a second postdoc. Now I'm back to doing research that I love in a functional lab, and I'm glad I persevered. But looking back, I wish I hadn't sunk so much time into my first postdoc lab. I should have quit and moved on much sooner. For others who may be in similar situations, here are tips to avoid drowning with a sinking ship.



"I wish I hadn't sunk so much time into my first postdoc."

DO NOT BE BLINDED BY PASSION. Enthusiasm and drive are key ingredients for scientific careers. However, they can be problematic when they prevent you from seeing warning signs clearly. My intense desire to find treatments to reverse hearing loss led me to mistakenly write off serious lab issues as small bumps in the road. Had I been more objective, I would have realized that those "bumps" were actually major obstacles.

TAKE PERSONNEL DYNAMICS SERIOUSLY. Collaboration and teamwork are essential in science; you can't function as an island. Blinded by passion, I disregarded the lack of honest communication with my supervisor about the problems in our lab. In retrospect, that was an obvious warning sign.

DO NOT BE TRAPPED BY FEAR. I fretted that if I didn't publish anything from my postdoc, no one would hire me. That's one reason I stuck with my ill-fated lab. But the concern turned out to be unfounded. Finding a new position after I was laid off wasn't easy, but I survived by being transparent about what happened and pushing forward with confidence. One thing that helped me move past my postdoc mess was looking back at my past successes to remind myself that I am a good scientist.

FOCUS ON YOURSELF. Pointing fingers is easy, but burning bridges—and wasting energy on casting blame—won't help you move forward. When problems arise, don't engage in pointless battles. Instead, take stock of your situation and decide what's best for you. Write down the pros and cons of your job; examine your career goals; and talk to your trusted mentors, colleagues, friends, and family. Along the way, be open to the possibility that it may be best to quit.

DO NOT WAIT FOR THE LAST STRIKE. Don't waste time in a bad environment. During my 3 years in my first postdoc lab, there were many times when I should have quit, but instead I hung on, hoping the situation would improve. Your life is not a game. Don't wait for strike three. ■

Victor S. C. Wong is a postdoctoral fellow at Weill Cornell Medicine in New York City. Send your career story to SciCareerEditor@aaas.org.

ILLUSTRATION: ROBERT NEUBECKER

Downloaded from http://science.sciencemag.org/ on January 21, 2019

Published by AAAS